NUCLEAR MAGNETIC RESONANCE IMAGING STUDIES OF ASPHALTENE PRECIPITATION IN AGED AND UNAGED ASPHALTS

Francis P. Miknis and Adam T. Pauli
Western Research Institute
365 N. 9th Street
Laramie, WY 82070-3380

Keywords: magnetic resonance imaging, asphalt, asphaltenes, aging

INTRODUCTION

Nuclear magnetic resonance (NMR) imaging is a powerful, relatively new technique that can be used for noninvasive chemical and physical characterization of local regions in the interior of intact samples. One of the more promising aspects of the technique is its ability to characterize chemical and physical processes noninvasively over time. Because of this ability and the optical opacity of asphalt systems, the potential of NMR imaging in the study of asphalts is being investigated [1]. The work reported here is an exploratory application of NMR imaging to study asphaltene precipitation in oxidatively aged asphalts. Although NMR imaging has been used mostly in medical applications, nonmedical applications are increasing and have recently been reviewed [2].

Historically, asphalts have been modeled as dispersions of associated molecules, referred to as asphaltenes, in an oily solvent phase referred to as maltenes. The asphaltenes are more aromatic and contain more heteroatoms than do the maltenes; therefore, their intermolecular interactions are generally more extensive. Consequently, asphaltenes are largely responsible for the internal structure of asphalts and tend to dominate many of the physical properties of asphalts [3]. The effectiveness by which asphaltenes are dispersed by the maltenes determines the compatibility of an asphalt. Compatible asphalts have smaller amounts of asphaltenes than incompatible asphalts. Thus, a measurement of the amount of asphaltenes in an asphalt is a measure of its compatibility.

The standard method to determine asphalt compatibility is the Heithaus test [4]. In this procedure, samples of asphalt are dissolved in an aromatic solvent, such as toluene, and titrated with an aliphatic solvent, such as n-heptane. The compatibility properties of an asphalt are then determined by measuring the onset of flocculation brought about by the addition of the titrating solvent to solutions of the dissolved asphalt at different concentrations. The Heithaus procedure is somewhat operator dependent. Recently, an automated Heithaus method has been developed to test neat asphalts, cross blended materials, and oxidatively aged asphalts that eliminates the operator dependency [5].

The compatibility of an asphalt is important for practical reasons because the degree of asphalt compatibility affects *inter alia* rutting propensities and oxidative age hardening. The effects of asphalt composition on these and other roadway failure mechanisms are currently being investigated at Western Research Institute under contract with the Federal Highway Administration. As part of that study, nuclear magnetic resonance (NMR) imaging methods are being explored to study asphaltene dispersion and aggregate behavior, and compatibility in oxidatively aged asphalts. Some results of this study are the subject of this paper.

EXPERIMENTAL

The asphalts studied are part of the Strategic Highway Research Program (SHRP) Core asphalts [6]. Their chemical properties have been characterized [7] and some are listed in Table 1. The asphalts were aged using a combination of thin film oven (TFO) and pressure aging vessel (PAV) aging [8]. NMRI measurements were made on asphalts AAB-1, AAD-1, AAK-1, AAM-1, and ABM-1 that were PAV aged for 12 hrs @ 100°C. Additional NMRI measurements were made on asphalts AAE and AAS-1 that were both PAV aged for 144 and 400 hrs at 60°C. In one set of experiments, asphalt

AAD-1 was aged using a combination of TFO aging only, and TFO aging followed by PAV aging. This produced a set of 4 samples consisting of unaged, TFO aged, and TFO followed by PAV aging for 4 and 12 hrs at 100°C.

Samples were prepared for NMRI imaging experiments in the following way: Aged and unaged asphalt samples were dissolved in toluene. To this mixture, isooctane was added to cause flocculation and asphaltene precipitation. The amount of isooctane needed to cause maximum flocculation was calculated from previous work on the development of an automated Heithaus method [5]. Two samples were prepared for each asphalt. In one case, the samples were stirred after the addition of the isooctane, and in the other case, the isooctane was added slowly to the asphalt-toluene solution to minimize mixing at the solvent interface. Images were acquired after the addition of the isooctane and for different times afterwards to observe settling of the asphaltenes.

NMR imaging experiments were carried out at a nominal proton resonance frequency of 200 MHz using a Chemagnetics/Otsuka Electronics microimaging probe. Samples for NMR imaging experiments were placed in 23 mm (OD) glass vials, which were then placed in 25 mm (OD) glass tubes. The tubes were inserted into the MRI probe and were positioned in the probe using O-rings such that the cross sections to be imaged were contained in the experimental field of view (FOV).

NMR images of asphaltene precipitation were made using the spin echo method. Images were acquired using a pulse delay of 1 s, a free induction decay size of 256 data points, 128 phase encodes, and a gradient strength of 34 G/cm. The echo time was varied from 40 to 80 ms. Eight slices, 1 mm thick and separated by 1 mm were obtained. The time required to obtain a set of images was about 35 minutes using these parameters.

RESULTS AND DISCUSSION

The effects of aging (oxidation) and stirring on asphaltene precipitation, as viewed with NMR imaging, are illustrated in Figure 1. In these images, and in the images in subsequent figures, only the 4th slice of an image set of 8 slices is shown. The 4th slice corresponds closely to the longitudinal cross section across the center of the sample vial. The times listed in Figure 1 are settling times and refer to the time elapsed between addition of isooctane and the time when the image was recorded. Also, in Figure 1 and in all other figures, the different contrasts represent regions of different molecular mobility. Thus, the lightest areas of contrast in Figure 1 are due to the hydrogens in molecules that have a fair degree of molecular mobility such as the dissolved asphalt, toluene and isooctane. The darker regions in the images are due to hydrogens in molecules having a greater degree of molecular association (hence less molecular mobility) such as the asphaltenes.

When isooctane was added to the unaged AAD-1 asphalt and the mixture stirred, the asphaltenes settled to the bottom of the vial in a normal fashion (Figure 1a). When isooctane was added to the sample of AAD-1 asphalt that was aged for 12 hrs at 100°C and the mixture stirred, the asphaltenes settled to the bottom of the vial also in a normal fashion (Figure 1b). However, when isooctane was added to the top of the aged AAD-1 asphalt/toluene solution without stirring, an additional layer of material formed at the isooctane-toluene/asphalt interface that appeared to have experienced different solvent interactions than did the asphaltenes. This is illustrated by the dark band in Figure 1c that formed at about the level of the original isooctane-toluene/asphalt interface and which appeared to be quite stable upon setting for some periods of time. As these are cross sectional images, the dark band is actually a layer at the interface.

The time evolution of the interface layer is shown in Figure 2a-d by the images taken at different settling times after addition of the isooctane. The first image (Figure 2a) shows the asphalt dissolved in toluene before addition of the isooctane. Figure 2b was taken after isooctane was added, unstirred to the sample vial, and before the asphaltenes could settle to the bottom. In this image a thin layer of additional material, which also contains spherical globules, can already be seen forming at the solvent interface. After one day of undisturbed settling, (Figure 2c) the layer is becoming more prominent and additional globules can be seen forming near the interface layer. The precipitation of asphaltenes is also noted by the darker diffuse band developing below the interface (Figure 2b). After one week (168 hrs) of settling, the interface layer is still apparent and the asphaltenes can be seen settling to the bottom of the vial (Figure 2d). On other samples, the layer has been imaged for settling times of up to 648 hrs. A set of radial images, 1 mm thick and separated by 1mm, through the interface layer of Figure 2d is shown in Figure 3a-d. This set of images shows the inhomogeneity of the asphalt solution. The distribution of spherical globules in and near the interface is shown in Figure 3b and c.

The formation of the dark layer appears to be related to the degree of aging. In Figure 4a-d, the asphaltene layer is seen at the bottom of the vial in all images for a settling time of 1 week and no dark layer is visible in the unaged and mildly (TFO) aged samples (Figure 4a and b). However, the dark layer is present at the interface for the PAV aged samples (Figure 4c and d) and is most pronounced for the asphalt sample that was aged the longest.

The formation of the interface layer appears to depend also on the concentration of asphaltenes in the unaged asphalt. In addition to asphalt AAD-1, the layering was observed in asphalts AAB-1, AAK-1 and AAE. All of these asphalts have asphaltene concentrations of about 20% or greater (Table 1). The layering was not observed in asphalts AAM-1 and ABM-1, which have low asphaltene concentrations, nor was it observed in asphalt AAS-1, which has a high asphaltene concentration. The reasons for the anomalous behavior of asphalt AAS-1 are not known at present. Asphalts AAS-1 and AAE were both PAV aged at a lower temperature (60°C), but for longer periods of time (144 and 400 hrs). Both have high concentrations of asphaltenes, but only AAE demonstrated the effect. The effects of time and temperature on asphaltene precipitation are currently under study.

The chemical nature of the material near the isooctane-toluene/asphalt interface is not known. This layer could be due to asphaltenes that are becoming more rigid with time at the isooctane-toluene/asphalt interface. A more rigid system would have shorter relaxation times and would appear darker in the NMR images. The layer could also be due to oxidation of the maltenes, which are then attracted to the highly polar surface of the asphaltenes and form a distinct layer at the interface. Compositional factors such as the amounts of strong and weak acids, bases and neutrals probably also contribute to the extent of oxidation and the associated interactions. Other possibilities exist. Nevertheless, the layer of material at the interface appears to have properties that are different from the asphaltenes and the maltenes. For example, the dark layer appears to be a more rigid material than the asphaltene layer. If the sample is stirred with a spatula the dark layer breaks into pieces. An example is shown in Figure 5. The top two images show the breakup of the interface layer longitudinally across the solvent-asphaltene boundary. The bottom two images show the breakup of the interface layer radially across the solvent-asphaltene boundary. In both types of images, the rigid nature of the interface layer is apparent. This material will need to be characterized in the future to determine how it might affect asphalt compatibility.

SUMMARY

Applications of magnetic resonance imaging to study various aspects of asphalts are in their infancy. Consequently, a number of imaging methods and instrumental parameters need to be investigated to determine the feasibility of MRI to study asphalts. In this study, exploratory MRI measurements were made on the effects of aging on the flocculation and precipitation of asphaltenes from asphalt. NMR images were obtained on asphalts which were dissolved in toluene and titrated with isooctane to the point of maximum flocculation. When the titrant was added slowly to minimize mixing at the isooctane-asphalt/toluene interface, the images showed that a layer of material formed at the solvent interface which was different from the asphaltenes or the maltenes. The formation of this layer appeared to be dependent on asphaltene concentration and degree of aging, i.e., the greater the asphaltene content and the degree of aging, the more prominent the layer. These observations suggest that NMR imaging might be used to assess the compatibility of aged asphalts and work is in progress along these lines.

DISCLAIMER

This document is disseminated under the sponsorship of the Department of Transportation in the interest of information exchange. The United States Government assumes no liability for its contents or use thereof.

The contents of this report reflect the views of WRI which is responsible for the facts and the accuracy of the data presented herein. The contents do not necessarily reflect the official views or the policy of the Department of Transportation.

Mention of specific brand names or models of equipment is for information only and does not imply endorsement of any particular brand to the exclusion of others that may be suitable.

ACKNOWLEDGMENTS

The authors gratefully acknowledge support of this work by the Federal Highway Administration under Contract No. DTFH61-92C-00170.

REFERENCES

1. Miknis, F. P.; Netzel, D. A., *Prepr. Pap.-Am. Chem. Soc., Div. Fuel Chem.* **1996**, 41(4), 1327-1331.

2. Komoroski, R. A., Anal. Chem., **1993**, 65, 1068A.

3. Boduszynski, M. M., in *Chemistry of Asphalts*, J. W. Bunger and N. C. Li, eds, Advances in Chemistry Series, **195**, Amer. Chem. Soc., Washington, DC, 1981, 119-135.

4. Heithaus J. J., *J. Inst. Petrol.*, **1960**, 48, 45-53.

5. Pauli, A. T., *Prepr. Pap.-Am. Chem. Soc., Div. Fuel Chem.*, **1996,** 41(4), 1327-1331.

6. Cominsky, R. J.; Moulthrop, J. S.; Elmore, W. E.; Kennedy, T. W., *SHRP Materials Reference Library Asphalt Selection Process*; Report No. SHRP-IR-A-89-002; Strategic Highway Research Program, National Research Council, Washington, DC, 1989, 31 pp.

7. Branthaver, J. F., et al., SHRP-A-368, *Binder Characterization and Evaluation, Volume 2: Chemistry*, Strategic Highway Research Program, National Research Council, Washington, DC, 1993, 193 pp.

8. Petersen, J. C., et al., SHRP-A-370, *Binder Characterization and Evaluation, Volume 4: Test Methods,* Strategic Highway Research Program, National Research Council, Washington, DC, 1994, 479 pp.

Table 1. Summary of Chemical Properties of Selected Asphalts

Property	**AAB-1**	**AAD-1**	**AAE**	**AAK-1**	**AAM-1**	**ABM-1**	**AAS-1**
Asphalt Grade	AC-10	AR-4000	60/70	AC-30	AC-20	AR-4000	AC-20
Crude Source	WY Sour	Calif.	Lloydminster air blown	Boscan	West Tex. Intermed.	Calif. Valley	Arab Heavy
Component Analysis, %							
Asphaltenes	19.3	23.9	24.8	22.9	9.4	8.3	21.3
Polar Aromatics	38.3	41.3	30.5	41.8	50.3	52.4	34.1
Napthene Aromatics	33.4	25.1	31.6	30.0	41.9	29.6	39.7
Saturates	8.6	8.6	12.7	5.1	1.9	9.0	5.9
Other Properties							
Carbon Aromaticities	0.32	0.24	0.33	0.32	0.25	--	--
Hydrogen Aromaticities	0.071	0.068	0.087	0.068	0.065	--	--
H/C	1.55	1.59	1.45	1.46	1.55	1.43	1.43
Molecular Weight (in toluene)	840	700	--	860	1300	--	960

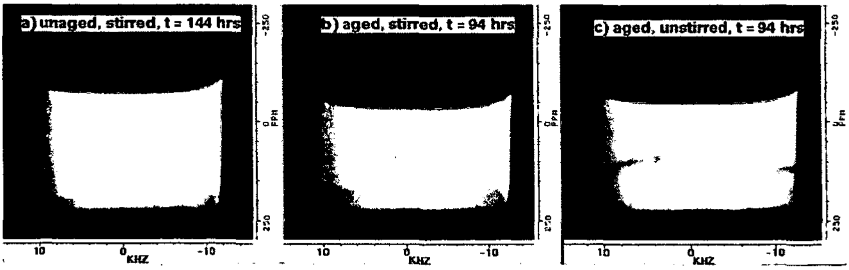

Figure 1. NMR images illustrating effects of aging and stirring on asphaltene precipitation. Times listed are settling times and refer to the time elapsed between addition of isooctane and the time when the image was recorded.

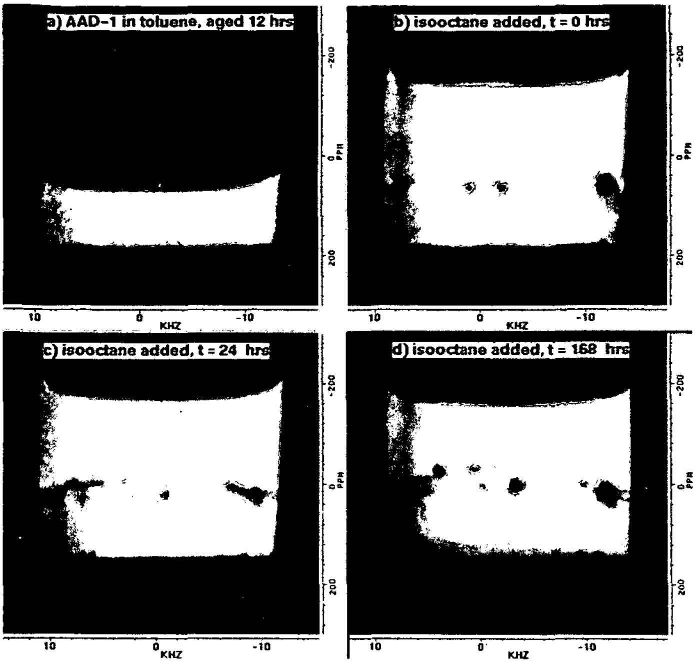
a) AAD-1 in toluene, aged 12 hrs
b) isooctane added, t = 0 hrs
c) isooctane added, t = 24 hrs
d) isooctane added, t = 168 hrs
10
0
-10
KHZ
-200
0
PPM
200

Figure 2. NMR images illustrating time evolution of interface layer in aged asphalt. Times listed are settling times.

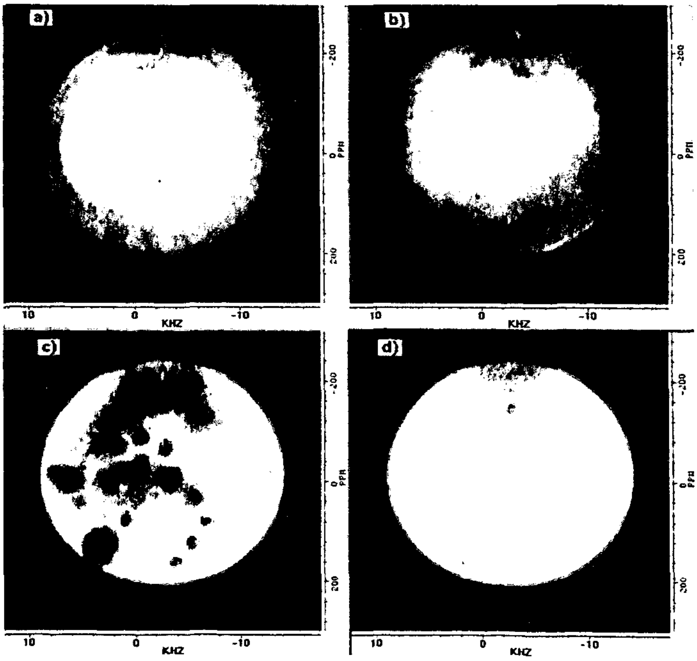
a)
b)
c)
d)
10
0
-10
KHZ
-200
0
PPM
200

Figure 3. Radial NMR images at different depths illustrating spherical globules in the solvent interface layer.

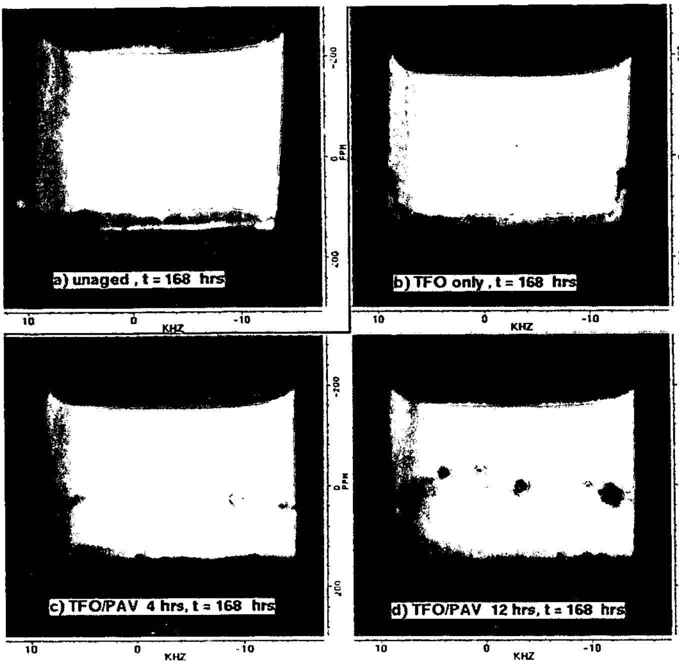
a) unaged , t = 168 hrs
b) TFO only , t = 168 hrs
c) TFO/PAV 4 hrs, t = 168 hrs
d) TFO/PAV 12 hrs, t = 168 hrs
10
0
-10
KHZ
-200
0
PPM
200

Figure 4. NMR images illustrating the effect of aging on asphaltene settling.

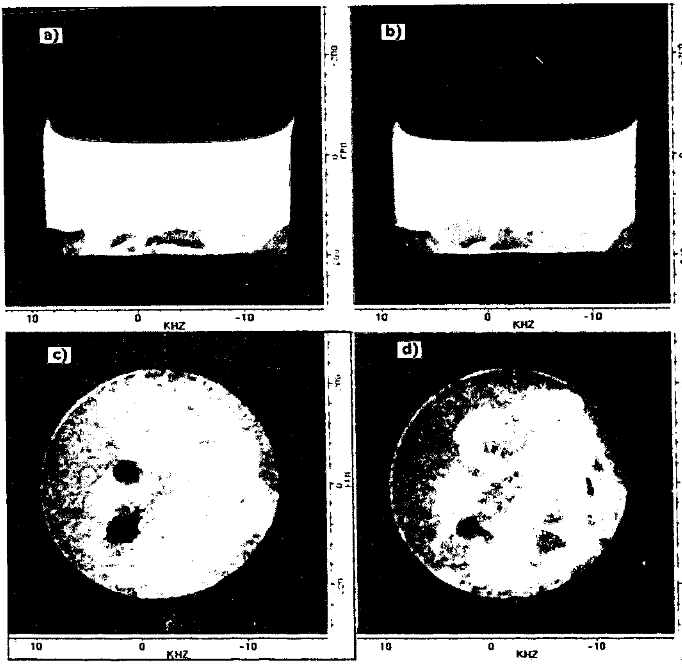
a)
b)
c)
d)
10
0
-10
KHZ
-200
0
PPM
200

Figure 5. NMR images illustrating breakup of interface layer with stirring. a), b) Longitudinal cross-section images at different positions, c), d) Radial cross-section images at different positions.

MEASUREMENTS OF VAPOR PRESSURES OF COAL TARS USING THE NON-ISOTHERMAL KNUDSEN EFFUSION METHOD

Vahur Oja and Eric M. Suuberg
Division of Engineering
Brown University, Providence, RI, 02912

Keywords: Coal Tars, Coal Pyrolysis, Vapor Pressures

INTRODUCTION

Vapor pressures of high molecular weight thermal decomposition products of coals (i.e., tars) are sometimes an important parameter in modeling the combustion behavior of the coals. The extent to which the tars can vaporize, before retrograde reactions reincorporate them into a char, plays a key role in determining the flux of combustibles to the flame front. This is reflected in various pyrolysis models [1-8]. There has been a lively debate in the coal pyrolysis literature concerning what values to assume for the vapor pressures of coal tars, since there have never been actual measurements of this property. What relevant data have been available have come from highly hydrogenated coal liquids [9] or from pure model compounds, and uncertainties of an order of magnitude have not been uncommon. The significance is that models of the coal pyrolysis tar yield are quite sensitive to this input parameter. Comparisons of the behavior of various proposed correlations are offered elsewhere [5,10].

In this study, the vapor pressures of primary coal tars have been examined using the Knudsen Effusion method, modified for application to mixtures containing components with a wide range of volatilities. The Knudsen effusion technique was selected because of the thermally labile nature of the primary tars (those that have not undergone secondary cracking). This requires that the vapor pressures be determined at temperatures well below those of pyrolysis, i.e., below 250 °C. This, in turn, means that the vapor pressures will be very low, because the tars have molecular weights of several hundred dalton.

EXPERIMENTAL

The Knudsen Effusion Technique for Vapor Pressure Measurement

The vapor pressures of actual coal tars and model "tars", consisting of mixtures of PAH, are measured, using a molecular effusion/TGA technique. The various so-called "effusion" methods are based on the molecular effusion of a vapor from a surface, or through an orifice [11]. Of these methods, that which has been selected for use here, is the Knudsen method [12,13], in which a substance of interest effuses through a small pinhole of known area, in an otherwise sealed container or cell. The Knudsen method is used for the measurement of low vapor pressures in the range from 1 to 10^{-6} torr, under molecular flow conditions. This ideally requires that pressures inside and outside the sample cell are low enough that the frequency of collisions of vapor molecules with gas phase species are low in comparison with the frequency of collisions with the cell. The measurement of vapor pressure involves determining the rate of loss of molecules of the evaporating substance from the effusion cell under these conditions. Measurements are typically made under isothermal conditions, with weight loss from the cell being recorded as a function of time, generally in a TGA-type apparatus. We have, however, modified the technique for non-isothermal operation, as described further below.

The basic theory of the effusion method has been often reviewed in the literature [12-14]. The theory of method is actually based upon the basic kinetic theory of gases. From these classical results, Knudsen derived an expression for the slow isothermal flow out of a cell with a small hole in it. The vapor pressure of a material in the cell can be calculated from Knudsen's original effusion rate result:

$$P_1 - P_2 = \frac{G}{t}\,\frac{w_1 + w_2}{\sqrt{\rho}}$$

where P_1 is the pressure of saturated vapor inside the cell, P_2 is the pressure outside of the effusion cell, w_1 is the resistance of hole in the cell, w_2 is the resistance of cell containing the sample, G is the mass lost by effusion, t is the effusion time, ρ is the density of the vapor at the temperature of experiment. The relation simplifies upon applying several simplifying assumptions, including the ideal gas law, that the pinhole leak is the main flow resistance, and assuming $P_1 >> P_2$, yielding:

$$P = \frac{m}{t\,A_0}\left(\frac{2\pi R T}{M}\right)^{1/2}$$

The above result is called the ideal Knudsen equation, in which P is the desired vapor pressure, m the mass loss during the effusion time interval , A_0 is orifice area, M the substance molecular weight , t the effusion time, and T the absolute temperature of the experiment. It is further assumed when applying this equation to the effusion process that the equilibrium vapor pressure of the effusing species obtains within the cell, that the orifice walls do not intercept and return into the cell an appreciable fraction of molecular current entering the hole, that there is no back flux into the orifice exit and the number of intermolecular collisions in the vapor phase occurring within the orifice is negligible.

In our implementation, the mass loss rate was continuously recorded, using a Cahn 2000 recording electrobalance. The cell containing the pinhole leak was suspended on one arm of the balance, which has nominal sensitivity in the μg level. The backpressure in the TGA system was maintained at 10^{-7} torr, which has been noted to be sufficient so as to provide accuracy in the 10^{-6} torr range of vapor pressures. The cell itself was maintained inside of a black capsule within the TGA, and was in close proximity to a thermocouple within the capsule. This was necessary in order to achieve the 0.1°K accuracy in temperature measurement required in vapor pressure work at low temperatures. The temperature measurement issue will be further discussed below.

The Non-Isothermal Knudsen Effusion Technique

One modification of the Knudsen effusion technique was required in order to apply it to materials as complicated as coal tars. Very complex mixtures, which contain materials exhibiting a wide variety of vapor pressures, cannot be conveniently studied by the traditional Knudsen effusion methods involving increasing temperature in isothermal steps. Typically, mixtures of components exhibiting a wide range of volatility are examined by a non-isothermal distillation procedure, for example ASTM D86, D216, D447, D850 and D 1078. The difficulties in applying these methods have led to various alternative methods, including the well-known "simulated distillation" as performed by gas chromatograph, and thermogravimetric methods [15]. These ordinary distillation techniques are not, however, acceptable in our case. Here, as noted above, the temperatures that would be typically involved in an ambient pressure , or mild vacuum, distillation would still be unacceptably high. We are forced to work at the high vacuums of the Knudsen effusion method in order to keep temperatures below those for decomposition of the tars. In contrast to the ASTM-type procedures, however, the pressure outside of the cell is of no consequence, provided that it is below the vapor pressure of the sample by at least an order of magnitude, and as long as the situation in the pinhole leak approximates collisionless flow.

The non-isothermal Knudsen effusion method was developed in response to the above need. The method allows a very wide range of temperatures to be scanned quickly, and with modest amounts of mass loss. The latter is important in the case of a mixture, in which the properties of the sample will change with mass loss. Reliable measurements using the Knudsen effusion method require particular attention to the problem of the measuring and controlling the temperature of the Knudsen cell. Most discrepancies between the results of the different workers using the Knudsen or related techniques are the result of insufficient attention to temperature measurement. As the sample must receive heat purely by radiation (since the cell is operated in a high vacuum) a long time is required to reach thermal equilibrium in an isothermal experiment. In our case, the main thermal lag is associated with heating of the five gram capsule which surrounds the sample cell. However, the sample cell has a view factor of the capsule which approaches one. Together with the fact that the effusion cell has a much smaller mass, 0.15 grams, it thus tracks the capsule temperature well. Thus a long equilibration time, associated with changing the capsule temperature in isothermal experiments, is avoided if an experiment is carried out non-isothermally.

RESULTS AND DISCUSSION

The performance of the non-isothermal technique was checked using anthracene and naphthacene, since the vapor pressures of these compounds have earlier successfully measured by us, using the standard isothermal Knudsen effusion method. Figure 1 shows the non-isothermal measurement results for anthracene at heating and cooling rates of 5 °C/min. It is apparent that there is a significant deviation of the results from the isothermal technique data. The fact that the heating data under-predict, and the cooling data over-predict, the real vapor pressures might be anticipated. This performance suggests that the cell temperature is lagging the surrounding capsule temperature, and that the heat transfer limitation has shifted to the capsule-cell transport process. For this reason, it is logical to expect that by decreasing the rate at which the capsule is driven in temperature, this limitation can be minimized. This is borne out by the results obtained at 0.8 °C/min heating rate, shown in Figure 2. There is in this case good agreement between the results obtained from the non-isothermal and isothermal techniques.

Figure 3 shows the results of the isothermal technique applied to naphthacene, in "cooling" mode. As seen in Figure 3, there is again good agreement between the results of isothermal and non-isothermal methods. Thus the reliability of the non-isothermal method appears to be established.

The results of the first application of the non-isothermal method to coal tars is shown in Figure 4. The results were applied to a fresh coal tar in this case. The tar was produced by the pyrolysis of a Bruceton "standard" Pittsburgh No. 8 high volatile bituminous coal, in a fluidized bed at approximately 550°C. The Bruceton coal has the following elemental composition: C-80.4%, H-5.3%, O-6.7%, N-1.6%, S-1.0%, ash 4.6%, all on a dry basis. The tar was collected in THF, and carefully dried prior to measurement.

In the vapor pressure experiments, the temperature of the tar sample was continually raised from an initial value of 60 °C to a final temperature of 220 °C, at a rate of 0.5 °C/min. Because the tar changes in composition during evaporative loss of its components, the ability to quickly scan the whole temperature space of interest is of great importance. The results of Figure 4 show that the tars evaporate in a "distillation-like" fashion. More volatile species are lost earlier in the process, leaving behind a progressively less volatile residue. The experiments of Figure 4 involved tracking the vapor pressure during both heatup and cooldown cycles. It can be seen that the trace of each heatup cycle (at a progressively higher total level of mass loss) tracks well the immediately preceding cooldown curve. This is not surprising, because during cooldown, the rates of mass loss fall quite low, and until the temperature is again raised to considerably higher values, little further mass loss occurs. Thus there should be little change in vapor pressure attributable to mass loss during the cooldown and early part of the next heatup cycle.

It can be noted that the vapor pressure remains in the range from about 7×10^{-5} to 7×10^{-3} torr as the temperature of the sample is raised from 60°C to 225°C, as a result of loss of progressively less volatile components. Using an earlier derived correlation for the vapor pressures of coal tars [16]:

$$P\ [\text{torr}] = 4.45 \times 10^{6} \exp(-255\, M^{0.586}/T)$$

if the mid-range of the pressure and temperatures of Figure 4 are taken to be $\ln P = -7.5$ (or $P = 5.5 \times 10^{-4}$ torr) and $1/T = 0.00255$ (or $T = 392$ K), then the value of M would be calculated to be about 430 daltons, which is in good agreement with the measured molecular weight of the middle fractions of the tar, from both present measurements and earlier results [16].

More recently, there has developed a concern about condensation-type reactions influencing the results of the vapor pressure measurements, even at these modest temperatures. Indirect evidence of a problem comes from the decreasing solubility of the tar after the vapor pressure experiments have been carried out. If a non-volatile component were to form during the vapor pressure measurement, then the volume fraction of volatile species would be decreased, and assuming that ideal solution behavior is maintained, the vapor pressure would decrease in proportion to the fraction of non-volatile material. At any given temperature, the shift of vapor pressure with cycling involves many orders of magnitude of pressure. We feel, at this point, that selective distillation of lighter fractions may be the more important effect, because there is an overall upward shift in molecular weight during the experiment, but no evidence of formation of large amounts of condensation products.

The data of Figure 4 allow one to judge that there is little change in the latent heat of vaporization during the experiment. This implies that a relatively narrow range of molecular weight is involved. The tar boiling point curve for an arbitrarily selected pressure of 10^{-4} torr is shown in Figure 5.

CONCLUSIONS

The non-isothermal Knudsen effusion method has been shown to be a useful and reliable method for measuring the vapor pressures of pure components and complex mixtures. It is considerably faster and more convenient than the conventional isothermal Knudsen effusion method.

ACKNOWLEDGMENT

The financial support of the U.S. Department of Energy, under grant DE-FG22-92PC92544, is gratefully acknowledged.

REFERENCES

1. Suuberg, E.M., in *Chemistry of Coal Conversion* (R. Schlosberg, Ed.), Plenum, 1985.
2. Unger, P.E., Suuberg, E.M., *18th Symp. (Int.) on Comb.*, The Comb. Inst., p. 1203, 1981.
3. Niksa, S. *AIChE J*, *34*, 790 (1988).
4. Niksa, S. and Kerstein, A., *Energy Fuels*, *5*, 647 (1991).
5. Fletcher,T., Kerstein,A. , Pugmire, R., Solum, M., Grant, D. *Energy Fuels*, *6*, 414 (1992).
6. Solomon, P.R., Serio, M.A., and Suuberg, E.M., *Prog. Energy Comb. Sci.*, *18*, 133 (1992).
7. Solomon, P.R., Hamblen, D.G., Carangelo, R.M., Serio, M.A., Deshpande, G.V., *Energy Fuels*, *2*, 405 (1988).
8. Oh, M.S., Peters, W.A., and Howard, J.B., *AIChEJ*, *35*, 776 (1989).
9. Tsonopoulos, C., Heidman, J., and Hwang, S.-C., *Thermodynamic and Transport Properties of Coal Liquids*, Wiley, 1986.
10. Oja , V. and Suuberg, E.M., *ACS Div. Fuel Chem. Prepr.*, *41*, 82 (1996).
11. Dushman, S., *Scientific Foundations of Vacuum Technique*, Wiley, 2nd edition, 1962.
12. Knudsen, M., *Ann. Physik.*, *28*, 999, 1909.
13. Knudsen, M., *Ann. Physik.*, *29*, 179, 1909.
14. Hollahan, J., *J. Chem. Educ.*, *39*, 23, 1962.
15. Huang, H., Wang, K., Wang. S., Klein, M. and Calkins, W. H., *ACS Div. Fuel Chem. Prepr.*, *41*, 87 (1996).
16. Suuberg,E.M., Unger, P.E., and Lilly, W.D., *Fuel*, *64*, 956 (1985).

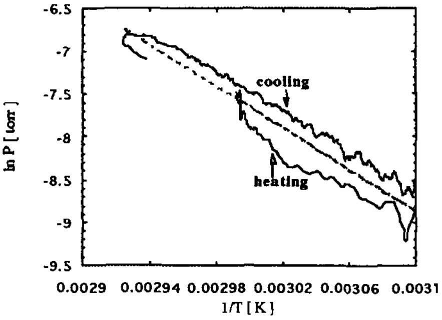

Figure 1. A comparison of vapor pressure results obtained using the non-isothermal and isothermal effusion methods on anthracene. The isothermal data are shown as the dashed line. Heating and cooling rates are 5 °C/min.

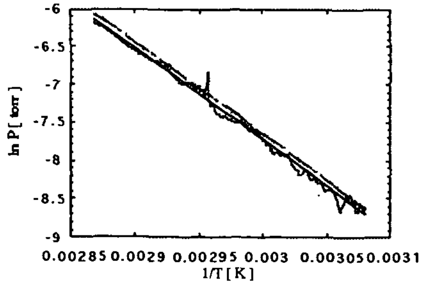

Figure 2. A comparison of the results on anthracene, obtained at 0.8°C/min heating and cooling rates.

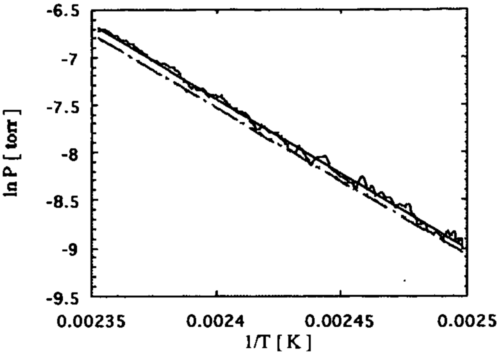

Figure 3. The non-isothermal effusion method applied to measuring the vapor pressure of naphthacene. Cooling rate 0.8°C/min.

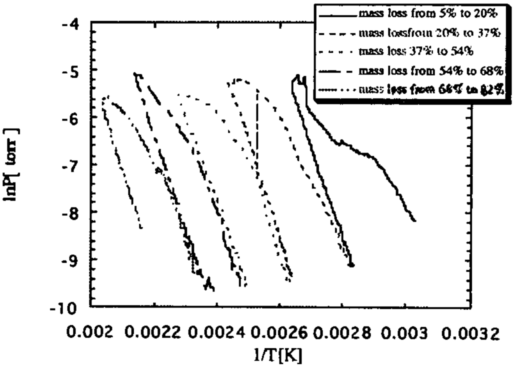

Figure 4. The non-isothermal Knudsen effusion method applied to Bruceton coal tar.

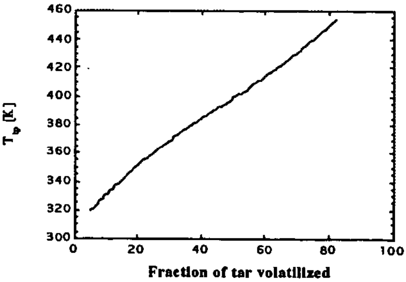

Figure 5. Boiling point distribution of Bruceton coal tar, 0.1 mtorr pressure.

CORRELATION BETWEEN CARBON RESIDUE AND MOLECULAR WEIGHT

John F. Schabron and James G. Speight
Western Research Institute,
365 N. 9th St., Laramie, WY 82070-3380

Key Words: Petroleum Residua, Carbon Residue, Molecular Weight

INTRODUCTION

Petroleum residua are materials obtained by nondestructive distillation of petroleum, usually below 350°C (660°F) since thermal decomposition can be substantial above this temperature (1). Distillation can be at atmospheric pressure (atmospheric residuum) or reduced pressure (vacuum residuum). Residua are usually tacky (atmospheric) or hard (vacuum) at room temperature. These materials typically have low atomic hydrogen-to-carbon ratios, which require hydrogen addition or carbon rejection (coking) schemes to convert them to liquid fuels. They can be difficult to process because of relatively high concentrations of elements other than carbon and hydrogen, and high viscosities (1).

Simple physical property measurements were once considered adequate to predict feedstock behavior in petroleum refining (1,2). The use of various types of residua available worldwide with different properties has added complexity to these considerations (3). Residua composition and properties must be understood to optimize refining strategies (4). Measurements such as elemental analysis, metals content, asphaltene content, and carbon residue provide some indication of residua behavior, but are not single predictors for upgrading processes (5). More insight is needed about the components of residua that cause specific problems in processing (6). The possibility exists that data from various analyses can be combined in a manner to provide insight into behavior during refining (7).

Molecular weight and molecular size are the most misunderstood parameters of petroleum constituents. There are many reports of high molecular weights (100,000-300,000 Daltons) for asphaltenes (8). True molecular weights for asphaltenes very rarely exceed 3,000. Apparent higher values are due to molecular association effects due to the presence of polar constituents causing inter- and intramolecular interactions.

EXPERIMENTAL

The samples were vacuum residua and commercial grade asphalt materials from various sources. Asphaltenes were determined by adding n-heptane at a 40:1 volume ratio (9). Microcarbon residue (MCR) values were determined according to ASTM D-4530. This requires less than 1 g of sample and correlates with the Conradson carbon residue (CCR) test, which consumes 5-10 g sample (10). Number average molecular weights were determined by ASTM D-2503 using a Knaur vapor pressure osmometer (VPO) in toluene at 140°F (60°C). Although pyridine would be considered more desirable for breaking up molecular associations between more polar materials, toluene was used in this study since complete solubility could not be achieved in pyridine for residua asphaltenes.

RESULTS AND DISCUSSION

Ideally, a predictive model can be applied to various feedstocks from different sources and of different types such as waxy, resinous, etc. to predict MCR or CCR values, which are predictors of coke yield. Carbon residue values are related to phase separation and delayed coking tendencies in a refinery (1,7,11). Asphaltene content can be used to provide a rough correlation with carbon residue values (12). For the twelve residua considered in the current study, the correlation between percent asphaltenes and MCR yields a correlation coefficient (r) value of only 0.584. Additional refinement is needed to be a useful predictor of residue formation tendencies. This refinement involves including association effects. Residua with relatively low heteroatom contents yield MCR values significantly lower thanresidua with relatively higher heteroatom contents (13).

A correlation relating asphaltene content, molecular weight and heteroatom content with CCR and MCR of whole residua has been developed (14). Subsequent results suggest that the inclusion of heteroatoms is not necessary, since heteroatom associative affects are already taken into account by measuring the apparent molecular weights of the asphaltenes. In the previous study, the intercept was 8.19 wt.% MCR, which is due to contributions from other aromatic and polar materials in the residua.

The fractional contributions of the various constituents of residua to MCR have been shown to be additive (13). Thus, by considering the contribution of all the fractions, a more universal correlation can be obtained. A new correlation with MCR values and apparent molecular weights in toluene is shown in Figure 1. This consists of twelve residua, six asphaltenes and twelve chromatographic fractions (six aromatics and six polars) considered as whole materials, and the six asphaltenes and the twelve chromatographic fractions considered as fractional contributions

(13,15) Saturate fractions containing no significant aromatic structures and providing no contribution to MCR are not included. The correlation coefficient is 0.943 for 44 points, with a slope of 0.0198 and an intercept of -0.42. This is within experimental error of 0 wt.% MCR. These results suggest a generic universality for residua constituents between molecular weights and residue forming tendencies.

In Figure 1, two asphaltenes fall near the line, while four do not. The four that do not exhibit unrealistically high molecular weights relative to their MCR values. These latter four were not included in the linear equation. The high molecular weights are most likely due to severe associations of these very polar materials in toluene. The two asphaltenes which fell near the line have heteroatom content (N+O+S) of less than 6 wt.%, while the four that are far to the right of the line have heteroatom contents greater than 6 wt.%. The high heteroatom content contributes to polarity and association effects.

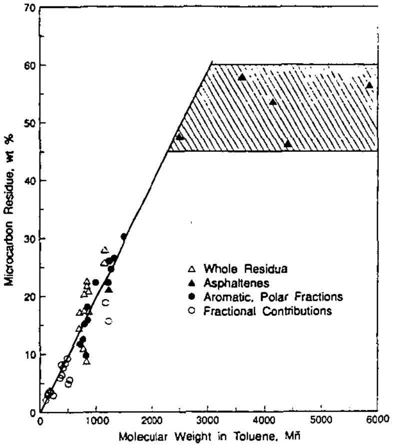

Figure 1. Microcarbon Residue vs. Molecular Weight for Residua Asphaltenes, Chromatographic Fractions, and Fractional Contributions in Toluene.

In an unrelated study (16,17) Athabasca bitumen pentane asphaltenes were separated into four ion exchange chromatography fractions. These materials were fully soluble in pyridine. The MCR values for these materials are plotted against their weights in pyridine. For reference, the toluene correlation line developed in Figure 1 is shown in Figure 2, and also the MCR value of the whole asphaltenes plotted against the molecular weight in benzene, which is essentially the same value one would expect in toluene.

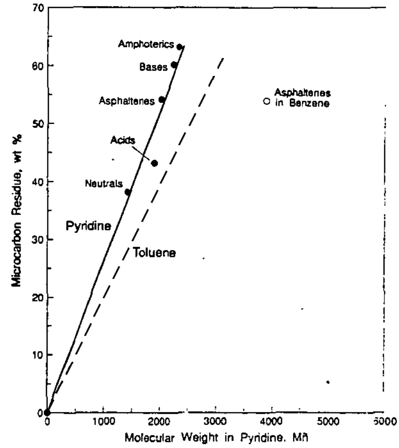

Figure 2. Microcarbon Residue vs. Molecular Weight for Athabasca Asphaltenes and Asphaltene IEC Fractions in Pyridine

The MCR values decrease in the order amphoteric, base, whole asphaltenes, acid, and polar neutral fractions (16). The point for the original asphaltene molecular weight in benzene falls far to the right of the line, with a MCR value of 54.0 and a molecular weight value of 3,890 Daltons. The pyridine molecular weight for the whole asphaltene is 2,018 Daltons (17). The equation for the pyridine line was calculated by including the origin point (0,0) to obtain a slope of 0.0262 and an intercept of -0.46, with a correlation coefficient of 0.990. The slope of the toluene line (0.0198) is smaller than the slope of the pyridine line, which is due to less association in pyridine.

The correlation lines can be used as a tool to gauge association. For example, to bring the asphaltene with the highest apparent molecular weight of 5,850 Daltons to the toluene line in Figure 1 without changing its MCR value would require a molecular weight of about 2,950 Daltons. Thus, it appears that the association tendency for this material is 5,850 â 2,950 = 2.0 units average in an associative complex in toluene solution. Using the pyridine line in Figure 2, the same MCR value yields a molecular weight value of 2,250, or 2.6 average units in an associative complex in toluene. The associative forming tendencies do not appear to have a direct affect on MCR values. This is suggested by the flattening of the correlation above a molecular weight of 3,000 Daltons in toluene (Figure 1), which appears to be due mainly to associative effects. The associations are broken up by the severe heating conditions involved in carbon residue formation.

A correlation which is more useful for the highly associated species is between carbon residue and H/C atomic ratios (Figure 3). Figure 3 includes points for all the materials in Figures 1 and 2. The correlation coefficient is 0.975, for 33 points with a slope and intercept of -105 and 173, respectively. Two points lying far off the line, correspond to a very waxy residuum and its wax-containing asphaltenes and these were not included in the calculation. The point of intersection at MCR = 0 wt.% occurs at a H/C ratio of 1.65. This implies that for residua constituents that there will be no carbon residue contribution for most species with H/C atomic ratiosgreaterthanabout 1.65.

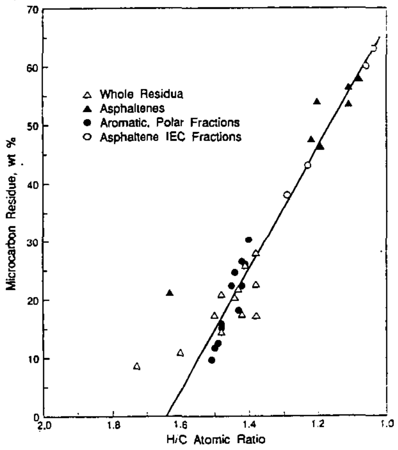

Figure 3. Microcarbon Residue vs. H/C Atomic Ratio for Residua, Asphaltenes, and Chromatographic Fractions

LITERATURE CITED

1. Speight, J.G., The Chemistry and Technology of Petroleum. 2nd Edition. Marcel Dekker, New York, NY (1991).
2. Speight, J.G., The Desulfurization of Heavy Oils and Residua. Marcel Dekker, New York, NY (1981).
3. Dolbear, G., A. Tang, and E. Moorhead, Upgrading Studies with California, Mexican, and Middle Eastern Heavy Oils. In Metal Complexes in Fossil Fuels, R. Filby and J. Branthaver, eds., American Chemical Society, Washington, DC, 220-232 (1987).
4. Schuetze, B., and H. Hofmann, Hydrocarbon Proc., Feb., 75-82 (1984).
5. Dawson, W.H., E. Chornet, P. Tiwari, and M. Heitz, PREPRINTS, Div. Petrol. Chem., Am. Chem. Soc., 34, 384 (1989).
6. Gray, M.R., AOSTRA J. Res., 6, 185 (1990).
7. Gary, J.H., and Handwerk, G.E., Petroleum Refining: Technology and Economics. Second Edition. Marcel Dekker Inc., New York (1984).
8. Speight, J.G., D.L. Wernick, K.A. Gould, R.E. Overfield, B.M.L. Rao, and D.W. Savage, Revue De L'Institut Francais Du Petrole, 40(1), 51 (1987).
9. Speight, J.G., R.B. Long, and T.D. Trowbridge, Fuel, 63, 616 (1984).

10. Long, R.B., and J.G. Speight, Revue de L'Institut Francais du Petrole, 44(2), 205 (1989).
11. Speight, J.G., Chemical and Physical Studies of Petroleum Asphaltenes. In Asphaltenes and Asphalts, 1, T.F. Yen and G.V. Chilingarian (Editors), Elsevier, Amsterdam, 12, 54 (1994).
12. Wiehe, I.A., PREPRINTS, Div. Petrol. Chem. Am. Chem. Soc., 38(2), 428 (1993).
13. Schabron, J.F, G.W. Gardner, J.K. Hart, N.D. Niss, G. Miyake, and D.A. Netzel, The Characterization of Petroleum Residua, U.S. Department of Energy Report DE/MC/11076-3539 (1993).
14. Schabron, J.F. and J.G. Speight, Revue de L'Institut Francais du Petrole, in press (1997).
15. Branthaver, J.F., J.C. Petersen, R.E. Robertson, J.J. Duvall, S.S. Kim, P.M. Harnsberger, T. Mill, E.K. Ensley, F.A. Barbour, and J.F. Schabron, "Binder Characterization and Evaluation", Strategic Highway Research Program Report SHRP-A-368, Volume 2: Chemistry, National Research Council, Washington, D.C. (1993).
16. Speight, J.G., PREPRINTS, Div. Fuel and Ind. Eng. Chem., Am. Chem. Soc., 31(3), 818 (1986).
17. Moschopedis, S.E., J.F. Fryer, and J.G. Speight, Fuel, 55, 227 (1976).

NOVEL CHARACTERIZATION OF PETROLEUM RESIDS BY LIQUID CHROMATOGRAPHY COUPLED WITH MASS SPECTROMETRY

C. S. Hsu
Analytical Sciences Laboratory
Exxon Research and Engineering Company
Route 22 East, Clinton Township
Annandale, NJ 08801

Keywords: characterization of petroleum resids and asphaltenes, thermospray, liquid chromatography-mass spectrometry.

The characterization of petroleum resids and asphaltenes has remained a tremendous challenge to mass spectrometry. These fractions contain thousands of heavy molecules that are difficult to separate into individual components or less complex subfractions by distillation or solvent elution due to high intermolecular van der Waals force and dipole -dipole interactions. The molecules usually lack volatility to provide a stable stream of vapor for mass spectrometric analysis. The number of isomers for a given molecular formula can be tremendous, that makes the differentiation of isomers, particularly steoroisomers, impractical and meaningless. High resolution accurate mass measurement is also very difficult because of the large number of possible elemental combinations that would require very high resolving power and mass measurement stability of the mass spectrometer. Mass spectrometric analysis of these fractions are therefore generally for the determination of molecular weight distribution. However, if high mass resolving power by mass spectrometry or molecular class separation by chromatography is achievable, then compound type and carbon number distributions would be useful information for the studies of upgrading these fractions. Due to multitude of molecules present, it would be desirable to ionize these molecule intact without fragmentation to facilitate mass spectral analysis.

Among low energy ionization techniques, field ionization (FI) and field desorption (FD) are commonly used (see Figure 1). In both FI and FD techniques, the molecules are ionized by a fine emitter with a high voltage (ca. 10-13 kilovolts) between the emitter and a counter-electrode at a short distance that creates a high electric field. The only difference between these two techniques is sample introduction. In FI, the sample is volatilized under mass spectrometric vacuum to produce vapor in the vicinity of the emitter for ionization. However, the temperature required for volatilizing resids and asphaltenes can be too high to cause thermal decomposition of the molecules. To avoid thermal decomposition, FD is used in which the sample is deposited onto a fine emitter which is inserted into mass spectrometer via a vacuum lock. When a high electric field is applied on the emitter, molecules are ionized by quantum tunneling to produce low internal energy molecular ions. To provide fluidity of the sample some emitter current is also applied during ionization. Once ions are formed, they are repelled off the emitter by Coulombic repulsion. In FD, therefore, the sample is ionized without volatilization.

The FD technique, however, suffers from two major drawbacks: weak signal and cluster formation. Since only limited surface area is available on the emitter for field ionization and field desorption, the emitter is usually activated in indene, acetonitrile or acetone vapor to grow microneedles (whiskers) to increase high-field sites or area. Nonetheless, the number of molecules accessible to the high-field sites are still limited. In addition, ionization efficiency by quantum tunneling is very low, compared to other ionization techniques, such as electron-impact ionization and chemical ionization. As a result, low ion yield and weak signal are obtained. Due to transient nature of the signal, medium and high resolution mass measurement is difficult to perform. With a somewhat larger sample load, several layers of molecules are present between the surfaces of the emitter and the sample matrix. Ions formed on the surface of the emitter will have to penetrate through these layers before they are expelled out of the source region. Some of them are neutralized, charge transferred, or undergone ion-molecule reactions. Figure 2 shows a 875-1026°F distillate from a Californian crude oil with an average molecular weight near 500. The presence of dimers with molecular weights between 700 and 1300 is also apparent.

We have resolved the difficulties encountered in FD by using thermospray (TSP) ionization, a technique used in liquid chromatography/mass spectrometry (LC/MS). In TSP, sample is dissolved in a mobile phase that is sprayed out of a heated nebulizer. A heavy duty filament or a discharge electrode is placed near the nebulizer as an ionization means. Excess amounts of solvent (mobile phase) molecules are preferentially ionized by electron bombardment of a heavy duty filament or discharge ionization of a discharge electrode. These solvent ions then ionize sample molecules via protonation, hydride extraction, or charge exchange. Since the sample molecules are not directly heated and ionized by high energy electron beams, intact protonated, hydride-abstracted, or molecular ions are formed in TSP.

The sample molecules are well-separated by an excess amount of solvent so that ion-molecule reaction between sample ions and molecules can be avoided. Thus, cluster formation encountered in FD is eliminated. The same distillate as in the FD experiment mentioned above was dissolved in a mobile phase of 75% methylene chloride and 25% hexane. A discharge electrode is used as an external source for TSP ionization, yielding a TSP spectrum as shown in Figure 3. The most noticeable feature of the TSP spectrum is the absence of dimer cluster in the 700-1300 mass range. The distribution of the ions in TSP is quite similar to that in FD except the absence of peaks corresponding to saturated hydrocarbons. Not being able to ionize saturated hydrocarbons is a major disadvantage of TSP because all of the suitable solvents for TSP experiments have similar or higher proton affinity than saturated hydrocarbons. Hence, saturated hydrocarbons have to be separated from aromatic hydrocarbons and analyzed separately. However, there are many other advantages of using TSP for petroleum resids and asphaltenes to compensate for such limitation.

One advantage of TSP is its stable ion current. Figure 4 compares the TSP and FD spectra of a 1120-1305°F DISTACT distillate of a Middle East crude oil. Both show similar molecular distribution in the mass range of 300-1400 with an average molecular weight of about 800. A much stronger ion current was obtained in TSP, compared to a weak current in FD. With high intensity and stability of ion current, slower scans for medium/high resolution mass measurement can be performed in TSP. Another advantage of TSP is its ability of on-line coupling with liquid chromatography (1). Liquid chromatography (LC) separates aromatic hydrocarbons by increasing polarity into monoaromatic, diaromatic, triaromatic, tetraaromatic, and polar elution regions. It greatly facilitates the differentiation of overlapping aromatic and naphthenoaromatic hydrocarbons (2). Figure 5 shows monoaromatic, diaromatic, triaromatic, and tetraaromatic elution regions of the above DISTACT distillate separated by LC. It can be seen that the average molecular weight gradually decreases with increasing aromaticity. The average molecular weights are about 850 for monoaromatics, 820 for diaromatics, 790 for triaromatics, and 730 for tetraaromatics, respectively. That is, in a given distillation range LC elution regions containing compounds with higher aromaticity have lower average molecular weights.

With increasing resolving power, it is also possible to obtain accurate mass measurement for elemental composition of the compounds (3). Figure 6 shows the compound type distributions obtained from medium resolution (ca. 5000 resolving power) measurement of the monoaromatic, diaromatic, triaromatic, and tetraaromatic elution regions shown in Figure 5. The distributions are shown as relative abundance as a function of the z-number of equivalent hydrocarbon series. For this specific sample, indenes or dinaphthenobenzenes were found to be the most abundant series in monoaromatics, benzothiophenes in diaromatics, dibenzothiophenes in triaromatics, and pyrene in tetraaromatics. The use of a mass spectrometer with higher resolving power, such as Fourier-transform ion cyclotron resonance mass spectrometry (FT-ICR), would be required for further confirmation of these compound series at high masses (4).

We have demonstrated that petroleum resids and asphaltenes can be characterized in fair details by using thermospray ionization technique. This technique can also be used in on-line liquid chromatography-mass spectrometry to further define the type of molecules present in these heavy high boiling petroleum fractions. To overcome intermolecular interaction between resid and asphaltene molecules for aggregate formation, dispersing the molecules in a solvent medium appears to be a reasonable approach for obtaining molecular information of these fractions. It would be worthwhile to study the behavior of these molecules in other type of LC/MS, such as atmospheric pressure chemical ionization (APCI) and electrospray, for the characterization of petroleum resids and asphaltenes.

(1) C. S. Hsu and K. Qian, *Energy Fuels*, 7, 268-272 (1993)
(2) K. Qian and C. S. Hsu, *Anal. Chem.*, **64**, 2327-2333 (1992)
(3) C. S. Hsu, K. Qian and Y. C. Chen, *Anal. Chim. Acta*, **264**, 79-89 (1992)
(4) C. S. Hsu, Z. Liang and J. E. Campana, *Anal. Chem.*, **66**, 850-855 (1994)

Figure 1 Simplified schematic diagram of a field ionization/field desorption ion source.

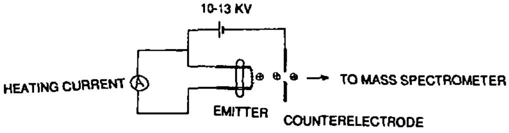
10-13 KV
HEATING CURRENT
A
EMITTER
COUNTERELECTRODE
TO MASS SPECTROMETER

Figure 2 Field desorption mass spectrum of a 875-1026°F distillate from a Californian crude oil, showing the presence of dimers formed during ionization.

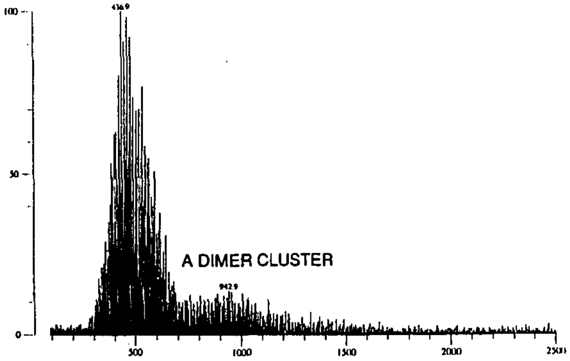

Figure 3 Thermospray ionization mass spectrum of a 875-1026°F distillate from a Californian crude oil, no dimers formed.

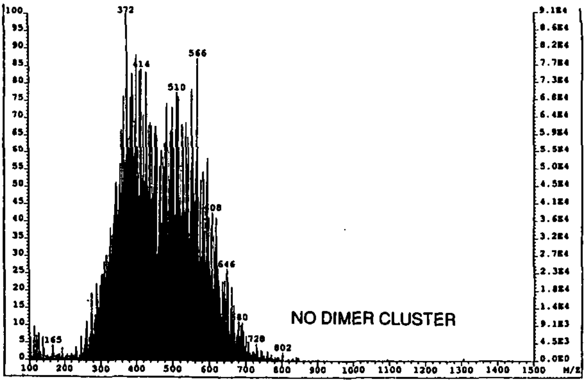

Figure 4 Similar molecular weight distributions are obtained by field desorption and thermospray of a 1120-1305°F DISTACT fraction of a Middle East crude oil.

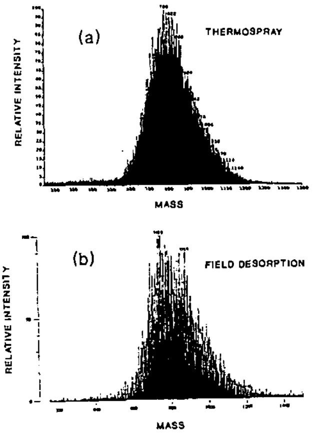

Figure 5 Molecular distributions of a 1120-1305°F DISTACT fraction of a Middle East crude oil in the monoaromatic, diaromatic, triaromatic and tetraaromatic elution regions of normal phase liquid chromatography.

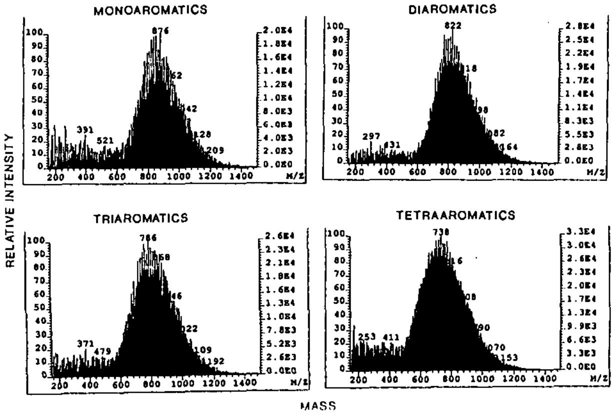

Figure 6 Compound type distributions of a 1120-1305°F DISTACT fraction of a Middle East crude oil in the monoaromatic, diaromatic, triaromatic and tetraaromatic elution regions of normal phase liquid chromatography.

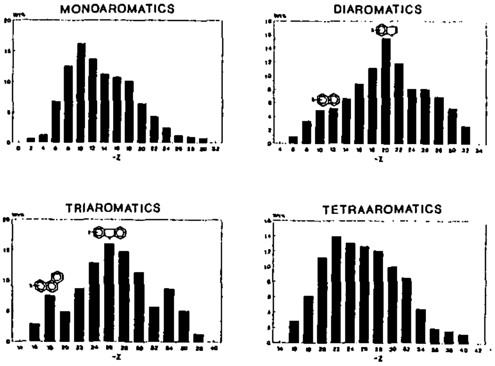

INTERFACIAL PROPERTIES OF ACID, BASIC AND NEUTRAL FRACTIONS DERIVED FROM ORINOCO BELT CRUDE OIL,

Cesar Ovalles*, Maria del Carmen García, Eduardo Lujano, Williams Aular, Reinaldo Bermudez,
Edgar Cotte, INTEVEP, S. A., P. O. Box 77343, Caracas 1080A, Venezuela.

Key Words: Extraheavy Crude Oil, Interfacial Properties, ABN Separation

INTRODUCTION

The interfacial properties of acid fractions play an important role in the stabilization of crude/water emulsions mainly because of their behavior as natural surfactants [1-13]. Also, acid compounds are used as biomarkers in geochemical correlations [14]. On the other hand, acid fraction are known to be coke precursor compounds [14], contributed to deactivation of heterogeneous catalysts used in refining operations and to stabilize water/crude oil emulsions making difficult crude dehydration during oil production processes [10-14].

In 1956, Reisherg and Doscher [1] demonstrated that interfacially active components present in Ventura crude oil are of acidic nature, whereas, in 1964, Newman [2] reported that the later fraction is constituted mainly of phenolic compounds for a Eichlingen-Niedersachsen crude. From these studies and for a Rio Bravo crude oil, Bartle and Niederhausen [3] concluded that the interfacially active materials are concentrated principally in the resins and asphaltene fractions.

Schramm and coworkers [4] studied the influence of the concentration of indigenous surfactants on the recovery of Athabasca bitumen using steam at high pH values. The interfacially active components were separated from the crude oil using the tendency of the former substances to concentrate at the interface of a foam. Using this method, the authors proposed [4] a general chemical structure which consists of naphtenic rings with carboxylic acid sustituents. The surfactants ($R\text{-}O^-$) were generated by addition of sodium hydroxide (eq. 1) in order to enhance bitumen separation from the oil sand [4].

$$R\text{-}OH + NaOH \rightleftharpoons R\text{-}O^- + Na^+ + H_2O \qquad (1)$$

Unfortunately, the extraction of the natural surfactant at high pH value (>10) can generate species, via hydrolysis (eq. 2), which were not originally present in the crude oil. These new species may present substantially different interfacial activity than that found for the indigenous compounds [7-8].

$$RCOOR' \xrightarrow{OH^-} RCOO^- + R'OH \qquad (2)$$

Speight and coworkers [5] extracted phenolic and carboxylic acid compounds from Athabasca bitumen using solvents of different polarities and ion-exchange resins. The authors concluded that oxygenated compounds present in the asphaltene fraction have phenolic sustituents, whereas resins concentrate the carboxylic acid moieties [6]. No details were given on the interfacial activity of the isolated fractions.

Seifert and Howells [7-8] extracted anionic compounds with NaOH/EtOH from a parafinic crude oil (Midway-Sunset) and characterized the interfacially active compounds at pH values greater than 10. By comparison of interfaeial tension vs pH of the original crude and its acid fractions (strong and weak), the authors concluded that their extraction method was efficient for the isolation of the surface active compounds. However, the authors reported the generation, via hydrolysis (eq. 2), between 40 and 50% of tensoactive materials which was not originally present in the crude oil [7-8].

Acevedo *et al.* [9] studied the interfacial activity of SARA fractions separated from Orinoco Belt crude oils and concluded that natural surfactants were present mainly in the resin fractions. From interfacial tension vs pH determinations for the crude oil and its extracts and the lower molecular weights found for methylated asphaltenes, the author suggested that carboxylic acid species were responsible for the observed interfacial activity. However, no further characterization were reported [9].

Sjoblom and coworkers [10-12] extracted surface active compounds from North Sea crude oil using a consecutive adsorption technique. The interfacial properties of the extracted fractions were evaluated using a decane/water (1:1) model system. It was found that the interfacial tension decreased and the stability of the emulsion w/o formed was higher as the polarity of the fraction increased. Sjoblom *et al.* [13] found a molecular weight for the indigenous surfactants between 900 and 1500 g/mole and, based on spectroscopic methods, proposed an average structure which contains a long alkylic chain bonded with phenol, nitrogen or carboxylic acid sustituents. However, the effects of the presence of strong (carboxylic) and weak (phenols) acids on the surface activity of the indigenous surfactants were not studied in detail.

From the previous literature, it can be concluded that the relationships between chemical structure and surface activity of acid fractions, which in turn at higher pH values behave as natural surfactants, are still widely unknown. Furthermore, the effects of the nature of the hydrocarbon chain, R, on the interfacial properties of these fractions have not been addressed in detail. This R group controls not only the acid strength (pKa) of an anionic surfactant but also its hydrophilic-lipophilic balance.

In this work, acid, basic and neutral fractions from Orinoco Belt Crude Oil (Cerro Negro) were isolated by ion-exchange chromatography and characterized by spectroscopic methods (FTIR, H- and ^{13}C-NMR), titration with KOH and molecular weight measurements using vapor pressure osmometry (VPO). The ion-exchange chromatography method was chosen because it is based on separation by functional group, induces little changes on the nature of the crude oils and reasonable mass balances can be easily obtained [14-15]. For measuring the interfacial activity, the method reported by Acevedo and coworkers [9] was used.

EXPERIMENTAL

All reagents were analytical grade and were used without further purification. The Cerro Negro crude oil used in this study came from the Morichal oil field (southeastern part of Venezuela) and has the following characteristics (wt %): °API = 8.1°, % C = 80.32, % H = 9.88, % S = 3.7, % Asphaltenes, = 11.50, [V] = 367 ppm, [Ni] = 95.5 ppm, acidity = 3.7 mg KOH/g, Conradson Carbon = 17,22 %.

FTIR spectra were carried out using CH_2Cl_2 as solvent and KBr cells. $CDCl_3$ was used as solvent and TMS as reference for H- and ^{13}C-NMR analysis. VPO molecular weight determinations were carried out in $CHCl_3$ as solvent.

For the isolation of the total acid fraction (TAF), a column of quaternary alkylamonium chloride supported on a crosslinked styrene-divinylbencene resin (Bio Rad AG-1, 200-400 mesh) was used as reported previously by Green and coworkers [14-16]. For the separation of the strong acid fraction (SAF) the method used was developed originally by McCarthy and Duthie [17].

The interfacial tension measurements were carried out using a toluene/water model system was used [9] (Robal Electronics Balance) and the values were reported at equilibrium at room temperature. The samples were dissolved in toluene and the concentrations were calculated with respect to the oleic phase. The pH of the aquous phase was adjusted with KOH [9, 18].

RESULTS AND DISCUSSION

Total and strong acid fractions (TAF and SAF) were isolated from the crude oil by ion-exchange chromatography using a styrene-divinylbencene resin [14-16] and KOH/SiO_2 [17] columns, respectively. In general, mass balances were between 90 and 95% with average percentages of extraction of 18% and 4% for TAF and SAT with respect to the original crude oil. The characterization by FTIR showed the presence of a band at 1710 cm^{-1} which was assigned to the carbonyl groups of the acid moiety [15-16]. Also, other bands were observed which corresponded very well with the to reported values for: $\nu(\phi\text{-OH}) = 3590\ cm^{-1}$, $\nu(N\text{-}H)_{arom} = 3460\ cm^{-1}$, $\nu(C\text{-}H)_{arom} = 3000\ cm^{-1}$, $\nu(C\text{-}H)_{aliph} = 2800\ cm^{-1}$, $\nu(C{=}C)_{arom} = 1600\ cm^{-1}$ [15-17]. From the analysis of the absorbance ratio of $\nu(C{=}O)/\nu(C{=}C)$ and $\nu(\phi\text{-OH})/\nu(NH)$ bands and their total acid Numbers (Table 1) it can be concluded that SAF present higher concentration of carboxylic acid groups than TAF, whereas the later has more phenolic containing compounds than the former.

H-NMR characterization showed, besides the normal signals between 7.2 and 8.5 ppm for aromatic protons and between 0.1 and 3.8 ppm for aliphatic protons, a broad band in the range 9-10 ppm which was attributed to the carboxylic acid proton as reported in the literature [19]. ^{13}C-NMR analysis showed a small signal at 168 ppm which is consistent with the presence of carboxylic acid in TAF and SAF.

The interfacial activity vs pH was evaluated using a toluene/water model system and the results are shown in Fig. 1. As can be seen, this system presents very small interfacial activity in the pH range studied. On the other hand at pH greater than 13, a very small value for the interfacial tension (<1 dynes/cm) was obtained for the original Cerro Negro crude oil (CNC) as it is reported previously in the literature [7-9]. Furthermore, a reconstituted sample of the Cerro Negro Crude oil (prepared by mixing TAF and BNF in the 18/82 ratio) showed similar interfacial activity than that found for the original CNC (Fig. 1). These results indicate that the separation method induced little changes on the interfacial properties on the crude oil as stated in the Introduction.

The effect of the pH on the interfacial activity of Cerro Negro crude oil and its fractions can be seen in Fig. 2A. It was found that the TAF present lower interfacial tension (2.1 dynes/cm) than those found for the original crude oil (5.3 dynes/cm) and BNT (4.6 dynes/cm) at 1000 mg/l and pH = 12. Similar results were obtained (Fig. 2B) by changing the concentration of the sample in the 100-15000 mg/l range at pH = 12. In general, the interfacial activity decreased in the order TAF > CNC > BNT.

In the same way, SAF showed lower interfacial tension (0.8 dynes/cm) than those determined for CNC (5.3 dynes/cm) and BNF (4.6 dynes/cm) at 1000 mg/l and pH = 12 (Fig. 3A). Also, a similar order of interfacial activity was found, SAF > CNC > BNT (Fig. 3B). From these results can be concluded that interfacially active compounds at high pH values are concentrated mainly in the acid fractions (TAF and SAF) of the crude as expected from the analysis of the literature [1-12].

Chemical characterization (FTIR, total acid number, H-NMR and molecular weight by VPO) and interfacial properties (interfacial tension at pH= 12, interfacial saturation, ISC, and excess, Γ, concentrations and area occupied at interphase) of Cerro Negro crude oil and its acid, basic and neutral fractions can be seen in Table 1. It is important to point out that in case of traditional surfactants, the ISC is better known as critical micelar concentration or CMC. Because the fractions studied in this work are very complex mixtures of a large variety of compounds and formation of micelles in these systems is not confirmed [20], it is preferred to use the term ISC instead of CMC. Therefore, ISC is defined as the concentration in which the interfacial tension remains constant at a given pH value.

As can be seen in Table 1, the interfacialy active fractions TAF showed higher concentration of acids and phenols, measured by absorbance ratio of $\nu(C=O)/\nu(C=C)$ and $\nu(\phi\text{-}OH)/\nu(NH)$, in comparison with the crude oil and its basic and neutral fractions. It is reported that the intensity of these bands increases as the activity of the natural surfactants increases for stabilization of water/crude emulsion [10-12]. Also, it can be observed in Table 1 and Fig. 2 that interfacial activity increases (lower interfacial tension and ISC) as the acidity of the sample increases for TAF, CNC and BNT.

In the same way, H-NMR analysis showed that the percentage of aromatic protons in TAF is higher (7.5%) that those found for the CNC (5.9%) and BNT (5.1%) whereas the molecular weight of TAF is higher (929 g/mol) than CNC (638 g/mol). Therefore, it can be concluded that the hydrophobic portion of the natural surfactants has higher aromatic character and molecular weight whereas the hydrophilic region showed higher acidity and concentration of polar sustituents in comparison with the original Cerro Negro crude oil.

As seen in Table 1, the strong acid fraction showed an interfacial tension value (measured above its ISC) similar to the original crude and TAF (0.7, 0.6 and 1.2 dynes/cm, respectively). However, the ISC found for SAF is aproximatively one fourth of CNC but two fold of TAF (1050, 4000, 650 mg/l, respectively). On the other hand, the molecular weight of SAF is higher (774 g/mol) than that found for CNC (638 g/mol) but smaller with respect to TAF (929 g/mol).

Also, the area occupied at the interfase for SAT is greater (156 Å) than those found for CNC and TAF (113 and 132 Å, respectively). These results indicate that SAF has **lower interfacial activity per molecule** than TAF due to higher value of ISC, greater area occupied at interfase but lower molecular weight of the former in comparison with the later extract. Therefore, the results can be explained in terms of a better hydrophilic-lipophilic balance of the TAF, (higher molecular weight, lower concentration of polar groups and higher total acid number) in comparison with the SAF. All the results presented in this work constitute an important contribution toward the understanding the chemical structure-surface activity relationships of the natural surfactants present in Venezuelan crude oil.

REFERENCES

1) Reisberg, J.; Doscher, T. M. Producers Monthly, 20, 46 (1956).

2) Neuman, H. J. Erdon und Khole, 17, 346 (1964).

3) Bartell, F. E.; Niederhauser, D. O., Fundamental Research on Occurrence and Recovery of Petroleum, American Petroleum Institute, N. Y., 57 (1946-7).

4) Schramm, L. L.; Smith, R. G.; Stone, J. A., Aostra Journal of Research, 1, 5 (1984).

5) Moschopedis, S. E.; Speight, J. G., Fuel, 55, 334 (1976).

6) Moschopedis, S. E.; Speight, J. G., Fuel, 55, 187 (1976).

7) Seifert, W. K.; Howells, W. G.,Amer. Chem. Soc., Div. Pet. Chem. Prepr., 14, 73 (1969).
8) Seifert, W. K., Amer. Chem. Soc., Div. Pet. Chem. Prepr., 14, 87 (1969).
9) Layrisse I.; Rivas, H.; Acevedo, S. J. Disp. Sci. Tech., 5, 1 (1984).
10) Nordli, K. G.; Sjoblom, J.; Kizling, J.; Stenius, P. Colloids. & Surf., 57, 83 (1991).
11)Sjoblom, J.; Mingyuan, L.; Christy, A. A.; Ronningsen, H. P., Coll. & Surf., 96, 261 (1995).
12) Sjoblom, J.; Mingyan, L.; Christy, A. A.; Gu, T. Colloids. & Surf., 66, 55 (1992).
13) Urdahl, O.; Brekke, T.; Sjoblom, J., Fuel, 71, 739 (1992).
14) Green, J. B.; Sturm, G. P., Jr.; Reynolds, J. W.; Thomson, J. S.; Yu, S. K.-T.; Grigsby, R. D.; Tang, S.-Y.; Shay, J. Y.; Hirsh, D. E.; Sanchez, V., U. S. Department of Energy, DE 90000200, Fossil Energy, Niper-161 (1988) and references therein.
15) Green, J. B.; Hoff, R. J.; Woodward, P. W.; Stevens, L. L., Fuel, 63 (1984).
16) Green, J. B.; Yu, S. K.-T.; Green, J. A.; Doughty, D. A.; Vogh, J. W.; Grigsoy, R. D.; Vrana, R. P.; Thomson, J. S.; Carbognani, L., U. S. Department of Energy, DE 90000200, Fossil Energy, Niper-322 (1989).
17) McCarthy, R. D.; Suthie, A. H., J. Lipid Research, 3, 117 (1962).
18) Acevedo, S.; Escobar, G.; Gutierrez, L.; Rivas, H.; Fuel, 71, 619 (1992).
19) Silverstein, R. M.; Bassler, G. C.; Morrill, T. C., Spectrometric Identification of Organic Compounds, Wiley, New York, p249 (1981).
20) Speight, J. G.; Wernick, D. L.; Gould, K. A.; Overfield, R. E; Rao, B. M., Savage, D. W. Revue de L'Institut Fraçais du Pétrole. 40, 51 (1985)

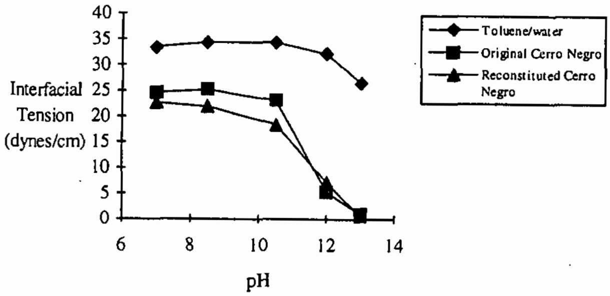

Fig. 1. Interfacial tension vs pH for original and reconstituted Cerro Negro crude oil. Concentration = 1000 mg/l. Toluene/water model system (pH = 12).

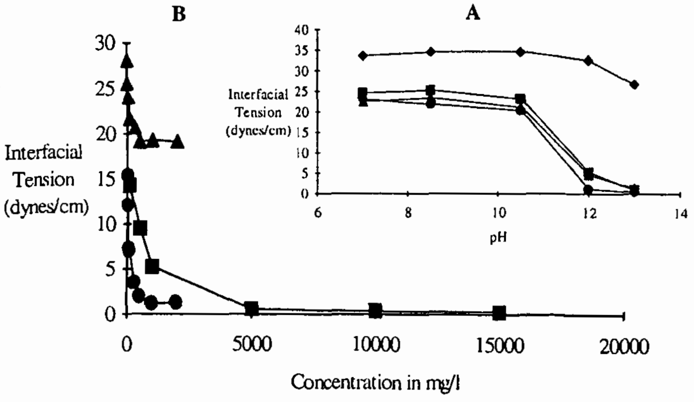

Fig. 2. Effects of (A) pH (at 1000 mg/l) and (B) concentration (at pH = 12) on the interfacial tension for Cerro Negro crude oil (CNC, ■) and its total acid (TAF, ●), basic and neutral (BNT, ▲) fractions using a toluene/water model system (♦).

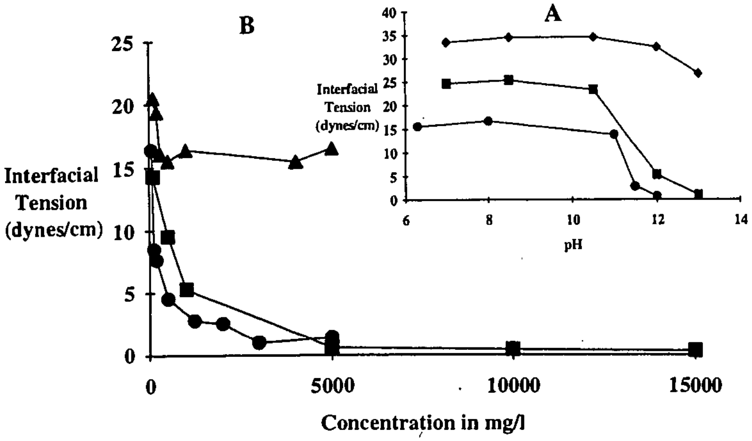

Fig. 3. Effects of (A) pH (at 1000 mg/l) and (B) concentration (at pH = 12) on the interfacial tension for Cerro Negro crude oil (CNC, ■) and its strong acid (SAF, ●), basic and neutral (BNF, ▲) fractions using a toluene/water model system (◆).

Table 1. Chemical and interfacial characterization of Cerro Negro crude oil and its acid, basic and neutral fractions[a].

	Fraction				
Chemical Characterization	CNC[b] (100%)	TAF[c] (18%)	BNT[d] (82%)	SAF[e] (4%)	BNF[f] (96%)
$\nu(C=O)/\nu(C=C)$[g]	0.57	0.97	0.37	3.38	0.06
$\nu(\phi\text{-}OH)/\nu(NH)$[h]	0.18	0.64	0.50	0.52	0.77
Total acid No.[i]	3.7	4.1	0.95	71.8	0.2
$\%H_{arom}$[j]	5.9	7.5	5.1	7.5	6.9
$\%H_{alif}$[k]	93.9	92.5	95.0	92.9	93.1
Mol. Weight.[l]	638	929	477	774	518
Interfacial Properties					
Interf. Tension.[m]	0.6	1.2	11.1	0.7	15.5
ISC[n]	4000	650	500	1050	3700
Interf. Area[p]	113	132	187	156	[o]
Interf.Conc.ex.(Γ)[q]	1.47	1.26	0.89	1.06	[o]

[a] The fractions were separated by ion-exchanged chromatography according with the literature [14-17]. Numbers in bracket indicate percentage w/w with respect to Cerro Negro Crude oil. [b] Cerro Negro Crude oil. [c] Total acid fraction. [d] Basic an neutral fraction obtained from TAF separation. [e] Strong basic fraction. [f] Basic an neutral fraction obtaiened from SAF separation. [g] Absorbance ratio between $\nu(C=O)$ at 1700-1710 cm^{-1} and $\nu(C=C)$ at 1600 cm^{-1}. [h] Absorbance ratio between phenolic $\nu(O\text{-}H)$ at 3590 cm^{-1} and aromatic $\nu(N\text{-}H)$ at 3460 cm^{-1}. [i] Total acid number in mg of KOH/gr of sample. [j] Percentage of aromatic protons determined by H-NMR. [k] Percentage of aliphatic protons determined by H-NMR. [l] Molecular weight determined by VPO. Error ±5%. [m] Interfacial tension (in dynes/cm ±1) above its concentration of saturation for a toluene/water model system at room temperature and pH = 12. Interfacial tension without additive = 32.5 dynes/cm. [o] It did not show a typical Gibbs isotherm. [n] Interface saturation concentration in. mg/l. [p] Area occupied at the interface in $Å^2$. [q] Interfacial concentration in excess x 10^{10} moles/cm^2.

IDENTIFICATION OF ACIDIC CONSTITUENTS IN A CALIFORNIA HEAVY CRUDE

N.A. Tomczyk, R.E. Winans
Chemistry Division, Argonne National Laboratory, Argonne IL 60439

J.H. Shinn
Chevron Research and Technology Company, Richmond, CA 94802-0627

Keywords: Crude, Analysis, Acidic Constituents

Abstract

Acidic constituents of heavy California crudes cause corrosion in the processing equipment. Many of the smaller acids have been identified, and this paper will focus on the heavier acidic compounds from a San Joaquin Valley crude. The acidic fraction is isolated by base extraction, methylated and analyzed by desorption high resolution mass spectrometry, NMR, and FTIR. The majority of the compound groups have been identified. The effect of mild hydrotreating on the distribution of acidic components will be discussed.

Introduction

A well known and significant problem in crude oil processing is corrosion due to acidic constituents. It is the goal of this study to first determine the acidic compounds responsible for the corrosion, then develop an online system to treat the crude before it enters the high temperature processes. In this work, we examine the composition of acid fractions in oils before and after mild hydrotreating, a process known to reduce the corrosivity in oils with very little change in composition in other than the acidic fractions. An online system to monitor the process will be the subject of future work.

Samples of pre- and post-treated San Joaquin Valley (SJV) crudes were extracted with base. Prior to methylation, the samples were analyzed by Fourier Transform - Infrared Spectroscopy (FTIR) and by C^{13} Nuclear Magnetic Resonance (NMR). Then, after methylation, they were analyzed by High Resolution Mass Spectrometry (HRMS); the results of which will be the focus of this paper.

Description of Samples Used

The oil was sourced from California's San Joaquin Valley, and was desalted in the commercial refinery operation. The hydrotreating consisted of heating the crude to temperatures between 550 and 650 F at hydrogen pressures between 100 and 500 psig over a commercial hydrotreating catalyst in a continuous-flow pilot plant system. Samples were taken throughout the run at various severities.

A common measure of acidity in oils was used to compare samples before and after treatment. This method, known as Neutralization Number or Total Acid Number, involves addition of potassium hydroxide (KOH) to the samples until a neutral pH is achieved, and recording the amount of base required to achieve neutrality as milligrams of base per gram of oil. The Neutralization Numbers for the untreated and treated oils discussed in this paper were 5.18 and 0.87, respectively.

Extraction

The extraction procedure used is a version of the one developed by Seifert and Howells [1]. It requires a 45 g sample to be dissolved in 67 g of isopentane. The mixture is then extracted ten times with a base solution of 70% ethanol and 1% NaOH, followed by two time with a 70% ethanol solution. The solution is centrifuged after each extraction to separate the layers. Centrifuging often results in three layers, an organic and an aqueous separated by solids, which contain asphaltenes. These solid layers are set off to the side until the extraction of the oil is complete. The solids are then dissolved in xylene and extracted with base. The two base extracts are then combined prior to cleanup and acidification at 0°C. Once acidified, the solution is extracted with ethyl ether. The ether is washed with distilled water to neutrality and dried with $MgSO_4$. Approximately 100 mg of extract is methylated with BF_3 in MeOH. Percent yields were 4.90% and 2.55% for the crude and the treated oils respectively.

Results

The samples were analyzed on a 3-sector MS-50 high resolution mass spectrometer [2]. The instrument was run in the electron impact mode. The analysis was performed using low electron voltage (17 eV) at 40,000 resolution. The samples were heated from 200 to 400° C on a probe inserted directly in the source. Mass measurements were a result of averaging the data from all the scans taken throughout the temperature range.

The spectra generated by the HRMS were analyzed by a program written in house. It calculates possible formulas for the masses detected by the instrument and categorizes them according to heteroatom substitution (i.e. NO_x, O_x, S_x...) and hydrogen deficiency. The notation of substitution, such as N_2O_3, only indicates that a compound contains two nitrogen and three oxygen. It is written as such to aid in the ease of presenting the data.

The first change that is evident is the shift in average mass. As can be seen in figure 1, the peak mass in the crude distribution is approximately 580 mass units. In the hydrotreated distribution, the peak mass is around 250 mass units.

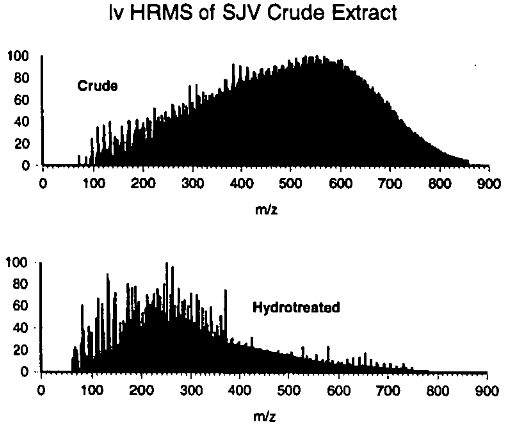

Figure 1. Mass distribution of SJV Crude and most treated product

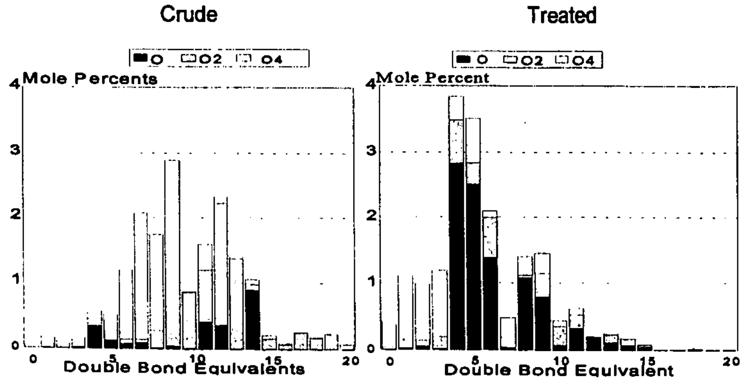

Figure 2. Distribution of oxygen containing species

Looking at figure 2, it is evident that there is a shift in the distribution of the compounds to smaller molecules. There also appears to be a shift from the O_4 functional groups dominating in the crude sample to predominantly single oxygen functional groups in the treated sample without a loss of apparent compound concentration. The groupings of O_2, and O_3, O_5, and O_6 (not shown in graph) exhibited an overall reduction in concentration and compound size.

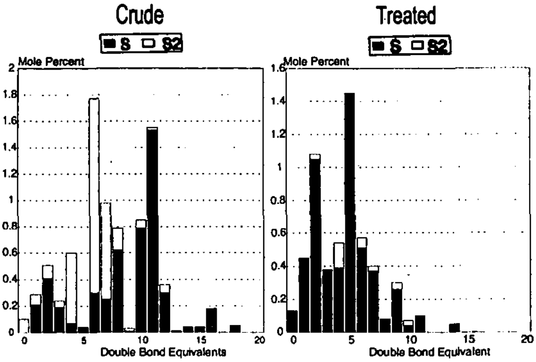

Figure 3. Distribution of sulfur containing species

In figure 3, there is not a significant loss of compounds from the crude to the treated sample. There is, however, an almost complete reduction in S_2 species in the treated sample, thus increasing the concentration of compounds containing one sulfur. There is also a shift towards smaller molecules. In the crude, the compounds are distributed between 0 and 18 DBE, where as, in the treated sample, they are clustered almost entirely below 10 DBE.

Figure 4 shows a significant decrease in the concentration of SO_3 (which designates compounds with a sulfur and three oxygens that are not necessarily together in one functional group) and SO_2 in the treated sample coupled with an increase of SO containing compounds. There also appears to be a loss of compounds in this group. Though the concentration of the compounds between DBE zero and DBE 10 is not reduced, the compounds above DBE 10 are almost completely gone.

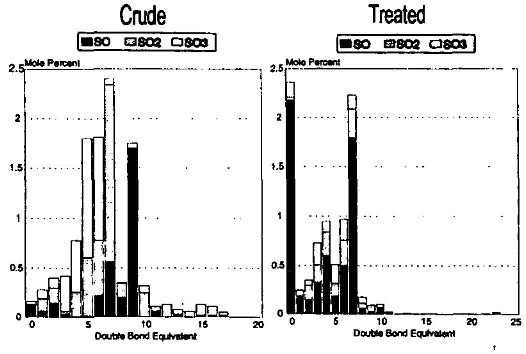

Figure 4. Distribution of SO_x containing species

For the nitrogen functional groups, in figure 5, there is a sharp reduction in the N through N_2 moieties coupled with an increase in N_3 groupings in the treated sample. While the distribution across the size of the molecules appears to be intact, there appears to be an overall reduction of compound concentration.

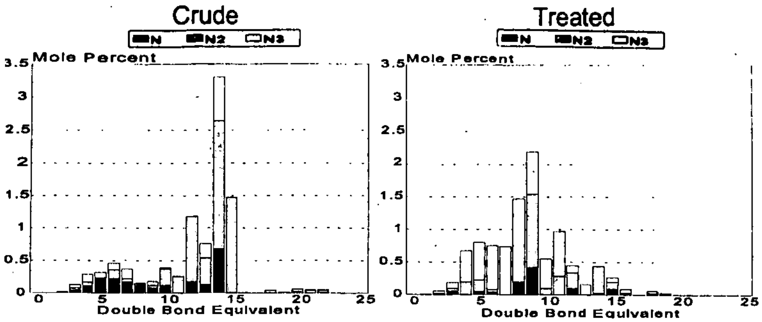

Figure 5. Distribution of nitrogen containing compounds

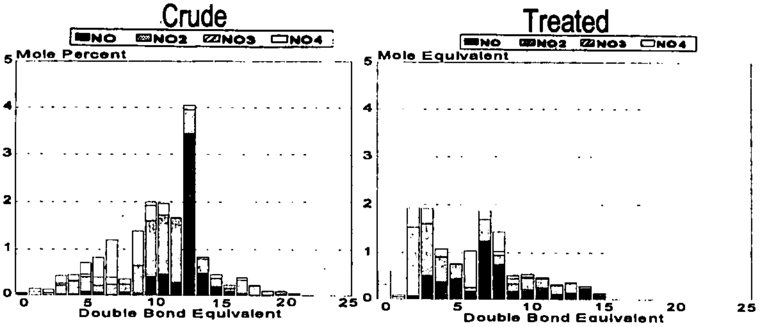

Figure 6. Distribution of NO_x containing compounds

Nitrogen-oxygen compounds appear to have had their concentration redistributed (figure 6). In the crude, it appears that the most prevalent class of compounds are those with 13 DBE (mole percent of 3.5), with lesser amounts spread between 3 and 21 DBE. In the treated sample, the distribution shifts to smaller DBE,(i.e. smaller molecule sizes). Looking at the other three NO_x moieties, appear to shift to smaller compounds coupled with a slight reduction in overall concentration.

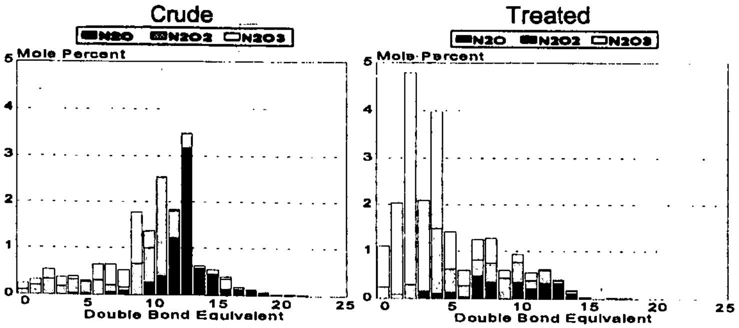

Figure 7. Distribution of N_2O_x containing compounds

The most obvious change in figure 7 is the N_2O_3 grouping. There is a significant increase in the amount of compounds in the treated sample. This change is coupled with a significant a concurrent decrease in N_2O. The N_2O_2 moieties are only slightly decreased in the treated sample. The redistribution of the entire series is only minor. It is the center of the concentration that is shifted from 13 DBE to 3 DBE.

Not surprisingly, the overall trend appears to be towards smaller compounds. However, while the S_x, O_x, and SO_x groupings show a tendency towards fewer heteroatoms in the compounds, the N_x and the N_2O_x groupings appear to become more complex and keep their larger molecules.

Conclusions and Future Work

The techniques employed in this study allow us to identify the relative concentrations of various important acidic groups in crude oils and processed products. A broad molecular-weight range of species containing various levels of oxygen, sulfur, and nitrogen are observed. The species identified include aromatic, aliphatic, and phenolic acids. Hydrotreating of acidic crudes to reduce their acid content has different impacts on the different species present. Changes in the number of species with high heteroatom content, and changes in molecular size of certain groups of species have been observed. Our current work applies these techniques to a focused group of samples designed to help understand which components most strongly relate to corrosive behavior in oils, how to facilitate measuring the corrosive species, and how to convert these species to non-corrosive forms.

Acknowledgement

This work was performed under the auspices of the U.S. Department of Energy, under contract number W-31-109-ENG-38. This work was supported by a CRADA agreement between Chevron Research and Technology Company and Argonne National Laboratory under the U. S. Department of Energy-Bartlesville, Fossil Energy Project.

References

1) Seifert, W.K. and W.G. Howells, "Interfacially Active Acids in a California Crude Oil", *Analytical Chemistry*, 41(4), 554-562 (1968).

2) Winans, R.E., "Mass Spectrometric Studies of Coal and Coal Macerals," *Advances in Spectroscopy*, H.L.C. Meuzelaar (ed.), Plenum Press, New York, 1992, 255.

DYNAMICS OF ASPHALTENES SOLUTIONS IN TOLUENE STUDIED BY MEANS OF THEIR ADSORPTIONS ON GLASS SURFACES

Sócrates Acevedo, Gaston Escobar, María A. Ranaudo,
Marisol García and Jimmy Castillo
Universidad Central de Venezuela, Facultad de Ciencias,
Centro de Química Organica, 47102 Caracas, 1041 Venezuela.

Keywords: asphaltene dynamics, molecular weights, aggregation, thermal lens spectroscopy

Using conventional VPO measurements in toluene and thermal lens spectroscopy (a laser technique) to measure the adsorption of asphaltenes on a glass surface from toluene solutions, the dynamics of Hamaca asphaltene solutions have been studied. The results described below are consistent with two dynamic events occuring at very different rates. In the first one the adsorbed asphaltenes were measured directly by the above laser method. When the signal corresponding to this adsorbed sample was plotted against time (solution concentration: 4000 mgl^{-1}) a maximum, near 125 min was observed. A much lower and steady value for the signal was observed after 300 min. A similar experiment was performed with resins and a low and constant signal was observed in this case. The second event was the slow increase of average molecular weight where the number average molecular weight M_n increased, during a period of two days, from 4230 to 17420 in toluene.

Experimental.

Two Hamaca asphaltene samples were examined. Sample A_1 were asphaltenes precipitated from extraheavy (8° API) Hamaca crude oil by adding 40 volumes of n-heptane to a 1:1 mixture of crude and toluene as described earlier. This sample contains about 80% asphaltenes and 20% of resins. Sample A_2 was a resin-free asphaltene obtained by washing the above A_1 sample with boiling n-heptane in a soxhlet apparatus during a period of three days.

M_n determinations.

These were measured in toluene at 50°C in a concentration range from 1 to 5 gl^{-1} as described earlier[1]. Results are shown on Table 1 for Hamaca and for similar samples of asphaltenes obtained from another extraheavy crude oil (Cerro Negro) wich are included for companson. As shown in this table, the M_n for the A_1 samples could be averaged whereas the values for A_2 increase steadily with time. Due to limitations of the VPO technique it was imposible to measure M_n values higher than those shown on Table 1.

Hamaca Asphaltenes,							
			Time (hours)				
	0	24	48	72	96	144	216
$A_1{}^a$	2760	2820	2850 .	3350	2380	3010	2230
A_2	4230	4330	17420	b	b	b	b
	a:average 2770±375						
Cerro Negro Asphaltenes							
$A_1{}^c$	2570	3220	2880	2570	-	3500	3100
A_2	5350	5470	10720	15170	b	b	b
	b: M_n too high to be measured by this method **c:average 2970±370**						

Table 1. M_n values vs time for asphaltene samples.

Thermal Lens Spectroscopy.

For thermal lens measurements we have used a home made thermal lens spectrometer with a collinear dual-beam configuration (see Figure 1).

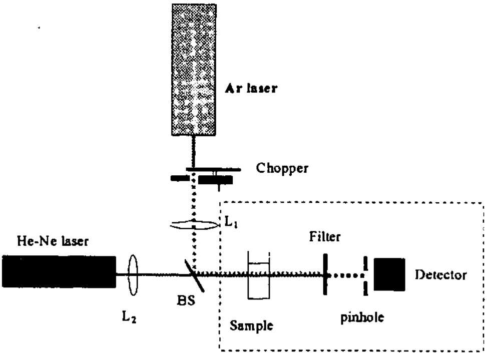

Figure 1. Experimental set-up for thermal lens spectroscopy.

A Coherent Innova 300 argon ion laser (250 mW, 488 nm3 was used as a pump or excitation beam whose amplitud was modulated by a chopper and was focused onto the sample with a lens L_1 (200 mm focal lenght). In the present case, the sample cell was the glass slide described below. A 5 mW He-Ne laser (632.8 nm) was used as probe beam and focused with lens L_2 (200 mm focal lenght). The probe beam focus is placed 6 cm before the sample cell. A 50% beam splitter (BS) was used in order to direct collineary the exitation and probe beam through" the sample cell. The signal was obtained by sampling the intensity at the center of the probe beam with a precision pinhole and a silicon photodiode. The detector-pinhole system was mounted on a XYZ translator in order to localize the laser beam center.

Adsorption Measurements.

Toluene solutions of the above A_2 Hamaca samples were prepared as required using an ultrasound apparatus to dissolve the asphaltenes as fast as possible. For diluted solutions (< 1 gl^{-1}) this required less than a minute whereas for the more concentrated the solutions were sonicated for 15 minutes to ensure completed dissolution. Glass slides (4 cm x 1 cm), used as adsorption surfaces, were dipped in the above solutions and stored in stoppered compartments. After the appropriate times, these were withdrawn, dried and analyzed using the the above thermal lens spectroscopy. Signal averages were obtained by impinging the beams on differents spots on the glass surface. Two types of experiments were performed: In the first, we monitored the signal against the time for a 4 gl^{-1} solution of asphaltene in toluene. The results are plotted in Figure 2. In the second type, toluene solutions of different concentrations were prepared, the glass slides were dipped in and measurements were recorded after 78 hours. The results are plotted on Figure 3.

Disscusion.

a. Time dependent experiments.

The results shown on Figure 2, could be analyzed in terms of the following considerations: During the first stages of the dissolution process the asphaltenes are present in solution as large particles formed by the association of aggregates.

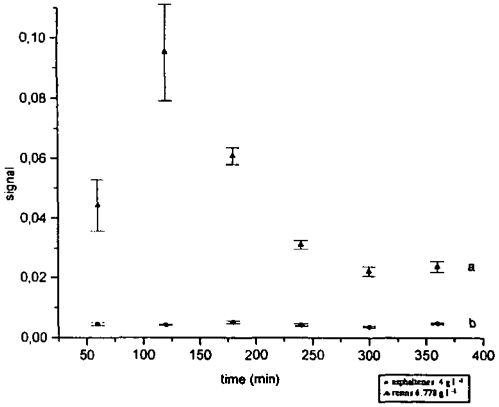

Figure 2. Adsorption of A_2 Type asphaltenes (a) and resins (b) on a glass surface as a function of time.

To simplify the arguments these could be represented as A_n where each A component is an asphaltene aggregate formed by a range of molecular weight compounds from large (A_L) to small (A_s) molecular weight components. The A_n and A macrostructures and composition would depend on the precipitation conditions used to obtain the samples (A_1 type) as well as on any further treatment employed to purify the sample (A_2 type). For instance, in macrostructure A the large components A_L, formed by aromatic structures bonded through aliphatic chains in a way similar to that suggested by Strausz *et al*[2] would be placed at the perifery of A enclosing smaller molecular weight components. In any case we suggest that during the first stages of the adsorption process, the predominant species present in solution would be the A_n whose adsorption would account for the increase in the signal S(t) in Figure 2. After a while, dissociation of A_n in their A components will set in leading to the observed decrease in S(t) since in principle adsorption of a lower molecular weight species (A) leads to a decrease in S(t). As shown in Figure 2, this process occurs during the first 300 minutes of measurements.

To account for the behaviour of M_n measured for the A_1 and A_2 samples (see Table 1) we suggest that due to entropic factors, the solvent will enter the A macrostructure breaking internal weak bonds between their components and releasing some of them. Then, the system will move to an equilibrium state consistent with the prevailing conditions of solvent, concentration and temperature. The above dynamic behaviour could be summarized by noting that both A_n and A macrostructures, as they are in samples A_1 and A_2 are not equilibrium macrostructures in toluene. For instance, the increase in M_n with time, for samples A_2 is likely due to the removal or resins from asphaltene sites active for molecular interaction when the sample is dissolved in toluene.

b. Concentration dependent experiments.

The adsorption isotherms of asphaltenes on inorganic surfaces, using conventional UV absorption spectroscopy, have been studied in our labs earlier[3]. However, due to experimental limitations inherent to this technique which leads to errors comparable or larger than the amount of sample adsorbed, the measumerents have to be made at very low concentrations, usually below 200 mgl^{-1}. Figure 3 show clearly that use of the above thermal lens technique leads to fairly good results at low and high concentrations, due to the direct measurement of the amount adsorbed and to the high sensitivity of the laser beam. The adsorption isotherm shown in Figure 3 for Hamaca (A_2 sample) is consistent with a Langmiur type adsorption at low concentration. As discussed elsewhere[3], the "jump" near 1000 mgl^{-1} is probably due to the adsorption of aggregates formed after the cmc corresponding to this sample.

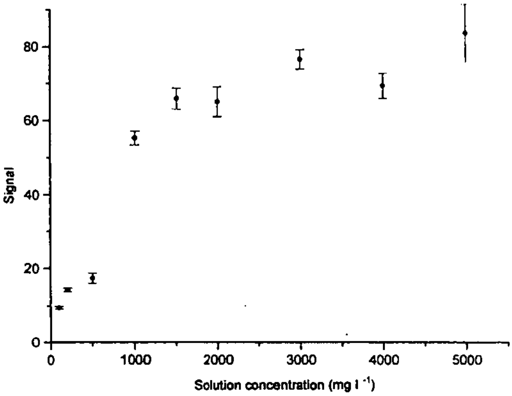

Figure 3. Adsortion isotherm of Hamaca asphaltenes (A_2 Type). Solvent: Toluene. Temperature: 25°C.

References.

1. Acevedo, S., Mendez, B., Rojas, A., Layrissc, I, and Rivas, H., Fuel, 64, 1741 (1985).

2. Strausz, O. P., Mojelsky, T. W., and Lown, R.M., Fuel, 71, 1355 (1992).

3. Acevedo, S., Ranaudo, M. A., Escobar, G., Gutierrez, L., and Ortega, P., Fuel, 74, 595 (1995).

SEPARATION OF FRACTIONS EXHIBITING VARIABLE PARAMAGNETISM FROM HEAVY OILS AND THE STUDY OF THEIR PROPERTIES

V.A. Martynova, L.N. Andreyeva, A.A. Velikov, F.G. Unger
Institute of Petroleum Chemistry, Russian Academy of Sciences,
634055, Tomsk, RUSSIA

Keywords: asphaltene, resins, paramagnetism

Scanty knowledge of nature of resins and asphaltenes is the main obstacle to effective and complex use of heavy oils. There are many theoretical concepts which consider the nature of supermolecular interactions in oil dispersed systems (ODS) from the positions of electrolytic dissociation, donor-acceptor interaction, π - π interactions of polyconjugated systems, exchange (quantum) interaction and etc.

In spite of different views on the nature of resins and asphaltenes the scientists have defined that just the formation and destruction conditions for supermolecular structures in oil dispersions decisively affect the processes of extraction and thermal destruction of the system components as well as predetermine the structure and physio-chemical properties of the end products of oil processing. Based on the researches carried out at the Institute of Petroleum Chemistry RAS concerned with the paramagnetic nature of oil dispersions, asphaltenes have been found to be a concentrate of paramagnetic molecules existing as associates with diamagnetic molecules. Paramagnetic molecules and reversible homolytic transformations of diamagnetic molecules into paramagnetic ones play the main role in the transformation of supermolecular structures in oil dispersed systems and are responsible for thermodynamically unstable equilibrium of the system as a whole [1-4].

Long-term studies of ODS paramagnetic nature made it possible to substantiate theoretically: i) the presence of such molecule types in ODS which under change of external effects rather easily go from diamagnetic to paramagnetic state and if the effect is removed they return to the initial state and ii) extraction of molecule concentrates from high-viscous oils exhibiting variable paramagnetic properties [5-7]. The method developed allows to divide heavy oils into fractions with different paramagnetism. The studies of fraction behavoiur by ESR- and IR-spectroscopies and by microcalorimetry during dissolution and heating showed that the level and width of energy slot for a reversible diamagnetic-paramagnetic transitions depend on structure and chemical composition of molecules. Homolytic mechanism of supermolecular structure transformations has been presented based on quantum-mechanic insight into the nature of intermolecular interactions in ODS [8-10].

EXPERIMENTAL

At the Institute of Petroleum Chemistry RAS a method has been developed to separate fractions with variable paramagnetic properties (FVP) from crude oils and heavy residues. A specially designed device was employed. The mathod is based on destruction of ODS supermolecular structures from the exposure to external factors (temperature, pressure, solvent type and time delay) and on the sequential selection of concentrates of FVP molecules different in the energyof reversable diamagnetic-paramagnetic transitions, i.e. in their stability to external effects.

Presented are the results on the study of initial petrol deasphaltizate obteined from commercial mixture of West Siberian oils and of extracted FVP. FVP-1 and FVP-6 exhibiting different paramagnetism are characterised in Table 1.

Table 1.

Physico-chemical characteristics of ODS

Test sample	Molecular mass (cryoscopy)	PMS, n x 10^{18} spin/cm^3	Elemental composition, wt. %						
			C	H	N	S	O	n x 10^2 V	n x 10^2 Ni
Deasphaltizate	751	2.76	83.40	9.66	0.65	2.52	1.78	0.90	0.40
FVP -1	693	2.13	85.16	10.00	0.54	2.43	0.96	0.49	0.21
FVP -6	1403	71.40	85.50	8.58	1.05	2.60	2.26	3.14	1.43

FVP properties dependent on external effects (temperature and solvent amount) were studied by ESR-, IR-spectroscopies and by microcalorimetry. The effect of the nature of different solvents on the change in the concentration of paramagnetic sites (PMS, spin/cm^3) in ODS has been studied previously. In the present work we used chloroform as a solvent.

I. ESR-SPECTROSCOPY

The changes in PMS concentrations (spin/cm^3) in ODS dependent on external factors were studied by ESR-spectrometer "SEX-2544" (Poland). Detailed procedure features are described in [4,8]. The results of ESR-studies of the three ODS samples (deasphaltizate, FVP-1 and FVP-6) are presented in Figs. 1-4.

Fig. 1 presents the change in paramagnetic properties of the test samples versus the temperature. The test samples were vacuum pretreated and sealed in quartz ampoules. The change in ODS paramagnetism versus the solvent concentrations in chloroform is shown in Fig. 2. The change in FVP-1 paramagnetic properties versus solvent and temperature is given in Fig. 3. As is seen from ESR-spectra presented in Fig. 4, the quantitative view of the spectrum varies because of temperature and solvent effects.

Relative change in the intensity of ESR-signal for ODS versus the temperature

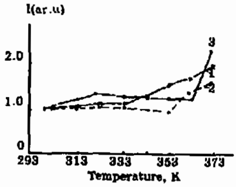

Fig. 1.
1. deasphaltizate
2. FVP-1
3. FVP-6

Relative change in the intensity of ESR signal for ODS in chloroform versus the concentration.

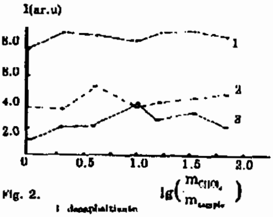

Fig. 2.
1. deasphaltizate
2. FVP-1
3. FVP-6

Relative change in the intensity of ESR-signal for FVP-1 in chloroform versus the concentration and temperature

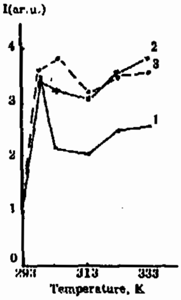

The results of ESR-studies are expressed in arbitrary units (ar.u.).
PMS concentration (spin/cm³) of vacuum-treated ODS samples at 298 K is takes as a unit.

Fig. 3.
1. FVP-1 : CHCl3 wt. ratio 1:1
2. - " - 1:2
3. - " - 1:10

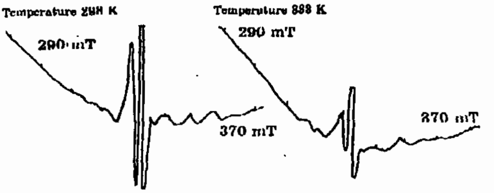

a) FVP : CHCl3 wt. ratio - 1:1

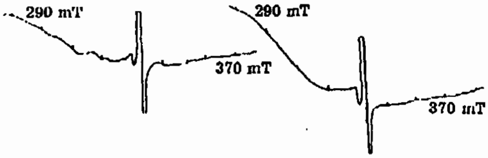

b) FVP : CHCl3 wt. ratio - 1:2

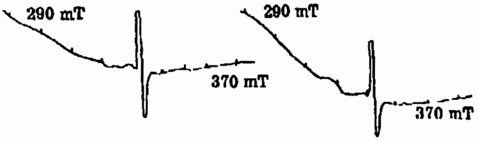

c) FVP : CHCl3 wt. ratio - 1:10

Fig. 4 (a,b,c). ESR-spectra for FVP-1 in chloroform obtained at different concentrations and temperatures

II. IR-SPECTROSCOPY

IR-spectra were registered by "SPECORD" M-80 (Germany) in sodium chloride cells. Recorded were review solution spectra in chloroform relative to chloroform as well as film spectra of the test samples obtained from chloroform solutions in KBr window relative to air. Detailed procedure features of IR-spectra recording are given in [6,9]. The aims of IR-studies were: i) to reveal structural fragments of the molecules included in FVP and responsible for their behaviour and ii) to study the changes in D_{opt} characteristic absorption bands under dilution in chloroform.

Table 2 and Figure 5 present the results of IR-spectroscopic studies. The analyses of IR-spectra made it possible the observations in the following range of wave numbers: 3600-3200; 1900-1500; 1400-1300 and 1100-800 cm^{-1}, respectively.

II. IR - SPECTROSCOPY

Table 2.

Reference of characteristic absorption bands for ODS solutions in chloroform studied by IR-spectroscopy

Wave number, cm^{-1}	Vibrations	Possible structures
3476	$>N-H$	pyrrol cycle
3382	$-OH$	hydroxyl group
1692	$C=O$	carbonyl group
1600	$C \overset{...}{=} C$	benzene rings
1308	$S=O$	sulfones, sulfonamides
1016	$R-O-C-O-R'$	acetoxy-group
868	$^{\nu}C-N$	nitro-, amino-groups
	$^{\sigma}C-H_{arom}$	

Relative change in optical absorption under dilution of FVP-1 in chloroform

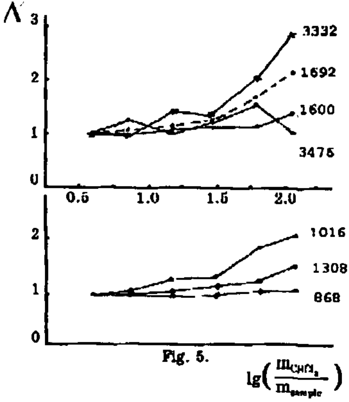

Fig. 5.

III. MICROCALORIMETRY

Thermodynamic characteristics (Q, J and ΔH, kJ/mol) of ODS samples dilution in chloroform were studied by differential microcalorimeter MKDP-2, designed at the Institute of Petroleum Chemistry RAS. The sensitivity of the device is $2x10^{-5}$ J. Detailed procedure of ODS microcalorimetric studies is given in [4,10]. The results of ODS microcalorimetric studies are given in Figs. 6-7 and in Tables 3-4. They were carried out under the conditions similar to those observed in ESR- and IR-spectroscopies.

III. MICROCALORIMETRY

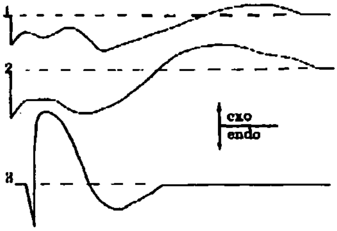

Fig.6. Dilution curves for ODS in chloroform at 298 K (ODS : $CHCl_3$ wt.ratio 1:10)

1- deasphaltizate
2- FVP-1
3- FVP-6

Table 3.

Enthalpies of ODS dilution in chloroform at different concentrations (298 K)

ODS : solvent wt. ratio	ΔH, kJ/ mol		
	deasphaltizate	FVP-1	FVP-6
1 : 10	+ 4.35 - 0.59	+ 4.59 - 1.16	- 6.07 + 2.24
1 : 20	+ 4.70 - 0.25	+ 4.21	- 6.75 + 0.20
1 : 30	+ 5.66 - 0.59	+ 3.45	- 2.29 + 3.20
1 : 40	+ 5.85	+ 5.87	- 3.35 + 0.54
1 : 100	+ 12.35	+ 4.28	- 4.28 + 4.94

the " + " sigh - endothermic process
the " - " sigh - exothermic process

III. MICROCALORIMETRY

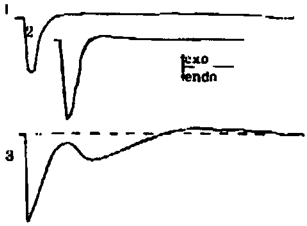

Fig.7. Dilution curves for ODS in chloroform at 333 K (ODS : $CHCl_3$ wt.ratio 1:10)

1- deasphaltizate
2- FVP-1
3- FVP-6

Table 4.

Enthalpies of ODS dilution in chloroform at different temperatures (ODS : $CHCl_3$ wt.ratio 1:10)

Test sample	Δ H, kJ / mol		
	Temperature, K		
	298	318	333
Deasphaltizate	+ 4.35 - 0.59	+ 4.28 - 0.36	+ 1.13 1.04
FVP-1	+ 4.59 - 1.15	+ 2.72 - 0.46	+ 1.08
FVP-6	6.07 + 2.24	- 5.08 + 3.37	+ 10.20 - 2.08

the " + " sigh - endothermic process
the " - " sigh - exothermic process

CONCLUSION

Thus the results of ESR-studies allow to conclude that FVP really differ in their paramagnetism and under external effects exhibit variable paramagnetic properties, i.e. their components are the carriers of ODS labile properties. FVP-1 was found to be the most susceptible to external changes. Under the conditions of separation this fraction had to contain compounds with low energy of diamagnetic-paramagnetic transitions. Biradicals are known to exhibit such paramagnetic properties in the initial state and in the solutions. They are likely included in a concentrate of separated molecules (FVP) and are responsible for their variable paramagnetism as well as for unstable thermodynamic equilibrium of ODS.

IR-studies were carried out to reveal structural fragments responsible for such FVP behaviour. Seven characteristic absorption bands have been indentified for all the separated FVP fractions. They differ only in their intensities. The lowest D_{opt} values were obtained for FVP-1 while the highest ones - for FVP-6. Based on elemental analysis and IR-spectroscopy it has been determined that the presence of cyclic and aromatic compounds of a polyconjugated type with S, N and O-containing fragments is typical for FVP. IR-spectra of FVP are similar and the differencies in the elemental compositions are insignificant. Based only on these data it was difficult to explain a great difference in fraction behaviours determined by ESR-spectroscopy. Therefore we carried out IR-studies of FVP relative to solution concentration in chloroform.

The comparison of data obtained by ESR- and IR-spectroscopies allowed: i) to define that for ODS solutions Lambert-Buger-Behr law becomes invalid and ii) to conclude that increasing solvent portion (by kT change) in the system intensifies intermolecular interactions bewteen solvent molecules and the components of supermolecular ODS structures. It results in the strengthened vibrations of atoms in structural fragments up to the break of separate bonds and/or to transition of a part of ODS molecules into a triple state. ESR- and IR-spectroscopes data indicate the proceeding of homolytic processes in ODS. The specific features of FVP behaviour are caused by biradical state of individual ODS components.

At present nitrite, hydrazile, phenoxyl, hydrocarbon and mixed bi- and polyradicals are well known. They include the following fragments:

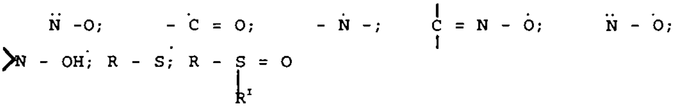

$$\ddot{N}-O;\quad -\dot{C}=O;\quad -\dot{N}-;\quad \overset{|}{\underset{|}{C}}=N-\dot{O};\quad \ddot{N}-\dot{O};$$

$$>N-O\dot{H};\quad R-\dot{S};\quad R-\underset{\underset{R^{I}}{|}}{\dot{S}}=O$$

and etc. corroborated by our studies.

Stable biradicals with similar fragments may be attributed to a group of "biradicals with heteroatoms", the non-paired electron of which is to a great extent located on S, N and O atoms. The presence of biradicals of "metal ketyls" group is also possible.

Microcalorimetric measurements of enthalpies of ODS dilution dependent on external factors (solvent amount, temperature) indicate that these processes proceed at low energies (1-15 kJ/mol). Dilution curves have complex profile of thermal effects of dilution, which can be explained by different rate of dilution for individual ODS components as well as by transformations of supermolecular structures in the solution after a complete dilution. Sign inversion (exo-, endo-) indicates deep character of the phenomena. Comparison of the data on the relative change in PMS concentration in the system and the data on the change in dilution enthalpies (ΔH, kJ/mol), obtained under similar conditions, indicates that the processes of dilution associate formation in ODS have a predominat-radical nature (endo-effects_, which intensify under external effects (change of kT system), i.e. depend on the initial concentration of PMS in ODS, different capacity of concentrates of FVP molecules to singlet-triplet changes, on the solvent type and solvent amount and on temperatures.

The authors consider the search for mechanisms intended to control homolytic processes proceeding in ODS to be a key to solve many problems of technological preparation, transportation and processing of high-viscous crude oil and heavy oil residues.

REFERENCES

NEUTRON SCATTERING CHARACTERIZATION OF ASPHALTENE PARTICLES

Min Y. Lin
Reactor Radiation Division, NIST, Gaithersburg, MD 20899
and
E.B. Sirota and H. Gang
Exxon Research and Engineering Co., Annandale, NJ 08801

Keywords: Asphaltene; particles; small angle neutron scattering

1. Introduction

The question of structure and association of asphaltene molecules in model solutions as well as in crude oils remains largely unanswered. It is however essential to the understanding of behavior of asphaltenes, specifically, their high viscosity. With small angle scattering techniques of neutrons and x-ray (SANS and SAXS), which probes length scales ranging from nanometers to near microns, it is possible to study the structure and aggregation behavior of asphaltene solutions, hence gaining the crucial information about their particle size, shape, physical interaction and phase behavior. Until recently, most such studies have concentrated on the basic asphaltene particles/micelles and their size, shape, while leaving larger size groups and long range correlations untouched, due to the difficulties of probing such long range length scales using SANS or SAXS. As a result, the high viscosity structure correlation of those solutions is still unclear.

In this work, we present first the conventional experimental data (momentum transfer Q > 0.01 Å^{-1}) obtained with SANS, which can be interpreted with a model of disk like shape for the basic asphaltene particles. These particles have an average radius of gyration around 40 Å. Even though the size distribution is fairly polydisperse, most of the particles are below 100 Å. At larger length scales (Q < 0.01Å^{-1}), high resolution SANS data show that the scattering profile continue to rise, suggesting large length scale correlation or large particles present. While the large length scale correlation is the popular explanation, we try to interpret it as the signature of the presence of large particles. Unfortunately, those particles are so large that no scattering technique currently can probe their Guinier range to directly measure their size. Indirectly, we estimate their size based upon scaling arguments.

2. Basic Particles

Figure 1 shows a typical scattering intensity profile obtained from a dilute asphaltene solution with SANS. The intensity I(Q) as a function of the momentum transfer Q is over a "conventional" small angle range, i.e., 0.006 < Q < 0.2 Å^{-1}. In this range, the data can be fitted with a model for the particles with certain shape and size distribution. While no model is unique[1], we use a model of disk-shape and a Shultz distribution for the radius. Except at the lowest Q, the fitted curve shown in Fig. 1 ia a good representative for the data. The fit results in an average radius (first moment of the radius distribution) a = 14 Å with a standard deviation of $\sigma = 92\%$, and the thickness of the disk is l = 20 Å.

The radius distribution is shown in Fig. 2. As can be seen, the distribution is rather broad. Indeed, if one uses the first moment to calculate the radius of gyration of the disk, it is

$$\langle R_g \rangle_1 = \left(a^2/2 + l^2/3 \right)^{1/2} = 11.5\ \text{Å},$$

which is quite small compared to the radius of gyration $\langle R_g \rangle_G$ obtained in a Guinier fit for the same data which is close to 40 Å. This is because that the Guinier fit represents a higher, different moment of the distribution.

The Shultz distribution has the following form: it is the product of a power law and an exponential decay:

$$P(r) = A\, r^{\alpha-1} \exp(-\beta r)$$

where $\alpha = 1/\sigma^2$, $\beta = \alpha/\langle r \rangle$, and A is a normalization constant. $\langle r \rangle$ is its first moment, and is typically used as the average. It can be shown that the nth moment is

$$\langle r^n \rangle = \langle r \rangle^n (\alpha+n-1)\ldots(\alpha+2)(\alpha+1)/\alpha^n$$

The Gunier radius of gyration is obtained as

$$(\langle R_g \rangle_G)^2 = -3 \frac{\partial}{\partial(Q^2)} \ln I(Q \to 0) = \langle m^2 R_g^2 \rangle / \langle m^2 \rangle.$$

For the disk model, it is related to the 6th moment, and therefore is

$$(\langle R_g \rangle_G)^2 = \langle r^6 \rangle / 2 \langle r^4 \rangle + l/3 = 47.8\ \text{Å},$$

which is more than 4 times larger than the first moment.

3. Large Size Particles

Even though the size distribution of the "basic" asphaltene particles are fairly broad, a typical particle size is well below 100 Å. The rheological property of the solutions can hardly be understood by the merely existence of these particles, if no further interaction or association of them is considered. However, in the Q range shown in Fig. 1, scattering intensity for concentration below 5% scales with the concentration, suggesting no interaction in the length scales probed[2]. The only interaction shown by SANS is the rise in intensity for $Q < 0.01$ Å^{-1}. Unfortunately, this has been largely ignored, mostly due to the limited range it is probed. However, it could be an important clue for the interaction or structure that is responsible for the macroscopic properties.

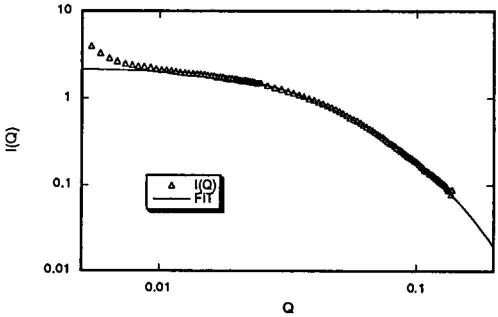

Fig. 1 SANS intensity as a function of Q. It was taken from a 2.5 wt% asphaltene (C7) solution in 1-methyl naphthalene-d10 at temperature 60 °C. The solid line is a fit with a disk-like particle shape. The distribution of the radius of the disk is shown in Fig. 2.

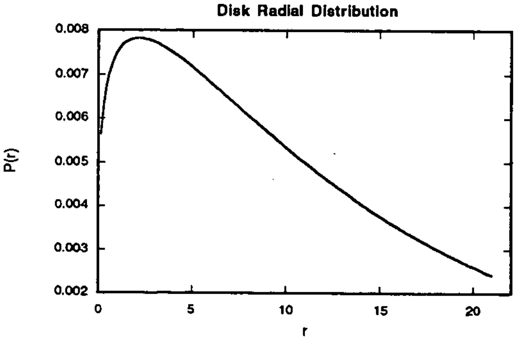

Fig. 2 Shultz distribution of the disk radius used to fit the data in Fig. 1. The average radius is <r> = 14 Å, and standard deviation is σ = 0.92.

In Fig. 3, we show two SANS data sets taken to Q below 0.005 Å^{-1}. In this extended Q range, the low-Q rise in intensity is more dominant. A quantitative analysis of the low-Q data in terms of the interactions of the basic particles is still difficult, although a fractal model has been proposed[3]. In our data, however, the slope shown at low Q is close to $s = -4$, the Porod slope, therefore it is not possible for a fractal structure (a mass fractal has $s > -3$, where $-s$ is the fractal dimension). On the other hand, a slope of -4 is typical for a compact object, in a Porod region of scattering intensity, much like those basic particles, which show a similar behavior, but at much larger Q (Q > 0.1 Å^{-1}), as shown also in the Figure. We can speculate that there are very large particles present in the solution, which could be compact aggregates of the basic, much smaller particles discussed above. However, the Guinier range of those large particles are in such a Q that is too small to measure by today's small angle scattering instruments. Light scattering would provide a right Q range, but the high absorption of light by those particles makes a light scattering measurement very difficult, if not impossible.

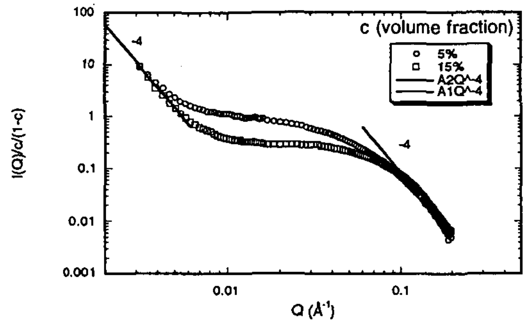

Fig. 3 SANS intensity normalized by the concentration for 5.0 wt% (circles) and 15 wt% (squares) in 1-methylnaphthalene-d10 at room temperature. At both lowest and highest Q ranges, the data show a -4 slope (Porod scattering).

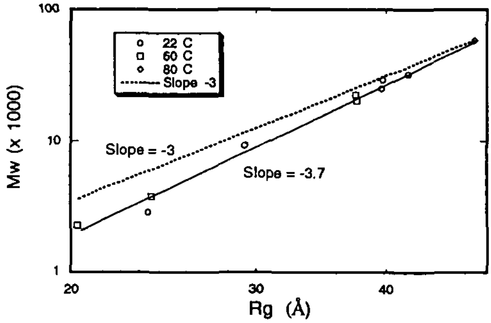

Fig. 4 Molecular weights and radii of gyration obtained from several solutions ranging from 0.5 wt% to 24 wt% at varying temperatures. Each point represents one solution at one temperature.

In Fig. 4, we plot the radius of gyration $<R_g>_G$ as a function of its molecular weight Mw (particle mass multiplied by the Avgadro constant) of the basic particle obtained for several solutions at different temperatures. While both $<R_g>_G$ and Mw are obtained from the same curve, they are actually independent. Although some of the solutions are higher than 5%, we assume that there are no interactions between the basic particles for both numbers to be meaningful. This assumption is related to, and consistent with the other assumption that the low Q behavior of the scattering is due to another group of particles with much larger sizes. Drawing a straight line through the points in the logarithmic plot, we find a slope of $s = 3.7$. Since $M \sim R^d$, where R and M are the size and mass of a particle, we should have $s = d$. The dimension d can never be larger than 3 in 3 dimension space where the asphaltene solutions are, unless the mass is not conserved.

This is actually consistent with the assumption that there are another group of mass present in the solution, and the total mass of the basic particles is indeed not conserved. It flows back and forth to the large size group, as conditions like concentration and temperature change. When concentration is increased or temperature lowered, there are more basic particles aggregated to form larger particles, resulting in a decrease of the total mass for the basic particles. If we assume both groups are compact particles ($d = 3$) as suggested by the slopes of -4 in Fig. 3, we can draw another line in the figure, with a slope of $s = d = 3$. The interception of the two lines is at a point taken from a 0.5 wt% solution at 80 C, where the low Q scattering is almost flat, suggesting no large size group present. The vertical distance between the two lines relative to the height of the upper line gives the percentage of mass missing from the smaller size group, and therefore is the percentage of mass residing in the large size group. Since we know the total concentration of the solution c, we then know from the graph c_1 and c_2, the concentrations of each group, as $c = c_1 + c_2$, the total mass *has* to be conserved.

Furthermore, the amplitude of the intensity in a Porod region is proportional to both concentration c and S/V, where the surface to volume ratio for most low aspect ratio objects is in turn proportional to $1/R_g$, its size inversed. Thus for the two groups in the same solution under certain temperature, we have

$$\frac{A_1}{A_2} = \frac{c_1 R_{g2}}{c_2 R_{g1}}$$

or

$$R_{g2} = \frac{A_1 c_2}{A_2 c_1} R_{g1}.$$

Since we know all the quantities on the right side, we can then calculate the larger size R_{g2}. For the 15 wt% solution, we obtain $R_{g2} \approx 9.7\ \mu m$. The size is fairly large, and we need independent verification.

4. Conclusion

We present an analysis for asphaltene solution data obtained with SANS that suggest the presence of two distinctive groups of particles, vastly different in their sizes. The "basic" group, while smaller in size, is the majority when the solution is very dilute and temperature is high. Their typical size is about 40 Å and is readily seen by SANS and SAXS. For the other group, the size is larger than 1000 Å and therefore is hard to probe even by high resolution SANS or SAXS. They are mostly results of the aggregation of the smaller-size particles when concentration is high and temperature is low. From thermodynamic point of view, it is not totally unreasonable. However, many questions remain, e.g., one of which is why no particles in the intermediate size range exist.

This analysis is in contradiction to the conventional understanding that the low Q behavior of the scattering merely reflects the interactions among the basic particles. More recently we performed experiments before and after dilute solutions were filtered with sub-micron filters, partially confirming the results of our analysis.

References

1. E.Y. Sheu, and D.A. Storm, in E.Y. Sheu and O.C. Mullins (editors) *Asphaltenes, Fundamentals and Applications*, Plenum Press, New York, (1993).
2. M.Y. Lin et al, unpublished.
3. J. Briant, G. Hotier, *Revue de l'Institut Francais du Petrole*, **38**(1), 83 (1983); and Y.C. Liu, E.Y. Sheu, S.H. Chen and D.A. Storm, *Fuel* **74**, 1352 (1995).

AN IMPROVED CHROMATOGRAPHIC METHOD FORTHE SEPARATION OF SATURATED HYDROCARBONS, AROMATIC HYDROCARBONS, RESINS AND ASPHALTENESFROM HEAVY CRUDE OILS

Carlos De La Cruz*; Nelson Márquez, Marcos Escobar and Soraya Segovia

Laboratorio de Espectroscopía Molecular y Atómica, and Laboratorio de Petroquímica y
Surfactantes, Departamento de Química, Facultad Experimental de Ciencias,
La Universidad del Zulia, Maracaibo-VENEZUELA.

Keywords: Heavy crude oils, resins, asphaltenes.

INTRODUCTION.

Two general chromatographic methods have been used to isolate molecular fractions from heavy crude oils. The first of these involves initially a n-paraffinic extraction of the maltenes (solubles) and asphaltenes (insolubles) from heavy crude oils, and later the liquid-solid chromatographic separation of the maltenes into saturated hydrocarbons and polar compounds such as "polar aromatics" and resins (1). The second chromatographic method involves the direct separation of saturated and aromatic hydrocarbons, resins and asphaltenes from heavy crude oils using appropriate solvents and adsorbents (2,3,4). The main disadvantage of both methods is the lack of reproducible results due to the very complex and similar resin and asphaltene molecular structures (5,6).

We report in this paper an improved chromatographic method for the separation of 5 molecular fractions from a typical heavy crude oil, and study the reproducibility of it. The isolated fractions are charaterized using UV-Visible and Atomic Absorption Spectroscopies. The results obtained with this method are compared with those of the standard literature.

EXPERIMENTAL.

Sample.

The heavy crude oil (10.3° API gravity) comes from the Boscán Field, near Maracaibo city, Venezuela. It was kindly provided without water and sediments by INPELUZ.

Chromatographic separation.

The chromatography consists of the extraction of 5 molecular fractions from an activated alumina (Brockman, Activity I, 80-200 mesh, Fisher, Pittsburgh-USA)/ alumina-impregnated heavy crude oil/ activated alumina in a 2.5 cm x 75 cm glass column. The elucidation of the fractions was based upon de Snyder polarities (7). The solvents, followed in brackets by their polarities, and fractions were:

(a) n-heptane (0,2)/ saturated hydrocarbons,
(b) 75:25 n-heptane:toluene (0,75)/ aromatic hydrocarbons I;
(c) Toluene (2,4)/ aromatic hydrocarbons II;
(d) 94:6 toluene:MeOH (2,57)/ resins;
(e) 13,3:26,7:60 MeOH: N,N Dimethyl formamide (DMF): CH_3CN(5,9) / asphaltenes.

The separation between saturated hydrocarbons and aromatic hydrocarbons I was monitored using a UV-lamp. The aromatic hydrocarbons I was a light yellow fraction. The aromatic hydrocarbons II, resins and asphaltenes were orange, black and black-brown fractions, respectively.

UV-Vis spectroscopy.

The UV-Vis spectra of the saturated hydrocarbons, aromatic hydrocarbons I, aromatic hydrocarbons II, resins, asphaltenes and vanadyl octaethylporphine (obtained fram Strem Chemicals, Newbutyport-USA; and used for quantification, see results and discussion below) in spectranalized CH_2Cl_2 were determined in a double-beam ratio recording Perkin Elmer Lambda 3B Spectrophotometer.

Atomic Absorption spectroscopy.

The Fe, Ni, and V contents of the resins, asphaltenes and standards of ferric chloride (Fisher, Pittsburgh-USA), metallic nickel (Fisher, Pittsburgh-USA), and ammonium metavanadate (Strem Chemicals, Newburyport-USA) were determined with a Perkin Elmer Atomic Absorption 3100 Spectrophotometer.

RESULTS AND DISCUSSION.

Table I shows the type of molecular fraction, the percentage of each fraction weight divided by the heavy crude oil weight (wt % original crude) and the Fe, Ni and V contents (in mg x Kg or ppm) of the last two fractions obtained using our chromatographic method. It also compares our results with those obtained from two standard chromatographic methods reported by ASTM (1) and Barwise and his co-worker (4).

TABLE I.
THE MOLECULAR FRACTIONS FROM A TYPICAL HEAVY CRUDE OIL.

Method	Molecular Fraction*	Wt % of Original Crude	Fe (ppm)	Ni (ppm)	V (ppm)	V-P** (ppm)
ASTM (1)	S	10,1				
	AR	13,8				
	R	27,2	40,4	132,2	814,7	624,8
	A	29,3	177,4	373,2	2884,2	1120,9
BARWISE (4)	S	32,8				
	AR	12,8				
	R	1,4?				
	A	24,3	334,4	195,6	3580,9	2065,6
THIS WORK	S	19,3				
	ARI	21,3				
	ARII	15,3				
	R	25,1	42,6	208,8	1560,6	1045,6
	A	11,3	124,8	325,5	3748,4	1540,4

* S: Saturated Hydrocarbons; AR: Aromatic Hydrocarbons, R: Resins; A: Asphaltenes.
** V-P: Vanadium in Porphyrins.

It is important to point out that the ASTM method starts with a n-pentane extraction of the maltenes and asphaltenes. Then the maltenes are fractionated into saturated hydrocarbons (i.e., paraffins and naphthenes) with n-pentane, and polar compounds (i.e., *polar aromatics* and resins) with a 50:50 benzene:acetone solution in two parallel assembled columns packed with Attapulgas clay (30-60 mesh) and clay/silica gel. Aromatics are calculated by difference, or alternatively they can be recovered using toluene. The Barwise method starts with an extraction of the saturated hydrocarbons with n-heptane, and then follows it with the extraction of the aromatic hydrocarbons, *Ni-porphyrins, V-porphyrins and a residual polar fraction (resins?)* with 80:20 n-heptane:CH_2Cl_2 solution, 50:50 n-heptane:CH_2Cl_2, CH_2Cl_2, 50:50 toluene: CH_3OH solution, respectively in a column packed with silica. We consider that the Ni-porphyrins and V-porphyrins form basically the asphaltene fraction.

The addition of the wt % of the original crude values for each method in Table I gives the following total recovery sequence: this work (92,3%, of which 55,9% corresponds to saturated and aromatic hydrocarbons, and 36,4% to resins and asphaltenes) > ASTM (80,4%, 23,9%, 56,6%) > Barwise (71,3%, 45,6%, 25,7%). Similarly, the atomic absorption spectroscopic sequence for the total Fe, Ni and V contents for each method is: this work (6010,7 ppm, of which 5309 corresponds to V) > ASTM (4422,1 ppm, 3698,9 ppm) > Barwise (4110,9 ppm, 3580,9 ppm). The V content can be divided into porphyrinic vanadium (V-P) and non-porphyrinic vanadium (8) using the Soret band at 409 nm in the UV-Visible spectra of the collected fractions and the model vanadium compound. This procedure indicates that our method removed 2586 ppm and 2723 ppm of porphyrinic and non-porphyrinic vanadium, respectively. The Barwise and ASTM methods removed (2065,6 ppm, 1515,3 ppm) and (1745,7 ppm, 1953,2 ppm), respectively. Table I shows that the porphyrinic and non-porphyrinic vanadium is found in the resinic and asphaltenic fractions. The UV-Visible spectra of these fractions show basically a very strong and sharp band at ca. 234 nm, two strong and very broad overlapped bands at ca. 274 nm and ca. 300 nm and the already mentioned Soret band (see for example the UV-Visible spectra of Figure I). The 234, 274 and 300-nm bands can be associated with condensed di-aromatic and poly-aromatic compounds that probably carry alkyl and alicyclic chains with heteroelements (i.e.

nitrogen, oxygen and sulfur). This indicates the intimate relationship between resins and asphaltenes, and the difficulty to obtain pure chromatographic fractions .

Finally, we had performed our chromatographic separation several times, and obtained very similar results to those reported above.

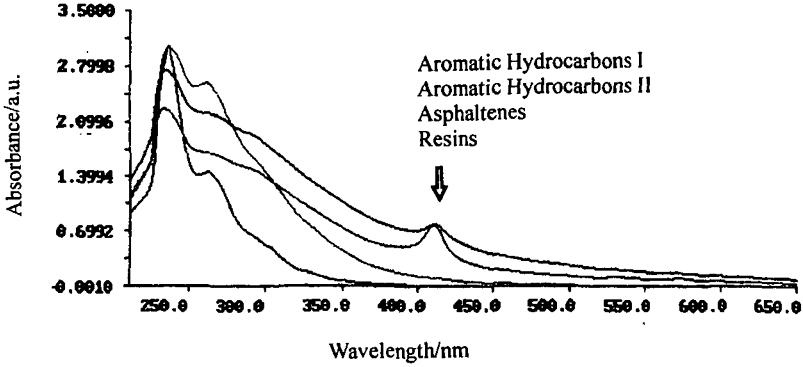

FIGURE I.
The UV-Visible spectra of the molecular fractions of a heavy crude oil.

ACKNOWLEDGMENTS

The authors would like to thank CONDES and CONICIT for providing financial support for this research.

LITERATURE CITED

(1) American Society for Testing and Materials, ASTM-D-2007-75, Annual Book of ASTM, Standard Part 37, 542 (1975).

(2) Osorio, E., Angulo, E., Segovia, S., Ysambertt, F, Márquez, N and De La Cruz, C., **Act. Cient. Venez.,** 45, 1 (1994).

(3) Márquez, N., Gall, C., Tudares, C., Paredes, J. and De La Cruz, C., **A.C.S. Preprints, Div. Petrol. Chem.,** 34, 292 (1989).

(4) Barwise, A. J.C. and Roberts, I., **Org. Geochem.,** 6, 167 (1984).

(5) Speight, J. G., **A.C.S. Preprints, Div. Petrol. Chem,** 34, 321 (1989).

(6) Mitra-Kirtley, S., Mullins, O.C., Van Elp, J., George, S.J., Chen, J. and Cramer, S. P., **J. Amer. Chem. Soc.,** 115, 252 (1993).

(7) Snyder, L. R., **J. Chromatogr. Sci.,** 16, 223 (1978).

(8) Ysambertt, F., Márquez, N., Rangel, B., Bauza, R. and De La Cruz. C., **Sep. Sci. Technol.** 30, 2539 (1995).

ANALYSIS OF SULFUR X-RAY ABSORPTION NEAR-EDGE SPECTROSCOPY IN ASPHALTENES, RESINS, AND MALTENES OF TWO DIFFERENT CRUDE OILS

Sudipa Mitra-Kirtley[*], Oliver C. Mullins[†], Corie Ralston[§], Dean Sellis[*], and Courtney Pareis[*]
[*]Rose-Hulman Institute of Technology, Terre Haute, IN 47803
[†]Schlumberger-Doll Research, Old Quarry Road, Ridgefield, CT 06877
[§]University of California, Davis, CA 95616

Keywords: XANES, sulfur, asphaltenes, resins, maltenes

Sulfur chemical structures present in crude oil products such as petroleum asphaltenes, resins, and maltenes obtained from two different oils have been determined using X-ray absorption near-edge structure (XANES) spectroscopy. Maltenes are pentane soluble portions, resins are pentane insoluble and heptane soluble portions, and asphaltenes are heptane insoluble portions of crude oil. The sulfur forms in these six fossil fuel samples are predominately organic; of them thiophene, sulfide and sulfoxide are the main contributors. One of the crude oils is known to have a high sulfoxide content; results from this study showed that there is a considerable amount of sulfoxide present in its asphaltene, resin, and maltene fractions. In spite of the fact that asphaltenes are known to be more polar than the other two fractions, and also that sulfoxide is a very polar chemical moiety, this structure is present in considerable amounts also in the resin and the maltene fractions of this particular crude oil. The second oil, lower in oxygen content, showed consistently less amount of sulfoxide in all its asphaltene, resin, and maltene fractions. Furthermore, no evidence for higher oxides such as sulfones, sulfonates, and sulfates are found in the three fractions of either of the crude oils.

INTRODUCTION

Asphaltenes, resins, and maltenes are some of the components of crude oil, and are of considerable interest.[1-3] The usual definition of these fractions are: maltenes are pentane soluble portions, resins are pentane insoluble and heptane soluble portions, and asphaltenes are heptane insoluble portions of crude oil. Asphaltenes are the heaviest, the next are resins, and the lightest parts of a crude oil are the maltenes. These fractions contain undesired heteroatoms; these heteroatoms are an issue in atmospheric pollution in the utilization of the resources. The study of heteroatoms, such as sulfur, in these components obtained from a particular crude oil is therefore of much interest, also in order to better understand the complex processes of crude oil formation.

Non-destructive and direct XANES spectroscopy methods have been very promising in analyzing the heteroatom structures of complex fossil-fuel samples. XANES spectroscopy has been recently employed to probe the chemical nature of sulfur in different fossil-fuel components[3] such as asphaltenes,[4-6] crude oils[7] and coal[8]. In asphaltenes the sulfur is found in mostly thiophenic and sulfidic forms, and the oxidized sulfur component in sulfoxide forms. In coal, sulfur exists in both organic and inorganic forms. Nitrogen XANES studies[9] on asphaltenes have shown that nitrogen occurs mostly in aromatic forms in pyrrolic and pyridinic forms.

In this study we present preliminary results of sulfur XANES spectroscopy on asphaltenes, resins, and maltenes obtained from two different crude oils. Several sulfur model compounds have been studied, and it is found that consistent with earlier results,[7] the s⇒p electronic transition peak in the XANES spectra vary in energies as the formal oxidation number of sulfur changes. The sulfoxide signature is well separated from the thiophenic signature, by about 3.00 eV. The organic sulfide peak also is separated from thiophenic peak by about 1.00 eV. The asphaltene fraction of one of the crude oils, CAL, is known to have a high sulfoxide content; the resin, and maltene fractions from this oil also consistently show much higher sulfoxide content than the three fractions from the other crude oil. In spite of the fact that asphaltenes are known to be more polar than the other two fractions, and also that sulfoxide is a very polar chemical moiety, this structure is present in considerable amounts also in the resin and the maltene fractions of this particular crude oil. Other forms of oxidized sulfur are not prominent in any of these samples.

EXPERIMENTAL

Our sulfur data have been collected at beamline X-19A at National Synchrotron Light Source at Brookhaven National Laboratory. We used a double crystal monochromator of Si (111) crystals. The model samples were first diluted in boric acid, finely ground, and then smeared on sulfur-free Mylar film; the fossil fuel samples were either ground and mounted on the film, or diluted in CCl_4 and smeared to dry on the film.

All sulfur models were obtained from Aldrich Chemical Company; they were dibenzyl sulfide, dibenzothiophene, thianaphthene, dibenzyl sulfoxide, iron(II) sulfide, potassium sulfate, and sodium thiosulfate. The fossil-fuel samples were asphaltenes, resins, and maltenes, obtained from CAL and KUW crude oils.

RESULTS AND DISCUSSIONS

Figure 1 plots the sulfur XANES of the asphaltene, maltene, and resin fractions obtained from CAL, KUW crude oils. Among the CAL suite, the most prominent region is around 2475.1 eV; the shoulder of this peak at around 2472.1 eV is quite prominent in all these samples. From the KUW suite, the most prominent feature occurs at 2472.1 eV, and the feature at 2475.1 eV is much less prominent. Thus from raw data it is evident that the structure with its s⇒p transition peak at 2475.1 eV is more abundant in the CAL suite than in the KUW suite. This trend is present in all the three fractions belonging to the same oil.

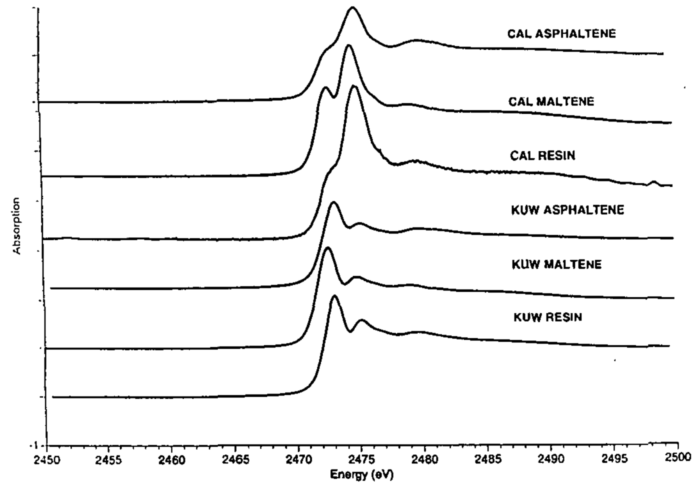

Figure 1: Sulfur XANES spectra of the asphaltene, maltene and resin fractions of CAL and KUW crude oils.

Figure 2 shows the XANES plots of several sulfur model compounds, studied by Waldo et al.[7] As mentioned earlier, the most prominent peak of a structure represents the s⇒p electronic transition peak. This figure shows that the different sulfur structures have s⇒p peaks located at different energies; these peaks shift to higher energies as the formal oxidation number of sulfur in the structure increases. As the formal oxidation number of sulfur in a structure increases, the electronics in the atom are more tightly bound to the nucleus, and it takes a larger energy to make the s⇒p transition. Our calibration procedure has resulted in a shift from these data by a few eV, but both the data sets show the same relative energy differences between the different sulfur structures. Dibenzyl sulfide, which has a formal oxidation number of zero, shows its prominent peak at 2474 eV (2471.1 eV in our case). Thiophene also has a formal oxidation number of zero, but the signature peak is shifted slightly from that of the sulfide, and occurs at 2475 eV (2472 eV in our case). The sulfoxide structure has a formal oxidation number of +2, and shows its signature peak much separated from the other two, at 2478 eV (2475.1 eV in our case).

XANES spectra of a maltene from the two different oils are shown in Figure 3. It is seen that the first peak of the KUW maltene appears at 2472.1 eV, the same energy as the main peak of our dibenzothiophene spectrum, and this feature appears only as a shoulder in the spectrum of CAL asphaltene. This leads one to the obvious conclusion that sulfoxide is present in larger percentage in CAL asphaltene than in the KUW sample.

A least-squares fitting program has been used in order to quantitatively analyze all the sulfur data. All the spectra of models and the fossil-fuels were first normalized with respect to the respective step heights, and then fit to a sum of several Lorentzian peaks and an arctangent step. The peaks specify bound to bound electrnic transitions, whereas the step signifies electronic transition tot he continuum. In order to be consistent, we held the width and the position of the steo function constant till the very end of the fitting procedure. We subtracted from the fossil-fuel spectra any secondary contribution from a structure appearing at the same energy as the s→p transition from a different structure.

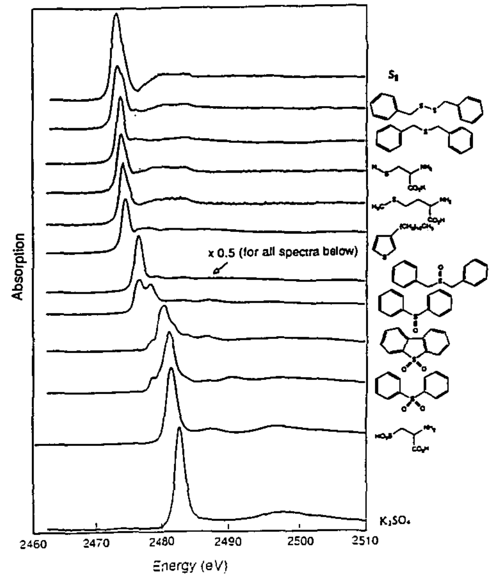

Figure 2: Sulfur XANES spectra of several model compounds[7]. The s→p transition peaks are blue shifted as the formal oxidation number of the structure increases.

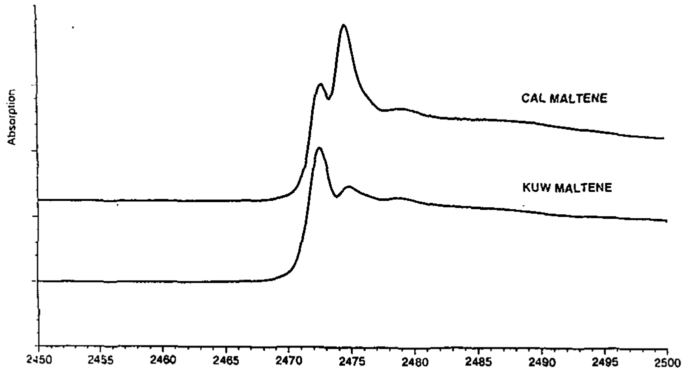

Figure 3: Sulfur XANES spectra of the maltene fractions from CAL and KUW. The differences in the resonance structures are very prominent.

Preliminary results of the sulfidic, thiophenic, and suloxide content of the asphaltenes, resins, and maltenes obtained from CAL and KUW crude oils show that the sulfoxide percentage in the CAL samples are higher not just in its asphaltene fraction, but also in the resin and maltene fractions. Asphaltene is known to be more polar than resin and maltene, and sulfoxide also has a very polar structure. It is interesting to note that in spute of this, all the CAL fractions showed higher sulfoxide percentages. Presence of high oxides, such as sulfone, and sulfate, in any of these samples was insignificant. There was no evidence of any inorganic sulfur structures in these samples.

CONCLUSIONS

Sulfur XANES spectroscopy is a very powerful way to ascertain the different chemical structures present in a complex material both qualitatively and quantitatively. Asphaltene, maltene, and resin extracted from CAL, which has a high sulfoxide content, all show consistently high sulfoxide percentages. Higher oxides of sulfur, such as sulfones, and sulfates are not present in significant quantities in any of these samples.

REFERENCES

1. G. V. Chilingarian, T. F. Yen, Editors, "Bitumens, Asphalts, and Tar Sands," Elsevier Scientific Publishing Co., New York (1978).

2. J. G. Speight, "The Chemistry and Technology of Petroleum," Marcel Dekker, Inc., New York (1980).
3. O. C. Mullins, Chapter 2, "Alphaltenes, Fundamentals and Applications," E. Y. Sheu, O. C. Mullins, Editors, Plenum Publishing Co., New York (1995).
4. G. N. George, M. L. Gorbaty, J. Am. Chem. Soc., 111, 3182 (1989).
5. M. L. Gorbaty, G. N. George, S. R. Kelemen, Fuel, 69, 945 (1990).
6. G. S. Waldo, O. C. Mullins, J. E. Penner-Hahn, and S. P. Cramer, Fuel, 71, 53 (1992).
7. G. S. Waldo, R. M. K. Carlson, J. M. Moldowan, K. E. Peters, J. E. Penner-Hahn, Geochimica et Cosmochimica Acta, 55, 801 (1991).
8. G. P. Huffman, S. Mitra-Kirtley, F. E. Huggins, N. Shah, S. Vaidya, and F. Lu, Energy and Fuels, 5, 574 (1991).
9. S. Mitra-Kirtley, O. C. Mullins, J. vanElp, S. J. George, J. Chen, and S. P. Cramer, J. AM. Chem. Soc., 115, 1, 252 (1993).

MAYA PETROLEUM ASPHALTENE IMAGING BY SCANNING TUNNELING MICROSCOPY: VERIFICATION OF STRUCTURE FROM ^{13}C AND PROTON NUCLEAR MAGNETIC RESONANCE

G. W. Zajac*, Amoco Corporation, N. K. Sethi and J. T. Joseph, Amoco Petroleum Products, P. O. Box 3011, Naperville, IL 60566.

Keywords: scanning tunneling microscopy, NMR structure, Maya asphaltene

Introduction

Petroleum resids are generally upgraded to higher value products by hydroprocessing. This process, however, is very demanding because of the highly aromatic nature of the constituent molecules, high metal and heteratom content. Most of the problems associated with resid upgrading are attributed to the presence of asphaltenes. Asphaltenes are generally believed to be the precursors of coke formation during resid processing, limiting the kinetics and economics of the process.

Asphaltene structure has been extensively investigated in the past (Speight, 1980; Strausz et al., 1992; Herzog et al., 1988; Ravey et al., 1988; Sheu et al., 1992; Storm, 1991). These studies have provided a global picture of asphaltene structure, which explains general asphaltene reactivity under thermal and catalytic conditions. Because of the dependence of the asphaltene structure on the origin of the crude oil, we performed a detailed study of this particular Maya asphaltene. This work describes a study focused on Maya asphaltenes, using carbon-13 and proton NMR and scanning tunneling microscopy.

NMR - STM Analysis - Experimental, Results & Discussion

The asphaltene sample used in this study was obtained by heptane precipitation from Maya vacuum resid and its preparation has been discussed in detail previously (Zajac, Sethi and Joseph 1994). The virgin asphaltene sample was analyzed by carbon-13 and H-1 NMR in solution on a Varian VXR-300 spectrometer operating at 300 Mhz proton frequency. Deuterated chloroform was used as the solvent. The asphaltene sample was completely soluble in chloroform. The solubility was confirmed by filtration through a 1 μm millipore filter that left no residue. The details of the analysis are discussed in our previous work (Zajac, Sethi and Joseph, 1994).

The average aromatic cluster parameters for virgin Maya asphaltene (heptane insolubles) were estimated from combined high resolution H-1 and C-13 NMR and atomic H/C data. Possible structural features of the virgin asphaltene molecule that include cyclic and linear aliphatic carbon atoms are illustrated in Figure 1. Three possible structural units of the virgin asphaltene are shown where the aliphatic sidechains repeat units range from n=1-5. Though no direct evidence of the precise structure groups that contain heteratoms, N, S, O etc., is available, these are assumed to be part of the ring structure, e.g., thiophenic functional groups for S. These NMR derived structural models form the basis of input for the scanning tunneling microscopy study.

The precipitated virgin asphaltene was diluted in THF to a concentration of 1-5 μg/ml which at the average molecular weight for the asphaltenes corresponds to a submonolayer coverage on an appropriate substrate if agglomeration does not occur. We have employed freshly cleaved highly oriented pyrolytic graphite (HOPG) as a substrate. Several microliters of the dilute solution are micropipetted on the surface and dried in dry nitrogen. A Digital instruments Nanoscope II equipped with a side viewing stereo microscope is employed. The tunneling tips are electrochemically AC etched tungsten (250 μm) in 1 M KOH which are subsequently rinsed in distilled water and stored in alcohol. The tunneling conditions were typically 100-600 mV bias voltage and 0.5-2.0 nA tunneling current.

Scanning tunneling microscopy is a direct real space probe of structure. The structure of adsorbates on model surfaces resolved at the molecular level has been applied to a number of systems (see e.g. Chiang, 1992). In an ambient environment, STM studies of the adsorption geometry of alkylcyanobiphenyl on graphite has resolved the individual aromatic groups and alkyl chains (Smith et al., 1990; Mizutani et al., 1990). Previous STM imaging of Rawati asphaltenes (Watson and Barteau, 1994) at high concentrations (1, 5 x 10^{-2} wt%) in pyridine has indicated the self-assembly nature of the alkyl sidechains with large regions of self-assembled asphaltenes.

A typical 140 Å image of a cluster of asphaltenes is shown in Figure 2. The atomically resolved graphite substrate is visible and a group of asphaltenes are observed as the higher contrast regions. The dimensions are measured as full widths of the observed current pertubations. In Fig. 2, a typical measurement sets the scale of such features ~ 13 Å. Another view of 102 Å STM image of a similar cluster of several asphaltenes is presented in Figure 3, the highlighted feature is of order ~ 12 Å. Because of the heterogeneous nature of this material it is difficult to distinquish aggregates versus individual structural units. Despite this difficulty we attempted a detailed measurement over twenty-four separate entities which were clearly isolated structures in approximately ten individual images yielding an average full width dimension of 10.4 Å ± 1.9 Å. A comparison is made to a random set of ten measurements from the possible NMR-derived asphaltene structural units shown in Figure 1, excluding the aliphatic sidechains. The measurements were made by calibration of the C-C bond length at 1.42 Å and making several measurements across the condensed ring portion of the three structural units presented. The average NMR dimension derived in this manner is 11.1 Å ± 1.4 Å for the condensed ring portion of the possible structural models. The reasonable agreement obtained between the NMR structural models and the STM observation argues in favor of the NMR molecular models.

An example of the heterogeneity in the distribution that we observe by STM is shown in Figures 4 & 5 where we find small structures in the presence of much larger structures. The larger structure shown in Fig. 4 of a 62 Å field of view is interesting for it appears to be comprised of three separate structural units which are individually < 20-30 Å. It is not clear if the large structure is an aggregate of three smaller units or a single structure connected by aliphatic linkages. Although we do not have evidence for the existence of aliphatic sidechains, there is weak fine structure existing in the vicinity of many of the structures that we observe. At low bias voltages aromatic structures would be emphasized and aliphatic regions suppressed, hence we might be biasing our observations toward the aromatic structures.

Summary and Conclusions

The C-13 and proton NMR analysis predicts small 6-9 ring condensed aromatic ring structural units with aliphatic sidechains for the virgin Maya asphaltene. The comparison of NMR structural models and STM direct observation reveals an agreement between the distribution of aromatic cluster sizes predicted and observed. The broad distribution ranges from several condensed rings to large macromolecular structures in excess of 30-50 Å. This study works in a very dilute limit (1-5 x 10^{-3} wt%). During hydroprocessing NMR has shown condensation reactions to occur and that the average aromatic cluster size grows in size and number. One is tempted to extrapolate to the high concentration regime where very large aggregates and self-assemblies might dominate and form the basis of coke precipitation during the hydroprocessing process.

References

Chiang, S. Molecular Imaging by STM in Scanning Tunneling Microscopy II, H. J. Guntherodt and R. Wiesendanger (Eds.) Springer-Verlag, New York. 1992, 181.

Herzog, P.; Tchoubar, D. and Espinat, D. Macrostructure of asphaltene dispersions by small angle x-ray scattering. Fuel 1988, 67, 245.

Mizutani, W; Shigeno, M.; Ono, M. and Kajimura, K. Voltage-dependent scanning tunneling microscopy images of liquid crystals on graphite. Appl. Phys. Lett. 1990, 56, 1974.

Ravey, J. C.; Ducouret, G. and Espinat, D. Asphaltene macrostructure by small angle neutron scattering. Fuel 1988, 67, 1560.

Sheu, E. Y.; DeTar M. M.; Storm, D. A. and DeCanio, S. J. Aggregation and kinetics of asphaltenes in organic solvents. Fuel 1992, 71, 299.

Smith, D. P. E.; Horber J. K. H.; Binnig, G. and Nejoh, G. Structure, registry and imaging mechanism of alkylcyanobiphenyl molecules by tunneling micrsocopy. Nature 1990, 344, 641.

Speight, J. G. The Chemistry and Technology of Petroleum Marcel Dekker, New York, 1980.

Storm, D. A.; Barresi, R. J.; DeCanio, S. J. Colloidal nature of vacuum residue. Fuel 1991, 70, 779.

Strausz, O. P.; Mojelsky, T. J.; Lown, E. M. The molecular structure of asphaltene: an unfolding story. Fuel 1992, 71, 1355.

Watson, B. A. and Barteau, M. A. Imaging Petroleum Asphaltenes using Scanning Tunneling Microscopy. Industrial and Engineering Chemistry Research 1994 33, 2358.

Zajac, G. W.; Sethi, N. K. and Joseph, J. T., Molecular Imaging of Petroleum Asphaltenes by Scanning Tunneling Microscopy: Verification of Structure from ^{13}C and Proton Nuclear Magnetic Resonance Data, Scanning Microscopy, 1994, 8, 463-470.

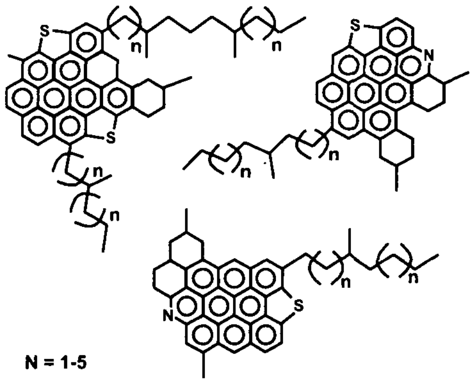
S
S
n
n
n
n
S
N
n
n
N
S
n
n
N = 1-5

Figure 1
The 13C and proton NMR derived average structural units in Maya asphaltenes.

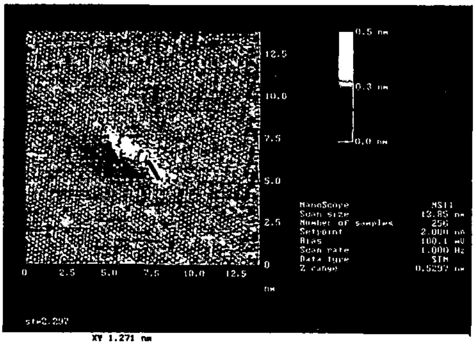
12.5
10.0
7.5
5.0
2.5
0
0 2.5 5.0 7.5 10.0 12.5
nm
0.5 nm
0.3 nm
0.0 nm
NanoScope NSII
Scan size 13.85 nm
Number of samples 256
Setpoint 2.000 nA
Bias 100.1 mV
Scan rate 1.000 Hz
Data type STM
Z range 0.5297 nm
st=2.297
XY 1.271 nm

Figure 2
A constant current STM 140Å view of graphite at atomic resolution with a cluster of asphaltenes appearing as bright current spots(V_T=100mV, I_T=2.0 nA). The white line marker indicated at bottom measures ~13Å.

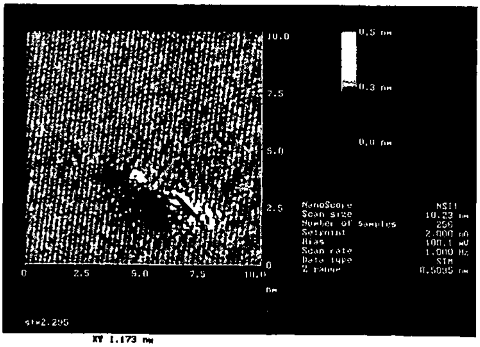
10.0
7.5
5.0
2.5
0
0 2.5 5.0 7.5 10.0
nm
0.5 nm
0.3 nm
0.0 nm
NanoScope NSII
Scan size 10.23 nm
Number of samples 256
Setpoint 2.000 nA
Bias 100.1 mV
Scan rate 1.000 Hz
Data type STM
Z range 0.5035 nm
st=2.295
XY 1.173 nm

Figure 3
A constant current STM 102Å view of graphite at atomic resolution with a cluster of asphaltenes, (V_T=100mV, I_T=2.0 nA). The marker indicates a dimension of ~12Å.

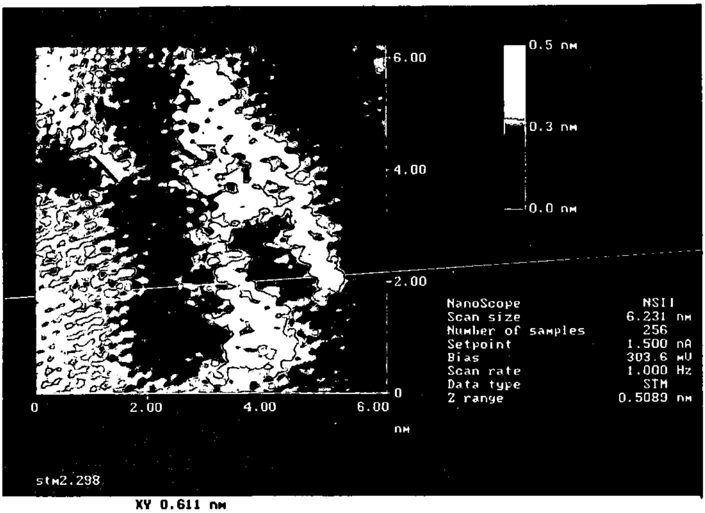
6.00
4.00
-2.00
0
0
2.00
4.00
6.00
nm
0.5 nm
0.3 nm
0.0 nm
stm2.298
XY 0.611 nm

NanoScope NSII
Scan size 6.231 nm
Number of samples 256
Setpoint 1.500 nA
Bias 303.6 mV
Scan rate 1.000 Hz
Data type STM
Z range 0.5089 nm

Figure 4
A constant current STM 62Å view of a large aggregated cluster of asphaltenes, (V_T=304mV, I_T=1.5 nA). The marker indicates an isolated structure of ~6Å.

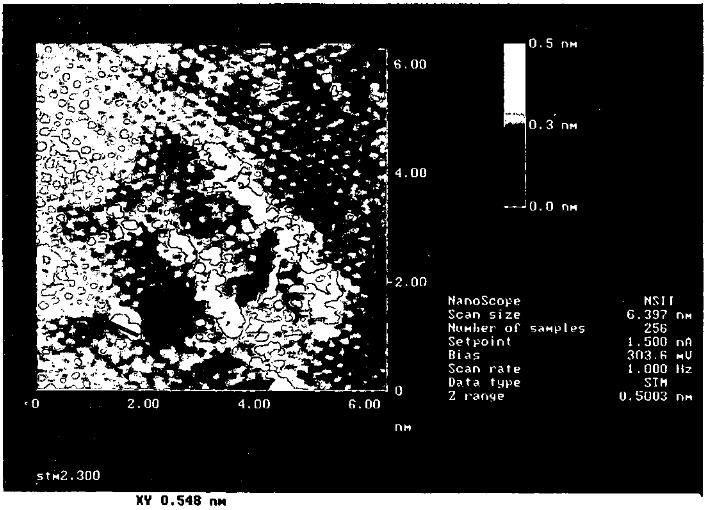
6.00
4.00
2.00
0
0
2.00
4.00
6.00
nm
0.5 nm
0.3 nm
0.0 nm
stm2.300
XY 0.548 nm

NanoScope NSII
Scan size 6.397 nm
Number of samples 256
Setpoint 1.500 nA
Bias 303.6 mV
Scan rate 1.000 Hz
Data type STM
Z range 0.5003 nm

Figure 5
A constant current STM image of 64Å field of view on graphite of another asphaltene cluster, (V_T=304mV, I_T=1.5 nA). The marker measures an isolated structure of ~5.5Å.

CHARACTERIZATION OF ASPHALTENES FROM PROCESSED RESIDS

Jerry E. Hunt and Randall E. Winans
Argonne National Laboratory, Chemistry Division
Argonne, IL 60439 USA
Jeffrey T. Miller
Amoco Corporation, Naperville, IL 60566

Keywords: asphaltene, ring size, molecular weight

Introduction

The current and future trend for petroleum processing is towards conversion of heavier and heavier fractions into useful products such as gasoline and diesel. Asphaltenes, the heptane insoluble fraction of heavy oils, are a solubility class and not a specific boiling range. They tend to be the hardest fraction to process in the refinery because of their high molecular mass, aromaticity and heteroatom and metal (S, N, Ni, V) content. Molecular characterization of asphaltenes is important since a more thorough understanding of the chemical nature of the constituents should lead to more efficient processing schemes.

A major hurdle in the accurate representation of the molecular structure of asphaltenes has been the determination of the molecular weight. The main problem is the formation of molecular aggregates depending upon factors such as polarity of the solvent, temperature, concentration and others. Over the past 15 years or so, the apparent molecular weight of asphaltenes has dropped significantly lower as the cause and effect of aggregation on molecular weight was determined. Molecular weights as high as 500,000 have been reported for some asphaltenes in the past with weights as low as 600 appearing in the literature recently depending on the analytical method used.[1-2]

The problem of molecular aggregation has been studied by a number of techniques [5-11] including SAXS and SANS. Using SANS, Thiyagarajan, *et al.* [12] found that at room temperature that asphaltenes are highly ordered rod like species with lengths up to 500Å. As asphaltene samples are heated up, these large aggregates are broken up into smaller rod like species with average lengths of less than 100Å at temperatures of above 50°C. Further shrinkage of the aggregates occurs when the asphaltene is heated to 340-400°C resulting in spherical particles with radii of about 12Å. Returning the sample to 20°C resulted in a low intensity signal implying irreversible thermochemistry. Espinat, *et al.* [14] also using SANS, found that the size of the colloidal asphaltene particles decreased with increasing temperature or with increasing dilution with resin material and increased with the addition of n-hexane. Finally, Storm, *et al.* [13] found by SAXS that for asphaltenes from several sources at 93°C that the colloidal particles had an average radii of 30-60 Å. They also found that the average particle size was independent of the heteroatom content of the asphaltene. The exact mechanism by which aggregation occurs has not been established.

Recently mass spectrometry has been used to determine a limiting lower value for the molecular weight for asphaltenes. This technique found that the upper limit for the molecular weight of Ratawi asphaltene was 814 versus 2360 from VPO. The upper limit for an asphaltene from the Alaskan North Slope was determined to be less than 1270 versus 3248 from VPO. High resolution mass spectrometry (HRMS) is a well-established technique for determination of composition of petroleum distillates by compound types. HRMS provides exact mass measurement of molecular and fragment ions, allowing distinction of molecular of equal nominal mass but of different double bond equivalents. The exact mass measurements also allow classification of hydrocarbon (saturated and unsaturated) and sub-classification into heteroatom-containing (e.g., nitrogen, oxygen and sulfur) molecules. In this paper we use high resolution sector field mass spectrometry to determine the comparative speciation of the composition of the asphaltenes from resid subjected to processing conditions.

Experimental

The resid was obtained by vacuum distillation of an asphaltene rich Maya crude oil. Asphaltenes were isolated by addition of a 40:1 excess of *n*-heptane to the Maya resid in toluene at 50 °C. The suspension was stirred overnight and filtered. The *n*-heptane was distilled from the filtrate to obtain the deasphalted oil (DAO). The yield of DAO was 83% of the resid. The precipitate was dissolved in a minimum of toluene and re-precipitated with a 40:1 excess of *n*-heptane. This precipitate was filtered, washed with *n*-pentane, and vacuum dried at 100 °C. The yield of asphaltene was 27% of the resid. The resid was processed under hydrotreating conditions at 425°C with 2000 psi H_2 with 0.05 weight per cent organic Mo catalyst. The extent of the reaction was monitored by GC methods.

A Kratos three-sector MS-50 mass spectrometer was used to obtain high resolution mass spectra of asphaltenes. The full-scan high-resolution (dynamic resolution of 10,000-40,000) electron ionization (EI) mass spectra were acquired with a Kratos MS50TA triple sector tandem mass spectrometer of EBE design. High boiling perfluorokerosene was introduced via a heated inlet. Calibration to mass 900 was routinely achieved at a scan rate of 10 s/decade. The source temperature was 250 °C. Ionization method was the electron impact (70 eV). The samples were inserted into the source on a high-temperature probe. The accelerating voltage was a nominal 8 kV. The spectra were collected and recorded on the MACH 3X data system. Group analysis for all scans with ions above background was averaged and only those which occur a minimum of at least four times was saved. Formulae which fit within ±3.5 millimass units are assigned for each averaged ion peak. The formulae are sorted by hydrogen deficiency and heteroatom content. Absolute response factors for each type of compound are not available, equal molar ionization sensitivities are assumed for all homologs in the analysis.

Results

The mass spectra from the asphaltene fraction generally show ion intensity from 100 to almost 850 amu. The average mass of the observed spectra is about 400 amu. While this does not represent the average molecular mass when one takes into consideration that fragmentation occurs under electron impact conditions, for very aromatic species electron impact is a good indicator for molecular distributions. When the fact that asphaltenes are highly aromatic (C_a~60%) is taken in account, the distributions may be only 50 to 100 amu higher. The elemental analysis calculated from the high resolution mass spectral data are in good agreement with those from traditional techniques, with aromaticity values slightly lower for the mass spectral data. This means that the mass spectral data is representative of the actual sample. Furthermore, at lest 90% of the asphaltene is volatilized in to the mass spectrometer.

In the high resolution mass spectrum thousands of peaks can be measured. This number of peaks makes reducing the data into a more manageable form necessary. The double bond equivalent (dbe) and the heteroatom content can be calculated from the exact mass data without any assumptions. Sulfur combinations may be misrepresented, but oxygen and nitrogen should not have a high probability of misrepresentation. However, the elemental analysis data extracted from the mass data show that these errors are minimal. Detailed distributions of asphaltene sulfur and nitrogen organic molecules as a function of double bond equivalent for three processing levels (35%, 70% and 85%) are shown in Figure 1.

Several features are readily apparent. First, the mass limit of the ions (~800 amu) suggests that the ring size may be as high as 10 rings. Second, the sulfur containing species are processed fairly efficiently. Heteroatomic sulfur in benzothiophenes (dbe=6) is particularly well removed by processing as almost no dbe=6 is observable in the most processed sample (compare Fig. 1A and Fig. 1C). Likewise those sulfur species of dbe=9, of which dibenzothiophenes are a possibility, are processed efficiently. However, the larger S-containing species in the range of 12-35 dbe are unchanged or even concentrated under these processing conditions. Based on the mass spectral exact mass formulae, the following structures are suggested:

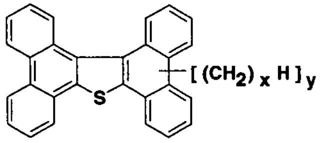

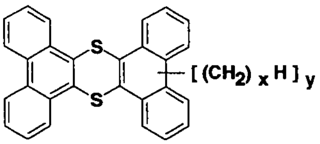

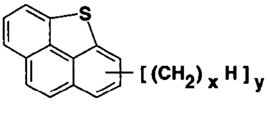

The y in the structures means that multiple substitution is observed in the mass spectrum and the x means that the chain length can vary.

The number of isomers of each species is quite high and mass spectrometry alone cannot discern them. A two-sulfur structure consistent with mass spectral data is also shown.

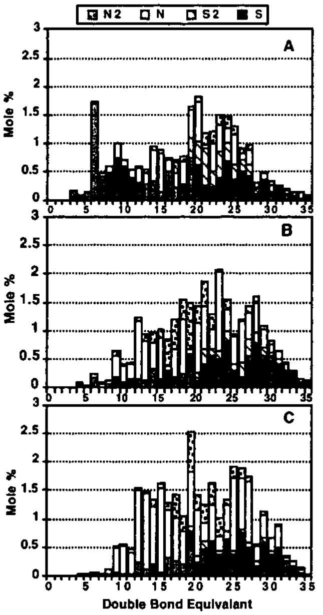

Figure 1. Sulfur and Nitrogen containing species for asphaltenes from processed resids. A, asphaltenes from 30% conversion; B, 70% conversion; C, 85% conversion.

Figure 2 shows the mass spectra for the three conversion levels of processing for a double-bond equivalent of 9. Although this class of molecules make up a small fraction of the total of the samples (~ 0.15 mole %), we can follow the processing on a molecular class basis. The asphaltenes in the 35% processed resid sample (Fig. 2A) show species from m/z 300 to 700, in addition to fragment and molecular species in the 180 to 250 range. These high mass species correspond to dibenzothiophenic structures with either multiple alkyl substitutions or chain lengths or combinations of both.

Chromatographic separation or tandem mass spectrometry could identify which combinations of chain length and substitution are present. Further processing as shown in Fig. 2 tends to shorten the chain length of the molecule leaving only few short chains on the molecule. We suggest that the most resistant molecules are probably those that are substituted at positions adjacent to the sulfur.

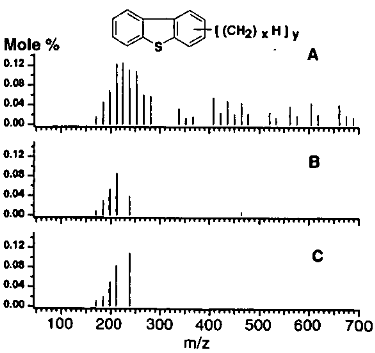

Figure 2. The mass distribution of sulfur-containing, double-bond equivalent=9 species. A, asphaltenes from 35% conversion; B, 70%; C, 85% conversion.

Nitrogen-containing species show a similar pattern to the sulfur pattern, but with one notable exception. The nitrogen species are much more resistant to processing. They are essentially untouched and perhaps concentrated. A similar pattern of multiple-alkyl substitution is found. Multiple nitrogens in rings systems are also present. Examples of suggested structures for the nitrogen-containing species follow:

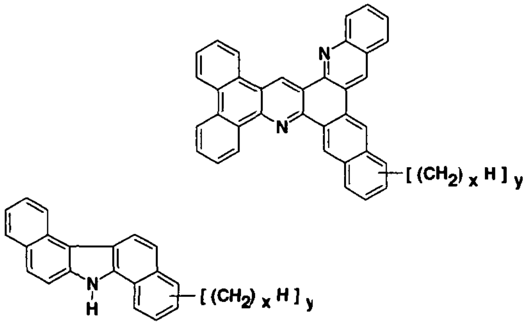

Such structures differ markedly from those published elsewhere. Others have shown more condensed structures. Our data do not support more condensed ring systems, but rather more open ring systems.

Hydrocarbon molecules are also found in the processed asphaltenes. As processing severity increases the mass intensity shifts to larger aromatic rings systems. The existence of hydrocarbons, while surprising may be explained in terms of the separation and aggregation properties of the asphaltenes. Asphaltenes are separated only by precipitation. As the asphaltenes precipitate they form aggregates which may trap hydrocarbons. In addition, if the asphaltenes aggregate under processing conditions, some of the aggregate may escape hydrotreating, leaving sources of large aromatic hydrocarbons in the asphaltene fraction.

Conclusion

Our mass spectral studies of asphaltenes from hydrotreated resid have shown them to be highly aromatic and present as extended open ring systems as high as 11 rings. Sulfur containing species with ring sizes smaller than 5 rings are effectively processed, while larger ring systems are more resistant to processing. The heteroatom containing species in the asphaltenes are multisubstituted with alkyl chains. Processing tends to remove the alkyl chains and/or reduce their, leaving the core ring system.

Acknowledgment

This work was performed under the auspices of the U. S. Department of Energy, under contract number W-31-109-ENG-38. This work was supported by a CRADA agreement between Amoco Corporation and Argonne National Laboratory under the U. S. Department of Energy-Bartlesville, Fossil Energy Project.

References

1. Dickie, J. P. and Yen, T. F.; *Anal. Chem.*, **39**, 1847 (1967).
2. Speight, D. A.; Wernick, D. L.; Gould, K. A.; Overfield, R. E.; Rao, B. M. L.; and Savage, D. W.; *Rev. Inst. Fr. Pet.*, **40**, 51 (1985).
3. Moschopedis, S. E.; Fryer, J. F.; Speight, J. G.; *Fuel*, **55**, 227 (1976).
4. Speight, J. G.; *Amer. Chem. Soc., Div. Fuel Chem., Prepr.*, **25**, 155 (1980).
5. Pfeiffer, J. P.; Saal, R. N.; *J. Phys. Chem.*, **44**, 139 (1940).
6. Ray, B. R.; Witherspoon, P. A.; Grim, R. E.; *J. Phys. Chem.*, **61**, 1296 (1957).
7. Dwiggins, C. W. Jr.; *J. Phys. Chem.*, **69**, 3500, (1964).
8. Dickie, J. P.; Yen, T. F.; *Anal. Chem.*, **39**, 1847 (1967).
9. Overfield, R. E.; Sheu, E. Y.; Sinha, S. K.; Liang, K. S.; *Fuel Sci. Technol. Int.*, **7**, 611 (1989).
10. Sheu, E. Y.; DeTar, M. M.; Storm, D. A.; DeCanio, S. J.; *Fuel*, **71**, 299 (1989).
11. Anderson, S. I.; Birdi, K. S.; *J. Colloid Interface Sci.*, **142**, 496 (1991).
12. Thiyagarajan, P.; Hunt, J. E.; Winans, R. E.; Anderson, K. E.; and Miller, J. T.; *Energy and Fuel*, **9**, 829 (1995).
13. Storm, D. A.; Sheu, E. Y.; DeTar, M. M.; *Fuel*, **72**, 977 (1993).
14. Espinat, D.; Ravey, J. C.; Guille, V.; Lambard, J. Zemb, T.; Cotton, J. P.; *J. De Phys. IV*, **3**, 181 (1993).

TLC-FID IN QUANTITATIVE HYDROCARBON GROUP TYPE ANALYSIS (HGTA) OF ASPHALTENES AND OTHER HEAVY FOSSIL FUELS

Vicente L. Cebolla, Jesús Vela, Luis Membrado, and Ana C. Ferrando
Departamento de Procesos Químicos
Instituto de Carboquímica, CSIC
P.O. Box 589, 50080 Zaragoza, Spain

Keywords: TLC-FID, petroleum asphaltenes and other heavy fossil fuels, TLC-scanning UV

INTRODUCTION

Thin-Layer Chromatography with Flame Ionization Detection (TLC-FID) is mostly used in fossil fuel chemistry for quantitative hydrocarbon group type analysis (HGTA) (1-3). From an instrumental point of view, polemics about quantitative results have been reported with regard to different detector designs and sample application systems (4). Moreover, inadequate sample selection with respect to volatility properties have caused some confusing results. In order to validate TLC-FID, results should be confirmed using other techniques. On the other hand, quantitation in Chromatography is performed by previous calibration because evolution of responses of different compounds with sample load depends on each detector. Calibration becomes difficult because of the complexity of fossil fuels. Thus, the most used absolute calibration method is time-consuming, and new rapid and quantitative procedures should be developed.

In this work, instrumental performances of a modern TLC-FID system were first tested on pure *n*-alkanes and several polycyclic aromatic compounds (PACs). Detector linearity was evaluated in function of sample load and scan speed, as well as absolute response factors of the standards. Thus, criteria were developed for accurate application of TLC-FID with regard to sample volatility. Likewise, measurements of chromarod and flame temperatures permit the evaluation of whether an evaporation of compounds outside the H_2 flame can take place. In a second step of the research, TLC-FID results *from absolute calibration* (comparing Medium Pressure Liquid Chromatography MPLC, and other alternative methods for fraction isolation: preparative TLC and Solid Phase Extraction, SPE), and *from an alternative, fast calibration* procedure (based on a variety of the internal normalization method, VINM) were compared for different fossil fuels including asphaltenes. Repeatability and ranges for VINM application for each type of sample are reported. Finally, results from TLC-FID were validated using TLC-dual wavelength scanning UV.

EXPERIMENTAL

Standards and products analyzed. Several *n*-alkanes, polycyclic aromatic hydrocarbons (PAHs, from 3 to 6 rings), heteronuclear-PACs, and hydroxy-PACs were used as standards (Across Chimica, Belgium). The studied fossil fuels were: *a heavy oil* (450°C+ vacuum Brent residue); several *petroleum asphaltenes*: a raw one (RAsph), their derived n-butylated asphaltene (BuAsph) and that treated with C_6H_5-CH_2 radical ($PhCH_2$ Asph), using reductive alkylation; *a coal-derived product,* obtained from hydroliquefaction of a Spanish coal at 430°C for 30 min, under a N_2/H_2 atmosphere, without solvent, and subsequently extracted with DCM.

TLC-FID runs. Procedure details have been reported in previous works (2, 5). Sample application (0.2-2 μL) was carried out using a 3202/IS-02 automatic sample spotter, (SES, Germany). Chromatographic separation was performed on S-III chromarods (silicagel, 5 μm particle size, 60 Å pore diameter). Quantification of peaks was carried out using an Iatroscan Mark 5 TLC-FID apparatus (Iatron Labs). Acquisition and treatment of data were carried out as reported elsewhere (5).

Samples were solubilized in DCM (15 mg mL^{-1}). Chromarods were developed after sample application, using two different elution sequences:

1) in the case of the studied heavy oil, n-hexane (38 min), toluene (3 min), DCM/methanol 95/5 v/v (30 sec). The following peaks were separated (± 0.01 min): saturates (retention time, r.t.: 0.18 min), aromatics (r.t.: 0.29 min), polars (r.t.: 0.39 min), and uneluted (r.t.: 0.47 min), and

2) in the case of the studied coal hydroliquefaction product and petroleum asphaltenes, n-hexane (38 min), toluene (20 min), and DCM/methanol 95/5 v/v (5 min). Peaks from sequence 2 were (± 0.01 min): saturates (r.t.: 0.14 min), aromatics (r.t.: 0.24 min), polars (r.t.: 0.36 min), and uneluted (r.t.: 0.48 min).

The amounts (μg) of the studied PACs reported throughout the text correspond to the mass effectively injected. The response of a given standard is defined as its corresponding area counts ($\mu V\ s^{-1}$), A. The response factor of each standard is defined as A per mass unit, m (μg). Only absolute response factors are used throughout this paper.

Flame and chromarod temperature measurements. These were made using a data acquisition system consisting of two thermocouples (Thermocoax, type K, 0'5 mm diameter, for the flame, and Thermocoax, type S, 1 mm diameter, for the chromarods), a Fluke Hydra 2620 multichannel data acquisition unit, and an HP-95 handheld computer to receive and store the data. A serial RS-232-C connection was used to send the data from the data acquisition unit to the computer.

Isolation of fractions for absolute calibration. *Preparative TLC* was carried out on a silicagel aluminium sheet (20 x 20 cm, 0.2 mm layer). Aromatic fraction was developed using toluene, and polar fraction using DCM/methanol 95/5, v/v. *Solid Phase Extraction (SPE)* was carried out on silicagel. Samples were preadsorbed in $CaCO_3$ using DCM. This solvent was further removed at 50°C under vacuum (15 mbar). The powder was placed on the top of a polypropylene syringe which contained 5 g of silicagel. Subsequently, 20 ml of toluene, and 40 ml of DCM were consecutively eluted through.

Purity of fractions were monitored using either TLC-FID or TLC-scanning UV.

TLC-scanning UV. Silicagel plates were also used. Eluants used for development were the same as in the case of TLC-FID. UV scanning was carried out using a Shimadzu CS9301PC densitometer, and its corresponding data acquisition and treatment software. Wavelength working range was 200-700 nm. Linear scanning in reflectance mode was used.

RESULTS AND DISCUSSION

TLC-FID instrumental performances with regard to quantitation

Given that one of the aims of this work was to evaluate the performance of TLC-FID technique without interferences related to the inherent volatility of the solutes, rubrene (5,6,11,12-tetraphenylnaphthacene) was chosen to allow an in-depth study of FID linearity, apart from the above-mentioned standards. Rubrene has a high Molecular Weight (MW= 532) and low volatility (i.e., $6.373*10^{-6}$ mm Hg at 171°C). Repeatability of absolute response factors (as RSD %, which was measured at 5 µg of sample load) was, in general, lower than 5 for all the standards, regardless of their volatilities.

Linearity was evaluated with regard to sample load and scan speed (Tables 1 and 2, Figure 1). Responses of standards were adequately fitted to logarithmic regressions in the whole mass range studied (0.1-12 µg) because deviations from linearity were found at sample loads lower than 1 µg. For the lowest mass range (< 1 µg), repeatabilities were worse (11% *RSD*) than those obtained at higher sample loads (< 5% *RSD*), and this should be considered when a quantitative analysis is to be done. For sample loads higher than 1 µg, linear regressions provide adequate regression coefficients and intercepts, with low relative errors.

A particular possibility of TLC-FID is to vary the scan speed. Fitting of responses at different scan speed showed the same pattern that those previously mentioned. As scan speed decreases: i) FID response also decreases, and ii) a greater deviation from the linearity for sample loads lower than 1 µg was found. Similar response factors were obtained using 30 or 35 s $scan^{-1}$. In the case of the slowest speeds (i.e., 60 s $scan^{-1}$), smaller, although linear, signals were obtained. This could be used in order to inject higher sample loads in cases in which a given mass saturates the detector.

Preliminary results, obtained from the measurements of chromarod and flame temperatures seems to indicate that volatilization of rubrene prior to combustion should not take place.

Criteria about sample volatility limits for TLC-FID analysis can be developed using pure standards. Although the absolute response factors vary for different petroleum fractions (saturates, aromatics, and polars), and for different homologous series of pure compounds, *they are reasonably uniform for alkanes longer than C_{24}, and aromatics with 4 or more rings*. In the case of alkanes studied, the response factor of n-C_{24} (0.1 mm Hg vapor pressure at 150°C) was 0.718, and that of a saturate fraction (C_{32+}) from a heavy oil was 0.801. n-Alkanes shorter than C_{24} (vapor pressures higher than 0.3 mm Hg at 150°C) showed significantly lower response factors. In the case of PAHs, response factors were near to unity for four or more-ringed standards, and for an aromatic fraction obtained from a heavy oil.

Calibration methods and quantitative TLC-FID results

The absolute calibration method is usually performed when a quantitative HGTA of fossil fuels is required. Thus, fractions isolated from the fossil fuel itself are used as external standards for each peak. MPLC is mostly used for fraction isolation. This is time-consuming although it is convenient when further characterization of peaks must be done using other external techniques. As well, linearity of responses for each standard is not a necessary condition for the application of this method.

A fast calibration method based on a variety of the internal normalization (VINM) was applied to several coal and petroleum products, in previous works (2, 5, 6). Its basis is as follows: if the FID response of each peak in a given sample versus the *mass of whole sample* can be linearized (*with forced zero intercept*), then this calibration procedure is theoretically equivalent to the absolute calibration. Therefore, *area percentage from the chromatogram is equal to mass percentage in the problem sample within the linear zone.* VINM is a quantitative, quality-control oriented procedure and no useful when preparative amounts of fractions are required. However, the tedious prefractionation required in the absolute calibration of fossil fuels is substituted for a rapid TLC-FID screening of several different masses of the whole sample, which can be done in 1 or 2 Iatroscan runs

(2-3 hours, and mililiters of eluants).
The agreement between both calibration methods for the studied asphaltenes is presented in Table 3. In this case, the isolation of fractions for absolute calibration was carried out using preparative TLC, instead of MPLC. Table 4 also shows an agreement between both calibration procedures for another type of sample: a coal hydroliquefaction product. Likewise, the use of either preparative TLC or SPE for absolute calibration gave similar results. These techniques save time when compared to that of MPLC (hours vs days) when absolute calibration is necessary.

Quantitative application of VINM for asphaltenes and other fossil fuels

Table 5 shows the linearity ranges from VINM in the case of the studied asphaltenes, and, for comparative purposes, in the case of a heavy oil. In this table, repeatability is expressed as a mass range semi-interval (± wt.%) for 95 % confidence level. A previous work (2) demonstrated that mass range semi-intervals for each peak from a heavy oil were narrower than those tolerated using the ASTM D2007. Furthermore, TLC-FID experiments are fast, and ASTM D2007 consists of a time-consuming preparative MPLC with a previous removal of asphaltenes.
Linearity from VINM is usually accomplished in restricted mass intervals, and the analyst has to choose the range of application depending on the obtained regression coefficients. Likewise, the range of sample load for application of this procedure depends on the sample nature. It must be stressed that this linearity interval refers to the whole sample and not to the mass of each fraction. Although regression coefficients are not good for the studied asphaltenes, experimental results confirmed the equivalence between the the two calibration procedures.
After performing the calibration and choosing the best linearity zone for each sample according to the regression coefficients, sufficient amount of sample must be applied onto the system in order to obtain quantitative results. Sample loads must be sufficiently high for the mass of each peak (taking into account its proportion) to be greater than 1 µg. As previously reported, masses lower than 1 µg present RSD % of nearly 11, and deviations from the linearity.
All the studied products present ranges more than sufficient for quantitative purposes in view of the small sample loads usually spotted using this technique.

Validation of TLC-FID results using an external technique (TLC-scanning UV)

As previously mentioned, TLC-FID is limited, to some extent, by volatility considerations. Although results from absolute calibration and VINM are in accordance, this would not necessarily imply that they are the true results. For this reason, results from TLC-FID were validated in this work using HPTLC-scanning UV with absolute calibration using the corresponding fractions as external standards. These were fractionated from the products using preparative TLC. Volatility is not a limitation for quantitative application of spectroscopic techniques, such as UV.
As samples used for validation must not contain alkanes, which do not absorb in the wavelength range used, one product without alkanes was chosen for validation test. Table 4 presents the agreement between the results from TLC-FID using both absolute calibration and VINM, and from HPTLC-scanning UV.

ACKNOWLEDGEMENTS

The authors are grateful to Spanish DGICYT (Project PB93-0100) and ECSC (European Steel & Coal Community, Project 7220-EC/765) for their financial support, and also Dr. R. Bacaud (CNRS, Villeurbanne) for fruithful discussions, and Dr. R. Gruber for providing asphaltene samples.

REFERENCES

1. Selucky, M.L. *Anal. Chem.* **1983**, *55*, 141.
2. Vela, J.; Cebolla, V.L.; Membrado, L.; Andrés, J.M. *J. Chromatogr. Sci.* **1995**, *33*, 417.
3. Barman, B.N. *J. Chromatogr. Sci.* **1996**, *34*, 219.
4. Shanta, N.C. *J. Chromatogr.* **1992**, *624*, 21.
5. Cebolla, V.L.; Vela, J.; Membrado, L.; Ferrando, A.C. *Chromatographia* **1996**, *42*, 295.
6. Cebolla, V.L.; Membrado, L.; Vela, J.; Bacaud, R.; Rouleau, L. *Energy & Fuels* **1995**, *9*, 901.

Table 1.- Linearity of FID detector with sample load.

Sample	**Linear Regression**	**Logaritmic regression**
n-Tetracosane	A = 663.4 * m - 19.26 (r = 0.9977)	Log A = 0.9363 * Log m + 2.849 (r = 0.9973)
Phenanthrene	A = 677.5 * m - 228.7 (r = 0.9977)	Log A = 1.105 * Log m + 2.719 (r = 0.9990)
Benzo-a-pyrene	A = 975.9 * m - 111.5 (r = 0.9986)	Log A = 1.0747 * Log m + 2.927 (r = 0.9973)
Fluorene	A = 573.0 * m - 102.0 (r = 0.9934)	Log A = 1.144 * Log m + 2.629 (r = 0.9972)
Fluoranthene	A = 886.0 * m - 390.5 (r = 0.9977)	Log A = 1.148 * Log m + 2.796 (r = 0.9991)
Pyrene	A = 761.2 * m + 205.4 (r = 0.9905)	Log A = 1.0747 * Log m + 2.895 (r = 0.9925)
Rubrene	A = 1074 * m -53.79 (r = 0.9990)	Log A = 1.084 * Log m + 2.976 (r = 0.9979)

Table 2.- Error percentage[1] of linear and logarithmic regression in the case of rubrene for different scan speds and sample loads.

	Linear Regression				
	Scan Speed (s scan $^{-1}$)				
Masa	*25*	*30*	*35*	*50*	*60*
0.6	-4.69	-11.93	-36.94	-61.55	-48.67
1.8	1.32	0.48	-0.72	-3.7	-5.2
2.9	0.14	-2.95	-4.65	-1.54	-7.36
4.1	5.22	1.64	3.23	-3.45	-7.73
5.3	-3.59	-0.06	-0.32	3.02	-6.54
Reg. Coef[2]	0.9979	0.9996	0.9984	0.9974	0.9923
	Logarithmic Regression				
0.6	-0.16	-0.45	-1.23	-2.08	-2.08
1.8	0.16	0.8	1.88	2.8	3.07
2.9	-0.06	-0.13	0.05	0.86	0.44
4.1	0.55	0.1	0.12	-0.81	-1.17
5.3	-0.51	-0.35	-0.96	-1.09	-0.6
Reg. Coef	0.9993	0.9993	0.9967	0.9942	0.9946

[1] Error % between the corresponding experimental value and that predicted from the corresponding fitting curve.

[2] Regression coefficient obtained in the mass range 0 - 5.3 µg.

Table 3.- Absolute and VINM calibration of petroleum asphaltenes using TLC-FID.

	Calibration method	***Aromatics***	***Polars***	***Uneluted***
RAsph	VINM	1.5	30.7	67.8
	Absolute Calibration	*1.8*	*33.8*	*64.4*
BuAsph	VINM	11.5	69.9	18.9
	Absolute Calibration	*13.0*	*68.0*	*19.1*
PhCH$_2$Asph	VINM	23.4	64.7	11.9
	Absolute Calibration	*20.9*	*67.1*	*12.0*

Table 4.- Validation of results for a coal hydroliquefaction product.

	TLC-FID			
	Isolation method	Aromatics	Polars	Uneluted
Absolute calibration	*TLC*	29.0	62.6	8.4
	SPE	30.6	60.4	9.0
VINM		31.2	60.7	8.1
	TLC-UVVIS			
Absolute Calibration	Isolation method	Aromatics	Polars	Uneluted
	TLC	30.1	62.2	7.7

Table 5.- Linearity intervals and repeatability from VINM (TLC-FID) of the studied asphaltenes and a heavy oil.

Sample	Average of Area* percentage (n=5)	95 % Confidence interval (wt%.±)	Usable linearity Interval (μg)**	Regression Coefficient (r)
RAsph				
Saturates	---	---	1 - 11.2 μg	---
Aromatics	1.5	1		0.8837
Polars	30.7	0.8		0.9935
Uneluted	67.8	1.2		0.9968
BuAsph				
Saturates	---	---	1 - 14.2 μg	---
Aromatics	11.5	2.3		0.9298
Polars	69.9	1.8		0.9824
Uneluted	18.9	1.2		0.9954
PhCH$_2$Asph				
Saturates	---	---	1 - 9.1 μg	---
Aromatics	23.4	2.6		0.9161
Polars	64.7	4.7		0.9993
Uneluted	11.9	2.9		0.9748
Heavy Oil				
Saturates	33.2	0.63	1 - 20.6 μg	0.9994
Aromatics	57.4	0.74		0.9931
Polars	12.9	0.19		0.9758
Uneluted	0.5	0.09		0.9697

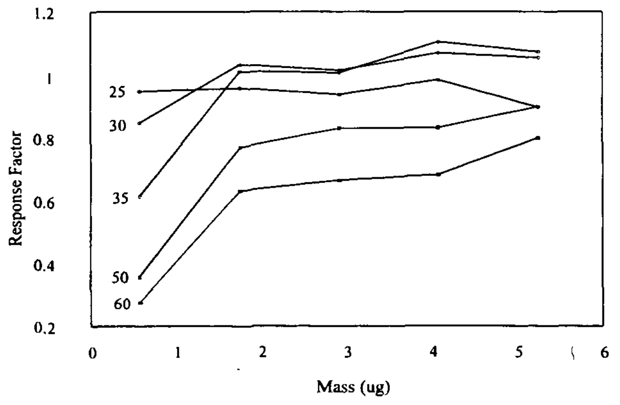

Figure 1.-Response factors (A/m) in the case of rubrene for different scan speeds and sample loads.

ASPHALENE SELF-ASSOCIATION - A COMPUTER SIMULATION STUDY

P.S. Subramanian and Eric Y. Sheu
Fuels and Lubricants Technology Department,
Texaco Inc., P.O. Box 509,Beacon, NY 12508

Key Words: Asphaltene, Molecular dynamic simulation, Aggregation

INTRODUCTION

Self-association of asphaltenes and the resulting colloidal-like particle structure, polydispersity, and other physical properties have drawn great scientific attention in the past decade. They are relevant to oil production, transportation and refining. One key question is yet to be answered is the energies that are involved in the self-association process. From thermodynamical point of view, the conventional micellization process is mainly driven by the hydrophilicity-hydrophobicity imbalance. Other energies, such as packing, double layer interacting, etc., often play minor roles only. The self-association of asphaltenes appear to be very different. Asphaltenes are defined based on the solubility. Their molecular structures are not unique. The molecules often consist of various degree of polynuclear aromaticity. No distinctive hydrophilic and hydrophobic portions in the molecules can be identified. Additionally, asphaltenes only self-associate in the organic environment with low permmittivities. This amounts to saying that the hydrophilicity-hydrophobicity imbalance should not be the governing factor, and that the interactions between molecules are short ranged. In the past decade, experiments, theories and computer simulations have been reported on this issue [1-3]. Good progress has been made, however, the fundamental understanding of the self-association mechanism is still lacking.

In this study, we performed a molecular dynamic simulation to study the self-association process. The aim is to identify the governing energy in this association process. One difficulty in this simulation is to mimic the real systems. It requires in-depth knowledge of the system. In our case, we chose the Ratawi vacuum residue (VR) derived asphaltene as the system. Ratawi VR asphaltene have been well studied in our laboratory. Data regarding its elemental analysis, chemical properties, and physical properties are readily available for us to construct the molecular structures, distribution and the initial configuration of the simulation.

COMPUTATIONAL DETAIL

The simulation consists of 64 asphaltene molecules ranging in size from 3 rings to 11 rings structure. The ring distribution was based on the Gaussian distribution with the peak at the 7 ring structure [4]. Two systems were modeled. One at a concentration of 0.015 wt % (below the critical micelle concentration, CMC) and the other at 5 wt % (above CMC). The size of the cell was chosen to represent the system at the desired densities. With the above concentrations, the corresponding cell dimensions are 743.0 Å and 108.8 Å respectively. The molecular dynamic (MD) simulation was performed using CERIUS2 [5]. The molecules were placed randomly in the cell using the amorphous cell module in the Cerius2 package to define the initial configuration. This was followed by energy minimization. During the energy minimization process, the Dreiding force field was used to account for both inter- and intra-molecular interactions except the electrostatic ones [6]. A dielectric continuum of 3.5 was used to model the solvent. Dreiding Force field was not used to compute the electrostatic interactions because it calculates the monopole-monopole interactions only. One can still use the Dreiding Force field for computing electrostatic interactions, provided the monopole-monopole interactions calculated can represent a good estimate of the intramolecular dipole moments. We tested several computation packages on this issue. We used charge equilibration, MOPAC6 [7], and CHARMM [8] to compute the electrostatic interations, then evaluate the dipole moments estimated and compared with the experimental values. Single ring and double ring molecules as the test cases. MOPAC6 was found to be far superior to the other two packages as far as dipole moment representation is concerned. We thus calculated the electrostatic charges using MOPAC6. The MD simulation was lasted for 250 picoseconds (ps) where the system energy starts to be stable.

RESULTS AND CONCLUSION

Figure 1 and 2 show the simulation results for the 0.015 wt % and 5 wt % respectively. As one can see, the 0.015 wt % does not show significant self-association. Dimers do exist, but no large aggregates are observed. On the other hand, the 5 wt % shows aggregates of various sizes. F (see figure 2) is a small aggregate while B, C, D and E are large ones of different shapes. Their common feature is the short range stacking phenomenon. The maximum stack observed contains approximately 7 asphaltene molecules. This was predicted by Yen based on the solid phase compounds. In solvent, these stacks appears to preserve. However, the stacks are loose and somewhat irregular (see D in figure 2). Aggregate B is a good example. It consists of many short range stacks linked loosely together. As a result the aggregate does not show well defined cylindrical shape. It appears more like a sphere. This is also true for aggregate A, C and E. Aggregate D is more like a cylinder although the stacking direction changes after 7th molecules. We also found a monomer in this simulation (unmarked molecule in Figure 2) which may or may not be significant. In order to evaluate the importance of the dipole-dipole interaction, we used the charges obtained from charge equilibration method to compute the electrostatic contribution, which under estimate the dipole moments for simple molecules. The result shows a collapse of the molecules into a single huge aggregate. Since experimental data from small angle neutron scattering (SANS) and small angle X-ray scattering (SAXS) [1,9] have indicated the average size of the aggregates to be approximately 30 ?, the occurrence of a collapse single aggregate phase should not be the case. This indicates, at least indirectly, that dipole-dipole interaction must play an important role in controlling the self-association process.

From the nucleation process point of view a system can undergo nucleation only when the dipole moment of the system is zero. If a non-zero dipole moment is introduced, the nucleation process would be terminated at a some point and the nucleation process would not be complete. This seems to be the case in asphaltene self-association process. The self-association of asphaltenes can be viewed as a nucleation process. It is initiated when concentration exceeds the CMC [9]. At the beginning stage, the molecules stack to form cylindrical-like aggregates. This process is then terminated partially due to non-homogeneous molecular structures which makes the stacks loose, but mainly due to non-zero dipole-dipole interactions. As a result, the phase separation occurs only at microscopic length scale, similar to a micelle solution, though the energies involved are completely different. The dipole moments can arise from the structural arrangement of the atoms in the molecules and the heteroatoms (Nitrogen, sulfur, nickel, vanadium etc.) that are commonly found in asphaltenes.

[1] For reference, see Asphaltene and Asphalts, Developments in Petroleum Sciences, edited by T. F. Yen and G. V. Ghilingarian, Elsevier, Amsterdam, (1994).
[2] J. G. Speight, The Chemistry and Technology of Petroleum, 2nd ed.; Marcel Dekker, New York, (1991).
[3] I. Kowalewski, M. Vandenbroucke, A. Y. Huc, M. J. Taylor, and J. L. Faulon, Energy & Fuels, 10, 97 (1996).
[4] C. Y. Ralston, S. Mitra-Kirtley and O. C. Mullins, Energy & Fuels, 10, 623 (1996).
[5] Cerius2 is marketed by BIOSYM/Molecular Simulations Inc., 9685 Scarnton Road, San Diego, California, USA.
[6] Mayo, S. L.; Olafson, B. D.; Goddard III, W. A. J. Phys. Chem. 1990, 94, 8897.
[7] MOPAC6 is a semi empirical package available from Quantum Chemistry Program Exchange (QCPE), Indiana University.
[8] CHARMm (Brooks, B. R.; Bruccoleri, R. E; Olafson, B. D.; States, D. J. ; Swaminathan, S.; Karplus, M., J. Comput. Chem., 1983, 4, 187).
[9] E. Y. Sheu, J. Phys. : Condens. Matter 8, A125 (1996).

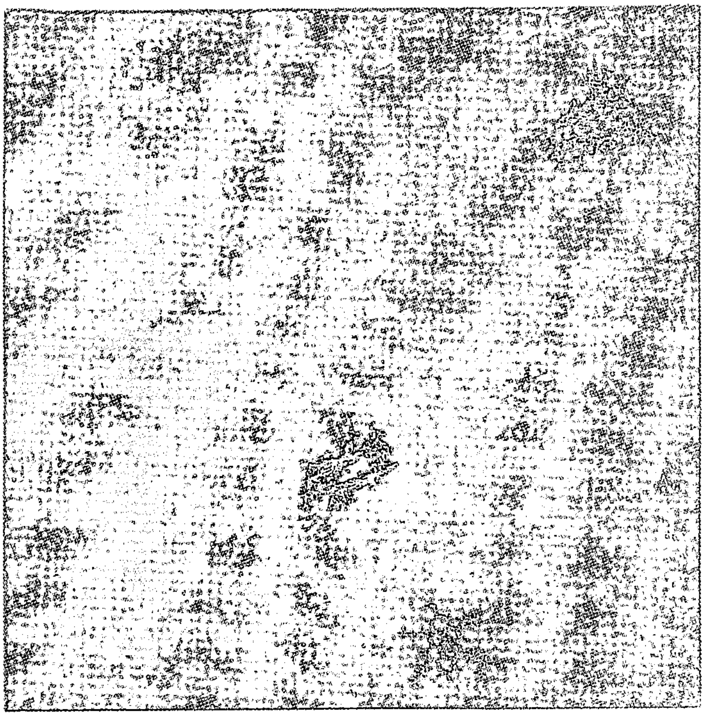

Figure 1. MD simulation for 0.015 wt % Ratawi Aphaltene in solvent.

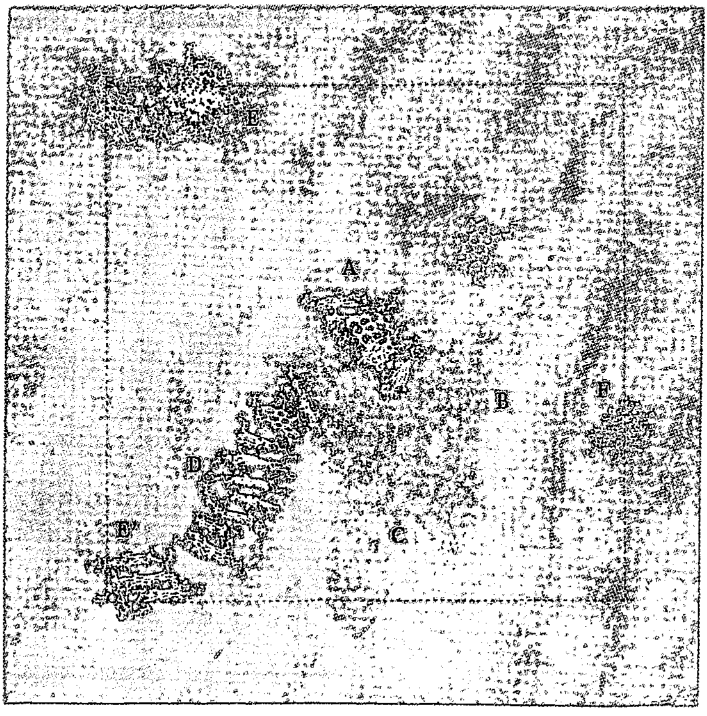

Figure 2. MD simulation for 5.0 wt % Ratawi Aphaltene in solvent.

HYDROCARBON BACKBONE OF POLAR FRACTIONS

R. A. Wolny (*), L. A. Green, J. G. Bendoraitis, L. B. Alemany (**)
Mobil Technology Company, Paulsboro, NJ 08066

(*) Current address: Saudi Aramco, LR&DC, Dhahran 31311, Kingdom of Saudi Arabia
(**) Current address: Rice University, Department of Chemistry, Houston TX 77005

Keywords: Polar, Hydrocarbon, Structure

SUMMARY

The quantity and composition of polar materials present in heavy process streams have an impact on the strategy used for their processing and the resulting yield structure. A chemical procedure was employed to deoxygenate the polar material which were later separated into aliphatic, aromatic, and residual polar fractions. These fractions were analyzed to determine their compositions. It was found that the deoxygenated hydrocarbon backbones of aliphatic and aromatic fractions derived from polar material are very similar in composition to the corresponding fractions separated from the original feed. However, structures that undergo easier oxidation are concentrated in the derived backbone fractions. The main components of the residual polar fractions obtained after deoxygenation are basic nitrogen compounds, polyheteroatom molecules, aliphatic sulfones, etc., that are resistant towards chemical processing.

INTRODUCTION

Most of the results published in the open literature concentrate on the analysis of polar compounds with a single functional group. For example, the carboxylic acids have been widely investigated (1-4). Seifert identified carboxylic acids associated with a variety of aliphatic, aromatic and heterocyclic (S- and N-containing) backbones (1,2). Cason isolated and identified isoprenoidal acids from California crudes (3,4). Sulfoxides represent another large group of polar compounds particularly in crudes that have a high total sulfur content. Strausz et al. described a method for converting polar sulfoxide molecules to low polarity sulfides that can later be separated from the polar matrix by chromatographic techniques (5). Basic nitrogen compounds represent the majority of nitrogen in the polar fraction (6-11). However, neutral and acidic nitrogen compounds with polar functional groups (e.g. carbonyl) are also present in the polar fraction (1). In this work we attempted to analyze the polar fraction of a crude and account for all polar functionalities and the hydrocarbon backbone with which these polar functionalities are associated.

EXPERIMENTAL PART

Reagents.

All solvents used were reagent or HPLC grade. Silica gel, mesh 100-200, Grade 923, supplied by Davison Chemical, was activated in an oven at 500°F for 24 hours. Alumina was purchased from ICN Biochemicals.

Instruments.

The GC/MS chromatograms were collected on Finnigan TSQ-70 and Kratos MS 80 instruments. The gas chromatographs on both instruments were equipped with J&W Scientific DB-5 columns, 30 m, 0.25 mm ID, 0.25 μm film thickness. Kratos MS 50 instrument was used to acquire field ionization mass spectra.

Simultaneous chromatograms (GC/FID, GC/FPD-sulfur) were recorded on a Varian 3400 instrument, using a J&W DB-5 column, 30 m, 0.53 mm ID, 1.5 μm film thickness.

The FTIR spectra were recorded on a Mattson Sirius 100 instrument.

PROCEDURE DESCRIPTION.

The polar fraction, 2.5 weight percent of the original material, was separated from the 550°F-1050°F fraction of a crude on silica gel. A sequence of hexane and toluene were used to elute aliphatic and aromatic fractions. The polar fraction was eluted with 50/50 vol% methanol/toluene and 50/50 vol% methylene chloride/acetone. The chemical procedure used to deoxygenate the polar fraction is similar to that described by Seifert et. al. (2). The sequence of LAH reduction, tosylation, and LAH reduction on the polar fraction gave an overall yield of 90.1 weight percent. Mass loss is expected due to removal of functional groups; however, some loss may be due to sample handling.

The chemically processed material was separated on silica gel into an aliphatic (Aliphatic Backbone), an aromatic (Aromatic Backbone), and a residual polar (Polar Backbone) fractions. The Aliphatic Backbone fraction was eluted with hexane, the Aromatic Backbone fraction was eluted with toluene, and the Polar Backbone fraction was eluted with 50/50 vol% methanol/toluene and 50/50 vol% methylene chloride/acetone. The aromatic fraction derived from the chemically processed polar fraction was further separated on alumina impregnated with 4% of silver nitrate (12). Aromatic Backbone Fraction-1 (ABF-1) and Aromatic Backbone Fraction-2 (ABF-2) were eluted with toluene, Aromatic Backbone Fraction-3 (ABF-3) with 5/95 vol% methanol/toluene, and Backbone Fraction-4 (ABF-4) with 30/70 vol% methanol/toluene and 50/50 vol% methanol/toluene. Residual silver nitrate was removed from ABF-3 and ABF-4 by extraction with distilled water.

RESULTS AND DISCUSSION

Selective reactions, outlined in the Experimental Part, remove reactive functional groups responsible for the polarity of molecules present in the polar fraction. Lithium aluminum hydride (LAH) reduces functional groups such as carboxylic acids, aldehydes, esters, ketones, acid anhydrides, and amides to hydroxyl groups (13). Then, hydroxyl groups are converted to the corresponding tosylates, which are later reduced with LAH to the hydrocarbon backbone (2).

The polar functional group can be associated with an aliphatic or an aromatic structure or attached to an aliphatic fragment of the aromatic molecule (naphthenic ring or alkyl side chain of an aromatic molecule). Also, a polar functional group can be attached to structures bearing a heteroatom.

Sulfoxides, another large group of polar compounds, are reduced to sulfides during the first reduction with LAH (5). Sulfides remain intact during tosylation and the second reduction with LAH.

Sulfones of thiophenes are easily reduced with LAH; however, sulfones of sulfides are difficult to convert back to sulfides. Reduction reactions of various functional groups with LAH are summarized by Hudlicky (13).

Infra-red

Infrared spectroscopy was used to quantify the contribution of various functional groups using average absorption coefficients reported in the literature (14,15). The result of this quantitative analysis is as follows: carboxylic acids and other carbonyls 8 weight percent; sulfoxides 47 weight percent; phenols and alcohols 12 weight percent.

Separations

The Aliphatic Backbone fraction represents only 4.5 weight percent of the chemically processed material (Table 1). Table 2 shows the group type distribution of the Aliphatic Backbone fraction and of the aliphatic fraction separated from the original crude fraction by a similar method. The Aliphatic Backbone derived from the polar fraction has a strong paraffinic character and absence of sulfur compounds (Figure 1). It is apparent from these data that the character of both aliphatic materials is similar.

The chemically processed polar fraction contains 65.2 weight percent as the Aromatic Backbone fraction (Table 1). This material contained high concentration of sulfides (Figure 1). This group of compounds was further separated from the rest of the aromatic matrix, as outlined in the Experimental Part.

The first two fractions eluted with toluene, were relatively small. The weight percent distributions and elemental analyses for ABF-1 and ABF-2 are shown in Table 1. ABF-1 and ABF-2 consist of aromatic hydrocarbons, thiophenic compounds, and nitrogen compounds having a pyrrolic ring that originated from the polar precursors. Pyrrolic nitrogen compounds are significant contributors to ABF-1 and ABF-2. Calculated from the average molecular weight and nitrogen content, determined by field ionization mass spectrometry (FIMS), ABF-1 and ABF-2 contain 43 and 63 weight percent of pyrrolic compounds, respectively. Mononaphthenocarbazole is the most abundant in this series.

Thiophenic compounds were identified in ABF-1 and ABF-2. Thiophenes could have originated from the corresponding sulfones or from thiophenes that had functional groups (R) reducible with LAH to hydroxyl. Based on sulfur measurements and average molecular weight from FIMS, ABF-1 and ABF-2 contain 6 and 11 weight percent of thiophenes, respectively.

ABF-3 and ABF-4 derived from the polar fraction constitute a majority of the total Aromatic Backbone fraction (Table 1). These two fractions contain predominantly sulfides and a small amount of pyrroles. Sulfides present in the ABF-3 and ABF-4 are very similar to the sulfides found in the corresponding fractions separated, by similar method, from the original crude fraction. Based on molecular weight from FIMS and nitrogen content, ABF-3 and ABF-4 contain 16 and 5 weight percent of pyrrolic nitrogen, respectively.

It is remarkable that the chemically processed polar fraction contains 46.6 weight percent of material defined as sulfides. This high concentration of sulfides is in very good agreement with 47 weight percent of sulfoxides quantified by IR. Pyrroles, aromatic hydrocarbons, and thiophenic compounds represent 12.9, 0.9, and 4.8 weight percent of the total polar fraction, respectively.

The residual polar material, Polar Backbone, represents 29.3 weight percent of the chemically processed polar fraction and contains 3.26 weight percent sulfur and 2.57 weight percent nitrogen (Table 1 and Figure 1). The Polar Backbone has substantial aromatic character (32% aromatic C and 9% aromatic H). Sulfur present in this fraction may exist in structures with polyheteroatoms, or sulfones and sulfoxides that are resistant towards reduction with LAH. Nitrogen is present mainly in the form of basic nitrogen compounds or polyheteroatom structures (8-13). Limited information was obtained from these data due to the high complexity of this fraction. More research is needed to characterize basic nitrogen and polyheteroatom compounds.

CONCLUSIONS

Removal of oxygen-bearing functional groups from the polar fraction produced non-aromatic and aromatic hydrocarbons (including those containing heteroatoms), and sulfides.

The low level of Aliphatic Backbone in the polar fraction results from minimal biodegradation of the original crude. Sulfoxides represent almost half of the polar fraction. It is suspected that sulfoxides may result from the oxidation during sample handling; however, indigenous sulfoxides can not be excluded. Pyrrolic nitrogen molecules that bear a polar group represent a significant part of the polar fraction. Pyrrolic molecules that contain naphthenic ring(s) are concentrated in the polar fraction.

Polar fraction bear a striking resemblance to non-polar material of the original crude. That is, polar fraction differ in functionality, but its backbone is consistent with compounds from the non-polar material. We believe that this observation can be applied to the polar materials from other petroleum feeds and products.

ACKNOWLEDGMENTS

Authors thank C.A. Simpson for acquiring the IR spectra, D.L. Parisi for assistance in acquiring FIMS spectra and P.P. Durand for his help in processing FIMS data.

REFERENCES

1. Seifert, W. K., Progress in the Chemistry of Organic Natural Products, **1972**, Vol. 32, pp. 1-49. Look also for citations in this publication.
2. Seifert, W. K., Teeter, R. M., Howells, W. G., Cantow, M. J., Analytical Chemistry, **1969**, Vol. 41, pp. 1638-1647.
3. Cason, J., Graham, D. W., Tetrahedron, **1965**, Vol. 21, pp. 471-483.
4. Cason, J., Khodair, A.I., J. Org. Chem., **1967**, Vol. 32, pp. 3430-3439.
5. Payzant, J. D., Montgomery, D. S., Strausz, O. P., Tetrahedron Letters, **1983**, Vol. 24, No. 7, pp. 651-654.
6. Ignatiadis, I., Schmitter, J. M., Arpino, P. J., Journal of Chromatography, **1985**, Vol. 324, pp. 87-111.
7. Schmitter, J. M., Ignatiadis, I., Arpino, P. J., Geochimica et Cosmochimica Acta, **1983**, Vol. 47, pp. 1975-1984.
8. Schmitter, J. M., Collin, H., Excoffier, J. L., Arpino, P. J., Analytical Chemistry, **1982**, Vol. 54, pp. 769-772.
9. Shive, B., Roberts, S. M., Mahan, R. I., Bailey, J. R., J. Am. Chem. Soc., **1942**, Vol. 64, pp. 909-912.
10. Schenck, L. M., Bailey, R. J., J. Am. Chem. Soc., **1941**, Vol. 63, pp. 1364-1365 and 1365-1367.
11. Bakel, A. J., Philp, R. P., Organic Geochemistry, **1990**, Vol. 16, No. 1-3, pp. 353-367.
12. Felsky, G., US Patent 4,430,205.
13. Reductions in Organic Chemistry, M. Hudlicky, published by Ellis Horwood Limited, 1984.
14. Petersen, J.C., Transportation Research Record 1096.
15. Petersen, J.C., Analytical Chemistry, **1975**, Vol. 47, No. 1, pp. 112-117.

TABLE 1. MASS, SULFUR, AND NITROGEN BALANCES FOR CHEMICALLY PROCESSED POLAR FRACTION.

	Mass Wt %	Sulfur in Sample wt% (*)	Sulfur in Total Polars wt%	Nitrogen in Sample wt% (**)	Nitrogen in Total Polars wt%
Starting Material (***)	100	3.97	3.97	1.28	1.28
Aliphatic Backbone	4.5	0.00	0.00	0.00	0.00
Aromatic Backbone Total	65.2	NM	3.09 (****)	NM	0.69
Aromatic Backbone Fraction 1 (ABF-1)	7.6	0.59	0.05	1.96	0.15
Aromatic Backbone Fraction 2 (ABF-2)	3.8	1.03	0.07	2.99	0.11
Aromatic Backbone Fraction 3 (ABF-3)	39.3	4.96	1.95	0.99	0.39
Aromatic Backbone Fraction 4 (ABF-4)	14.5	7.04	1.02	0.32	0.04
Polar Backbone	29.3	3.26	0.95	2.57	0.75
Balance	99.0		4.04		1.44

(*) Measured by D 1552
(**) Estimated from FIMS
(***) Charge to LC column after reactions
(****) Sum of ABF-1, ABF-2, ABF-3, and ABF-4

TABLE 2. GROUP TYPE DISTRIBUTION IN ALIPHATIC BACKBONE FRACTION AND ALIPHATIC FRACTION SEPARATED FROM ORIGINAL MATERIAL

Compounds	*Aliphatic Backbone*	*Aliphatics-original material*
Paraffins	46.5	50.5
Mononaphthenes	17.4	15.1
Dinaphthenes	11.3	13.0
Trinaphthenes	6.6	7.6
Tetranaphthenes	7.9	6.3
Pentanaphthenes	7.8	5.0
Hexanaphthenes	0.0	1.7

FIGURE 1. GC TRACES (FID & FPD-SULFUR) FOR CHEMICALLY PROCESSED POLAR FRACTION. (A) ALIPHATIC BACKBONE, (B) AROMATIC BACKBONE, (C) POLAR BACKBONE

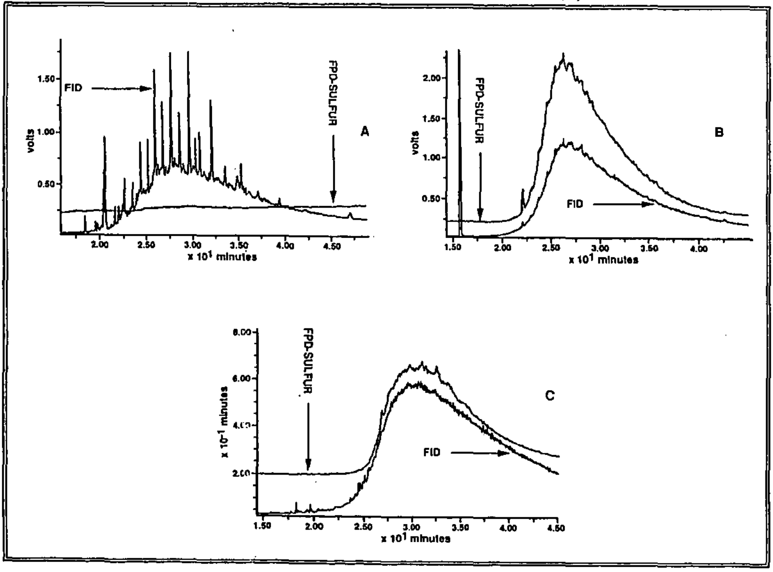

THE NATURE OF RESINS AND ASPHALTENES

Felix Unger, Institute of Petroleum Chemistry,
Russian Academy of Sciences, Siberian Division,
3 Akademichesky Ave., Tomsk, 634055, Russia

Keywords: asphaltene, resin, paramagnetic resonance, electrolytic dissociation

In 1944, Zavoisky [1] discovered electronic paramagnetic resonance (EPR), a tool for direct detection of unpaired electrons in molecular systems, which gave rise to a new avalanche of studies on radical reactions and paramagnetic phenomena, and in 1957 Garif'yanov and Kozyrev [2] found unpaired electrons in petroleum-like systems and thus proved the presence of free radicals in these systems. Thereafter, the role of radicals in petroleum-like systems was discussed rather [for example 3, 4]. However, it could not be evaluated adequately because of the absence of any methodical basis for correct determination of the number of unpaired electrons in the petroleum-like system under investigation. Thus, Flinn et al. [5], based on the published estimate for the paramagnetism of asphaltenes 10^{18} spins/g, arrived at the conclusion that for every 100 molecules there is one free radical. This estimate gave rise to the wide-spread opinion that the role of paramagnetics in asphaltene structures is insignificant. However, once a method for rigorous quantitative estimation of the fraction of paramagnetic molecules has been developed [6], the paramagnetism of petroleum-like systems is estimated as 10^{15} (for gasolines), 10^{17} -10^{18} (for oils), 10^{19} -10^{21} (for asphaltenes), and 10^{20} -10^{22} spins/g (for carbenes-carboids, some cokes, and insoluble carbonic materials). Even for some petroleums (e.g., Archinskoe petroleum of Tomsk region), the paramagnetism is abnormally high 10^{21} spins/g), which is a direct indication of the specific role played by paramagnetic molecules in petroleum-like systems.

Other evaluations of asphaltenic-resin systems are the following.

a. Those systems have no FREE IONS, namely the dissociation of molecules by action of the kinetic energy movement does not go through the heterolytic mechanism, but through the homolytic mechanism.

b. The experiments show that organic acids and bases concentrate not in asphaltenes, but into maltenes with minimum of their contents into the resins (carbon radioactive label), namely the oil systems (with the asphaltenes and resins) contain minimum (or zero) amount of polar molecules. This is confirmed by the value of dielectric constant of oil systems, which is close to benzene.

c. The quantmechanic calculations show, that the potential energy of attraction between the molecules of compounds in oil systems maybe the following:

1. Ion+ion. ATTRACTION. However, the ions are absent.
2. Radical+radical. ATTRACTION. Radical existing in the system and those formed as a result of homolytic reactions, recombine or transition into the singlet state or associate depending on volume restrictions.
3. Radical+charge-polarised molecules. ACIDATION. Therefore organic acids and bases concentrate into the maltene parts, but only minimum of their amount is found in resins.
4. Radical+charge and spin-neutral molecules. ACIDATION. Therefore, the radicals are rejected from the saturated carbon hydrogenates and other compounds with large dielectric constants. Under industrial conditions this process is entitled "DEASPHALTISATION".
5. Radicals+spin-polarised molecules. ATTRACTION. On this basis colloid particles of oil systems are built with radicals in the centre of a particle, surrounded with aromatic and heteroorganic molecules.
6. Spin-polarised+spin-polarised molecules. The DIFFERENT DEGREE OF THE ENERGIES of ATTRACTION. On this basis circumference stratums of colloid particles are built.
7. Spin-polarised+spin-neutral molecules. LITTLE, TILL TO ZERO ENERGIES OF ATTRACTION. On this basis the combination of the circumference stratums of colloid particles with encircling medium is built (with the paraffin-naphthene saturate hydrocarbons, in particular with maltenes in oil systems). A universal theoretical picture the common equation of potential energies maybe given for interaction between molecules:

$$V = K_0e^{-kr} + K_1r^{-1} + K_2r^{-2} + K_3r^{-3} + K_4r^{-4} + K_5r^{-5} + K_6r^{-6} \qquad (1)$$

where: k, K - coefficients, e - natural logarythm, r - distance between the interaction centres. The coefficient "K" may be either "+" or "-". The lattter denotes attraction.

The Zero member beats reflects exchangeable interactions between radicals, the first - charge between ions, the second - between ions and charge-polarised molecules, the third - between radicales and spin-polarised molecules, the fourth and fifth - between breakwater molecules with different degree of spin and charge polarization (multipole members), and the sixth - between neutral molecules (Van-der-Vaals member).

d. From quantum mechanics considerations the virial-theorem for compound-mixtures must be followed:

$$\langle T\rangle = 1/2n\langle V\rangle \qquad (2),$$

where "n" is the number of grade on the variable "r" in formula (1) with allowance for the sign of grade, and "T" - kinetic energy. The brackets <> denote the middle meanings of energies.

Out of formula follows the strict necessity of coordination of acts for the alteration of potential energies of attraction-acidation between molecules and of the kinetic energies of their movement with distance between interacting molecules in physical-chemical processes, into this numerals homolytise, heating, cooling, in chemical reactions and etc.

e. Molecules with unpaired spin will not give NMR-spectra (coordinately with quantum mechanics considerations). The oil samples with high number of spins give weak (low intensity) NMR-spectra, what is attributed from the few contribution of diamagnetic molecules (some of asphaltenes will not give NMR-spectra at all), that is well coordinated with theory. The theoretical and experimental results allow estimation and understanding of the nature of resins and asphaltenes in oil dispersed systems.

The contradictory explanation of the colloidal structures of petroleum systems in terms of charge phenomena (electrolytic dissociation, donor-acceptor interactions, hydrogen charge-dipole interactions, etc.) called for both a new theoretical base and a complex comprehensive interpretation of the information obtained by chemical and instrumental methods for analyzing petroleums, petroleum products, resins, asphaltenes, and other petroleum-like materials, which has been reduced to several basic principles that are in excellent agreement with all available experimental data. These principles are discussed here.

There is no doubt that, the process of excitation and/or homolytic dissociation is a process actually identifiable with the use of instruments intended for physical investigations; second, from theoretical (quantum mechanical) reasonings it should be stated that this process fails not to occur, and, third, this process does occur on introduction of a solvent into a disperse petroleum system and/or its heating. Therefore, the statement is valid that the study of the interaction of the molecules of the solvent introduced with the molecules of associative combinations under varied conditions may be of primary importance for the technology of raw petroleum transformation in the near future.

In view of the importance of these results for the chemistry of solvents, in particular, petroleums, we present below the fundamental aspects of the chemistry of petroleum-like systems inherent in any non-water solutions and in some low-polarity water solutions.

1. Asphaltenes (being a type of powder) are not involved as components in petroleum (petroleum-like) systems, but they are formed in the process of action of a solvent on the system as associative combination of molecules having a higher density than the solution and separated from the system to form a precipitate.

2. The reason for the appearance and existence of asphaltenes is the presence of paramagnetic molecules that have positive potential energies of interaction with respect to saturated hydrocarbon molecules (repulsion) or other type molecules with sigma-bound atoms.

3. The possibility for the prolonged existence of paramagnetic molecules in the medium of diamagnetic molecules is provided by a shell preventing radicals from recombination. The shell is formed by the same principles as the solvate shells in electrolytic solutions, but the forces therewith are quantum (exchange) rather than charge in nature. Low-activity radicals may have thin shells or none at all. Active radicals will have heavy shells; in their nearest vicinity there will be accumulated molecules with a high energy of interaction with paramagnetic molecules, and the interaction energy will decrease in going to the periphery of the associative combination of molecules. If the associate density is comparable with the medium density, no separation will

occur, and the paramagnetic molecule will be able to exist for an infinitely long time in the center of the associate and will not recombine notwithstanding its high activity.

4. Diamagnetic molecules which go into the triplet state or dissociate into radicals under minor energy actions (e.g., on the order of a dozen of kilojoules per mole) are the basic molecules consisting resins. Owing to the kinetic energy of molecules, paramagnetic molecules are always present in small amounts in resins, that appear and due in equilibrium homolysis-recombination reactions. The range of energies required for a molecule to go into the triplet state or to dissociate into radicals may be rather large in view of the variety of molecules; so asphaltenes (precipitates) may occur from resins under the action of saturated solvents at elevated temperatures in substantial amounts. However, the molecules of such precipitates, when the original low-temperature conditions are reverted, recombine to transform again into the resin diamagnetic molecules.

5. Resins are a potential source for asphaltenes owing to the high probability of homolytic processes; asphaltenes are a potential source for resins owing to the molecules present in the nearest surrounding of radicals in associative combinations.

6. The properties of resins and asphaltenes are fundamentally independent of the atomic composition but depends on the energy of the interaction of atoms in molecules and molecules with one another. The varied element composition of resins and asphaltenes from various raw materials imparts them some specific properties, but the principles of appearance and existence of these associative combinations are almost independent of the composition.

7. All properties of resins and asphaltenes are well explained by the quantum mechanical principles of the formation of homopolar interactions and fail to be explained in terms of heteropolar interactions.

8. The properties of asphaltenes and resins are inherent in all types of viscous and liquid homopolar systems (petroleums, tars, homopolar schistose resins, homopolar carbonic hydrogenation products, etc.) and have an universal nature.

9. The properties of homolytes and the regularities of the formation of associative combination in them dictate some rules for the application of instrumental techniques whose violation may result in artifacts.

-Spectral characteristics (intensities of peaks and their positions on the frequency or angle axis) should be calculated (measured) with respect to quantitative references.

-The references should not be introduced they may change (sometimes substantially) the system properties. For solid systems no changes of this type were noticed, with the exception of asphaltenes being concentrates of paramagnetic molecules with variable paramagnetism.

-To obtain the spectral characteristic of a material, it is necessary to use a complete referenced spectrum. If a partial spectrum is used, even with referencing it is impossible to estimate the contribution of a given parameter into the properties in total. If this contribution is small and this has been overlooked, an artifact is inavoidable.

10. The paramagnetic nature of disperse homolytes, the peculiarities of the physical chemistry of the prohibited singlet-triplet and triplet-singlet transitions (diamagnetic-to-paramagnetic and reverse transitions of molecules) in petroleum-like systems, as well as, the quantum mechanical prohibitions for the filling of phase spaces by bosons, fermions, and paulions offer the possibility to predict certain types of chemical interactions in such systems.

-The presence of molecules with a high degree of spin polarization and with unpaired electrons is responsible for the amphoteric nature of the properties of petroleum-like systems. Thus, the compounds precipitated on acid impregnates behave like the compounds precipitated on base impregnates. In a detailed analysis it is generally revealed that these are the same compounds which are precipitated in a way inherent in the precipitation of the high-polarity molecules whose high polarity is due to the readiness of forced charge polarization. Note that for this type of compounds both the ionization potential and the electron affinity are low.

-In petroleum-like liquid mixtures, molecules with pronounced charge polarization or electrolytic dissociative ions are practically absent. All electrophoretic and electrical conductance phenomena in these systems are the consequence of the field-assisted charge polarization of various spin-polarized molecules and radicals. Therefore, both the cathode and the anode masses strongly vary qualitatively and quantitatively with electric field to the extent that the direction of precipitation is changed which requires significant potentials, some orders of magnitude higher than those required for electrolytic dissociation.

-All reactions with petroleum-like media are homolytic in nature, and the touch of heterogeneity in them is conditioned by the pronounced charge properties of specially used electrolytic reagents. However, the propositions of the ionic mechanism are often not justified even for ferric chloride, sulfuric acid, and the like. A study of catalytic reactions should also be performed with due account of the regularities revealed.

11. As leads for further research, besides pending studies of already raised problems, it is noteworthy to develop adequate quantum mechanical and physicochemical models to describe:

-the DPS states;

-homolytic processes and the possibility of affecting their passage by fields;

-the thermolytic reactions in the existing chemical works;

-the catalytic reactions in the existing and predicted chemical works;

-the mechanism of action of additives for stabilization, inhibition, inflammation, quenching, ignition, etc;

-the DPS compounds showing the properties of radicals, biradicals, and spin-polarized particles with high and low degrees of spin polarization and the places of these compounds in the DPS.

12. The most important line of studies, going far beyond petroleum chemistry, is research in the field of theory of liquids. It is for the first time since the impressive studies on electrolytic dissociation performed by Arrenius that we may say that homolytic dissociation has equally attracted the attention of researchers and the possibility has appeared to develop a unified theory of dissociation based on the available and future achievements in quantum mechanics with the goal to gain an understanding of the structure of liquid systems of any origin.

In conclusion, we present several figures illustrating some experimental results to confirm the above fundamental inferences on the paramagnetic nature of the dispersions in petroleum-like systems.

References

[1] E.K. Zavoisky, J. Phys. (1945) v.9, N 3.
[2] I.S. Garif'yanov and B.M. Kozyrev, Zh. Eksper. Teor. Fiz. (1956) v.30, N.2 p.255.
[3] E.C. Tynan and T.F. Yen, Fuel, (1969) v.48, n.2, p.191.
[4] T.F. Yen, J.C. Erdman, and A.J. Saraceno, Ann. Chem., (1962) v.34, n.6, p.694.
[5] R.A. Flinn et al., Petrol. Refiner, (1955) v.40, n.4, p.139.
[6] F.G.Unger, L.N.Andreeva. Fundamental aspects of the oil chemistry. Nature of the resins and asphaltenes. Novosibirsk, Nauka, Siberian Publishing Firm RAN (1995).

GAS HYDRATE TUTORIAL

E. Dendy Sloan, Jr.
Center for Hydrate Research
Colorado School of Mines
Golden, Colorado 80401 USA

Keywords: natural gas hydrates, crystal structures, properties

ABSTRACT

The tutorial provides an overview of time-independent physical/chemical properties as related to crystal structures. Page limitations proscribe only a description of hydrate properties; applications are detailed in other papers in this gas hydrate symposium. The following seven points are illustrated in this tutorial:

1. Gas hydrates are crystalline compounds which form when small (<0.9nm) molecules contact water at temperatures above and below the ice point, with elevated pressures.
2. Properties of sI and sII hydrate crystals are well-defined; measurements have begun on sH.
3. Each volume of hydrate contains as much as 180 volumes (STP) of methane.
4. Physical and chemical properties of hydrates are approximated by three heuristics:
    - Mechanical properties approximate those of ice,
    - Phase equilibrium is set by the size ratio of guest molecules within host cages, and
    - Thermal properties are set by the hydrogen-bonded crystals within a range of guest sizes.
5. Three-phase (L_W-H-V) equilibrium pressure depends exponentially on temperature.
6. There is a need to characterize the hydrate phase directly (via diffraction, NMR, Raman, etc.).
7. No acceptable model exists for hydrate formation kinetics.

The reader may wish to investigate these details further, via references contained in several monographs, (Sloan, 1990; Sloan et al., 1994, Monfort, 1996).

INTRODUCTION

Gas clathrates (commonly called hydrates) are crystalline compounds which occur when water forms a cage-like structure around smaller guest molecules. While they are more commonly called hydrates, a careful distinction should be made between these non-stoichiometric clathrate hydrates of gas and other stoichiometric hydrate compounds which occur for example, when water combines with various salts.

Gas hydrates of current interest are composed of water and the following eight molecules: methane, ethane, propane, isobutane, normal butane, nitrogen, carbon dioxide, and hydrogen sulfide. Yet other apolar components between the sizes of argon (0.35 nm) and ethylcyclohexane (0.9nm) can form hydrates. Hydrate formation is a possibility where water exists in the vicinity of such molecules at temperatures above and below 273 K.

Hydrate discovery is credited in 1810 to Sir Humphrey Davy. Due to their crystalline, non-flowing nature, hydrates became of interest to the hydrocarbon industry in 1934 (Hammerschmidt, 1934), the time of their first observance blocking pipelines. Hydrates act to concentrate hydrocarbons: 1 cubic meter of hydrates may contain as much as 180 SCM of gas. Makogon, (1965) indicated that large natural reserves of hydrocarbons exist in hydrated form, both in deep oceans and in the permafrost. Evaluation of these reserves is highly uncertain, yet even the most conservative estimates concur that there is twice as much energy in hydrated form as in all other hydrocarbon sources combined. While one commercial example exists of gas recovery from hydrates, the problems of *in situ* hydrate dissemination in deepwater/permafrost environments will prevent their cost-effective recovery until the next millennium.

WHAT ARE HYDRATES: HOW DO STRUCTURE RELATE TO PROPERTIES?

Hydrates normally form in one of three repeating crystal structures shown in Figure 1. Structure I (sI), a body-centered cubic structure forms with small natural gas molecules found *in situ* in deep oceans. Structure II (sII), a diamond lattice within a cubic framework, forms when natural gases or oils contain molecules larger than ethane but smaller than pentane. sII represents hydrates which commonly occur in hydrocarbon production and processing conditions, as well as in many cases of gas seeps from faults in ocean environments.

The newest hydrate structure H, named for the hexagonal framework, was discovered and shown by Ripmeester et al. (1987, 1991) to have cavities large enough to contain molecules the size of common components of naphtha and gasoline. Initial physical properties, phase equilibrium data, and models have been advanced (Mehta and Sloan, 1993, 1994a,b, 1996a,b,c; Udachin et al. 1996), and Sassen et al. (1994) have found one instance of *in situ* sH in the Gulf of Mexico. Since information on structure H is in the fledgling stages, most of this tutorial concerns sI and sII.

HYDRATE CRYSTAL STRUCTURES.

Table 1 provides a hydrate structure summary for the three hydrate unit crystals (sI, sII, and sH) shown in Figure 1. The crystals structures are given with reference to the water skeleton, composed of a basic "building block" cavity which has twelve faces with five sides per face, given the abbreviation 5^{12}. By linking the vertices of 5^{12} cavities one obtains sI; linking the faces of 5^{12} cavities results in sII; in sH a layer of linked 5^{12} cavities provide connections.

Interstices between the 5^{12} cavities are larger cavities which contain twelve pentagonal faces and either two, four, or eight hexagonal faces: (denoted as $5^{12}6^2$ in sI, $5^{12}6^4$ in sII, or $5^{12}6^8$ in sH). In addition sH has a cavity with square, pentagonal, and hexagonal faces ($4^35^66^3$). Figure 1 depicts the five cavities of sI, sII, and sH. In Figure 1 a oxygen atom is located at the vertex of each angle in the cavities; the lines represent hydrogen bonds with which one chemically-bonded hydrogen connects to an oxygen on a neighbor water molecule.

Inside each cavity resides a maximum of one of the small, guest molecules, typified by the eight guests associated with 46 water molecules in sI ($2[5^{12}]\bullet 6[5^{12}6^2]\bullet 46H_2O$), indicating two guests in the 5^{12} and 6 guests in the $5^{12}6^2$ cavities of sI. Similar formulas for sII and sH are ($16[5^{12}]\bullet 8[5^{12}6^4]\bullet 136H_2O$) and ($3[512]\bullet 2[4^35^66^3]\bullet 1[5^{12}6^8]\bullet 34H_2O$) respectively.

Structure I a body-centered cubic structure forms with natural gases containing molecules smaller than propane; consequently sI hydrates are found *in situ* in deep oceans with biogenic gases containing mostly methane, carbon dioxide, and hydrogen sulfide. Structure II a diamond lattice within a cubic framework, forms when natural gases or oils contain molecules larger than ethane but smaller than pentane; sII represents hydrates from thermogenic gases. Finally structure H hydrates must have a small occupant (like methane, nitrogen, or carbon dioxide) for the 5^{12} and $4^35^66^3$ cages but the molecules in the $5^{12}6^8$ cage can be as large as 0.9nm (e.g. ethylcyclohexane).

TIME-INDEPENDENT PROPERTIES FROM HYDRATE CRYSTAL STRUCTURES.

Mechanical Properties of Hydrates. As may be calculated via Table 1, if all the cages of each structure are filled, all three hydrates have the amazing property of being approximately 85% (mol) water and 15% gas. The fact that the water content is so high suggests that the mechanical properties of the three hydrate structures should be similar to those of ice. This conclusion is true to a first approximation as shown in Table 2, with the exception of thermal conductivity and thermal expansivity (Davidson, 1983, Tse, 1994). Many mechanical properties of sH have not been measured to date.

Guest: Cavity Size Ratio: a Basis for Property Understanding. The hydrate cavity occupied is a function of the size ratio of the guest molecule within the cavity. To a first approximation, the concept of "a ball fitting within a ball" is a key to understanding many hydrate properties. Figure 2 (corrected from von Stackelberg, 1949) may be used to illustrate five points regarding the guest:cavity size ratio for hydrates formed of a single guest component in sI or sII.

1. The sizes of stabilizing guest molecules range between 0.35 and 0.75 nm. Below 0.35nm molecules will not stabilize sI and above 0.75 molecules will not stabilize sII.
2. Some molecules are too large to fit the smaller cavities of each structure (e.g. C_2H_6 fits in the $5^{12}6^2$ of sI; or i-C_4H_{10} fits the $5^{12}6^4$ of sII).
3. Other molecules such as CH_4 and N_2 are small enough to enter both cavities (labeled as either 5^{12}+$5^{12}6^2$ in sI or 5^{12}+$5^{12}6^4$ in sII) when hydrate is formed of those single components.
4. The largest molecules of a gas mixture usually determines the structure formed. For example, because propane and i-butane are present in many thermogenic natural gases, they will cause sII to form. In such cases, methane will distribute in both cavities of sII and ethane will enter only the $5^{12}6^4$ cavity of sII.
5. Molecules which are very close to the hatched lines separating the cavity sizes appear to exhibit the most non-stoichiometry, due to their inability to fit securely within the cavity.

Table 3 shows the size ratio of several common gas molecules within each of the four cavities of sI and sII. Note that a size ratio (guest molecule: cavity) of approximately 0.9 is necessary for stability of a simple hydrate, given by the superscript “^{J}”. When the size ratio exceeds unity, the molecule will not fit within the cavity and the structure will not form. When the ratio is significantly less than 0.9 the molecule cannot lend significant stability to the cavity.

Consider ethane, which forms in the $5^{12}6^{2}$ cavity in sI, because ethane is too large for the small 5^{12} cavities in either structure and too small to give much stability to the large $5^{12}6^{4}$ cavity in sII. Similarly propane is too large to fit any cavity except the $5^{12}6^{4}$ cavity in sII, so that gases of pure propane form sII hydrates from free water. On the other hand, methane's size is sufficient to lend stability to the 5^{12} cavity in either sI or sII, with a preference for sI, because CH_4 lends slightly higher stability to the $5^{12}6^{2}$ cavity in sI than the $5^{12}6^{4}$ cavity in sII.

Phase Equilibrium Properties. In Figure 3 pressure is plotted against temperature with gas composition as a parameter, for methane+propane mixtures. Consider a gas of any given composition (marked 0 through 100% propane) on a line in Figure 3. At conditions to the right of the line, a gas of that composition will exist in equilibrium with liquid water. As the temperature is reduced (or as the pressure is increased) hydrates form from gas and liquid water at the line, so three phases (liquid water + hydrates + gas) will be in equilibrium. With further reduction of temperature (or increase in pressure) the fluid phase which is not in excess (gas in ocean environments) will be exhausted, so that to the left of the line the hydrate will exist with the excess phase (water).

All of the conditions given in Figure 3 are for temperatures above 273K and pressures along the lines vary exponentially with temperature. Put explicitly, hydrate stability at the three-phase (L_W-H-V) condition is always much more sensitive to temperature than to pressure. Figure 3 also illustrates the dramatic effect of gas composition on hydrate stability; as any amount of propane is added to methane the structure changes (sI → sII) to a hydrate with much wider stability conditions. Note that a 50% decrease in pressure is needed to form sII hydrates, when as little as 1% propane is in the gas phase.

Any discussion of hydrate dissociation would be incomplete without indicating that hydrates provide the most industrially useful instance of statistical thermodynamics prediction of phase equilibria. The van der Waals and Platteeuw (1959) model was formulated after the determination of the crystal structures shown in Figure 1. With the model, one may predict the three-phase pressure or temperature of hydrate formation, by knowing the gas composition. For further discussion of these details the reader is referred to Sloan (1990, Chapter 5).

Heat of Dissociation. The heat of dissociation (ΔH_d) is defined as the enthalpy change to dissociate the hydrate phase to a vapor and aqueous liquid, with values given at temperatures just above the ice point. For sI and sII, Sloan and Fleyfel (1992) show that to a fair engineering approximation (±10%) ΔH_d is a function mostly of crystal hydrogen bonds, but also of the cavity occupied within a wide range of components sizes. Enthalpies of dissociation may be determined via the univariant slopes of phase equilibrium lines (ln P vs. 1/T) in the previous paragraphs, using the Clausius-Clapeyron relation [$\Delta H_d = -zR\ d(\ln P)/d(1/T)$].

As one illustration, simple hydrates of C_3H_8 or i-C_4H_{10} have similar ΔH_d of 129 and 133 kJ/mol (Handa, 1986) because the both occupy the $5^{12}6^{4}$ cavity, although their size:cavity ratios are somewhat different (0.943 and 0.976). As a second illustration, Figure 3 shows that mixtures of CH_4 + C_3H_8 have a value of ΔH_d = 79 kJ/mol over a wide range of composition. In such mixtures, C_3H_8 occupies most of the $5^{12}6^{4}$ cavities while CH_4 occupies a small number of $5^{12}6^{4}$ and many 5^{12}. In fact, most natural gases (which form sII) have similar values of ΔH_d. Figure 4 shows similar line slopes (and thus ΔH_d values) for binary mixtures of methane when the large guest is changed from C_3H_8, to i-C_4H_{10}, to n-C_4H_{10}. Similarly, over a wide range of composition for mixtures of methane and ethane, ΔH_d values are similar (74 kJ/mol) for components entering both cavities of sI. Identical arguments may be used to explain similar ΔH_d values of 79.5 ±7% kJ/mol (Mehta and Sloan, 1996c) for sH mixtures of methane with seventeen larger components.

CHALLENGES FOR FUTURE RESEARCH

A review of the literature suggests that there are two imminent challenges for future research. First we must characterize the hydrate phase both in the laboratory and in the field. Secondly we must characterize the kinetics hydrates formation and dissociation.

Measurements of the Hydrate Phase. For the hydrate phase there are two measurement techniques - diffraction and spectroscopic. Neutron diffraction (typified by Tse, 1994) can detect water atoms and guest molecules, while X-ray diffraction detects oxygen positions. Recently using X-ray diffraction Stern et al. (1996) have been remarkably successful at converting 97% of ice to water, by raising ice grain temperatures above the solidus while under high pressure.

Two types of spectroscopy are useful with hydrates: (1) nuclear magnetic resonance (NMR) with cross polarization (CP) and magic-angle spinning (MAS), and (2) Raman spectroscopy. Virtually all NMR hydrate work to date comes from the Canadian National Research Council. The first comprehensive review of NMR studies of clathrates was written by Davidson and Ripmeester (1984), and a thorough update has been written by Ripmeester and Ratcliffe (1991). Of NMR hydrate compounds Xe has obtained prominence due to its large (ca. 100 ppm) chemical shift.

Recently Sum et al. (1996) have shown that Raman spectroscopy can be used to determine the fraction of filled cages in hydrates, and the fraction of various components in the cages. Since Raman appears to be both more versatile and less resource intensive, it holds substantial

Measurements of Hydrate Kinetics. Most hydrate kinetics research has come from the laboratory of Bishnoi, notably the work of Englezos et al., (1987a,b). They modeled kinetics of methane and ethane hydrate after nucleation, for periods up to 100 minutes. A subsequent model was made by Skovborg and Rasmussen (1994); these workers assumed that the mass transfer of gas to the liquid phase was the rate-controlling step, so that hydrate kinetics and diffusion to the hydrate phase could be ignored.

However, even with these excellent beginnings, quantification of hydrate kinetics still pose substantial challenges to hydrate researchers. For example, no model of hydrate nucleation can acceptably fit all the data of a single experimenter; no universal nucleation model is available. As another example, all models of hydrate growth kinetics are apparatus-dependent. While the growth model may be a satisfactory fit for the apparatus in which the data were generated, the model will not fit data generated in other apparatuses. Determining time-dependent hydrate behavior s one of the most significant challenges for research.

CONCLUSIONS

This tutorial reviews hydrate crystal structures, and shows how properties such as phase equilibria and heat of dissociation relate to molecular structure. While many time-independent properties of sI and sII hydrates are determined, those for newer structures (e.g. sH) are just beginning to be explored. The time-dependent characteristics of all three hydrate structures are largely unspecified and kinetic models to date appear to be apparatus-dependent. Characterization of the hydrate phase constitutes a current challenge.

LITERATURE CITED

Davidson, D.W., in Natural Gas Hydrates: Properties, Occurrence and Recovery, J.L. Cox, ed., pg 1. Butterworths, Boston (1983)

Davidson, D.W., Ripmeester, J.A.,in Inclusion Compounds, Vol 3 Chapter 3, J.L. Atwood, J.E.D. Davies, and D.D. MacNichol,eds, Academic Press (1984)

Englezos, P., Kalogerakis, N., Dholabhai, P., Bishnoi,P., Chem. Eng. Sci., 42(11), 2647 (1987a)

Englezos, P., Kalogerakis, N., Dholabhai, P., Bishnoi,P., Chem. Eng. Sci., 42(11), 2659 (1987b)

Hammerschmidt, E.G., Ind. Eng. Chem. **26** 851 (1934)

Handa, Y.P., J. Chem. Thermo., 18, 891 (1986)

Makogon, Y.F., Gazov. Promst. 14 (1965)

Mehta, A.P., A Thermodynamic Investigation of Structure H Clathrate Hydrates, Ph.D. Thesis, Colorado School of Mines, Golden, CO (1996)

Mehta, A.P., Sloan, E.D., J. Chem. Eng. Data, **38**, 580 (1993)

Mehta, A.P., Sloan, E.D., J. Chem. Eng. Data, **39**, 887 (1994a)

Mehta, A.P., Sloan, E.D., AIChE Journal, **40**, 312 (1994b)

Mehta, A.P., Sloan, E.D., AIChE Journal, **42**, 2036(1996a)

Mehta, A.P., Sloan, E.D., in Proc. 2nd Intnl. Conf. on Natural Gas Hydrates, p1. Monfort, J.P., ed., Toulouse, 2-6 June (1996b)

Mehta, A.P., Sloan, E.D., "Structure H Hydrates: Implications for the Petroleum Industry,"Proc. 1996 Annual Tech Conf.,SPE 36742, 607 Denver, CO., 6-9 October (1996c)

Monfort, J.P., ed, Proc. 2nd Intnl. Conf. on Natural Gas Hydrates, F. Foucaud, Secretariat, 18 Chemin de la Loge, 31078 Toulouse Cedex, France 2-6 June (1996)

Ripmeester, J.A., Tse, J.A., Ratcliffe, C.I., Powell, B.M., Nature, **325**, 135 (1987)

Ripmeester, J.A., Ratcliffe, C.I., Solid State NMR Studies of Inclusion Compounds, National Research Council of Canada, Report C1181-89S, August 17 (1989)

Ripmeester, J.A., "The Role of Heavier Hydrocarbons in Hydrate Formation," presented at 1991 AIChE Spring Meeting, Houston, April 10 (1991)

Ripmeester, J.A., Ratcliffe, C.I., Klug, D.D., Tse, J.A., , in (First) International Conference on Natural Gas Hydrates, Annals of New York Academy of Sciences, Sloan, E.D., Happel, J., Hnatow, M.A., eds., **715**, p161, (1994)

Sassen, R., MacDonald, I.R., Org. Geochem. **22(6)** 1029 (1994)

Skovborg, P., Rasmussen, P., Chem. Eng. Sci., **49**, 1131 (1994)

Sloan, E.D., Clathrate Hydrates of Natural Gases, Marcel Dekker, Inc., New York (1990)

Sloan, E.D., Fleyfel, F., Fluid Phase Equil, **76**, 123 (1992)

Sloan,E.D., Happel, J., Hnatow, M.A., eds, (First) International Conference on Natural Gas Hydrates, Annals of New York Academy of Sciences,., **715**, (1994)

Stern, L.A., Kirby, S.H., Durham, W.B., Science, 273, 1843 (1996)

Sum, A., Burruss, R., Sloan, E.D., in Proc. 2nd Intnl. Conf. on Natural Gas Hydrates, p51. Monfort, J.P., ed., Toulouse, 2-6 June (1996b)

Tse, J.S., in (First) International Conference on Natural Gas Hydrates, Annals of New York Academy of Sciences, Sloan, E.D., Happel, J., Hnatow, M.A., eds., 715, p187, (1994)

van der Waals, J.H., and Platteeuw, J.C., "Clathrate Solutions," Adv. Chem. Phys.,vol **2**,1,(1959)

von Stackelberg, M., Naturwiss **36** 327, 359 (1949)

Table 1 Geometry of Cages in Three Hydrate Crystal Structures

Hydrate Crystal Structure	I		II		H		
Cavity	Small	Large	Small	Large	Small	Medium	Large
Description	5^{12}	$5^{12}6^2$	5^{12}	$5^{12}6^4$	5^{12}	$4^35^66^3$	$5^{12}6^8$
Number of Cavities/Unit Cell	2	6	16	8	3	2	1
Average Cavity Radius, Å	3.95	4.33	3.91	4.73	3.91[3]	4.06[3]	5.71[3]
Variation in Radius[1], %	3.4	14.4	5.5	1.73	Not Available		
Coordination Number[2]	20	24	20	28	20	20	36
Number of Waters/Unit Cell	46		136		34		

1. Variation in distance of oxygen atoms from center of cage.
2. Number of oxygens at the periphery of each cavity.
3. Estimates of structure H cavities from geometric models

Table 2 Comparison of Properties of Ice and sI and sII Hydrates[1]

Property	Ice	Structure I	Structure II
Spectroscopic			
Crystallographic Unit Cell			
Space Group	$P6_3/mmc$	Pm3n	Fd3m
No. H_2O molecules	4	46	136
Lattice Parameters at 273K	a =4.52 c =7.36	12.0	17.3
Dielectric Constant at 273 K	94	~58	58
Far infrared spectrum	Peak at 229 cm^{-1}.	Peak at 229 cm^{-1} with others	
H_2O Diffusion Correl Time, (μsec)	220	240	25
H_2O Diffusion Activ. Energy(kJ/m)	58.1	50	50
Mechanical Property			
Isothermal Young's modulus at 268 K (10^9 Pa)	9.5	8.4^{est}	8.2^{est}
Poisson's Ratio	0.33	~0.33	~0.33
Bulk Modulus (272 K)	8.8	5.6	NA
Shear Modulus (272 K)	3.9	2.4	NA
VelocityRatio(Comp/Shear):272K	1.88	1.95	NA
Thermodynamic Property			
Linear. Therm. Expn: 200K (K^{-1})	$56x10^{-6}$	$77x10^{-6}$	$52x10^{-6}$
AdiabBulkCompress:273K(10^{-11}Pa)	12	14^{est}	14^{est}
Speed Long Sound:273K(km/sec)	3.8	3.3	3.6
Transport			
Thermal Condctivity:263K(W/m-K)	2.23	0.49±.02	0.51±.02

1. Modified from Davidson (1983) and from Ripmeester et al. (1994)

Table 3 Ratios of Molecular Diameters to Cavity Diameters[1] for Some Molecules Including Natural Gas Hydrate Formers

		(Molecular Diameter) / (Cavity Diameter)			
		Structure I		Structure II	
	Cavity Type=>	5^{12}	$5^{12}6^{2}$	5^{12}	$5^{12}6^{4}$
Molecule	Guest Dmtr (Å)				
N_2	4.1	0.804	0.700	0.817✓	0.616✓
CH_4	4.36	0.855✓	0.744✓	0.868	0.655
H_2S	4.58	0.898✓	0.782✓	0.912	0.687
CO_2	5.12	1.00	0.834✓	1.02	0.769
C_2H_6	5.5	1.08	0.939✓	1.10	0.826
C_3H_8	6.28	1.23	1.07	1.25	0.943✓
i-C_4H_{10}	6.5	1.27	1.11	1.29	0.976✓
n-C_4H_{10}	7.1	1.39	1.21	1.41	1.07

✓ indicates the cavity occupied by the simple hydrate former

1. cavity radii from Table 2-1 minus 1.4Å water radii

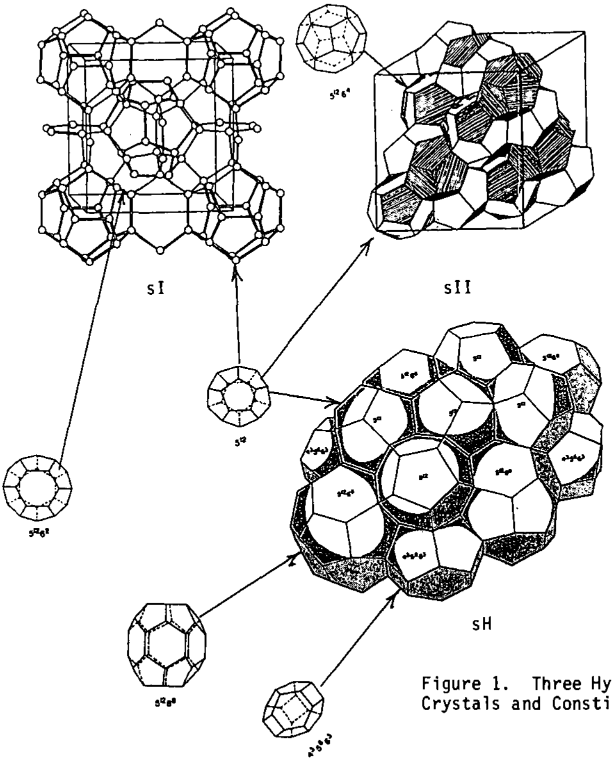
5¹²6⁴
sI
sII
5¹²
5¹²6²
sH
5¹²6⁸
4³5⁶6³

Figure 1. Three Hydrate Unit Crystals and Constituent Cavities

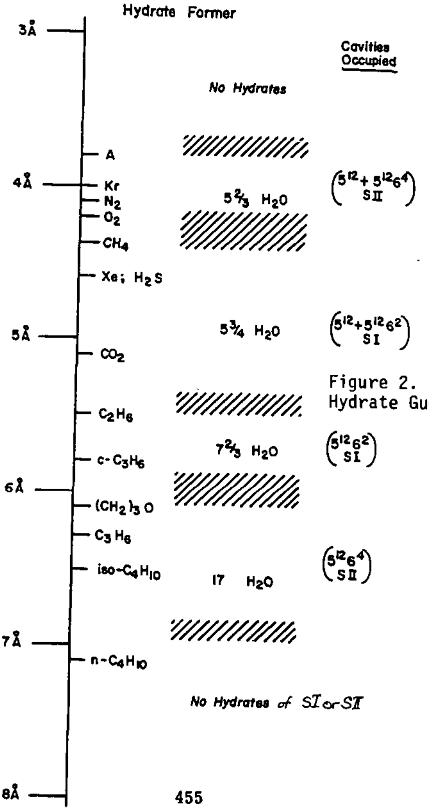
Hydrate Former
Cavities Occupied
3Å
No Hydrates
A
4Å
Kr
N₂
O₂
CH₄
Xe; H₂S
5⅔ H₂O
(5¹² + 5¹²6⁴ SII)
5Å
CO₂
5¾ H₂O
(5¹² + 5¹²6² SI)
C₂H₆
c-C₃H₆
7⅔ H₂O
(5¹²6² SI)
6Å
(CH₂)₃O
C₃H₈
iso-C₄H₁₀
17 H₂O
(5¹²6⁴ SII)
7Å
n-C₄H₁₀
No Hydrates of SI or SII
8Å

Figure 2. Relative Sizes of Hydrate Guest and Host Cavities

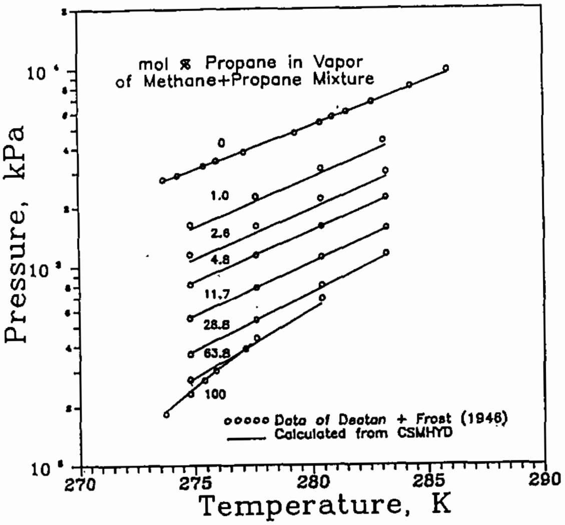

Figure 3. Three-Phase (Lw-H-V) Equilibria of Methane+ Propane Mixtures

---

Figure 4. Three-Phase Equiibria of Methane +(Propane and Two Butanes)

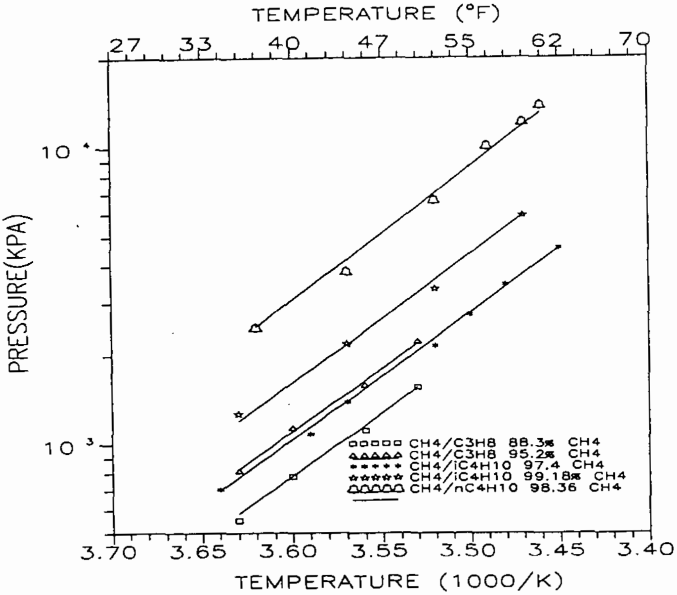

ASSESSMENT OF UNITED STATES GAS HYDRATE RESOURCES

Timothy S. Collett
U.S. Geological Survey, Denver Federal Center
Box 25046, MS-939, Denver, CO 80225

Keywords: gas hydrates, energy resources, natural gas

I. INTRODUCTION

Gas hydrates are crystalline substances composed of water and gas, in which a solid water-lattice accommodates gas molecules in a cage-like structure, or clathrate. Gas hydrates are widespread in permafrost regions and beneath the sea in sediment of outer continental margins. While methane, propane, and other gases can be included in the clathrate structure, methane hydrates appear to be the most common in nature[1]. The amount of methane sequestered in gas hydrates is probably enormous, but World estimates of the amounts are speculative and range over three orders-of-magnitude, from about 100,000 to 270,000,000 trillion cubic feet[2]. The estimated amount of gas in hydrate reservoirs of the world greatly exceeds the volume of known conventional gas reserves. The production history of the Russian Messoyakha gas hydrate field demonstrates that gas hydrates are an immediate source of natural gas that can be produced by conventional methods[3,4]. Gas hydrates also represent a significant drilling and production hazard. Russian, Canadian, and American researchers have described numerous problems associated with gas hydrates, including blowouts and casing failures[3,5,6]. As exploration and development activity moves into deeper water (>300 m) and high latitude arctic environments, the frequency of gas hydrate induced problems will likely increase.

One of the fundamental problems that links the gas hydrate resource and hazard issues is the need for accurate assessments of the gas volumes within a gas hydrate occurrence. Most of the published gas hydrate resource estimates have by necessity been made by broad extrapolation of only general knowledge of local geologic conditions[2]. The primary objectives of our gas hydrate research efforts in the U.S. Geological Survey are to document the geologic parameters that control the occurrence of gas hydrates and to assess the volume of natural gas stored within the onshore and offshore gas hydrate accumulations of the United States. This paper begins with a discussion of the geologic parameters that affect the stability and formation of gas hydrates, which is followed by a description of the methodology used to assess gas hydrate resources. This paper ends with a cumulative estimate of the *in-place* gas hydrate resources of the United States onshore and offshore regions.

II. GAS HYDRATE TECHNICAL REVIEW

Under appropriate conditions of temperature and pressure (figs. 1*A*, 1*B*, and 1*C*), gas hydrates usually form one of two basic crystal structures known as Structure I and Structure II. Each unit cell of Structure I gas hydrate consists of 46 water molecules that form two small dodecahedral voids and six large tetradecahedral voids. Structure I gas hydrates can only hold small gas molecules such as methane and ethane, with molecular diameters not exceeding 5.2 angstroms. The unit cell of Structure II gas hydrate consists of 16 small dodecahedral and 8 large hexakaidecahedral voids formed by 136 water molecules. Structure II gas hydrates may contain gases with molecular dimensions in the range of 5.9 to 6.9 angstroms, such as propane and isobutane. At conditions of standard temperature and pressure (STP), one volume of saturated methane hydrate (Structure I) will contain as much as 164 volumes of methane gas -- because of this large gas-storage capacity, gas hydrates are thought to represent an important source of natural gas. For a complete description of the structure and properties of hydrates see the summary by Sloan[7].

II.A. Permafrost Gas Hydrates

Onshore gas hydrates are known to be present in the West Siberian Basin[8] and are believed to occur in other permafrost areas of northern Russia, including the Timan-Pechora province, the eastern Siberian Craton, and the northeastern Siberia and Kamchatka areas[9]. Permafrost-associated gas hydrates are also present in the North American Arctic. Direct evidence for gas hydrates on the North Slope of Alaska comes from a core-test, and indirect evidence comes from drilling and open-hole industry well logs which suggest the presence of numerous gas hydrate layers in the area of the Prudhoe Bay and Kuparuk River oil fields[10,11]. Well-log responses attributed to the presence of gas hydrates have been obtained in about one-fifth of the wells drilled in the Mackenzie Delta, and more than half of the wells in the Arctic Islands are inferred to contain gas hydrates[12,13]. The combined information from Arctic gas-hydrate studies shows that, in permafrost regions, hydrates may exist at subsurface depths ranging from about 130 to 2,000 m[1].

II.B. Marine Gas Hydrates

The presence of gas hydrates in offshore continental margins has been inferred mainly from anomalous seismic reflectors that coincide with the predicted phase boundary at the base of the gas-hydrate stability zone. This reflector is commonly called a bottom-simulating reflector or BSR. BSRs have been mapped at depths below the sea floor ranging from about 100 to 1,100 m[1]. Gas hydrates have been recovered in gravity cores within 10 m of the sea floor in sediment of the Gulf of Mexico[14], the offshore portion of the Eel River Basin of California[15], the Black Sea[16], the Caspian Sea[17], and the Sea of Okhotsk[18]. Also, gas hydrates have been recovered at greater sub-bottom depths during research coring along the southeastern coast of the United States on the Blake Outer Ridge[19], in the Gulf of Mexico[20], in the Cascadia Basin near Oregon[21], the Middle America Trench[22,23], offshore Peru[24], and on both the eastern and western margins of Japan[25,26].

Because gas hydrates are widespread in permafrost regions and in offshore marine sediments, they may be a potential energy resource. In-place World estimates for the amount of natural gas in gas hydrate deposits range from 5.0×10^2 to 1.2×10^6 trillion cubic feet for permafrost areas and from 1.1×10^5 to 2.7×10^8 trillion cubic feet for oceanic sediments[2]. The published gas hydrate resource estimates show considerable variation, but oceanic sediments seem to be a much greater resource of natural gas than continental sediments. Current estimates of the amount of methane in the world gas hydrate accumulations are in rough accord at about 7×10^5 trillion cubic feet[2]. If these estimates are valid, then the amount of methane in gas hydrates is almost two orders of magnitude larger than the estimated total remaining recoverable conventional methane resources, estimated to be about 9×10^3 trillion cubic feet[27].

III. GEOLOGIC CONTROLS ON GAS HYDRATE DISTRIBUTION

Review of previous gas hydrate studies indicates that the formation and occurrence of gas hydrates is controlled by formation temperature, formation pore-pressure, gas chemistry, pore-water salinity, availability of gas and water, gas and water migration pathways, and the presence of reservoir rocks and seals. In the following section, these geologic controls on the stability and formation of gas hydrates will be reviewed and assessed.

III.A. Formation-Temperature, Formation Pore-Pressure, Gas Chemistry

Gas hydrates exist under a limited range of temperature and pressure conditions such that the depth and thickness of the zone of potential gas-hydrate stability can be calculated. Depicted in the temperature/depth plots of figures 1*A*, 1*B*, and 1*C* are a series subsurface temperature profiles from an onshore permafrost area and two laboratory-derived gas-hydrate stability curves for different natural gases[28]. These gas-hydrate phase-diagrams (figs. 1*A*, 1*B*, and 1*C*) illustrate how variations in formation-temperature, pore-pressure, and gas composition can affect the thickness of the gas-hydrate stability zone. In each phase-diagram, the mean-annual surface temperature is assumed to be -10°C; however, the depth to the base of permafrost (0°C isotherm) is varied for each temperature profile (assumed permafrost depths of 305 m, 610 m, and 914 m). Below permafrost, three different geothermal gradients (4.0°C/100 m, 3.2°C/100 m, and 2.0°C/100 m) are used to project the sub-permafrost temperature profiles. The two gas-hydrate stability curves represent gas hydrates with different gas chemistries. One of the stability curves is for a 100 percent methane hydrate, and the other is for a hydrate that contains 98 percent methane, 1.5 percent ethane, and 0.5 percent propane. The only difference among the three phase-diagrams (figs. 1*A*, 1*B*, and 1*C*) is the assumed pore-pressure gradient. Each phase diagram is constructed assuming different pore-pressure gradient; 9.048 kPa/m [0.400 psi/ft] (fig. 1*A*), 9.795 kPa/m [0.433 psi/ft] (fig. 1*B*), and 11.311 kPa/m [0.500 psi/ft] (fig. 1*C*).

The zone of potential gas-hydrate stability in each phase-diagram (figs. 1*A*, 1*B*, and 1*C*) lies in the area between the intersections of the geothermal gradient and the gas-hydrate stability curve. For example, in figure 1*B*, which assumes a hydrostatic pore-pressure gradient, the temperature profile projected to an assumed permafrost base of 610 m intersects the 100 percent methane-hydrate stability curve at about 200 m, thus marking the upper boundary of the methane-hydrate stability zone. A geothermal gradient of 4.0°C/100 m projected from the base of permafrost at 610 m intersects the 100 percent methane-hydrate stability curve at about 1,100 m; thus, the zone of potential methane-hydrate stability is approximately 900 m thick. However, if permafrost extended to a depth of 914 m and if the geothermal gradient below permafrost is 2.0°C/100 m, the zone of potential methane-hydrate stability would be approximately 2,100 m thick.

Most gas-hydrate stability studies assume that the pore-pressure gradient is hydrostatic (9.795 kPa/m; 0.433 psi/ft). Pore-pressure gradients greater than hydrostatic will correspond to higher pore-pressures with depth and a thicker gas-hydrate stability zone. A pore-pressure gradient less than hydrostatic will correspond to a thinner gas-hydrate stability zone. The effect of pore-pressure variations on the thickness of the gas-hydrate stability zone can be quantified by comparing each of the phase diagrams in figures 1*A*, 1*B*, and 1*C*. For example, in figure 1*A*, which assumes a 9.048 kPa/m (0.400 psi/ft) pore-pressure gradient, the thickness of the 100 percent methane-hydrate stability zone with a 610 m permafrost depth and a sub-permafrost geothermal gradient of 2.0°C/100 m would be about 1,600 m. However, if a pore-pressure gradient of 11.311 kPa/m (0.500 psi/ft) is assumed (fig. 1*C*) the thickness of the methane-hydrate stability zone would be increased to about 1,850 m.

The gas-hydrate stability curves in figures 1*A*, 1*B*, and 1*C* were obtained from laboratory data published in Holder and others[28]. The addition of 1.5 percent ethane and 0.5 percent propane to the pure methane gas system shifts the stability curve to the right, thus deepening the zone of potential gas-hydrate stability. For example, assuming a hydrostatic pore-pressure gradient (fig. 1*B*), a permafrost depth of 610 m, and a sub-permafrost geothermal gradient of 4.0°C/100 m, the zone of potential methane (100 percent methane) hydrate stability would be about 900 m thick; however, the addition of ethane (1.5 percent) and propane (0.5 percent) would thicken the potential gas-hydrate stability zone to 1,100 m.

III.B. Pore-Water Salinity

It is well known that dissolved salt can depress the freezing-point of water. For example, the base of the ice-bearing permafrost on the North Slope of Alaska does not coincide with the 0°C isotherm but with a lower temperature[10]. This freezing-point depression has been attributed in part to the presence of salt in the unfrozen pore-waters. Salt, such as NaCl, when added to a gas-hydrate system, also lowers the temperature at which gas hydrates form. Pore-water salts in contact with the gas during gas hydrate formation can reduce the crystallization temperature by about 0.06°C for each part per thousand of salt[28]. Therefore, a pore-water salinity similar to that of seawater (32 ppt) would shift the gas-hydrate stability curves in figures 1*A*, 1*B*, and 1*C* to the left about 2°C and reduce the thickness of the gas-hydrate stability zone.

III.C. Availability of Gas and Water

Most naturally occurring gas hydrates are characterized by two crystal structures known as Structure I and Structure II[7]. The ideal gas/water ratio of Structure I gas hydrate is 8/46, whereas the ideal gas/water ratio of Structure II gas hydrate is 24/136. These ideal ratios confirm the observation that gas hydrates contain a substantial volume of gas. For example, if all the cages of Structure I gas hydrate are occupied, each volume of gas hydrate will contain 189 volumes of gas at standard temperature and pressure. The ideal hydrate gas/water ratios also indicate that there is a substantial amount of water stored in the gas-hydrate structure. These high gas and water concentrations demonstrate that the formation of gas hydrate requires a large source of both gas and water. Thus, it becomes necessary to quantify the potential sources of gas and water when assessing a potential gas-hydrate accumulation.

III.D. Gas and Water Migration Pathways

Other factors controlling the availability of gas and water are the geologic controls on fluid migration. As previously shown, gas hydrates contain a substantial volume of gas and water that must be supplied to a developing gas-hydrate accumulation. If effective migration pathways are not available, it is unlikely that a significant volume of gas hydrates would accumulate. Therefore, geologic parameters such as rock permeability and the nature of faulting must be evaluated to determine if the required gas and water can be delivered to the potential hydrate reservoir.

III.E. Presence of Reservoir Rocks and Seals

The study of gas-hydrate samples recovered during research coring operations in oceanic sediments suggests that the physical nature of in-situ gas hydrates may be highly variable[7]. Gas hydrates were observed to be (1) occupying pores of coarse-grained rocks; (2) nodules disseminated within fine-grained rocks; (3) a solid, filling fractures; or (4) a massive unit composed mainly of solid gas hydrate with minor amounts of sediment. Because of the limited number of gas-hydrate samples, it is not known if gas hydrates are usually pore-filling material or occur as massive units. A study of well logs from northern Alaska indicate that gas hydrates occur there as pore-filling constituents within coarse-grained reservoir rocks[10]. This study suggests that porous rock intervals serve as reservoir rocks in which gas and water can be concentrated in the amounts necessary for gas-hydrate formation. Therefore, the presence of reservoir rocks may play a role in gas-hydrate formation, particularly in well-consolidated rock intervals. It is also speculated that the presence of effective reservoir seals or traps may play a role in gas-hydrate formation. Gas generated at depth moves upward, generally along tilted permeable carrier beds, until it either seeps at the surface or meets an impermeable barrier (trap) that stops or impedes its flow. As migrating gas accumulates below an effective seal, the total gas concentrations may reach the critical amounts necessary for the formation of gas hydrates. Thus, impermeable seals can provide a mechanism by which the required gas can be concentrated within reservoir rocks. Besides conventional reservoirs and trapping mechanisms, it is possible for gas hydrate to form its own reservoir and trap. As gas migrates into the zone of gas-hydrate stability, it may interact with the available pore water to generate gas hydrate. With the appropriate volumes of gas and water, the pore space within the reservoir rock could be completely filled, thus making the rock impermeable to further hydrocarbon migration. The plugging of gas pipelines and production tubing by gas hydrates is testimony to the sealing potential of gas hydrates[7]. It has also been shown that, in marine environments, gas hydrates can mechanically displace sediments to form their own reservoir. Thus, the availability of reservoir quality rocks may not always be a limiting factor.

IV. GAS HYDRATE RESOURCE ASSESSMENT

The major goal of this resource assessment is to estimate the gas hydrate resources in the United States, both onshore and offshore. Similar to the assessment of the conventional resources in the 1995 U.S. Geological Survey (USGS) Oil and Gas Assessment[29], this assessment of gas hydrates is based on a play-analysis scheme, which was conducted on a province-by-province basis. We have defined, described, and assessed all the gas-hydrate plays in the United States regardless of their current economic or technological status. Therefore, this assessment is concerned with the *in-place* gas hydrate resources--that is, the amount of gas that may exist within the gas hydrates without reference to its recoverability. In a play analysis method, prospects (potential hydrocarbon accumulations) are grouped according to their geologic characteristics into plays. The geologic settings of the hydrocarbon occurrences in the play are then modeled. Probabilities are assigned to the geologic attributes of the model necessary for generation and accumulation of hydrocarbons. In this assessment method, geologists make judgments about the geologic factors necessary for the formation of a hydrocarbon accumulation and quantitatively assess the geologic factors that determine its size.

In this assessment, 11 gas-hydrate plays were identified within four offshore and one onshore petroleum provinces (figure 2); for each play, *in-place* gas hydrate resources were estimated. Estimates for each of the 11 plays were aggregated to produce the estimate of total gas-hydrate resources in the United States. The offshore petroleum provinces assessed consist of the U.S. Exclusive Economic Zone (EEZ) adjacent to the lower 48 States and Alaska. The only onshore province assessed was the North Slope of Alaska, which included State water areas and some offshore Federal waters. The provinces shown in figure 2 are geographic in character; however, their formation represents an attempt to group the individual petroleum provinces along broad geologic lines. Maps depicting the geologic data required for this hydrate assessment have been included in the U.S. Geological Survey 1995 National Oil and Gas Assessment CD-ROM[29]. Maps of bathymetry, sedimentary thickness, total organic carbon (TOC) content of the sediments, seabed temperature, geothermal gradient, and hydrate stability zone thickness have been published for all four offshore provinces assessed in the U.S. Geological Survey 1995 National Oil and Gas Assessment CD-ROM[29]. Maps depicting the thickness of the onshore gas-hydrate stability zone in northern Alaska are also included in the Assessment CD-ROM[29].

The estimates of *in-place* gas-hydrate resources included in this report are presented in the form of complementary cumulative probability distributions (fig. 3). These distributions summarize the range of estimates generated by the FASPU computer program[29] as a single probability curve in a "greater than" format (fig. 3). Our estimates are reported at the mean and at the 95th, 75th, 50th, 25th, and 5th fractiles. We consider the 95th and 5th fractiles to be "reasonable" minimum and maximum values, respectively. In-place gas resources within the gas hydrates of the United States are estimated to range from 112,765 to 676,110 trillion cubic feet of gas (TCFG) [3,193 to 19,142 trillion cubic meters of gas (TCMG)], at the 0.95 and 0.05 probability levels, respectively (fig. 3). Although these ranges of values show a high degree of uncertainty, they do indicate the potential for enormous quantities of gas stored as gas hydrates. The mean in-place value for the entire United States is calculated to be 320,222 trillion cubic feet of gas (TCFG) [9,066 trillion cubic meters of gas (TCMG)]. This assessment of *in-place* gas hydrates represents those deposits that constitute the resource base *without reference to recoverability.*

V. REFERENCES CITED

1. Kvenvolden, K.A., 1988, Methane hydrate--A major reservoir of carbon in the shallow geosphere?: Chemical Geology, v. 71, p. 41-51.
2. Kvenvolden, K.A., 1993, Gas hydrates as a potential energy resource -- A review of their methane content, *in* Howell, D.G., ed., The Future of Energy Gases: U.S. Geological Survey Professional Paper 1570, p. 555-561.
3. Makogon, Y.F., 1981, Hydrates of natural gas: Tulsa, Penn Well Publishing Company, 237 p.
4. Collett, T.S, 1993, Natural gas production from Arctic gas hydrates, *in* Howell, D.G., ed., The Future of Energy Gases: U.S. Geological Survey Professional Paper 1570, p. 299-312.
5. Franklin, L.J., 1981, Hydrates in Arctic Islands, *in* Bowsher, A.L., ed., Proceedings of a Workshop on Clathrates (gas Hydrates) in the National Petroleum Reserve in Alaska, July 16-17, 1979, Menlo Park, California: U.S. Geological Survey Open-File Report 81-1298, p. 18-21.

6. Yakushev, V.S., and Collett, T.S., 1992, Gas hydrates in Arctic regions: risk to drilling and production: Second International Offshore and Polar Engineering Conference, June 14-19, 1992, San Francisco, California, Proceedings, p. 669-673.
7. Sloan, E.D., 1990, Clathrate hydrates of natural gases: New York, Marcel Dekker, Inc., 641 p.
8. Makogon, Y.F., Trebin, F.A., Trofimuk, A.A., Tsarev, V.P., and Cherskiy, N.V., 1972, Detection of a pool of natural gas in a solid (hydrate gas) state: Doklady Academy of Sciences U.S.S.R., Earth Science Section, v. 196, p. 197-200.
9. Cherskiy, N.V., Tsarev, V.P., and Nikitin, S.P., 1985, Investigation and prediction of conditions of accumulation of gas resources in gas-hydrate pools: Petroleum Geology, v. 21, p. 65-89.
10. Collett, T.S., 1993, Natural gas hydrates of the Prudhoe Bay and Kuparuk River area, North Slope, Alaska: American Association of Petroleum Geologists Bulletin, v. 77, no. 5, p. 793-812.
11. Collett, T.S., 1983, Detection and evaluation of natural gas hydrates from well logs, Prudhoe Bay, Alaska, in Proceedings of the Fourth International Conference on Permafrost, Fairbanks, Alaska: Washington D.C., National Academy of Sciences, p. 169-174.
12. Judge, A.S., 1988, Mapping the distribution and properties of natural gas hydrates in Canada: Proceedings of the American Chemical Society Third Chemical Congress of the North American Continent, June 6-7, Toronto, Ontario, Abstract no. 29.
13. Judge, A.S., and Majorowicz, J.A., 1992, Geothermal conditions for gas hydrate stability in the Beaufort-Mackenzie area: The global change aspect: Global and Planetary Change, v. 98, no. 2/3, p. 251-263.
14. Brooks, J.M., Cox, B.H., Bryant, W.R., Kennicutt, M.C., Mann, R.G., McDonald, T.J., 1986, Association of gas hydrates and oil seepage in the Gulf of Mexico: Organic Geochemistry, v. 10, p. 221-234.
15. Brooks, J.M., Field, M.E., and Kennicutt, M.C., 1991, Observations of gas hydrates in marine sediments, offshore northern California: Marine Geology, v. 96, p. 103-109.
16. Yefremova, A.G., and Zhizhchenko, B.P., 1974, Occurrence of crystal hydrates of gas in sediments of modern marine basins: Doklady Akademii Nauk SSSR, v. 214, p. 1179-1181.
17. Ginsburg, G.D., Guseinov, R.A., Dadashev, A.A., Ivanova, G.A., Kazantsev, S.A., Soloviev, V.A., Telepnev, Ye.V., Askery-Nasirov, R.E., Yesikov, A.D., Mal'tseva, V.I., Mashirov, Yu.G., and Shabayeva, I.Yu., 1992, Gas hydrates in the southern Caspian Sea: Izvestiya Akademii Nauk Serya Geologisheskaya, v. 7, p. 5-20.
18. Ginsburg, G.D., Soloviev, V.A., Cranston, R.E., Lorenson, T.D., and Kvenvolden, K.A., 1993, Gas hydrates from the continental slope, offshore from Sakhalin Island, Okhotsk Sea: Geo-Marine Letters, v. 13, p. 41-48.
19. Kvenvolden, K.A., and Barnard, L.A., 1983, Hydrates of natural gas in continental margins, *in* Watkins, J.S., and Drake, C.L., eds., Studies in Continental Margin Geology: American Association of Petroleum Geologists Memoir 34, p. 631-641.
20. Shipboard Scientific Party, 1986, Sites 614-624, *in* Bouma, A.H., and others, Proceedings, Deep Sea Drilling Project, Initial Reports, Washington D.C., U.S. Government Printing Office, v. 96, p. 3-424.
21. Shipboard Scientific Party, 1994, Site 892, *in* Westbrook, G.K., and others, Proceedings, Ocean Drilling Program, Initial Reports, College Station, Texas, v. 146, p. 301-375.
22. Kvenvolden, K.A., McDonald, T.J., 1985, Gas hydrates of the Middle America Trench, Deep Sea Drilling Project Leg 84, *in* von Huene, R., Aubouin, J., and others, Initial Reports Deep Sea Drilling Project, Washington, D.C., U.S. Government Printing Office, v. 84, p. 667- 682.
23. Shipley, T.H., and Didyk, B.M., 1982, Occurrence of methane hydrates offshore Mexico, *in* Watkins , J.S., Moore, J.C., and others, Initial Reports, Deep Sea Drilling Project: Washington D.C., U.S. Government Printing Office, v. 66, p. 547-555.
24. Kvenvolden, K.A., and Kastner, M., 1990, Gas hydrates of the Peruvian outer continental margin, *in* Suess, E., von Huene, R., and others, Proceedings, Ocean Drilling Program, Scientific Results, College Station, Texas, v. 112, p. 517-526.
25. Shipboard Scientific Party, 1990, Site 796, *in* Tamake, K., and others, Proceedings, Ocean Drilling Program, Initial Reports, College Station, Texas, v. 127, p. 247-322.
26. Shipboard Scientific Party, 1991, Site 808, *in* Taira, A., and others, Proceedings, Ocean Drilling Program, Initial Reports, College Station, Texas, v. 131, p. 71-269.
27. Masters, C.D., Root, D.H., and Attanasi, E.D., 1991, Resource constraints in petroleum production potential: Science, v. 253, p. 146-152.
28. Holder, G.D., Malone, R.D., Lawson, W.F., 1987, Effects of gas composition and geothermal properties on the thickness and depth of natural-gas-hydrate zone: Journal of Petroleum Technology, September, p.1147-1152.
29. Gautier, D.L., Dolton, G.L., Takahashi, K.I., and Varnes, K.L., 1995, National assessment of United States oil and gas resources on CD-ROM: U.S. Geological Survey Digital Data Series 30.

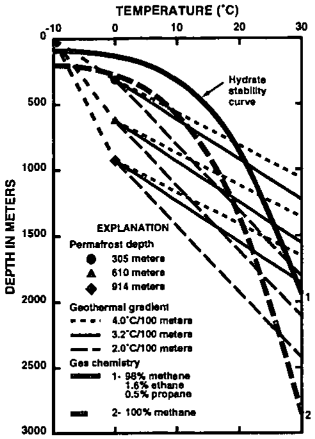

Figure 1*A*. Graph showing the depth-temperature zone in which gas hydrates are stable in a permafrost region [9.048 kPa/m pore-pressure gradient].[28]

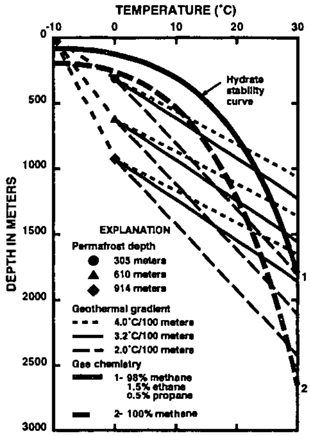

Figure 1*B*. Graph showing the depth-temperature zone in which gas hydrates are stable in a permafrost region [9.795 kPa/m pore-pressure gradient].[28]

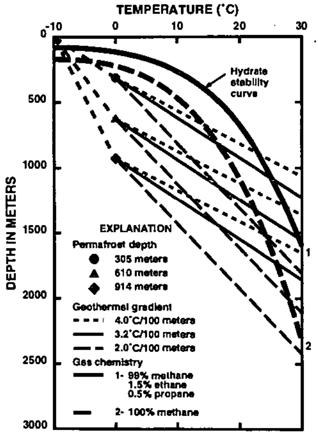

Figure 1*C*. Graph showing the depth-temperature zone in which gas hydrates are stable in a permafrost region [11.311 kPa/m pore-pressure gradient].[28]

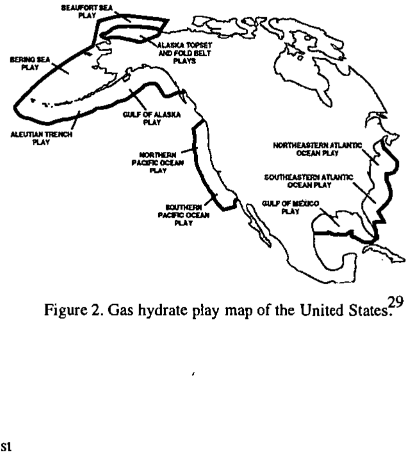
BEAUFORT SEA PLAY
ALASKA TOPSET AND FOLD BELT PLAYS
BERING SEA PLAY
GULF OF ALASKA PLAY
ALEUTIAN TRENCH PLAY
NORTHERN PACIFIC OCEAN PLAY
SOUTHERN PACIFIC OCEAN PLAY
NORTHEASTERN ATLANTIC OCEAN PLAY
SOUTHEASTERN ATLANTIC OCEAN PLAY
GULF OF MEXICO PLAY

Figure 2. Gas hydrate play map of the United States.[29]

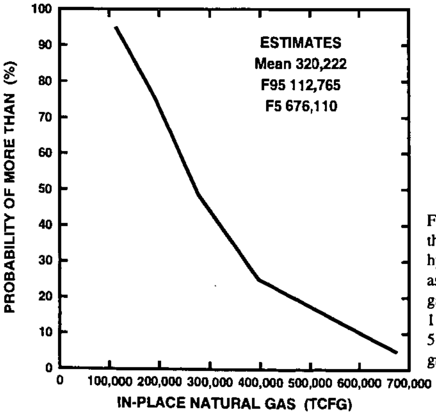

Figure 3. Cumulative probability curve showing the estimated in-place resources within the gas hydrates of the United States. The curve is read as follows: there is a 95 percent chance that the gas hydrate resource potential is greater than 112,765 trillion cubic feet of gas, and there is a 5 percent chance that the gas hydrate resource is greater than 676,110 trillion cubic feet of gas.[29]

CLATHRATE-BASED FUEL STORAGE AND TRANSPORT MEDIA: POTENTIAL IMPACT

M. D. Max, Code7420, R. E. Pellenbarg, Code6101, Naval Research Laboratory, Washington, D.C. 20375

Synthetic hydrate fuel, methane, gas

INTRODUCTION

Clatrhrates, particularly methane and other hydrocarbon gas hydrates, have been known as laboratory curiosities since chlorine hydrate ($Cl_2.6H_2O$),was reported (Faraday, 1823). In the 1930's and 1940's the natural gas industry had problems with the formation of a crystalline, wax-like substance in natural gas transport pipes. This material clogged the lines and research was focusedon understanding the origin and physical chemistry of the material so that its appearance in pipelines could be minimized. Methane hydrates are now recognized as being very widespread in marine sediments and in permafrost regions, and may constitute the largest store of fixed carbon on earth (Kvenvolden, 1993). Our present knowledge about methane hydrate physical chemistry, and the potential large volumes of recoverable methane from naturally occurring sources argues strongly that methane is likely to be the fuel of the future, especially if the aspect of compressing methane within a clathrate crystal lattice can utilized on an industrial scale.

There is currently an increasing interest in methane as a fuel because the technology for handling it as a fuel, and the direct (e.g., on-site combustion for heating) and indirect (electricity generation) energy conversion technologies are well understood and cost effective. Additionally, because methane contains more hydrogen atoms for each carbon atom in its molecule than any other hydrocarbon fuel, less carbon dioxide is produced upon combustion. Also, gas field methane is usually relatively pure and relatively easy to purify. Its use as a fuel is thus more environmentally benign than other more complex hydrocarbon fuels or coal. Methane also produces much less carbon dioxide per mole than alcohols, where OH substitutes for one molecule of H, and much less than in liquid petroleum and oil based fuels.

Methane ("natural gas") produced from conventional gas deposits is plentiful, easily delivered (as a gas) to the user by an in-place domestic distribution system, and as a fuel, methane is clean burning and has a respectable heat content. The prospect of methane recovery from vast oceanic gas hydrate deposits, however, argues for an almost indefinite supply of methane, the recovery of which will probably speed the development of the gas-energy economy to replace the current oil-based economy. In addition to this development being ecologically sound, oil may be viewed better as an industrial feedstock than as a direct fuel, so long as a convenient, alternate source of energy such as methane is made available.

Methane is particularly amenable to transport and handling as a gas in pipelines and transport to point use in pipes within contiguous land areas. In fact, most of the early work into the chemistry of methane hydrates was undertaken by the gas transport industry because hydrates were forming and clogging gas pipelines even at relatively high temperatures and moderate pressures. Current technology frequently requires that methane fuel be moved as either compressed gas or as liquefied gas, as when natural gas is imported to the U.S. distribution grid from foreign gas fields. Of course, many fixed-site utilizations for natural gas (e.g. space heating, electrical power generation, or cooking) rely exclusively on gaseous methane as a fuel stock. Where technical or geographic difficulties prohibit the use of piped distribution, however, other means of distributing gas must be developed for use. Storage of methane (e.g., compressed gas) at the point of use may also a problem so long as a continuous piped supply is not available.

Both compressed gas and liquified gas, as transport media, possess serious safety concerns associated with the flammability of the material (compressed natural gas) or the cold temperatures and ultimate flammability/potentially explosive nature of the liquefied medium. This paper suggests and examines a new application of clathrate chemistry, which could have a significant impact on methane fuel use and distribution if implemented. We call attention to a potential third alternative for bulk gas transport and point-of-use storage, which would be energy dense, fairly stable, non-flammable in bulk, easy to transport, and potentially useable as-is for motor fuels.

SYNTHETIC METHANE CLATHRATE FUEL (SMCF)

Naturally occurring methane hydrates are not stable at sea level ambient temperatures and pressures. However, it is not intended to use pure methane hydrate as the basis for the new fuel transport and storage media. Current experimental results show that hydrates can be fabricated both from natural gas more dense than methane (de Boer et al, 1985) with variable physical property ranges that are stable well above the normal methane hydrate P-T stability field (Sloan, 1990). Also, in the course of producing synthetic methane hydrate, metastabilities about the liquidus line exist (Stern et al., 1996), which may point toward controlling metastability ranges of methane hydrate rather than expanding the methane hydrate stability field. This broader stability of naturally occurring multiple gas clathrates, poorly understood metastability, and relative ease with which synthetic methane (based) hydrate can be formed, leads us to suggest that research fabricating special property methane clathrates is feasible and that research should be undertaken to fabricate a new methane fuel storage and transport media.

The gas to be transported would be carried as a stabilized water-gas hydrate, or as a clathrate utilizing selected (probably gaseous) additives which could expand the stability field for pure methane-pure water clathrates well beyond that of natural methane hydrate or even some of the other natural hydrates that are stable nearer standard T-P (Fig. 1). It is clear that development and adoption of a clathrate-based fuel transportation/distribution system, to augment the in-place domestic gaseous-state fuel distribution complex, would offer many advantages above and beyond those associated with safety.

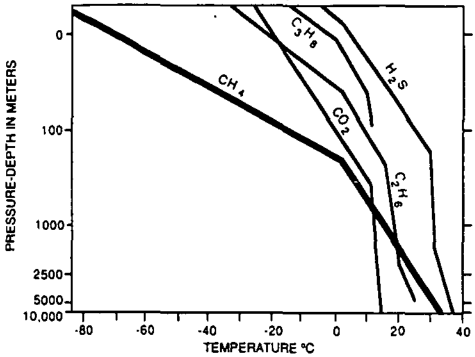

Figure 1. Natural hydrate phase boundaries for different common gases. From Makogon (1988). Replotted with temperature in normal scale and pressure-depth in meters seawater. 0 is atmospheric pressure at sea level. CH_4, methane; C_2H_6, ethane; C_3H_8, propane; C_4H_{10}, butane, the highest molecular weight of the paraffin gases, which most easily forms clathrates. CO_2, carbon Dioxide; H_2S, hydrogen sulphide.

Although the energy density of methane clathrate is low compared with common liquid fuels (Table 1), its potential energy density is actually greater than a similar volume of liquid methane, and up to 164 times (Kvenvolden, 1993) the same volume of methane gas (at STP). The compression factor is obtained because methane molecules are forced closer together in the crystalline solid methane hydrate than is obtained by any other form of methane compression. For our energy conversion factor we use 160 X compression factor, although it is unlikely that the industrial synthetic fuel will actually have a compression factor that high, because it is conservatively less than the maximum anticipated and results in even numbers appropriate for preliminary estimation.

Fuel or form of methane	Formula	Density g/cc	Energy Content Btu/lb	Energy Content Btu/ft3
Methane Gas	CH_4	7x10-4	160 *3	1,150 *3
Methane Liquid	CH_4	0.42*2	1,500 *4	152,000 *4
Methane-water solid (natural hydrate energy conversion equivalent)	$CH_4(H_2O)_6$	~ 1.0	277 *4	15,800 *4 *5
Methane-water solid (natural hydrate potential)	$CH_4(H_2O)_6$	~ 1.0	277 *4	184,000*4 *6
Octane (gasoline)	C_8H_{18}	0.70	19,000 *3	840,000 *3
JP-5 *1	$C_{14}H_{30}$	0.77	18,500 *3	930,000 *3

Table 1. Energy content of various Hydrocarbon Fuels. *1, Less volatile jet fuel used by Navy, mandated for use on carriers to reduce danger of explosion. *2, boiling point -161 C. *3, STP Conditions, gas phase. *4, Energy may be consumed producing gaseous methane from these forms or in containing them. *5. Combustion products are H_2O and CO_2. Energy content takes into account energy required to decompose hydrate to H_2) and CH_4; this figure represents energy content after conversion at 150 volumes of methane in hydrate per

volume of methane at STP . * 6. Total potential energy content with no account taken of dissociation energy requirements based on 160 volumes of methane in hydrate per 1 volume of methane at STP (engineering may reduce the energy requirements for dissociation from specially fabricated clathrate or natural heat sinks may be used as an energy source).

It must be pointed out that the precise nature of SMCF is not known because it has yet to be designed and fabricated. Thus, the energy density, energy losses upon fabrication and subsequent gasification, and the equivalent energy of methane after conversion, in addition to the cost of the conversion and other engineering necessary for an SMCF system need to be known before a commercial value can be placed on the SMCF media. The potential energy content of naturally occurring methane hydrate is high enough to allow for some system or usage diminution and still remain an attractive new fuel storage and transport media. Thus, if an energy efficient means for gasifying synthetic methane clathrate fuel (SMCF), can be found, it may prove to be a more efficient means of compressing methane than liquification.

Because it is unlikely that the energy density of a clathrate-based fuel media will ever significantly approach that of liquid petroleum fuels, the clathrate fuel is clearly not appropriate for all vehicles. For instance, vehicles with small volumes capacity for fuel storage, such as private motor vehicles and aircraft, where weight/volume is a major factor, are not likely end-point users. Larger platforms, however, such as ships and possibly high-speed trains which could be made environmentally benign (with respect to noise of energy generation and exhaust), might be possible end-users, especially when the other attributes of clathrate based fuel media, such as inhibiting uncontrolled fires and explosions in commercial applications and explosion damping and deflecting in military applications, are taken into consideration.

The proposed safer transport system utilizes gas hydrates (clathrates) which are physical associations of water ice and low molecular weight gas molecules (e.g. methane, ethane, propane or butane). These clathrates form spontaneously when water and a suitable low molecular weight gas (e.g. methane, carbon dioxide, hydrogen sulfide, chlorine) are mixed at suitable temperatures (generally low) and pressures (generally moderate). Indeed, the older literature contains many references to gas hydrates forming spontaneously in natural gas transmission pipelines, and often blocking them; this potential situation requires the drying of gas prior to pipeline transportation (DoE, 1987).

Research into the low pressure species has mainly concerned to developing techniques that will allow for industrial capability to efficiently dissolve, or gasify hydrates. Where bonding interaction between guest and host molecules might be enhanced somewhat, gas that normally does not hydrate, such as hydrogen, may be bound into specially formulated hydrates. If host cavities were to be lined with groups having a high hydrogen bonding character, such as hydroxyl or amino groups, other factors, such as the solubility parameter of the host, would be of less importance. Increased hydrogen bonding power might also be induced by charging guest molecules prior to exposure to hydrate lattice, or through the use of magnetic field charging (moving the fuel in a field, pulsing a field, or moving a field with respect to the orientation of the hydrate). Release of gas could be induced through heating, lowering of pressure, or electronic stimulation that would produce effects similar to that of microwaving food (where the frequency of the microwave is specific to water molecules).

FUEL SYSTEM REQUIREMENTS

The proposed SMCF storage and transport system would consist of three separate components: (1) Formation Module, (2) Transport Vessels, and (3) Gas Separation Unit.

(1). Hydrate Formation Module (HFM). Methane hydrates are stable under moderate pressures, and low temperatures (Fig. 1). The HFM will consist of a pressure vessel into which are pumped stabilizer, water spray, and methane; the P-T conditions of formation are presently uncertain but may be different from those needed for stability of the special hydrate during storage. Recent research shows that the methane hydrate forms immediately upon mixing water with the gas, when the system is within the stability field of the clathrate (Peter Brewer, MBARI, pers. comm., November, 1996). Once the hydrate is formed, the material would be removed from the HFM, and transferred to the transport vessel for movement to point of use or distribution.

(2) Hydrate Transport Vessel (HTV). The HTV would consist of a insulated container which could contain the stable special hydrate at ambient to moderate pressures. The insulation would more than likely consist of plastic foam such as is used by the refrigeration industry; vacuum jackets would be avoided because of cost and safety concerns. The HTV could be fabricated in any desired shape, and might evolve to be conformal to the hull or some interior structural members of the platform using the stored gas as a fuel, for example, in the double hull space of a ship.

(3) Gas Separation Unit (GSU). The GSU could be integral to the HTV, or separate, as mandated by the ultimate use of the released fuel gas. The clathrates are unstable in the presence of elevated heat; the hydrate could be decomposed by direct heating (e.g. a clathrate slush would be transferred to a heated vessel: gas evolves from the slush and escapes for use, and the water

from the hydrate is discarded or retained for use in making more hydrate later). Alternatively, the hydrate slush could be sprayed with water, the heat in which would be sufficient to decompose the hydrate. In either case, the evolved gas would be routed to a device (e.g. engine) which could use the combustible gas as a fuel.

It must be noted that there is no inherent reason why the units listed above would necessarily be separate components. For example, the storage vessel could contain integral sub-sections which would allow both formation of and decomposition of the gas hydrate right in the HTV. Further, it is technically possible to design and build an internal combustion engine which would use hydrate as the only, or majority, fuel; such a system would be similar to water-injection technology as applied to internal combustion engines, as in some experimental fighter plane engines and race cars.

CONCLUSIONS AND DISCUSSION

We have considered the feasibility of forming gas hydrates on demand, the utility of doing so (safe transportation of methane as a fuel), and potential end uses of gas moved as a hydrate (decomposition into gas for combustion, or design of engines to operate on hydrate itself). It is appropriate to examine the effects of adding a clathrate-based fuel on the current energy economy of a developed society.

Where would the SMCF system be applied and how would it develop? These questions cannot be fully answered because: 1. the engineering possibilities have yet to be explored, 2. the effect on market forces cannot be assessed beyond observing that the technology and potential fuel handling systems largely exist or can be developed at low cost, and, 3. government regulations that would apply (but do not yet exist) could either inhibit or promote development of both the SMCF itself and a world gas economy.

In the broadest sense, a SMCF-based fuel economy would be akin to the system based on liquid hydrocarbons. Specially formulated clathrates would be transported in the form of slush in much the same way as present liquid hydrocarbons. Transportation is solid form could utilize much of the present container-handling equipment and facilities including much of the sea, rail, and road equipment already in existence. Production as slush (Najafi and Schaetzle, 1989) would also allow pumped distribution. Moreover, where safety concems are paramount, the SMCF might be used because of could greatly enhance safety; even in the presence of open flames, methane is evolved slowly from hydrates through breakdown of the crystal structure. This means that all of the gas or liquid methane available as an explosive component in present conventional methane storage media can only be evolved at a rate at which it could feed a fire, but not an explosion without first collecting evolved gas. In addition, upon gas evolution, substantial quantities of water are also produced, whose presence could be engineered to inhibit accidental ignition attributes of the system.

A dedicated clathrate-based methane fuel economy, in existence and developing, would drive exploration and development to utilize the vast quantities of methane that are only now being recognized as present on the planet (Max and Lowrie, 1996). Current conservative estimates indicate that naturally occurring methane hydrates contain at least twice the amount of fixed carbon as do conventional methane, liquid hydrocarbons, and coal, combined, on Earth (Kvenvolden, 1993), and it is unlikely that this fuel source will remain untapped, especially if an SMCF system can be developed at a reasonable cost.

References

De Boer, R.B., Houbolt, J.J.H.C. & Lagrand, J. 1985. Formation of gas hydrates in a permeable medium. Geologie en Mijnbouw, 64, 245-249.

DoE, 1987. Gas hydrates Technology Status Report. Department of Energy DOE/METC-870246 (DE8700127) 54pp.

Faraday, M. 1823. On fluid chlorine. Philosophical Transactions Royal Society of London 22A, 160-189.

Kvenvolden, K.A. 1993. A primer on gas hydrate. In: Howell, D.G. et al. (eds). The future of energy gases. USGS Professional Paper 1570, 279-291.

Makogon, Yu.F. 1988. Gas-hydrate accumulations and permafrost development. In: Senneset, K. (ed). Permafrost. Fifth International Conference Proceedings, 95-101.

Max, M.D. & Lowrie, A. 1996. Methane hydrate: A frontier for exploration of new gas resources. Journal of Petroleum Geology, 19, 41-56.

Najafi, M. & Schaetzle, W.J. 1989. Analysis of clathrate solidification. IEEE CH2781-3/89/0000, 1839-1844.

Sloan, E.D., Jr. 1990. Clathrate Hydrates of Natural Gases. Marcel Dekker, Inc., New York and Basel. 641pp.

Stern, L.A., Kirby, S.H. & Durham, W.B. 1996. Peculiarities of methane clathrate hydrate formation and solid-state deformation, including possible superheating of water ice. Science, 273, 1843-1848.

CLATHRATE HYDRATES: SOME NEW STRUCTURAL INFORMATION[*]

Konstantin A. Udachin[♦], Gary D. Enright, Christopher I. Ratcliffe and John A. Ripmeester[†]
Steacie Institute for Molecular Sciences
National Research Council of Canada
Ottawa, Ontario, Canada K1A 0R6

Keywords: clathrate hydrates, crystal structure, structure H hydrate, CO_2 as small cage guest, bromine hydrate

INTRODUCTION

The accurate prediction of conditions for hydrate formation depends strongly on the availability of good structural information[1]. For clathrate hydrates, a complete description of structure involves not only the unit cell parameters and average atomic positions, but also the cage occupancies. In order to provide this kind of information, it is necessary to use techniques such as diffraction, which is sensitive to long range order, in combination with techniques such as NMR which are sensitive to local order[2]. Previously we have demonstrated the use of NMR methods for the determination of relative cage occupancies for structure I and II hydrates[3].

Although the crystal structures of Str. I and II hydrates have been known for a considerable length of time[4], the detailed lattice information on Str. H hydrate has remained unknown until recently[5]. It is also remarkable that a number of other apparently simple clathrate hydrate structures remain unsolved. Examples are the low hydrate of dimethyl ether[6] and bromine hydrate. The latter is especially intriguing as the hydrate was first reported in 1829[7], and it has been studied on and off for over 160 years[8]. A crystal space group and a set of lattice parameters were reported by Allen and Jeffrey[9], although atomic coordinates were not obtained. More recently, Dyadin and co-workers[8] have claimed that on the basis of hydration numbers which range from ~ 7 to 12, and the different crystal morphologies reported that there is evidence for as many as four different structures. We have now shown that a single crystal structure accounts for all of the different hydration numbers and crystal morphologies.

Another factor that is relatively unappreciated is the fact that although the small 5^{12} (D) cage is common to all 3 structures, I, II and H, the symmetry and size of these small cages is different[10], and hence their behaviour towards guest molecules should also be quite different. This is very directly evident from the chemical shift parameters of xenon trapped in the small cages which suggest that the structure II and H small cages are significantly larger and less symmetric than the Structure I small cage. Experiments with CO_2 have confirmed this idea.

Experimental

Bromine hydrate single crystals suitable for diffraction were grown from solutions of different concentrations to give material of different morphologies and hydration numbers see table 1. The crystal structures were determined on a Siemens diffractometer equipped with a CCD detector using Mo K_α radiation. In all, 16 different crystals were examined. The structures were solved with the Shextl software package.

Double hydrates of xenon or $^{13}CO_2$ were made by sealing into 10mm pyrex tubes measured quantities of powdered ice, along with the appropriate large cage and small cage guests. Samples were conditioned for times lasting from ~ 1 day to several weeks. NMR spectra were measured on an Bruker MSL 200 spectrometer equipped with a double-tuned solenoid probe suitable for cross-polarization and dipolar decoupling[2]. Temperature variation was achieved with a cold gas-flow system and a temperature controller. Spectral simulations were carried out with the Bruker Xedplot package.

RESULTS AND DISCUSSION

a) The structure of bromine hydrate

As was pointed out in the introduction, bromine hydrate can be made with different hydration numbers and vastly different morphologies[8]. Hydration numbers have been reported by at least 13 different authors and vary from 7 to 12[8]. For the crystals used in this study, the composition of the crystals was controlled by changing the concentration of the starting solutions from ($Br:H_2O$) 1:20 to 1:5. (table 1). The morphology of the different crystals is shown in fig. 1. Six crystals were studied in detail in order to come to a satisfactory solution of the structure, the space group and cell parameters for ten other crystals were determined to cover the different crystal morphologies. For all of the crystals studied, the space group turned out to be the one reported by Allen and Jeffrey [9]: $P4_2/mnm$. At -100°C the lattice parameters are a=23.044, c=12.075 Å.

One view of the structure is shown in fig.2. The unit cell can be represented[11] as follows: $2D_A.8D_B.8T_A.8T_B.4P.172H_2O$ with a $5^{12}6^3$ (P) cage, two distinct $5^{12}6^2$ (T_A, T_B) cages similar to those in str. I, and two kinds of 5^{12} (D_A, D_B) cages. The reason for the difficulty in finding a good structural solution becomes apparent when examining the guest positions in fig. 2. As opposed to structures with hydrocarbon guests, in the bromine hydrate case the scattering is dominated by the highly disordered bromine guest: the P cage has as many as 12 possible positions for bromine; the T cages each have 14 (T_A) or 15 (T_B), with the site occupancies varying from 20 down to 2 %. The highly anisotropic site distribution is evident especially for the T cages, where the centre of the cavity can be seen to be clear as the bromine atoms are confined to be near to the equatorial plane of the cage. The variable hydration numbers observed for bromine hydrate arise from the variable degree of filling of the large cages (table 1). The minimum hydration number possible is 8.6.

It will be another challenge to work out a thermodynamic model for bromine hydrate, as the clathrate has 3 types of large cage (P, T_A, T_B) suitable for bromine, and two small cages (D_A, D_B) which may contain oxygen or nitrogen from the air (some electron density in the small cages was indeed observed). The bromine hydrate structure is the only one of its type, as all other molecules of this size form str. II hydrate. Attempts to form a different hydrate with xenon as helpgas initially gave a structure II hydrate, but with time this was seen to revert back to the bromine hydrate structure. The fact that the large cages do not need to be full seems to be unique as well. This suggests that guest - guest interactions may play an important role in dictating structure type. Significant guest - guest interactions are likely for the electron-rich bromine molecule which should have a sizable molecular quadrupole moment. Another challenge is the understanding of the reasons for the different crystal morphologies. It appears that some kind of "self-inhibition " takes place to suppress the growth of certain crystal faces when the bromine concentration varies in the growth solution.

b) NMR Chemical Shifts and Cage Size

One of the first applications of ^{129}Xe NMR spectroscopy was the chemical shift resolution of the distinct sites in str. I hydrate[2]. It was also noted that the chemical shifts for the 5^{12} cages in str. I and II were quite different[10]. According to the empirical chemical shift - cage size relationship, the D cage in str. II is larger than that in str. I. Since little is known about potential helpgases for str. H, it was thought that the Xe NMR parameters could give some guidance for the prediction of the suitability of CO_2 as such a helpgas for the two small cages. ^{129} Xe chemical shift for different hydrate cages are summarized in table 2 along with the point symmetry of the cages.

We note that str. I has the only pseudospherical D cage. From the chemical shift data, the other D cages are not only less symmetric, as indicated by non-zero chemical shift anisotropies, but also somewhat larger, as seen from the smaller shifts. This is likely to be of some importance for all small cage guests, since in str. I the fact that the small cage occupancy decreases with increasing guest size suggests that it is the repulsive interactions that limit the cage occupancy. Also, especially for non-spherical guests small departures from spherical symmetry are likely to be important. CO_2 is a good test molecule, as it appears to be a marginal guest for the 5^{12} cages. An indirectly determined hydration number from thermodynamic measurements is 7.0[12], which leads to an occupancy ratio $\theta_S/\theta_L \sim 0.\ 3$ through the relationship between hydration number and guest occupancy ratio once the free energy difference between the hypothetical empty lattice and ice is known[3] . In a previous NMR study[13], small cage CO_2 guests were not observed, as the central region of the spectrum is dominated by contributions from liquid and/or gaseous CO_2. By using the appropriate polarization transfer pulse technique, these contributions can be eliminated from the spectrum, leaving the small cage contribution visible (fig. 3 (top)). On the other hand, for a double hydrate of propane and CO_2, the ^{13}C spectrum indicates that nearly all of the CO_2 molecules are now located in the 5^{12} cage, that, from the Xe spectrum, is slightly larger and shaped like an oblate spheroid. The very weak central line indicates that there is almost no CO_2 in the large cage of the hydrate. The two propane ^{13}C resonance lines aren't resolved and occur as a single peak at ~ 18 ppm.

Based on these observations, what would one expect for the Str. H small cages ? From the ^{129}Xe spectra, the D and D' cages should be as large as the str. II D cage and also quite asymmetric. An attempt was made to produce a hydrate sample of neohexane with CO_2 as small cage guest. The product gave the ^{13}C spectrum shown in fig. 4. Indeed, contributions can be found from CO_2 in both D and D' cages with NMR lineshapes characteristic of axial and non-axial symmetry. We can conclude that CO_2 is indeed suitable as a small cage guest in str. H hydrate.

CONCLUSIONS

The long outstanding problem of the structure(s) of bromine hydrate has been solved succesfully by examining 16 crystals of different morphologies and hydration numbers. There is just one structure, now solved in detail, and it is the tetragonal form originally suggested by Jeffrey.

By using the Xe NMR spectrum observed for xenon trapped in the small cages in str. I, II and H, it was predicted that the small cages in str. II and H should be good sites for CO_2. This was confirmed by using ^{13}C NMR spectroscopy to examine a number of CO_2 -containing hydrates. CO_2 is now also confirmed as a possible helpgas molecule for the structure H hydrate. The fact that all of the small cages (D and D' in str I, II and H) have different shapes and sizes (especially as defined by ^{129}Xe NMR) suggests that the Langmuir constants which define the affinity of small guests for these cages should also be different.

Acknowledgments: KAU and CIR thank the NATO Science Program for a Research Visit Grant.

[*] Published as NRCC no:39129

[•] Permanent address: Institute of Inorganic Chemistry, Russian Academy of Sciences, Novosibirsk, Russia

[1] Author for correspondence

---

[1] Davidson, D. W. in " Water. A Comprehensive Treatise. Franks, F. Ed., Plenum, New York, N. Y., *1973*, Vol. 2; Sloan, Jr., E. D. " Hydrates of Natural Gas ", Marcel Dekker, New York, N. Y., *1991*

[2] Davidson, D. W, Handa, Y. P., Ripmeester, J. A., J. Phys. Chem. *1986* **90**, 6549

[3] Collins, M., Ratcliffe, C. I., Ripmeester, J. A., J. Phys. Chem. *1990* **94**, 157

[4] Ripmeester, J. A., Tse, J. S., Ratcliffe, C. I., Powell, B. S., Nature *1987* **325**, 135

[5] Udachin, K. A., Enright, G. A., Ratcliffe, C. I., Ripmeester, J. A., Supramol. Chem. (in press)

[6] Miller, S. L., Gough, S. R., Davidson, D. W., J. Phys. Chem., *1977* **81**, 2154

[7] Lowig, Ann. Pogg., *1829* **16**, 376

[8] Dyadin, Y. A., Belosludov, V. R., in Comprehensive Supramolecular Chemistry, Atwood, J. L., Davies, J. E. D., MacNicol, D. D., Vogtle, F., Ed., Pergamon, *1996* **6**, 789

[9] Allen, K. W., Jeffrey, G. A., J. Chem. Phys. *1963* **38**, 2304

[10] Ripmeester, J. A., Ratcliffe, C. I., Tse, J. S., J. Chem. Soc. Faraday Trans. I *1988*, 3731

[11] Jeffrey, G. A., in Inclusion Compounds, Atwood, J. L., Davies, J. E. D., MacNicol, D. D., Ed., Pergamon, *1982*, Vol. 1

[12] Bozzo, A. T., Chen, H-S., Kass, J. R., Barduhn, A., Desalination, *1975* **16**, 303

[13] Ratcliffe, C. I., Ripmeester, J. A. J. Phys. Chem. *1986* **90**, 1259

Table 1. Some details on the crystals of bromine hydrate studied

Initial composition of solution (Br_2:H_2O)	Average degree of filling of large cavities[a] (P, T_A, T_B)	Crystal Stoichiometry[a] (Br_2:H_2O)
1:20	0.805	1:10.68
1:14	0.914	1:9.41
1:10	0.946	1:9.09
1:7	0.962	1:8.94
1:5	0.998	1:8.62

[a] from analysis of crystal structure data

Table 2 . Hydrate cages, cage sizes and ^{129}Xe chemical shift data

Structure	cage type	symmetry	radius/Å[a]	σ_{Xe}(iso)[b] (ppm)	δ[c] (ppm)	η[d]
I	5^{12}(D)	m3	2.50	-242	0	
I	$5^{12}6^2$(T)	42m	2.93	-152	-21	
II	5^{12}(D)	3m	2.50	-231	-16	
II	$5^{12}6^4$(H)	43m	3.28	-80	0	
H	5^{12}(D)	mmm	2.50	-231	-13.6	0.8
H	$4^35^66^3$(D')	62m	2.50	-212.4	-31.8	
H	$5^{12}6^8$(E)	6/mm	4.1	---------	-------	

[a] estimate from X-ray diffraction data; [b] isotropic chemical shift;[c] $\delta=(2/3)\Delta\sigma$ - chemical shift anisotropy;[d] asymmetry parameter - departure of cage geometry from axial symmetry

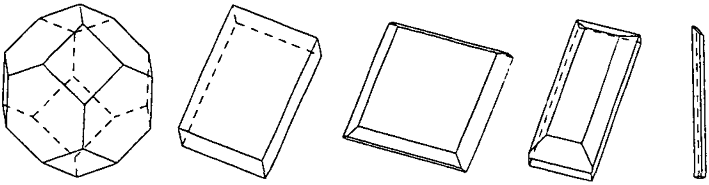

Figure 1. Morphology of different bromine hydrate crystals studied. In general, the massive form is seen most readily in dilute solutions, the needles in concentrated solutions.

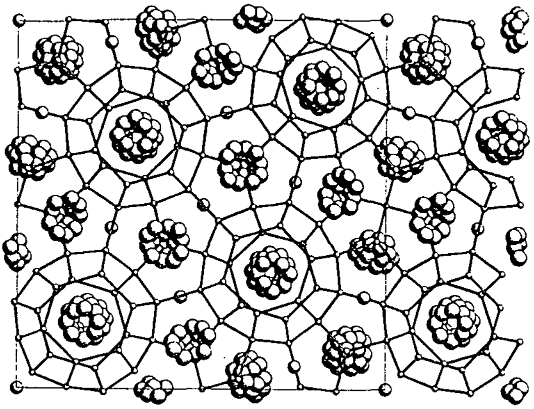

Figure 2. General view of the bromine hydrate structure with the view approximately along the z direction; hydrogen atoms are omitted for clarity; the bromine atoms are shown in their many possible disordered positions in the cages, the maximum occupancy being one molecule per cage

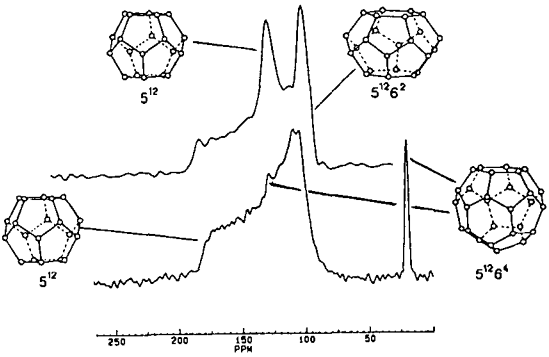

Figure 3. ^{13}C NMR powder patterns obtained for a) CO_2 hydrate b) double hydrate of CO_2 and propane. Note that the symmetry rather than the cage size determine the chemical shift patterns which reflect the nature of the guest motion (isotropic vs anisotropic). Pseudo-spherical cages give the sharp central lines (since cross-polarization methods were used, the liquid and gaseous CO2 are not visible).

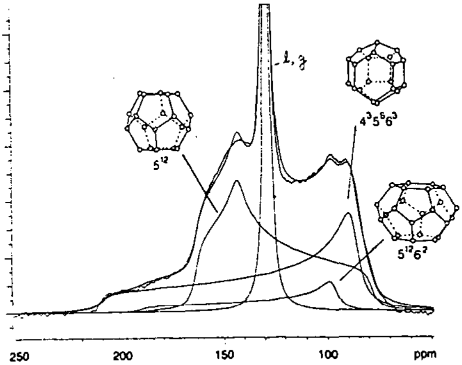

Figure 4. ^{13}C NMR spectrum for a str.H hydrate of CO_2 and 2,2 dimethyl butane. There is a small amount of str. I CO_2 hydrate present also. This spectrum does show liquid and gaseous CO_2 as a sharp line in the centre of the spectrum, as it was not recorded with a cross -polarization technique. The ^{13}C tensor pattern is axially symmetric for the $4^{3}5^{6}6^{3}$ (D') cage, and is a general tensor pattern for the low symmetry 5^{12} (D) cage.

THERMOGENIC GAS HYDRATES, GULF OF MEXICO CONTINENTAL SLOPE

Roger Sassen and Ian R. MacDonald

Geochemical and Environmental Research Group, Texas A&M University, College Station, Texas 77845

Keywords: gas hydrates, thermogenic hydrocarbons, Gulf of Mexico

INTRODUCTION

The Gulf of Mexico continental slope is a natural laboratory for gas hydrates that contain hydrocarbons from deeply buried thermogenic sources. Thermogenic hydrocarbons (oil and gas) from actively generating Mesozoic source rocks (>6 km burial depth) migrate vertically along conduits associated with actively-moving salt structures and faults to subsurface reservoirs (2-4 km) of Tertiary age[1]. The hydrocarbon trapping system is so "leaky" that large volumes of thermogenic hydrocarbons reach the sea floor[1], and enter the water column[2].

Although biogenic gas hydrates are abundant on the Gulf slope[3], oil and gas from deep source rocks create a geochemically complex and physically dynamic environment for thermogenic gas hydrates at the sea floor. Structure II gas hydrate containing C_1-C_4 thermogenic hydrocarbon gases was first sampled in 1984 by piston cores in 530-560 m water depths on the Gulf slope offshore Louisiana[4]. Identification of the hydrate as structure II was based on the relative abundance of the C_3 and i-C_4 hydrocarbons[4]. The structural assignment was corroborated using solid-state nuclear magnetic resonance (NMR)[5]. Research on gas hydrates of the Gulf slope, however, has advanced rapidly in the last few years, and our objective here is to summarize new results.

THE BUSH HILL STUDY AREA

The Bush Hill site in the Green Canyon area of the Gulf slope offshore Louisiana is a well-documented site for study of thermogenic gas hydrates (27°47.5' N and 91°15.0' W). Bush Hill is a fault-related sea-floor mound about 500 m wide, with relief of about 40 m[6]. Water depth of the mound crest is about 540 m, where mean water temperature is about 7° C (range = 6 to 11° C) Phase equilibria models indicate that Bush Hill is within the stability zone of thermogenic gas hydrates (Sloan, E.D., pers. communication).

Sea-floor sediments contain crude oil and related free hydrocarbon gases. Bacterial oxidation of these hydrocarbons produces CO_2 which precipitates as authigenic carbonate rock with isotopically-light $\delta^{13}C$ values[7]. The crest of the mound is colonized by seep-dependent chemosynthetic organisms including bacterial mats, vestimentiferan tube worms, and methanotrophic mussels[8]. Persistent natural oil slicks appear on satellite remote sensing images of the sea surface over Bush Hill[2].

Thermogenic gas hydrates and gases that vent to the water column at the mound crest are readily sampled by research submarines. Copious streams of gas vent continuously to the water column where subsurface migration conduits intersect the sea floor[9,10]. Thermogenic gas hydrates form around the orifices of gas vents. The gas hydrates at vents are not dispersed in sediments as nodules or thin seams, but instead occur as continuous masses. Lens-shaped masses of yellow to orange gas hydrates breach the sea-floor at numerous locations on the crest of Bush Hill[9,10]. The hydrates form sediment-draped mounds 30-50 cm high and up to several m in width, with exposed gas hydrate visible at the edges of mounds[10].

Vent Gases

The C_1-C_5 hydrocarbons of the vent gases are dominated by methane (C_1 = 91.1-94.7%), and $\delta^{13}C$ values of C_1 are within the narrow range of -42.4 to -45.6 ‰ PDB (Table 1). The C_1-C_5 distributions and $\delta^{13}C$ of C_1 of the vent gases (Table 1) correlate to gases from underlying subsurface reservoirs of Jolliet Field[11].

Table 1. Normalized C_1-C_5 hydrocarbon compositions and methane $\delta^{13}C$ of vent gases and thermogenic gas hydrates (Structure II and Structure H) at Bush Hill. Number in superscript indicates the citation to the data.

Sample	C_1	$\delta^{13}C$	C_2	C_3	*i*-C_4	*n*-C_4	*i*-C_5
Vent Gas [10]	93.2	-43.3	4.3	1.5	0.3	0.6	0.3
Vent Gas [10]	93.5	-42.5	4.3	1.4	0.2	0.4	0.2
Vent Gas [10]	94.7	-45.6	3.9	0.7	0.1	0.5	0.2
Vent Gas [10]	94.6	-43.8	3.8	0.7	0.1	0.5	0.3
Vent Gas [10]	91.1	-42.4	4.8	1.8	0.4	1.2	0.8
Hydrate (II)[10]	71.7	-36.3	10.6	12.6	2.6	1.7	0.8
Hydrate (II)[10]	80.2	-38.5	9.4	7.3	1.6	1.2	0.3
Hydrate (II)[10]	72.1	-39.9	12.4	11.4	2.3	1.6	0.3
Hydrate (H)[6]	21.2	-29.3	9.5	7.5	2.5	17.5	41.1

Structure II hydrate

Hydrocarbon compositions of massive hydrate lenses of Bush Hill are shown in Table 1. The C_1-C_5 hydrocarbons of the hydrate gases are dominated by C_1 (71.7-80.2%). The $\delta^{13}C$ values of C_1 are in the range of -36.3 to -39.9 ‰ PDB, somewhat heavier than vent gases, possibly because of bacterial activity[10]. The C_2 and C_3 hydrocarbons are both present in similar but relatively high percentages compared with the vent gas (Table 1). Preliminary NMR of an intact hydrate sample preserved in liquid nitrogen is consistent with structure II hydrate (Ripmeester, J., pers. communication).

Structure H gas hydrate

Structure H hydrates produced in the laboratory can enclose larger molecules than structure I or II hydrates, including common thermogenic hydrocarbons such as *i*-C_5. Given the widespread occurrence of petroleum, it was postulated in 1993 that structure H hydrate could co-exist in nature with structure II hydrate[12].

Evidence for the natural occurrence of structure H gas hydrate at the Bush Hill locality was first reported in 1994[6]. Massive amber-colored gas hydrate breached the sea-floor. It had been exposed when a buoyant lobe of hydrate broke free of the sediment and floated upwards into the water column. Identification of structure H hydrate was based on abundant *i*-C_5, which represented 41.1% of the total C_1-C_5 hydrocarbon distribution of the sample (Table 1). The δ^{13} C of C_1 from the sample is heavy (-29.3 ‰ PDB), possibly because of bacterial activity[6].

Experimentally-Precipitated gas hydrate

Gas hydrate was experimentally precipitated at the crest of Bush Hill in 1995 using natural vent gases as the starting material[10]. Water temperatures during experiments were 9.0-9.2°C. Precipitation of white to yellow gas hydrate was noted to occur within minutes.

The hydrocarbon compositions of experimentally precipitated gas hydrates are similar to vent gas compositions[10]. The C_1-C_5 hydrocarbons of the experimentally precipitated gas hydrates gases are dominated by methane (C_1 = 87.7-93.9%), and the $\delta^{13}C$ values of C_1 are within the -40.5 to -45.3 ‰ PDB range.

CONCLUSIONS

Thermogenic gas hydrates occur on the Gulf of Mexico continental slope because of active vertical migration of oil and gas to the sea floor within their stability zone. The Bush Hill seep site on the Gulf slope is an important case history. Massive thermogenic gas hydrates occur in association with the orifices of hydrocarbon vents. Both structure II and structure H hydrates appear to co-exist in this environment. Gas hydrate is also rapidly precipitated in sea-floor experiments using natural vent gas as the starting material. More sophisticated sampling and experiments from research submarine platforms could significantly enhance our understanding of thermogenic gas hydrate formation in the deep sea.

ACKNOWLEDGEMENTS

Support for research was provided by the NOAA National Undersea Research Center, University of North Carolina at Wilmington, and the Minerals Management Service, New Orleans.

REFERENCES

1. R. Sassen; J.M. Brooks; I.R. MacDonald; M.C. Kennicutt II; N.L. Guinasso; A. G. Requejo Trans. Gulf Coast Assoc. Geol. Socs 1993 43 349-355.

2. MacDonald, I.R.; N.L. Guinasso, Jr.;S.G. Ackleson; J.F. Amos; R. Duckworth; R. Sassen; J.M. Brooks J. Geophys. Res. 1993 98 16,351-16,364.

3. J.S. Booth; M. M. Rowe; K. Fischer U.S. Geological Survey Open-File Report 96-272, June 1966.

4. Brooks J.M.; M.C. Kennicutt II; R.R. Fay; T.J. McDonald; Sassen R. Science 1984 225 409-411.

5. Davidson, D.W.; S.K. Garg, S.R. Gough, Y.P. Handa; C.I. Ratcliffe; J.A. Ripmeester; J.S. Tse; W.F. Lawson Geochim. Cosmochim. Acta. 1986 50 619-623.

6. Sassen, R.; I.R. MacDonald Org. Geochem. 1994 22 1029-1032.

7. Sassen R.; H.H. Roberts; P. Aharon; J. Larkin; E.W. Chinn; R. Carney Org. Geochem. 1993 20 77-89.

8. MacDonald I.R; G.S. Boland; J.S. Baker: J.M. Brooks; M.C. Kennicutt II; R.R. Bidigare R.R. Marine Biol. 1989 101 235-247.

9. MacDonald, I.R.; N.L. Guinasso; R. Sassen; J.M. Brooks; L. Lee; K.T. Scott Geology 1994 22 699-702.

10. Sassen, R.; I.R. MacDonald. Org. Geochem. 1996, in press.

11. Kennicutt II, M.C.; J.M. Brooks; G.J. Denoux Mar. Chem. 1988 24 39-59.

12. Mehta, A.P.; Sloan, E.D. J. Chem. Eng. Data 1993 38 580-582.

HYDRATE FORMATION DURING CONTROLLED RELEASE OF CH_4 AND CO_2 IN MONTEREY BAY

Peter G. Brewer [*], Franklin M. Orr [+], Jr., G. Friederich [*], K.A. Kvenvolden [#], and D.L. Orange [*]
* Monterey Bay Aquarium Research Institute, P.O. Box 628, Moss Landing CA 95039
+ School of Earth Sciences, Stanford University, Stanford CA 94305
# U.S. Geological Survey, 345 Middlefield Road, Menlo Park CA 94025

Keywords: Methane hydrate, CO_2 hydrate, ocean chemistry

INTRODUCTION

We have initiated a program of research into gas hydrate formation in the deep sea by controlled release of gas into natural sea water and marine sediments with the object of investigating the formation rates and growth patterns in natural systems, and the geochemical stability of the reaction products over time. Here we present a brief account of the experiments we have performed to date, we describe the novel experimental apparatus and procedures developed by our group for *in situ* oceanic work, and comment briefly on the significance of our results.

Laboratory experiments on the formation of hydrates are well known (1,2,3) and the techniques typically involve rocking or shaking the reactants in a pressure vessel, and initiation of the reaction with ice crystals or by supercooling. The experience of laboratory researchers is that significant (> 24 hours for methane) induction times delay the onset of hydrate formation (4), and several mechanistic theories have arisen to explain this lag in terms of the activation barrier associated with cluster formation. The growth of hydrates in nature does not involve shaking the reactants, nor is supercooling or the presence of ice crystals part of the deep sea natural environment, and therefore we approached our first *in situ* experiment with genuine curiosity as to whether the reaction would proceed via simple injection of the gas within the time frame of a few hours available to us for observation. We report here that we have repeatedly observed the formation of hydrates in a few seconds from methane, methane+ethane+propane, and CO_2, under various oceanic conditions, and have begun a program of time series observations of material left in place in our natural laboratory on the sea floor for an extended period of time.

EXPERIMENTAL METHODS

We have made use of Remotely Operated Vehicle (ROV) technology, and specifically the ROV *Ventana* (5,6) operated by the Monterey Bay Aquarium Research Institute from the research vessel *Point Lobos*, to carry out our experiments. The basic vehicle has a depth rating of 1,850 m and is powered by a 40 hp electro/hydraulic power pack. The vehicle is linked to the surface by a Kevlar armored tether with five copper conductors and an optical fiber core of ten elements which carry all control and telemetry signals. Imaging is provided by a Sony DXC-3000 three-chip color video camera with a Fujinon 5.5 to 40 mm zoom lens through which we observed and recorded the experiment. A Conductivity - Temperature - Pressure sensor (CTD; Sea Bird Instruments) is mounted on the vehicle and data is telemetered in real time to the control room.

Below the main frame of the vehicle is an open tool sled structure which housed the gas tank for the methane, and mixed gas experiments. The basic system is similar to that described earlier by us (7). A pressure regulator set to 0.7 Mpa above ambient pressure and a needle valve that limited the flow rate to about 125 ml per minute were in line. Gas was distributed to the reaction chambers by four hydraulically actuated pistons (Allenair) operating quarter turn valves that were controlled directly by us through the *Point Lobos* control room interface. The valves and reaction tubes were mounted on an aluminum box frame carried on the front of the vehicle and positioned for optimum viewing. The reaction tubes were vented to the outside ocean by an overflow tube at the top of the cylinder, arranged so as to trap a small gas bubble at all times while allowing for pressure equalization. A peristaltic pump was attached to all reaction cylinders to flush sea water at the local temperature and salinity through the apparatus prior to gas injection. The gas flow schematics are illustrated in Fig. 1.

For CO_2 release we faced the problem of dispensing a liquid at the pressures and temperatures encountered. Two systems were used: overpressuring the liquid CO_2 with a bubble of He gas to expel the fluid from a vertically mounted tank; and use of a hydraulically activated piston to expel the liquid CO_2 from a pressured reservoir. Once the CO_2 was expelled the gas flow, valving and reaction vessel were identical to that for methane.

The gas was expelled into acrylic reaction cylinders (60 x 4.5 cm; volume 954 cm^3) mounted vertically on the frame; a second reaction chamber with a plane viewing surface, and large enough to contain a temperature probe of five thermistors was also constructed and used in the later experiments. The chambers contained either sea water alone, or were partially filled with sediments of varying grain sizes. No provision was made for sample recovery on board ship at this time, and the observations were purely visual, although the environmental conditions for the experiment are well defined by the CTD sensor.

OBSERVATIONS

Methane Hydrate Formation

In our first experiment (January, 1996) we used pure methane gas (Linde); the thermodynamic boundary for methane hydrate formation posed by the local hydrographic (P,T,S) conditions in Monterey Bay is close to 525 m water depth. We paused at about 500m to inject a small amount of gas as a precaution to clear the lines, then drove *Ventana* to a depth of about 910m and switched on the peristaltic pump to flush the system of trapped sea water and achieve T,S equilibrium with the external medium (approximately 3.9^0C; $34.42\%_0$). Once the system had flushed we injected methane gas by bubble stream through a 10 µm porous frit at the bottom of the reaction cylinders. Methane hydrate formation occurred within a few seconds, seen easily as a bright reflective bubbly mass at the gas/water interface at the top of the tube. The hydrate formed as a white rind on the gas bubble surface that appeared to separate the water and gas from further rapid reaction unless some mechanical disturbance occurred. The reaction was reproducible; an injection into a second reaction cylinder produced an identical result. No significant induction period was observed, nor was anything other than gas and natural sea water present.

Of the two remaining reaction cylinders one contained about 20 cm of coarse sand, and the other a similar amount of fine grained mud. Here the hydrate formation was again first seen at the top of the tube. But the pores of the coarse sand matrix were soon observed to be flooded with hydrate, which sealed off further gas flow. The effect was to create cracking and then lifting of a major piece of the solidified sand column. Gas flow through the fine mud caused channels to open up since the capillary pressure for the gas to enter the pore spaces was higher than that required to displace the sediment. White hydrate masses quickly formed on the walls of the channels and gas created void spaces with an appearance and effect quite different from the coarse sand matrix. On recovery of the vehicle the hydrates formed in our experiment dissociated during transit to the surface, and we were not able to recover specimens for analysis.

CO_2 Hydrate Formation

In a second dive with an almost identical experimental arrangement (water, and sediment containing, reaction cylinders) we observed hydrate formation with CO_2. Here the local thermodynamic boundary for CO_2 hydrate formation occurs at about 350m water depth. We added a small amount of helium gas to the CO_2 cylinder prior to the dive so as to create an overpressure to drive the liquid CO_2 out of the primary reservoir. *Ventana* was then driven to about 568 m, and gas injected as before. White hydrate "whiskers" appeared at the frit within a few seconds, and a mass of hydrate coated bubbles formed quickly at the upper gas/water interface. Any induction period for hydrate formation was so short as to be negligible.

Our inspection of the performance of the apparatus at depth, and leakage of gas around valves, lead us to believe that our stratagem of using He to overpressure the CO_2 had in fact created a CO_2/ He gas mixture, and that this particular experiment cannot therefore be strictly interpreted as pure CO_2 hydrate formation. Since He does not form a hydrate under any conditions the overall effect is likely to be small. Interestingly all CO_2 hydrates formed were buoyant, and rose rapidly through the sea water to rest at the interface between gas and water. The density of CO_2 hydrate is substantially greater than sea water, and the buoyancy is an indication of trapped unreacted liquid CO_2 (plus a small amount of dissolved He) in the formed product. Visual inspection, by close camera focus, of the bubbles of hydrate confirmed the presence of a liquid layer inside the hydrate sheath. Injection of CO_2 into the sediment containing cylinders produced a sequence of results very close to that observed for methane.

Mixed Gas Experiment

An experiment with a methane (90%) ethane (5%) and propane (5%) mixture was also carried out. Here the presence of propane as a hydrate Structure II former significantly shifts the hydrate boundary to shallower depths than that for methane alone; moreover the presence of propane is widely regarded as acting to reduce any induction period for hydrate formation. Since we have observed a very short formation time for CH_4 hydrate, the differential effect of using this gas mixture was insignificant and equally rapid hydrate formation on bubble surfaces was seen.

Liquid CO_2 injection

In an effort to create pure CO_2 hydrate without the complexity of probable He contamination in the mixture, we rebuilt the gas release apparatus so as to contain liquid CO_2 in a piston actuated cylinder. Care was taken to apply pressure from ROV system hydraulics to the open side of the cylinder throughout the dive so as to maintain a positive pressure over ambient and thus avoid pressures in the incorrect sense on the gas regulator. Here we dove to about 910m, and released CO_2 into the apparatus. At this depth only the liquid CO_2 phase is present. No fine pore frit, but a simple small bore tube, was used for sample introduction in this experiment for fear of plugging the apparatus completely. The effect was to create globules of liquid CO_2 which, after sticking temporarily to the release port, rose slowly to the upper interface. There it appeared that a fine film of accreting hydrate gave a pearly appearance to the external surface of the globules, which did not coalesce but remained as separated units.

Thermal Signatures

In a modification of our apparatus we replaced one of the cylindrical reaction tubes with a plane faced larger unit for better viewing. In this unit we placed a heat flow probe constructed by the Woods Hole Oceanographic Institution's Alvin group. This consists of a metal rod about 1 m long with five thermistors each separated by about 10 cm. Readout from the probe was fed directly to the control room for real time monitoring of the experiment. Working with pure CH_4 gas in sea water we observed the temperature rise from the heat of formation during hydrate creation on bubble surfaces at the gas/water interface. Disturbance of the upper boundary by bubble flow created a mixed layer several centimeters deep which served to dissipate the heat, and it was not possible to gain a more quantitative estimate of the amount of hydrate formed.

On termination of the experiment and on raising *Ventana* to shallower depths we immediately observed a temperature drop due to quasi-adiabatic expansion cooling of the unreacted gas in the head space. Adiabatic cooling of the sea water itself is much smaller, but can be evaluated since the equation of state for sea water is well known (8). The temperature drop associated with gas expansion continued on raising until the hydrate decomposition point was reached. This point was not identical with the external oceanic boundary condition for dissociation due to the lower temperature at equal pressure within the apparatus, but it was clearly defined by a sharp break in the temperature trend due to cooling from the heat of dissociation.

Longer Term Observations

We intend to make longer term studies of the *in situ* stability of the hydrates we form than can be afforded within the confines of a one day dive schedule. This has meant devising a means to leave the apparatus on the sea floor for an extended period, and to return to it periodically for inspection and sampling of the trends. We have begun this process by constructing a square frame designed to sit above the sea floor and to hold the reaction tubes in place at a level where they can be viewed by the vehicle camera on return visits. This requires some means to first form the hydrate, then sever the connecting gas lines, pick up the frame with the vehicle robotic arm, and place it away from *Ventana* so that we can exit the site. Return to the location is provided for by deploying an interrogatable acoustic beacon nearby.

We have completed the first step and have left in place both CH_4 and CO_2 hydrate containing reaction cylinders at about 905 m depth at the "Clamfield" site in Monterey Bay. Revisits to this site after approximately 3 days, and 3 weeks, showed very little change in the hydrate structures we first formed. The cylinder containing CH_4 hydrate, unreacted gas, and sea water, was characterized by a bright white bubbly appearance. The bubbles with hydrate rind had not significantly coalesced or changed dimensions in the 3 week period. The CO_2 hydrate system, again containing liquid CO_2, hydrate and sea water, had the afforementioned appearance of pearly globules that remained as distinct entities separated by their hydrate sheath for the full observation period to date.

DISCUSSION

From the experiments we have carried out to date we can make some interesting conclusions about the manner and characteristics of hydrate formation in the deep sea, where the reaction medium contains the normal assemblage of suspended particles, bacteria, and trace gases which characterize the natural environment. Firstly we have repeatedly made hydrates of several gases, each within the period of a very few minutes or seconds, by the simple technique of direct gas injection with no shaking or ice nucleation step whatsoever. The initial manifestation of this was the creation of hydrate coated bubbles at the gas/water interface; but hydrate also formed in seconds to minutes within the pore spaces of marine sediments where no provision was made for gas trapping. We surmise that passage of the gas bubbles around the sediment grains caused sufficient surface renewal that hydrate formed in a similar manner to the more easily visualized upper boundary, but with smaller unit size granules. No significant induction or lag period was observed for hydrate formation for any gas yet injected in this manner.

Once formed the hydrate structures appeared quite stable. That behavior is consistent with the idea that the hydrate rind on bubble surfaces separates the inside gas from the outside water well enough that further growth must occur only slowly by diffusion of the reactants through the hydrate skin. Unless some defect or fracturing of the hydrate rind occurs, this appears to be the rate limiting step.

Growth of hydrate in marine sediments is critically dependent on the grain size of the material. In a coarse material (sand) flooding of the pores results in cementing of the sediment into a massy unified structure within seconds, yet yields no hydrate nodules of the kind often reported in nature (9). These nodular structures were observed in the process of forming in the flow channels carved by gas in experiments in fine grained mud, and the contrast between hydrate formation in the coarse and fine matrices was dramatic.

Our work with CO_2 hydrate has yielded results relevant to the proposed disposal of CO_2 in the deep ocean (10). For instance the ease with which CO_2 hydrate forms will pose a challenge to deep injection facilities concerned with plugging of the system; and the observation of the relative stability of the hydrate coated globules restricts interaction between disposed CO_2 and the surrounding ocean water. Furthermore, CO_2 hydrate did not separate spontaneously from unreacted CO_2; instead it formed a mass of intermediate density between sea water and liquid CO_2. Our observations were consistent with the description by Sakai et al. (11) of the natural venting of CO_2 rich fluids on the ocean floor.

Our experience with CO_2 hydrate formation is that the liquid CO_2 used experimentally requires excellent technique to handle. Post cruise analysis of our experiment carried out with He overpressure indicated by formal calculation (using the Peng-Robinson (12) equation of state) that the gas injected was indeed a CO_2/He mixture, since under the conditions we used (about 4.4^0 C, 1800 psia) to prepare the gas reservoir then about 10 mol% He will dissolve in the liquid CO_2. Release of this at our *in situ* experimental conditions will form a mixture of about 20 volume % liquid phase, and 80 volume % vapor, accounting for our observations.

Once formed from sea water/gas (or liquid) contact, the hydrates are stable over a period of several weeks, and quite possibly very much longer indeed, even though sea water and unreacted gas or liquid are separated only by a thin hydrate film. The initial attempt we made to study this was successful in separating the experimental apparatus from the vehicle, and leaving it in place. In future experiments we will leave hydrates within sediment matrices for later recovery, and arrange for greater sea water/hydrate contact, since water flow around the hydrates was quite restricted in the present system.

Finally we are devising means for surface recovery of the experimental material for laboratory investigation, and wish to apply the knowledge we have gained to a variety of important geochemical and gas disposal problems.

REFERENCES

1. Sloan, E.D. Jr. *Clathrate Hydrates of Natural Gases.* Marcel Dekker. **1990** pp 641.
2. Stern, L.A.; Kirby, S.H.; Durham,W.B. *Science* **1996**, 273, 1843-1848.
3. Dickens, G.R.; Quinby Hunt, M.S. *Geophys. Res. Lett.* **1994**, 8, 2115-2118.
4. Sloan, E.D. In: *Gas Hydrates: Relevance to World Margin Stability and Climatic Change* **1996**, pp. 1-38.
5. Robison, B.H. *Mar. Tech. Soc. J.* **1993**, 26, 45-53.
6. Newman, J.B.; Robison, B.H. *Mar. Tech. Soc. J.* **1993**, 26, 45-53.
7. Brewer, P.G.; Orr, F.M., Jr.; Friederich, G.; Kvenvolden, K.A.; Orange, D.L.; McFarlane, J.; Kirkwood, W. *Geology* **1996** submitted.
8. Millero, F.J.; Chen, C.T.; Bradshaw, A.L.; Schleicher, K. *Deep-Sea Res.* **1980**, 27, 255-264.
9. Brooks, J.M.; Field, M.E.; Kennicutt, M.C. *Mar. Geol.* **1991**, 96, 103-109.
10. Golomb, D. *Energy Convers. Manage.* **1993**, 34, 967- 976.
11. Sakai, H.; Gamo, T.; Kim, Es.; Tsutumi, T.; Tanaka, T.; Ishibashi, J.; Wakita, H.; Yamano, M.; Oomori, T. *Science* **1990**, 248, 1093-1096.
12. Peng, D.Y.; Robinson, D.B. *Ind. Eng. Chem. Fundam.***1976**, 15, 59- 64.

ACKNOWLEDGEMENTS

We wish to thank the Captain and crew of the RV *Point Lobos*, and the pilots of the ROV *Ventana* for their outstanding work in making these experiments possible. Support was provided by the David and Lucile Packard Foundation, and by Stanford University (F.M.O.) and the United States Geological Survey (K.A.K.)

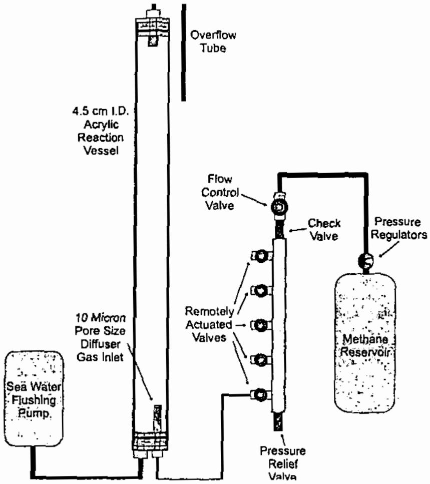
Overflow Tube
4.5 cm I.D. Acrylic Reaction Vessel
Flow Control Valve
Check Valve
Pressure Regulators
Remotely Actuated Valves
10 Micron Pore Size Diffuser Gas Inlet
Sea Water Flushing Pump
Methane Reservoir
Pressure Relief Valve

1. Line diagram of the experimental apparatus used for hydrate generation from the ROV Ventana; the various pieces are not to scale.

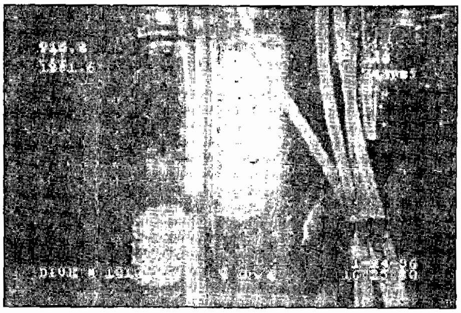

2. Image of methane hydrate formed at the upper gas/water interface. The hydrate rind on bubble surfaces is plainly seen. The digital information on the screen gives (top, upper left) depth, and date and time (lower right). The reaction cylinders are 4.5 cm. diameter.

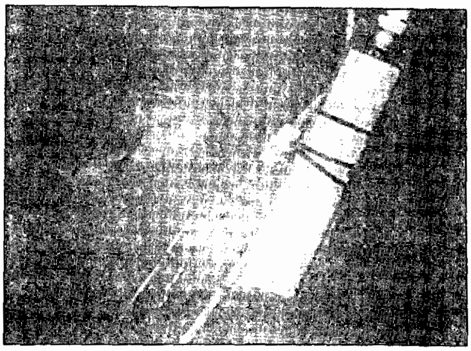

3. Image of both methane (right, white) and carbon dioxide (left, gray) hydrates approximately 3 weeks after initial formation in experimental apparatus left on the sea floor. The granular appearance of the methane hydrate is retained; the less rounded blobs of liquid carbon dioxide have a thin veneer of hydrate that apparently prevents surrounding sea water from further reaction.

ACCUMULATION OF SUBMARINE GAS HYDRATES

Gabriel D. Ginsburg and Valery A. Soloviev
Research Institute for Geology and Mineral Resources of the Ocean
1, Angliyskiy prospekt, St.Petersburg, 190121 Russia

Keywords: submarine gas hydrates, accumulation mechanisms, fluid migration

INTRODUCTION

During last fifteen years the authors have been studying the generation and accumulation of submarine gas hydrates. In particular, expeditions have been carried out in the Caspian, Black, and Okhotsk seas (Ginsburg et al., 1990, 1992, 1993), and the Norwegian Sea (1996, unpublished) The results of our investigations have been summarized in a monograph (Ginsburg and Soloviev, 1994). That is the basis of this presentation.

RESULTS AND DISCUSSION

The analysis of the worldwide observational data suggests that submarine hydrates largely occur in local accumulations (Ginsburg and Soloviev, 1994, 1995). All observed submarine gas hydrates are readily divisible into two groups: associated and non-associated with fluid vents. Hydrates of the first group, which have been observed close to the sea floor in the Caspian, Black, Okhotsk and Norwegian seas, the Gulf of Mexico, and in several other sites (altogether in 11 regions, Fig.1) are controlled by fluid conduits: mud volcanoes, diapirs, and faults. As for the second group of gas-hydrates (deep-seated), their control by fluid flow may be usually deduced from an association with indirect borehole indications of fluid flows, such as relatively coarse-grained sediments and anomalies of pore water chlorinity (Figs.2, 3).

The generation, accumulation and disappearance of any water-soluble naturally occurring compound in terms of water availability are governed by solubility variations of this compound. This is true also in regard to gas hydrates. It is extremely important for natural gas hydrate formation that the solubility of methane (which is the major component of natural hydrates) in water in terms of hydrate stability is little affected by the general (hydrostatic) pressure (contrary to "normal" conditions of hydrate instability) but is dictated essentially by the equilibrium pressure of hydrate formation, which is temperature-dependent. Since the equilibrium pressure of hydrate stability is diminished with decreasing temperature, methane solubility in water also decreases (Fig.4, solid line). Because of this, the solubility of methane in pore waters generally decreases towards the sea floor within the submarine gas hydrate stability zone (Fig.5). The higher the geothermal gradient, accordingly the thinner the hydrate stability zone, the sharper is the methane solubility decrease.

Three major mechanisms of methane transport in sediments can be distinguished: dissolved in pore water flows, as free gas flows, and molecular diffusion. Hydrate precipitation from ascending methane-saturated water is thought to be the most straightforward (Ginsburg, 1990; Ginsburg and Soloviev, 1994). The hydrate zone forms a gas-geochemical barrier for methane-saturated water which rises either from below or from within this zone: as the water cools it should precipitate hydrate. The amount of precipitated hydrate obviously corresponds to the excess of dissolved methane (i.e., over the solubility). Clearly the effectiveness of this process depends, in particular, on the rate of water flow and the water temperature; in the case of focused flow of warm water, the thickness of the submarine hydrate zone can decrease to zero. Gas hydrates being precipitated from infiltrated waters are progressively filling the sediment pore space and/or fracture porosity and eventually cement them, producing massive and vein hydrate sediment structures.

Gas hydrates associated with free gas flows discharging on the sea floor were observed in the Gulf of Mexico (Brooks et al., 1994) and in the Okhotsk Sea (Ginsburg et al., 1993). Clearly, the gas seeping through the hydrate stability zone has no time to crystallize as a hydrate. After a hydrate film forms at the gas-water interface, each succeeding portion of free gas, prior to hydration, has to penetrate this film. Thus the rate of hydrate formation in the vicinity of free gas flows is limited by the rate of this penetration (i.e., the rate of molecular diffusion), and hydrates are accumulated primarily from the water-dissolved gas: a solid (hydrate) phase grows at a distance from free gas. The lateral outward diffusion of methane of the ascending gas flow appears to be governed by the difference between chemical potentials of gaseous and dissolved methane at common depths. The above difference is deduced from the difference between the pressure of a free methane close to the hydrostatic pressure and the vapour pressure of dissolved methane, which in terms of pore water saturation should be close to the equilibrium pressure of gas hydrate formation (compare P_h and P_{eq} on Fig.6). Since this difference decreases with increasing subbottom depth, hydrate accumulations associated with ascending free gas flows are assumed to taper off downward. Accumulations of this type at great water depths should be more extensive than shallow ones (other factors being equal) because the considered difference increases with deepening water. It is self-evident that this model simplifies the matter. In fact, the heat release caused by hydrate formation enhances the outward methane transport and extends the diffusion aureole around ascending gas flow. Within this aureole the hydrates are thought to result not only from outward diffusing methane but also from upward diffusion, the intensity of which is controlled by high gradients of concentration and vapor pressure of water-dissolved methane in the hydrate zone (in terms of methane-saturated water); these gradients greatly exceed values outside the hydrate zone (Figs.5 and 6).

A similar pattern of methane diffusion and gas hydrate accumulation should also characterize the vicinity of ascending flows of gas-saturated water. In particular this is possible around the water flows which are too warm for hydrate precipitation. High gradient of temperature nearby these flows provides favorable conditions for rapid gas hydrate accumulation.

It is generally believed that diffusion plays only a destructive role in the history of hydrocarbon accumulations. In contrast, Egorov (1988) has put forward the concept of "directional diffusion recondensation". This implies the diffusional transfer of hydrocarbons which saturate water in the presence of a temperature-controlled solubility gradient. According to this concept, the formation and accumulation of a hydrocarbon phase in the region of lower temperature results from such a transfer. We suggest that directional diffusion recondensation is just the process which governs gas hydrate accumulation in the vicinity of free gas and gas-saturated water flows, as well as within and above the sediment sections where biochemical methane is intensively generated. Relatively impervious sediments may act as a cap in this process. DSDP-ODP data offer examples of gas hydrate occurrences close to the boundary between relatively coarse- and fine-grained sediments (Ginsburg and Soloviev, 1994).

Thus, gas hydrates accumulate from water solutions, no matter whether methane is delivered into the reaction zone, by infiltration or diffusion. The important distinction between two modes of hydrate accumulation in sediments (aside from the process rate) lies in the source of hydrate water. In the case of hydrate precipitation from infiltrated gas-saturated water this source is flow itself; in the case of diffusional methane delivery the hydrate water is extracted from sediment pore water in-situ.

We have proposed the term segregation to designate the mechanism of hydrate accumulation from diffusing gas and from water being extracted from sediments (Ginsburg and Soloviev, 1994). A continuous delivery of methane and the associated formation of hydrate generates a migration of pure water into the reaction zone from the adjacent sediments or sea water. This mechanism of water migration is thought to be diffusion-osmotic. Hydrate inclusions of a different shape are formed during this process due to the dewatering of surrounding sediments if the latter are compacted. The shape of inclusions is obviously caused by the factors controlling the fields of gas and water chemical potentials. In particular the subhorizontal lenticular-bedded hydrate sediment structure observed in association with submarine gas vents in the Okhotsk Sea (Ginsburg et al., 1993) may result from the subhorizontal extension of isotherms.

As a result of water redistribution during segregational gas hydrate accumulation, the total water content of hydrate-bearing sediments may turn out to be higher than that of the adjacent nonhydrated ones, as has been observed in the Okhotsk Sea (Ginsburg et al., 1993). A water content of sediments directly proportional to their hydrate content has been demonstrated in the Caspian Sea (Ginsburg et al., 1992). Hence the hydrate accumulation in sediments may imply not only gathering of gas but also of water. Due to hydrate water abundance, a sediment may become fluidized upon decomposition of hydrate.

Diffusion is known to be an ubiquitous process in marine sediments. Since a hydrate of any origin is subject to subsequent decomposition and possible diffusional recondensation of the released hydrate methane, segregational hydrates are thought to be more common than those precipitated by infiltrated water.

We mentioned two kinds of inhomogeneity of the geological medium exerting influence upon gas hydrate accumulation: permeability variations, which control fluid conduits and gas hydrate caps, and geothermal inhomogeneity (geothermal gradient), which predominantly governs gas solubility in water. In addition two other kinds of inhomogeneity - hydrochemical and lithological can have a pronounced effect on this process. It is well-known that water-dissolved salts inhibit (prevent) gas hydrate formation, i.e. hydrates form more readily from fresh water. Therefore, a gradient of water salinity within the hydrate zone under gas-saturation conditions must provoke a diffusional flux of methane into fresh water, where this arriving methane should be hydrated. Such a situation may occur near boundaries of water flows. It is necessary to emphasize here that the solubility of methane in the fresh gas-saturated water is known to be higher than in saline water, whereas the corresponding methane fugacity, which actually should be considered as a driving force of diffusion, is higher in saline water (Handa,1990).

A lithological (or in more exact terms, a porometric) inhomogeneity implies, in particular, a distinction of sediment pore size (we do not consider here a shape of sediment pores and their specific properties, which of course also affect gas hydrate accumulation). The pore medium influences the hydrate equilibrium (thermodynamic effect) and the kinetics of hydrate formation. The thermodynamic effect essentially is as follows: a pore surface is hydrophilic and therefore lowers the pore water chemical potential. As a result, a higher thermodynamic concentration of methane is required for the formation of hydrate. In principle, this effect is similar to the influence of salts dissolved in water. This surface effect was studied by many authors and had been found negligible in terms of natural sediment water content. The kinetic effect lies in the fact that a pore size may be less than a gas hydrate critical nucleus size at a given temperature. In this case, for hydrate formation to start, more significant overcooling or oversaturation is required (Chersky and Mikhailov, 1990). We suggest that the essence of both effects (thermodynamic and kinetic) can be understood by examination of hydrate formation in adjacent sediments having different pore sizes. It is evident that the hydrate formation in coarse-pored sediments has an advantage over fine-pored ones - the same gas concentration in water may turn out to be sufficient to form hydrates in the former case and insufficient in the latter. What this means is hydrate can accumulate rather in relatively large pores in the course of sediment compaction and/or biochemical gas generation.

CONCLUSIONS

Submarine gas hydrates mostly occur locally and are linked to fluid flows. They accumulate from methane-saturated water, in the course of pore water infiltration and methane diffusion. Apart from the methane availability the accumulation of hydrates is controlled by physical factors such as temperature gradient, pore water salinity gradient and lithological variability. The hydrates precipitate at lower temperatures and from less saline water; relatively coarse-grained sediments make better hydrate reservoirs than fine-grained sediments.

REFERENCES

Brooks, J.M., Anderson, A.L., Sassen, R., MacDonald, I.R., Kennicutt II, M.C. and Guinasso, N.L., Jr., 1994. Hydrate occurrences in shallow subsurface cores from continental slope sediments. In: E.D. Sloan, Jr., J. Happel and M.A. Hnatow (Eds.), Int. Conf. on Natural Gas Hydrates. Annals of the New York Acad. Sci., 715: 381-391.

Cherskiy, N.V. and Mikhailov, N.E., 1990. Size of equilibrium critical nuclei of gas hydrates. Doklady Akademii Nauk SSSR, 312(4): 968-971 (in Russian).

Egorov, A.V., 1988. Diffusional Mechanisms of Hydrocarbons Primary Migration and Accumulation in Offshore Sedimentary Basins, Thesis. Institut Okeanologii Akademii Nauk SSSR, Moscow, 218pp. (in Russian).

Gieskes, J.M., Johnston, K., Boehm, M., 1985. Appendix. Interstitial water studies. Leg 66. In: von Huene, R., Aubouin, J. et al. Init. Repts. DSDP, 84: Washington, D.C.: 961-967.

Ginsburg, G.D., 1990. Submarine gas hydrate formation from seeping gas-saturated underground waters. Doklady Akademii Nauk SSSR, 313(2): 410-412 (in Russian).

Ginsburg, G.D. and Soloviev, V.A., 1994. Submarine Gas Hydrates. VNIIOkeangeologia, St.Petersburg, 199 pp. (in Russian, with English abstract).

Ginsburg, G.D. and Soloviev, V.A., 1995. Submarine gas hydrate estimation: theoretical and empirical approaches. Proc. 27th Annu. OTC., Houston, Texas, USA, 1-4 May 1995: 513-518.

Ginsburg, G.D., Kremlev, A.N., Grigor'ev, M.N., Larkin, G.V., Pavlenkin, A.D. and Saltykova, N.A., 1990. Filtrogenic gas hydrates in the Black Sea (twenty-first voyage of the research vessel "Evpatoriya"). Soviet Geology and Geophysics (Geologia i Geofizika), 31(3): 8-16.

Ginsburg, G.D., Guseynov, R.A., Dadashev, G.A., Ivanova, G.A., Kazantsev, S.A., Solov'yev, V.A., Telepnev, E.V., Askeri-Nasirov, R.Ye., Yesikov,A.D., Mal'tseva, V.I., Mashirov, Yu.G. and Shabayeva, I.Yu., 1992. Gas hydrates of the Southern Caspian. Int. Geol. Rev., 34(8): 765-782.

Ginsburg, G.D., Soloviev, V.A., Cranston, R.E., Lorenson, T.D., Kvenvolden, K.A., 1993. Gas hydrates from continental slope offshore from Sakhalin Island, Okhotsk Sea. Geo-Marine Letters, 13: 41-48.

Handa, Y.P., 1990. Effect of hydrostatic pressure and salinity on the stability of gas hydrates. Journ. Phys. Chem., 94(6): 2652-2657.

Makogon, Yu.F. and Davidson, D.W., 1983. Influence of excessive pressure on methane hydrate stability. Gazovaya promyshlennost', 4: 37-40 (in Russian).

Namiot, A.Yu., 1991. Solubility of Gases in Water. Reference Textbook. Nedra, Moscow, 167 pp. (in Russian).

von Huene, R., Aubouin, J. et al., 1985. Init. Repts. DSDP, 84: Washington, D.C.

Watkins, J.S., Moore, J.C. et al., 1981. Init. Repts. DSDP, 66: Washington, D.C.

FIGURES

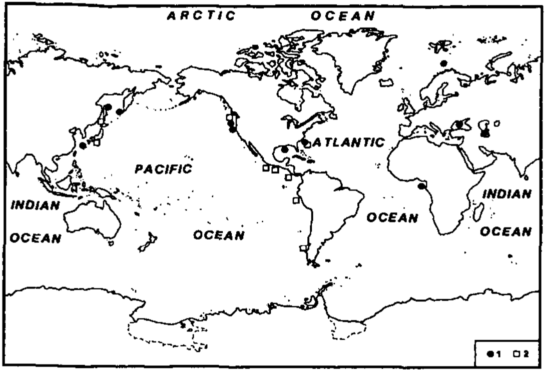

Fig.1.
Worldwide locations of observed submarine gas hydrates. Updated after Ginsburg and Soloviev, 1994. 1, 2 - sea floor seepage-associated and non-associated gas hydrates, respectively.

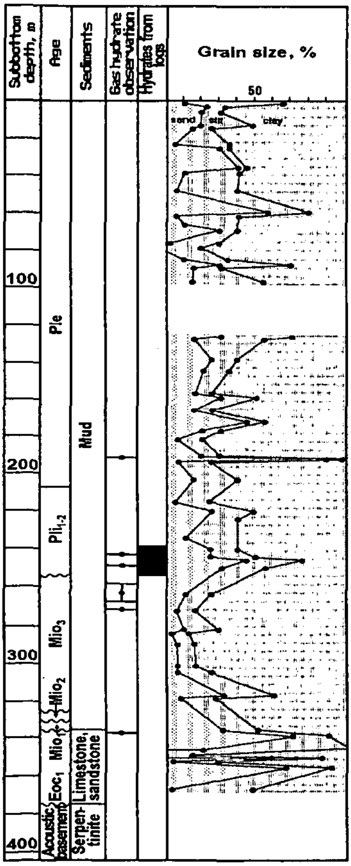

Fig.2. Gas hydrate shows and sediment grain size in geological section at DSDP Site 570, Middle America Trench. Compiled from von Huene, Aubouin et al., 1985.

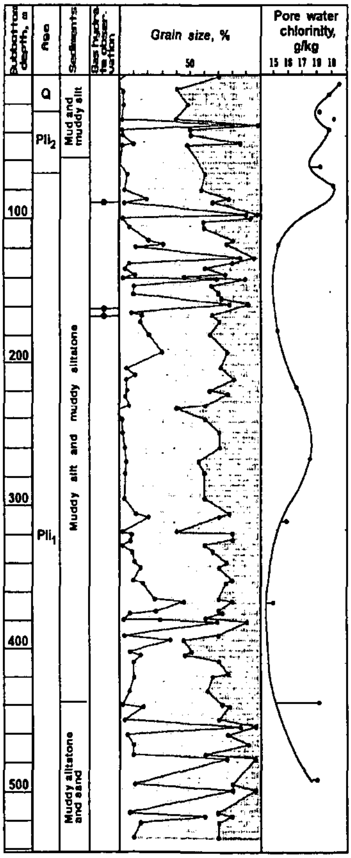

Fig.3. Gas hydrate shows, sediment grain size, and pore water chlorinity in geological section at DSDP Site 491, Middle America Trench. Compiled from Watkins, Moore et al., 1981, and Gieskes et al., 1985. The chlorinity curve is drawn using sulfate as a measure of sample contamination with the sea water. For symbols of sediment grain size see Fig.2.

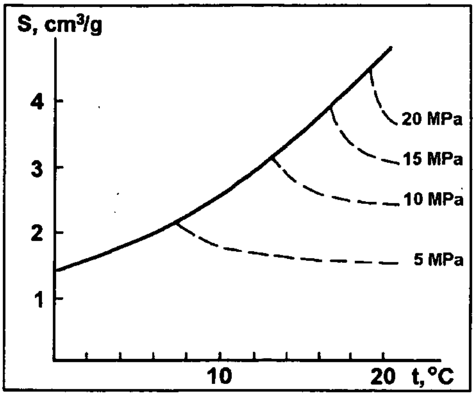

Fig.4. Solubility of methane (S) in pure water plotted against temperature (t): isobars of solubility in terms of gas hydrate instability (set of dashed lines), and solubility in equilibrium with hydrate (solid line). Compiled using the data of Makogon and Davidson (1983) and Namiot (1991).

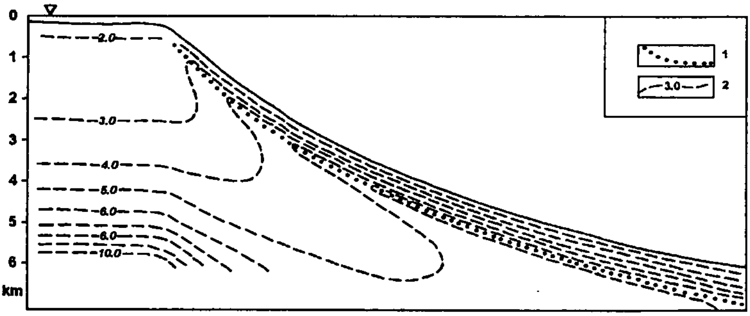

Fig.5. Vertical cross-section demonstrating solubility of methane in water under thermobaric conditions of continental margins (after Ginsburg and Soloviev, 1994). The dashed lines are isolines of solubility numbered in STP cm^3/g. Dotted line is the base of thermobaric gas hydrate stability zone. Compiled using the data of Makogon and Davidson (1983) and Namiot (1991). Accepted assumptions: water is pure; bottom water temperature is 5°C for water depths down to 500 m, and 2°C at greater depths; geothermal gradient is 30°C/km; hydrobaric gradient is 10 MPa/km.

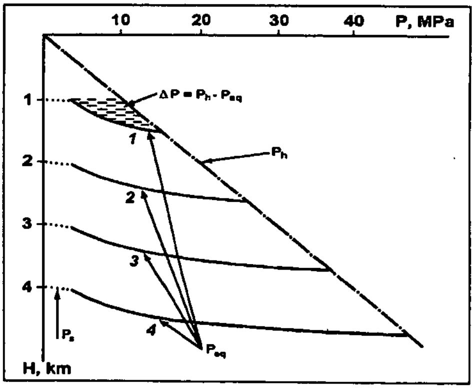

Fig.6. Relationship between different kinds of pressure (P) affecting diffusion of methane in subbottom conditions. H is total depth = water depth + subbottom depth. P_h is conventional hydrostatic pressure. P_{eq} is equilibrium pressure of methane hydrate; curves 1-4 relate to water depths 1, 2, 3, 4 km, respectively. P_s is saturation pressure of dissolved methane within sulfate reduction zone. Accepted assumptions: water is pure, gas is pure methane (see also Fig.5). The P_{eq} curves are the usual PT gas hydrate equilibrium curves but the temperature axis is replaced by the depth axis based on the accepted assumptions.

ON THE MECHANISM OF GAS HYDRATE FORMATION IN SUBSEA SEDIMENTS

B. Tohidi, A. Danesh, and A.C. Todd
Department of Petroleum Engineering, Heriot-Watt University
Edinburgh EH14 4AS, Scotland.

Keywords: Gas Hydrates, Gas Solubility, Subsea Sediments

INTRODUCTION

Gas hydrates are crystalline molecular complexes formed from mixtures of water and suitably sized gas molecules. Based on hydrogen bonding, water molecules form unstable lattice structures with several interstitial cavities. The gas molecules can occupy the lattice cavities and, when a minimum number of cavities are occupied, the crystalline structure becomes stable and solid gas hydrates are formed, even at temperatures well above the ice point[1]. The known gas hydrate structures are; structure-I, structure-II, and the recently discovered structure-H[2].

The necessary condition for hydrate formation is the presence of water or ice, suitably sized non-polar or slightly polar molecules, together with appropriate pressure and temperature conditions. In subsea environments, the sediments are normally saturated with sea water and a combination of the geothermal gradient and the weight of the column of water (which causes a hydrostatic pressure) could provide the right conditions for hydrate formation. Under these conditions, gas released from biogenic activities (or seepage from oil and gas reservoirs) could form gas hydrates. Current estimates show that the amount of energy in the gas hydrates is twice that of the total fossil fuel reserves, indicating a huge source of energy which could be exploited in the right economical conditions[1].

Although most scientists agree on the process of hydrate formation in subsea sediments, the mechanism of gas hydrate formation is the subject of some debate. Some researchers suggest that the presence of the free gas phase is necessary and gas hydrates form in the gas-water interface. Others believe that at least a local supersaturation of gas with respect to gas-water equilibria is required. Some propose that this supersaturation will result in the evolution of micro-bubbles and hence formation of gas hydrates. While others suggest that there is no need for the presence of gas bubbles for the hydrates to be stable[1,3-5].

In this presentation, a thermodynamic model, validated against experimental data, is used to predict the solubility of methane in pure or saline water. The results show that gas hydrates could form from dissolved gas as well as from free gas. Based on the above findings, two mechanisms for hydrate formation in subsea sediments have been suggested and discussed.

It should be noted that, the hydrate forming gas is assumed to be pure methane to simplify the argument. Obviously for multi-component systems, upon hydrate formation, some compositional variation will occur which will result in changes in equilibrium conditions. Also, any effect due to capillary forces and the type of rock has been ignored in this work.

THERMODYNAMIC MODEL

The fugacity of each component in all fluid phases, including the salt free water-rich phase, have been calculated by an equation of state (EoS). The saline water phase has been modelled by combining the EoS with the modified Debye-Hückel electrostatic term, using only one interaction parameter. In optimising the water-salt interaction parameters, water vapour pressure depression data at 373.15 K and freezing point depression data have been used. For the gas-salt interaction coefficient, gas solubility data in single electrolyte solutions at different temperatures and salt concentrations have been used. The model has been extended to mixed electrolyte solutions with nine salts in its library. A detailed description of modelling vapour, liquid hydrocarbon, salt free water phase, hydrate phases, ice phase, and saline water phase is given elsewhere[6, 7].

Figure-1 shows methane solubility in distilled water at different temperatures. There is a good agreement between experimental[8] data and predictions which demonstrates the success of the EoS in representing highly polar systems.

Methane solubility in distilled water and in 1 and 4 molar NaCl solutions are presented in Figure-2. The agreement between experimental[9] data and predictions is very good, which indicates the reliability of the thermodynamic model. (There are some deviations for pure water at higher pressures, which could be due to the inaccuracy of experimental data, as Figure-1 shows better agreement for the case of pure water).

RESULTS AND DISCUSSIONS

Figure-3 shows the predicted methane solubility in the water-rich phase in a wide temperature range (i.e., 275 to 400 K), at different isobars. This figure indicates that methane solubility passes through a minimum. The dashed lines show the methane solubility in metastable conditions. Also in the above figure, the concentration of methane in the water-rich phase at water-hydrate and water-hydrate-methane phase equilibria are presented.

For simplicity, the sea water in subsea sediments is represented by 3.5 Wt% NaCl aqueous solution. Methane solubility in the water-rich phase in the presence of sea water, is depicted in Figure-4. Constant pressure lines are replaced by depth, taking into account the density of the sea water. Again the dashed lines, which are the extension of methane solubility in water-gas equilibria, show the methane solubility in the water-rich phase at metastable conditions. For simplicity, pressure (or depth) is assumed to be constant; by cooling and moving along the constant pressure line, the system will approach the water-hydrate-methane equilibrium point, i.e. the potential hydrate formation temperature. Assuming no subcooling is required, methane hydrates could form at this point. In the absence of a free gas phase, a further reduction in temperature will cause more hydrates to form and the methane concentration in equilibrium with hydrates to reduce. Nevertheless, for hydrate formation, a certain degree of subcooling is required. Therefore, the methane concentration in the water rich phase could be as high as those presented by the dash lines. However, when hydrate formation is initiated the equilibrium methane concentration in the water-rich phase is much lower. This means that gas hydrates could form without the presence of a free gas phase.

In the presence of a free gas phase and under the above conditions (constant pressure, temperature, and composition), hydrate formation would cease only when one of the phases (i.e., water or the free gas phase) disappears. However, in the presence of sea water the increase in the concentration of salts (due to hydrate formation) could inhibit the further formation of hydrates, as discussed later.

The effect of salt(s) on the equilibrium concentration of methane in the water-rich phase is presented in Figure-5. As shown, the presence of salt(s) will reduce the methane solubility, and inhibit hydrate formation, as the hydrate-water-methane point for 3.5 Wt% NaCl solution is at a lower temperature compared to pure water.

Figure-6a shows the mole% hydrates formed from dissolved gas in 3.5 Wt% NaCl solution at 280 K. The x-axis is pressure (or depth). As an example, at 20 MPa (1993 m depth), the dissolved gas in the metastable condition is enough to form 1% hydrates. However, the amount of hydrates could be as high as 2.2% for 60 MPa pressure (5980 m depth).

As shown in Figure-6b, the 1% hydrates will increase the salt concentration by 0.03 Wt%, i.e., the salt concentration will increase from 3.5 to 3.53 Wt%. However, the effect on phase equilibria conditions is insignificant (an inhibition of 0.013 K). This means that for further hydrate formation, the controlling factor is most likely to be the supply of gas. As the gas concentration in the hydrate stability zone is significantly lower, the gas could be transported by diffusion. Convection is also another means of supplying gas to the hydrate suability zone.

Based on the above results the following two mechanisms are proposed for hydrate formation in subsea sediments:

1. Hydrate formation from dissolved gas:

- Gas released from biogenic and thermogenic sources are dissolved in sea water.
- The dissolved gas reaches the hydrate stability zone by diffusion, or the water containing the dissolved gas reaches the hydrate stability zone by convection/advection.
- Hydrate formation initiates at a certain degree of subcooling and the concentration of gas in the water-rich phase is reduced, as shown in Figure-4. Therefore, the gas concentration (in the water-rich phase) outside the hydrate stability zone would be higher than that inside the hydrate stability zone.
- More gas is provided to the hydrate suability zone by diffusion (due to the concentration gradient) for further hydrate formation.

As mentioned previously, the increase in salt concentration due to hydrate formation is very small. Therefore, the diffusion of gas from the high concentration region to the hydrate stability zone is likely to be the controlling factor.

2. Hydrate formation from free gas:
- Free gas is generated in-situ, or reaches the hydrate stability zone by convection.
- Large amounts of hydrates could be formed which could result in the consumption of all the free gas, or a significant increase in the salt concentration in the pores.
- The increase in salt concentration could inhibit further hydrate formation (Figure-5), unless the salt concentration is reduced by diffusion.
- More free gas is converted into hydrates. This process will terminate when all the gas (or water) is converted into hydrates.

In the above mechanism, the transfer of salts by diffusion is likely to be the controlling factor.

ACKNOWLEDGEMENTS

The authors would like to thank Professor Westbrook and Dr Minshull for very useful discussions.

REFERENCES

1. Sloan, E. D., Clathrate Hydrates of Natural Gases, Marcel Dekker Inc., New York, (1990).
2. Ripmeester, J.A., Tse, J.S, Ratcliffe, C.I., and Powell, B.M., "A New Clathrate Hydrate Structure", Nature, Vol. 325, No. 135, , pp. 135-136, (1987).
3. Miller, S.L., "The Nature and Occurrence of Clathrate Hydrates", Natural gases in Marine Sediments, Ed. Kaplan, I.R., Plenum Press, New York, (1974).
4. Makogon, Y., "Gas Hydrate Formation in Porous Media", Proceed. of the 2nd International Conference on Natural Gas Hydrates, pp. 275-289, (1996).
5. Brown, K.M., Bangs, N.L., Froelich, Kvenolden, K.A., "The Nature, Distribution, and Origin of Gas Hydrate in the Chile Triple Junction Region", Earth and Planetary Science Letter, Vol. 139, pp. 471-483, (1996).
6. Tohidi, B., Danesh, A., and Todd, A.C., "Modelling Single and Mixed Electrolyte Solutions and its Applications to Gas Hydrates", Chem. Eng. Res. and Des., Vol. 73 (May), Part A, pp. 464-472, (1995).
7. Tohidi, B., Danesh, A., Burgass, R.W., and Todd, A.C., "Gas Solubility in Saline Water and Its Effect on Hydrate Equilibria", Proceedings of the 5th International Offshore and Polar Engineering Conference (ISOPE-95), Vol. 1, pp. 263-268, (1995).
8. Culberson, O.L., and McKetta, J.J., Petrol. Trans. AIME, Vol. 192, P. 223, (1951).
9. O'Sullivan, T.D., and Smith, N.O., "The Solubility and Partial Molar Volume of Nitrogen and Methane in Water and in Aqueous Sodium Chloride from 50 to 125 ° and 100 to 600 Atm", J Phys Chem, Vol 74, No 7, pp. 1460-1466, (1970).

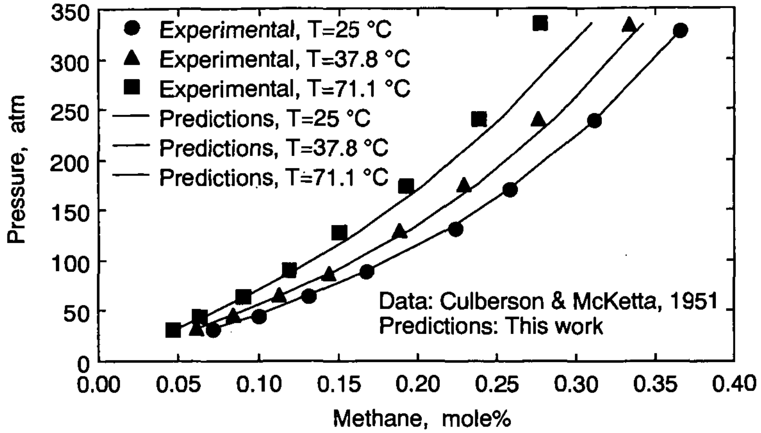

Figure-1 Experimental and predicted methane solubilities in distilled water.

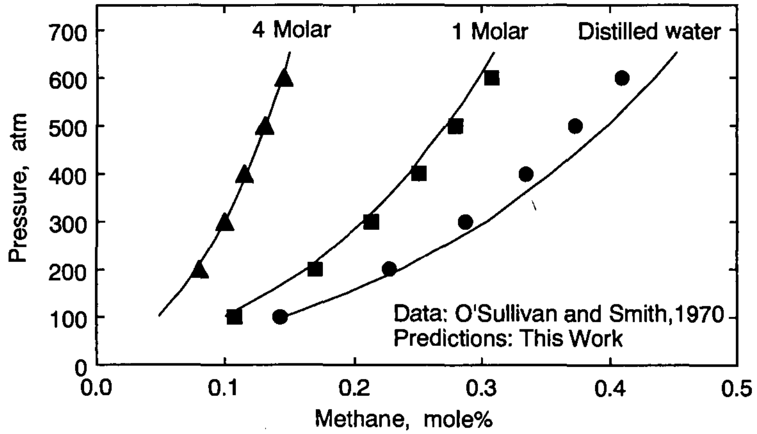

Figure-2 Experimental and predicted methane solubilities in distilled water and NaCl aqueous solutions.

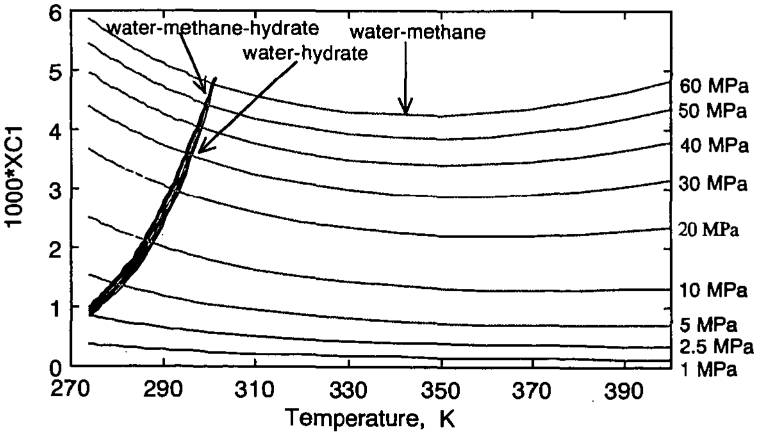

Figure-3 Predicted methane concentrations in the water-rich phases (Salt free) of water-methane, water-methane-hydrate, and water-hydrate equilibria.

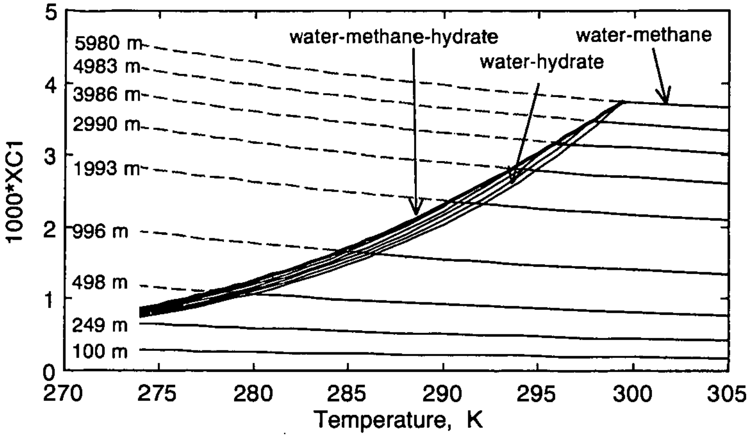

Figure-4 Predicted methane concentrations in the water-rich phases (3.5 Wt% NaCl) of water-methane, water-methane-hydrate, and water-hydrate equilibria.

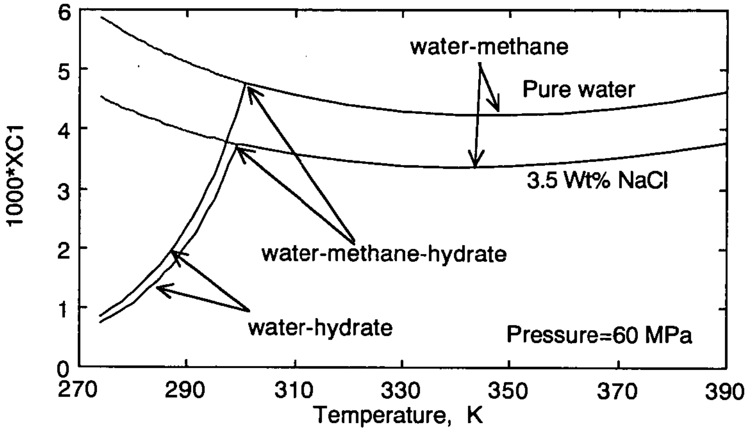

Figure-5 Effect of water salinity on methane concentration.

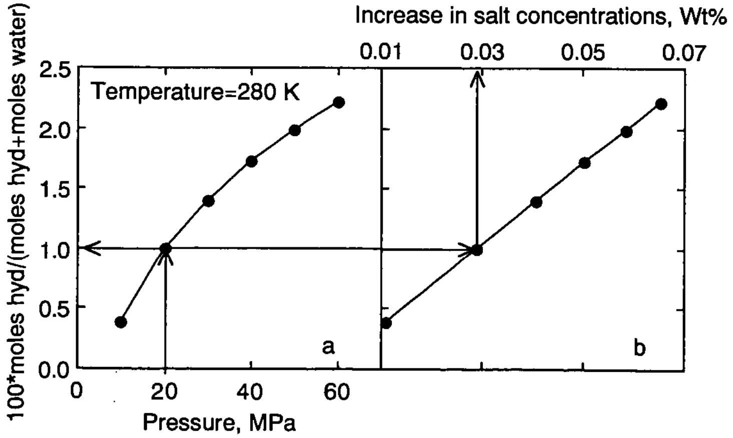

Figure-6 Percent hydrates formed from the dissolved methane and the increase in salt concentration.

KINETICS OF METHANE HYDRATE FORMATION IN PURE WATER AND INHIBITOR CONTAINING SYSTEMS

Tian-Min Guo and Jun-Hong Qiu
High Pressure Fluid Phase Behavior & Property Research Laboratory
University of Petroleum
Beijing, P.R. China 100083

Keywords: Kinetics, Methane hydrate formation, Brines

INTRODUCTION

The discovery of huge deposits of methane hydrate *in situ* (a possible energy source in the future), the production problems associated with the offshore oil/gas exploitation/transportation, and the new applications of hydrate technology have renewed interest in hydrate research in the past decade.

The two basic problems to be studied are the hydrate equilibrium thermodynamics and the hydrate formation/dissociation kinetics. Most of the papers published previously have been related to the former topic, a number of engineering applicable thermodynamic models has been developed, including recent models for salt-containing systems (Zuo et al., 1996; etc.). Compared to hydrate equilibrium thermodynamics, our knowledge on the kinetics of hydrate formation are far from mature. Due to the complexity of the dynamic process of hydrate formation, and the lack of consistent experimental data, a generalized kinetic model is not yet available. Since knowledge of the kinetics of hydrate formation is of critical importance in the transportation pipeline design, effective utilization of the methane hydrate resource *in situ*, and the various applications of hydrate technology, it has received increasing attention in recent years. Comprehensive reviews on the progress are available (Sloan, 1990; Makogon, 1981; Englezos, 1993; and Qiu and Guo, 1995).

The major objectives of this work are: (1) Measure the kinetic data of methane hydrate formation in the presence of pure water, brines containing single salt and mixed salts, and aqueous solutions of ethylene glycol (EG)/(salt + EG). (2) Develop a new kinetic model of hydrate formation for the methane + pure water systems based on a four-step formation mechanism and reaction kinetics approach. (3) Explore the feasibility of extending the proposed kinetic model to salt(s) and EG containing systems.

EXPERIMENTAL SECTION

Apparatus. It is well known that the specific equipment used in the study of hydrate formation kinetics has significant influence on the experimental results. There are basically two types of equipment, fixed boundary type and turbulent boundary type. The former is more suitable for simulating the hydrate formation/dissociation *in situ*, and the latter is closer to the conditions in the transportation pipelines and natural gas processing equipment. The apparatus used in this work belongs to the latter type. The schematic diagram of the experimental system is shown in Fig. 1, and the major parts are briefly described as follows:

Transparent sapphire cell: The 2.5 cm i.d. sapphire cell was purchased from the DB Robinson Design & Manufacturing Ltd. (Canada), the total volume and the effective volume (excluding the piston and stirrer volume) are 78 and 59 mL, respectively. The working volume of the cell can be adjusted by a floating piston driven by a positive displacement pump. The maximum working pressure and temperature are 20 MPa and 423 K, respectively.

Air bath: The air bath was manufactured by Shanghai Instruments Corp., the working temperature range is 263 ~ 373 K and can be controlled to within ±0.2 K by a digital programmable temperature controller.

Agitation system: The agitation system consists of a magnetic stirrer coupled with a permanent magnet mounted outside of the cell. A variable speed DC motor equipped with an rpm-controller provides up and down reciprocating motion of the magnet.

Pressure measurement: The pressure in the cell was measured through pressure transducer and pressure gauge simultaneously. A differential pressure transducer (Honeywell Inc.) was connected with the data acquisition system. The precision of the DP transducer at the working span (0 ~ 10 MPa) is ±0.1 %. A 0 ~ 25 MPa Heise pressure gauge was also installed for taking parallel pressure readings. The pressure measurement system was calibrated against a Ruska standard dead-weight gauge, and the precision of the pressure measurements is estimated at ±0.015 MPa.

Experimental Procedure. The kinetics of hydrate formation can be studied in two modes: the constant temperature-constant pressure mode and the constant temperature-constant volume mode. In the former mode, to maintain constant system pressure, the hydrate former gas consumed in the hydrate formation process is continuously supplemented from outside. In the latter mode, the system is closed, with its volume kept constant, and the system pressure is lowered gradually in the hydrate formation process. The latter mode was applied in this study.

Prior to performing the experiment, the floating piston was lowered to the bottom of the sapphire cell and its position was unchanged during the measuring process. About 12 mL liquid sample was charged into the evacuated sapphire cell. When the system temperature stabilized at the preset value, methane was introduced into the cell until the pressure was raised to about 4.0 MPa. The gas was then discharged to eliminate the trace amounts of residual air in the cell. Methane was again charged until the preset initial system pressure was attained, then the DC motor to actuate the magnetic stirrer was started with the stirrer was moving up and down at a rate of four strokes per minute. The system temperature and the change of system pressure were recorded through the data acquisition system every 30 seconds, and displayed on the monitor screen.

Experiments Performed. The systems studied and the corresponding operating conditions are summarized in Table 1. A total of 30 sets of kinetic data were measured for the following systems: methane + water, methane + water + salt(s), methane + water + EG, and methane + water + salt + EG.

Experimental Results. A typical pressure vs. time ($P \sim t$) curve measured for the methane hydrate formation process is shown in Fig. 2. The curve can be roughly divided into three zones. The first zone (from t_o to t_s) is called the "*gas dissolution zone*", P_s stands for the system pressure when saturation of the dissolved gas is established. The second zone (from t_s to t_r) is called the "*nucleation zone*", system pressure remains nearly at constant in this zone. The time interval from t_o to t_r is the so called *induction period.* The third zone, from t_r to t_d, is called the "*crystal growth zone*", in this zone the system pressure falls gradually from P_r to P_d and remains stabilized after time t_d. The three zones are divided rather arbitrarily, as in fact, nucleation could proceed simultaneously with the gas dissolution process. The relative time distribution of the three zones in the 30 experiments performed are also listed in Table 1. The detailed $P \sim t$ data for typical experiments are given in Table 3 and Figs. 3 ~ 5 along with the calculated results which are discussed below.

Analysis of the Experimental Results. From Table 1, it can be seen that the time interval of the gas dissolution period is, in general, 1 ~ 2 hours, however, the time interval of nucleation period differs appreciably for the experiments performed, from ~ 25 minutes (E04, E08, and E25) to ~ 5 hours (E16), and for some experiments (E01 and E20) no crystal nucleus was formed even after 10 hours. Since during the nucleation period, the liquid phase is in the *metastable state*, the nucleation process is sensitive to very small perturbations to the system. This caused difficulty in obtaining repeatable results even when the experiments were run under identical temperature and initial pressure conditions (E09a ~ E09c). The time period for crystal growth also differed significantly for experiments run under different operating conditions, from 80 minutes (E04) to more than 5 hours (E28).

Under the same operating temperatures, the initial pressure has little effect on the time interval of gas dissolution period (E01 ~ E04 and E05 ~ E09), however, its influence on the nucleation period is significant. In general, the lower the initial pressure, the longer of the nucleation period. Similar initial pressure effect was observed in the crystal growth period (E02 ~ E04 and E07 ~ E09).

The temperature effect on the time interval of gas dissolution and nucleation periods (under same initial pressure) is, in general, the higher the temperature, the longer the time period (E10 and E12, E08 and E11). The effect increases with the lowering of the initial pressure. Significant temperature effect was also observed in the crystal growth period; the time interval increase almost linearly with the increase of temperature, however, the temperature effect seemed not as sensitive to the initial pressure in this period.

The effects of inhibitors (salt/ethylene glycol) on the hydrate formation process are quite complex. When the concentration of the inhibitor is less than 1.0 mass%, the effect of concentration is not obvious on the time distribution of the three periods (E13 and E14, E17 and E18, E21 and E22).

For concentrations greater than 1.0 mass%, the time interval of gas dissolution period is little effected by the inhibitor concentration, however, the concentration has significant effect on the time interval of nucleation period, the higher the concentration the longer the time interval (E15 and E16, E19 and E20, E23 an E24, E26 and E28). The order of inhibition effect is as follows (when concentration of inhibitor > 1.0 mass%): EG > $NaHCO_3$ > NaCl > (NaCl + $NaHCO_3$) > ($NaHCO_3$ + EG) > (NaCl + EG).

An interesting phenomenon observed in the experiments is that when the concentration of inhibitor is less than 1.0 mass% (E13, E14, E17, E18 and E25), the induction time (gas dissolution period + nucleation period) is significantly shorter as compared with the methane + pure water systems (run under similar temperature and initial pressure conditions). It is in consistency with the observation of Yousif et al. (1994), that the hydrate formation could be *enhanced* at low inhibitor concentration.

MECHANISM OF METHANE HYDRATE FORMATION

In this work, the mechanism of methane hydrate formation in pure water was described by the following four steps.

Step 1: A portion of the methane molecules in the gas phase dissolve into the aqueous phase, and the dissolved methane molecules are clathrated by *n* water molecules to form a metastable cluster (i.e. the water molecules comprising the clusters may be replaced by other water molecules in the bulk),

$$CH_4(g) \underset{k_{-1}}{\overset{k_1}{\rightleftharpoons}} CH_4(aq) \tag{1}$$

$$CH_4(aq) + nH_2O \underset{k_{-2}}{\overset{k_2}{\rightleftharpoons}} CH_4 \cdot nH_2O \tag{2}$$

Following Long and Sloan (1993), the coordination number n was taken as 20. Since the structure of this labile cluster is similar to the 5^{12} hydrate cavity (Christiansen and Sloan, 1994), we assume their size is also similar, i.e. ~ 0.5 nm.

Step 2: The link of clusters to form a crystal unit.

$$m(CH_4 \cdot nH_2O) \underset{k_{-3}}{\overset{k_3}{\rightleftharpoons}} mCH_4 \cdot rH_2O + (mn - r)H_2O \tag{3}$$

It has been well established that methane forms structure I hydrate, the structure I hydrate crystal unit cell contains 46 water molecules, and consists of two 5^{12} and six $5^{12}6^2$ crystal cavities. The maximum number of methane molecules per unit cell is 8. Assume the crystal unit in Eq. (3), $mCH_4 \cdot rH_2O$, is an ideal crystal unit cell (with its cavities fully occupied), thus $m = 8$, and $r = 46$. It is also assumed that the size of the crystal unit cell $mCH_4 \cdot rH_2O$ is the same as the crystal unit cell of structure I hydrate, and is thus taken as 1.2 nm (van der Waals and Platteeuw, 1959). Since the size of the crystal unit is smaller than the *critical size*, some of the crystal units could be dissociated back to individual labile molecular clusters, and the others will be further linked to form a stable *crystal nucleus*, its size exceeding a certain critical size.

Step 3: Crystal units linked to form crystal nucleus N,

$$l(mCH_4 \cdot rH_2O) \xrightarrow{k_4} N \tag{4}$$

Englezos et al. (1987) proposed an equation for calculating the critical size of hydrate crystal nucleus. Based on the proposed equation, Natarajan et al. (1994) calculated the critical size of the methane hydrate crystal nucleus to be approximately 10~30 nm. That means, about 8~25 unit cells with a size of 1.2 nm are required to form a crystal nucleus of the critical size, i.e. l = 8~25. Thus, approximately 64~200 methane molecules and 368~1150 water molecules are required to form a crystal nucleus of critical size.

Step 4: Crystal nucleus growing to form hydrate crystal H,

$$pCH_4(aq) + N + qH_2O \xrightarrow{k_5} H \tag{5}$$

During the crystal nucleus growing period, hydrate crystals H with different sizes could be formed. Graauw and Rutten (1970) has measured the size distribution of propane hydrate crystals (structure II) in a continuous stirred tank crystalizer, the results showed that the crystal size is within 10 ~ 35 μm, the average being about 20 μm. Bylov and Rasmussen (1996), Monfort and Nzihou (1993) have also studied the crystal size distribution. Based on the size distribution data available, we can conclude that the size of the methane hydrate crystal is at least three times in magnitude larger than the size of the critical crystal nucleus. The magnitude of p and q in Eq. (5) should be 10^5 and 10^6, respectively.

KINETIC EQUATIONS

For simplifying the derivation of the rate equations involved in the hydrate formation process, the following assumptions were made:

(1) The rate of concentration change of each component (r_i) in the reactions shown in Eqs. (1) to (5) can be expressed in the following polynomial form,

$$r_i = -\frac{dC_i}{dt} = kC_i^{\alpha}C_j^{\beta} \cdots \tag{6}$$

where C_i and C_j represent the concentration (mol/L) of components i and j, α and β denote the order of concentration change.

(2) The order of concentration change is unity for all components (α=β=1.0).

(3) The water content in the aqueous phase is constant during the hydrate formation process.

(4) The volume of gas phase and liquid phase remain unchanged during the hydrate formation process.

Based on the above assumptions, the following rate equations can be derived:

$$\frac{dC_G}{dt} = -k_1C_G + k_{-1}C_A \tag{7}$$

$$\frac{dC_A}{dt} = k_1C_G - k_{-1}C_A - k_2C_A + k_{-2}C_B - pk_5C_AC_N \tag{8}$$

$$\frac{dC_B}{dt} = k_2C_A - k_{-2}C_B - mk_3C_B + mk_{-3}C_D \tag{9}$$

$$\frac{dC_D}{dt} = k_3C_B - k_{-3}C_D - lk_4C_D \tag{10}$$

$$\frac{dC_N}{dt} = k_4C_D - k_5C_AC_N \tag{11}$$

$$\frac{dC_H}{dt} = k_5C_AC_N \tag{12}$$

where C_G stands for the apparent mole concentration of methane in the gas phase (mole of methane in gas phase per liter of liquid phase), C_A, C_B, C_D, C_N and C_H denote the concentrations (mol/L) of $CH_4(aq)$, $CH_4 \cdot nH_2O$, $mCH_4 \cdot rH_2O$, N and H, respectively. Based on assumption (3), the concentration of water in the liquid phase does not appear in the rate equations. At initial conditions: $t = 0$, $C_G = C_G^o$, $C_A = C_B = C_D = C_N = C_H = 0$, from mass balance of methane we have:

$$C_G^o = C_G + C_A + C_B + mC_D + lmC_N + (p + lm)C_H \tag{13}$$

Since C_G, C_A, C_B, C_D, C_N and C_H are restrained by Eq. (13), only five of the above six concentration variables are independent. The concentration of the metastable molecular cluster C_B was chosen as a dependent variable. From Eq. (13) we have:

$$C_B = C_G^o - C_G - C_A - mC_D - lmC_N - (p + lm)C_H \tag{14}$$

Eq. (9) can then be removed from the rate equation set. Substituting Eq. (14) into Eqs. (8) and (10) yields:

$$\frac{dC_A}{dt} = k_{-2}C_G^o + (k_1 - k_{-2})C_G - (k_{-1} + k_2 + k_{-2})C_A - mk_{-2}C_D - lmk_{-2}C_N - (p + lm)k_{-2}C_H - pk_5C_AC_N \tag{15}$$

$$\frac{dC_D}{dt} = k_3(C_G^o - C_G) - k_3C_A - (mk_3 + k_{-3} + lk_4)C_D - lmk_3C_N - (p + lm)k_3C_H \tag{16}$$

The initial conditions are changed to: $t = 0$, $C_G = C_G^o$, $C_A = C_D = C_N = C_H = 0$.

Eqs. (7), (11), (12), (15) and (16) coupled with the corresponding initial conditions constitute the mathematical model of the kinetic behavior of methane hydrate formation in pure water.

THE LEAST SQUARE ESTIMATION OF THE KINETIC PARAMETERS

In the rate equations established in the previous section, there are eight unknown parameters: k_1, k_{-1}, k_2, k_{-2}, k_3, k_{-3}, k_4 and k_5. As k_1 and k_{-1} are restrained by the following expression of equilibrium constant K_c (derivation is referred to the expanded manuscript):

$$K_c = \frac{k_1}{k_{-1}} = \frac{C_w^oZRTV_l}{HV_g} \tag{17}$$

where C_w^o, Z and H denote the initial water concentration, compressibility of methane and Henry's constant of methane, respectively. k_{-1} can be calculated through k_1 as follows:

$$k_{-1} = \frac{k_1}{K_c} = \frac{k_1HV_g}{C_w^oZRTV_l} \tag{18}$$

Thus, only seven unknown parameters (k_1, k_2, k_{-2}, k_3, k_{-3}, k_4 and k_5) in the kinetic equations needed to be determined.

The damped nonlinear least square method was used for parameter estimation, the details of the algorithm are also given in the expanded manuscript (which is available on request). The regressed parameter values for the methane + water systems are tabulated in Table 2, and a typical comparison between experimental and calculated $P \sim t$ data for Experiment E09b is shown in Fig. 3.

TEST ON THE PROPOSED KINETIC MODEL

Sensitivity on Initial Pressure. Experiments E01 ~ E04 were run under the same temperature (273.65 K) and different initial pressures. Tests were performed on the prediction of the $P \sim t$ data of E01 ~ E03 based on the parameter values determined from E04. The test results show that, in the gas dissolution zone the deviations between experimental and calculated gas phase pressure are in the range of –0.11% ~ –0.50%; in the nucleation zone, the maximum relative deviations are –0.37% for E02 and E03, and 0.74% for E01(no hydrate finally formed); and in the hydrate growth zone, the maximum relative deviation is –0.29% for E02 and E03. Typical comparison between the experimental and predicted $P \sim t$ curves for E01 is shown in Fig. 4.

Experiments E05 ~ E09 were also run at the same temperature (274.15 K) and different initial pressures. The $P \sim t$ data of Experiments E08, E09b and E09c were predicted by using the parameter values determined from E07. In the gas dissolution zone, the measured and calculated gas phase pressures are close, the maximum relative deviation is 0.38%. In the nucleation zone, the maximum deviations are –0.059% for E08, and 0.54% for E09b and E09c. In the crystal growth zone, the maximum deviations for E08, E09b and E09c are 0.78%, 1.01% and 0.52%, respectively.

The test results indicate that although the kinetic data of hydrate formation depend on the initial pressure, the model parameters determined from a specific run are capable of predicting the $P \sim t$ data of runs carried out at different initial pressures (under same temperature) with good accuracy.

Prediction of the $P \sim t$ Data for Salt/EG Containing Systems. The prediction of the kinetic data of methane hydrate formation in brines and aqueous solution of EG are of particular interest in real production processes and has not been previously reported. It is well known that the presence of salt(s) and alcohol in the aqueous phase can inhibit the hydrate formation (similar to the freezing point depression), as the solubility of methane will be significantly lowered, and the physical properties (viscosity, density, diffusivity, interfacial tension, etc.) of the aqueous phase will in turn be significantly changed. As a preliminary attempt to extend the proposed kinetic model to the salt/ethylene glycol containing systems, we assumed the solubility of methane in the aqueous phase (expressed in terms of the Henry's constant of methane) is the critical factor affecting the inhibition of methane hydrate formation. The larger the Henry's constant, the greater the inhibition effect.

Among the eight parameters in the proposed kinetic model, k_{-1} is the only parameter related to Henry's constant, hence, the other model parameters determined from methane + pure water system can be applied directly to the salt/ethylene glycol containing systems. For illustration purposes, the $P \sim t$ data of methane hydrate formation in 5.0 mass% NaCl solution (Experiment E16) were predicted by using the kinetic parameters determined from Experiment E09b performed on methane + pure water system (E16 and E09b were run at the same temperature and initial pressure conditions). The Henry's constant of methane in the 5.0 mass% NaCl solution at 274.15 K was taken from Cramer (1984), $H = 3.642 \times 10^3$. The comparison between the predicted and experimental results is presented in Fig. 5. Fairly good prediction results were observed, the maximum deviations of the predicted gas phase pressure are −0.13 % in the gas dissolution zone, and 0.31 % in the nucleation and crystal growth zones.

CONCLUSIONS

(1) The new kinetic model developed from a four-step hydrate formation mechanism and reaction kinetics approach is capable of describing the $P \sim t$ data measured in this work.

(2) Under identical temperature condition, the kinetic parameters determined for a specific initial pressure can be applied to estimate the $P \sim t$ data run at other initial pressures (within the pressure range of this study), the maximum deviation is within 0.3%.

(3) The kinetic model developed for methane + water systems can be extended to inhibitor containing systems by replacing the Henry's constant of methane in corresponding aqueous phase.

(4) As the dynamic behavior of hydrate formation is strongly dependent on the type of equipment and agitation intensity, the kinetic data measured in this work can only be considered as typical for a mildly agitated non-flowing system.

ACKNOWLEDGMENT

Financial support received from the China National Science Foundation, Postdoctoral Research Foundation and the China National Petroleum & Natural Gas Corporation are gratefully acknowledged.

REFERENCES

M. Bylov and P. Rasmussen, A new technique for measuring gas hydrate kinetics, Proceedings of the 2nd International Conference on Natural Gas Hydrates, June 2-6, 1996, Toulouse, France, 259-266.

R. L. Christiansen and E. D. Sloan, Mechanisms and kinetics of hydrate formation, Annals of the New York Academy of Sciences, Vol. 715 (1994) 283-305.

S. D. Cramer, Solubility of methane in brines from 0 to 300 °C, Ind. Eng. Chem. Proc. Des. Dev., 23 (1984) 533-538.

J. de Graauw and J. J. Rutten, The mechanism and the rate of hydrate formation, Proceedings 3rd Int. Symp. on Fresh Water from the Sea, 1970, Athens, 103-116.

P. Englezos, N. Kalogerakis, P. D. Dholabhai and P. R. Bishnois, Kinetics of formation of methane and ethane gas hydrates, Chem. Eng. Sci., 42 (1987) 2647-2658.

P. Englezos, Clathrate hydrates, Ind. Eng. Chem. Res., 32 (1993) 1251-1274.

J. Long and E. D. Sloan, Quantized water clusters around apolar molecules, J. Mol. Simul., 11 (1993) 145-161.

Y. F. Makogon, Hydrates of Natural Gas (translated from Russian by W. J. Cieslewicz), PennWell, Tulsa, 1983.

J. P. Monfort and A. Nzihou, Light scattering kinetics study of cyclopropane hydrate growth J. Crystal Growth, 128 (1994) 1182-1186.

V. Natarajan, P. R. Bishnoi and N. Kalogerakis, Induction phenomena in gas hydrate nucleation, Chem. Eng. Sci., 49 (1994) 2075-2087.

J.-H. Qiu and T.-M. Guo, Status of the kinetic studies on the hydrate formation/dissociation, J. Ind. & Eng. Chem. (China), 46 (1996) 741-756.

P. Skovborg, H. J. Ng, P. Rasmussen and U. Mohn, Measurement of induction times for the formation of methane and ethane hydrates, Chem. Eng. Sci., 48 (1993) 445-453.

E. D. Sloan, Clathrate Hydrates of Natural Gas, Marcel Dekker, New York, 1990.

J. A. van der Waals and J. C. Platteeuw, Clathrate solutions, Adv. Chem. Phys., 2 (1959) 2-57.

M. H. Yousif, R. B. Dorshow and D. B. Young, Testing of hydrate kinetic inhibitors using laser scattering technique, Annals of the New York Academy of Sciences, Vol. 715 (1994) 330-340.

Y.-X. Zuo, S. Gommesen and T.-M. Guo, Equation of state based hydrate model for natural gas systems containing brine and polar inhibitor, Chinese J. Chem. Eng. (in English), 4 (1996) 189-202.

Table 1. Summary of the methane hydrate systems studied and the time distribution of three zones

Exp. No.	Aqueous phase*	Temp. (K)	Initial Press. (MPa)	Gas dissolution zone (min)	Nucleation zone (min)	Crystal growth zone (min)
E01	H_2O	273.65	4.47	100	645#	–
E02	H_2O	273.65	5.46	100	80	150
E03	H_2O	273.65	7.45	100	100	125
E04	H_2O	273.65	8.47	95	25	80
E05	H_2O	274.15	4.49	100	575#	–
E06	H_2O	274.15	5.10	105	510#	–
E07	H_2O	274.15	5.46	95	90	205
E08	H_2O	274.15	5.96	95	25	185
E09a	H_2O	274.15	6.46	105	195#	–
E09b	H_2O	274.15	6.46	105	105	160
E09c	H_2O	274.15	6.47	105	32	183
E10	H_2O	274.65	6.47	90	30	195
E11	H_2O	275.15	6.00	130	165	280
E12	H_2O	276.15	6.47	110	40	390
E13	NaCl (0.5)+H_2O	274.15	6.46	60	38	160
E14	NaCl (1.0)+H_2O	274.15	6.47	65	30	185
E15	NaCl (3.0)+H_2O	273.65	6.47	110	150#	–
E16	NaCl (5.0)+H_2O	274.15	6.45	110	325	150
E17	$NaHCO_3$ (0.5)+H_2O	274.15	6.45	65	32	168
E18	$NaHCO_3$ (1.0)+H_2O	274.15	6.46	65	30	200
E19a	$NaHCO_3$ (3.0)+H_2O	274.15	6.47	115	210	195
E19b	$NaHCO_3$ (3.0)+H_2O	274.15	6.48	115	200	200
E20	$NaHCO_3$ (5.0)+H_2O	273.65	6.46	120	615#	–
E21	EG (0.5)+H_2O	274.15	6.47	110	340#	–
E22	EG (1.0)+H_2O	274.15	6.46	115	345#	–
E23	EG (5.0)+H_2O	273.65	6.47	115	25	185
E24	EG (10.0)+H_2O	273.65	6.47	120	505#	–
E25	NaCl (0.5)+ $NaHCO_3$ (0.5)+H_2O	274.15	6.47	60	25	185
E26	NaCl (1.5)+ $NaHCO_3$ (1.5)+H_2O	274.15	6.47	90	35	250
E27	NaCl (2.5)+ $NaHCO_3$ (2.5)+H_2O	273.65	6.47	100	65	290
E28	NaCl (2.5)+ $NaHCO_3$ (2.5)+H_2O	274.15	6.47	95	60	320
E29	NaCl (2.5)+ EG (2.5)+H_2O	273.65	6.47	90	55	235
E30	$NaHCO_3$ (2.5) + EG (2.5)+H_2O	273.65	6.47	90	112	203

* Numbers in parentheses are mass percent of inhibitor; EG stands for ethylene glycol.

# No hydrate crystal formed in this time period.

Table 2. Estimated kinetic parameter k_j values for various experiments on methane + water systems

Exp. No.	$k_1 \times 10^3$	$k_2 \times 10^2$	$k_{-2} \times 10$	$k_3 \times 10^3$	$k_{-3} \times 10^2$	$k_4 \times 10$	k_5
E02	33.99	135.1	45.37	0.3735	5.037	0.4297	6.626
E03	32.95	187.3	41.57	0.2669	8.527	0.1839	5.261
E04	19.46	12.13	28.48	1.470	5.386	4.097	10.93
E07	29.05	0.8026	6.543	6.374	9.195	10.94	4.976
E08	15.54	55.59	0.3661	0.01616	3.923	6.708	0.5876
E09b	14.15	0.03878	1.189	139.2	0.2266	0.7779	4.224
E09c	8.539	21.95	0.3699	0.03070	4.771	4.390	0.8824
E10	13.74	10.64	34.31	1.447	34.34	28.15	9.487
E11	21.28	0.9161	4.622	1.792	6.435	8.710	3.455
E12	10.22	94.46	3.016	0.02347	4.746	7.368	0.9024

Table 3. Comparison of the experimental and calculated gas phase pressure for the Experiments E09b and E16*

Experiment E09b				Experiment E16			
t (min)	P_{exp} (MPa)	P_{cal} (MPa)	Rel. Dev. (%)	t (min)	P_{exp} (MPa)	P_{cal} (MPa)	Rel. Dev. (%)
0.0	6.465	–	–	0.0	6.447	–	–
10.0	6.452	6.453	- 0.018	15.0	6.430	6.431	−0.022
20.0	6.441	6.444	- 0.040	30.0	6.417	6.422	−0.078
30.0	6.429	6.436	- 0.110	40.0	6.412	6.418	−0.088
45.0	6.424	6.426	- 0.034	55.0	6.405	6.414	−0.13
60.0	6.421	6.419	+ 0.036	75.0	6.401	6.410	−0.14
75.0	6.412	6.414	- 0.034	95.0	6.400	6.408	−0.13
85.0	6.412	6.411	+ 0.013	110.0	6.399	6.407	−0.13
105.0	6.410	6.407	+ 0.049	135.0	6.399	6.406	−0.11
125.0	6.406	6.404	+ 0.028	150.0	6.399	6.405	−0.10
140.0	6.405	6.402	+ 0.040	170.0	6.398	6.405	−0.11
165.0	6.405	6.400	+ 0.082	200.0	6.398	6.403	−0.081
190.0	6.405	6.397	+ 0.120	230.0	6.397	6.401	−0.068
210.0	6.405	6.395	+ 0.150	260.0	6.397	6.399	−0.028
220.0	6.399	6.395	+ 0.065	290.0	6.396	6.396	+0.003
230.0	6.398	6.394	+ 0.066	350.0	6.395	6.392	+0.11
240.0	6.393	6.393	+ 0.004	410.0	6.394	6.378	+0.24
260.0	6.387	6.391	- 0.066	445.0	6.392	6.372	+0.31
280.0	6.381	6.389	- 0.120	480.0	6.382	6.367	+0.23
310.0	6.375	6.384	- 0.140	515.0	6.376	6.361	+0.23
340.0	6.371	6.378	- 0.120	540.0	6.372	6.356	+0.24
370.0	6.370	6.371	- 0.022	575.0	6.368	6.350	+0.29

* Calculations for E16 were based on the parameter values determined from E09b.

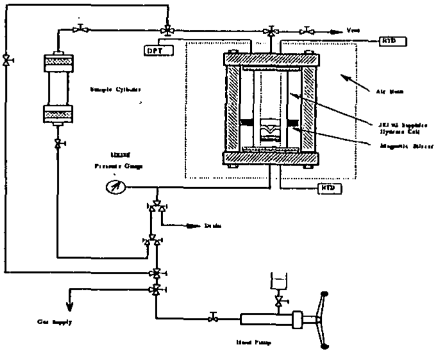

Fig. 1. Schematic diagram of the experimental system
DPT—differential pressure transducer
RTD—resistance thermocouple detector

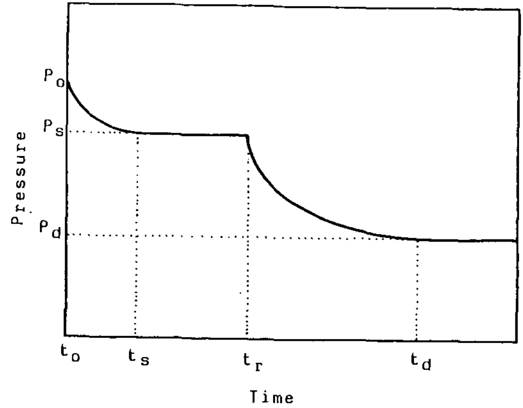

Fig. 2. A typical $P \sim t$ curve measured in this study

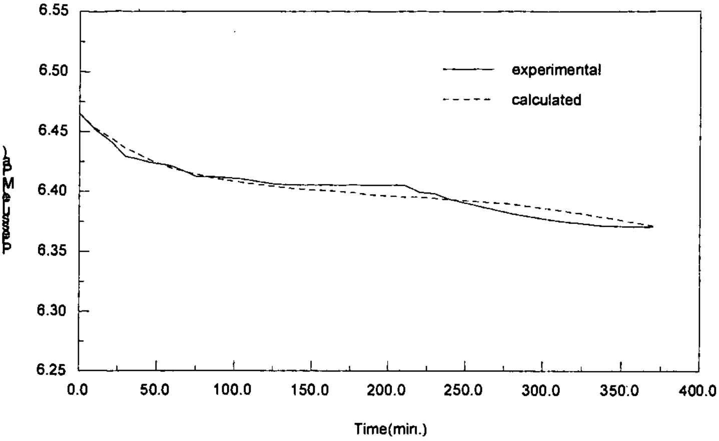

Fig. 3. The experimental and calculated $P \sim t$ curve for Experiment E09b

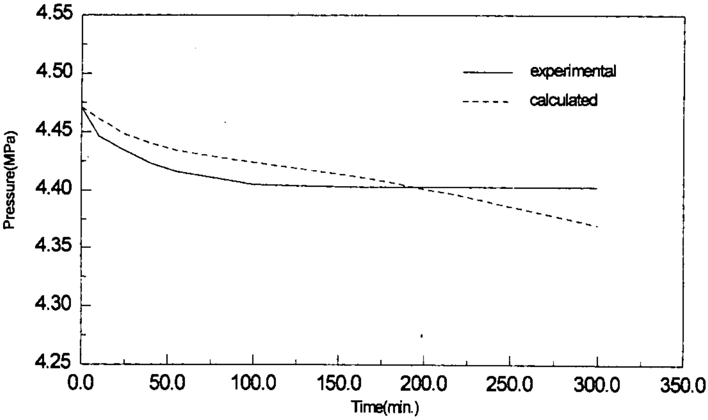

Fig. 4. The experimental and calculated $P \sim t$ curve for Experiment E01 (calculation based on the parameters determined for E04)

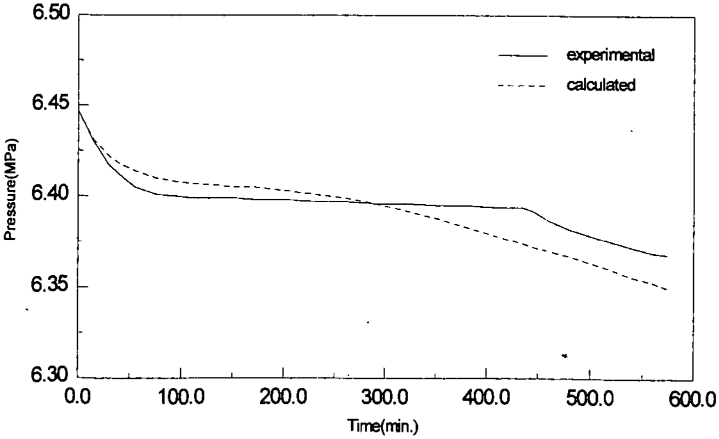

Fig. 5. The experimental and calculated $P \sim t$ curve for Experiment E16 (calculation based on the parameters determined for E09b)

"Experimental testing and evaluation of a kinetic gas hydrate inhibitor in different fluid systems"

Olav Urdahl*[1], Are Lund[2], Lars Henrik Gjertsen[1] and Torstein Austvik[1]

1 Statoil Research Centre, Field Development Technology, Postuttak, 7005 Trondheim, NORWAY
2 SINTEF, Applied Chemistry, 7000 Trondheim, NORWAY
*Corresponding author

Key words: hydrate inhibition, kinetic inhibitor, flowing system, performance

Introduction

The development of offshore mature basins such as the North Sea is increasingly characterized by marginal reservoirs. Feasible economic development of these reservoirs requires a shift towards total subsea production systems without fixed or floating production platforms. Unprocessed or minimum processed reservoir fluids will be transported to a central processing facility or ultimately to shore. One of the key issues of total subsea production systems is multiphase flow technology with particular emphasize on gas hydrate control technology.

Subsea transportation of unprocessed or minimum processed well fluids over long distances today requires the use of large amounts of methanol or glycols for hydrate inhibition. The effect of these additives is to decrease the water activity to an extent that markedly reduces its ability to participate in hydrate formation, and thereby in a lowering of the hydrate formation temperature. The amount of inhibitor necessary to obtain the desired lowering of the hydrate formation temperature is substantial, usually in the range of 20-40 weight% of the aqueous phase. This has prompted the search for new types of additives capable of inhibiting hydrate formation at far lower concentrations (1-5).

Statoil performs intensive research on hydrates; methods to prevent hydrate problems as well as studies on the formation and removal of hydrate plugs. This paper focuses on the robustness of a commercially available additive from T. R. Oil Services (Hytreat 525) with respect to degree of subcooling, pressure, salinity of the aqueous phase and the impact from having a defoamer or a corrosion inhibitor in the system. The inhibitor is tested both at continuous flow conditions and at re-starts after shut-ins. Results from tests on two different condensate systems as well as two crude oils are summarized.

Experimental

The experiments were carried out in a high pressure loop formed as a wheel. The system is illustrated in **Figure 1**. The test wheel was filled with the desired fluid at a specified temperature and pressure, and then set under rotation. The rotation creates a relative velocity between the pipe wall and the fluid thus simulating transport through a pipeline.

The high pressure wheel is made from stainless steel with an inner tube diameter of 52.5 mm and a wheel diameter of 2.0 m. The volume is 13.4 liters. The wheel includes two high pressure windows for visual inspection, and one of these is equipped with a video camera.

The flow simulator is placed in a temperature controlled chamber. The temperature is controlled using a programmable regulator, a heating fan and a refrigeration system. The temperature development in the chamber as a function of time is preset in the regulator.

The wheel is attached to a motor/gearbox system enabling a variation of the peripheral velocity of the wheel between 0.3 m/s and 5.0 m/s. A torque sensor is installed as a part of the rotational shaft enabling torque measurements to be performed during rotation. Pressure and temperature sensors on the wheel have ranges of 0-250 bara and -10 to +150 °C respectively. All signals are transferred through cables and slip rings to a real time PC-based data acquisition system.

The accuracy of the measurements is estimated to be ±0.2 Nm for torque, ±0.5 bar for pressure, ±0.1°C for fluid temperature in the wheel and ±1.0 °C for temperature in the chamber.

Experimental procedure

1 Continuous flow

The wheel is rotated at a constant peripheral velocity (1.0 m/s) as the temperature is reduced from about 60°C to 4°C at a given cooling rate. In the following, these experiments are referred to as continuous flow experiments. In condensate systems without emulsifiers added, a velocity of 1.0 m/s creates separated liquid phases (prior to hydrate formation). The phases are generally mixed at this velocity when black oil systems are used.

2 Start-up

The system is cooled as the wheel is rotating (peripheral velocity of 1 m/s) to about 30 °C before the wheel is stopped. The wheel is then cooled to a temperature of 4°C and kept constant for a period of minimum 12 hours. The wheel do not move during this period. Then the wheel is restarted and rotated at a constant peripheral velocity of 1.0 m/s for the rest of the experiment. These experiments are referred to as start-up experiments.

In order to minimize the number of adjustable parameters for the experiments, only one given cooling rate is used both for the continuous flow experiments and the start-up experiments.

Results and discussion

The hydrate inhibitor tested in this work is a commercially available kinetic inhibitor concisting of a blend of different polymer/surfactants.

In this specific study the inhibitor was tested in the high-pressure system using two different crude oils and two gas condensates. Also the presence of a coorosion inhibitor or a defoamer on the performance was investigated for some of the fluid systems. Results from 27 experiments performed in the flow simulator with the different hydrocarbon fluids are presented. A summary of the experimental conditions and observations from these experiments is given in **Table 1.** It should be stressed that the subcoolings given in the **Table 1** have been corrrected for the actual salinity of the systems.The results are discussed in more detail below.

Condensate A

Impact of corrosion inhibitor

Based on the visual information from the experiments the addition of the corrosion inhibitor changed the physical properties of the system with respect to foaming tendency. No significant change of performance of the hydrate inhibiting properties was observed. In all the inhibitor experiments there was a considerable kinetic effect but there was a decrease in transporability at hydrate formation compared to the pure system.

Impact of salinity

The salinity of the aqueous phase in these experiments was varied from 0-3,5 wt%. Increased salinity resulted in an increased delay of hydrate formation from 80 min to 20 hours. Previous studies (1,3,5) have shown that the optimal salinity for this inhibitor is approx. 3,5 wt%. The improved performance is due to conformational changes in the polymer systems in the inhibitor. A salinity of 0,25 wt% corresponds to the actual salinity of the produced water from the field.

Impact of subcooling

As seen from **Table 1** the subcooling in the experiments are varied from 9°C to 13°C. At continuous flow mode an addition of 0.5 wt% of the hydrate inhibitor prevented hydrate formation at a subcooling of approximately 9°C for the test period of 36 hours when the salinity was 0,25 wt%. Also restarts after a shut-in of 12 hours was successfullly carried out at this temperature, although there were hydrates present in the system. However, at subcoolings above 9°C, the hydrate inhibitor tested was not able to fully prevent the hydrate formation during continuous flow. But in all the experiments hydrate formation was delayed compared to experiments on the blank Condensate A fluid.

Condensate B

Impact of subcooling

Experiments were here performed with a inhibitor concentration of 0.5 wt% of the aqueous phase . As seen from exp. 15, no hydrate formation were observed in this system at a subcooling of 11°C at a pressure of 70 bar within an experimental time of 80 hours. When the subcooling was increased to 13°C, hydrate formation was observed after 9 hours. When increasing the pressure to 140 bar (exp.16) keeping the subcooling constant at 11°C, hydrates were formed after 6 hours, and the flowloop plugged 1 hour after hydrate initiation. In these experiments the aqueous phase contained 3.5 wt% NaCl.

Crude oil A

The kinetic inhibitor was tested with and without the presence of a corrosion inhibitor both in continuous flow experiments and in shut-in experiments. In exp. 17-20 also a defoamer was present in the system.

Impact of defoamer and corrosion inhibitor

From **Table 1** one can observe from experiments 17-26 that the prescence of the defoamer reduces the performance of the hydrate inhibitor dramatically. For practical purposes it does not work at all.

During the continuous flow experiments without the defoamer present a significant delay of the hydrate formation was observed both with and without the prescence of the corrosion inhibitor. At a subcooling of 11°C the presence of the corrosion inhibitor improved the performance compared to the system with only the hydrate inhibitor present. Hydrate formation was not initiated during a period of 60 hours.

In the start-up experiments, however, the induction time was reduced. Hydrates were formed during the stagnant period (12 hours), and the wheel was plugged shortly after restart.
The transportability of the hydrates formed was better in the presence of the corrosion inhibitor. This is opposite to what was observed for condensate A, and it illustrates the importance of fluid effects when this kind of technology is considered for use.

Impact of subcooling
The subcooling in the experiments was varied fom 7°C to 13°C. The chemical was not capable of fully preventing the hydrate formation in any of the experiments. However, at subcoolings below 10°C the hydrates formed were transportable.

Crude oil A
Impact of subcooling
During continuous experiments at a subcooling of 7.3°C and 0.5wt% of hydrate inhibitor no hydrate formation was observed for almost 10 hours. The formation rate was then very slow for 2 hours before it increased rapidly resulting in a viscosity increase of the system. No hydrate plugging was observed.

In the start-up at a subcooling of 9.5°C, hydrates started to form very slowly after start-up. After approx. 4 hours the formation rate increased drastically and flow problems were observed due to the high viscosity of the system. However, no "solid" hydrate plug was observed in the experiment.

Fluid and flow dependency
The inhibitor were tested in 4 different fluids with different composition and physicochemical properties. The performance of the inhibitor is different for all these fluids. It is not possible to extrapolate the results from one condensate to another, or one black oil system to another. It is known tha parameters like aliphatic/aromatic ratio, amount and state of asphaltenes and resins and also wax content will influence on the performance, and these factors will always vary between different fluids.

Regarding the influence of flow properties it has for all the systems investigated been shown that stagnant conditions are more difficult to handle then continuos flow. This aspect should be investigated further and will be adressed more thoroughly in a forthcoming paper.

Summary and conclusions

A commercially available kinetic hydrate inhibitor in a high pressure flowing system at various conditions and for different fluid systems. Also the presence of other production chemicals have been adressed. The conclusions can be summarized as follows:
- the defoamer has a negative effect. It reduces the performance to nearly zero.
- the corrosion inhibitor results in an increased mixing/emulsification of the system. This might be a benefit in some systems (black oils) but not in others (condensates).
- the salinity is crucial for the performance.
- the maximum subcooling to be handled is in the range 7-11°C depending on the fluid system.
- the effect of the inhibitor is reduced at stagnant conditions.

The results strengthen the knowledge that results from one fluid system should not be extrapolated to another. These kind of chemicals have to be qualified for each given fluid before they can be applied at real conditions.

Acknowledgements

The Statoil Multiphase Flow Program is acknowledged for giving permission to publish the results. T.R.Oil Services is acknowledged for supplying the kinetic hydrate inhibitor.

References

(1) O.Urdahl, A.Lund, P.Mørk and T.N.Nilsen.*Chem. Eng. Sci.*, **50 (5)**, 863-870, (1995).

(2) A. Lund, O. Urdahl and S.S. Kirkhorn, *Chem. Eng. Sci.*, **51(13)**, 3449-3458, (1996).

(3) A. Lund, O. Urdahl, L.H. Gjertsen, S.S. Kirkhorn and F.H. Fadnes, Proceedings from the *2nd International Conference on Naural Gas Hydrates*", p. 407, Toulouse, France, July, (1996)

(4) L.H. Gjertsen, T. Austvik and O. Urdahl, Proceedings from the *2nd International Conference on Naural Gas Hydrates*", p. 155, Toulouse, France, July, (1996).

(5) A. Lund, O. Urdahl and S.S. Kirkhorn, *J. Pet. Sci. and Tech.*, Submitted.

Table 1: *Experimental conditions and observations from the experiments*

Exp.	Fluid	Inhibitor conc. (wt%)	Water cut (vol%)	Conc. of corr.inh. (ppm)	Salinity (wt%)	Mode	Sub cooling (°C)	Comments
1	Cond. A	0	20	-	0.25	Cont	8.5	Hydrate formation started immediately and the pipe was plugged after 23 min.
2	Cond. A	0.50	20	800	0.25	Cont+ start-up	13.0	Hydrate formation and plugging after 16 hours. Hydrate lumps and depositions at the window.
3	Cond. A	0.50	20	800	3.5	Cont+ st.up	11.0	No hydrate formation observed during dynamic period. A hydrate plug formed during shut-in
4	Cond. A	0.50	20	800	3.50	Cont+ start-up	11.0	A lot of foam in the condensate phase during dyn. conditions.. The foam broke down 5 hours after shut-in. Hydrate formation started after 9 hours. Plugged before restart.
5	Cond. A	0.50	20	-	0.25	Cont.	13.0	Foam observed in the condensate phase from start of experiment. Emulsification after 90 minutes and hydrate formation and plugging after 26 hours (dynamic conditions).
6	Cond. A	0.50	20	-	0.25	Cont+ start-up	9.0	No hydrate formation observed during dynamic condition. 4 hours after shut-in hydrate formation started at interface growing into both condensate and aqueous phase. Loose hydrates. Smooth restart with minor depositis at the window.
7	Cond. A	0.50	20	-	0.25	Cont+ start-up	11.0	Hydrate formation observed after 4 hours during dynamic conditions. Plugged before restart.
8	Cond. A	0.50	20	-	0	Cont.	10.5	No hydrate formation observed during the experimental time of 11 hours
9	Cond. A	0.50	20	-	0	Cont	13.0	Hydrate formation and immediate plugging after 80 min.
10	Cond. A	0.50	20	-	3.5	Cont.	11	No hydrate formation observed for the experimental time of 25 hours.
11	Cond. A	0.50	20	-	3.5	Cont.	13	Hydrate formation and immediate plugging after 20 hours.
12	Cond. B	0	20	-	3.5	Start-up	14.5	Deposits and plugging within 11 min. after start of hydrate formation.
13	Cond. B	0.50	20	-	3.5	Start-up	13/15	No hydrate formation after 3 hours at 4°C. When temp. was lowered to 2°C rapid hydrate formation was initiated after 3.5 hours
14	Cond. B	0.50	20	-	3.5	Start-up	13	Rapid hydrate formation after 9.5 hours.
15	Cond. B	0.50	20	-	3.5	Cont.	11	No hydrate formation was observed within the experimental time of 80 hours
16	Cond. B	0.50	20	-	0	Start-up	11	Viscous emulsion after restart. Hydrate formation started 1.5 hours after restart.
17	Crude A	0	33	-	3	Start-up	13	Deposits at restart Plugging after 2 minutes.
18	Crude A	0.27	33	-	3	Start-up	13	Deposits at restart. Plugging after 1 minute
19	Crude A	0.27	33	-	3	Start-up	7	Hydrates formed 27 min. after restart Transportable hydrates but very viscous.
20	Crude A	0.50	33	-	3	Start-up	13	Hydrate deposits at restart. Plugging after 1 minute
21	Crude A	0	33	-	3	Start-up	10.5	Emulsion layer at the interface. Blocked 80 sec. after restart.

Exp.	Fluid	Inhibitor conc. (wt%)	Water cut (vol%)	Conc. of corr.inh. (ppm)	Salinity (wt%)	Mode	Sub cooling (°C)	Comments
23	Crude A	0.50	33	-	3	Cont.	11	Slow hydrate formation initiated after 7 hours. Formation rate increased later in the exp.
24	Crude A	0.50	33	-	3	Start-up	11.5	After stop of wheel the phases remained emulsified for 50 min. High formation rate 3 hours after start-up.
25	Crude A	33	0.50	800	3	Start-up	9	Droplets of water mixed in the oil phase. No hydrate formation for 68 hours. When subcooling was increased to 13°C the loop plugged.
26	Crude A	33	0.50	800	3	Start-up	11.2	Brown water phase during shut-in. Loop plugged 12 hours after restart.
27	Crude B	40	0	-	5	Start-up	7.6	Depositions and plugging 2 min. after start-up.
28	Crude B	40	0.5	-	5	Cont.	7.3	Slow hydrate formation initiated after 9.5 hours. More rapid formation after 11.5 hours andd also large increase in viscosity.
29	Crude B	40	0.5	-	5	Start-up	9.5	No deposits observed at start-up, but slow hydrate formation observed. After 3.5 hours rapid hydrate formation occurs resulting in a very viscous system that nearly blocks the loop.

Figure 1: An illustration of the flow loop.

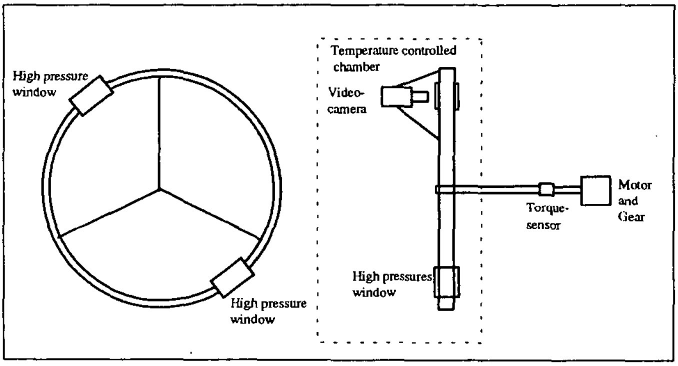
High pressure window
Temperature controlled chamber
Video-camera
Torque-sensor
Motor and Gear
High pressures window
High pressure window

ENHANCED HYDRATE INHIBITORS: POWERFUL SYNERGISM WITH GLYCOL ETHERS

William D. Young, Jeff M. Cohen, and Philip F. Wolf
International Specialty Products
1361 Alps Rd., Wayne, NJ 07470

Keywords: Gas hydrates, hydrate inhibition, gas production

INTRODUCTION

Since natural gas hydrates frequently plug oil and gas production lines, various chemical and thermal methods have been developed to prevent hydrate formation. Conventional chemical treatment involves injecting 20-50 weight % methanol in the water phase at the wellhead or downhole to depress the freezing point of hydrates below the minimum fluid temperature in the line. However, high methanol injection rates are expensive and may exacerbate pipeline corrosion. Alternative chemical treatment methods are needed.

Recently Lederhos, et al[1] reported that certain water soluble polymers effectively inhibit hydrates at treatment levels of 0.1 to 1.0 wt% in the water phase, far less than required by methanol. At typical flowline conditions, these polymers slow the rates of hydrate nucleation and growth to such an extent that virtually no hydrates form in the wellstream during transport to processing facilities. Since the polymers slow hydrate formation rather than depress the freezing point, they are called 'kinetic inhibitors.' Under favorable conditions, kinetic inhibitors have prevented hydrates for more than 5 days. Industry field tests have demonstrated the viability of this technology.[2,3]

The most successful of the kinetic inhibitors are vinylcaprolactam (VCL) and vinylpyrrolidone (VP) based polymers, including Gaffix VC-713, a terpolymer of VCL, VP, and dimethylaminoethylmethacrylate (DMAEMA), and PVCL homopolymer. In addition, PVP, although not as effective as VC-713 and PVCL, has been widely used because it costs less and provides adequate protection in less demanding applications.[1,4]

ISP manufactures a full line of hydrate inhibitors including VC-713, PVCL, PVP and VCL/VP copolymers. These inhibitors are tested in the high pressure laboratory at realistic pipeline conditions. We have observed that several glycol ether solvents (for example, 2-butoxyethanol) significantly enhance the performance of the polymeric hydrate inhibitors. Better inhibitors provide lower polymer treatment levels and lower overall cost. This paper presents the results of our experimental study on hydrate inhibitors containing glycol ether solvents.

EXPERIMENTAL

The tests were conducted in a 300 ml stainless steel stirred reactor at high pressure and low temperature. A diagram of the apparatus is shown in Figure 1. Following the procedure of Long, et al,[4] 30 stainless steel balls are placed in the bottom of the reactor to increase nucleation sites. The reactor is immersed in a refrigerated bath, which normally maintains temperature to within 0.5°F. The pressure in the reactor is controlled to within 5 psi by a programmable syringe pump. The pump displaces hydraulic oil into a piston cylinder which contains the hydrate-forming gas on one side and hydraulic oil on the other. The volume of oil displaced by the syringe pump to maintain constant pressure indicates gas consumption in the reactor.

The inhibitors were tested at 0.5 wt% dry polymer and 0.75 wt% glycol ether in the salt solution. In a typical experiment, 0.6 g dry polymer and 0.9 g glycol ether liquid were added to 120 g of a 3.5 wt%, filtered, synthetic sea salt solution and mixed for at least one hour. The resulting solution was transferred to the 300 ml reactor, sealed, and immersed in the temperature bath at 39.2°F (4°C). The pressure was then increased to 1000 psig with green canyon gas and held constant to within about 5 psi with the syringe pump. After the pressure reached 1000 psig, the reactor stirrer was turned on to 1000 rpm. The gas volume, as measured by the syringe pump, and the reactor pressure and temperature were recorded electronically at 1 minute intervals throughout the experiment.

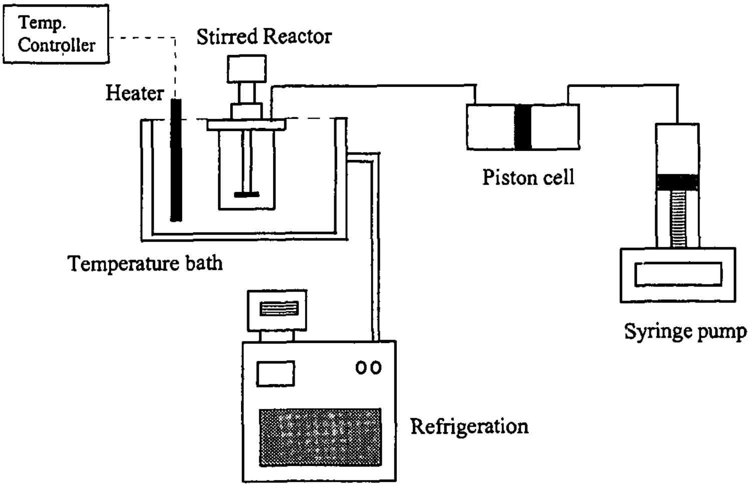

Figure 1: Gas hydrate test apparatus. The 300 ml reactor was charged with 120 g of sea salt solution containing 0.5% dissolved inhibitor. Tests were conducted at constant 39.2°F and 1000 psig for 20 hours. See text for more detail.

MATERIALS

Gaffix VC-713 is a terpolymer of VCL, VP, and DMAEMA. For consistency, all experiments reported here were conducted with the same manufacturing lot of VC-713.

Butyl Cellosolve, or 2-butoxyethanol, has the formula n-$C_4H_9OC_2H_4OH$. It is an industrial solvent with a boiling point of 171°C manufactured by Union Carbide. This material and the other glycol ethers listed in Table 2 were obtained from Aldrich and have a purity of about 99%.

The synthetic sea salt corresponds to ASTM 'Standard Specification for Substitute Ocean Water' and was purchased from Marine Enterprises of Baltimore, Maryland.

Green canyon gas is a typical natural gas mixture. It has the composition listed in Table 1.

Component	Mole %
nitrogen	0.4
methane	87.2
ethane	7.6
propane	3.1
isobutane	0.5
n-butane	0.8
i-pentane	0.2
n-pentane	0.2
total	100

Table 1: Green canyon gas composition

RESULTS AND DISCUSSION

Figure 2 shows the result of adding 0.75 wt% butyl Cellosolve to a mixture of 0.5 wt% VC-713 in sea salt solution. For comparison, the figure also shows the test results for 3.5 wt% sea salt solution with no inhibitor, 0.5 wt% VC-713 in sea salt solution, and butyl Cellosolve in sea salt solution. Each test was conducted at 39.2°F and 1000 psig. At these conditions green canyon gas has an equilibrium dissociation temperature of 64.7°F in deionized water, giving a total subcooling of 25.5°F. The gas consumption was calculated from measured volume change with the real gas law (compressibility factor = 0.83).

As the figure shows, this particular lot of VC-713 inhibits hydrates for only about 40 minutes at the test conditions. Adding 0.75 wt% butyl Cellosolve dramatically increases the performance of the inhibitor, to the extent that no detectable hydrates form for the duration of the 20 hour test. The figure also shows that butyl Cellosolve does not inhibit hydrates without polymer present.

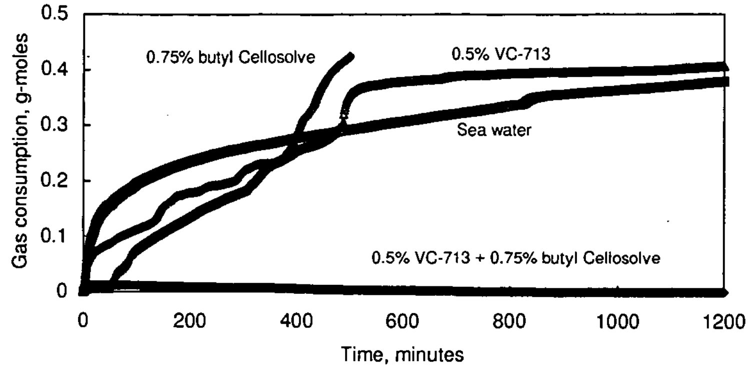

Figure 2: Hydrate inhibition test results at 39.2°F and 1000 psig (subcooling = 25.5°F). The aqueous phase is 3.5 wt% sea salt in all four tests. Concentrations are expressed as weight % in the aqueous phase.

Following up on the result with butyl Cellosolve, other glycol ethers with similar structures were tested at the same concentrations and conditions. Table 2 lists the observed induction times for each material, where induction time has been defined as the time at which detectable gas consumption begins, even if hydrate growth is slow beyond that point.

The data indicate that glycol ethers with 3 or 4 carbons in their alkoxy group significantly enhanced the performance of VC-713. Lower homologs did not appear to have any effect. Higher homologs were insoluble in the salt solution.

Glycol ether	Formula	Induction time (min)
2-butoxy ethanol	$n\text{-}C_4H_9OC_2H_4OH$	>1200
2-isopropoxy ethanol	$CH_3CH(CH_3)OC_2H_4OH$	800
1-propoxy-2-propanol	$C_3H_7OCH_2CH(CH_3)OH$	600
2-(2-butoxyethoxy) ethanol	$n\text{-}C_4H_9OC_2H_4OC_2H_4OH$	440
1-butoxy-2-propanol	$n\text{-}C_4H_9OCH_2CH(CH_3)OH$	450
2-propoxy ethanol	$n\text{-}C_3H_7OC_2H_4OH$	350
2-ethoxy ethanol	$C_2H_4OC_2H_4OH$	10
1-methoxy-2-propanol	$CH_3OCH_2CH(CH_3)OH$	10
none (sea water only)		0
none (VC-713 only)		40

Table 2: Induction times for 0.75 wt% glycol ether plus 0.5 wt% VC-713 in 120 g of sea salt water at 39.2°F and 1000 psig.

Butyl Cellosolve also showed strong synergism with other kinetic inhibitors. Table 3 compares the induction times for polyvinylcaprolactam homopolymer (PVCL) and 50/50 VCL/VP copolymer with and without butyl Cellosolve. Test conditions were identical to those described above.

Table 4 lists the surface tension of aqueous solutions of glycol ethers as reported in the manufacturer's literature.[5] The data indicate that the higher homologs are surface active. If this hydrophobicity of the hydrocarbon chain also causes the chain to associate with the dissolved polymer, then the glycol ether may allow the polymer conformation to expand in solution. This could occur if the surfactant breaks the weak bonds between polymer segments which pull the coils together and tighten the conformation. An extended polymer would presumably have more of its length available for interaction with the crystal surface, which may account for its improved performance as a hydrate inhibitor.

	Induction times (minutes)	
Inhibitor (0.5%)	No additive	0.75% butyl Cellosolve
Gaffix VC-713	40	>1200
PVCL	0	>1200
50/50 VCL/VP	0	350

Table 3: Comparison of induction times for kinetic inhibitors with and without butyl Cellosolve added, at 39.2°F and 1000 psig in sea water solution.

Solvent	Mol. weight	Boiling point, °C	Surface tension at 25°C, for 25% aq. solution, by volume (dynes/cm)
methyl Cellosolve	76.1	124.5	54.3
Cellosolve	90.1	134.9	47.1
propyl Cellosolve	104.2	150.1	32.3
butyl Cellosolve	118.2	171.2	28.9

Table 4: Surface tension and other properties of the 2-alkoxy ethanol homologs. All data was obtained from manufacturer's literature.[5]

REFERENCES

1. Lederhos, J. P.; Long, J. P.; Sum, A.; Christiansen, R. L.; Sloan, E. D., Jr., "Effective Kinetic Inhibitors for Natural Gas Hydrates," *Chemical Engineering Science*, 51 (8), (1996) 1221.
2. Notz, K.; Bumgartner, S. B.; Schaneman, B. D.; Todd, J. L., "The Application of Kinetic Inhibitors to Gas Hydrate Problems," *27th Annual Offshore Technology Conference*, Houston, TX, 1-4 May 1995, 719.
3. Bloys, B.; Lacey, C.; Lynch, P., "Laboratory Testing and Field Trial of a New Kinetic Hydrate Inhibitor," *27th Annual Offshore Technology Conference*, Houston, TX, 1-4 May 1995, 691.
4. Long, J.; Lederhos, J.; Sum, A.; Christiansen, R.; Sloan, E. D., "Kinetic Inhibitors of Natural Gas Hydrates," *Proceedings of the Seventy-Third GPA Annual Convention*, New Orleans, LA, 7-9 March 1994, 85.
5. Union Carbide, *Glycol Ethers*, (1993).

THE EFFECT OF IMPURITIES ON ETHANE HYDRATE INDUCTION TIMES

Martin Bylov
Calsep A/S
Gl.Lundtoftevej 7, 2800 Lyngby
Denmark

Peter Rasmussen
Department of Chemical Engineering, The Technical University of Denmark
Building 229, 2800 Lyngby
Denmark

Keywords: Hydrates, Induction Time, Growth Rate.

ABSTRACT

Three series of ethane hydrate formation experiments have been performed. The first series was carried out at 14 bar and 3 °C. Very scattered induction times (40,000 to 340,000 seconds) and less scattered growth rates were observed. Before the next series the cell was cleaned very thoroughly. With similar experimental conditions the induction time was longer than three weeks after which period of time the pressure was increased to 21 bar. Scattered induction times (10,000 to 150,000 seconds) and slightly higher growth rates were obtained. The third series was carried out at 20 bar and with 20 mg of impurities added. Short induction times and slightly lower growth rates were observed. All the experiments have been simulated using the hydrate kinetics model proposed by Skovborg (3). The experiments lead to the overall conclusion that impurities almost eliminate the induction time. This should be considered when transferring laboratory results to field conditions.

INTRODUCTION

The original scope of the presented experimental work was to establish an experimental procedure which would result in reproducible induction times. In the work by Skyum (1) and Andersen (2) numerous ethane hydrate experiments were carried out. Between each experiment the cell was opened, emptied and cleaned. Under seemingly identical conditions, large variations in the induction times were observed. It was assumed that a random amount of dust/dirt would be present in the cell in each experiment resulting in the observed variations in the induction times. Consequently it was decided to keep the cell closed between experiments thus having the same amount of dust/dirt in the cell throughout the measurement series.

EXPERIMENTAL SETUP AND PROCEDURE

The experimental setup is outlined in figure 1. The cell is a stainless steel container with a volume of 66.5 cm^3. Sapphire windows are placed on two opposing sides. The cell is closed with a lid, through which the gas and water are lead to the cell. The pressure sensor is placed in the lid while the temperature sensor is placed in an oil filled pocket in the cell. The temperature in the cell is controlled by flowing a water/ethanol mixture through the cooling jacket. The cell is placed on top of a magnetic stirrer, that can rotate a teflon coated magnetic rod in the cell. The maximum working pressure of the cell is 60 bar.

Before the first experiment in a series, the cell is cleaned and then evacuated. The desired amount of water is introduced and the pressure is increased to the desired level using ethane gas. The cooling flow is started and gas hydrates will eventually form. When no further gas hydrate formation takes place, the cooling flow is stopped The cell with content is left for 4-5 hours to dissociate all formed hydrates and to heat up the cell to ambient temperature. The cooling flow is then restarted, and a new experiment can start.

RESULTS - SERIES 1

Before the first series the cell was cleaned in the same way as used by Skyum (1) and Andersen (2). This means rinsing with distilled water and drying using compressed air. The cell was evacuated and loaded with 20 cm^3 of distilled water and ethane at 21°C. Series 1 was started with a temperature setting of 3 °C. Figure 2 shows the pressure transient and part of the temperature transient of the first experiment (M6). The pressure initially drops from 15.3 bar to 14.0 bar due to the reduction in temperature from 21 °C to 3 °C. The pressure and the temperature then remain constant until the end of the induction time. As hydrates start to form the pressure drops dramatically due to gas consumption and there is a small increase in the temperature due to the heat evolved. The course of events in experiment M6 is representative for all the experiments in series 1 and 2.

A total of 11 experiments is included in series 1 and the results are shown in table 1 and in figure 3. The induction time is here defined as the time that elapses from the cooling flow is started and until the pressure starts to drop due to hydrate formation. To calculate the amounts of hydrate formed within 600 and 3600 seconds respectively after the induction period, the computer program HYLAB has been used. The HYLAB program is essentially based on the gas hydrate kinetics model proposed by Skovborg (3):

$$\frac{dn}{dt} = k * A * c_{w0} * (x_{int} - x_b) \tag{1}$$

dn/dt : Gas consumption rate.
k : Mass transfer coefficient.
A : Gas/water interfacial area.
c_{w0} : Molar concentration of water in the water phase.
x_{int} : Mole fraction of gas in water phase at the gas/water interface in equilibrium with the gas phase.
x_b : Mole fraction of gas in the water phase in equilibrium with the gas hydrate.

In principle the model requires knowledge of the product k*A to be able to calculate the gas consumption rate and the pressure drop with time.

When analysing experimental data as here the model is rearranged to allow a measured pressure drop to be converted into a gas consumption rate giving as the results the amount of hydrate formed and the product k*A.

The induction time varies between 38209 seconds and 341430 seconds whereas the growth rates are much more uniform.

RESULTS - SERIES 2

After discovering that simply keeping the cell closed between experiments thus keeping the composition constant did not yield reproducible induction times it was decided to try to eliminate the effect of presence of impurities. The cell was consequently cleaned much more thoroughly using only double distilled water and drying with dust free paper. Similar conditions to those used in series 1 were established. More than three weeks (~2,000,000 seconds) passed after pressurizing the cell and no hydrates were formed. The pressure was then increased to 21 bar. Approximately 38500 seconds later hydrates eventually formed. Series 2 comprises this and five more experiments at 3 °C and 21 bar. The results are shown in table 2 and in figure 3. Not surprisingly the growth rates were higher in series 2 than in series 1. The induction times were on the average lower (table 4) but still very scattered

RESULTS - SERIES 3

The results in series 1 and 2 showed that even minor amounts of impurities have some effect on the induction time. Consequently it was decided to add a large amount of impurities to the system to make it insensitive to addition of further impurities. It was decided that the "composition" of the added impurities should to some degree match the solid material found in multiphase pipelines. The impurities consist of equal amounts of $CaCO_3$, $BaSO_4$, rust and asphaltenes. Before addition of water and gas to the cell, 20 mg impurities was added and conditions similar to those of series 2 were established. The course of events in the experiments of series 3 differs drastically from that of the other experiments. In series 3 the pressure initially not only drops due to reduction in temperature but also because hydrates were formed shortly after the hydrate equilibrium temperature is reached. The observed induction time in table 3 is the time from the beginning of cooling until some hydrate particles were seen. In table 3 is also listed the time it takes before the conditions in the cell are favourable for hydrate formation from an equilibrium model (4) point of view. It can be seen that hydrates were often observed before the conditions for their formation were favourable. This cannot be contributed to low accuracy in the gas hydrate model used, but rather to the fact that there is some time delay in the temperature measurement. In all experiments performed in the cell the pressure start dropping for approximately 30 seconds before any change in the temperature is seen. For that reason it seems likely that gas hydrates start to form shortly after the actual conditions in cell are favourable for their formation.

DISCUSSION

The results in series 1 and 2 indicate that induction times are very hard to reproduce even under seemingly identical conditions. Series 3 indicates that addition of large amounts of impurities almost eliminates the induction time. It is however difficult from the present data to say whether the standard deviation on the induction times in series 3 is as large as for the other experiments. Comparison between the observed induction times in series 3 and the time after which the hydrate formation is favourable could indicate that the induction times also in this case are scattered, though very short.

The growth rates are for all series much less scattered than the induction times and thus easier to compare. It is no surprise that the growth rate in series 2 is larger than in series 1 since the driving force for hydrate formation is considerably higher. Expressed in terms of the Skovborg model, the difference $x_{int} - x_b$ is larger in series 2 ($\sim 3.7 * 10^{-4}$) than in series 1 ($\sim 1.8 * 10^{-4}$).

When looking at the average A*k which is needed to describe the experiments in series 1 and 2, it is interesting to note that a smaller value applies for series 2. One must assume that the interfacial area is the same in both series, i.e. k must differ. This observation has two possible explanations. Either the mass transfer coefficient is pressure dependent or the mass transfer of ethane from the gas phase to the water phase is not the only significant kinetic step. If for example the building up of gas hydrate crystals is also a significant kinetic step, one must assume that x_b will be higher than predicted from a gas hydrate equilibrium point of view. If x_b is in fact higher than predicted by the model, an analysis of the data assuming equilibrium between the water phase and the hydrate phase will result in a higher value of A*k as it is the case in series 1 compared to series 2. This could suggest that when the driving force for hydrate formation is small, the building up of crystals is a significant step, whereas it becomes less significant for larger driving forces.

When analysing the amount of hydrate formed in series 3 it is seen that during the first 600 seconds it is even lower than the results obtained in series 1, whereas at later times the results are comparable to those of series 2 (table 4). The explanation is probably that the driving force for hydrate formation is small in the beginning of the series 3 experiments and the conditions of the experiments resemble those of series 2 at later stages. In series 3 the standard deviation on the amount of hydrates formed is higher compared to the previous series, indicating that impurities in some way make the growth rate more random.

One can also observe that the average A*k gets smaller as more hydrates are formed. This is most likely due to the reduction of the interfacial area caused by formation of a hydrate slurry layer between the two fluid phases.

CONCLUSIONS

Reproducing induction times in "clean" laboratory conditions seems very difficult if not impossible. Deliberate addition of impurities to the system seems to eliminate the induction time. Extreme caution should therefore be taken when operating a multiphase pipeline under conditions favourable for hydrate formation. Kinetic inhibitors that supposedly prolong the induction time should be evaluated also in the presence of considerable amounts of impurities.

The experiments reveal that the growth rate depend on the driving force. This may either be interpreted as a pressure dependence of the parameter k in the model by Skovborg or it may indicate that the building up of crystals is also a significant kinetic step. From the present experiments it is not possible to say which explanation is correct.

When analysing kinetic experiments one should consider that the system investigated may not be in thermal equilibrium at all times.

ACKNOWLEDGMENT

We are grateful to KSLA-ST/2 , Amsterdam, The Netherlands for lending us the measurement cell, and to K.S. Pedersen, Calsep A/S for many productive discussions.

REFERENCES

(1) Skyum L., 1995, "Hydrate Kinetics", M.Sc. Thesis, Department of Chemical Engineering, The Technical University of Denmark.

(2) Andersen B.D., 1995, "Formation of Gas Hydrates", M.Sc. Thesis, Department of Chemical Engineering, The Technical University of Denmark.

(3) Skovborg P. and Rasmussen P., 1994, "A Mass Transport Limited Model for the Growth of Methane and Ethane Gas Hydrates", Chem. Eng. Sci., **49**, 1131-1142.

(4) Munck J., Skjold-Jørgensen S. and Rasmussen P.,1988, "Computations of the Formation of Gas Hydrates", Chem. Eng. Sci., **43**, 2661-2672.

Series 1 Experiment No.	Induction time /s	Moles of hydrate formed in 600 s.	Moles of hydrate formed in 3600 s.
M6	38209	0.0247	0.0804
M7	41827	0.0229	0.0792
M8	60066	0.0205	0.0768
M9	45509	0.0245	0.0802
M10	155361	0.0222	0.0786
M12	104444	0.0230	0.0797
M13	298416	0.0134	0.0631
M14	341430	0.0216	0.0785
M16	106390	0.0233	0.0804
M17	117085	0.0243	0.0807
M18	77961	0.0188	0.0733

Table 1. Results of series 1. T = 3 °C. Hydrate formation starts at 14 bar.

Series 2 Experiment No.	Induction time/s	Moles of hydrate formed in 600 s.	Moles of hydrate formed in 3600 s.
M20	38489	0.0294	0.1112
M21	147025	0.0262	0.1097
M22	67392	0.0275	0.1003
M23	122524	0.0313	0.1139
M24	47379	0.0222	0.1027
M25	10096	0.0269	0.0960

Table 2. Results of series 2. Thoroughly cleaned cell. T=3 °C. Hydrate formation starts at 21 bar.

Series 3 Experiment No.	Observed Induction time/s	Time for favourable hydrate conditions /s.	Moles of hydrate formed in 600 s.	Moles of hydrate formed in 3600 s.
M30	280	285	0.0183	0.0892
M31	239	290	0.0148	0.0822
M32	229	230	0.0248	0.1038
M33	174	205	0.0193	0.0990
M34	227	235	0.0168	0.0778
M35	220	215	0.0243	0.01095
M36	233	185	0.0239	0.01029

Table 3. Results of series 3. Initial conditions similar to those of series 2.

	Moles of hydrate formed in 600 s.	Moles of hydrate formed in 3600 s.	Induction time/s
Series 1 Average	0.0217	0.0774	126063
Series 1 Standard dev.	15.2%	6.7%	81.6%
Series 1 Average k*A cm^3/s	0.40	0.31	-
Series 2 Average	0.0273	0.1056	72151
Series 2 Standard dev.	11.3%	6.6%	72.7%
Series 2 Average k*A cm^3	0.22	0.17	-
Series 3 Average	0.0203	0.0949	-
Series 3 Standard dev.	19.8%	12.6%	-
Series 3 Average k*A cm^3	0.26	0.17	-

Table 4. Key results of the three measurements series.

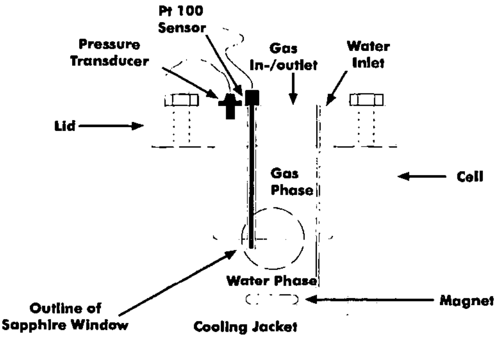
Pt 100
Sensor
Pressure
Transducer
Gas
In-/outlet
Water
Inlet
Lid
Gas
Phase
Cell
Water Phase
Outline of
Sapphire Window
Magnet
Cooling Jacket

Figure 1. The Experimental Apparatus.

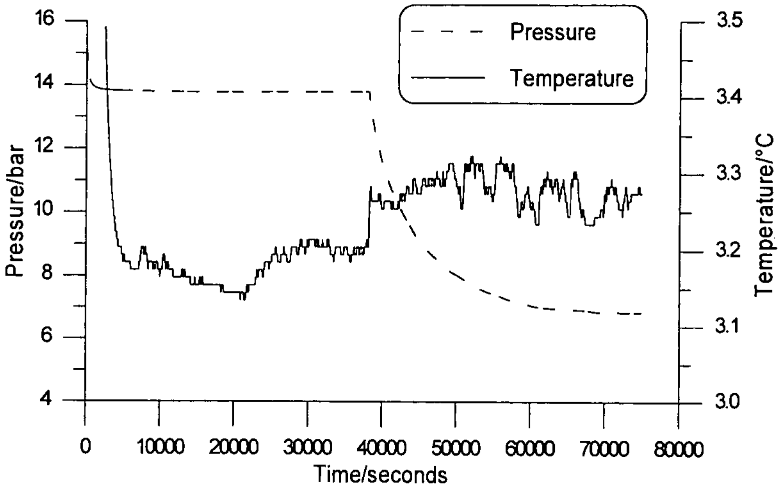

Figure 2. Pressure and temperature vs. time in a typical experiment (M6).

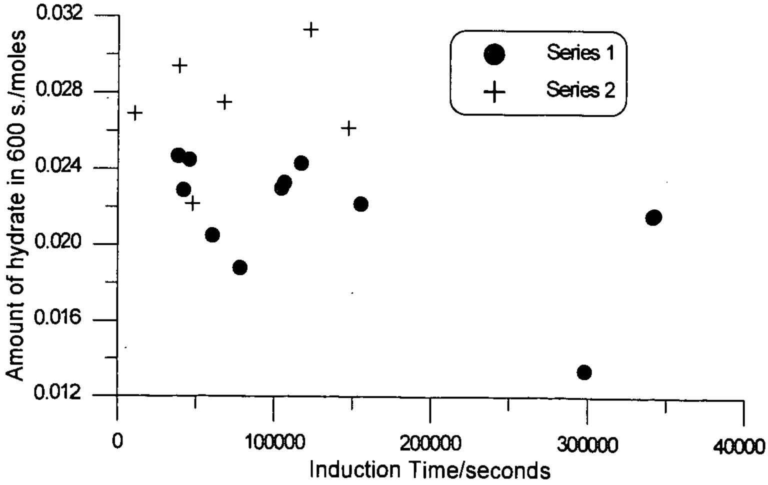

Figure 3. Growth rate vs. induction time for series 1 and 2.

AN EXPERIMENTAL STUDY OF HYDRATE CRYSTAL GROWTH FROM METHANE, CARBON DIOXIDE, AND METHANE+PROPANE MIXTURES

S.-Y. Lee, E. McGregor, and G. D. Holder
University of Pittsburgh
Chemical and Petroleum Engineering Department
Pittsburgh, PA 15261

Keyword: Gas Hydrates, Methane, Pipelines

Introduction and Background

Gas hydrates are crystalline inclusion compounds composed of water and natural gas in non-stoichiometeric ratios varying from 5.67 to 17 water molecules per hydrated gas molecule (Holder, Zetts and Pradham, 1988; Sloan, 1990). Hydrate crystals represent one on of the few phases and perhaps the only condensed phase where water and light non-polar gases exist together in significant proportions and are of particular interest to the petroleum and natural gas industries because of their potential as a separating agent, their potential as a storage vehicle and their undesired ability to plug gas transportation lines (Holder and Enick, 1995).

Gas-water mixtures will form crystals which coat the walls of and potentially plug gas transportation lines causing the ceasation of gas or gas+oil flow (Lingelem, Majeed and Stange, 1994). When producing oil or gas, one goal of industry is to understand the conditions under which operation is possible without plugging. One such operating condition is where the hydrates are thermodynamically unstable. Such conditions are generally present when operating at temperatures above 25 C, although the temperature depends upon pressure, usually 50-200 Mpa, and gas composition, usually 95+% methane. Sufficiently high temperatures are generally not present when producing gas in offshore operations, because deep ocean waters are seldom warmer than 4-8 C. To prevent hydrate formation operators will generally inject methanol which acts as an antifreeze and destabilizes hydrates. Effective methanol concentrations are generally 10-50%, by weight, of the water+methanol liquid.

Sometimes, it is not desirable or possible to operate at conditions where hydrates are thermodynamically unstable. Such conditions may occur if methanol injection facilities fail or in cases where methanol injection and recovery are prohibitively expensive. In such cases it is desirable to understand for what duration, operation of a gas transportation line is possible without the complete plugging of the line by hydrates. To more completely understand this question, the rates at which hydrates form must be understood. The process includes the nucleation of hydrates on a heterogeneous surface, such as the pipewall, and the growth of these hydrates towards the center of the pipeline. This scenario for hydrate growth is deemed most likely for two reasons. First, the pipewall is generally the coldest part of the transportion line and hence the location where hydrates are most thermodynamically stable. Second, the formation of crystalline hydrates normally requires a solid nucleation site and the pipewall is generally the only source of such sites. Crystals can subsequently abraid from the pipewall and be transported down the pipeline, but such abraided crystals are not expected to be the primary cause of initial flow constriction.

In the present study, we determine the rates at which hydrates nucleate and grow on the surface of a cold pipewall over which gas is flowing at rates comparable to those which might exist in a pipeline.

Experimental

The apparatus for studying the precipitation and growth of solids is a variation of that described elsewhere (Figure 1 Holder and Enick, 1995). The apparatus consists of two coaxial cylinders. Hydrates form in the annular space by growing radically inward from the cooled outer wall. To form hydrates, the temperature controlled vessel is pressurized with the appropriate gas, 100-150 ml of water are injected and the inner cylinder rotated. The vessel can be operated in a vertical position as shown in Figure 1 or in a horizontal position. For these experiments a horizontal position was used exclusively. The fundamental improvement of this apparatus relative to cells used in the past is that gas will flow in the annular space over the hydrate formation surface rather than remaining static. This will provide a means of investigating the effects of gas shear stress at the hydrate forming surface in pipelines.

Temperature gradients within this vessel are established by flowing methanol/water mixtures from separate isothermal baths through cooling coils on the outside of the vessel and the inner cooling chamber. The water in the vessel would coat the rotating inner cylinder, evaporate, and condense on the inside of the outer cylinder.

A temperature gradient was established across the annular gap. The surface of the water was then in direct contact with the flowing methane at 273K - 275K. Hydrates began to form inside the outer cylinder. Pressure decreased as the methane from the gas phase entered the hydrate phase and was used to deliver the amount of water converted to hydrate.

Experiments continued until either 1) the pressure of the methane remained constant, indicating that hydrate formation had ceased or 2) the rotation of the inner cylinder ceased because small amounts of hydrates clogged the bearings and friction surfaces. The system was then depressurized and the hydrate crystals examined before they had an opportunity to completely dissociate. The hydrates formed a relatively uniform layer of frost-like solid in the annular gap.

Results

We have measured the linear growth rate of hydrates formed from pure methane, pure carbon dioxide, two mixtures of methane+propane whose compositions were (95% methane and 5% propane) and (97% methane and 3% propane). The important variables in these studies were gas flow rate, gas composition, temperature, and pressure. Table 1 lists the results.

Gas flow rate: Higher gas flow rates (reported as RPM) tend to produce higher rates of hydrate formation. This is because the higher gas flow rates dissipate the considerable heat release generated during hydrate formation (50-100 kJ per mole of hydrated gas) and because the higher gas flow rates improve the mass transfer of water to the hydrate forming surface. It is still not clear which of these factors is most significant. However, the effect of gas flow rate appears to level off at the highest rates. This means that mass and heat transfer are no longer limiting and a true kinetic value for hydrate growth is obtained. The higher gas flow rates used here are comparable to pipeline Reynolds numbers in excess of 10,000 and thus these conditions are those that might be obtained in an actual gas pipeline.

Gas composition: It was observed that no clear difference in growth rates for the 95% methane and 97% methane mixtures were observed, but rates for gas mixtures and for carbon dioxide were faster than for pure methane. The methane hydrate is the least thermodynamically stable and it appears that the thermodynamic driving force (difference between the equilibrium temperature and the actual experimental temperature at the hydrate surface) affects the rate at which hydrates form. Another factor which may be important is the ability to stabilize the large cavity of the hydrate structure. Propane stabilizes the large cavity of structure II better than methane and carbon dioxide stabilizes the large cavity of structure I better than methane. The ability to stabilize the large cavity may play a role in the kinetics. The current experimental evidence is not conclusive on this issue.

Another variable of interest for the methane+propane mixtures is that the gas composition changes as the hydrates form since the propane concentration in the hydrates is much higher than in the gas phase. As more hydrates form a eutectic mixture of methane and propane containing less than 1% propane should be present. This mixture should result in the simultaneous formation of both structure I and structure II hydrate.

Temperature: In general, temperature is thought to increase the rate of any kinetic process. However, higher gas temperatures decrease the thermodynamic driving force and will tend to impede the rate.

Pressure: The range of pressures used was small, but the results indicate that higher pressures increased the rate of hydrate formation.

Inhibitors: Both WAX and PVP reduced the rate of hydrate formation to negligible values when present. Both were applied to the inside surface of the outer cylinder prior to hydrate formation.

The overall correlation for growth rate for both methane + propane mixture is

$$\text{linear rate} = 0.001535\,(\text{RPM}) + 9.3 \times 10^{-6}\,(\text{P/KPA}) - 0.0178\,(\text{Cooling Coil (T/K)}.$$

This correlation has a R^2 of 0.75.

Conclusion

The rates of hydrate formation along pipe walls will likely be comparable to the rates measured in this study. Linear growth rates of 0.2 cm/hr are likely to represent the maximum growth rate that could be expected in gas transportation lines. As the hydrates thicken, they can serve as insulators of the line which will result in slower cooling of the produced fluids (which come out of the earth at higher temperatures than exist in the transportation line). The insulation will produce higher transportation temperatures and could either enhance or inhibit hydrate formation rates.

Based upon the rates measured here, transportation lines could be operated for hundreds or thousands of hours prior to their blockage by hydrates.

Acknowledgment

We would like to thank GRI for their partial support of the early stages of this research under contract GRI5091-260-2121.

References

Holder, G.D. and R.M. Enick, "Solid Deposition in Hydrocarbon Systems-Kinetics of Waxes, Ashpaltenes and Diamondoids", Final Report, Gas Research Institute, GRI, 1995.

Holder, G.D., S. Zetts, and N. Pradhan, **Reviews in Chemical Engineering**, 5(1), 1, 1988.

Holder, G.D.; Zele, S.; Enick, R.; LeBlond, C.*Ann. N.Y. Acad. Sci.* **1994**, *715*, 344.

M.N. Lingelem, A.I. Majeed, and E. Stange, "Industrial Experience in Evaluation of Hydrate Formation, Inhibition, and Dissociation in Pipeline Design and Operation", in **Natural Gas Hydrates**, Annals of the NY Academy of Science, E.D. Sloan et al, editors, New York, p75, 1994.

Sloan, E.D., **Clathrate Hydrates of Natural Gas**, Marcel Dekker, New York, 1990.

Figure 1. High Pressure Tangential Annular Flow Apparatus

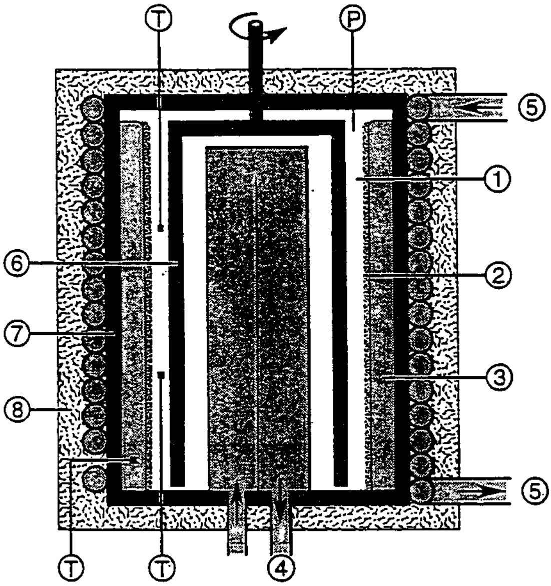

1. High Pressure Gas
2. Gas Hydrate
3.
4. Gas Cooling Fluid Flowing in Cylinder
5. Ice Cooling Fluid Flowing in Coils
6. Rotating Cylinder
7. High Pressure Cell
8. Insulation

T - Thermocouples
P - Pressure Transducer

Table 1: Growth Rate of Hydrates

Gas Composition	Bulk gas Temp (K)	Cooling coil Temp (K)	Initial Press (KPa)	RPM	Linear growth rate (cm/hr)
100%C_1	283.7 +/- 0.4	273.7 +/- 0.3	6509	7	0.02
100%C_1	283.5 +/- 0.5	271.4 +/- 0.1	6039	8	0.02
100%C_1	282.9 +/- 0.4	272.0 +/- 0.3	6021	8	0.05
100%C_1	282.1 +/- 0.4	271.9 +/- 0.1	6023	8	0.00
100%C_1	281.9 +/- 0.3	272.1 +/- 0.1	5987	30	0.02
100%C_1	283.0 +/- 0.5	271.8 +/- 0.1	6004	2	0.01
100%C_1	282.3 +/- 0.7	271.9 +/- 0.2	6019	8	0.02
100%C_1	279.7 +/- 0.6	271.5 +/- 0.2	6861	25	0.02
100%C_1	276.5 +/- 0.2	271.5 +/- 0.2	6618	15	0.02
5%C_3:95%C_1	291.1 +/- 0.3	272.9 +/- 0.1	7014	7	0.08
5%C_3:95%C_1	288.9 +/- 0.4	273.6 +/- 0.2	7110	15	0.11
5%C_3:95%C_1	288.7 +/- 0.6	270 +/- 0.1	6905	60	0.15
5%C_3:95%C_1	288.4 +/- 0.7	271.1 +/- 0.1	6940	1	0.03
5%C_3:95%C_1	287 +/- 0.9	270 +/- 0.1	7089	30	0.17
3%C_3:97%C_1	284.7 +/- 0.7	271.6 +/- 0.1	6781	7	0.03
3%C_3:97%C_1	288.1 +/- 0.1	273.2 +/- 0.1	7036	7	0.05
3%C_3:97%C_1	284.5 +/- 0.1	271.7 +/- 0.1	6782	60	0.15
3%C_3:97%C_1	286.8 +/- 0.2	274 +/- 0.1	7016	2	0.08
3%C_3:97%C_1	287.5	271.5 +/- 0.1	6927	2	0.13
3%C_3:95%C_1	286.4 +/- 0.1	273 +/- 0.1	7011	30	0.06
CO_2	282 +/- 0.3	271.4 +/- 0.1	3555	8	0.10
CH_4/WAX	277.8 +/- 0.7	271.6 +/- 0.2	5296	15	0.002
CH_4/PVP	278.6 +/- 0.6	272.1 +/- 0.2	5482	15	0.000

METHANOL: CLATHRATE HYDRATE FORMER OR INHIBITOR ?[*]

Hirokazu Nakayama[a#], Darren H. Brouwer[a], Y. Paul Handa[b], Dennis D. Klug[a], John S. Tse[a], Christopher I. Ratcliffe[a] , Xu Zhu[a] and John A. Ripmeester[a†]
[a]Steacie Institute for Molecular Sciences, [b]Institute for Chemical Processing and Environmental Technology, National Research Council of Canada, Ottawa, Ontario, Canada K1A 0R6

Keywords: methanol, hydrate, methanol monohydrate, hydrate inhibitor, clathrate hydrate

INTRODUCTION

Methanol has long been in use as an inhibitor of hydrate formation[1]. It acts as a classical antifreeze, that is by lowering the activity of the water, and generally shifts the equilibrium lines for hydrate formation in the phase diagram to lower temperatures. It has been shown that in water - hydrate former - methanol systems the methanol is excluded from the clathrate hydrate when the material is frozen[2]. From a molecular point of view, one may argue that methanol interacts strongly with water by hydrogen bonding, thus interfering with the structure formation required for the formation of solid ice and ice-like lattices. Thus, methanol is one of few small molecules that do not form clathrate hydrates at ordinary temperatures (~ 0° C). The propensity for small water-soluble molecules to form hydrates depends on a balance between hydrophobic and hydrophilic interactions, as many of the water soluble ethers readily form clathrate hydrates[3]. Ethanol is known to form two different hydrates[4] at low temperatures which are probably semi-clathrates structurally related to Str.I and Str.II hydrates (Pm3m, a=11.88 Å, F4,32, a=17.25 Å respectively). Isopropanol, t-butanol and iso-amyl alcohol all are known to form double hydrates with small help-gas molecules[5].

In 1991, a report appeared[6] which suggested that methanol, when co-deposited with water in a vacuum at low temperatures, forms a clathrate hydrate of structure II with a lattice constant of 16.3 Å. This observation poses a number of questions regarding the ability of methanol to both inhibit and promote hydrate formation. If one is a high temperature property, and the other a low temperature property, at which temperature do they cross over and what are the responsible interactions ? On the other hand, there are some general questions regarding the interpretation of the results. For instance, the usual structure II lattice parameter is 17.1 ± 0.1 Å[7], so it isn't easy to see how the structure II lattice can adapt to a ~ 12% volume reduction.

Also, size considerations alone would suggest that methanol (an ethane-sized molecule) should form a structure I rather than a structure II hydrate. As noted above, the larger (propane-sized) ethanol molecule apparently forms semi-clathrates similar to both str. I and str II. In this sense it is pertinent to note that calculations have been performed on a str. I hydrate lattice containing methanol guests[8]. A third point is that the report does not acknowledge the possible presence of methanol monohydrate, which was reported in a study of the methanol -water phase diagram in 1961[9]. These questions led us to have a close look at the low temperature behaviour of the methanol - water system.

EXPERIMENTAL

Methanol and water were co-deposited from metered amounts of the vapours on the cold plate (~ 20K) of a Displex closed cycle refrigerator. Sample stoichiometry was varied from 20:1 to 1:1. Pure amorphous ice and methanol phases were prepared as well. Samples were handled and stored under liquid nitrogen. Some samples of a 1:1 stoichiometry were prepared by direct mixing of the liquids followed by quenching to 77K and annealing above the eutectic temperature at ~ 150K.

Sample characterization was carried out by differential scanning calorimetry (DSC), powder X-ray diffraction (XRD) and NMR spectroscopy. Samples for NMR were isotopically enriched in ^{2}H for either the water or methanol phases.

Thermal events were recorded by means of a Tian Calvet heat-flow calorimeter (Setaram, Model BT2.15). The details of the calorimeter and the operating procedure have been described previously[10]. A sample size of about 2 g was used, the sample temperature always remaining below 80K during loading. Samples were scanned from 78K to room temperature at 10 K°/h with nitrogen at 200 mbar as heat exchange gas. XRD measurements were performed on a Rigaku Θ - Θ powder diffractometer equipped with a Paar temperature controller. Samples were loaded cold, and XRD patterns were taken at 80K. Samples were annealed for 10 min. at the appropriate temperatures then cooled for the recording of the XRD pattern. The various phases which appear on crystallization of the amorphous deposits and mixtures were identified by comparison with data obtained for the pure crystalline materials or from literature data.

^{2}H NMR powder patterns were recorded at a frequency of 30 MHz on a Bruker MSL 200 NMR spectrometer equipped with a 5mm solenoid probe. Quadrupole echo sequences were used with a 90° pulse length of ~ 2.5 μsec and an echo delay time of 30 μsec. Samples of 1:1 stoichiometry were quenched and conditioned in the probe at temperatures somewhat above 150K. Quadrupole coupling parameters were determined by a fitting procedure using the Bruker Winfit package.

RESULTS AND DISCUSSION

Table 1 offers a summary of the calorimetric data which was obtained for a range of samples which reasonably well cover the methanol-water phase diagram. The column on the left is in good agreement with previously reported work on vapour-deposited ice. We note that all starting materials are amorphous, and that the first event to take place on warming is crystallization, or crystallization preceded by a glass transition. This is in agreement with the reported phase diagram, where devitrification is reported to take place between 110 and 120K. We note that it doesn't seem to matter much whether samples are produced by quenching the liquid mixture, or by vapour deposition.

A critically important component of the work is to identify the phases present in the low temperature region, that is after the glass transition/crystallization events. The XRD patterns of Ice Ih, Ice Ic and the clathrate hydrates are well documented. XRD patterns for the α and β phases of methanol were recorded in order to be able to recognize the presence of these phases.

In all of the experiments carried out, it was found that a number of reflections appeared which could not be assigned to one of the aforementioned crystal phases. These reflections appeared to be strongest for samples approaching a composition of 1:1 methanol/ water. Another experiment showed that these reflections disappeared when the sample was warmed to 175K, leaving only the Ice Ih pattern, but reappeared on cooling. We can conclude that these reflections should be assigned to the methanol monohydrate which is known to melt incongruently at ~ 171K. Although methanol monohydrate has been known to exist for many years, so far no information is available on its structure. In order to facilitate further study, a good sample of methanol monohydrate was prepared by quenching a 1:1 mixture of methanol and water and annealing at 150K for 10 hrs. The sample still contained a significant quantity of hexagonal ice as impurity, however, the remaining 19 reflections could be indexed in terms of tetragonal Laue symmetry and a fit of the d spacings was obtained with unit cell dimensions of a = 4.660(1), c=13.813(5) Å.

With the identification of the methanol monohydrate phase, all of the reflections can be accounted for for all of the samples considered in this study. The crystallization processes which transform the lowest temperature amorphous phases are outlined below for a range of sample compositions.

Ice ⇒ Ice Ic
methanol/water (1:20, 1:10) ⇒ methanol monohydrate + Ice Ih + Ice Ic (trace)
methanol/water (1: 2) ⇒ methanol monohydrate + Ice Ih + methanol
methanol ⇒ α - methanol

Perhaps the most unusual observation is the near disappearance of cubic ice as a distinct phase in the presence of methanol. Figure 1 shows a typical XRD run on a codeposit (1:2 methanol- water) initially annealed at 120K. The ice Ih reflections clearly are present for all temperatures. The calorimetric data is in agreement with this, as the only evidence for the crystallization of cubic ice is from a very weak exotherm near 148K in the 10:1 deposit (see table 1), and the subsequent transformation of ice Ic to ice Ih occurs near 179K; these events occur near 142K and 195K for pure ice. Methanol seems to act as a catalyst in the direct conversion of amorphous ice to ice Ih.

How do our results relate to those reported for the " methanol clathrate " [6]? The material prepared was thought to be a clathrate mixed with some cubic ice based on the assignment of 10 reflections to a 16.3 Å clathrate lattice plus 1 reflection due to cubic ice. By comparing the diffraction data for the two studies it becomes apparent that all of the observed reflections in both studies can be accounted for in terms of ice

Ih and methanol monohydrate. It should be noted that the small angle reflections (hkl = 111, 220 and 311 for str. II) which are essential for assigning the clathrate structures in mixed-phase systems were not observed. Certainly in light of our data there is no need to propose a structure II clathrate hydrate with an unusual lattice parameter.

Although the XRD powder data have given a good indication of the symmetry and size of the unit cell in the crystal, the detailed structure remains as yet unknown. Some additional information on the methanol monohydrate can be obtained from NMR spectroscopy. The ^2H NMR quadrupole coupling parameters obtained for the water lattice are useful, as these can be used to give information both on the strength of the hydrogen bonds and the dynamics of the water lattice. The ^2H NMR lineshape for a sample of $CH_3OH.\ D_2O$ yielded a quadrupole coupling constant χ (= e^2Qq/h) of 206.9 kHz and an asymmetry parameter η= 0.09. These values are very near to those for ice Ih (215 kHz, 0.1[11]), and are characteristic of a fully hydrogen-bonded network. The χ value is an average for the D_2O and CH_3OD deuterons, as exchange must produce the deuterium-substituted methanol. The small decrease in χ indicates that the O - O distances are, if anything, on average slightly shorter than those in ice Ih. The temperature dependence of the lineshape (fig. 2) gives a rough indication of the rate of the dynamic processes in which water molecules are involved. Above about 140K, the lineshape develops a central component which is a manifestation of slow reorientation of the water molecules within the lattice. A comparison with the lineshapes obtained for pure ice Ih indicates that the water molecules in the methanol hydrate at ~ 150K have the same motional correlation time as those in ice Ih at ~260K. Since the water reorientation in ice is defect-driven, the implied low activation energy for water reorientation in methanol monohydrate must reflect the ease with which defects can be generated. A more detailed analysis of D_2O dynamics is complicated by the fact that besides the water molecules there are two kinds of methanol O-D bonds that must be involved in restricted dynamic processes (see below). Examination of a corresponding $CD_3OD.H_2O$ (fig. 2, below) sample showed that there are two dynamically inequivalent CD_3 groups, as there are two overlapping powder doublets. Both CD_3 groups show rapid rotation about their 3-fold axes, one of the two shows little or no additional motion, the second shows the presence of another process which formally can be explained by a jump between two positions with ~ 40° between the directions of the CD_3 group symmetry axes. The central line (fig. 2, right) arises from the more mobile OD and HOD deuterons. The NMR measurements show quite clearly that molecular motion is possible at much lower temperatures than in a pure ice lattice.

CONCLUSIONS

On the basis of results reported here it appears unnecessary to propose the existence of a clathrate hydrate of methanol. In vapour-deposited or quenched water - methanol mixtures the crystallization products include mainly methanol monohydrate and Ice Ih on the water-rich side of the composition diagram. Methanol seems to act as a catalyst for the direct conversion of glassy ices to ice Ih. On the basis of XRD it is proposed that the methanol monohydrate is tetragonal with unit cell dimensions a= 4.660, c= 13.813 Å. NMR results indicate that both water and methanol are part of a fully hydrogen-bonded network, but that water reorientation takes place much more easily than in pure ice Ih and in most clathrate hydrates. Finally, one can say that methanol by all accounts remains an inhibitor of hydrate formation.

[•] Issued as NRCC no:39128

[#] Permanent adress: Department of Chemistry, Osaka University,Osaka, Japan

[†] Author for correspondence

---

[1] Sloan, Jr., E. D. " Hydrates of Natural Gas ", Marcel Dekker, New York, N. Y. *1991*

[2] Davidson, D. W., Gough, S. R., Ripmeester, J. A., Nakayama, H., Canad. J. Chem. *1981* **59**, 2587

[3] Davidson, D. W. , in " Water a Comprehensive Treatise, Franks, F., Ed., Plenum, N. Y., *1973*, Vol.2

[4] Calvert, L. D., Srivastava, P., Acta Crystallogr. Sect. A *1969*, **25**, S131

[5] Ripmeester, J. A., Ratcliffe, C. I., J. Phys. Chem. J. Phys. Chem. *1990* **94**, 8773

[6] Blake, D., Allamandola, L., Sandford, S., Hudgins. D., Friedemann, F., Science *1991* **254**, 548

[7] Davidson, D. W., Handa, Y. P., Ratcliffe, C. I., Ripmeester, J. A., Tse, J. S., Dahn, J. R., Lee., F., Calvert, L. D., Mol. Cryst. Liq. Cryst. *1986*, **141**, 141

[8] Wallqvist, A., J. Chem. Phys. *1992* **96**, 5377

[9] Vuillard, G., Sanchez, M., Bull. Chem. Soc. Fr. *1961*, 1877

[10] Handa, Y. P., Hawkins, R. E., Murray, J. J., J. Chem. Thermodyn. *1984*, **16**, 623; Y. P. Handa, J. Chem. Thermodyn. *1986*, **18**, 891

[11] Ripmeester, J. A., Ratcliffe, C. I., Klug, D. D., J. Chem. Phys. *1992*, **96**, 8503

Table 1. Summary of Calorimetric Data ; thermal events are shown in italics, phases present in bold type

Starting material			
ice (a)	10:1 mixture (a)	1:1 mixture (quenched)	methanol (a)
ice Ih			
		liquid mixture	**liquid**
195K(en)			
		183K (en; w)	
	179K (en; w)		*178K*(en)
	Ice Ih + liq	**Ice Ih + liq**	
	173K (en)	*174K* (en)	**β phase + liq.**
Ice Ic			
	MeOH.H$_2$O + Ice Ih	**MeOH.H$_2$O + Ice Ih + eutectic mixture**	*168K* (en)
			α phase + eutectic mixture
		158K (en,w)	*158K* (en,w)
	148K (ex, w)		
142K (ex)		**MeOH.H$_2$O + Ice Ih + eutectic mixture** (s)	**α phase + eutectic mixture** (s)
136K (g)			
	131K (ex)		
		122K (ex)	
Ice (a)	**amorphous mixture**	*112K* (g)	
			102K (ex)
		amorphous mixture	**methanol (a)**

a = amorphous; ex = exotherm; en = endotherm; w = weak; g = glass transition, s = solid

Figure 1. X-ray powder diffraction patterns for a 1:2 methanol-water mixture obtained at 90K; the sample was annealed for 6 hours at 120K before the other patterns were obtained at the temperatures indicated. The crystalline phases present are: ice Ih (marked on the 180K pattern); methanol monohydrate (marked on the 160K pattern); α and β methanol (marked on the 140K pattern). the amorphous material shows up as broad background scattering especially at low temperatures, liquid as broad background at 180K.

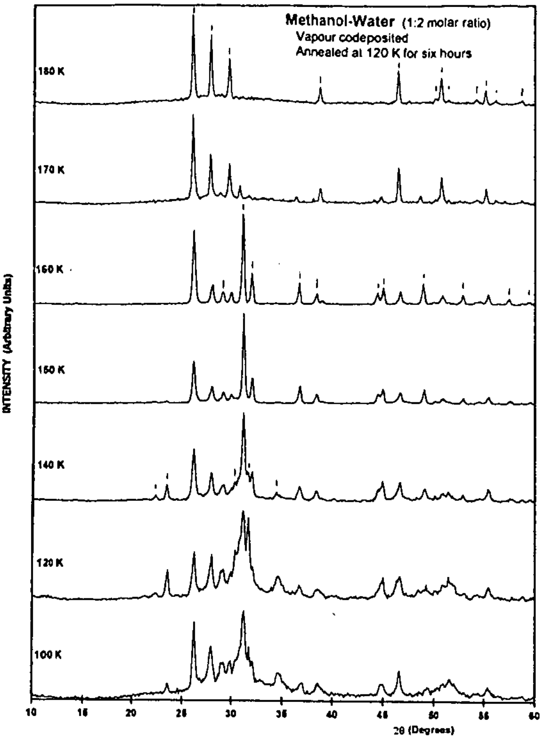

Figure 2. ^{2}H NMR powder patterns for (right) $CH_3OH.D_2O$ - temperature dependence; (below) $CD_3OD.H_2O$ at 140 K experimental and simulated patterns (parameters for outer and inner powder doublets χ = 46.83 kHz, η = 0.04; χ = 37.80, η = 0.18)

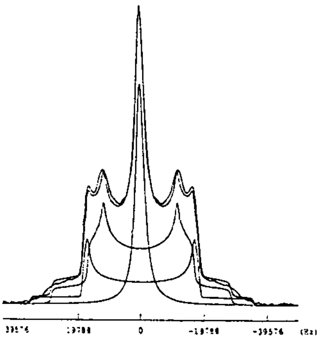

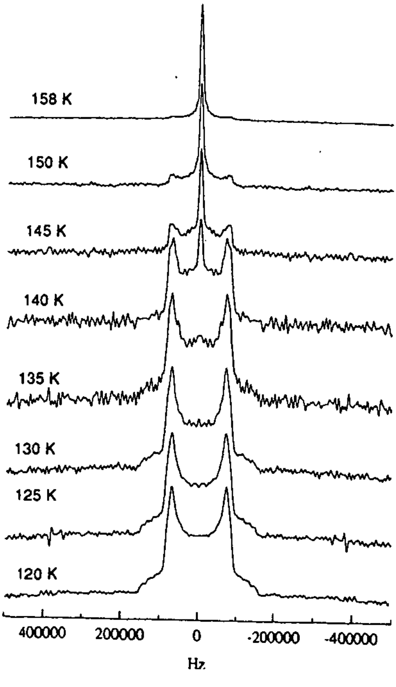

A SIMPLE METHOD FOR PREDICTING GAS HYDRATE FORMING CONDITIONS IN AQUEOUS MIXED ELECTROLYTE SOLUTIONS

Jafar Javanmardi and Mahmood Moshfeghian
Department of Chemical Engineering
Shiraz University, Shiraz, Iran
and
Robert N. Maddox
School of Chemical Engineering
Oklahoma State University, Stillwater, OK, USA

Key Words: Hydrate; Electrolyte; Gas

ABSTRACT:

A simple thermodynamic model is proposed for predicting hydrate forming conditions for natural gas components in the presence of single component or mixed electrolyte solutions. The parameters required for use of the model are developed and presented. The model is quite accurate with average deviations between calculated and experimental values of less than 0.5°C for systems not included in the model parameter determination.

INTRODUCTION:

Gas hydrates are a form of clathrate -- compounds in which guest molecules are entrapped in a cage lattice structure composed of host molecules. They were first discovered by Davy in 1810 who produced chlorine hydrate (24). Natural gas hydrates were first produced by Villard in 1888 (25). Hydrates of natural gas components are ice-like solid compounds that can form under temperature conditions 25°C (40°F) or more above the freezing point of water.

Several different hydrate structures are known. Most polar and some weakly polar gases form either a structure I or structure II hydrate. The hydrate formed depends primarily on the size of the guest molecule. Methane and ethane form structure I hydrates while propane and iso-butane form structure II hydrates. Parrish and Prausnitz (18) reported the physical characteristics of structure I and II hydrates.

Gas hydrates are ice-like clathrate compounds that are solids. They can accumulate in low places or around valves and fittings causing gas gathering and flow lines to become clogged and shut off gas flow. This is a particular problem in cold weather when line temperatures are most likely to be in the hydrate forming range. Knowledge of hydrate forming conditions and ways of preventing hydrates from forming are important to the natural gas industry. These areas are well developed and reliable methods are available for both natural gas mixtures (Maddox, et al. 14) and gas mixtures with inhibitors present (Moshfeghian and Maddox, 16).

Salt solutions and brine are frequently produced along with natural gas. Also, hydrates have been suggested as one way of making sea water potable (Knox, et al., 12) and as a possible way of storing natural gas in salt pits (Miller and Strong, 15). Capabilities for predicting natural gas forming conditions in the presence of weak electrolytes need improvement. That is the justification for the work presented here.

APPROACH

The approach used to develop the procedure for estimating hydrate forming conditions for gases over electrolytes is similar to that used by Moshfeghian and Maddox (1990) for their work on inhibited water solutions. They predicted the conditions for hydrate formation over pure water and then calculated an adjustment, or change, in those conditions to account for the presence of the inhibitor.

In the present work the method of Holder, Corbin and Papadopoulos (1980) is used to calculate the conditions for hydrate formation over pure water, and equations are developed to adjust those conditions for the presence of electrolyte. Holder and co-workers used experimental measurements to generate chemical potential, enthalpy and heat capacity functions. No gas species dependent adjustable parameters are required.

THERMODYNAMIC MODEL

The equations used for predicting the influence of weak electrolyte solutions on natural gas hydrate forming conditions were developed from the work of van der Waals and Platteeuw, (23). The value of the Langmuir constant depends on temperature and potential energy function parameters and was evaluated using the mathematical expressions of Parrish and Prausnitz (18).

At equilibrium the chemical potential of water is equal in all phases present. If the free water is present as ice, none of the ice will be incorporated within the hydrate structure, and the chemical potential of the water in the hydrate will be equal to that of ice. If liquid water is present the free water and the water in the hydrate will have the same chemical potential.

The way in which the activity of water is evaluated depends on the components present in the system under consideration. If pure liquid water is present Holder, et al. (8) suggest that gas solubility in the water phase will be so slight that x_w, the mole fraction of water, may be used without creating significant error. If, on the other hand, water is present in an electrolyte solution with an appreciable concentration of salt present, the model suggested by Pitzer and Mayorga (22) can be used to estimate the activity of water in the electrolyte. Following Englezos and Bishnoi (5) and Tohidi, et al. (26) this work has used the Pitzer and Mayorga activity model for predicting conditions necessary for hydrate formation in the presence of electrolyte solutions.

In case there is more than one electrolyte present in the solution, the procedure proposed by Patwardhan and Kumar (19) is used to estimate the water activity.

Formation of hydrate from gas and liquid water molecules where G molecules of gas involve N molecules of water can be represented by the following chemical reaction:

$$G + N(H_2O) \longleftrightarrow GN(H_2O)$$

For this representation Maddox, et al. (14) showed that the effect of a non electrolyte inhibitor on the hydrate temperature of a natural gas could be explained as:

$$\lambda n(a_w) = \frac{-\Delta H}{NR}\left(\frac{1}{T} - \frac{1}{T_w}\right) \qquad (1)$$

The derivation of equation (1) is discussed in detail by Pieroen (21). The electrolyte can be treated as an "inhibitor" if the procedure developed is used for estimating electrolyte activities and other parameters. In this work (ΔH/NR), the enthalpy of hydrate formation per water molecule in the hydrate lattice in equation (1) is assumed to be a function of pressure and the ionic strength of the electrolyte solution and to take the following form:

$$\frac{\Delta H}{NR} = \frac{e_1 I^{e_2}}{1 + e_3 P + e_4(\lambda n P)} \qquad (2)$$

with e_1, e_2, e_3 and e_4 being adjustable parameters determined from experimental electrolyte solution hydrate data.

Experimental measurements of the hydrate temperature of methane (1, 2, 23) and ethane (6,26) in the presence of liquid water and electrolyte solutions and propane (8, 10, 13, 26) in the presence of ice, liquid water and electrolyte solution were used to evaluate the parameters in equation (2). The values are: e_1= 597.33; e_2=-0.0409; e_3=0.0000227; e_4=-0.0751. These are global parameters that apply for any gas and any single or mixed electrolyte solution. They reproduce the measurements of Blanc and Tournier-Lasserve (1), Dholabhai, et al. (3), and Roo, et al. (23) for methane (CH_4) with an average absolute temperature deviation of 0.33°C; The experimental determinations by Englezos and Bishnoi (6) and Tohidi, et al. (26) for ethane are reproduced with an average absolute deviation of 0.56°C across all data points. Experimental data for propane by Englezos and Ngan (8), Holder and Godbole (10), Kubota, et al. (13), and Tohidi, et al. (26) are reproduced with an average absolute deviation for all propane data points of 0.35°C. A summary of these results is shown in Table 1.

CALCULATION PROCEDURE

Based on the discussion above a procedure for calculating the hydrate forming temperature and pressure for natural gas components in contact with water containing one or more electrolyte salts can be suggested. Assuming that the pressure is fixed and the hydrate forming temperature is required, the sequential steps in the procedure are:

1. Assume that the hydrate forming temperature in the presence of water with no electrolyte present is above 273.15K, the freezing point of water. If the hydrate temperature is lower than this, that fact will become evident and the assumed temperature can be changed. Use equations 3, 7 and 13 to evaluate T^0.
2. Calculate the activity of water and ΔH/NR.
3. Calculate the hydrate temperature in the presence of electrolyte.
4. If the temperature calculated in step 3 is greater than 273.15K, all is well; if it is lower than 273.15K return to step 1, assume the temperature is less than 273.15K, and repeat steps 2 and 3.

RESULTS

The procedure outlined has been used to predict hydrate forming conditions for carbon dioxide (CO_2) over electrolyte solutions. CO_2 is a different gas than light hydrocarbons in that it displays appreciable solubility in water, even at moderate pressures. There are cases in which gas solubility is high enough that the mole fraction of water in the water phase departs substantially from 1.0. The solubility of CO_2 in water can be expressed as:

$$x_{CO_2} = \left\{ \frac{f^V_{CO_2}}{(g_1 + g_2 T)\exp\left[(g_3 - P^{g_4})/P^{g_4}\right]} \right\} \tag{3}$$

where:

g_1 = -725919.22
g_2 = 2898.54
g_3 = 0.05127
g_4 = -0.11228

Calculations of CO_2 solubility using equation (3) match the experimental measurements of CO_2 solubility made by Stewart and Munjal (25) within an average absolute mole fraction CO_2 deviation of 0.00042 over temperatures from 259 to 281K and pressures from 1.0 to 4.25 MPa. Using equation (3) for CO_2 solubility in water and the hydrate prediction procedure developed here, the hydrate forming conditions for CO_2 over electrolyte solutions have been calculated and compared with experimental determinations made by Dholabhai, et al. (4), and Englezos (7). The results for CO_2 are summarized in Table 1. The 161 CO_2 data points show an average absolute temperature deviation of 0.46°C over the full temperature, electrolyte composition and pressure range of the data.

CONCLUSION

The model developed for predicting hydrate forming conditions in the presence of electrolyte solutions does an excellent job of reproducing experimental measurements. It also has the capability to make accurate predictions of hydrate formation in cases where the gas shows appreciable solubility in the water phase. It represents a significant step in predicting hydrate forming conditions for constituents of natural gas.

NOMENCLATURE

a_w = activity of water
a^0_w = activity of water in the single salt solution defined by m^0_k
A_ϕ = Debye-Hückel coefficient = 0.392 for water at 25°C
β_0 = parameter in equation (10)
β_1 = parameter in equation (10)
β_2 = parameter in equation (10)
C_{mj} = Langmuir constant
C_P = specific heat, cal/g-mole-K
f_λ = gas-phase fugacity of the λth gas species
h = molar enthalpy, cal/g-mole
m = molality of electrolyte solution
m_k = molality of electrolyte k in mixed electrolyte solution
m^0_k = molality of electrolyte k in a solution containing only electrolyte k and that has the same ionic strength as the mixed solution
n = formula of electrolyte
n_+ = number of positive ions in electrolyte formula
n_- = number of negative ions in electrolyte formula
nc = total number of components in gas phase
R = gas constant, 1.987 cal/g-mole-K
T = absolute temperature, K
V = molar volume cm^3/g-mole
μ^H_w = chemical potential of water in the gas occupied lattice, cal/g-mole
$\Delta\mu^H_w$ = change in chemical potential of water caused by hydrate formation, cal/g-mole
μ^β_w = chemical potential of water in the unoccupied lattice, cal/g-mole
μ^i_w = chemical potential of ice, cal/g-mole
μ^λ_w = chemical potential of pure water, cal/g-mole
θ_{mj} = fraction of the type m cavities which are occupied by a j-type gas molecule
υ_m = ratio of the number of type m cavities to the number of water molecules in the hydrate phase
z = charge on ions in electrolyte formula

REFERENCES

1. Blanc, C., and J. Tournier-Lasserve, World Oil, November (1990).
2. Carson, D. B. and D. L. Katz, "Trans. AIME," 146, (1942).
3. Dholabhai, P. D., P. Englezos, N. Kalogerakis and P. R. Bishnoi, "Can. J. Chem. Eng.," 69, 800, (1991).
4. Dholabhai, P. D., N. Kalogerakis and P. R. Bishnoi, "J. Chem. Eng. Data," 38, (4), 650 (1993).
5. Englezos, P. and P. R. Bishnoi, "AIChE J.," 34, (10), 1718, (1988).
6. Englezos, P. and P. R. Bishnoi, "Ind. Eng. Chem. Res.," 30, (7), 1655, (1991).
7. Englezos, P., "Ind. Eng. Chem. Res.," 31, (9), 2232, (1992).
8. Englezos, P. and Y. T. Ngan, "J. Chem. Eng. Data," 38, (2), 250, (1993).
9. Holder, G. D. and G. Gorbin, "Ind. Eng. Chem. Fund.," 19, (3), 282, (1980).
10. Holder, G. D. and S. P. Godbole, "AIChE J.," 28, 930, (1982)
11. Jeffrey, G. A. and R. R. McMullan, "Prog. Inorg. Chem.," 8, 43 (1967).
12. Knox, W. G., M. Hess, G. E. Jones and H. B. Smith, "Chem. Eng. Prog.," 57, (2), 66 (1961).
13. Kubota, H., K. Shimizu, Y. Tanaka and T. Makita, "J. Chem. Eng. Japan," 17, (4), 423, (1984).
14. Maddox, R. N., M. Moshfeghian, E. Lopez, C. H. Tu, A. Shariat and J. Flynn, Laurence Reid Gas Conditioning Conference, March 4-6, 1991.
15. Miller, B. and E. K. Strong, "Amer. Gas Assoc. Monthly," 28, (2), 63, (1946).
16. Moshfeghian, M. and R. N. Maddox, "Oil & Gas J.," 30, 78, (1993).
17. Moshfeghian, M, and R. N. Maddox, Annals of New York Academy of Science, 715, (1994)
18. Parrish, W. R. and J. M. Prausnitz, "Ind. Eng. Chem. Proc. Dev.," 11, 26 (1972).
19. Patwardhan, V. S. and A. Kumar, "AIChE J.,"32, (9), 1419, (1986).
20. Peng, D. Y. and D. B. Robinson, "Ind. Eng. Chem. Fund.," 59, (1976).
21. Pieroen, A. P., Recueil Trav. Chem., Vol. 74, 995-1002, (1955)
22. Pitzer, K. S. and G. Mayorga, "J. Phys. Chem.," 77, (19), 2300, (1973).
23. Roo, J. L., C. J. Peters, R. N. Lichenthaler and G. A. Diepen, "AIChE J.," 29, (4), 651, (1983).
24. Schroeder, W., Sammlung Chemischer & Chemisch-Technischer Vortäge, Ahren's, 1926.
25. Stewart, P. B. and P. Munjal, "J. Chem. Eng. Data," 15, (1), 67, (1970).
26. Tohidi, B., R. W. Burgass, A. Danesh and A. C. Todd, "SPE 26701," 255, (1993)
27. Van der Waals, J. H. and J. C. Platteeuw, "Advan. Chem. Phys.," 2, 1, (1959).
28. Villard, M., Compte Rendus, 1888, 106, 1602.

Table 1

Component	Electrolyte Concentration mol/L			Temperature Range K	Pressure Range MPa	AATD* K
	NaCl	KCl	$CaCl_2$			
CH_4	0-5.43	0-1.57	0-1.07	261-281	2.39-92.0	0.33
C_2H_6	0-4.28	0-1.88	0-1.59	265-283	0.50-2.0	0.56
C_3H_8	0.4.27	0-3.35	0-1.61	248-278	0.1-0.54	0.35
CO_2	0-4.29	0-2.36	0-2.24	259-281	1.0-4.23	0.46

* Average Absolute Temperature Deviation

MEASUREMENT OF GAS HYDRATE PHASE EQUILIBRIUM

Phillip Servio and Peter Englezos

Department of Chemical Engineering, The University of British Columbia
Vancouver BC, V6T 1Z4, CANADA

Keywords: hydrate equilibrium data, triethylene glycol, neohexane

ABSTRACT

Incipient equilibrium hydrate formation conditions for two systems are presented. The isothermal pressure search method was employed. First, structure II hydrate data for the propane-triethylene glycol water system at glycol concentrations of 0, 10 an 20 wt % are given. Triethylene glycol was shown to have considerable inhibiting effect on propane hydrate formation. The other data are hydrate formation conditions for the system methane-carbon dioxide-neohexane-water. The initial gas molar composition on a water-free basis was 80 % methane and 20 % carbon dioxide. At a given temperature, the incipient hydrate formation pressure was found to be within the range of the hydrate formation pressure for the methane-neohexane-water and the carbon dioxide-water systems. Thus, further analysis is required to elucidate the type of hydrate structure.

INTRODUCTION

During the past five years we have been measuring phase equilibrium data in gas hydrate forming systems in our laboratory. The broad objective of the work is to provide thermodynamic data which will be used either directly in process design of relevant operations in the oil and gas industry or can be used to test the validity of computational methods for phase equilibrium. We have studied the effect of glycols, water soluble polymers and electrolytes in hydrates from natural gas components. In the present work, we provide measurements for two systems: First, phase equilibrium data for the propane-water-triethylene glycol (TEG) system and second data for the methane-carbon dioxide-2,2-dimethyl butane (neohexane) system.

It has been known since the 1930s that natural gas and water can form a solid ice-like compound commonly called gas hydrate (Hammerschmidt, 1934). This may take place at temperatures above the normal freezing point of water. Because the formation of hydrates has severe economic consequences, in oil and gas operations, prevention of formation is major concem. The most common method to prevent hydrate formation is to inject methanol, glycol, or electrolytes (inhibiting substances). There is a growing interest to replace thermodynamic inhibitors with kinetic inhibitors i.e. chemicals which could perhaps prevent the agglomeration of gas hydrates after they have been formed (Muijs, 1991; Sloan et al. 1994; Englezos, 1996). In spite of this growing effort as well as the progress that has been made in hydrate thermodynamics, equilibrium data for gas hydrates are still needed not only for process design but also for the development and testing of predictive methods for hydrate equilibria (Sloan, 1990; Englezos, 1993; Sloan et al. 1994).

Triethylene glycol is an industrially used chemical to inhibit the formation of gas hydrates. Ross and Toczylkin (1992) have presented data on the effect of TEG on methane and ethane gas hydrates. These are known to be structure I hydrates. Hence, one of the objectives of this work is to report incipient equilibrium data for propane hydrate in aqueous triethylene glycol solutions. Propane hydrate is known to form structure II type hydrate crystal lattice.

Following the report from the National Research Council (NRC) of Canada in 1987 on a new hydrate structure, Sloan and co-workers reported the first structure H hydrate phase equilibrium data in 1992 (Ripmeester et al. 1987; Ripmeester and Ratcliffe,1990; Lederhos et al. 1992). The possibility of forming structure H hydrates in gas and oil reservoirs provides the motivation to obtain phase equilibrium data for structure H hydrates. Subsequently, additional data and a method to predict structure H equilibrium were reported from Sloan's laboratory (Lederhos et al. 1993; Mehta and Sloan,1993; 1994a; Mehta and Sloan,1994b; Makogon et al. 1996; Mehta and Sloan, 1996). Additional data were also reported by other laboratories (Danesh et al.1994; Hutz and Englezos, 1996).

Thus far only methane, nitrogen and argon have been used as light components in the formation of structure H hydrates. Carbon dioxide in conjunction with neohexane and ice also forms structure H hydrates (Ripmeester, 1996). In our laboratory, we attempted to prepare such hydrate but in liquid water. However, we were not able to form hydrates which could be of structure H. At a given temperature, the hydrate that was formed was stable at the carbon dioxide structure I hydrate equilibrium pressure.

Hence, we decided to work with a gas mixture of 80 % methane and 20 % carbon dioxide on a molar basis in conjunction with neohexane which serves as the heavy component.

APPARATUS AND PROCEDURE

A schematic of the apparatus is shown in Figure 1. It consists of a high pressure 316 stainless steel vessel which is immersed in a temperature controlled bath. It has two circular viewing windows on to the front and back. The top of the vessel is held in place by six stainless steel bolts and is sealed with a neoprene O-ring. The temperature control bath contains 30 L of a solution consisting of approximately 50/50 mass percent water and ethylene glycol. A motor driven mechanism is used to stir the contents of the bath. The temperature of the bath is controlled by an external refrigerator/heater (Forma Scientific model 2095, Caltech Scientific, Richmond, BC) with a capacity of 28.5 L. The refrigerator/heater also uses a 50-50 mass percent glycol-water mixture. Mixing of the cell contents is accomplished using a magnetic stir bar that is magnetically coupled to a set of two rotating magnets (Tormag Engineering, Vancouver, B.C.) placed directly underneath the cell. The set of magnets is driven by an electric motor. The temperature at the top, middle and near the bottom inside the cell is measured by three Omega copper-constantan thermocouples. Their accuracy is believed to be +/- 0.10 K. The pressure in the cell is measured by a Bourdon tube Heisse pressure gauge from Brian Controls (Burnaby, BC). The range of the gauge is 0-14 000 kPa and its accuracy is believed to be less than 0.25 percent of the span.

The objective of an experiment is to determine the minimum pressure, at a given temperature, where hydrate crystals can co-exist in equilibrium with a gas phase containing mostly propane and the aqueous liquid phase containing the triethylene glycol. In the structure H hydrate formation experiments, the equilibrium is among a gas phase rich in methane and carbon dioxide, an aqueous liquid phase, a liquid hydrocarbon phase rich in neohexane and the hydrate phase. The isothermal pressure search method is used for the determination of the hydrate formation conditions. We use this method because when a pressure change is imposed, the system can reach thermal equilibrium faster compared to the time required for an adjustment of the temperature. More detailed information on the equipment and the procedure to carry out the experiments is available elsewhere (Englezos and Ngan, 1994; Hutz and Englezos, 1996)

The solutions were prepared with deionized water. The purity of methane and propane was 99.9 and 99.5 % (by volume) respectively. These gases as well as the anaerobic grade carbon dioxide were supplied by Medigas. The neohexane (99%) was supplied from Aldrich. Triethylene glycol was also supplied by Aldrich and was 99% pure. The hydrate forming substances were used without any further purification. A Sartorius analytical balance with a readability of 0.05g was used to weigh the compounds used in the experiments.

RESULTS AND DISCUSSION

The propane-triethylene glycol-water system. The measured equilibrium hydrate formation conditions are shown in Figure 2 together with the vapour pressure of propane. As seen from the figure, the data indicate an inhibiting effect by TEG on propane hydrate equilibrium. One can read from the graph the hydrate point depression at a given pressure. For example at 300 kPa the hydrate point depression is 1.65 and 3.15 K for the 10 and 20 wt % TEG solutions respectively. At 400 kPa pressure, the hydrate point depressions are 1.70 and 3.25 K for the 10 and 20 wt % solutions respectively. It is noted that the freezing point depressions for these TEG solutions is 1.33 and 2.93 K. Comparing these values with our previous work with glycerol we note that, the inhibiting effectiveness of TEG is therefore comparable to glycerol but less than that of methanol and NaCl on the same weight % basis (Breland and Englezos, 1996). It is also noted that the difference in hydrate point depression for TEG solutions at different pressures are less than experimental uncertainty. Hence, it is assumed that the hydrate point depression values do not depend on pressure.

The methane-carbon dioxide-neohexane-water system. Experiments at NRC showed that carbon dioxide with neohexane forms structure H hydrate (Ripmeester, 1996). In spite of efforts to nucleate such hydrates but in liquid water and not in ice as was done at NRC, we were not able to obtain hydrates of structure H. The hydrate we obtained was stable within the carbon dioxide structure I hydrate equilibrium conditions. Since these experiments were inconclusive, we decided to work with an 80-20 % methane-carbon dioxide-neohexane-water system. Figure 3 shows the hydrate equilibrium measurements. The results indicate that the measured conditions are within the range of the methane-neohexane structure H and the carbon dioxide structure I hydrate formation conditions. At this stage, it is premature to decide upon the structure of the hydrate. We plan to analyze the gas and the solid phase in order to elucidate the structure.

CONCLUSIONS

The effect of triethylene glycol (TEG) on the formation of propane hydrate was studied at 0, 10 and 20 wt % aqueous TEG solutions. TEG was found to have a significant inhibiting effect comparable to glycerol but weaker than methanol or NaCl. The experiments with a 80-20 % methane carbon dioxide mixture together with neohexane in liquid water were not conclusive with respect to the structure formed. However, the incipient equilibrium formation conditions for this system were determined.

REFERENCES

1. Breland, E., and P. Englezos 1996. Equilibrium Hydrate Formation Data for Carbon Dioxide in Aqueous Glycerol Solutions. *J. Chem. Eng. Data*, 41(1), 11-13.
2. Danesh, A., B. Tohidi, R.W. Burgass and A.C. Todd, 1994. Hydrate equilibrium data of methyl cyclo-pentane with methane or nitrogen. *Trans I Chem E* (Chem. Eng. Res. Des.), 72, PartA: 197-200.
3. Englezos, P., 1993. Clathrate hydrates. *Ind. Eng. Chem. Res.*, 32(7): 1251-1274. Englezos, P. 1996. Nucleation and Growth of Gas Hydrate Crystals in Relation to Kinetic Inhibition. *Revue de l'Institut français du pétrole*, (in press).
4. Englezos, P. and Ngan, Y. T.,1994. Effect of polyethylene oxide on gas hydrate phase equilibria. *Fluid Phase Equilibria*, 92: 271-288.
5. Hammerschmidt, E.G. 1934. Formation of Gas Hydrates in Natural Gas Transmission Lines. *Ind. Eng. Chem.* 26 (8), 851-855.
6. Hütz, U., and P. Englezos, 1996. Measurement of Structure H Hydrate Phase Equilibrium and the Effect of Electrolytes. *Fluid Phase Equilibria,* 117, 178-185.
7. Lederhos, J.P., Christiansen, R. L. and Sloan, E.D., 1993. A first order method of hydrate equilibrium estimation and its use with new structures. *Fluid Phase Equilibria*, 83: 445-454.
8. Lederhos, J.P., Metha, A.P., Nyberg, G.B., Warn, K.J. and Sloan, E.D., 1992. Structure H clathrate hydrate equilibria of methane and adamantane. *AIChE J.*, 38(7): 1045-1048.
9. Metha, A.P. and Sloan E.D.Jr., 1993. Structure H hydrate phase equilibria of methane + liquid hydrocarbon mixtures. *J. Chem. Eng. Data*, 38: 580-582.
10. Metha, A.P. and Sloan E.D.Jr., 1994a. A thermodynamic model for structure-H hydrates, *AIChE J.*, 40(2): 312-320.
11. Metha, A.P. and Sloan E.D.Jr., 1994b. Structure-H phase equilibria of paraffins, naphthenes, and olefins with methane, *J. Chem. Eng. Data*, 39, 887-888.
12. Metha, A.P. and Sloan E.D.Jr., 1996. Improved thermodynamic parameters for prediction of structure-H hydrate equilibria, *AIChE J.*, 42(7): 2036-2046.
13. Muijs, H.M. 1991. Surfactants in Oil Production, in Chemicals in the Oil Industry: Developments and Applications; Ogden, P.H., Ed., *Roy. Soc. Chem. pp.*277-297.
14. Ripmeester, J.A. 1996. Personal Communication.
15. Ripmeester, J.A., Tse, J.S., Ratcliffe,C.I. and Powell, B.M., 1987. A new clathrate hydrate structure. *Nature*, 325: 135-136.
16. Ripmeester, J.A. and Ratcliffe, C.I., 1990. 129 Xe NMR studies of clathrate hydrates: new guests for structure II and structure H. J. *Phys. Chem.*, 94: 8773-8776.
17. Ross, M.J. and L.S. Toczylkin, 1992. Hydrate Dissociation Pressures for Methane or Ethane in the Presence of Aqueous Solutions of Triethylene Glycol, J. Chem. Eng. Data, 37, 488-491.
18. Sloan, E. D. Jr., 1990. *Clathrates Hydrates of Natural Gases.* Marcel Dekker, New York.
19. Sloan, E.D.; Happel, J.; Hnatow, M.A. 1994. International Conference on Natural Gas Hydrates, *Annals of the New York Academy of Sciences*, Vol. 715, New York.

ACKNOWLEDGMENT

The financial support from the *Natural Sciences and Engineering Research Council of Canada* (NSERC) is greatly appreciated.

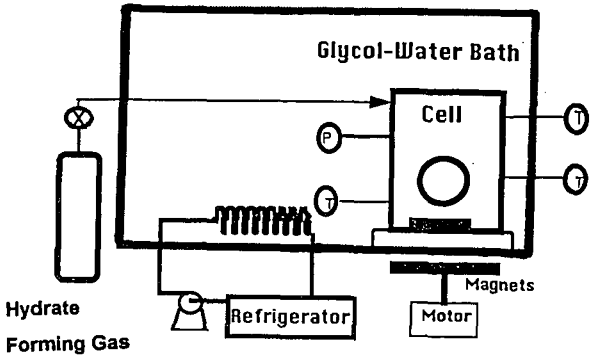
Glycol-Water Bath
Cell
P
T
T
T
Magnets
Motor
Refrigerator
Hydrate
Forming Gas

Figure 1. Experimental apparatus

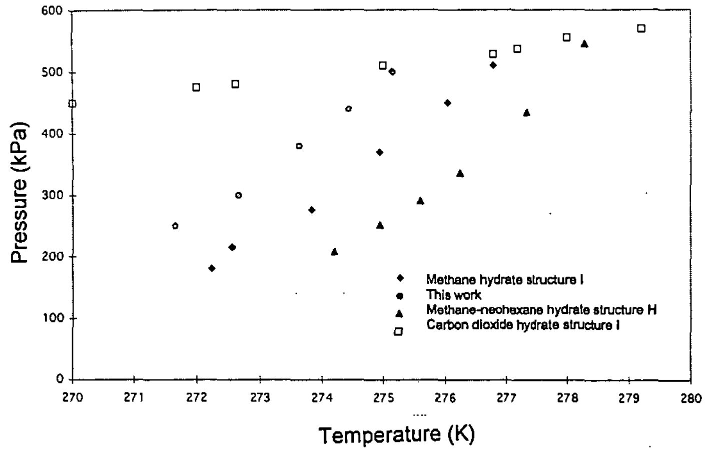

Figure 2. Incipient equilibrium propane hydrate formation conditions in aqueous triethylene glycol solutions.

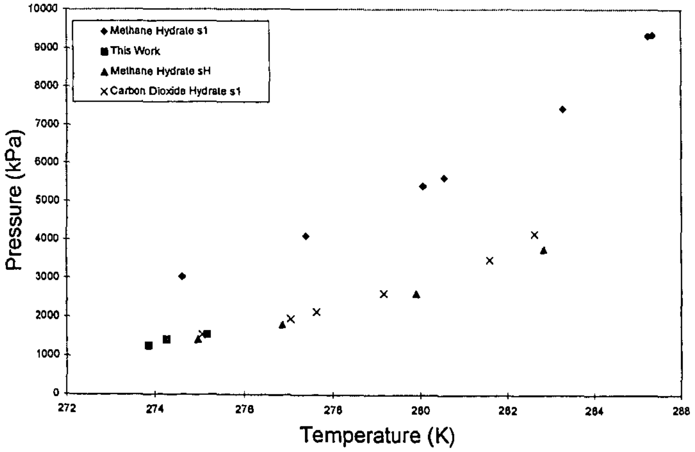

Figure 3. Incipient equilibrium hydrate formation conditions for the methane-carbon dioxide-neohexane-water system.

"MEASUREMENTS AND MODELING OF HYDRATE EQUILIBRIUM CONDITIONS OF SYSTEMS CONTAINING HEAVY HYDRATE FORMERS"

F.H. Fadnes[1*], T. Jakobsen[2] and A. Lund[3]

1 Norsk Hydro A/S, N-5020 Bergen, Norway
2 Terra Environment A/S, N-5028 Bergen, Norway
3 Sintef Applied Chemistry, N-7034 Trondheim, Norway

- Corresponding author

Keywords: Gas Hydrates, equilibrium, cyclopentane

INTRODUCTION

Gas hydrates were, until recently, considered to be a phenomenon associated with small diameter hydrocarbon molecules. For systems relevant to the oil industry, the upper limit was set by n-butane.
In 1987, Ripmeester et al (1,2) discovered a new hydrate structure called structure H. This structure has cavities larger than those of the former known structures I and II and can therefore be stabilized by heavier guest molecules. Of components foud in real hydrocarbon fluids, isopentane, methylcyclopentane, methylcyclohexane and 2,3-dimethylbutane were identified as potential structure H formers while benzene, cyclohexane and cyclopentane were identified as potential structure II formers.
Recently, Thoidi et. al (3) presented experimental and prediction results on the effect of isopentane, methylcyclopentane, cyclopentane and cyclohexane on the hydrate equilibrium properties of two natural gas mixtures. They concluded that structure II heavy hydrate formers increase the hydrate stability of the two hydrocarbon gas mixtures, where as structure H heavy hydrate formers do not have significant effect on the hydrate phase boundary.
In the oil industry the hydrate prevention strategy makes extensive use of hydrate prediction programs. To our knowledge, none of the present commercially available programs take account of the heavy hydrate formers. If some heavy hydrate formers, found in a real hydrocarbon fluid, have a significant effect on the hydrate equilibrium temperature these have to be included in the prediction programs.
In this work the hydrate equilibrium properties of isopentane, cyclopentane and cyclohexane in a synthetic hydrocarbon fluid have been determined. The vapor phase was simulated by either pure methane - a structure I former, or a synthetic gas mixture assuring formation of structure II. The hydrocarbon liquid phase was in all experiments Exxsol D60, which is a paraffinic C9 - C13 distillation cut.
Also presented is a survey of the content of cyclopentane in a selection of real hydrocarbon fluids from the North Sea area.

EXPERIMENTAL

All experiments were performed in a high pressure sapphire PVT-cell. The cell is placed in a temperature controlled air bath in which the temperature can be varied between -40 and +200 °C. The temperature stability is 0.1 °C and the resolution is 0.01°C. The cell has a maximum working pressure of 500 bara. The accuracy of the pressure measurement is estimated to be within 0.5 bar and the resolution is 0.1 bar. The cell volume is controlled and varied using a piston directly coupled to a computerized brushless motor. Volumes are read with a resolution of 0.0001 cm^3. The estimated accuracy is 0.005 cm^3. Maximum cell volume is 100 cm^3.
Stirring is provided by a magnetically coupled stirrer, driven by a computer controlled, variable speed motor. Maximum speed is 1000 rpm. Rheology changes of the experimental fluids are continuously monitored by measurement of the effect required to keep the motor running at constant speed.

Experimental procedures. The sapphire cell was cleaned and evacuated prior to filling of the experimental fluids. All fluids were added gravimetrieally in the following sequence: Water (purified by reversed osmosis), hydrocarbon liquid phase (D60 - added various amounts of heavy hydrate formers) and finally the hydrocarbon vapor phase (C1 or synthetic gas mixture). The water cut was, in all experiments, approximately 50%. The hydrocarbon phase were recombined and the saturation point, at ambient temperature, were determined.
Hydrate formation was initiated by cooling the system at a constant rate, 3 - 5 °C/hours, while continuously stirring the cell. After a period of time, allowing for equilibrium to be established, the system was reheated at a rate of 0.25 °C/hours until the hydrates were completely melted. The experiment gives information of the hydrate equilibrium temperature, the degree of sub cooling and the visual appearance of the formed hydrates. Hydrate formation and decomposition are indicated by deflections in a volume vs. temperature plot (the isobar) and by a change in the rheology of the system (the apparent viscosity). The experiments were performed at isobaric conditions, at 100, 200 and 300 bara.
All experiments were documented by video recordings.

Experimental fluids. The synthetic gas mixture were composed of C1, C2 and C3 in the ratio 74.89, 16.47 and 8.64 mole %, respectively. All components were minimum 99.9 % pure. Analysis of the mixture did not show significant contamination of any other components.

Methane were 99.95 % pure. Isopentane, cyclopentane and cyclohexane were all of analytical grade purity.

Exxsol D60 is a commercial paraffinic solvent. The composition of D60 is given in table 1.

The compositions of the different experimental systems are given in tables 2 and 3. The measured saturation pressure and the recombination gas/oil ratio are given along with the composition.

RESULTS AND DISCUSSION

The results from the experiments involving the potential heavy hydrate formers isopentane cyclopentane and cyclohexane, are presented in tables 2 and 3 and figures 1 to 4. Also included in these figures are predictions of the hydrate equilibrium conditions. These predictions were performed by use of PVTsim, a commercially available PVT and phase behavior simulation program.

Isopentane was expected to form structure H while cyclopentane and cyclohexane were expected to form structure II. As can be seen from the figures, only cyclopentane seems to have a significant effect on the hydrate equilibrium conditions for the tested systems. The effect of cyclopentane is, on the other hand, remarkable as hydrate equilibrium temperatures close to 30 °C were observed.

Isopentane: The effect of isopentane is demonstrated in figure 1. As can bee seen from this figure, the hydrate equilibrium conditions for the C1/D60 system are not significantly altered by addition of isopentane at a concentration of 9.2 mole %. The C1/D60 system forms a structure I hydrate and our results indieates that, in this system, isopentane do not stabilize either structure II or structure H hydrate.

Cyclopentane: The effects of cyclopentane in a C1/D60 system are presented in figure 2. At concentrations of 9.4 and 4.6 mole % are the equilibrium temperature shifted to higher temperatures and it is reason to assume that the structure is shifted from I to II. At a concentration of 0.9 mole % are the hydrate equilibrium conditions for the C1/D60 system not significantly altered. It can thus be assumed that cyclopentane do not participate in the hydrate formation at this concentration.

The effects of cyclopentane in a synthetic gas/D60 system are presented in figure 3. This system forms structure II also when heavy hydrate formers are not added. The effect of adding 11 mole % cyclopentane to this system is seen by the significant increase in the hydrate equilibrium temperature.

Addition of 1.1 mole % cyclopentane to the synthetic gas system gives only a marginal increase (0.2 °C) of the hydrate equilibrium temperature.

Cyclohexane. The results from the experiments involving cyclohexane in a C1/D60 system are presented in figure 4. There were not observed any stabilizing effects in this system, which is expected to form structure I when no heavy hydrate formers are added. It seems therefore reasonable to conclude that cyclohexane, at this concentration, do not stabilize either structure II or structure H.

Significance for the hydrate prevention strategy. Figure 2 and 3 clearly states that cyclopentane at concentrations of 9.4 and 4.6 mole % significantly increases the hydrate equilibrium temperature. 1.0 mole % cyclopentane has, on the other hand, no significant impact on the hydrate equilibrium.

For the two systems tested, C1/D60 and synthetic gas/D60, our hydrate prediction program PVTsim predicts structure I and II, respectively. Cyclopentane is not included as a hydrate former in this program and the only predicted effect of adding cyclopentane to the test systems are a dilution of the hydrate formers and thus a slight reduction of the hydrate formation temperatures. At higher concentrations of cyclopentane will this clearly lead to a significant miscalculation of the hydrate equilibrium conditions.

Neither the concentration at which cyclopentane is able to switch from structure I to structure II, nor the concentration at which cyclopentane is able to significantly change the equilibrium temperature of structure II hydrate, are known. It seems, however, that 0.9 - 1.1 mole % is below the critical concentration where cyclopentane affect the hydrate equilibrium.

A survey of the content of cyclopentane in a selection of North Sea oil is given in table 4. As can be seen from this table the concentration seems, in general, to be below the critical concentration for having any significant impact on the hydrate equilibrium conditions.

CONCLUSIONS

1 The hydrate formation characteristics of two synthetic hydrocarbon system containing three heavy hydrate formers have been investigated.

2 9.2 mole % isopentane do not promote formation of structure II or structure H in a methane/D60 system. The hydrate equilibrium conditions are not significantly influenced.

3 9.4 and 4.6 mole % cyclopentane promotes formation of hydrate structure II in both the methane/D60 system and the synthetic gas/D60 system. The hydrate equilibrium conditions were shifted to higher temperatures.

4 1.0 mole % cyclopentane do not change the hydrate structure from I to II in the methane/D60 system and do not significantly increase hydrate the stability of structure II in the synthetic gas/D60 system.

5 8.0 mole % cyclohexane in a methane/D60 system do not promote formation of hydrate structure II or structure H and do not affect the hydrate equilibrium conditions.

6 In 13 different North Sea oil surveyed, are the concentrations of cyclopentane too low to affect the hydrate stability. We believe that the hydrate equilibrium conditions, for these oils, can be predicted with reasonable accuracy.

REFERENCES

(1) Ripmeester, J.A., Tse, J.S., Ratcliffe, C.I. and Powell, B.M.:
"A New Clathrate Hydrate Structure", Nature (1987) 325.

(2) Ripmeester, J.A., Ratcliffe, C.I. and McLaurin, G.E.:
"The role of heavier Hydrocarbons in Hydrate Formation",
AIChE Spring Meeting (1991)

(3) Thohidi, B., Danesh, A., Burgass, R.W. and Todd, A.C.:
SPE35568 "Effects of Heavy Hydrate Formers on the Hydrate Free Zone of Real Reservoir Fluids", European Production Operations Conference & Exhibition (1996)

Table 1. Composition and properties of Exxsol D60.

Carbon no.	C9	C10	C11	C12	C13
N + Iso paraffin (wt.%)	0	5	23	23	6
Naphtenes (wt.%)	1	13	18	8	3
Mw	126.2	140.8	155.4	169.8	183.7
Density (kg/m3)	768	778	788	797	805

Table 2. The synthetic gas/D60 system. Composition and hydrate equilibrium data.

System	S.0	S.1	S.2
C1 (mole %)	41.16	38.02	39.9
C2 (mole %)	9.05	8.36	8.78
C3 (mole %)	4.75	4.39	4.60
Cy-C5 (mole %)		10.97	1.07
D60 (mole %)	45.03	38.26	45.66
GOR (Sm^3/Sm^3)	144	139	132
Psat (Bara)	131 @23.1 °C	125 @23.9 °C	141@29°C
Hydrate equilibrium (°C):			
@ 100 Bara	19.7	25.3	19.9
@ 200 Bara	22.0	27.4	22.2

Table 3. The methane/D60 system. Composition and hydrate equilibrium data.

System	C.0	C.1	C.3
C1 (mole %)	60.87	57.69	57.67
i-C5 (mole %)		9.22	
Cy-C5 (mole %)			9.43
D60 (mole %)	39.13	33.09	32.90
GOR (Sm^3/Sm^3)	182	182	183
Psat (Bara)	253 @24 °C	227 @23.6 °C	228 @24.5 °C
Hydrate equilibrium (°C):			
@ 100 Bara	13.7	12.9	25.7
@ 200 Bara			29.4
@ 300 Bara			29.8

Table 3 cont. The methane/D60 system. Composition and hydrate equilibrium data.

System		C.4	C.5	C.6
C1	(mole %)	59.02	59.75	58.47
C2	(mole %)			
Cy-C5	(mole %)	4.61	0.92	
Cy-C6	(mole %)			8.01
D60	(mole %)	36.37	39.33	33.52
GOR	(Sm^3/Sm^3)	180	176	182
Psat	(Bara)	247 @25.4 °C	247 @21.7 °C	244 @24 °C
Hydrate equilibrium (°C):				
@ 100 Bara		22.4	13.1	13.6
@ 200 Bara			18.6	.
@ 300 Bara			20.9	

Table 4. Content of cyclopentane in North sea oils.

Oil I.D.	Cyclopentane (mole %)	Cyclopentane (wt %)
1	0.04	0.01
2	0.03	0.01
3	0.07	0.05
4	0.07	0.05
5	0.12	0.11
6	0.04	0.04
7	0.05	0.04
8	0.06	0.05
9	0.05	0.04
10	0.09	0.09
11	0.08	0.08
12	0.04	0.02
13	0.07	0.03

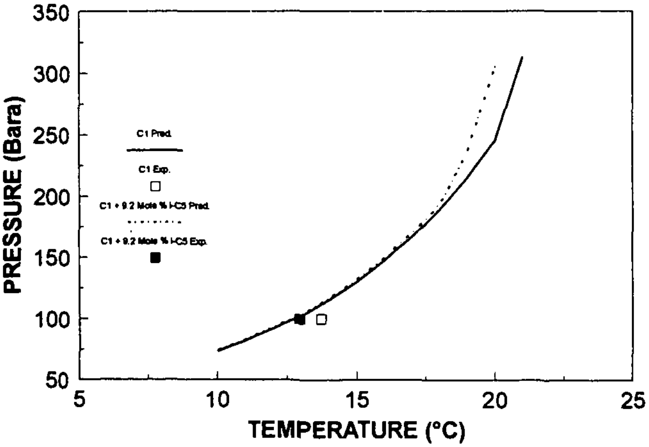

Figure 1. Experimental and predicted hydrate equilibrium conditions for a methane/D60 system containing isopentane.

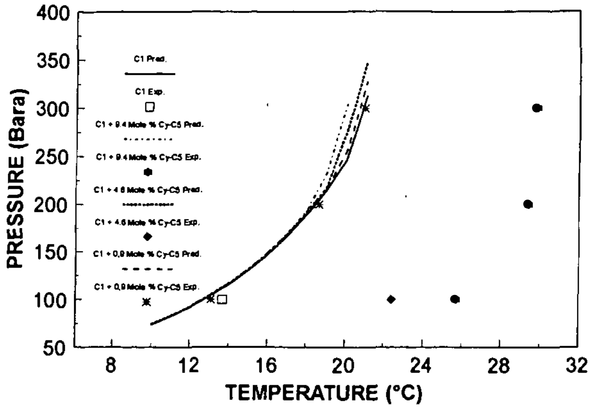

Figure 2. Experimental and predicted hydrate equilibrium conditions for a methane/D60 system containing cyclopentane.

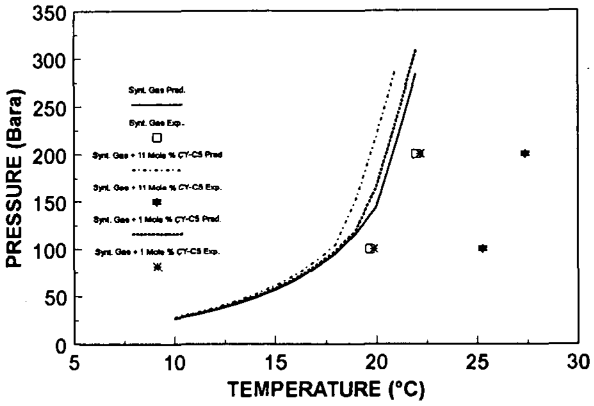

Figure 3. Experimental and predicted hydrate equilibrium conditions for a synthetic gas/D60 system containing cyclopentane.

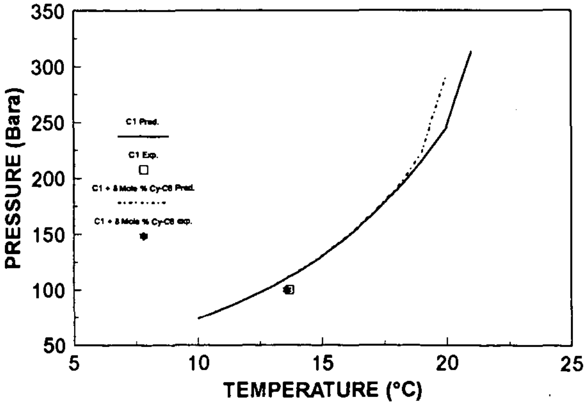

Figure 4. Experimental and predicted hydrate equilibrium conditions for a methane/D60 system containing cyhexane.

ELECTRONIC AND VIBRATONAL PROPERTIES OF GAS HYDRATES

J.S. Tse, Steacie Institute for Molecular Sciences, National Research Council of Canada, Ottawa, Ontario, Canada K1J 9B2, V. Shpakov and V. Belosludov, Institute for Inorganic Chemistry, Novosibirski, Russia 630090 and V.I. Murashov, Department of Chemistry, Dalhousie University, Halifax, Nova Scotia, Canada B3H 4J3.

Keywords : lattice vibration, thermal conductivity, clathrate hydrate

INTRODUCTION

The most unique physical property of gas hydrate is the anomalous low and unexpected glassy-like thermal conductivity [1,2]. This interesting behaviour has both significant practical and scientific consequences. Thermal conductivity is a vital parameter required for the computer modelling of the recovery of natural gas from the hydrate [3]. A knowledge on the variation of the thermal conductivity with pressure and temperature is a prerequisite to the exploitation of this important natural resource. Despite the well defined crystalline structures for gas hydrates [4,5], their thermal conductivities are characteristic of amorphous materials. The understanding of the causes responsible for this unusual phenomenon will sled light on the mechanism of thermal transport in the disorder system. In solid, the thermal energy is transported and dissipated by the acoustic lattice vibrations. These vibrations are normally too low in energy to be effectively studied by infrared and Raman spectroscopy. However, they can be conveniently probed by neutron incoherent inelastic spectroscopy. In the following, the results from such measurements will be presented and discussed with the aid of computer simulation of the guest and lattice vibrations with lattice dynamics and molecular dynamics methods.

EXPERIMENTAL AND THEORETICAL DETAILS

Methane hydrate in deuteriated water was prepared by condensation of the gas into a pressure vessel equipped with rolling rods at very low temperature. The vessel was then allowed to warm slowly to -30° C and annealed at this temperature with gentle rotation for 24 hours. The hydrate sample was carefully removed and stored under liquid nitrogen. The neutron incoherent inelastic experiments were performed at the C3 triple axis spectrometer at Chalk River Nuclear Laboratory [6]. Lattice dynamics [7] and molecular dynamics calculations [8] were performed on a single unit cell of 8 methane and 46 water molecules using the SPC [9] and TIP4P [10] water intermolecular potential, respectively.

RESULTS AND DISCUSSION

The experimental vibrational frequencies for the motions of the methane in the cavities of the hydrate can be obtained directly from the neutron scattering experiments. At 5 K, two peaks were observed at 32, 57 and 72 cm^{-1} in the experimental spectrum which are in excellent agreement with the theoretical predicted values [11,6] at 35, 54 and 78 cm^{-1}. These results reassured the reliability of the interaction potential models employed in the calculations. The motions of the enclathrated methane in the hydrate cages can be examined from the variation of the intensity of the J = 0 →1 rotational excitation peak with the neutron momentum transfer (Q) (fig.1). If the methane is freely rotating the intensity of the excitation peak will be proportional to the first order Bessel function $j_1(Qr)$, where r is the C-H distance. A fit to the experimental data gives an effective C-H distance of 1.23 A

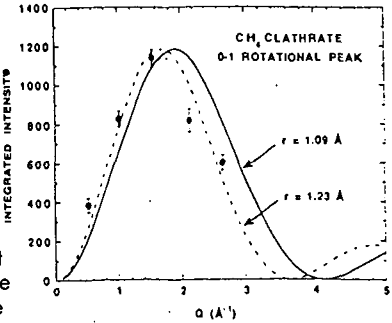

Fig. 1 Variation of the intensity (I) of the rotational peak with neutron momentum transfer (Q)

which is close to the correct value of 1.09 A. This result indicates that the methane molecules rotate almost freely inside the hydrate cages and are in complete agreement with a previous NMR study [12]. Another important observation is the lack of energy dispersion in the rotational mode as the temperature is raised (fig.2). This effect is the consequence of a strong coupling between the low frequency acoustic lattice vibrations with the localized methane motions [13]. A clear picture of the interactions between the enclathrated methane with the host water lattice is now emerged from the neutron experiment. Although the methane molecule behaves like a free molecules, its motions are directly coupled with the lattice vibrations. This coupling provides a plausible mechanism for the transfer of thermal energy from the lattice to the methane. The heat transport can be dissipated via the thermal excitation of the methane thus reducing the thermal conductivity of the material

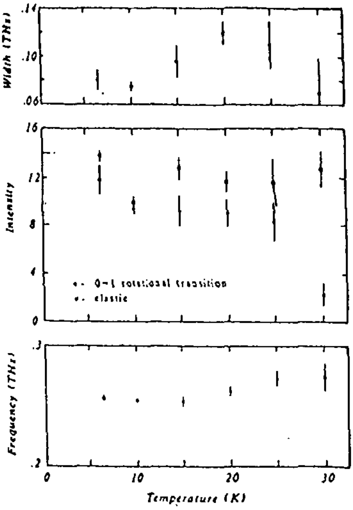

Fig. 2 The variation of the position, lineshape and intensity of the rotational peak with temperature.

The interaction between the lattice acoustic vibrations with the localized motions of the guest has been proposed on the basis of molecular dynamics calculations [6] and experimental measurement of the lattice vibrational spectra of the gas hydrates [12]. This proposal can be quantified through the calculation of the cross time correlation function of the lattice and the guest motions by molecular dynamics techniques. The fourier transform of the correlation function gives the vibrational modes of the motions are correlated. If there is no correlation between the motions of the guest and the water lattice, time function will decay exponetially with time. Otherwise, the time decay will be modulated by the appropriate coupling frequencies. The results for such calculation for the structure I xenon hydrate and a hypothetical "light xenon" hydrate where the mass of the xenon has been set to 1 amu but retaining the interaction potentials as in the real xenon hydrate are shown in figs. 3 and 4. Inspection of the time correlation functions and their fourier transforms provide valuable information on the role of the guest-host coupling mechanism. In the case of the real xenon hydrate, it is evident that the correlation time extends to very long time (10 psec). The vibrational frequencies that couple the lattice and the guest vibrations occur at 23, 34 and 52 cm^{-1}. These frequencies are the same as the localized vibrations calculated for xenon [14] and fall within the acoustic region of the lattice vibrations [15]. Since the vibrational frequency of the rattling motion of the guest is inversely proportional to the square root of the reduced-mass [14], a "light xenon" should

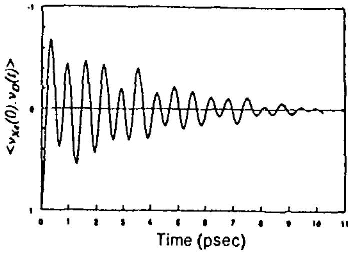

Light Xe (M_{xe} = 1)

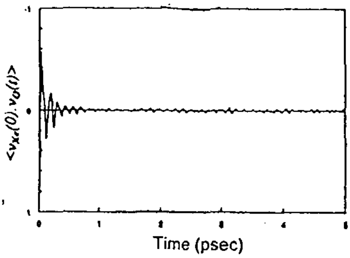

Fig. 3 The cross velocity correlation function for xenon and "light xenon" hydrate.

moves the guest vibrations out of the lattice acoustic region. This fact is shown in the calculations on the hypothetical hydrate. The correlation time between the " light xenon" and the lattice is extremely short and less than 1 psec. The corresponding " coupled" vibrations are located from 250 to 600 cm^{-1}, which are outside the translational region of the lattice vibrations. To summarized, it is shown from the present molecular dynamics calculations, the coupling between the guest and water lattice vibrations only occurs at the low frequency region. In practice, the hydrocarbons enclathrated in the hydrate structure all possess low frequency librational and rattling motions thus permitting the exchange of thermal energy with the host lattice.

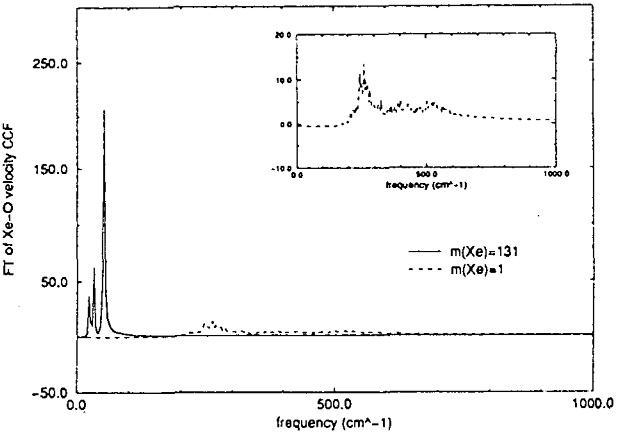

Fig. 4 The fourier transform of the cross velocity correlation function for xenon and " light xenon" hydrate.

Strong interactions between the guest and water lattice are also expected from a factor group analysis of the symmetry of the translational vibrational modes [13]. It can be easily shown that at the Brilluoin zone center, both the guest and lattice translational vibrations possess the T_{1u} representation. However, the lattice acoustic lattice vibrations are strongly dispersive but the guest vibrations are largely localized and non-dispersive. A symmetry avoided crossing between the two vibrational branches must then occur along certain phonon wavevector between the zone center and the zone boundary. The resonance of two vibrational modes of the same symmetry can be a mechanism for energy transfer. A schematic representation of this interaction is shown in fig.5. A lattice dynamics calculations on xenon hydrate indeed shows a considerable mixing of the positional displacements of the xenon and the water in the eigenvectors associated with the acoustic vibrations after the intersection of the phonon branches.

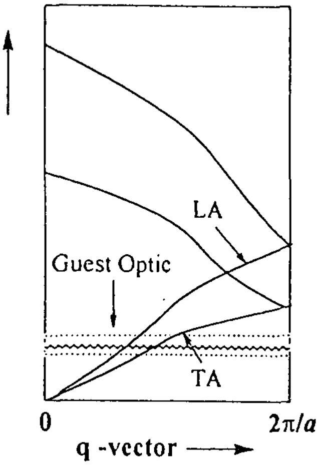

Fig. 5 Schematic diagram for the symmetry avoided crossing of the acoustic branch with the guest localized vibrations.

Realizing the basic mechanism for the coupling between the guest and host lattice, a simple model based on a modified Einstein model can be used to predict the thermal conductivity of gas hydrate [16,17]. One important feature of this thermal conductivity model is that only the molecular properties are needed as input parameters for the calculation of the thermal conductivity In this model, the localized vibrations are assumed to be heavily damped with lifetimes of half a period of the oscillation and the distribution of the localized modes in a solid can be approximate by the Debye model. Using the equivalent of the gas kinetic equation, an expression for the minimum thermal conductivity Λ_{min} can be derived.

$$\frac{\Lambda_{min}}{\Lambda_\infty} = 2\left(\frac{T}{\Theta_D}\right)^2 \int_0^{\Theta_D/T} \frac{x^3 e^x}{\left(e^x - 1\right)^2} dx$$

At high temperature when $T >> \Theta_D$, the transport integral approaches unity and the limiting thermal conductivity Λ_∞ is given by

$$\Lambda_\infty = \frac{1}{2}\left(\frac{\pi}{6}\right)^{\frac{1}{3}} k_B n^{\frac{2}{3}} \left(2v_t + v_l\right)$$

Where k_B is the Boltzman constant, n is the number density and v_l and v_t are the longitudinal and transverse sound velocity of the hydrate. Therefore, once the experimental density and acoustic sound velocities are known, the thermal conductivity at any temperature can be estimated. Previous calculations show that the calculated thermal conductivities for several gas hydrates employing these are in good accord with experiment [17].

The electrostatic field created by the water froming the cavities in a hydrate has important effects on the vibrations of the guest molecules. In view of the potential use of vibrational - infrared and Raman spectroscopies as an alternative means of the determination of the hydration number, it is imperative to understand these electrostatic effects. An electrostatic potential map (MEP) for the hydrate cavity can be computed from quantum mechanical method. We have computed the MEP for the small and large cage of a structure I hydrate. The MEP can be used to derive appropriate point charge model for the water molecules for the future simulation of the interactions between the guest and the cavities. Details of the computational results will be published elsewhere.

REFRERENCES

1. Ross, R.G., P. Andersson, G. Backstrom, 1981, Nature, **290**, 322.
2. Tse, J.S., White, M.A., 1988, J. Phys. Chem., **92**, 5006.
3. Holder, G., Angert, P.F., Pereira, 1983, "Natural Gas Hydrates", Cox, J.L. ed., Butterowrth Publishers.
4. McMullan, R.K., Jeffrey, G.A., 1965, J. Chem. Phys., **42**, 2725.
5. Mak, T.C.W., McMullan, R.K., 1965, J. Chem. Phys., **42**, 2732.
6. Tse, J.S., Powell, B.M., Sears, V.F., Handa, Y.P., 1993, Chem. Phys. Lett., **215**, 383.
7. Shpakov, V.P., Tse, J.S., Belosludov, V.R., Belosludov, R.V., 1996, J. Phys., Conden. Mat., (submitted).
8. Tse, J.S., Klein, M.L., McDonald, I.R., 1983, J. Phys. Chem., **92**, 5006.
9. Berendsen, H.J.C., Postma, J.P.M., van Gunsteren, Hermans, J., 1981. "Intermolecular Forces", Pullman, B. ed., Reidel Dordrecht, the Netherlands.
10. Jorgenson, W. 79 L., Chandraskhar, J.D., Madura, J.D., Impey, R.E., Klein, M.L., 1983, J. Chem. Phys.,**79**, 926.
11. Tse, J.S., Klein, M.L., McDonald, I.R., 1987, J. Chem. Phys., **91**, 5786.
12. Garg, S.K., Gough, S.R., Davidson, D.W., 1975, J. Chem. Phys., **63**, 1646.

13. Tse, J.S., Ratcliffe, C.I., Powell, B.M., Sears, V.I., Handa, Y.P., 1997, J. Phys. Chem., in press.
14. Tse, J.S., Klein, M.L., McDonald, I.R., 1983, J. Chem. Phys., **78**, 2096.
15. Tse, J.S., Klein, M.L., McDonald, I.R., 1984, J. Chem. Phys., **81**, 6124.
16. Cahill, D.G., Pohl, R.O., 1988, Ann. Rev. Phys. Chem., **39**, 93.
17. Tse, J.S., 1994, J. Incl. Phenmon., **17**, 259.

DIRECT FREE ENERGY CALCULATIONS FOR GAS HYDRATES.

R.E. Westacott and P.M. Rodger
Chemistry Department, University of Reading, Whiteknights, Reading, Berks., RG6 2AD, UK.

Abstract.

In this work we present an efficient method for calculation of free energies for molecular crystals. This method is a generalization of the local harmonic approximation and allows full coordinate free energy minimization at finite temperatures and pressures. In terms of gas hydrates, this method provides a first principles route to the chemical potential of water in the hydrate lattice. This quantity has been calculated for different levels of cavity occupancy for the type I hydrate of methane. The values obtained indicate that the number of occupied cavities has a significant effect on the chemical potential of water. Further, we have used this method to calculate the total free energy of methane hydrate and ice. Using the integrated form of the equation of state for a Lennard-Jones fluid we have also calculated the free energy of the free guest species. With these three values the methane/ice/methane hydrate three-phase co-existence line can be obtained.

I. Introduction.

The ability to calculate free energy in an efficient manner is of paramount importance in the structural and thermodynamic study of gas hydrate systems. In principle, it is possible to fully characterize the structural and thermodynamic properties of the system from a knowledge of the free energy. In most cases, this involves calculating the structural or thermodynamic property as a function of temperature and pressure. If this is the case, the free energy must be calculated at many different state points. Thus the efficiency of the free energy calculation becomes the limiting factor and determines the scale of the calculations which can be undertaken.

The development of theories for free energy calculations on atomic solids based on local atomic vibrational behaviour has been an important contribution in this area[1]. In the Local Harmonic Model (LHM) the atoms are modelled as Einstein oscillators which vibrate in the field created by the other atoms, but there is no interatomic vibrational coupling. The LHM is computationally inexpensive and has been shown to give a good description of the thermodynamic properties of atomic solids[1]. It should be mentioned that analogous theories exist, notably the second moment model of Sutton[2], which is equivalent to the LHM only the nature of the approximation to the density of states differs. In this work we have further developed the LHM for complex molecular crystals and applied the theory to gas hydrates.

At present most attempts to explain the stability and properties of gas hydrates are based on the van der Waals and Platteeuw cell theory. According to this model the water molecules form a wee-defined crystal lattice containing cavities into which the guest molecules may be absorbed. The theory also assumes that the free energy of the water lattice is independent of which molecules, if any, occupy the cavities. Thus the contribution of the water lattice to the total free energy of the system must be the same when all the cavities are empty as when all the cavities are occupied. Recent computer simulations by Rodger[3] indicate some fundamental difficulties with the van der Waals and Platteeuw theory. His results indicate that the empty lattice is unstable rather than metastable. If this is the case, the guests must serve to dampen out the critical lattice vibrations that lead to the rearrangement of the host lattice. Tanaka[4] has considered distortion of hydrate cages around xenon and carbon tetrafluoride guests. The work showed that the smaller xenon atoms did not distort the hydrate cages, while the carbon tetrafluoride caused significant distortion of the small cages. This deformation gave rise to a change in the water chemical potential and casts further doubt on the validity of the primary assumption of the cell theory.

In this paper we present the extension to the LHM for molecular crystals and its application to gas hydrates. The method provides a simple, computationally cheap tool for the investigation of the lattice relaxation in gas hydrates and their structural and thermodynamic properties. We present optimum cell lengths over a range of temperatures and pressures for methane hydrate obtained using a single co-ordinate free energy minimisation and a range of other properties. Also we present values of the free energy difference between ice and the β-hydrate, and between the β-hydrate and the water lattice of hydrates of various occupancies. We demonstrate how the three phase line (ice-hydrate-vapour) can be calculated using this method. Finally, we show the necessity for a full co-ordinate (*i.e.* all atomic co-ordinates) free energy minimisation rather than the single co-ordinate (*i.e.* unit cell length) calculation using the dissociation pressure calculated using each method compared to the experimental value.

Method.

The essence of the LHM is the ease of calculation of the vibrational partition function, q_{vib}

$$q_{vib} = \frac{1}{1 - e^{-\frac{h\upsilon}{k_B T}}} \tag{1}$$

which is simple to calculate from the vibrational frequency, υ

$$\upsilon^2 = \frac{\partial^2 U}{\partial r^2}\frac{1}{4\pi m^2} \tag{2}$$

The Helmholtz free energy can then be calculated from

$$A = -k_B T \ln q_{vib} \tag{3}$$

In the classical limit, where $k_B T$ is much greater than $h\upsilon$, equation (1) simplifies to

$$q_{vib} = \frac{k_B T}{h\upsilon} \tag{4}$$

For a perfect crystal with a unit cell of N atoms, the quasi-harmonic approximation gives the Helmholtz free energy as

$$A = U + kT\sum_{i}^{3N} \ln\left(2\sinh\left(\frac{\hbar\upsilon_i}{2kT}\right)\right) \tag{5}$$

where U is the potential energy and the vibrational frequency of atom i, υ_i, is obtained from the dynamical matrix with elements

$$D_{ij} = \frac{\partial^2 U}{\partial r_i \partial r_j} \tag{6}$$

as the square root of the eigenvalues of the matrix $\boldsymbol{M}^{-1}\boldsymbol{D}$, where $\boldsymbol{M}$ is the mass matrix. In the LHM, D_{ij} is set to zero unless i and j refer to co-ordinates of the same atom. Thus $\boldsymbol{D}$ is reduced from a $3N$x$3N$ matrix to N 3x3 matrices and the diagonalisation becomes substantially easier. Equation (5) is, therefore, a 3-dimensional, many-atom representation of equation (3).

However, for a molecular system, this neglect of interatomic coupling is only valid for atoms in different molecules. Within the same molecule the vibrations of the atoms are strongly coupled through the presence of covalent bonds. So, in the Molecular Local Harmonic Model (MLHM), the dynamical matrix can still be reduced to block diagonal form, except in this case each block represents a set of molecular co-ordinates rather than a set of atomic co-ordinates. Thus $\boldsymbol{D}$ is reduced to M 9x9 matrices. The expression for the Helmholtz free energy in the MLHM is

$$A = U + kT\sum_{i}^{m}\sum_{j}^{N_i} \ln\left(2\sinh\left(\frac{\hbar\omega_{j,i}}{2kT}\right)\right) \tag{6}$$

where N_i is the number of atoms in molecule i, m is the number of molecules and $(\omega_{ij})^2$ are the eigenvalues of the molecular matrices $\boldsymbol{M}_i^{-1}\boldsymbol{D}_i$.

We have used the SPC model[5] for water and a single Lennard-Jones site for the methane. Using a grid search method we have performed a single co-ordinate minimisation by calculating the free energy over a range of unit cell lengths. This is a simple application of the MLHM and provides optimum cell lengths and gradient properties such as thermal expansivity, isobaric compressibility and heat capacities. We have also performed full atomic co-ordinate free energy minimisation using a conjugate gradient-type approach, where the atoms are moved according to the free energy force. For the calculation of hydrate dissociation pressures we have used an equation of state for a Lennard-Jones fluid[6] to describe the properties of the fluid guest.

III. Results.

In figure 1(a) we show the effect of temperature on the unit cell length of methane hydrate at 1 atmosphere. It is noticeable that the effect is linear and that the cell length values obtained are comparable with those of experiments[7]. In figure 1(b), we show the effect of pressure on the unit cell length of methane hydrate at 260 K. Again, the effect is linear and the cell length values are similar to experimental values[8]. The thermal expansivity calculated using the values shown in figure 1(a) is $1.78\text{x}10^{-4}$ K^{-1}. This compares favourably with $0.77\text{x}10^{-4}$ K^{-1} obtained experimentally by Tse *et al.*[9]. The compressibility calculated from figure 1(b) is $3.3\text{x}10^{-11}$ Pa^{-1}, which compares well with the estimate of $14\text{x}10^{-11}$ Pa^{-1} given by Sloan[10]. The heat capacities calculated from our work are of the order of 50 to 55 J mol^{-1} K^{-1}, which is are a factor of 4 to 5 smaller than the experimental values of Handa[11].

Initial observations of these results suggest that there is some effect of the guest molecules on the host lattice. The difference in Gibbs free energy between the β-hydrate and the water lattice of the occupied hydrates is approximately 1.1 kJ/mol. These differences are very similar to empirical estimates obtained by the cell theory for the free energy difference between the hydrate water lattice and ice (1.2-1.3 kJ/mol at 273 K[12]). There are also differences between the Gibbs free energies of the water lattices of the occupied systems. This difference is approximately 0.1 kJ/mol. On closer inspection, inclusion of guest molecules appears to stabilise the water lattice. However, it seems that enhanced stability and guest inclusion have a complex relationship. The fully occupied methane hydrate may have the lowest total Gibbs free energy, but it does not have the most stable water lattice. Occupation of the two 5^{12} cavities has the greatest stabilising effect on the water lattice.

There seems to be some degree of variation of the effect of guest molecules on the host water lattice with temperature and pressure. The biggest differences, around 1.1 kJ/mol, are experienced at the higher temperatures and lower pressures that we have studied. These are precisely the conditions of interest in industrial applications. Given that the magnitude of these changes in the free energy of the water lattice, ΔG_H,.is comparable with $\Delta\mu_w^\beta$, it must be expected that the accuracy of the cell theory predictions will vary with composition. At low temperatures and higher pressures the difference is considerably smaller, about 0.2 kJ/mol.

From the full atomic co-ordinate free energy minimisation we observe similar trends, such that the fully occupied hydrate is always the most stable hydrate, but the hydrates of intermediate occupancy have the more stable water lattice than either the β-hydrate or the fully occupied hydrate. The magnitude of ΔG_H seems to be temperature dependent, so that at higher temperatures the difference is larger. This is a reflection of the fact that the free energy minimisation is entropy driven. Our calculations show that ΔG_H can be as high as 2.3 kJ/mol at higher temperatures. Such differences in the thermodynamic properties are currently ignored in the cell theory, which assumes that the properties of the water lattice of occupied hydrates are the same as the β-hydrate. Thus $\Delta\mu^{\alpha-\beta}$ in the cell theory ignores any occupancy-dependent properties. Holder and Hand[13], for example, used an optimum value for $\Delta\mu^{\alpha-\beta}$ of 1.115 kJ/mol. It is clear that occupancy-dependent changes in $\Delta\mu^{\alpha-\beta}$ of about 2.3 kJ/mol will be very significant and inclusion of such guest perturbation of the host lattice will be necessary to correct errors experienced when using the cell theory to determine hydrate dissociation pressures.

The MLHM, when coupled with an appropriate equation of state to describe the thermodynamics of the bulk guest phase, can be used to calculate hydrate dissociation pressures by calculating points on the ice/gas/hydrate phase line. We have used results from the unit cell optimisation and the full co-ordinate minimisation in order that we may determine whether the full co-ordinate minimisation is necessary to correctly describe gas hydrate properties, or whether the single co-ordinate minimisation is sufficient. In figure 2, we illustrate the dissociation pressure calculated using the unit cell optimisation. The point where the two lines cross indicates the dissociation pressure and in this case, methane hydrate at 270 K, it is approximately 40 MPa. In figure 3, we illustrate the case for full co-ordinate minimisation. Here we calculate the dissociation pressure to be 2.5 MPa. This is in excellent agreement with the experimental value[8] of 2.32 MPa. The quality of this agreement must be contemplated given the errors within the SPC model[14], although SPC water has been shown to yield the correct melting temperatures for methane hydrate[15].

IV. Conclusions.

In this paper we have shown the development of a simple model for free energy minimisation of complex molecular crystals. We have applied this model to gas hydrates and shown that calculation of thermodynamic properties using this method yields values in good comparison to experiment. We have demonstrated the importance of lattice relaxation in the calculation of some of these properties and illustrated this using the calculation of dissociation pressure as an example.

---

[1] LeSar, R., Najafabadi, R. and Srolovitz, D.J., Phys. Rev. Lett., **63**, 624 (1989)
[2] Sutton, A.P., Phil.Mag. A., **60**, 147 (1989)
[3] Rodger, P.M., J. Phys. Chem., **93**, 6850 (1989)
[4] Tanaka, H., Chem. Phys. Lett., **202**,345 (1993)
[5] Berendsen, H.J.C. *et al.*, in *Molecular Dynamics and Protein Structure*, ed. J. Hermans, Polycrystal Book Service, Illinois (1985)
[6] Nicholas, J., Gubbins, K., Street, W.B., and Tildesley, D.J., Mol. Phys., **37**, 1429 (1979)
[7] Bertie, J.E. and Jacobs, S.M., J. Chem. Phys., **77**, 3230 (1982)
[8] Tse, J.S., McKinnon, W.R. and Marchi, M., J. Chem. Phys., **91**, 4188 (1987)
[9] Handa, Y.P. *et al.*, J. Chem. Phys., **94**, 623 (1991)
[10] Sloan, E.D., *Clathrate Hydrates of Natural Gases*, Dekker, New York (1990)
[11] Handa, Y.P., J. Chem. Thermo., **18**, 891 (1986)
[12] Holder, G.D., Corbin, G. and Papadopolous, K., Ind. Eng. Chem. Fundam., **19**, 282 (1980)
[13] Holder, G.D. and Hand, J.H., AIChE J., **28**, 440 (1982)
[14] Karim, O.A., Kay, P.A. and Haymet, A.D.J., J. Chem. Phys., **92**, 4634 (1990)
[15] Rodger, P.M., Forrester, T.R. and Smith, W., Fluid Phase Equilibria, **116**, 326 (1996)

Figure 1(a) Effect of Temperature on Unit Cell Length.

Methane Hydrate.

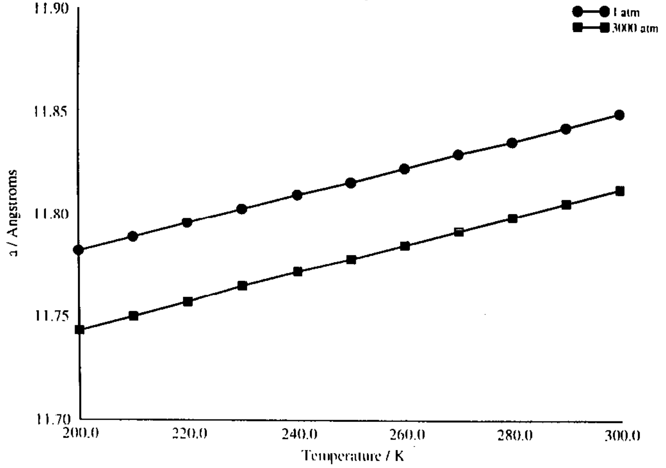

Figure 1(b) Effect of Pressure on Unit Cell Length.

Methane Hydrate.

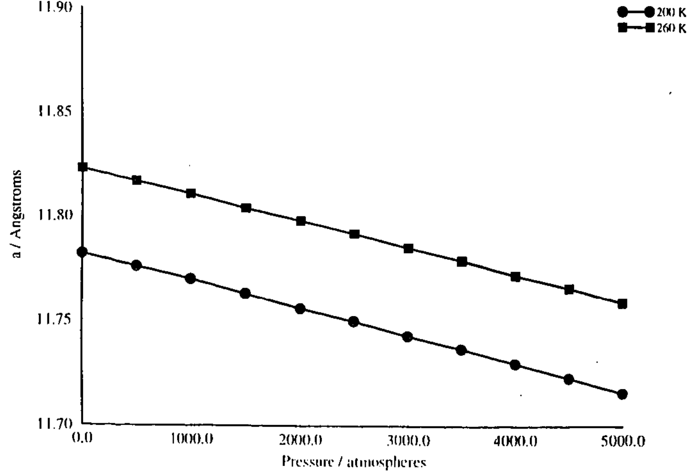

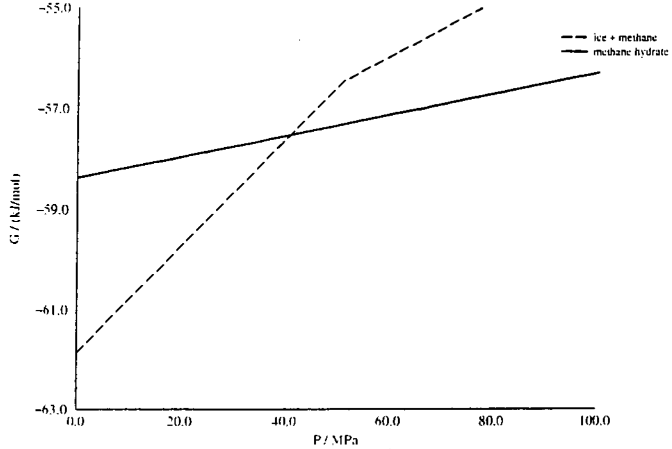

Figure 2. Dissociation Pressure of Methane Hydrate.

Using Unit Cell Optimisation.

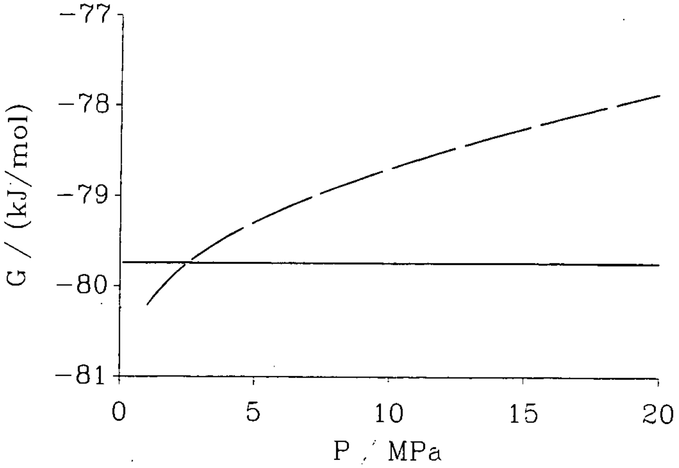

Figure 3. Dissociation Pressure of Methane Hydrate. Using full coordinate optimisation.

SYNTHESIS OF POLYCRYSTALLINE METHANE HYDRATE, AND ITS PHASE STABILITY AND MECHANICAL PROPERTIES AT ELEVATED PRESSURE

Laura A. Stern, Stephen H. Kirby (both at: USGS, Menlo Park, CA 94025)
and William B. Durham (UCLLNL, Livermore, California, 94550)

Key words: *gas hydrate synthesis; reaction kinetics; mechanical properties*

Abstract

Test specimens of methane hydrate were grown under static conditions by combining cold, pressurized CH_4 gas with H_2O ice grains, then warming the system to promote the reaction CH_4 (g) + $6H_2O$ ($s \rightarrow l$) $\rightarrow$ $CH_4{\cdot}6H_2O$. Hydrate formation evidently occurs at the nascent ice/liquid water interface, and complete reaction was achieved by warming the system above 271.5 K and up to 289 K, at 25-30 MPa, for approximately 8 hours. The resulting material is pure methane hydrate with controlled grain size and random texture. Fabrication conditions placed the H_2O ice well above its melting temperature before reaction completed, yet samples and run records showed no evidence for bulk melting of the ice grains. Control experiments using Ne, a non-hydrate-forming gas, verified that under otherwise identical conditions, the pressure reduction and latent heat associated with ice melting is easily detectable in our fabrication apparatus. These results suggest that under hydrate-forming conditions, H_2O ice can persist metastably at temperatures well above its melting point.

Methane hydrate samples were then tested in constant-strain-rate deformation experiments at T= 140-200 K, P_c= 50-100 MPa, and $\dot{\varepsilon}= 10^{-4}$-$10^{-6}$ s^{-1}. Measurements in both the brittle and ductile fields showed that methane hydrate has measurably different strength than H_2O ice, and work hardens to a higher degree compared to other ices as well as to most metals and ceramics at high homologous temperatures. This work hardening may be related to a changing stoichiometry under pressure during plastic deformation; x-ray analyses showed that methane hydrate undergoes a process of solid-state disproportionation or exsolution during deformation at conditions well within its conventional stability field.

INTRODUCTION

Methane hydrate is a nonstoichiometric compound consisting of a network of H_2O molecules that are hydrogen-bonded in a manner similar to ice and interstitially encaging CH_4 gas molecules *(1)*. Distributed globally in shallow marine and permafrost environments, methane hydrate harbors a significant yet virtually untapped hydrocarbon source *(2,3,4)*. Despite scientific interest in this compound and potential commercial importance, many of the physical and material properties of methane hydrate are as yet poorly constrained or unmeasured, and a full understanding of these properties will eventually be needed to turn potential energy projections into practical plans for its recovery. We have now established optimal growth parameters for efficient synthesis of methane hydrate suitable for such testing, and have measured these samples in deformation experiments to determine fracture and flow characteristics. The results revealed some anomalous behavior in the formation, plastic flow behavior, and stability of methane hydrate at elevated pressure *(5)*.

SAMPLE SYNTHESIS

Our objective was to synthesize large-volume, cohesive, low-porosity, polycrystalline hydrate aggregates with controlled, fine grain size and random crystallographic grain orientation. Our technique differs from previous studies *(6)*, most of which involve continuous agitation of reaction mixtures, resulting in strongly textured material unsuitable for materials testing. We produced samples of virtually pure methane hydrate by the general reaction CH_4 (g) +$6H_2O$ ($s \rightarrow l$) $\rightarrow$ $CH_4{\cdot}6H_2O$ (s), by the mixing and subsequent slow, regulated heating of sieved granular ice and cold, pressurized CH_4 gas in an approximately constant-volume reaction vessel (Figs. 1, 2, & 3A).

Sample fabrication details are as follows: CH_4 gas from a source bottle is initially boosted in pressure (P) by a gas intensifier and routed into sample molding vessels housed in a deep freezer. The sample assembly (Fig. 2) consists of two steel vessels immersed in an ethyl alcohol bath initially held at freezer temperature (T) of 250 K. One vessel serves as a reservoir to store and chill pressurized CH_4 gas, and the other houses the sample mold. The mold consists of a hollow split-cylinder that encases an indium sleeve filled with 26 g of H_2O ice "seed" grains, packed to 40% porosity. Seed material is made from a virtually gas-free, single-crystal block of triply distilled H_2O ice, ground and sieved to 180-250 µm grain size. Initially, the sample chamber with seed ice is closed off from the reservoir and is evacuated. A loosely fitting top disk inserted on top of the packed seed ice grains (Fig. 2) prevents displacement of the packed ice grains during evacuation.

The reservoir vessel is first charged with pressurized CH_4 gas to 34 MPa, and cools to 250 K. The reservoir is then opened to the pre-evacuated sample chamber, and CH_4 pressure drops to roughly 22 MPa. These steps serve to fill the porosity between the ice grains at a molar ratio of CH_4 to H_2O in the sample vessel well in excess of that required for full hydrate formation *(7, 8)*. The bath T is then slowly raised by means of the hot plate situated beneath the alcohol bath (Fig. 2). As the sample and reservoir warm, they self-pressurize. Pressure increases steadily with increasing T until reaction initiates, at which point consumption of CH_4 gas by hydrate formation slows the rate of P increase. Data-acquisition software (LabVIEW, National Instruments) was used to monitor and record P and T conditions throughout each run, and the extent of reaction was determined by the measured P_{CH4} offset from the reversible CH_4 expansion curve.

Following full reaction, the heat source is turned off and the system slowly cools back down to 250 K. The sample chamber is then quenched in liquid nitrogen, isolated from the reservoir, vented, disconnected from the apparatus, and opened. The inner, hollow split-cylinder containing the sample is pushed from the mold and pried off the jacketed sample. Samples are then stored in liquid nitrogen until mechanical testing.

THE HYDRATE-FORMING REACTION & POSSIBLE SUPERHEATED ICE

Representative pressure-temperature (P-T) and temperature-time (T-t) histories during a reaction run are shown in Figure 4. Up to at least 271.5 K, CH_4 pressure increases approximately linearly with T with a slope largely governed by the equilibrium thermal expansion of free CH_4 in the reservoir and sample reaction vessel. Progress of the hydrate-forming reaction was monitored by observing the deflection of P from this linear P-T curve, a deflection that accompanies the volume reduction associated with reaction. Completion of the reaction is marked by a P offset (ΔP_r) of 1.8± 0.1 MPa at a peak T of ~ 289 K, a state that is reached over a heating time interval of about 8 hours after the vessel crosses the 271.5 K isotherm (Fig. 4). After cooling to 77 K while venting unreacted CH_4, the resulting samples were shown by x-ray diffraction measurements to be virtually pure methane hydrate, with minor amounts of ice (0-3%) being the only additional phase (Fig. 3). That practically all the H_2O reacted to form hydrate was also consistent with both the calculated molar volume reduction of the reaction *(9)*, and with the lack of a P-T anomaly associated with freezing of unreacted liquid water (Fig. 4A, cooling curve). Measurements of the mass uptake of CH_4 in fully reacted samples also were consistent with essentially complete reaction of the original H_2O to form hydrate of composition near $CH_4{\cdot}6.1H_2O$ ($\pm 0.1H_2O$), which is the expected equilibrium stoichiometry for this compound at approximately 25-30 MPa methane pressure *(9, 10)*. The resulting samples are translucent, white, cohesive aggregates of uniformly fine, equant grains with 250 ± 50 µm grain size. The samples contain 28-30% porosity after full reaction *(9)*. This porosity is eliminated by externally pressurizing sealed samples while venting the pore space gas, which we discuss later.

The detailed P-T-t curves (Fig. 4) and analyses of recovered samples revealed unexpected aspects of the reaction process. Figure 4 shows that deviation of the P-T record from the CH_4 self-pressurization curve first occurs just above the expected melting T of H_2O ice, 271.5 K at 28 MPa. As time proceeds, the rate of P increase slows as the hydrate-forming reaction consumes CH_4 gas *(9)*. X-ray diffraction patterns of samples from runs with maximum temperatures below the ice melting curve showed no evidence of hydrate, and no deflections were observed in the P records to indicate any significant CH_4 mass uptake. Lack of appreciable reaction of CH_4 with ice below the H_2O liquidus was expected, in light of earlier investigations *(6, 8)*.

After approximately 45% ΔP_r, the reaction rate decreases markedly. Full reaction was found to be most readily achieved by continuing to warm the system to conditions approaching the hydrate dissociation curve and well above the metastable extension of the H_2O melting curve (Figs. 1 & 4). To determine the rate of conversion of ice to hydrate at these conditions of T and P as a function of time, a series of partial-reaction experiments were quenched at various points along the full reaction curve, and subsequently weighed and x-rayed to determine hydrate content (Fig. 4, runs A - E). These partial-reaction tests indicate that during the early stages of reaction up to values of roughly 0.5 ΔP_r, the slow rate of seed ice melting still "outpaces" hydrate formation, as there is less hydrate in the samples than would be predicted by ΔP_r [see *(5)* for further discussion]. After this period, the rate of hydrate formation essentially keeps pace with incipient melting for the remainder of the 8 hours needed for full reaction at these conditions.

Figure 4 shows that there are no P-T discontinuities in the fabrication records to indicate bulk melting of the seed ice in the sample molds, even though full reaction to form hydrate at these conditions requires about 8 hours at temperatures well above the H_2O melting curve. The positive slope of the P-T curve within a few degrees above 271.5 K shows that there is not immediate and full melting of the ice as it is warmed above its liquidus, and there is a period of several tens of minutes after crossing the liquidus before there is any substantial indication of either ice melting or hydrate forming. These observations point to the conclusion that a large fraction of the seed ice exists in a superheated state for the many hours needed for full hydrate conversion.

This conclusion was verified by control experiments using neon (Ne, a non-hydrate-forming gas) in place of CH_4 gas, under the same environmental conditions and in the same apparatus as the methane hydrate samples (Fig. 5). We have previously described these results *(5)* and briefly outline them here. The Ne experiments confirmed that rapid, wholesale melting of the H_2O ice during the heating phase and refreezing of ice during the cooling phase of the tests (Fig. 5A) occurs in our apparatus when ice is not in the presence of a hydrate-forming gas, and that the associated P-T anomalies are easily detected. The T measured by the Ne sample thermocouple lags the rising T in the surrounding alcohol bath during the time interval over which the pressure drops (Fig. 5B), a phenomenon that we attribute to the absorption of heat by the expected endothermic melting of ice. In comparison, the T records of CH_4 runs displayed no such thermal anomalies, indicating that rapid, wholesale melting did not occur (Fig. 5B) *(12)*. A prominent refreezing P-T anomaly occurred during the cooling phase of the Ne runs, and no P offset was detected after returning to the starting temperature (Fig. 5A). Visual inspection and x-ray identification of the final, quenched samples from the Ne experiments showed that they consist of clear cylinders of H_2O ice in the bottom of the mold, and that the loosely fitting top disk had sunk to the bottom, indicating full melting. In contrast, fully reacted methane hydrate samples have uniformly fine-grained granular textures and no displacement of the top disk. The Ne control experiments thus demonstrate that all the indicators of ice melting expected in our apparatus are actually observed when a non-hydrate-forming gas is used in the place of methane. The lack of such indicators in the methane experiments implies that such melting does not occur when hydrate is forming at our fabrication conditions.

The apparent suppression of macroscopic ice melting during methane hydrate synthesis raises several important questions; namely, why is full reaction achieved only after many hours at temperatures well above the the H_2O ice melting point, and why is there no evidence for wholesale melting of unreacted seed ice during this time? Probably of greatest influence is the availability of fresh ice surfaces to nucleate hydrate formation. For hydrate formation from either water or ice, the formation rate greatly diminishes once a surface layer of hydrate has formed, and vigorous shaking or stirring to crack the hydrate encasement and renew CH_4 access to ice/water surfaces is needed in order to continue the formation process at appreciable rates *(13)*. Hwang and colleagues *(8)*, however, grew methane hydrate on disks of melting ice to measure hydrate growth rates at constant temperatures under static conditions. They observed two stages of methane hydrate formation, an initial "nucleation" period during which the formation rate increased with time, followed by a "growth" period, during which the formation rate decayed with time until no more ice remained on the disks. Hydrate growth rates were shown not only to be determined by the rate of the supply of the hydrate-forming species to the growth surface, but also by the rate of removal of the exothermic heat of formation from the forming surface *(14)*. They concluded that the onset of melting ice along exposed surfaces not only promoted hydrate formation by providing a "template" for the formation of hydrates, but moreover, provided a heat sink for absorbing the heat of formation during hydrate growth. Once a rind of hydrate has encased an ice grain, the most likely process of continued hydrate formation involves solid-state diffusion of methane gas through the hydrate shell to the ice core *(8, 15)*.

Our observations are in accord with the interpretations of Hwang et al. *(8)*, and additionally we conclude from our sample textures and run records that this surface layer of hydrate encasing each seed ice grain not only rate limits reaction in the grain interior, but also serves to shield the ice grain from nucleating melt by removing the existence of a free external ice surface. A similar superheating effect has been measured in gold-plated silver single crystals, and results suggest that either a free external surface or internal defects or dislocations are critical for melting to take place at the normal "thermodynamic" melting point *(16)*. In our experiments, methane hydrate may be producing a similar effect by shielding the ice cores from nucleating melt and from establishing a liquid-solid H_2O interface, by rapid reaction of incipient melt nuclei with CH_4 gas to form hydrate. We note that our method of seed ice preparation produces grains with few internal grain boundaries, and additionally, the ice grains are likely to anneal at the warm temperatures during fabrication, thus removing many of the internal defects for melt to nucleate on.

SOLID-STATE DEFORMATION TESTING & RESULTS

The strengths of methane hydrate specimens made by the above techniques were measured in constant-strain-rate tests in compression, at conditions ranging from T= 140 to 200 K, confining pressure (P_c) = 50 to 100 MPa, and strain rates ($\dot{\varepsilon}$) = 3.5 x 10^{-4} to 10^{-6} s^{-1} (Table 1).

The testing apparatus is a 0.6 GPa gas deformation apparatus outfitted for cryogenic use, in which N_2 or He gas provides the P_c medium *(17, 18)* (Fig. 6). The thin, soft, indium jackets in which the samples were grown serve to encapsulate them during testing to exclude the P_c medium. Sample interiors were vented to room conditions by means of small-diameter tubing to allow initial compaction to eliminate porosity. The pressurized column within the apparatus consists of an internal force gauge, the jacketed sample, and a moving piston that compresses the sample axially against the internal force gauge at a fixed selected displacement rate ($\dot{u}$). Elastic distortion of the force gauge is measured outside the vessel and changes only with P_c and with the differential load that the piston exerts on the sample. In these experiments, differential force (F) and piston displacement (u) are recorded, corrected for changes from initial cross-sectional area and length (A_o, L_o) to instantaneous values (A, L), and converted to differential stress (σ), axial shortening strain (ε) and strain rate ($\dot{\varepsilon}$) by the relationships: $\varepsilon = u/L_o$; $\dot{\varepsilon} = \dot{u}/L$; $A \cdot L = A_o \cdot L_o$; $\sigma = F/A$. The force-time record (which we convert to stress-strain, as in Fig. 7B) usually reveals a transient response followed by a strength that ceases evolving with time, when various processes of work hardening and recovery have reached a steady-state condition.

Samples were subjected to a hydrostatic pressurization and compaction sequence at 170 K, prior to deformation. During this procedure, P_c was slowly "stepped" up to 100 MPa in increments of about 20 MPa. Following each P step, the piston was advanced to touch and square the bottom of the sample, then advanced just sufficiently to lightly compress the sample in order to compact it with minimal plastic deformation. Six of the samples were compacted using the internal vent line to eliminate the pore-space gas, and two of the samples were compacted without the venting capability. One sample (run 366, Table 1) was examined after compaction in the undeformed state. Volumetric measurements showed that virtually all porosity was eliminated, and that a cylindrical shape was largely maintained with only minor distortion of the sample. X-ray analysis showed evidence of a small fraction of H_2O ice in the sample ($\approx 7\pm3\%$), likely due to a disproportionation of hydrate as increasing P effects a stoichiometric change from $CH_4 \cdot 6.1H_2O$ to $CH_4 \cdot 5.8H_2O$ *(10)*.

A suite of seven hydrostatically-compacted samples of methane hydrate were then tested by the methods described above and at the conditions shown in Table 1. Samples displayed measurably different steady-state strengths than H_2O ice, and results are summarized in Figure 7A. Moreover, the characteristics of transient deformation are markedly different. A typical stress-strain curve for methane hydrate is shown in Figure 7B; whereas H_2O ice ordinarily exhibits a strength maximum before leveling off to steady flow stress, usually within the first 5 - 10% of strain, methane hydrate exhibits monotonic work hardening (or strain hardening) that continues over more than 15% strain. This hardening effect persists to an extreme degree not only relative to other ices, but to most metals and ceramics as well.

Comparison of pre- and post-deformation x-ray diffraction analyses shows that samples underwent further structural changes while deforming within the nominal hydrate stability field. All deformed samples showed a significant volume fraction of ice in their final x-ray patterns (25% ± 10%, Fig. 4B) compared with virtually no ice in their pre-test x-ray patterns (<3%, Fig. 4A), and also showed larger fractions of ice than detected in the pressurized-only sample (run 366). It is possible, however, that either heterogeneous ice precipitation or deformation-enhanced textural and grain size changes in the precipitated ice increased the apparent ice peak intensities. No peaks were observed in post-deformation x-ray patterns to indicate growth of any other new phase besides ice and structure I hydrate. We note that the two non-vented samples (281 & 282), showed equally large fractions of ice in their post-deformation x-ray patterns as the vented samples. After first detecting this apparent solid-state disproportionation of the hydrate, a gas collection system was attached to the vent line for two of the runs to observe and collect possible CH_4 gas evolving during deformation. The only gas that appeared from the vent, however, was that squeezed from the pores during initial pressurization before deformation. No gas evolved from the system during any portion of deformation testing or subsequent unloading. While collapse of the hydrate structure could occur if as-molded material were strongly nonstoichiometric and contained significant lattice vacancies, this is unlikely as we measured nearly full uptake of CH_4 gas into the as-molded material. Double occupancy in lattice cages also seems unlikely as a possible explanation due to spacial considerations. We therefore conclude that at the deformation conditions of this study, methane hydrate appears to undergo a form of stress-enhanced exsolution and/or precipitation process within its nominal stability field. Precipitating H_2O ice may likely be causing a dispersion hardening process during hydrate deformation, a process that will be targeted in further studies.

SUMMARY

Methane hydrate displays exceptional characteristics that merit further investigation into the nature and behavior of this important compound. In the course of establishing optimal growth parameters for synthesizing hydrate samples suitable for rheological testing, we demonstrated that under conditions favorable to hydrate formation, the rate of H_2O ice melting may be suppressed to allow short-lived superheating of ice to temperatures well above its melting point. Deformation tests showed that not only does methane hydrate have a measurably different rheology than H_2O ice, but that it also undergoes extensive work hardening accompanied by a process of solid-state disproportionation during deformation at conditions well within its equilibrium stability field. Such unexpected consequences of methane hydrate formation and deformation may affect the physical, mechanical, and geochemical properties of hydrate-bearing sediments in ways not previously appreciated. In particular, hydrate instability under nonhydrostatic stress may affect environments such as those underlying continental shelves or in associated accretionary prisms prone to regional tectonic influences, where the presence of hydrates influences the strength, stability, porosity, pore-fluid composition, and migration pathways of hydrate-cemented sediments.

REFERENCES & NOTES

1. Natural gas hydrates belong to either of two crystal structures; methane hydrate ($CH_4{\cdot}6H_2O$) is a structure I hydrate (1.2 nm cubic unit cell, space group *Pm3n*), constructed from 46 H_2O molecules and eight cavities available for CH_4 gas molecules.
2. E. Sloan, *Clathrate Hydrates of Natural Gases,* Marcel Dekker, Inc., New York, 641 p., 1990.
3. K. Kvenvolden, *Chemical Geology,* **71**, 41-51, 1988.
4. Because hydrates concentrate methane by a factor of 170 with respect to STP gas and as little as 10% of the recovered energy is required for dissociation, hydrate reservoirs are considered a substantial future energy resource; it has been estimated that the total amount of gas in this solid form may surpass the energy content of the total fossil fuel reserves by as much as a factor of two [*(2)*, *(3)*, also Claypool, G.E., and I. R. Kaplan, in: Kaplan, I. R., (ed), *Natural Gases in Marine Sediments,* Plenum Press, New York, 99-139, 1974].
5. L. Stern, S. Kirby, and W. Durham, *Science,* **273**, 1843-1848, 1996.
6. R. Barrer and D. Ruzicka, *Trans. Faraday Soc.*, **58**, 2253, 1962; R. Barrer and A. Edge, *Proc. Roy Soc.* (London), **A300**, 1, 1967; B. Falabella and M. Vanpee *Ind. Eng. Chem. Fund.*, **13**, 228, 1974; K. Aoyogi, K. Song, R. Kobayashi, E. Sloan, and P. Dharmawardhana, *Gas Processors Assn. Research Report No. 45,* Tulsa, OK, 1980; see Sloan *(2)* for full review of fabrication techniques.
7. Hwang et al *(8)* noted that for hydrate formation from melting ice, higher gas P yields higher formation rates. Makogon *(15)* had earlier suggested that as hydrate formation is an interfacial process, high concentrations of hydrate-forming species are required at the interface.
8. Hwang, M.J., D.A. Wright, A. Kapur, and G. D. Holder, *J. Inclusion Phenom.*, **8**, 103-116, 1990.
9. The volume of an empty structure I hydrate lattice is 16% greater than the equivalent mass of ice I [the empty structure I lattice has a density of 0.78, and stoichiometric methane hydrate has a density near ice (0.90 vs 0.92 for ice)], but there is a large $-\Delta V$ associated with hydrate formation due to the volume reduction of the gas phase into the hydrate structure. Here, we start with 26 g of seed ice, and the actual molar reaction is: $1.4H_2O + 0.23\ CH_4(g) \rightarrow 0.23(CH_4{\cdot}6.1H_2O)$. The 3.8 g of CH_4 uptake measured after sample synthesis confirms this hydrate stoichiometry and is consistant with *(10)*. Independent measurement of CH_4 collected from a dissociating sample also verified this stoichiometry (K. Kvenvolden and T. Lorenson, personal communication). While ΔV of the reaction is nearly 21%, we only measure a 6.4% associated drop from the starting P due to the large volume of the combined reservoir plus sample chamber.
10. Gas hydrate number *n* varies with P; increasing P maximizes guest-molecule site occupancy. At sample synthesis conditions (~28 MPa) *n* for methane hydrate should be 6.1 ± 0.1, and at 100 MPa $n = 5.85 \pm 0.05$ (S. Saito, D. Marshall, and R. Kobayashi, *AICE J.*, **10**, 734, 1964; also see *(11)*, p.54.)
11. *Handbook of gas hydrate properties and occurrence.* U.S. DOE Publication DOE/MC/19239-1546, 234p., 1983.
12. The reaction $CH_4\ (g) + 6H_2O\ (ice) \rightarrow CH_4{\cdot}6H_2O$ liberates a small amount of latent heat {≈ 20 ± 0.3 kJ/mol at 273 K and a CH_4 P of 28 MPa, determined from the Clapeyron slope (T. Makogon and E. Sloan, *J. Chem. and Eng. Data* **39**, 2, 351-353, 1994), the measured enthalpy of formation at standard conditions (Y. Handa, *Chem Thermodynamics* **18**, 915-921, 1986), ΔV_r *(9)*, and its variation with P *(11)*.} This heat is not reflected as a T anomaly (Fig. 5B), evidently because reaction occurs over a period of 8 hours and such heat would be small compared with the exchange of heat of the sample with its surroundings by conduction. (The standard enthalpy for melting of ice is -6.01 kJ/mol, or -36 kJ/ 6 moles for comparison with the hydrate-forming reaction).
13. The importance of vigorous agitation to renew ice/water surfaces for hydrate formation was established by Villard (P. Villard, *Compt. Rend.*, **106**, 1602, 1888) and is also discussed by Sloan *(2)* and Hwang et al *(8)*.
14. Hwang et al. *(8)* note that as hydrate formation is an exothermic process, the heat released by the phase change increases the T at the formation interface. This effect is greater for hydrate formation from liquid water than from ice since the heat of formation is partially absorbed by the melting ice.
15. Y. Makogon, *Hydrates of Natural Gases,* W.H. Cielewicz Translation, PennWell Publishing, Tulsa OK, 1981.
16. J. Daeges, H. Gleiter, and J. Perepezko, *Phys. Lett.*, **119A**, 79, 1986. See also: S. Phillpot, J. Lutsko, D. Wolf, and S. Yip, *Phys. Rev. B*, **40** (5), 283-2840, 1989, and S. Phillpot, S. Yip, and D. Wolf, *Computers in Physics*, **3**, 20-31, 1989, for further discussion of results.
17. H. Heard, W. Durham, C. Boro, and S. Kirby, in *The Brittle-Ductile Transition in Rocks, Geophysical Monograph* **56**, ed. by A. G. Duba et al., American Geophysical Union, Washington, D. C., 225-228, 1990.
18. W. Durham, S. Kirby, and L. Stern, *J. Geophys. Res.* **97**, E12, 20,883-20,897, 1992; also S. Kirby, W. Durham, M. Beeman, H. Heard, and M. Daley, *J. Phys.*, **48**, suppl., 227-232, 1987.
19. This work was supported under NASA order W-18927, and was performed in part under the auspices of the USGS and in part by the U. S. DOE by the Lawrence Livermore National Laboratory under contract W-7405-ENG-48.

Table 1. Mechanical test conditions and results.

Run# (step)		T (K)	P_C (MPa)	$\dot{\varepsilon}$ (s^{-1})	ε_t	σ_y (MPa)	σ_{ss} (MPa)	Comments
281	1	160	50	3.5×10^{-4}	0.125	---	>85	Strain hardening.
	2	160	50	3.5×10^{-6}	0.150	---	60	Strain hardening.
	3	160	50	3.5×10^{-4}	0.160	100	---	Brittle failure. ≈25% H_2O ice[b].
282	1	140	50	3.5×10^{-6}	---	71	---	Failure, multiple events.
	2	140	50	3.5×10^{-4}	0.160	94	---	Failure, multiple events. ≈25% ice[b].
366	1	168	100	---	---	---	---	Pressurization & compaction only[c];
367	1	185	100	3.5×10^{-5}	0.138	---	71	Strain hardening at 10^{-5} step.
	2	185	100	3.5×10^{-4}	0.215	96	90	≈30% ice post-deformation.
368	1	168	100	3.5×10^{-5}	0.185	---	102	Strain hardening. 25% ice[b].
369	1	168	100	3.5×10^{-5}	0.16	---	100	Identical run as 368[d]. No evolved CH_4 gas.
370	1	200	100	3.5×10^{-5}	0.120	---	62	Strain hardening at 10^{-5}. No evolved gas[d].
	2	200	100	3.5×10^{-4}	0.230	85	80	≈30% ice post-deformation.

[a] P_c *is confining pressure gas medium;* ε_t *is total strain;* σ_y *is yield strength;* σ_{ss} *is steady-state strength.*
[b] Post-deformation, determined by x-ray diffraction.
[c] Samples 367, 368, 369, & 370 all underwent identical pressurization and compaction as 366 prior to testing.
[d] Runs 369 & 370 had a gas collection system attached throughout testing to detect evolved CH_4 gas.

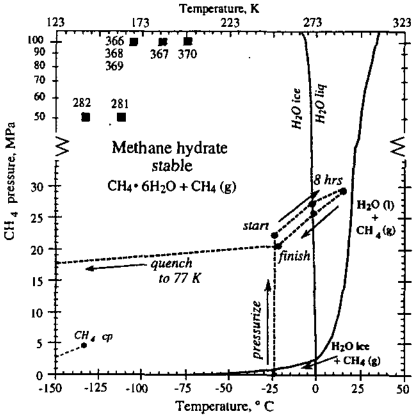

Figure 1: Phase diagram for the CH_4-H_2O system. Shaded region shows field of methane hydrate stability. At low pressures or high temperatures, methane hydrate dissociates to H_2O (ice or liquid) plus CH_4 gas. The metastable extension of the H_2O melting curve is shown by the grey curve. Dashed lines trace the sample fabrication reaction path (described in text.) Solid squares show pressure and temperature conditions of deformation tests (note change in pressure scale on y-axis from linear to log scale.) CH_4 cp designates methane critical point.

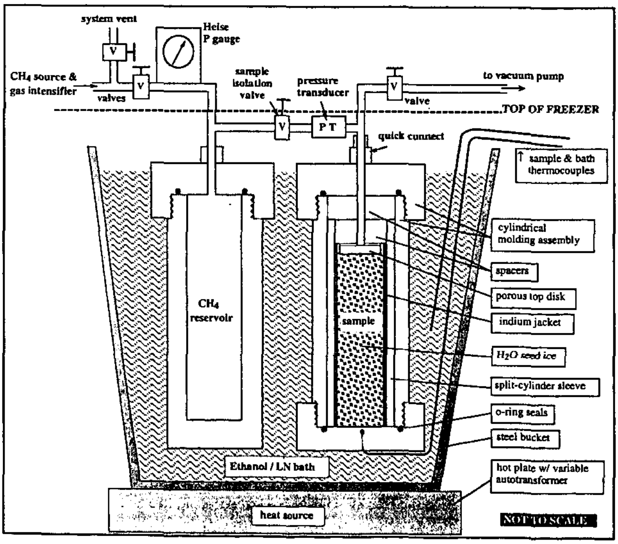
system vent
Heise P gauge
V
CH4 source & gas intensifier
valves
sample isolation valve
pressure transducer
V
valve
to vacuum pump
TOP OF FREEZER
V
PT
quick connect
sample & bath thermocouples
cylindrical molding assembly
spacers
porous top disk
indium jacket
H2O seed ice
split-cylinder sleeve
o-ring seals
steel bucket
hot plate w/ variable autotransformer
CH4 reservoir
sample
Ethanol / LN bath
heat source
NOT TO SCALE

Figure 2: Apparatus for fabricating cylindrical test specimens of methane hydrate from CH_4 gas and melting ice. The sample assembly is housed in a freezer at 250 K, and consists of two steel vessels immersed in an ethyl alcohol bath. One vessel stores a reservoir of cold, pressurized CH_4 gas at 35 MPa and 250 K, and the second contains the sample mold with pre-jacketed and pre-evacuated H_2O "seed" ice. Two-way valves allow isolation of any component of the assembly, and a vacuum pump connected to the sample chamber permits evacuation of the system. The sample chamber is warmed by a hot plate situated beneath the alcohol bath and controlled remotely with a variable autotransformer. Temperature is monitored by thermocouples enplaced in the base of the sample mold and in the bath, and pressure is measured by the gauge and transducer, as shown. Procedures promoting methane hydrate crystallization are described in the text.

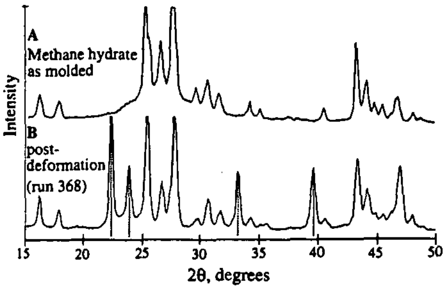

Figure 3:

X-ray powder diffraction patterns for methane hydrate as grown (**A**) and after mechanical testing (**B**). Methane hydrate deformed under nonhydrostatic stress undergoes a partial solid-state disproportionation, as evidenced by H_2O ice peaks (dotted lines) found in post-deformation x-ray diffraction patterns.

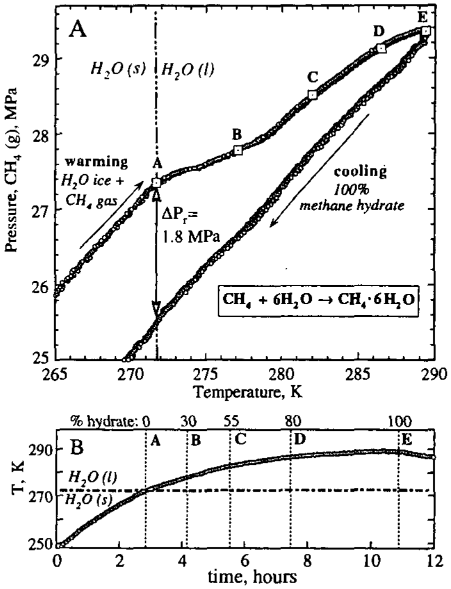

Figure 4:

(**A**) Temperature-pressure profile of sample fabrication conditions promoting the hydrate-forming reaction: CH_4 (g) + H_2O (ice) → $CH_4{\cdot}6H_2O$. Warming the ice + gas mixture above the H_2O solidus (dot-dashed line, point A) initiates reaction. Increasing temperature slowly to 289 K, over an 8 hour span, accelerates full reaction. Complete reaction in our apparatus is marked by a 1.8 MPa pressure drop (ΔP_r) from start to finish. Squares A-E correspond to individual samples that were quenched at specific intervals during hydrate formation to determine hydrate content as a function of ΔP_r and time.

(**B**) Temperature-time profile during hyrate formation. Hydrate content (vol.%) of samples A-E given on top scale bar, and show how the rate of hydrate formation decays with time under static growth conditions.

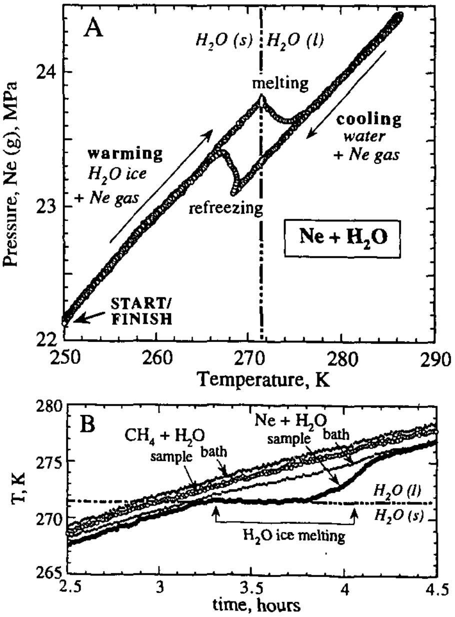

Figure 5:

(**A**) Temperature-pressure record of neon gas + H_2O ice experiment demonstrates full melting and refreezing of H_2O ice near its solidus when in the presence of non-hydrate-forming gas. The Ne + ice run shows no net pressure drop associated with melting and refreezing, so start-finish conditions are coincident.

(**B**) Detail of temperature-time history of Ne (g) + H_2O ice in the region of ice melting, showing the lag of the sample temperature compared to the bath temperature associated with the absorption of heat by the endothermic melting of ice. No such effect is displayed by the themal history of the methane hydrate experiment, also shown (grey open circles).

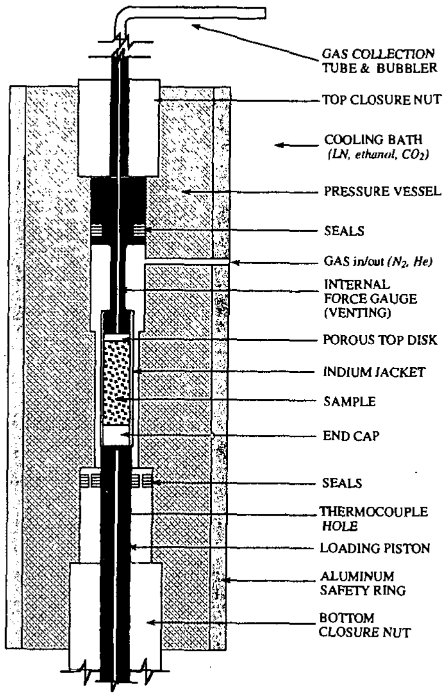
GAS COLLECTION TUBE & BUBBLER
TOP CLOSURE NUT
COOLING BATH (LN, ethanol, CO_2)
PRESSURE VESSEL
SEALS
GAS in/out (N_2, He)
INTERNAL FORCE GAUGE (VENTING)
POROUS TOP DISK
INDIUM JACKET
SAMPLE
END CAP
SEALS
THERMOCOUPLE HOLE
LOADING PISTON
ALUMINUM SAFETY RING
BOTTOM CLOSURE NUT

Figure 6:

Schematic of triaxial gas deformation apparatus set up for methane hydrate testing at cryogenic temperatures. The indium-jacketed sample sits within a cylindrical pressure vessel in which N_2 or He gas provides the confining medium. A sliding piston moves through dynamic seals from below to impose constant axial shortening. Samples are mounted on to a "venting" internal force gauge permitting sample communication with room conditions and allowing initial hydrostatic pressurization to elliminate residual porosity prior to deformation. The gas collection system (shown at top) was attached during several tests to monitor possible loss of methane gas during deformation.

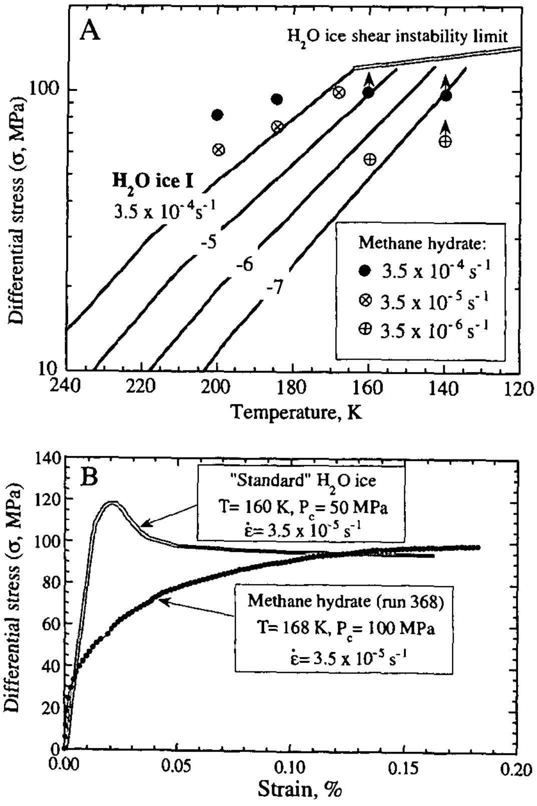

Figure 7:

(**A**) Strength measurements of methane hydrate show that it has measurably different strength than H_2O ice. Ice flow constants are from *(18)*. Methane hydrate data points with arrows indicate faulting behavior.

(**B**) Stress-strain curves of deformed methane hydrate (run 368) compared to "standard" polycrystalline H_2O ice. While the strengths of the two compounds are comparable, methane hydrate undergoes systematic strain hardening to an extreme degree (over 18% strain) while H_2O ice typically displays an ultimate yield strength followed by relaxation to steady state behavior.

NEW METHOD OF TEMPERATURE-RAMPING, ISOBARIC EXPERIMENTS TO STUDY THE HYDRATE FORMATION AND DECOMPOSITION

Guillaume Besnard, Kyoo Y. Song, Joe W. Hightower, Riki Kobayashi, Doug Elliot*, and Roger Chen*, Department of Chemical Engineering, MS-362, Rice University, 6100 Main Street, Houston, Texas 77005-1892.
* International Process Services, Inc., a subsidiary company of the Bechtel Corp., P. O. Box 2166, Houston, Texas 77252-2166.

Key Words: Hydrate, Methane, Solubility, Enthalpy, Entropy

Gas hydrate formation and decomposition involving methane in water has been studied in a series of temperature-ramping, isobaric, variable-volume experiments. Results obtained have provided novel information on (1) gas solubility in the liquid phase at temperatures in the vicinity of hydrate formation, (2) derived thermo-physical properties such as enthalpy, entropy, etc., and (3) details of the mechanism of hydrate formation/decomposition. Also, heats of dissolution/formation may be obtained indirectly from these results. An attempt was made to overcome experimental difficulties which had been imposed by the appearance of the hydrate solid phase. Such detailed solubility information will add substantially to the scarce data currently available in the literature.

INTRODUCTION

Though the existence of hydrates was demonstrated by Davy (1) in the early part of the nineteenth century, current interest dates from 1934 when Hammerschmidt (2) discovered that hydrates were responsible for plugging natural gas lines. This discovery stimulated numerous studies to determine the hydrate structure and its formation and decomposition conditions. The authors have recently employed a temperature-ramped, isobaric (constant pressure), variable-volume technique that is capable of providing continuous details of hydrate formation and decomposition. Furthermore, the method enables a straightforward calculation of solubility of the hydrate former in the host phase which may be pure water or aqueous solutions.

Information on the solubility of gases like CH_4 in pure water is very useful for the calculation of some derived thermo-physical properties such as the enthalpy of solution, the enthalpy of formation, and the entropy change of the solution. Gas solubility has been extensively studied (5-12) and found to be extremely low. It has been generally reported for temperatures above ambient. However, the same information at the low temperatures and high pressures is very scarce. The solubility of hydrate formers, such as methane, ethane, carbon dioxide, etc., is not easily measurable due to the appearance of the hydrate solid phase, metastable phases, etc. The increase of the solubility with decreasing temperature can be explained by the formation of an ice-like structure (i.e. pentagonal dodecahedra) in the solvent (13-16). Another explanation is that displacement of solvation equilibrium occurs with changes in temperature ($\Delta H_{solv}<0$) and that the solute introduces low entropy structures in water (15-17). The solvation of gas, R, is considered as a relaxation to the equilibrium process described as follows:

$$R + nH_2O = R(H_2O)n.$$

First introduced by Pauling (3) in 1957 and expanded in recent studies (12-18), a concept has developed that the hydrate structure has a geometry similar to basic water structure and the liquid forms its own "buckyballs". The "buckyball" includes 21 water molecules, 20 of which form a pentagonal dodecahedron with one molecule in the middle to add stability to the cage. At ambient temperature, it was proved that these structures are metastable and flicker in and out of existence (19). Sloan and Fleyfel (4) in 1991 proposed a kinetic model of gas hydrate formation from ice assuming that during the nucleation period considerable metastability occurs because of the forming and breaking of structures. Although many more detailed studies are required, our experiments have made it possible to detect the different steps suggested by Sloan et al. (4).

The solubilities of methane and ethane in water at low pressures (3.45 and 0.66 MPa, respectively) have been reported earlier (20). This paper reports results for methane obtained at higher pressures (10.48 and 13.93 MPa) in the temperature range 291.2 to 278.2 K, which includes the hydrate formation conditions, and divergence of these measurements from solubility predicted by Henry's law is presented.

EXPERIMENTAL SECTION

Experimental Apparatus

Calorimeter

A differential calorimeter, which is a variation of the common heat flux calorimeter (21), used in these studies consists of two symmetrical containment vessels, both thermally insulated from the surrounding aluminum block. One containment vessel serves as the sample cell while the other vessel serves as a reference. The surrounding block temperature is ramped at a fixed rate, (by using heating and/or refrigeration), allowing a steady-state heat flux between the sample vessel and the surroundings. But the calorimeter can also be used in an "isoperibolic" operation where the surrounding block is held at a constant temperature (22). The calorimeter is equipped with an internal electrical conductivity cell to track the amount of water in the hydrate and liquid phase by monitoring the conductivity of a dilute KCl solution during hydrate formation.

Moreover, any heat exchange between the containment vessel and the surrounding block occurs almost exclusively by conduction and is measured by two thermopiles. The resulting differences in voltage for the two thermopiles represent the differential heat flux for the two containment vessels. Integrating this voltage over time gives the total heat transfer associated with "the event." However, for this work, the heats of dissociation have been calculated from the solubility of methane since the thermopile values were not reliable enough to provide us with consistent data. Figure 1 shows the apparatus and the pressure-maintaining system.

Computer/data acquisition

Performance of the calorimeter strongly depends on the control and data acquisition program for the computer. Our program is capable of handling various data acquisitions while controlling the pressure and the temperature precisely. The program has been written in "Visual Basic" and can set heater load and pump position (i.e. volume of gas added to the cell during the ramping experiments). The pressure is controlled every four seconds, and the data are collected every minute, allowing precise control of the temperature-ramping, isobaric experiments. Measurements were made during the data acquisition from two pressure transducers, three PRTs, a thermopile, and an electrical conductivity device.

The stepping motor, Genrad RLC Digibridge, HP multimeter, and Keithley digital multimeter are controlled via an IEEE interface. Pressure transducers and a temperature controller are interfaced via an RS232. Figure 2 shows a block diagram of the control and data acquisition systems.

Experimental Procedure

The right cell of the calorimeter shown in Figure 1 is first charged with roughly 650 grams of the dilute aqueous potassium chloride solution (~0.004 normal) prepared with ultra-pure water (17.0 megaohm-cm resistance) and Baker Analyzed Reagent grade salt. This solution fills approximately two thirds of the cell, in order to insure that the electrical conductivity cell be immersed, and magnedrive propellers provide vigorous mixing of the cell contents. After the system has been evacuated to remove air, methane gas is introduced to the system comprising the calorimeter cell, the right pump, and the pressure lines.

The fundamental measurement is the change in volume of the digital pump during the temperature-ramping experiments while the pump is controlled by a stepping motor to maintain the pressure constant. The stepping motor is actuated by a digital-based driver which is controlled by a computer through the IEEE interface. The system consists of the stepping motor, Digidrive, transformer, and 2100 Indexer with an IEEE interface. Flow rates range from 5 to 96 cc/min has been achieved. The pump is able to add to or withdraw gas from the cell at very precise rates. But precise control of the isobaric operation strongly depends on the pressure transducer that closes the loop. They are rated at 10,000 psia with an accuracy of 0.07%. The displacement of the plunger of the pump gives us the volume of methane gas added to the cell, hence the solubility of methane in water-rich phase.

RESULTS AND DISCUSSION

Plots of changes in the system volume versus temperature, as shown in Figure 3, present typical experimental results in a way similar to that used previously (20). However, the current pressures (10.48 and 13.93 MPa) are much higher than the previous one, 3.45 MPa. Figure 3 shows different regions along the curve which are:

a) Cooling

(1) An interstitial solubility where gas is dissolved into water according to

Henry's law.

(2) Solubility of the gas begins to increase beyond that accounted for by Henry's law.

(3) The gas intake by the water increases, and this point is commonly called a catastrophic temperature(Tc). The solubility continues to increase.

(4) Catastrophic hydrate formation occurs, and the amount of solid present in the water has drastically increases.

(5) Solidification starts but the magnetic stirrer is still running.

b) Heating

(6) Dissociation of the hydrates begins. The hydrate crystals start melting and the volume maintains a constant value.

(7) The volume drops very fast and the hydrates are almost completely decomposed. The volume returns to its initial value.

Figures 4 and 5 show calculated methane solubility of (log[mole fraction CH_4 in water]) at 13.93 MPa (2020 psia) plotted vs. (1/T) and Ln (T), respectively, while Figure 6 presents the solubility of methane (1000 * X_{CH4}) vs. temperature at 10.48 MPa (1520 psia). Table 1 provides the solubility of methane gas in pure water obtained during the temperature-ramping experiment at a rate of 1.2°C/hr, for both pressures of 10.48 and 13.93 MPa. Table 2 presents the changes of enthalpy and entropy obtained by plotting Ln(x) versus 1/T (T in K) from the relation of

$$d\,Ln(x) / d\,(1/T) = -\Delta H/R$$

and Ln (X) vs. Ln (T) (again, T in K) by the relation:

$$d\,Ln(x) / d\,ln(T) = +\Delta S/R\ .$$

We had to extrapolate the available literature data of methane solubility in water far above hydrate formation condition (5) to establish a reference for the solubility of methane in pure water in the low temperature region.

Figures 3 and 4 demonstrate a sudden increase of the gas solubility from the extrapolated values. Below 17°C, the liquid solution becomes supersaturated with methane gas. Song et al. (20) attributed this increase to a "sorption" effect with the ordering of water molecules into an ice-like structure with the water molecules surrounding the hydrocarbon molecules. These ordered structures result from contact of the hydrocarbon with water which induces small dipole moments into the hydrocarbon molecules and allows some ordering through weak dipole-induced dipole interactions with the water. The number of water molecules affected by the interaction with the hydrocarbon solute is related to the size of the guest molecule, i.e. the contact surface of the guest molecule. Therefore, the size of the "ice-like" structures will increase with the size of the hydrocarbon (24).

At Tc, the catastrophic temerature at which hydrate crystals start to form, the solubility is increased by 78 % for 10.48 MPa and 51 % for 13.93 MPa. After hydrate crystals are formed, the solubility still increases, showing a high level of supersaturation of methane gas in liquid water, which started just before and just after Tc. These solubility measurements emphasize the crystallization-like process taking place during hydrate formation. The dissolved gas molecules form the nuclei which initiate the process of hydrate precipitation and crystal growth. One might state that around Tc, the nucleation occurs as a result of a fluctuation in free energy due to the local temperature and pressure fluctuations, of sufficient importance to surmount the free energy barrier (12).

From an energy point of view, the changes of enthalpies and entropies are negative and in agreement with reported values (20, 22, 25). The changes in enthalpy and entropy, as the temperature approaches Tc, could be compared with ice formation on one hand and experimental heats of dissociation on the other. The enthalpy of dissociation for the methane hydrate at 13.93 MPa is very close to the enthalpy of dissolution of the same gas when Tc is approached, as found previously (12). Moreover, the comparison of the entropies of solution derived here with corresponding values based on the same standard state for gases in non-polar solvents at 25°C shows that the entropies of solution in water are all negative by a large amount. The partial molal entropy of solution is influenced by the size of the cavity created by the gas molecules when the estimate of the cavity size is made by bond distances. Frank and Evans (15), and Song el al. (20) have demonstrated that the large negative values for partial molal entropies of solution of non-polar gases in water can be understood as the creation of a more highly ordered state in water or "icebergs". As the temperature is increased, these quasi-ice-like structures break up and ΔS becomes positive.

CONCLUSION

A fully automated calorimeter with some modifications has facilitated isobaric (constant pressure), variable-volume, and temperature-ramped experiments, and the experimental procedure has enabled us to elucidate discrete steps involved in the hydrate formation and decompostion for a high pressure methane-water system in a continuous manner.

Simultaneously, the measured volumes were utilized to determine directly methane gas solubility in the water phase in a way that minimizes uncertainties associated with the appearance of the solid hydrate phase.

Of importance, it has been confirmed that the solubility of methane gas in water in the vicinity of the incipient hydrate formation temperature is much greater than that would be predicted by Henry's law, a frequently-used conventional calculation procedure.

Finally, the obtained solubility was used to calculate derived thermo-physical properties, i.e. changes of enthalpy and entropy of the solution.

LITERATURE CITED

(1) Davy, H. *Phil. Trans. Roy. Soc.*, London **1811**, *101*, 1.
(2) Hammerschmidt, E. G. *Ind. Eng. Chem.* **1934**, *26*, 851.
(3) Pauling, L. The Structure of Water Hydrogen Bonding. Hadzi, D. Pergamon Press, **1959**.
(4) Sloan, E. D.; Fleyfel, F., *J. AIChE* **1991**, *37*, 1281.
(5) Culberson, L.; McKetta, J. *AIME Trans* **1950**, *189*, 1.
(6) Kobayashi, R. *Vapor-LIquid Equilibrium in Binary Hydrocarbon-Water systems.* Ph-D Dissertation, University of Michigan, **1951**.
(7) Katz, D.L.; Cornell, D.; Vary, J.; Kobayashi, R.; Elenbaas, J.R.; Poettman,F.H.; Weinang, C.F. *Handbook of Natural Gas Engineering* **1959.**
(8) Clever, H.L.; Han, C.H. *ACS Symp. Ser.* **1980**, *133*, 513.
(9) Clever, H.L.; Battino, R. *Role. Data Sci. Prog.* **1986**, *9*, 209.
(10) Battino, R. *Sol. Data Ser.* **1986**, *24*, 1.
(11) Battino, R. *Sol. Data Ser.* **1987**, *27*, 1.
(12) Feneyrou, G. *Elucidation of the Formation and Decomposition of Clathrate Hydrates of Natural Gases through Gas solubility Measurements.* M.S Dissertation, Rice University, **1996** .
(13) Klotz, I.M. *In Protein Structure and Function,* Brookhaven Symposia in biology **1960**, *13*, 25.
(14) Patterson, D.; Barke, M. *J. Phys. chem.* **1976**, *80*, 2435.
(15) Frank, H.S.; Evans, M.W. *J. Chem. Phys.* **1945**, *13*, 507.
(16) Kauzmann, W. *Adv. Protein Chem.* **1959**, *14*, 1.
(17) Nemety, G.; Scheraga, H.A. *J. Phys. Chem.* **1962**, *36*, 3401.
(18) Fleyfel, F.; Song, K.Y.; Kook, A.; Martin, R.; Kobayashi, R. *J. Phys. Chem.* **1993**, *25*, 6722.
(19) Bernal, J.D. *Royal Society on Physics of Water and Ice* published in Hydrogen Bonding, Pergamon Press **1957.**
(20) Song, K.Y.; Feneyrou, G.; Fleyfel, F.; Martin, R. Lievois, J.S.; Kobayashi, R. *Solubility Measurements of Methane and Ethane At and Near Hydrate Conditions, in press,* Fluid Phase Equilibria **1996.**
(21) Calvet, E.; Prat, H. *Recents Progres en Microcalorimetrie* Dunod Edition Paris **1958.**
(22) Lievois, J.S. *Development of an Automated, High Pressure Heat flux Calorimeter and its Application to Measure the Heat of Dissociation of Methane Hydrate.* Ph-D Dissertation, Rice University, **1987.**
(23) Frank, H.S.; Wen, W.Y. *Discussion Faraday Society* **1957**, *24*, 133.
(24) Himmelblau, D.M. *Partial Molal Heats and Entropies of Solution for Gases Dissolved in Water from the Freezing Point to Near the Critical Point.* J. Phys. Chem. **1959**, *63*, 1803.
(25) Rettich, T.R.; Handa, Y.P.; Battino, R.; Wilhem, E. *Solubility of Gases in Liquids. High-Precision Determination of Henry's Constants for Methane and Ethane in Liquid Water at 275 to 328 K* J. Phys. Chem. **1981**, *85*, 3230.
(26) CSMHYD - hydrate program developed by the Colorado School of Mines (Dendy E. Sloan), available through the Gas Processors Association (GPA), Tulsa, Ok.

Table I. Solubility of Methane Gas in Water (Obtained from Temperature-Ramping (1.2 °C/hr), Variable-Volume, Isobaric Experiments)

pressure, MPa a (psia)	temp., K (°C)	sol. of CH_4, X_{CH4} *1000	pressure, MPa a (psia)	temp., K (°C)	sol. of CH_4, X_{CH4} *1000
10.48	291 (18.0)	2.04	13.93	292 (19.0)	2.96
(1520)	289 (16.0)	2.41	(2020)	290 (17.0)	3.22
	288 (15.0)	2.61		289 (16.0)	3.92
T^a =11.6 °C	285 (12.0)	3.62	T^a =14.6 °C	289 (15.5)	4.23
T^b =16.0 °C	285 (11.6)	4.09	T^b =18.0°C	288 (14.6)	5.03
T^* =13.8 °C	284 (11.0)	4.45	T^* =16.24°C	287 (14.0)	6.68
	283 (10.0)	5.17		286 (13.0)	11.29
	282 (9.0)	5.92		285 (12.0)	6.72
	280 (7.0)	7.54		283 (10.0)	25.70
	279 (6.0)	9.17		280 (7.0)	37.20
	278 (5.0)	11.41		279 (6.0)	44.95
				278 (5.2)	52.44
	298 (25.0)^c	1.98			
				298 (25.0)^c	2.62

a initial hydrate formation temperature,
b final decomposition temperature,
* predicted from hydrate program of Colorado School of Mines (22),
c obtained from Culberson and McKetta (1).

Table II. Derived Thermo-Physical Properties of a Methane-Water System (Obtained from Solubility Measurements)

pressure, MPa a (psia)	range of temp., °C	change of enthalpy, ΔH, KCal/mole of gas	change of entropy, ΔS, Cal/mole.K
10.483	16.0 to 12.0	-16.8	-58.6
(1520)	12.0 to 11.6	-47.7	-170.5
T^a = 11.6 °C	11.6 to 7.0	-21.1	-74.7
T^b =16.0 °C	7.0 to 5.0	-32.0	-115.9
T^* =13.8 °C			
13.931	19.0 to 17.0	-7.1	-24.4
(2020)	16.0 to 14.6	-27.5	-95.2
T^a = 14.6 °C	14.6 to 13.0	-87.8	-308.9
T^b = 18.0 °C	12.0 to 6.0	-26.1	-92.3
T^* = 16.24 °C			

a initial hydrate formation temperature,
b final decomposition temperature,
* predicted from hydrate program of Colorado School of Mines (22).

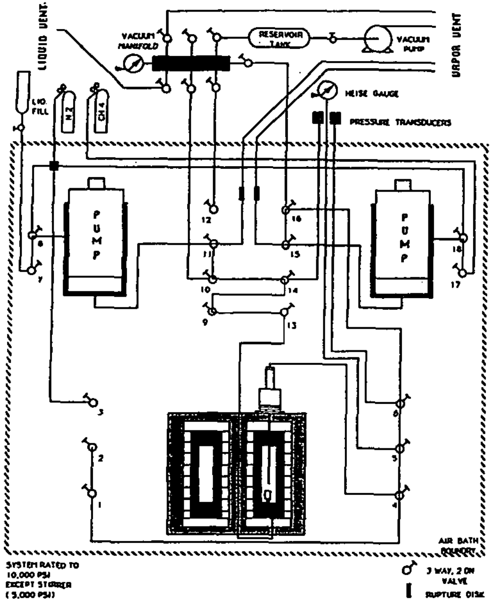
LIQUID VENT.
VACUUM MANIFOLD
RESERVOIR TANK
VACUUM PUMP
VAPOR VENT
LIQ. FILL
N2
CH4
HEISE GAUGE
PRESSURE TRANSDUCERS
PUMP
PUMP
1
2
3
4
5
6
7
8
9
10
11
12
13
14
15
16
17
18
AIR BATH BOUNDARY
SYSTEM RATED TO 10,000 PSI EXCEPT STIRRER (5,000 PSI)
3 WAY, 2 ON VALVE
RUPTURE DISK

Figure 1. Calorimeter apparatus used for temp.-ramped, isobaric, and volume-variable experiments.

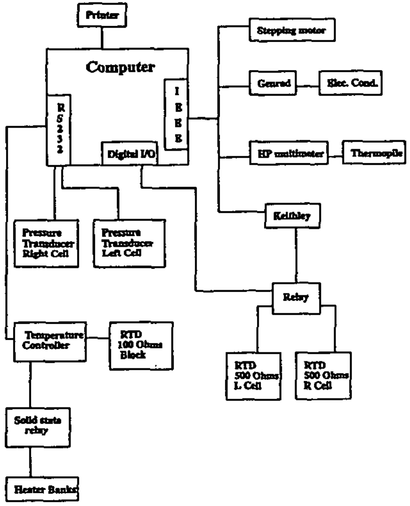
Printer
Computer
RS232
IEEE
Digital I/O
Stepping motor
Geared
Elec. Cond.
HP multimeter
Thermopile
Keithley
Relay
RTD 500 Ohms L Cell
RTD 500 Ohms R Cell
Pressure Transducer Right Cell
Pressure Transducer Left Cell
Temperature Controller
RTD 100 Ohms Block
Solid state relay
Heater Banks

Figure 2. Block diagram of pressure and temperature controls and data logging system.

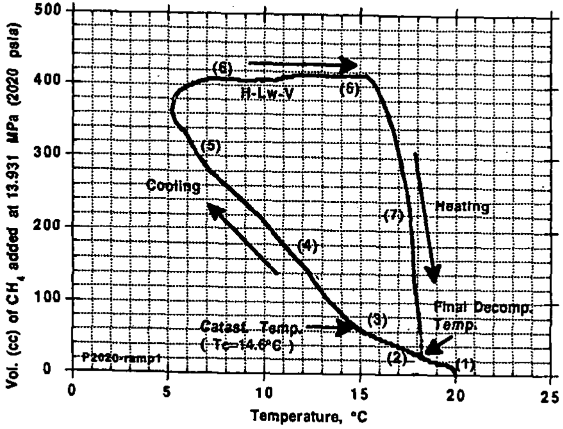

Figure 3. Change of system vol. vs. temp. for a methane and water system at 13.931 MPa (2020 psia) when the air bath temp. was ramped at 1.2°C/hr.

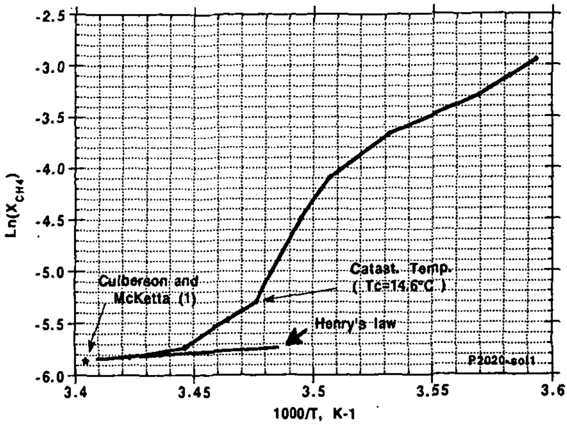

Figure 4. Logarithm of solubility (mole fraction) of methane in the water phase vs. reciprocal of the absolute temp. for a methane and water system at 13.931 MPa (2020 psia).

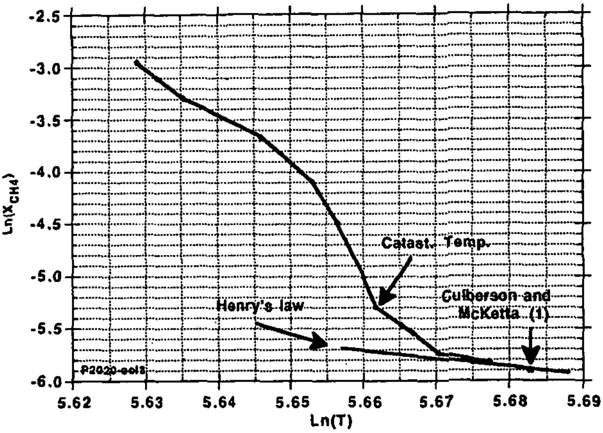

Figure 5. Logarithm of solubility (mole fraction) of methane in the water phase vs. logarithm of absolute temp. for a methane and water system at 13.931 MPa (2020 psia).

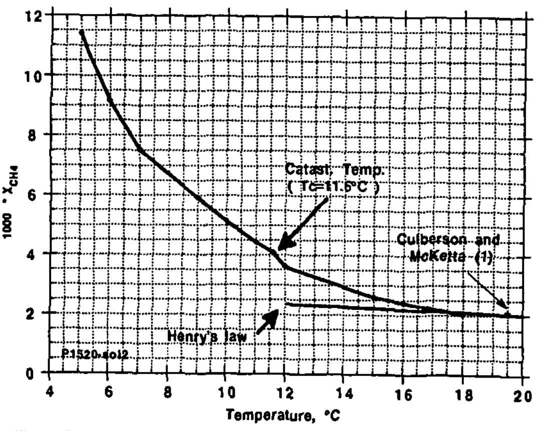

Figure 6. Solubility (mole fraction) of methane in the water phase vs. temp. for a methane and water system at 10.483 Mpa (1520 psia).

GROWTH AND INHIBITION PHENOMENA OF SINGLE HYDRATE CRYSTALS

Roar Larsen,
Norwegian University of Science and Technology, N-7034 Trondheim, Norway
Taras Y. Makogon,
Colorado School of Mines, Golden, CO, 80401
Charles A. Knight,
National Center for Atmospheric Research, Boulder, CO, 80307
E. Dendy Sloan, Jr.,
Colorado School of Mines, Golden, CO, 80401

Keywords: hydrate single crystals, crystal growth habit, hydrate inhibition

ABSTRACT

Single crystals of structure II (sII) and structure I (sI) hydrates were grown in aqueous tetrahydrofuran (THF) and ethylene oxide (EO) solutions. Normal growth habits from the melt are {111} crystallographic planes for sII, and {110} for sI. Addition of polymeric inhibitors in very small amounts changed the growth habit of sII to thin, 2-dimensional hexagonal {111} plates, and caused rapid small-scale branching of sI crystals. The highly branched sI crystals were found to still be single crystals. Higher concentrations of inhibitor were found to stop the growth of sII crystals completely. These concentrations were as low as 0.1 wt% at low supercooling. The minimum concentration needed to stop growth changed with temperature, polymer characteristics and solution agitation. Experiments showed the polymer adsorption to be practically irreversible, and an inhibition hypothesis was developed.

INTRODUCTION

Natural gas hydrates are of great interest from several different viewpoints. Historically, hydrates have been studied as a nuisance causing problems in the oil and gas industry (Englezos, 1993). Over the previous decade another motivation for study has been their role as deposits of immense energy resources in subsea sediments and subterranean permafrost (Kvenvolden, 1994). Just recently, the economics of using hydrates as a suitable storage and transport medium for natural gas have been addressed anew (Gudmundsson and Bϕrrehaug, 1996). A comprehensive overview of hydrates is given by Sloan (1990).

This work uses model systems as an analogue to natural gas hydrates. To circumvent the need for high pressures or very low temperatures, tetrahydrofuran (THF) and ethylene oxide (EO) aqueous solutions are used to form structure II (sII) and structure I (sI) hydrates, respectively. THF and water mixed at the stoichiometric ratio for hydrates (17 water molecules per THF molecule) has a hydrate equilibrium melting point of about 4.4°C at 1 atm. pressure. For ethylene oxide at stoichiometry (23 water molecules per 3 EO molecules) the equilibrium melting temperature is about 11°C. In natural gas applications, sII is the predominant structure.

Over the past 50 years, the thermodynamics of hydrates have been studied extensively, to the point where commercially available simulation codes can predict equilibrium conditions with an accuracy good enough for most practical purposes. The kinetics of hydrate growth have not reached nearly the same level of resolution. Several groundbreaking studies have increased our understanding, but much work still remains to be done. This work takes a very basic approach, studying single crystals of the hydrate structures.

In addition to the basics of crystal growth, the main focus of this work is to study the effects of addition of inhibitors to the systems. Thermodynamic inhibitors like methanol have traditionally been used to alleviate or avoid problems with hydrates in the oil and gas industry, but the use of these can have severe implications for economy, logistics and product quality. There has therefore been a significant driving force towards finding better inhibitors which will work at much lower concentrations. There are two main classes of these inhibitors: anti-agglomerants (emulsifying agents) and kinetic inhibitors (chemicals that interfere with the growth process of the hydrate crystals). We have studied three of the best-known kinetic inhibitors in some detail. These are poly(vinylpyrrolidone) (PVP), poly(vinylcaprolactam) (PVCap) and a terpolymer of vinylpyrrolidone, vinyl caprolactam and dimethylaminoethylmethacrylate (VC-713) (Lederhos et al., 1996).

EXPERIMENTAL PROCEDURES

The growth cell used in our experiments is shown in Fig. 1. It consists of a transparent plexiglass cooling jacket for temperature control to within 0.1 K. Glass test tubes extend into this cooling chamber, and are filled with the experimental solution. The temperature is set to a predetermined level of supercooling and the solutions are left to equilibrate before proceeding. A rubber cap holds a thin glass pipette in the middle of the test tubes (open to the atmosphere at the top and to the experimental solution at the bottom). Crystal nucleation and initial growth is forced by inserting a cold wire into the pipette, creating a momentarily large local supercooling as well as a nucleation surface. The crystal growth then progresses inside the pipette, and, more often than not, nicely defined single crystals emerge into the test solution when the growth reaches the tip of the pipette. The cooling chamber has several test tubes, enabling quick transfer of crystals between uninhibited and inhibited solutions at the same temperature.

RESULTS

Uninhibited crystal growth

THF hydrate sII crystals grown from the melt (the stoichiometric solution) exhibit the {111} crystallographic planes, in the form of regular octahedra. One such crystal is shown in Fig. 2. Irregularities in form were sometimes observed, but at moderate supercooling (0-4 K) the {111} planes were always dominant. Higher supercooling resulted in skeletal crystals while still retaining the octahedral outline. Even higher supercooling (>8 K) resulted in dendritic growth of the crystals. Over the supercooling range of 0-5 K, the growth rate of these crystals was found to be exponential as a function of the supercooling.

Crystals of EO hydrate (sI) grown from the melt exhibit the {110} crystallographic planes, in the form of a dodecahedron with rhombic faces. This is the same shape as the common garnet. Fig. 3 shows one such crystal grown at a supercooling of 0.5 K. So far, no clear evidence of other crystallographic planes has been found for this system.

Crystal growth with inhibitors

For the THF hydrates, substantial changes in growth habit is observed already at very low concentrations of inhibitor in the system. For a supercooling of 1.4 K, concentrations lower than 0.1 wt% of PVP, PVCap or VC-713 all change the growth from octahedra to two-dimensional hexagonal plates. The large faces of these plates are still {111} planes, but some questions remain as to the orientation of their thin edges. The orientation of these planes is shown in Fig. 4, where an uninhibited octahedral crystal was transferred to a solution with inhibitor. The planes grow off the edges of the existing crystal, or sprout from its body, but are always parallel to the facets of the original crystal.

At slightly higher concentrations of the inhibitors PVCap and VC-713, further crystal growth is inhibited completely. At a magnification of 50x, no growth of the crystal faces could be measured over a period of more than 24 hours. This phenomenon is seen at concentrations from 0.1 wt% at 1.4 K supercooling for the best inhibitor polymers. The minimum concentration needed to achieve full inhibition depends strongly on the supercooling and to some degree also on the polymer type and molecular weight, as well as solution agitation. Fig. 5 shows one example of the dependence on supercooling. PVP does not produce complete inhibition, even at concentrations as high as 5.0 wt%.

To study the assumed adsorption of the polymers to the crystal surface, a set of experiments were conducted in which crystals which had been exposed to the no-growth solutions for periods ranging from 5 minutes to several hours were transferred back to uninhibited solutions. None of these crystals showed any further growth until at least 3 hours after being transferred back, and then only from the vertices of the original crystals, or from the interface between the crystals and the glass pipettes. The new growth quickly grew throughout the tubes and obscured any further investigation of the surface of the original crystals.

As control experiments, several tests with known non-inhibitors were performed. Polyvinyl alcohol, urea, hydroxyethylcellulose and polyacrylamide show no impact on the growth habits of the sII crystals at all. These chemicals were chosen because of their solubility in water, and in some cases for their similarity to the polymeric inhibitors in having a vinyl backbone and high hydrogen bonding capability.

EO hydrate crystals show an even more dramatic change of growth habit when a small amount of inhibitor is added to the melt. Low concentrations (0.1-0.2 wt%) produce rapid, small-scale branching of the crystals, producing spherical globules with flimsy branches. This effect was obtained only with PVCap and VC-713. Further experiments in flat capillaries on a cooled bed under a microscope revealed that the branching EO crystals are most likely still single crystals. At intermediate concentration of inhibitor, when the branching had clearly started but were still visibly faceted, the individual branches were seen to preserve a constant crystallographic orientation throughout (Fig. 6).

The EO hydrate system is still under investigation concerning the possibility of complete inhibition.

DISCUSSION

Crystal growth planes which are exhibited macroscopically are the slowest growing planes (faster-growing planes grow out of existence). Studying molecular models of the sII hydrate, it is evident that the 6-membered rings of the large cavities all lie in the {111} planes. This suggests a hypothesis for the normal growth habit, appealing to a presumed higher energy barrier against producing these rings compared to the 5-membered rings. The H-bonds between water molecules are strained more from their natural angle in forming 6-membered rings than in forming 5-membered ones. We therefore believe this process is slower, and may result in the planes containing these rings being the slowest growing. This hypothesis is strengthened when noting that 5-membered rings seem to be naturally occurring structures in water (Rahman and Stillinger, 1973). This contrasts with Smelik and King (1996) who describe a mechanism where forming of the 5^{12} cages is viewed as the controlling factor. Our hypothesis does not transfer directly to the sI hydrate, but a similar argument can be made about specific {110} planes having a higher number of hexagonal rings per unit area (although not parallel to the plane) than e.g. the {100} or the {111} planes. No clear evidence for either of these hypotheses has been presented to date.

The exponential shape of the curve for growth rate vs. supercooling would indicate that the so-called Jackson α-factor is greater than 3 (Myerson, 1993), suggesting that the surface of the growing THF hydrate is molecularly smooth, and that the growth mechanism is creation and propagation of steps on the faces. We believe that surface nucleation is the most probable mechanism for this, as invoking screw dislocations as the dominating factor does not explain orientation preference and homogeneity. However, in the very few cases where other planes than {111} are seen, screw dislocations on {111} might be invoked as an explanation for speeding these planes up and exhibiting otherwise outgrown facets.

We have no completely satisfying explanation for the 2-dimensional growth at intermediate concentrations of inhibitor. The question is complicated by the fact that in some cases, the edges of these plates have been identified as also being {111}, and this is puzzling, as it implies that some {111} planes grow faster than others. Fundamentally there seems to be only two options to explain this, since just at an edge one expects the physical conditions in the liquid containing the crystal to be virtually identical on the two faces very close to their common edge. One possibility is an imperfection of some kind that stimulates growth on one of the faces (the thin edge), and the other is some kind of time-dependent adsorption effect for the inhibitor.

The first of these explanations has some precedent in he effect caused by stacking faults (van de Waal, 1996). Such faults would not be unexpected on the sII {111} planes. We do not rule out this mechanism, but we are skeptical of it because of the complete lack of macroscopic morphological evidence of such faults. The second possible explanation appeals to a mechanism where a fast-growing plane pushes aside the inhibitor as it grows, quickly enough that the polymer can not reorient and find its structural fit and bond onto the leading surface. This phenomenon has some precedence also, in the effect of kinetic inhibitors on ice growth (Harrison et al., 1987). We do not feel confident in choosing one of these explanations over the other at present, and may eventually have to appeal to a combination of the two. The results indicate preferential adsorption on {111}, but this question is not completely resolved, as the crystals also only exhibit {111} in their uninhibited state.

We believe that the complete growth inhibition is a result of polymer adsorption to the crystal surface, with the adsorbed molecules acting as barriers to further growth. When the concentration is high enough, polymer molecules will sit closer on the surface than twice the critical radius for crystal growth at the corresponding temperature, and the crystal will not be able to grow between the polymer strands. The adsorption process is fairly rapid, as no measurable growth takes place after a crystal is transferred to an inhibited solution, and the minimum no-growth concentration is probably close to the concentration needed at the surface, as the diffusivity of the polymer is much lower than any other component in the system. However, there has to be some time involved in diffusion and orientation of the inhibitor, if the latter of the above hypotheses for 2-dimensional growth is physically correct.

The tests with non-inhibitors show that it is not enough to have long molecules acting as diffusion barriers or molecules with a high capacity for H-bonding. We think that the pendant groups of our polymers are important in achieving strong adsorption. One possible explanation is that the pendants fit as pseudo-guest molecules in unfinished large cavities, with extra binding to the surface caused by H-bonds from the carbonyl groups on the pendants. There is some evidence from molecular simulations suggesting that this might happen (Makogon (1997), Carver et al. (1995)). The experiments where inhibited crystals were transferred back into uninhibited solutions, show that the adsorption is practically irreversible. Each pendant group or H-bonding site on its own probably shows equilibrium adsorption and desorption, but in the case where numerous sites along a polymer chain are engaged in this process, desorption of some of them would have little influence on the overall molecule, and these sites would be kept close to their adsorption area, and could easily re-adsorb. For the entire polymer to desorb, all the adsorption sites would have to "let loose" at the same time, an event which is statistically unlikely after a certain number of adsorption points has been achieved for each molecule. When desorption and further growth was found to occur, it happened in areas where it is easy to imagine the polymer fit to be less than perfect: at the vertices and at the interface between the crystal and the glass pipettes.

The EO hydrates grown with inhibitor have not yet been studied in as much detail as the THF system, but the preliminary results show some parallels to the sII hydrates. PVCap and VC-713 show different results than PVP, indicating that the difference in inhibition performance might be more fundamental than just a difference in degree of effectiveness. We believe that this is mainly due to the pendant group of PVP being smaller and not having the same stabilizing effect to provide strong adsorption. The dramatic small-scale branching of the EO hydrate crystals with inhibitor is somewhat similar to what is known in the crystallographic literature as spherulitic growth. However, our experiments indicate that these crystals are still single crystals with constant orientation throughout, whereas for spherulites, the orientation will be off by some degree for each new branch. We believe that this is a new phenomenon, as we have not been able to find reports of such growth in the literature, and remains a topic for further investigation.

ACKNOWLEDGMENTS

The following companies are gratefully acknowledged for their financial support of this work: Amoco, ARCO, Chevron, Conoco, Exxon, Mobil, Oryx, Petrobras, Phillips, Statoil and Texaco.

REFERENCES

Carver, T.J., Drew, M.G.B., Rodger, P.M., *J. Chem. Soc. Faraday Trans.*, 91(19), pp 3449-3469 (1995)

Gudmundsson, J. and Bϕrrehaug, A., Proc. 2nd Int. Conf. on Nat. Gas Hydrates, pp 415-422, Toulouse, France, June 2-6 (1996)

Harrison,K.,Hallett,J.,Burcham,T.S.,Feeney,R.E.,Kerr,W.L.,Yeh,Y., *Nature*, 32, p 241 (1987)

Englezos, P., *I&EC Research*, vol. 32, pp 1251-1274 (1993)

Kvenvolden, K.A., *Ann. New York Acad. Sci.*, vol. 75, pp 232-246 (1994)

Lederhos, J.P., Long, J.P., Sum, A., Christiansen, R.L., Sloan, E.D., *Chem. Eng. Sci.*, 51, (1996)

Makogon, T.Y, Ph.D. thesis, Colorado School of Mines (1997).

Myerson, A.S., Handbook of Industrial Crystallization, Butterworth-Heinemann, Boston (1993)

Rahman, A., Stillinger, F.H., *J.Am.Chem.Soc.*, 95, pp 7943-7948 (1973)

Sloan, E.D., Clathrate Hydrates of Natural Gases, Marcel-Dekker, New York (1990)

Smelik, E.A. and King, H.E., *Am. Mineralogist*, accepted for publication (1996)

van de Waal, B.W., *J. of Crystal Growth*, vol. 158, pp 153-165 (1996)

FIGURES

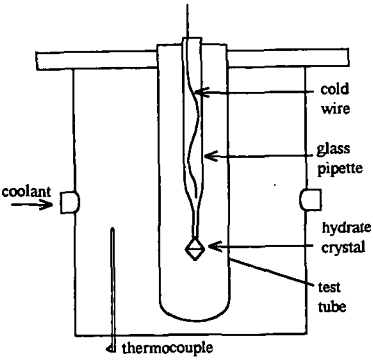
cold wire
glass pipette
coolant
hydrate crystal
test tube
thermocouple

Figure 1 The experimental cell. Water or water-glycol mixtures are used as coolant. The test tubes are ~2.5 cm outer diameter, screwcapped pyrex glass.

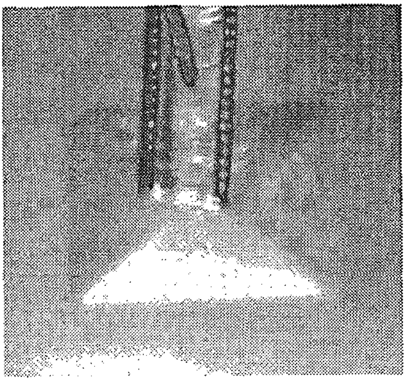

Figure 2 Octahedral s II {111} crystal of THF hydrate grown without any additives at ΔT= 3.4 K. Pipette end is approximately 2 mm across.

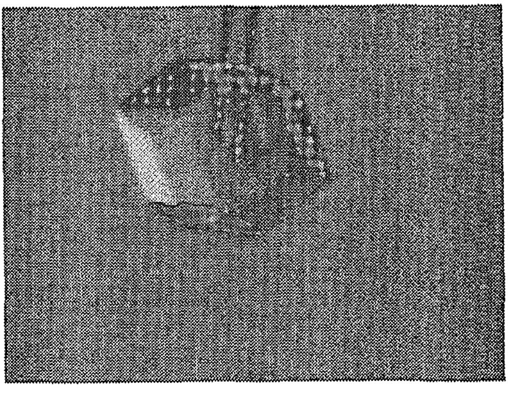

Figure 3 Dodecahedral s I {110} crystal of EO hydrate grown without any additives at ΔT= 0.5 K. Pipette end is approximately 0.2 mm across.

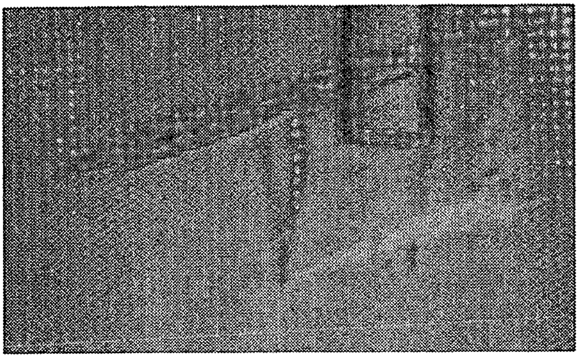

Figure 4 THF hydrate crystal growing in solution with 0.25 wt% VC-713 at $\Delta T = 2$ K. Original crystal outline is seen, with the induced 2-d plates sprouting from it. Pipette end is approximately 2 mm across.

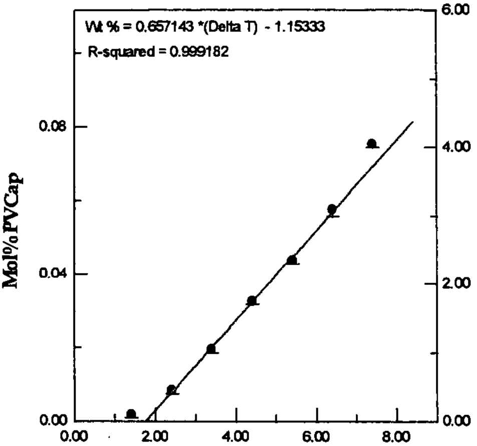

Figure 5 Complete inhibition and its dependence on supercooling. ΔT vs. concentration of inhibitor shows minimum concentration required to have complete inhibition of crystal growth. THF hydrates, sII. The inhibitor is a PVCap.

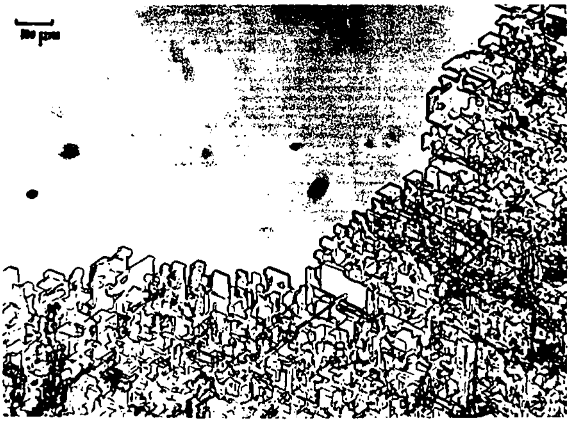

Figure 6 EO sI crystal grown in capillary at $\Delta T = 0.5$ K. Intermediate concentration of inhibitor between unaffected and highly branched crystal, 0.08 wt % PVCap. Note preservation of crystallographic orientation throughout.

NEUTRON DIFFRACTION MEASUREMENTS OF THE NUCLEATION AND GROWTH MECHANISMS OF METHANE HYDRATE.

C.A. Koh[†], A.K. Soper[‡], R.E. Westacott[†], R.P. Wisbey[†], X.Wu[†], W. Zhang[†], and J.L. Savidge[††]
[†] Chemistry Department, King's College, London, Strand, London WC2R 2LS, UK
[‡] ISIS, Rutherford-Appleton Laboratory, Chilton, Didcot, Oxon, OX11 0QX, UK
[††] Gas Research Institute, West Bryn Mawr Drive, Chicago, Illinois, IL 60631, USA

Abstract.

In this paper we present the results of our *in-situ* x-ray and neutron diffraction experiments during the formation of gas hydrates under industry operating conditions. We have performed energy dispersive x-ray diffraction to investigate the crystalline nature of species formed during the hydrate formation process. These experiments have been performed on carbon dioxide and propane hydrate. We show that Bragg peaks, indicating crystal structures, appear during the formation process. Some of these peaks appear in the final hydrate diffraction pattern and others do not. However, in the intermediate stages there is a lot of amorphous structure which could not be interpreted. In an effort to understand this part of the formation process we have performed neutron diffraction experiments on the Small Angle Neutron Diffraction for Amorphous and Liquid Samples (SANDALS) instrument at the Rutherford Appleton Laboratory. This instrument is designed to look at short range structure and provides information on the water structure around the guest molecules in the liquid phase. We present examples of the solvation sphere around methane molecules during the formation of methane hydrate, together with the average size and variance of the co-ordination sphere

Introduction.

A substantial body of information is now available on the equilibrium properties of clathrate hydrates [1-5]. This data has been collected over several decades during which it has been used to support the development of fundamental models to explain chemical and engineering aspects of gas hydrate knowledge [6]. However, these properties and the information currently available fail to identify the mechanisms through which gas hydrates nucleate, grow or decompose, and in some cases fail to accurately determine the thermodynamic properties. Hydrate research has recently concentrated on the kinetics of gas hydrate formation. The methods for the prevention of hydrate formation have also concentrated on kinetic control rather than thermodynamic control.

The work described in this paper uses x-ray and neutron diffraction to investigate the structure in liquid water before and during hydrate formation. We have used the Energy Dispersive X-Ray Diffraction (EDXD) instrument at the Daresbury Laboratory to monitor the formation and decomposition of gas hydrates. We have also used the SANDALS (Small Angle Neutron Diffraction of Amorphous and Liquid Samples) at the Rutherford-Appleton Laboratory to monitor structure in the liquid phase before and during hydrate growth.

Methodology.

Both types of experiment have been conducted in specially designed high pressure cells. Temperature, pressure and composition were selected and controlled throughout the experiments. The experiments were conducted *in-situ*, such that gas consumed during hydrate formation is replaced by gas from the cylinder and the pressure maintained.

The x-ray diffraction experiments were carried out over a 250 to 300 K temperature range and 0.1 to 3.5 MPa pressure range [7,8]. The detector angle was fixed at 5.042°. *In-situ* experiments were conducted for carbon dioxide/water and propane/water systems. Diffraction patterns were recorded every 200 second throughout the experiments. Data was collected as a series of intensity *vs.* energy spectra recorded with time throughout the experiments.

The neutron diffraction experiments on the methane/water system were carried out at constant pressure (2100 psi) and the temperature varied using a ramping procedure. Two scattering patterns were recorded at each temperature. The first stage of the experiment was carried out at a temperature in the water/gas region of the phase diagram (291 K). The scattering pattern was recorded over a 30 minute period. The temperature was reduced to a point within the hydrate region of the phase diagram (283 K). Further scattering patterns were obtained. The temperature was further reduced to 277 K and subsequently reduced to 263 K were the complete sample was frozen. Any ice obtained was melted by reheating to 277 K, where the final scattering patterns were obtained.

Spherical Harmonic Analyses were performed to obtain detailed views of the local intermolecular orientational correlation function [9-11]. Reverse Monte Carlo (RMC) simulations were performed on one scattering pattern at each of the four temperature set points (291 K, 283 K, 277 K (cooling) and 277 K (heating)). The original simulation cell contained 12 methane molecules and 1500 water molecules arranged in a random configuration. The RMC simulation were carried out over 5 million trials, using an empirical water model. The results for the RMC simulations were deemed to be more realistic than our previous results using a Spherical Harmonic Reconstruction [9-11].

Results.

The EDXD experiments lead to some interesting preliminary results. In figure 1, we show the diffraction patterns taken during an experiment. At time zero, the diffraction pattern indicates an amorphous sample, *i.e.* the liquid and gas mixture. As the experiment progresses, sharp peaks appear in the diffraction pattern. These peaks are due to Bragg reflections from a crystalline material. The final pattern is comparable with the diffraction pattern of the complete hydrate structure. That is, the calculated unit cell length is in agreement with literature values and the indexed peaks correspond to Bragg reflections obtained from the single crystal diffraction patterns.

The intermediate stages of this experiment are more difficult to interpret (see figure 2). These diffraction patterns contain a mixture of amorphous and crystalline species. At present, we cannot determine whether Bragg peaks in these intermediate stages which do not appear in the the final hydrate are due to a preferred orientation effect or a crystalline intermediate, which may or may not exist in some form in the product. Methods for interpreting these intermediate stages are currently under investigation.

The EDXD experiments are primarily designed to look at definite crystal structures, as the x-rays are diffracted by planes of electron density in the crystal. Neutrons, on the otherhand, are diffracted by atomic nuclei and therefore provides the possibility of investigating short-range order in liquids. The data shown here were subjected to a spherical harmonic analysis to assess the degree of orientational correlation of water around the methane. The first term in this series expansion of the data is simply the centres correlation function, methane carbon to water oxygen. This is shown in Figure 3 for the four cases. A pronounced co-ordination sphere is found in all instances, but changes quite abruptly for case (4) when a significant amount of methane hydrate is formed. It can be seen from cases (1) - (3), the co-ordination sphere peaks at an average distance of about 3.6 A for case (1) and then gradually moves to larger radius values as the water/methane system is pushed towards the formation of hydrate by decreasing of temperature. The fits that were obtained are shown in figures 4 and 5.

The RMC simulations aim to reproduce the total corrected scattering pattern of the sample. In figure 3, we show the CH_4-O pair correlation function obtained from the scattering patterns obtained at each of the four temperatures described above. The changing correlation function from (a) to (d) indicates an increase in the average number of water molecules in the co-ordination sphere around methane. This is taken from the area under the first peak in the pair correlation function in each case. The position of the peak also indicates that the co-ordination sphere contracts in radius as the experiment progresses. These distances have been used to extract examples of the co-ordination spheres from the final RMC structures. The regions extracted from these structures give some indication of the water structure around the methane molecules during each stage of the experiment. Firstly, we should point out that the number of water molecules within the required distance of the methane molecules is not the same for each methane at each stage of the experiment. The area under the first peak in the pair correlation function indicates the average number of water molecules in the first co-ordination sphere. In Table 1 we present the average and variance of the number of water molecules in the co-ordination spheres for each stage of the experiment. It is interesting to note that there are distorted ring tetramers, pentamers and hexamers in these structures. It is noticeable that the average number of water molecules in the co-ordination spheres increases from part (a) to part (d). This is a consequence of hydrate formation where the expected average number of water molecules in the co-ordination sphere is 23 assuming full conversion to hydrate.

Conclusions

We have demonstrated that the use of energy dispersive x-ray and small angle neutron diffraction techniques can provide complementary information on the formation of natural gas clathrate hydrates.

Acknowledgements

The authors would like to acknowledge the management and financial support of the GRI and funding from the Rutherford-Appleton Laboratory, ISIS Facility. Thanks are also due to C.C. Tang and A. Neild at the Daresbury Laboratory.

References

1. Van der Waals, J. H. & J. C. Platteeuw. *Adv. Chem. Phys.* **2**. 1, 1959
2. Makogan, Y. F. *Hydrates of natural gases.* Translated from Russian by W. J. Cieslesicz. Penn Well Books. Tulsa, Oklahoma, 1981.
3. Interml Conf. Natural Gas Hydrates, Toulouse, 1996.
4. Bishnoi, P. R., V. Natarajan & N. Kalogerakis. Annuals of the New York Academy of Sciences. **715**. 311-321, 1994.
5. Bishnoi, P. R. & P. D. Dholabhai. *Fluid phase equilibria.* **83**. 455, 462, 1993.
6. Annuals of the New York Academy of Sciences. **715**. 24-28, 1994.
7. C.A. Koh, J.L. Savidge, C.C. Tang, J. Phys. Chem. 100, 6412-6414, 1996.
8. C.C. Tang, C.A. Koh, A.A. Neild, R.J. Cernick, R.E. Motie, R.I. Nooney, J. Synchrotron Rad. 3, 220-224, 1996.
9. Finney, J. L. & A. K. Soper. *Chemical Society Review.* **23**, 1, 1994
10. Soper, A. K. 1993. *Physical Review* E, **47**, 2598, 1993.
11. Soper, A. K. *J Chem Phys* **101**, 6888, 1994.

Figure 1:
x-ray diffractogram for carbon dioxide hydrate.

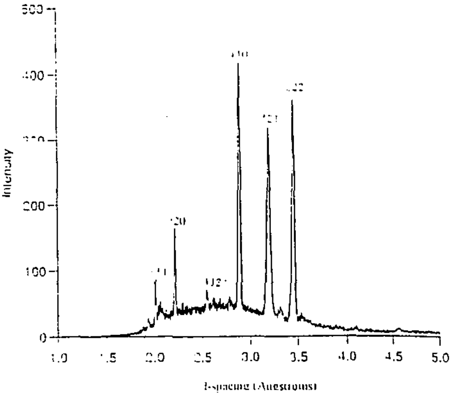

Figure 2:
x-ray diffractograms for carbon dioxide hydrate growth.

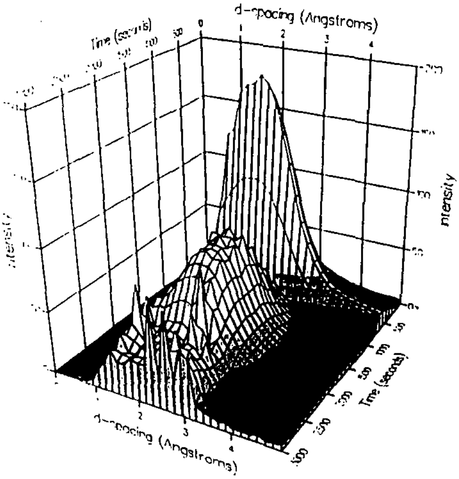

Figure 3:
radial distribution functions for methane carbon and water oxygen during methane hydrate growth.

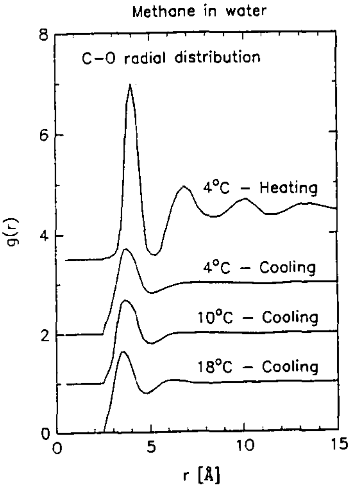

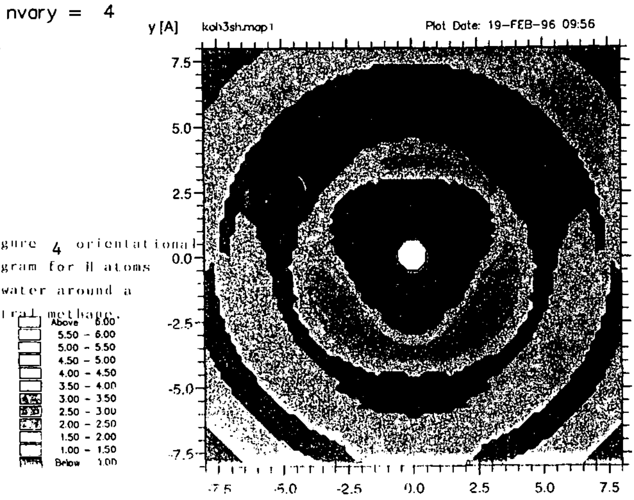

Figure 4 orientational diagram for H atoms of water around a central methane.

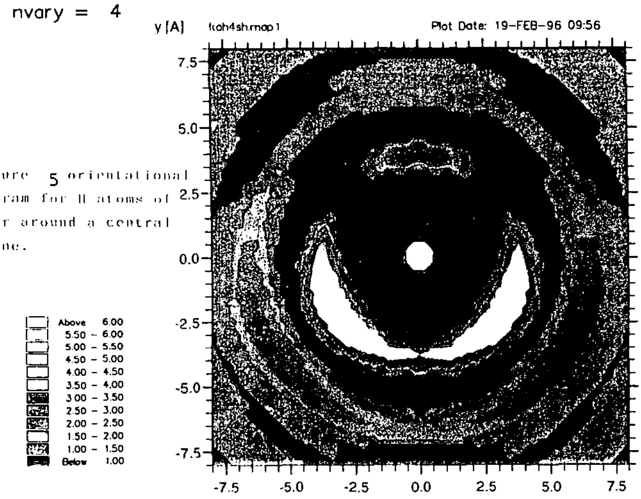

Figure 5 orientational diagram for H atoms of water around a central methane.

Equilibrium Properties and Kinetics of Methane and Carbon Dioxide Gas Hydrate Formation/Dissociation

Takeshi Komai, Yoshitaka Yamamoto and Sanshiro Ikegami
National Institute for Resources and Environment, MITI, Japan
16-3, Onogawa, Tsukuba, Ibaraki, 305 Japan
E-mail:koma@nire.go.jp

Keywords: Gas Hydrate, Methane Hydrate, Phase Equilibria, Formation and Dissociation

INTRODUCTION

Large quantities of gas hydrates, clathrate compounds of water and gases formed under high pressure and low temperature, are found in marine sediments and in cold regions. To produce large amount of methane gas from the reservoir with a reasonable way, it is necessary to obtain fundamentals on the mechanism of formation and dissociation and the properties under the practical situations, including phase equilibria and kinetics of gas hydrates. In addition, we have proposed the displacing method of gas hydrates, so that methane gas is extracted from the reservoir by displacing methane with carbon dioxide in molecular level. The main purposes of this research are to acquire the further understanding for the mechanism of hydrate formation/dissociation, and also to aceumulate engineering data for completing the original concept of displaeing method. We have carried out a experiment on the formation and dissociation of methane and carbon dioxide, using an apparatus consisting of extremely high pressure vessel and observation windows. This paper presents the experimental results on the properties of gas hydrates formation and dissociation under the condition of three phase equilibrium, and some discussion on kinetics and the mechanism of gas hydrate formation.

EXPERIMENTAL

The experimental apparatus, in which the formation and dissociation of gas hydrate could be observed, was designed and manufactured, so that the several conditions of pressure, temperature and concentration of gases could be precisely controlled. Fig.1 illustrates the schematic diagram of the apparatus and the measuring system of the experiment. The pressure cell (1), made of stainless steel and with 90 ml in internal volume, can be used under the pressure condition of up to 40 MPa. It contains three glass windows (2) for observation, a magnetic type mixing equipment (3), and some nozzles (4) for introducing gas and liquid component. The pressure cell is installed within a constant temperature bath (5) filled with cooling agent of ethylene glycol, where the temperature can be controlled with the accuracy of ±0.2 ℃. Gas and liquid fluids are introduced into the cell using a high pressure pump (6) and a fluid supplier system (7), and then are adjusted so that the pressure would be kept constant or free to change by means of two cylinder type controllers (8). The accuracy of controlled pressure is designed to be ±0.05 MPa. Four transducer for detecting and controlling the pressures are equipped, and five thermocouples are installed for measuring the temperatures inside the cell as shown in Fig.1. The observation system including a optical fiber borescope (9) and a CCD camera (10) can be utilized for this apparatus.

The procedure of the experiment on the three phase equilibrium of gas hydrate are described in the following. First, a quantity of pure water is supplied by the high pressure pump into the pressure cell, and other portion of the volume is filled with pressurized gas component by the fluid supplier system. The quantities can be calculated as equivalent volume portions needed for hydrate structure. The internal pressure can be adjusted, using both the cylinder units in liquid phase and the supplier system in gas phase. The formation of gas hydrate is observed during the temperature of whole system going down, while the pressure is no longer controlled at this situation. The accumulation of hydrate would complete for about a couple of hours, after which the temperature is controlled to go up with the constant rate for getting the equilibrium data of dissociation. The optical cell and the spectrometric system are equipped at the glass window for detecting the nucleation and the change of liquid phase structure. A lot of experimental data, such as temperatures, pressures and gas concentrations, and other experimental conditions, are measured and analyzed using the data acquisition system.

RESULTS AND DISCUSSION

The solubility of gases and gas transport into liquid phase are important factors to promote the formation of gas hydrates in the three phase equilibrium condition. In this experiment, two types of mixing and bubbling operations were adopted for the promotion of nucleation. Fig.2 shows photographic figures for the formation of methane hydrate, observed through the glass window. These results were obtained under the same condition as the pressure was approximately 10 MPa and the temperature was 4.0 to 6.0 ℃. As shown in the left figure, a lot of fine fragments of methane hydrate were formed around the mixing blade and were accumulated in the liquid phase. On the contrary, as shown in the right figure, a lot of gas bubbles from the nozzle turned into solid phase droplets of methane hydrate at the interface of gas and liquid phase. The following experimental results are mainly related to the mixing operation, because it enables the equilibrium properties to become more favorable and reproductive. For keeping sufficient saturation or dissolved condition of gases into liquid phase, each experiment requires previous mixing operation for 30 minutes and enough mixing speed of no lower than 170 rpm.

Plenty of experiments using the gas hydrate formation apparatus have been conducted under the conditions, such as gas component, initial pressure and temperature, and restating hysteresis situation. Fig.3 shows the trend curves for temperature and pressure, obtained using the gas component of CH_4 (100%). TEMP1 represents the temperature measured by No.1 thermocouple at the center of the cell, and TEMP2 the controlled one outside the cell. PRES means the pressure of liquid phase inside the cell. This figure shows that the formation of gas hydrates eventually started during the process of temperature decreasing, because slight increases of temperature appeared after the nucleation point due to the heat of formation. The rapid decrease of pressure was observed around the formation point, while the pressure gradually decreased as the temperature became lower due to the change of solubility. On the other hand, the dissociation of gas hydrate was observed during the process of temperature increasing, from which the increase of temperature started to decline. Fig.4 shows the trend curve of differential temperature measured by No.1 and No.5 thermocouples as a heat balance in the experiment. The first peak on the curve indicates the exothermic heat of formation, and the last one the endothermic heat of dissociation. According to these relations and the observation, critical temperatures and pressures necessary for gas hydrate formation and dissociation can be determined as in Table 1. These results include the properties for the three phase equilibrium. Compared with data in experiments No.4 and No.9 for CO_2 and CH_4 hydrate, the critical temperatures of CH_4 hydrate formation and dissociation are much higher than those of CO_2 hydrate. Further, it is found that the critical temperatures of formation and dissociation increase as the initial pressures become higher in both cases of CO_2 and CH_4 hydrates.

Fig.5 shows the three phase equilibrium relation obtained through the series of experiment for CO_2 and CH_4 hydrate. Upper two lines are the formation and dissociation equilibrium curves for CH_4 gas hydrate, the relation between critical temperatures T and pressures P, and lower lines for CO_2 gas hydrate. In other words, gas hydrate can be present as solid phase with gas and liquid components at higher position from curves for formation, and it no longer exists at lower position from curves for dissociation. From the results it is clear that the relation between P and T is approximately linear in semi-log plotting, and that the critical pressures of CH_4 are relatively higher than those of CO_2 assuming the same temperature condition. This suggests that the formation of CH_4 hydrate requires much higher potential or activation energy rather than in the case of CO_2 hydrate. In addition, it is found that the equilibrium curves for the formation of hydrates are placed at upper position compared with those for the dissociation. Further, the equilibrium data measured in case of dissociation agree well with estimated values using theoretical methods of kinetics, but those in case of formation largely differ from the theoretical values. These large differences may include interesting phenomena and fundamentals on the mechanism of gas hydrate formation. Thus, further experiments were carried out on the behavior of history and hysteresis observed the process of formation and dissociation of gas hydrates.

Fig.6 illustrates the history curve of P and T obtained in the experiment No.39 for CH_4 hydrate. The formation process proceeds on the oscillated curve between A and D, and the dissociation process on the curve between E and F. The differences of temperature and pressure between formation and dissociation equilibria are approximately 3.5 ℃ and 0.5 MPa, respectively. The history of P and T is usually regarded to be the super cooling effect in the process of formation. The temperature differences obtained by the experiment using CO_2 were quite smaller than that in case of CH_4. In addition, the super cooling effect clearly appeared in the case that the gas component was introduced by the way of bubbling. These results suggest that the supper cooling effect in the history behavior might be largely related to the interface conditions, the way of gas introduction, and the component of gas and liquid.

Fig.7 shows the hysteresis curves for demonstrating the effect of restarting situations, obtained by continuous three experimental runs in the same conditions. The second and third runs were restarted immediately after completing the previous run. In the first run of experiment, the temperature of initiating formation was 15.2 ℃ at the pressure of 17.5 MPa. However, the formation temperature was shifted to 16.6 ℃ in the second run, and up to 16.8 ℃ in the third run. This means that the formation temperatures increase in case of restarting situations, so that they approach the dissociation temperatures or the theoretical temperature for three phase equilibrium. Another experimental run showed that the formation temperature of second run shifted by 2.5 to 3 ℃ compared with that of the first run, but that of third run recovered to the level of first run if the liquid with dissolved gas was left as the final condition of second run for 12 hours. These results may suggest that the hysteresis behavior for gas hydrate formation largely depends on the presence of cluster structure in liquid phase, the promotion process of nucleation, and the saturation or dissolved condition of gases into liquid phase.

CONCLUSIONS

Experimental studies on the properties of three phase equilibrium and the process of formation and dissociation of gas hydrates have been carried out, using the specially designed experimental apparatus. As a result, it was found that measured equilibrium data in case of dissociation agree well with estimated values using theoretical methods, but those in case of formation largely depend on the interface conditions, the way of gas introduction, the structure of liquid phase, and the history and hysteresis process of hydrate formation. Thermodynamics properties of gas hydrates were also discussed on the basis of temperature and pressure data in formation and dissociation of gas hydrate. In order to make clear the effects of liquid structure and interface condition on the detail process of formation of gas hydrates, further experimental and theoretical approaches are necessary on the mechanism of nucleation and cluster structure.

ACKNOWLEDGMENT

The authors gratefully acknowledge Dr. T. Saito, Mr. F. Kiyono, Dr. R. Nagaosa and Dr. H. Nada in NIRE for their great assistance in developing the original concept of experimental method and the theoretical analysis of gas hydrates, and thank the New Energy and Industrial Technology Development Organization(NEDO) for the financial assistance in conducting the research project.

REFERENCES

Burrus, R.C.: Cristallization of Natural Gas Hydrate: Video Microscopy and Mass Balance on Nucleation and Grouth, Proc. Conf. Drilling Hydrates in Offshore, Japan, 182, (1995)

Holder, G.D., Zett, S.P. and Pradhan, N.: Phase Behavior in Systems Containing Clathrate Hydrates: A Review:, Reviews in Chemical Engineering, 5, 1-70, (1988)

Uchida, T., Hondoh, T. and Mae, S.: Effects of Temperature and Pressure on the Transformation Rate from Air Bubbles to Hydrate Crystals, Ann. Glaciol., 20, 143-147, (1994)

Matsumoto, R.: Feasibility of Methane Hydrate under the Sea as a Natural Gas Resource, J. Jap. Assoc. Petro. Tech., 60(2), 147-156, (1995)

Table 1 Experimental results of the formation and dissociation equilibrium data.

Exp.No.	Initial Pressure (MPa)	Formation Equilibrium		Dissociation Equilibrium		
		Pressure (MPa)	Temperature (℃)	Pressure (MPa)	Temperature (℃)	
EXMH09	5.80	5.4	4.4	4.2	5.0	
EXMH08	8.05	7.1	5.8	6.8	10.6	
EXMH24	10.20	9.4	8.1	8.6	11.7	
EXMH11	10.50	9.7	8.8	8.6	12.0	CH_4
EXMH07	11.90	10.8	8.8	9.9	13.2	
EXMH06	13.38	12.5	11.0	11.6	14.1	
EXMH29	17.97	17.0	12.9	16.8	17.1	
EXMH30	20.00	18.8	14.2	18.6	18.0	
EXMH12	3.1	2.4	4.0	1.9	5.0	
EXMH13	4.0	3.4	6.0	2.6	6.9	CO_2
EXMH04	4.9	4.2	9.4	4.1	9.9	

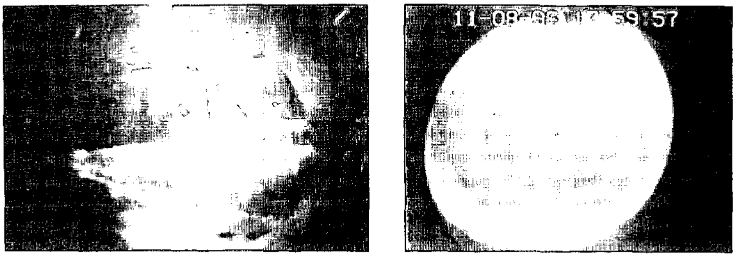

Fig.2 The observation of methane gas hydrate formation.

(Left figure) In case of mixing operation. (Right figure) In case of bubbling operation.

P=10.0 MPa, T=8.0 ℃ P=10.0 MPa, T=4.0 ℃

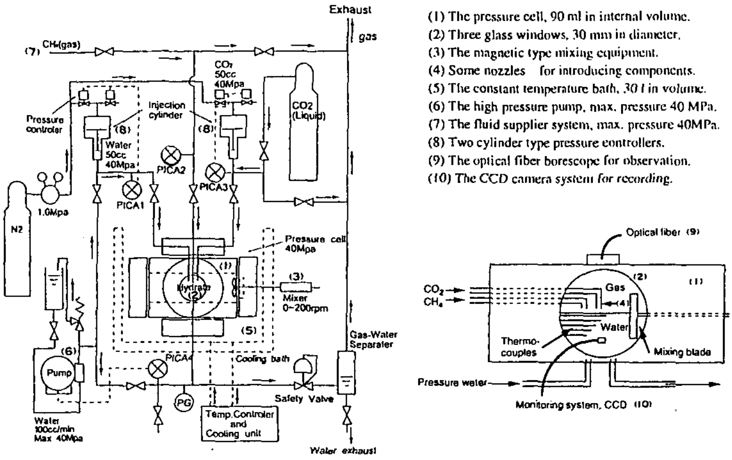
Exhaust
gas
(7) CH₄(gas)
CO₂
50cc
40Mpa
CO2
(Liquid)
Pressure controler
Injection cylinder
(8)
(8)
Water
50cc
40Mpa
PICA1
PICA2
PICA3
PICA4
N2
1.0Mpa
Pressure cell
40Mpa
(1)
Hydrate
(2)
(3)
Mixer
0~200rpm
(5)
Cooling bath
(6)
Pump
Water
100cc/min
Max 40Mpa
PG
Temp.Controler and Cooling unit
Safety Valve
Gas-Water Separater
Water exhaust
Optical fiber (9)
(1)
(2)
Gas
(4)
Water
CO₂
CH₄
Thermo-couples
Mixing blade
Pressure water
Monitoring system, CCD (10)

(1) The pressure cell, 90 ml in internal volume.
(2) Three glass windows, 30 mm in diameter.
(3) The magnetic type mixing equipment.
(4) Some nozzles for introducing components.
(5) The constant temperature bath, 30 *l* in volume.
(6) The high pressure pump, max. pressure 40 MPa.
(7) The fluid supplier system, max. pressure 40MPa.
(8) Two cylinder type pressure controllers.
(9) The optical fiber borescope for observation.
(10) The CCD camera system for recording.

Fig.1 The schematic diagram of the experimental apparatus and the measuring system. (Upper figure) Main system. (Lower figure) Pressure cell and measuring sensors.

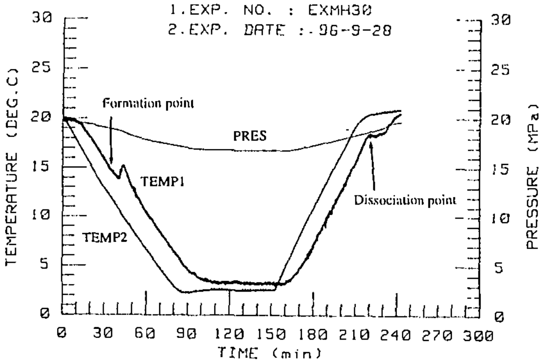

Fig.3 The trend curves of pressure and temperature obtained in the experiment for methane gas hydrate formation and dissociation.

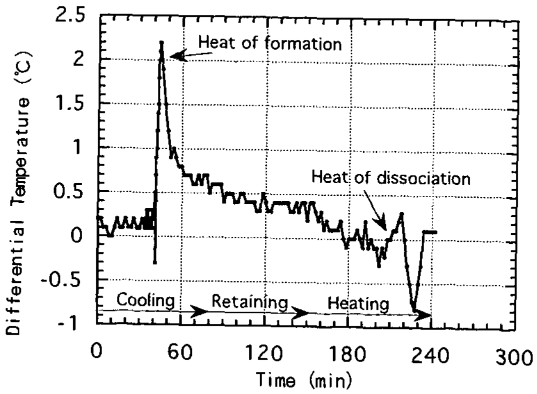

Fig.4 The change in differential temperature, and heat valance of gas hydrate formation and dissociation.

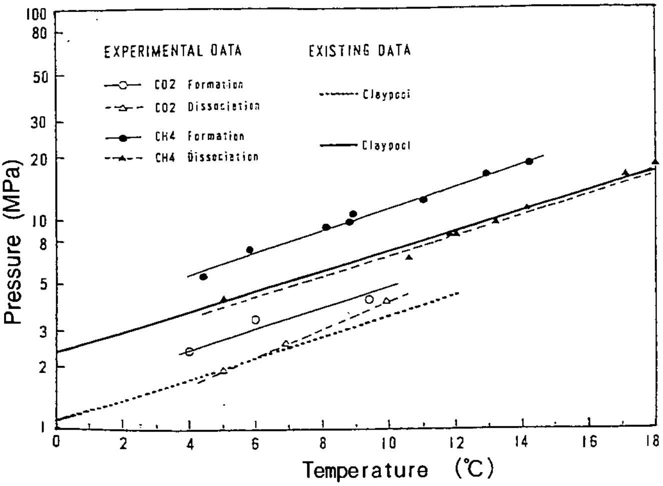

Fig.5 The relations between pressure and temperature in three phase equilibrium condition for CO_2 and CH_4 gas hydrates.

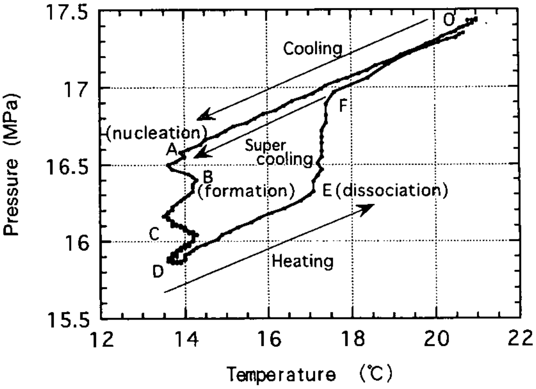

Fig.6 The history curve of pressure and temperature in the process of gas hydrate formation and dissociation.

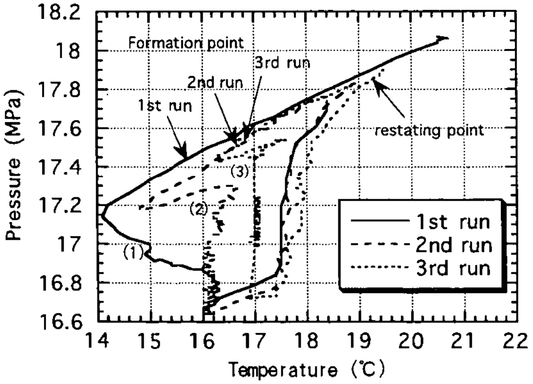

Fig.7 The hysteresis curves of pressure and temperature in the process of gas hydrate formation and dissociation.

STUDY ON FORMATION / DISSOCIATION MECHANISM OF GAS HYDRATES AND RECOVERY OF PURE HYDRATE CRYSTAL USING HIGH PRESSURE CRYSTALLIZATION TECHNIQUE

Yoshitaka Yamamoto*, Takeshi Komai*, Sanshiro Ikegami* and Akihiro Wakisaka**

*National Institute for Resources and Environment, 16-3, Onogawa, Tsukuba-shi,
Ibaraki 305, Japan
**National Institute for Advanced Interdisciplinary Research, 1-1-4, Higashi, Tsukuba-shi,
Ibaraki 305, Japan

Keywords: gas hydrate, high pressure crystallization, separation of pure crystal

INTRODUCTION

Gas hydrate is the species that guest molecules (CO_2, CH_4 etc.) are included in the cage of hydrogen-bonding network of water molecules. Recently, it was found that there are great quantity of methane hydrate in the sediment below the sea bottom. Since Japan has no natural energy resources, we pay much attention to the natural gas hydrates as one of the hopeful energy source for the future. To establish elemental technologies for mining methane hydrate, we started fundamental and also practical study of gas hydrate.

The observation of real crystallization process is indispensable to study formation / dissociation mechanism precisely. On the other hand, it is important for establish methane hydrate recovering method to get pure hydrate crystals and measure accurate physical and chemical property of them.

To achieve these objects, we are constructing high pressure crystallization apparatus with optical window. In this presentation, we will report the resent result of hydrate crystal formation and recovery experiment with this apparatus.

As a fundamental research on the gas hydrate formation, we are interested in molecular clustering structure of aqueous solution. As for the interaction of magic numbered water cluster, $H^+(H_2O)_{21}$, which has dodecahedral structure, with organic molecules, it was observed that tetrahydrofuran (THF) did not dissociate the hydrogen-bonding network of $H^+(H_2O)_{21}$ cluster; however, methanol dissociated it. In the mass spectra of clusters generated from THF-water and methanol-water mixtures, $H^+(H_2O)_{21}$ clusters contact with THF, $H^+(H_2O)_{21}(THF)_n$:n=1,2,3..., and $H^+(H_2O)_{21}$ clusters substituted by methanol, $H^+(H_2O)_{21-n}(CH3OH)_n$: n=1,2,3..., were observed, respectively[1]. Such molecular structures in aqueous solutions seem to be related with the nucleation mechanism of hydrate. That is, THF makes hydrates, but methanol works as gas hydrate inhibitor. We also intend to carry out methane hydrate formation experiment with any additives such as THF or CH_3OH,etc., and discuss nucleation mechanism of gas hydrate with the clustering structure of water molecules which were observed by cluster beam mass spectrometer.

EXPERIMENTAL

High pressure crystallization apparatus with optical vessel

Fig.1 shows the schematic diagram of the high pressure crystallization apparatus with optical vessel. Photographs of this apparatus and main vessel are also shown in Fig.2 and Fig.3 respectively. As shown in Fig.1, main vessel (C1) and sub vessel (C2) are piston-cylinder type high pressure vessels. Inner diameter and volume of these vessels are 15 mm and 20 mℓ respectively. The main vessel has a pair of sapphire windows to observe crystallization process on both side and stainless filter to separate liquid phase from solid phase on the bottom. Main vessel is soaked in a silicon oil bath[Temperature control range ; -30℃~+130℃]. This oil bath also has optical windows and crystallization process can be observed through these windows with microscope or multi channel spectrophotometer. Compression of vessels is carried out by using oil pressure equipment (19). Main vessel is connected with gas supplying system, which can supply host gases continuously under high pressure(max. under 400kg/cm^2). Control of gas flow rate is carried out by flow controller for high flow rate (3) [0.5~5N ℓ/min] and low flow rate (4) [0.01~0.1N ℓ/min]. Maximum pressure of crystallization unit is 4000kg/cm^2.

Crystallization and separation procedure

Sample mixtures (pure water and THF, pure water and CH_4 etc.) are injected into the main vessel (**C1**) and compressed to form hydrate crystals. The excess liquid phase is removed from the crystals in the main vessel (**C1**) to the sub vessel (**C2**), keeping the pressure in the main vessel constant and slightly decreasing the pressure in the sub vessel. After separation process is finished, stop valve between two vessels (**VH1**) is shut and crystals are recovered.

To confirm performance of the apparatus, crystallization and separation of pure indole from indole/isoquinoline mixture was carried out. Then, we started hydrate formation experiment of THF/water system and CH_4/water system. In case of methane/water system, to prevent dissociation of methane hydrate, the main vessel is cooled to about 80℃ by dry ice/methanol bath before the decreasing of main vessel pressure and taking out of hydrate crystal.

RESULT AND DISCUSSION

Formation and separation of high purity indole crystal by high pressure crystallization method

Fig.4 shows the typical operation diagram of high pressure crystallization. Sample solution is indole-isoquinoline mixture (80mol%-indole). Separation process is as follows.

1) Inject sample mixture into main vessel (**C1**) and compressed to 1000kg/cm^2 step wise under 50 ℃. In this process, pure indole crystal is formed and impurities concentrated into liquid phase

2) Hold the pressure of main vessel at 1000kg/cm^2 until solid-liquid phase equilibrium is achieved.

3) Open the stop bulb (**VH1**) between main and sub vessel and remove liquid phase from the crystal. In this process, pressure in the main vessel is constant (1000kg/cm^2) all the way. However, as sown in Fig.4, after almost stop the piston displacement, the pressure which is indicated in pressure gauge (**PH1**) gradually decreased and finally reach almost atmospheric pressure. This means that almost all the liquid is removed and pressure in the main vessel can not transmitted to pressure gauge (**PH1**). At that time, crystal in main vessel is squeezed under 1000kg/cm^2 and remained liquid is perfectly separated.

4) Pressure of main vessel is decreased to atmospheric pressure and separated crystal is recovered.

The purity of recovered solid was measured by gas chromatography. Indole concentration of that crystal was 98mol% and it was known that high purity crystal can be separated by this high pressure crystallization apparatus.

Formation and separation of THF hydrate and methane hydrate

Generally, autoclave type high pressure vessels were used for hydrate formation experiment and it is said that stirring of the vessel is important to form hydrate crystal. However, it is difficult to stir sample in main vessel (**C1**) in our apparatus. As mechanical stirring is not performed at natural hydrate formation process, stirring seems to be not always necessary. To confirm if methane hydrate formation is occurred without stirring or not, we slowly injected methane gas into an autoclave type optical vessel which is filled with pure water. (details will be described in another presentation of our group in this meeting by Dr.Komai.) As a result, film like hydrate crystal was formed almost instantly with rising of methane gas babble under the condition of 2℃、100kg/cm^2. Though it seemed to need fairly long time to make methane gas included in the hydrate film into crystal perfectly, it was confirmed that nucleation of hydrate can be occurred without mechanical stirring. According to this result, we tried hydrate formation experiment with the high pressure crystallization apparatus.

First, THF/water (THF : H_2O = 1 : 25 molar ratio) mixture was injected into the apparatus and examined efficiency of hydrate formation and separation. Temperature and separation pressure are 4℃ and 200kg/cm^2. After separation of excess water, main vessel was cooled to -10℃ and THF hydrate was recovered. From the pressure which is indicated on pressure gauge (PH1), we confirmed that hydrate and excess water was perfectly separated as same as indole-isoquinoline mixture. Photograph of recovered THF hydrate is shown in Fig.5.

Next, methane hydrate formation and separation experiment was performed with this apparatus. 6mℓ of pure water and 4 mℓ of methane gas was injected into main vessel1, and hydrate was formed under

4℃,400kg/cm^2. After separation of methane hydrate from water phase was finished, hydrate crystal was cooled to about -80℃ by methanol/dry ice bath. (Under -80℃, the dissociation pressure of methane hydrate become lower than atmospheric pressure.) Then, pressure of main vessel was decreased to atmospheric pressure and formed crystal was recovered. Photograph of recovered solid is shown in Fig.6. Recovered crystal is flammable white solid and dissolve with discharging babbles. Though It thought to be a methane hydrate, detailed analyses was still not performed and purity of crystal is not confirmed for the moment.

CONCLUSION

We constructed the gas hydrate formation/separation apparatus using high pressure crystallization method and confirmed a formation and recovery of gas hydrate by this equipment. For the present, adjustment of gas supplying unit was not finished perfectly and strict control of crystal formation is not achieved. Also, the system for observation of hydrate crystal formation is under adjustment.

From now on, we try to improve high pressure mass controller in gas supplying unit and structure of optical system and establish the technique for formation of pure hydrate and recover it. With the separated gas hydrate, we are going to measure physical and chemical property of it precisely.

We are also carrying out methane hydrate formation experiment with THF or CH_3OH. we will also make a discussion about influence of these additives to methane hydrate formation with the comparison of the clustering structure of water molecules which was observed by cluster beam mass spectrometer.

ACKNOWLEDGEMENT

This study is financially supported by NEDO (New Energy and Industrial Technology Development Organization).

REFERENCE

1. Yamamoto, Y. and Wakisaka. A, *Proc.Int.Conf.on Natural Gas Hydrate*, Toulouse, June , 1996, 355

2. Yamamoto,Y., Sato,Y. , Ebina, T., Yokoyama, Ch., Takahashi, S., Nishiguchi, N. and Tanabe,H., *Nenryou kyoukaishi* ,1991, **70**, 533

3. Yamamoto,Y., Sato,Y., Mito, Y., Tanabe, H., Nishiguchi, N. and Nagaoka, K. *Proc. Int. Symp. on Prep. of Func. Mat.*, 1989, 195

4. Yamamoto, Y., Sato,Y., Ebina, T.,Yokoyama, Ch., Takahashi, S., Mito,Y., Tanabe, H., Nishiguchi, N. and Nagaoka, K., *Fuel*,1991, **70**, 565

5. Yamamoto, Y., Sato, Y. and Wakisaka, A., *J.Chem.Soc., Chem.Commun.*, 1994, 2727

6. Wakisaka, A, Shimizu, Y., Nishi, N., Tokumaru, K. and Sakuragi, H., *J.Chem.Soc., Faraday Trans.*, 1992, **88**, 1129

7. Christiansen, R.L. and E.D.Sloan, Jr., *Proc.Int.Conf.on Natural Gas Hydrate*, N.Y., April, 1994, **19**, 283

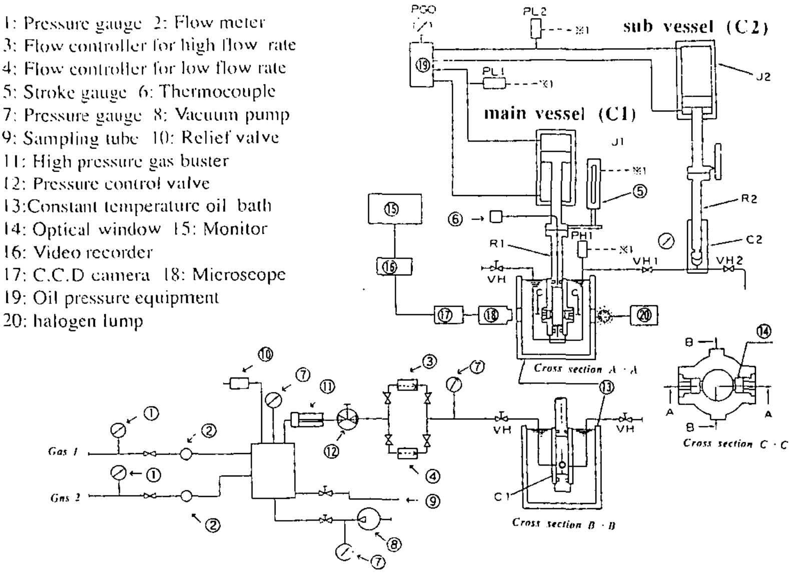
PGO
PL2
※1
sub vessel (C2)
J2
PL1
※1
main vessel (C1)
J1
※1
R2
R1
PH1
※1
C2
VH
VH1
VH2
Cross section A · A
B
A
A
B
Cross section C · C
Gas 1
Gas 2
VH
VH
C1
Cross section B · B

1: Pressure gauge 2: Flow meter
3: Flow controller for high flow rate
4: Flow controller for low flow rate
5: Stroke gauge 6: Thermocouple
7: Pressure gauge 8: Vacuum pump
9: Sampling tube 10: Relief valve
11: High pressure gas buster
12: Pressure control valve
13:Constant temperature oil bath
14: Optical window 15: Monitor
16: Video recorder
17: C.C.D camera 18: Microscope
19: Oil pressure equipment
20: halogen lump

Fig.1 Schematic diagram of the high pressure crystallization apparatus with optical vessel

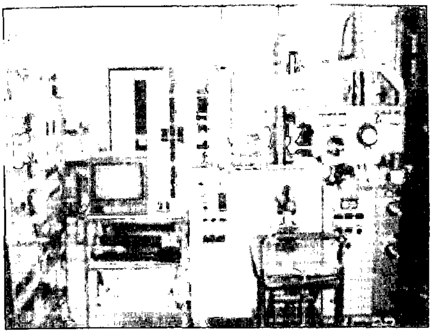

Fig.2 Photograph of the high pressure crystallization apparatus.

Fig.3 Photograph of the main vessel (C1)

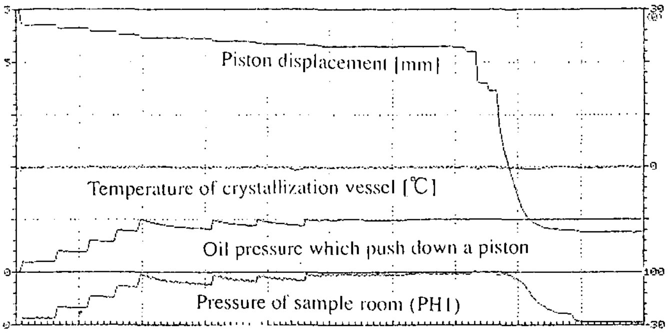

Fig.4 Operation diagram of crystallization and separation of pure indole from indole/isoquinoline mixture using high pressure crystallization technique (Indole concentration is 80mol%, separation temperature = 50℃, separation pressure = 1000kg/cm^2)

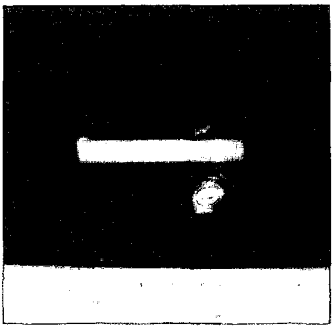

Fig.5 Photograph of recovered THF hydrate (separation temperature=1℃, separation pressure=200kg/cm^2)

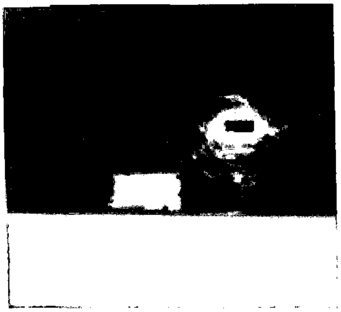

Fig.6 Photograph of recovered CH_4 hydrate (separation temperature=4℃, separation pressure=400kg/cm^2)

THE EFFECT OF CO_2 CLATHRATE HYDRATE ON THE OCEAN DISPOSAL OF CO_2: A REVIEW OF DOE-SPONSORED RESEARCH

Robert P. Warzinski, Perry D. Bergman
U.S. Department of Energy, Federal Energy Technology Center, Pittsburgh, PA 15236

Stephen M. Masutani
University of Hawaii, Hawaii Natural Energy Institute, Honolulu, HI 96822

Gerald D. Holder
University of Pittsburgh, School of Engineering, Pittsburgh, PA 15261

Keywords: carbon dioxide, ocean disposal, clathrate hydrate

INTRODUCTION

Deep ocean disposal of CO_2 is an option to mitigate rises in atmospheric levels of CO_2 if other measures are ineffective and the worst global warming scenarios begin to occur. Through its Office of Fossil Energy, the U.S. Department of Energy (DOE) supports research directed at evaluating the feasibility of this option for long-term CO_2 disposal. Two projects, managed at the Federal Energy Technology Center (FETC) in Pittsburgh, Pennsylvania, are being conducted that specifically address the technical issues associated with deep-ocean disposal of CO_2. One of the projects is being conducted at FETC; the other at the University of Hawaii at Manoa (UHM) in Honolulu, Hawaii. The purpose of this paper is to describe the scope of these projects and summarize current experimental and theoretical results.

BACKGROUND

In 1993, a research needs assessment for capture, utilization, and disposal of CO_2 from fossil fuel-fired power plants was prepared for DOE by the Massachusetts Institute of Technology (1). This well-received report concluded that establishing the feasibility of large-scale disposal options should be assigned the highest research priority of all needs identified. Of the large-scale disposal options considered at that time, the principal ones were those using the deep ocean or deep confined aquifers for storage. With respect to ocean disposal, the key research recommendations focused on the impact of the CO_2 clathrate hydrate on the effectiveness of this disposal option.

Depth is a key factor in ocean disposal of CO_2. To avoid premature escape of the CO_2 from surface waters to the atmosphere, injection below a depth of about 500 m would be required. From approximately 500-m to 3000-m ocean depth, undissolved CO_2 would exist as a buoyant liquid. At greater depths, the liquid CO_2 would sink. In the absence of hydrate formation, the minimum depth for effective CO_2 sequestration would be around 700 m. Drops released at this depth would completely dissolve before reaching a depth of 500 m (1).

CO_2 clathrate hydrate ($CO_2 \cdot nH_2O$, $6<n<8$) is a crystalline compound that can form under temperature and pressure conditions associated with CO_2 disposal in the ocean below a 500-m depth. The hydrate can form either as solid crystalline particles or as a coating on the surface of liquid CO_2 drops. The solid hydrate particles should sink in the ocean, facilitating sequestration; however, thin hydrate shells on liquid CO_2 drops would limit dissolution of the CO_2 and complicate sequestration attempts. During transport to depth and injection, hydrate formation may clog submerged conduits, erode and foul injector nozzles, and negatively impact CO_2 dispersion. The U.S. DOE supports experimental and theoretical research at FETC and at UHM to address these concerns. A small high-pressure viewcell at FETC and a large pressurized tank at UHM are being utilized in the experimental programs. Mathematical modeling of these phenomena is also being performed at both FETC and UHM.

RESEARCH AT FETC

The work at FETC was initiated in 1993. All of the experimental work has been performed in a high-pressure, variable-volume viewcell (HVVC) that has a maximum working volume of about 40 cm^3. A description of the HVVC system and basic experimental procedures have been published (2,3). The HVVC system can operate at temperatures down to near 0°C and at pressures up to 69 MPa (10,000 psig). The HVVC system can therefore be used to simulate ocean depths down to 6900 m. This is more than adequate for studying the behavior of CO_2 at the depths currently being considered for unconfined release of CO_2 in the ocean (1000 m to 1500 m) (4).

To enable more accurate prediction of the fate of CO_2 injected into the ocean, experiments at FETC have focused on determining the relative density of the hydrate in water (2,5) and seawater and on the formation of hydrate shells on drops of CO_2 and their effect on drop dissolution (2,6). With respect to the relative density of the hydrate, observations in two-phase systems with water and either gaseous or liquid CO_2 showed that the hydrates which formed at the CO_2/H_2O interface were initially snowlike in appearance and buoyant in the water-rich phase. With time, the hydrates became icelike (transparent) in appearance and sank. Trapped, unconverted CO_2 may have caused the bulk density of the initially formed hydrates to be less than that of the water-rich phase. Eventually, this trapped CO_2 either escaped or was converted to hydrate, causing the density to increase and the appearance to change. In contrast, when formed from dissolved CO_2, the hydrates were initially icelike in appearance and sank. Buoyant hydrate particles would frustrate sequestration in the ocean by causing the CO_2 to rise to unacceptably shallow depths. On the other hand, sinking hydrate particles would facilitate sequestration by causing the CO_2 to descend to greater depths before dissolution and thus increase its residence time in the ocean.

Some of the above experiments with water and CO_2 have recently been repeated using General Purpose Seawater (GPS) from Ocean Scientific International Ltd. As in the fresh-water experiments, hydrates formed from CO_2 dissolved in the seawater were icelike in appearance and sank in the seawater-rich phase.

Observations of the rate of hydrate shell formation on CO_2 drops in water and seawater have also been performed at FETC. In these experiments, a CO_2 drop is introduced into the viewcell and comes in contact with either existing hydrate particles or the glass or stainless steel parts of the viewcell itself. In all such cases, hydrate shell formation began at the point where the bubble or drop contacted the crystalline hydrate or viewcell, then rapidly spread out along the bubble or drop surface. Others have also reported similar phenomena (7). Specific examples from our experimental work have been previously described (6). The rate of growth of the hydrate shell on CO_2 drops (0.5 cm to 1 cm in diameter) in water has been estimated at 0.5 to 1.0 cm^2/s. Recent observations in seawater gave similar results.

The rate of dissolution of hydrate-covered CO_2 drops has also been studied in water (2) and more recently in seawater. In these experiments, the rate of decrease in drop radius was measured. Rates in the range of 0.0045 to 0.02 cm/h have been observed for hydrate-covered drops. These rates are slower than those obtained by other workers (2). The differences between the results are likely due to dissimilar experimental conditions and equipment. Data from the recent experiments in the viewcell indicate that the rate of shrinkage of CO_2 drops in seawater appears to be slower than in fresh water for drops of similar size under similar conditions. The reason for the slower rate in seawater is the topic of current investigations.

To overcome the limitations of the viewcell and more realistically simulate the environment that a CO_2 drop encounters in the ocean, a high-pressure water tunnel facility has been planned. This device is patterned after a similar apparatus developed by others for the study of methane hydrates (8). A low-pressure model is currently under construction to verify the flow patterns in the proposed test section of the tunnel.

Recent mathematical modeling efforts at FETC have been directed at determining the thickness of the hydrate shell that forms on CO_2 drops under conditions expected for ocean disposal (6). The model was developed to estimate both the thickness of the initially-formed shell and the bounds on the ultimate thicknesses of shells after reaching steady state in saturated and unsaturated environments. The degree of saturation is determined relative to the equilibrium CO_2 concentration at the hydrate equilibrium pressure, C_H, at the temperature of the system. Under anticipated ocean disposal conditions, the system can actually be oversaturated owing to the induction period that often accompanies hydrate formation (6).

The model assumes that the ultimate thickness of the shell is governed by the diffusion of the CO_2 through the hydrate shell and diffusion or convection of dissolved CO_2 away from the hydrate-covered particle. It was demonstrated that a very thin hydrate shell (<0.1 cm) would initially form around drops of injected CO_2. If injected into unsaturated water, a stable hydrate thickness on the order of 10^{-2} to 10^{-4} times the radius of the drop would form. The model therefore implies that the initially formed shell would become thinner in an unsaturated environment. The thinning of the hydrate shell after formation has been experimentally observed in the viewcell experiments and is reflected by changes in both the texture and transparency of hydrate-covered drops. Initially, the shell has rough texture and is opaque. Within a few minutes the shell becomes smooth and relatively transparent.

For a CO_2 drop injected into saturated water, the model predicts that with time the hydrate shell would thicken, possibly approaching 10^{-1} cm in thickness for growth periods well in excess of 100 hours. Such conditions could occur in the vicinity of the injection. Since the water is saturated with respect to hydrate-forming conditions, the hydrate shell serves only to slow the diffusion of CO_2 and thus limit the formation of additional hydrate from the injected CO_2. Results for this scenario are shown in Figure 1. The diffusivity values for CO_2 through the hydrate shell, D_H, used in Figure 1 are in the range of values for diffusivities in solids. Experimental determination of this value would be required for validation of this portion of the model.

In water oversaturated with CO_2 relative to C_H, the shell could also thicken by addition to the hydrate layer from the CO_2 dissolved in the water. This mode of growth was the subject of an earlier paper (9). The above model also did not take into consideration the effect of varying salt concentration at the surface of drop as hydrates form. Current modeling efforts at FETC are directed at incorporating this effect.

RESEARCH AT UHM

A 36-month research grant to investigate ocean disposal of CO_2 was awarded by DOE to the University of Hawaii at Manoa in August 1995. The laboratory study is being conducted by the Hawaii Natural Energy Institute of the School of Ocean and Earth Science and Technology. The principal objective of the study is to obtain data on liquid CO_2 discharge jet instability and on drop dispersion, interactions, and dissolution under conditions representative of the deep ocean. These data will be applied to the development and validation of predictive models to perform (ocean) environmental hazard assessments and to devise injection methods that ensure effective containment of the CO_2 from the atmosphere.

Experiments at UHM employ a unique High-Pressure CO_2 Mixing Facility (HCMF), designed specifically to investigate the oceanic CO_2 disposal process. The HCMF comprises a cylindrical pressure vessel, systems to hold and supply liquid CO_2 and chilled (ambient to 0°C) water, and diagnostics and data acquisition equipment. The insulated steel pressure vessel has an I.D. of 0.55 m and is 2.46-m tall. During experiments, it is partially filled with fresh or seawater and pressurized with an inert gas to simulate conditions in the ocean down to depths of approximately 600 m. A photograph of the pressurized test vessel is shown in Figure 2. Numerous viewports provide access for quantitative optical probes and for flow visualization. Details of the construction and operation of the HCMF have been reported (10).

Two types of tests will be conducted using the HCMF: (1) continuous discharging of liquid CO_2 through a variety of orifices over a range of conditions to study effluent breakup and injector performance; and (2) monitoring of single CO_2 droplets or droplet pairs as they dissolve and interact during simulated buoyant rise through the ocean. In the continuous discharge experiments, a non-intrusive, laser scattering diagnostic will be employed to map droplet size distribution spectra, velocity, and number density in the region immediately downstream from the injector. These data on initial CO_2 droplet size distributions and spatial dispersion are needed to model accurately the disposal process. The primary experimental variables include jet velocity, simulated depth of discharge, and injector orifice size and geometry.

In the droplet dissolution experiments, a transparent diffuser will be submerged in the pressure vessel aligned with its vertical axis. Water from the vessel is pumped downward through the diffuser to stabilize in space buoyant liquid CO_2 droplets that have been bled into the diffuser. By this means, the unrestrained rise through the ocean can be simulated in a facility of finite height. Close-up image acquisition and analysis will be employed to document droplet dissolution and interaction phenomena.

In both the continuous discharge and dissolution tests, experiments will be repeated under ambient water conditions that either foster or preclude the formation of the CO_2 clathrate hydrate. As of this writing, facility preparations and diagnostic development are being completed.

Complementary mathematical modeling to date has focused on theoretical analyses of CO_2 jet instabilities and the generation of the dispersed droplet phase. The effects of hydrate formation on these instabilities have been considered (11). Results suggest that if hydrate formation kinetics proceed more rapidly than the amplification of the jet instability, then breakup may be modified and the dispersed droplet phase size distribution altered. At the extreme, a solid hydrate layer could grow and deposit around the injection orifice, encasing the jet and possibly closing it off. While calculations indicate that hydrate formation effects will be restricted to situations involving relatively large injector orifices (> 1-cm diameter) and low jet velocities (< 6 cm/s), the uncertainty in some parameters used in these calculations, notably the rate constant for hydrate formation, warrant experimental confirmation.

Recently, the DOE-funded experimental research at UHM has attracted international interest. Additional funds have been committed to the project by ABB Management, Ltd. in Switzerland and Statoil (Norway) has offered the use of instrumentation and the professional assistance of research personnel from the University of Bergen. Interest in collaborative studies has also been expressed by Japanese investigators.

SUMMARY

DOE-sponsored research at FETC and UHM is addressing important issues related to the effect of hydrates on the ocean disposal of CO_2. These issues include: 1) the relative density of hydrate particles and how to either preclude hydrate formation or form particles that would sink in the ocean and thus facilitate sequestration efforts; 2) the behavior of hydrates during formation either as particles or as shells around liquid CO_2 drops, and how their formation would impact CO_2 dissolution and jet dynamics; and 3) the dissolution behavior of hydrate-covered CO_2 drops and the fate of these drops in the ocean. Data are being sought to help develop and validate predictive models which can be employed to identify effective sequestration strategies and to evaluate impacts on the marine environment.

DISCLAIMER

Reference in this report to any specific product, process, or service is to facilitate understanding and does not imply its endorsement or favoring by the United States Department of Energy.

REFERENCES

1. A Research Needs Assessment for the Capture, Utilization and Disposal of Carbon Dioxide from Fossil Fuel-Fired Power Plants, DOE Report DOE/ER-30194, July 1993 (available NTIS).
2. Warzinski, R. P.; Cugini, A. V.; Holder, G. D. Proc. Int. Conf. Coal Sci. **1995**, 2, 1931-1934.
3. Warzinski, R. P.; Lee, C.-H.; Holder, G. D. J. Supercrit. Fluids **1992**, 5, 60-71.
4. Omerod, B.; Angel, M. Ocean Storage of Carbon Dioxide: Workshop 2 - Environmental Impact, IEA Greenhouse Gas R&D Programme Report, June 1996.
5. Holder, G. D.; Cugini, A. V.; Warzinski, R. P. Environ. Sci. Tech. **1995**, 29, 276-278.
6. Holder, G. D.; Warzinski, R. P. Prepr. Pap. -Am. Chem. Soc., Div. Fuel Chem. **1996**, 41(4), 1452-1457.
7. Burruss as reported by E.D. Sloan, Jr. in International Conference on Natural Gas Hydrates; E.D. Sloan, Jr.; J. Happel; M.A. Hnatow, Eds.; Annals of the New York Academy of Sciences; Vol. 715; p 17.
8. Maini, B. B.; Bishnoi, P. R. Chem. Engng. Sci. **1981**, 36, 183-189.
9. Holder, G. D.; Cugini, A. V.; Warzinski, R. P. Environ. Sci. Tech. **1995**, 29, 276-278.
10. Masutani, S. M.; Kinoshita, C. M.; Nihous, G. C.; Ho, T.; Vega, L. A. Energy Convers. Mgmt. **1993**, 34(9-11), 865-872.
11. Teng, H.; Masutani, S. M.; Kinoshita, C. M.; Nihous, G. C. Prepr. Pap. -Am. Chem. Soc., Div. Fuel Chem. **1996**, 41(4), 1447-1451.

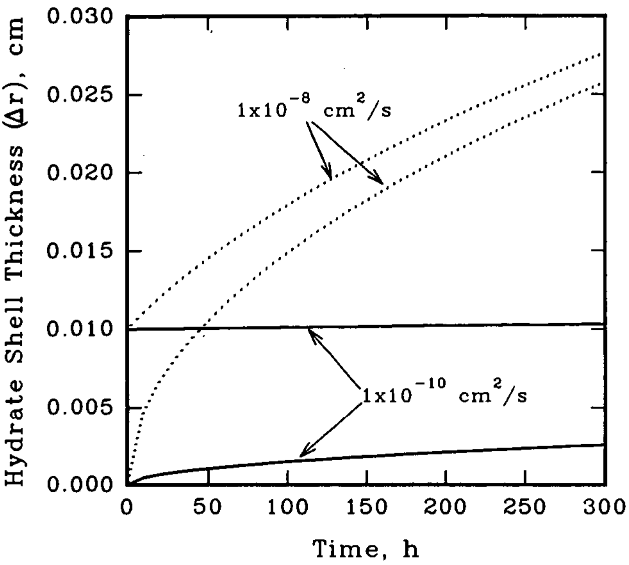

Figure 1. Thickening of the hydrate shell in a saturated reservoir as a function of time and solid-phase diffusivity, D_H (values shown in figure), and the initial thickness of the hydrate shell (indicated at time = 0).

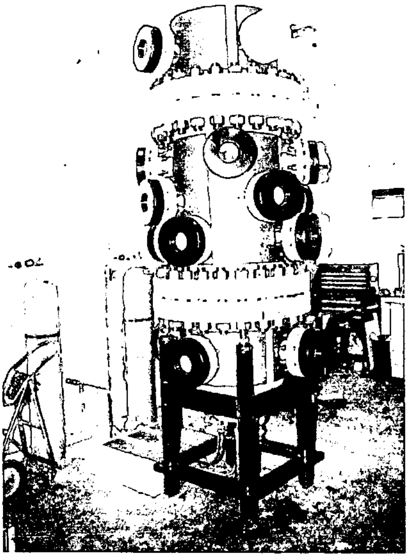

Figure 2. Photograph of the pressurized test vessel used in the High Pressure CO_2 Mixing Facility at the University of Hawaii at Manoa.

DOE INDIRECT COAL LIQUEFACTION - HURDLES AND OPPORTUNITIES FOR ITS EARLY COMMERCIALIZATION.

John Shen and Edward Schmetz, U.S. Department of Energy, Germantown, MD 20874, Gary Stiegel and Richard Tischer, U.S. Department of Energy, P.O. Box 10940, Pittsburgh, PA 15236

Keywords: Fischer-Tropsch, Slurry phase reactor, Co-production

INTRODUCTION

Coal is the most abundant domestic energy resource in the United States. The Fossil Energy organization within the U.S. Department of Energy (DOE) has been supporting a coal liquefaction program to develop improved technologies for converting coal to clean and cost-effective liquid fuels and/or chemicals to complement the dwindling supply of domestic petroleum crude. The goal of this program is to produce coal liquids that are competitive with crude at $25 per barrel. Indirect and direct liquefaction routes are the two technologies being pursued under the DOE coal liquefaction program. In indirect liquefaction, the emphasis is on the development of improved liquid phase reactor technology to convert "lean syngas" (low hydrogen to carbon monoxide ratio) produced from advanced coal gasifiers. In this paper, the terms of "liquid phase reactor" and "slurry phase reactor " are considered interchangeable.

An overview of the DOE indirect liquefaction program, including the development highlights of the Liquid Phase Methanol technology which is undergoing commercial demonstration at the Eastman Chemicals plant in Kingsport, Tennessee within the DOE Clean Coal Program, can be found elsewhere (Shen, et al. 1996). This paper will update the status of DOE indirect liquefaction program, and briefly review the recent development in the commercial liquid phase reactor design. It also will discuss the hurdles and opportunities for the early commercialization of this technology.

UPDATED STATUS OF DOE INDIRECT LIQUEFACTION PROGRAM

Slurry Phase Fischer-Tropsch Three slurry phase Fischer-Tropsch runs have been made at the proof-of-concept (POC) unit at LaPorte, Texas between 1992 and 1996, with costs shared by industrial consortiums headed by Air Products and Chemicals (APCI). The first two runs used iron catalysts and the third one a cobalt catalyst. Highlights of the first two runs have been reported earlier (Shen, et al. 1996). More detailed review of the first run data also has been published (Bhatt, et al. 1995)..These results indicate that, with the system to convert lean syngas over iron catalysts, more work is needed to improve the correlations between the autoclave and POC slurry phase reactor data. Also, efforts should be directed to explore the advantages of iron over cobalt catalysts to produce a more versatile product slate including olefins. Finally, more fundamental study is needed to gain a better understanding of the iron catalyst behavior in a slurry phase F-T reactor. Data workup for the third run with a cobalt catalyst is now underway

Liquid Phase Dimethyl Ether (DME) The feasibility of liquid phase DME technology was first demonstrated by APCI at the LaPorte POC unit in 1991. Since then, there have been considerable industrial interests in this one-step syngas to DME technology, which could reduce the DME cost as a fuel or a precursor to chemicals. Recent work at bench scale unit has been aimed to further reduce the deactivation rate for the physical mixture of methanol synthesis and methanol dehydration catalysts present in a liquid phase reactor. Results obtained with APCI's improved proprietary dehydration catalyst appear encouraging (Parris, et al. 1996). The commercial demonstration of liquid phase DME technology at the Liquid Phase Methanol project site at Kingsport is tentatively scheduled for year 2000.

Synthesis Gas to Oxygenates and Chemicals Novel catalyst R&D has been underway to convert synthesis gas to oxygenates and chemicals under cost-shared contracts. The products include mixed alcohols including isobutanol (Xu, et al. 1996), vinyl acetate monomer (Tustin, et al. 1996), methyl methacrylate (Spivey, et al. 1996), and dimethyl carbonate (Hagen, 1996). The industrial participants in this program include APCI, Eastman Chemicals, RTI, Bechtel, and Amoco.

Commercial Liquid Phase Reactor Development

A recent media release indicates that Sasol has placed orders for seven SAS (Sasol Advanced Synthol) gas phase reactors with diameters up to 10.7 meters (Sasol 1996). It seems reasonable to assume that the same size reactor also can be used for slurry phase reactor applications. In an earlier DOE supported study, Bechtel has designed a commercial slurry phase reactor with a diameter of 4.8 meters (Fox, et al. 1990). At that time considerable considerations have been given to the reactor physical constraints including the weight of tube sheets holding the internal tube exchanger. It seems prudent that, in view of the Sasol announcement, the commercial slurry phase reactor design should be revisited to evaluate the various impacts of a larger reactor size.

Hurdles and Opportunities for the Early Commercialization of Indirect Liquefaction Technology

Due to the federal budget constraints, DOE has been exploring the use of "financial incentives" rather than "cost-sharing" to promote the commercial demonstration of slurry phase F-T technology. Preliminary results from this scoping study, conducted by Mitretek with DOE support, will be reported in a separate paper at this meeting (Gray, et al. 1997). Under this proposal, an industrial consortium would be formed to lead the effort, with DOE to cost-share the Phase Zero project feasibility study and to serve as an advocate for the use of incentives. Use of incentives is deemed necessary to mitigate the high risks associated with these projects. It is also consistent with our precedents to offer "limited" incentives to introduce a new domestic resource based transportation fuel because of its vital importance to the economic well-being of our country.

IGCC (integrated gasification combined cycle) system, which is an integrated part of the indirect liquefaction technology, has recently received more commercial interests, partly in response to the emerging trend in tighter environmental regulations (Rhodes 1996; Aalund, 1996). In these applications and others under considerations, a variety of carbonaceous feedstock are used to address the local need to dispose the environmentally disadvantageous materials. With more and more these IGCC systems in place, the opportunity to co-produce power, premium quality transportation fuels and/or chemicals could offer the best prospect for the early commercial deployment of the slurry phase F-T technology. With the learning experience gained from these operations, a transition to coal based IGCC/slurry phase F-T could be underway between 2010 and 2015 when coal liquid is projected to be competitive with crude (Gray, et al. 1996).

CONCLUSIONS

We have presented an updated summary of the work performed under DOE indirect liquefaction program since 1994. In the slurry phase F-T area, we also have identified areas for future R&D work. A "financial incentives" based approach, to be led by an industrial consortium, has been proposed to promote the commercial demonstration of slurry phase F-T technology. The early commercial deployment of this technology could be in the IGCC based power plants to co-produce power, premium quality transportation fuels, and/or chemicals. The DOE supported slurry phase F-T technology is tailored for co-production applications with enhanced system efficiency.

REFERENCES

Aalund, L.R., "Italian Refinery Gasification Project to Make Electricity, Steam, and Hydrogen from Tar", Oil & Gas Journal, P. 33, October 21, 1996

Bhatt, B.L., R. Frame, A. Hoek, K. Kinnari, V.U.S. Rao, and F.L. Tungate 1995 "Catalyst Processing Scale-up for Fischer-Tropsch Synthesis", Topics in Catalysis 2 (1995) 235-257.

Fox, J.M., B.D. Degen, G. Cady, F.D. Deslate, and R.L. Summers 1990 "Slurry Reactor Design Studies: Slurry vs. Fixed-Bed Reactors for Fischer-Tropsch and Methanol", Final Report, DOE/PC/89867/T2, June 1990

Gray, D., and G. Tomlinson 1996 "Incentives for the Commercialization of Liquefaction Technologies", Paper Presented at the First Joint Power & Fuel Systems Contractors Conference, Pittsburgh, PA, July 9-11, 1996

Gray, D., and G. Tomlinson 1997 "Opportunities for Early Commercial Deployment of Indirect Liquefaction", Paper to be Presented at the American Chemical Society Meeting, San Francisco, CA, 4/13-4/17, 1997

Hagen, G.P. 1996 "Synthesis of Oxygenate Products for High Volume Fuels Applications", Paper Presented at the First Joint Power & Fuel Systems Contractors Conference, Pittsburgh, PA, July 9-11, 1996

Parris, G.E., X.D. Peng, and B.A. Toseland 1996 "Some Advances in Catalysis for Alternate Fuels", Paper Presented at the First Joint Power & Fuel Systems Contractors Conference, Pittsburgh, PA, July 9-11, 1996

Rhodes, A.K., "Kansas Refinery Starts Up Coke Gasification Unit", Oil & Gas Journal, P. 31, August 5, 1996

Sasol 1996 Media Release: "Sasol Awards Contract to the Consortium of Hitachi Zosen and Marubeni for Seven Advanced Synthol Reactors", October 22, 1996

Shen, J., G. Stiegel, and A. Bose 1996 "DOE Indirect Coal Liquefaction Program - An Overview", Fuel Sciences & Technology Int'l, 14(4), 559-576 (1996)

Spivey, J.J., M.R. Gogate, J.R. Zoeller, R.D. Colberg, G.N. Choi, and S.S. Tam 1996 "Synthesis of Methyl Methacrylate from Coal-Derived Syngas", Paper Presented at the First Joint Power & Fuel Systems Contractors Conference, Pittsburgh, PA, July 9-11, 1996

Tustin, G.C., J.R. Zoeller, and L. DePew 1996 "Synthesis of Vinyl Acetate Monomer from Synthesis Gas", Paper Presented at the First Joint Power & Fuel Systems Contractors Conference, Pittsburgh, PA, July 9-11, 1996

Xu, M., B.L. Stephens, M.J.L. Gines, and E. Iglesia 1996 "Reaction Pathways and Catalyst Requirements in the synthesis of Isobutanol from CO and Hydrogen", Paper Presented at the First Joint Power & Fuel Systems Contractors Conference, Pittsburgh, PA, July 9-11, 1996

AN EVALUATION OF PROPERTIES FOR CALIFORNIA REFORMULATED GASOLINE

Analisa R. Bevan, Tony R. Brasil, and James J. Guthrie
California Air Resources Board
2020 L Street
Sacramento, California 95814

Keywords: California, Reformulated, Gasoline

ABSTRACT

California began using a cleaner-burning reformulated gasoline in March 1996. The California reformulated gasoline regulations limit eight specific properties, with flexibility given to refiners to average properties, or to use a predictive model to blend gasolines having equivalent emission benefits. Data were collected from refiners, compliance fuel sample monitoring, and the California Energy Commission. These data are used to compile a picture of California reformulated gasoline's average properties and the range of properties. The properties evaluated include sulfur, aromatic hydrocarbon, benzene, olefin, and oxygen content, distillation temperatures at 50 and 90 percent volume, and Reid vapor pressure. Additionally, data have been collected pertaining to the energy density which affects the fuel economy of this cleaner-burning gasoline. This evaluation confirms the Air Resources Board's pre-regulation analysis on emission performance and fuel economy.

INTRODUCTION

Presented is an evaluation of data which illustrates the present composition of gasoline in California. California introduced a cleaner-burning reformulated gasoline (CaRFG) in 1996 as part of its comprehensive program to reduce air pollution. Since CaRFG's introduction, the Air Resources Board (ARB) has monitored the composition of gasoline sold in California through several mechanisms. An evaluation of this data was performed to verify that estimated emission benefits are being met. The ARB also calculated the energy difference of CaRFG on a subset of available data using oxygen content, specific gravity, distillation temperatures at 10, 50 and 90 percent volume (T10, T50 and T90), and aromatic hydrocarbon content.

BACKGROUND

Air Quality Compared to California Phase 1 gasoline (Post-1992), CaRFG reduces emissions of volatile organic compounds (VOC), oxides of nitrogen (NOX), and carbon monoxide (CO), as well as the risk from exposure to toxic air contaminants. Table 1 shows the emission reductions attributable to CaRFG.

CaRFG Regulation The CaRFG regulations set specifications for eight properties with several compliance options available to gasoline producers. Compliance options which provide refiners flexibility in meeting the regulation include; (1) compliance with regulation flat limits, (2) the use of averaging based on the regulation averaging limits; (3) the use of a predictive model; or (4) the use of an alternative formulation certified to have equivalent emission performance. Since the implementation of the CaRFG regulation, no fuel producers have used the alternative formulation method of compliance.

The CaRFG regulation sets cap limits for each of the eight regulated properties. The cap limits ensure that compliance can be demonstrated at all points of the distribution and marketing system. These limits are listed in Table 2.

Regulation Flat limits The regulation flat limits, listed in Table 2, are fixed for each regulated property and cannot be exceeded when complying by this method. Refiners are not required to report batch properties to the ARB when using this method of compliance.

Averaging Limits The averaging limits are listed in Table 2. Gasoline producers using the averaging limits to comply with the CaRFG must demonstrate that volume weighted gasoline production averages meet each specification limit by the end of the averaging period without exceeding the cap limit. As shown in Table 2, the averaging limits are lower than the flat limits. Under this compliance option refiners must report the measured properties and volumes of each batch of fuel produced to the ARB.

Predictive Model The Predictive Model provides fuel producers with flexibility to optimize the gasoline properties of fuel produced to match the capabilities of their facilities. The predictive model allows fuel producers to designate alternative flat limits and averaging limits while maintaining the emission benefits of the CaRFG regulation. The majority of producers have chosen to use this method of compliance. The compliance reporting requirements are similar to the compliance options described above. However, the specifications of the eight regulated properties must be reported to the ARB.

DATA COLLECTED

Regulation Flat Limits Since no reporting by fuel producers to the ARB is required for this option, it was assumed that fuel producers using this option produced fuel with properties at the regulation flat limits. The gasoline production volume was obtained from the California Energy Commission (CEC) from weekly production data.

Regulation or Predictive Model Averaging Limits Under this option, gasoline producers must report the properties and volume of each batch produced to the ARB; thus, the average properties were calculated directly from their compliance reports.

Predictive Model Flat Limits Many gasoline producers used several predictive model formulations in a given month. Since the volume of gasoline produced under each formulation was not reported, a typical formulation reported from each producer in a given month was used. The production volume for each producer was again estimated with CEC weekly gasoline production data.

Compliance Sample Data ARB compliance sampling data were used to evaluate energy density changes associated with CaRFG. A total of 103 samples comprised this subset of CaRFG data.

Presented Data

Table 3 lists the approximate volume weighted average properties of the gasoline being produced in California from March 1996 through September 1996.

Table 4 summarizes the properties found in samples of summertime CaRFG sold in 1996. The table also summarizes and provides a comparison to summertime California gasoline sold in 1990 and 1991.

DATA ANALYSIS

Evaluation CaRFG Regulatory Compliance Table 3 shows that the average CaRFG properties of fuel sold in California are very similar to the regulation flat limits. Of the eight properties, only the T90 specification is higher. It is higher because many fuel producers have been able to increase the T90 when meeting the predictive model flat limits.

Evaluation of Emissions Effects The predictive model provides the basis for the emissions characteristics of the formulations presented here. The predictive model predicts the relative change in emissions compared to the regulation flat limits or averaging limits. Although changes in emissions compared to changes in properties are not always linear, they can be estimated linearly for the range of properties allowed in the regulation. Because of this, the average emissions of each batch are expected to be similar to the emissions of the average properties of all batches.

The in-use California average gasoline properties have the same emissions benefits as anticipated by the ARB. Since the averaging limits are more stringent than the flat limits, the average properties of the in-use gasolines meeting averaging limit specifications were evaluated separately from those meeting flat limit specifications. Table 3 lists the average gasoline properties from March to September 1996 for gasoline meeting the flat limits, averaging limits, and the overall average gasoline properties.

Evaluation of Fuel Economy Effects All of the eight CaRFG property limits may have some impact on volumetric energy content (Btu/gal) and vehicle fuel economy (mpg). Vehicle fuel economy has been shown to correlate well with gasoline energy content as estimated by ASTM D 3338, modified by considering oxygenated contents separately (Hochhauser, et al, 1993). The most significant of the regulated properties to this procedure are oxygen content, aromatic hydrocarbon content, T50 and T90. The sulfur content has an insignificant impact at the levels found in CaRFG, and is not considered in our estimation of the energy contents of CaRFG.

The oxygen content requirement decreases energy content, because the oxygenated compounds have reduced lower heating values (Btu/lbm) than gasoline. Gasoline with 2 percent by weight oxygen has about a 2 percent lower volumetric energy content than non-oxygenated gasoline. The specific gravity is second only to the oxygen content in its significance to the energy content of CaRFG. Specific gravity is not a regulated property; however, all of the eight regulated properties may have some impact on the specific gravity. The reduction of Reid vapor pressure required of summertime CaRFG may be the only property regulation which tends to increase specific gravity and, consequently, energy content and fuel economy. Aromatic hydrocarbon content, T50 and T90 limits tend to decrease specific gravity, energy content, and fuel economy. The difference in the mean energy contents of CaRFG and Pre-CaRFG is shown in Table 4 to be -3.5 percent.

Consider a vehicle and engine operating at steady speed and load at a given excess-air factor (air-to-fuel ratio relative to theoretical). Ignore changes in thermal efficiency due to small changes in air, fuel, and exhaust flow, which are required to maintain the fixed conditions. Then, a small relative change in fuel energy content should result in an equivalent relative change in vehicle fuel economy (Blackmore and Thomas, 1977). Compared to a fuel with 3 percent greater energy content, under the same conditions the vehicle will travel a 3 percent shorter distance burning the same volume of lower energy fuel. Under the assumptions, a decrease in specific gravity and increase in oxygen content, such as from CaRFG regulations, do not change this relationship. However, under transient operation of the vehicle and engine, or with carburetion designed to maintain a fixed air-to-fuel ratio, the CaRFG regulations should result in reduced fuel mass flow and enleanment (excess-air factor increase) (API, 1988). A slight increase in fuel volume flow should have a negative effect on vehicle fuel economy. Enleanment could increase or decrease engine thermal efficiency; the decrease occurring only with enleanment beyond an excess-air factor of about 1.1 (Adler, 1986).

The change in thermal efficiency should have a corresponding effect on vehicle fuel economy. This theory suggests that, the relative change in vehicle fuel economy is proportional and roughly equivalent to the relative change in gasoline energy content under normal operation of most vehicles. Laboratory dynamometer testing of vehicles operated over the Federal Test Procedure cycle confirms this theory and suggests that the constant proportionality is less than one (Hochhauser, et al, 1993). We conclude that the percent change in average fuel economy of California's gasoline-fueled vehicles, due to the introduction of CaRFG, is less than the percent change in the average energy content of gasoline.

CONCLUSIONS

Our evaluation of CaRFG data shows that fuel producers have met the regulation property limits and that they have made use of available regulation flexibility by implementing various compliance options. Based on analysis performed on the average properties presented, it appears that emission benefits predicted for the regulation are being realized. Additionally, based on sample data and energy density calculations, the effect on fuel economy is relatively small. The overall evaluation of the data confirms pre-regulation analysis of emissions and fuel economy effects.

TABLE 1
Predicted Emission Benefits of California Reformulated Gasoline

Market Segment Reductions	VOC	NOx	CO
On-Road	17%	11%	11%
Off-Road	10%	--	--
Marketing Operations	7%	--	--
Total	**15%**	**11%**	**11%**

Note: Emission benefits of CaRFG for off-road and marketing operations are not separated from on-road categories.

TABLE 2
California Reformulated Gasoline Specification Limits

Property	**Flat Limits**	**Averaging Limits**	**Cap Limits**
Aromatic Hydrocarbon, vol%	25	22	30
Benzene, vol%	1.0	0.80	1.2
T50, F	210	200	220
T90, F	300	290	330
Olefins, vol%	6.0	4.0	10.0
RVP, psi	7.0	--	7.0
Sulfur, ppmw	40	30	80
Oxygen, vol%	1.8 to 2.2	--	1.8 to 2.7

TABLE 3
California Average Gasoline Properties
(March to September 1996)

Property	**Flat Limits**	**Averaging Limits**	**Overall**
Aromatic Hydrocarbon, vol%	24.5	23.9	24.2
Benzene, vol%	0.87	0.55	0.73
T50, F	204	200	202
T90, F	313	298	306
Olefins, vol%	6.6	3.6	5.2
RVP, psi	7.0	7.0	7.0
Sulfur, ppmw	41	14	29
Oxygen, vol%	2.0	1.8	1.9

TABLE 4
Evaluation of Fuel Economy Effects of CaRFG

	Oxygen (%wt)	AroHC (%vol)	RVP (psia)	T10 (F)	T50 (F)	T90 (F)	Sp.Grav. @ 60F	ASTM D 3338 (Btu/gal)
CaRFG (103 Samples)								
Minimum	1.30	9.5	5.96	139	162	276	0.7241	110,200
Maximum	2.90	31.6	7.19	158	229	339	0.7522	113,000
Median	2.17	22.9	6.73	144	201	308	0.7407	111,800
Mean	2.18	22.4	6.71	145	201	309	0.7400	111,700
Pre-CaRFG (90-91) (441 Samples)								
Minimum	Not Known, But Small	4.5	6.9	98	170	281	0.706	109,900
Maximum		60.8	9.3	156	251	362	0.795	120,300
Median		35.8	8.5	130	222	331	0.757	115,800
Mean		36.1	8.4	131	221	329	0.758	115,800
Difference of Means	+2	-13.7	-1.7	+14	-20	-20	-2.4%	-3.5%

REFERENCES

California Air Resources Board, Stationary Source Division, 1991. Proposed Regulations for California Reformulated Gasoline, Vol. 1, California Reformulated Gasoline Specifications, Staff Report. Sacramento, California.

California Air Resources Board, Stationary Source Division, 1994. Proposed Amendments to the California Phase 2 Reformulated Gasoline Regulations, Including Amendments Providing for the Use of a Predictive Model. Sacramento, California.

California Air Resources Board, 1994. Memorandum, "Phase 2 Reformulated Gasoline Emission Benefits." Peter D. Venturini to K.D. Drachand and Terry McGuire.

Adler, U, Editor-in-Chief, 1986. Automotive Handbook, Robert Bosch Gmbh, Stuttgart.

API, 1988. Alcohols and Ethers, A Technical Assessment of Their Application as Fuels and Fuel Components, API Publication 4261, American Petroleum Institute, Washington, D.C.

ASTM, 1992. "Standard Test Method for Estimation of Net Heat of Combustion of Aviation Fuels," ASTM D 3338-92, American Society for Testing and Materials, Philadelphia.

Blackmore and Thomas, editors, 1977. Fuel Economy of the Gasoline Engine: Fuel, Lubricant and Other Effects, John Wiley & Sons, New York.

Hochhauser, Benson, Burns, Gorse, Koehl, Painter, Reuter, and Rutherford, 1993. "Fuel Composition Effects on Automotive Fuel Economy--Auto/Oil Air Quality Improvement Research Program," SAE 930138, Society of Automotive Engineers, Inc, Warrendale, Pennsylvania.

ACKNOWLEDGMENTS

Staff of the Air Resources Board and California Energy Commission were valuable to the collection of data presented. Contributions from the following staff were appreciated: C. Beddow, D. Lum, and F. Schmidt (ARB Compliance Division); A. Hebert and J. Cohan (ARB Monitoring and Lab Division); D. Simeroth, J. Courtis, K. Macias, R. Vincent and N. Chan (ARB Stationary Source Division); G. Shremp (California Energy Commission).

DEVELOPMENT OF A CERAMIC MEMBRANE FOR UPGRADING METHANE TO HIGH-VALUE-ADDED CLEAN FUELS

U. Balachandran, J. T. Dusek, J. J. Picciolo, P. S. Maiya,
B. Ma, and R. L. Mieville
Argonne National Laboratory, Argonne, IL 60439

M. S. Kleefisch and C. A. Udovich
Amoco Exploration and Production, Naperville, IL 60566

Keywords: Mixed conductor, dense ceramic membrane, methane conversion

INTRODUCTION

The upgrading of natural gas (which consists mostly of methane) to high-value-added clean-burning fuels such as dimethyl ether, alcohols, and pollution-fighting fuel additives is driven by the abundance of natural gas discovered in remote areas. Recently, extensive efforts have focused on both direct and indirect conversion of methane to these value-added products [1,2]. The direct-conversion route is the most difficult approach because the products are more reactive than the starting reactant, methane [3]. Indirect routes require the partial oxidation of methane to synthesis gas (syngas, $CO + H_2$) in a first stage. The syngas is then converted to upgraded products in a second stage. The most significant cost associated with partial oxidation of methane to syngas is that of the oxygen plant. In this paper, we offer a technology that is based on dense ceramic membranes and that uses air as the oxidant for methane-conversion reactions, thus eliminating the need for the costly oxygen plant. Certain ceramic materials exhibit both electronic and oxide-ionic conductivities. These mixed-conductor materials transport not only oxygen ions (functioning as selective oxygen separators), but also electrons. No external electrodes are required and such a system will operate without an externally applied potential. Oxygen is transported across the ceramic material in the form of oxygen anions, not oxygen molecules.

Recent reports in the literature suggest that ceramic membranes made of these mixed conductors can successfully separate oxygen from air at flux rates that could be considered commercially feasible. Thus, they have potential applications for improving the economics of methane conversion [4-6].

Teraoka et al. [4] showed that oxides in the La-Sr-Fe-Co-O system exhibit mixed conductivity and appreciable oxygen permeability. However, we have found that these oxides are unstable when exposed to methane at elevated temperatures and are therefore unsuitable for syngas conversion. We have developed a novel ceramic composition, namely $SrFeCo_{0.5}O_x$, that is stable in methane and that has oxygen permeation suitable for the partial oxidation of methane [7,8].

EXPERIMENTAL

Ceramic powders of composition $SrFeCo_{0.5}O_x$ were made by solid-state reaction of the constituent cation salts. Appropriate amounts of $SrCO_3$, $Co(NO_3)_2{\cdot}6H_2O$, and Fe_2O_3 were mixed and milled in isopropanol with ZrO_2 media for ≈15 h. When dry, the mixtures were calcined in air at ≈850°C for ≈16 h, with intermittent grinding. After final calcination, we ground the powder with an agate mortar and pestle to an average particle size of ≈7 µm. The resulting powders were characterized by X-ray diffraction (XRD), scanning electron microscopy (SEM), and thermal analysis and were also analyzed for particle-size distribution.

The powder was made into a slip containing a solvent, dispersant, binder, and plasticizer. Membrane tubes were fabricated by extrusion of the slip to an outside diameter of ≈6.5 mm, lengths up to ≈30 cm, and wall thicknesses of 0.25-1.20 mm. The tubes were sintered at ≈1200°C, then characterized by SEM and XRD, and finally used in our methane partial-oxidation studies.

The tubes were evaluated for performance in a quartz reactor system, as shown in Fig. 1. The quartz reactor supports the ceramic membrane tube with hot Pyrex seals. An Rh-based reforming catalyst was loaded adjacent to the tube, and a gold wire mesh was wrapped around the tube to prevent solid-state reactions between the catalyst and the ceramic tube. Both the feed gas (generally 80% CH_4 and 20% Ar) and the effluents were analyzed with a gas chromatograph. Inside the membrane tube, air was the source of oxygen.

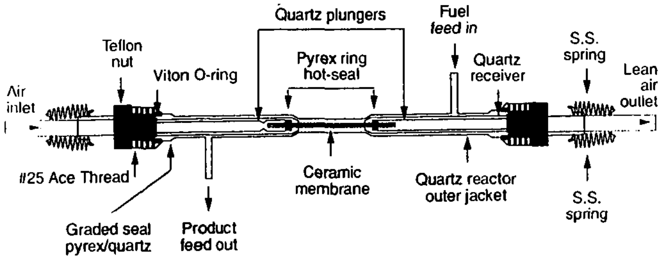

Fig. 1. Schematic diagram of ceramic membrane reactor.

Electrical conductivity was determined by a four-probe method that used a blocking electrode of yttria-stabilized zirconia (YSZ) for oxygen ion conduction [9], while the oxygen diffusion coefficient was measured by a time relaxation method. The sample was subjected to a sudden increase in oxygen partial pressure, and ionic conductivity was monitored as a function of time and temperature [10].

RESULTS AND DISCUSSION

The XRD pattern of an $SrFeCo_{0.5}O_x$ sample recorded at 850°C in an $Ar\text{-}O_2$ gas mixture is shown in Fig. 2. The material exhibited remarkable structural stability at high temperature, and no phase transition was observed as oxygen partial pressure was changed. This structural stability of $SrFeCo_{0.5}Ox$, when compared with that of other mixed conducting oxides of similar type, is reflected in its physical and mechanical properties, as shown in our earlier publications [7,11].

The measured electronic and ionic conductivities of $SrFeCo_{0.5}O_x$ and other materials of the same family are shown in Table 1. It is clear that this material is unique in that its ratio of ionic to electronic conductivity is close to unity. The chemical diffusion coefficient, as determined by the conductivity relaxation method [9], is shown in Fig. 3. The diffusion coefficient increases exponentially with temperature, and at 900°C, is ≈9 x 10^{-7} cm^2/s. Activation energy associated with oxygen diffusion is ≈0.9 eV, which indicates that oxide ions can move more easily in the $SrFeCo_{0.5}O_x$ sample than in other mixed-conducting oxides.

Figure 4 shows conversion data obtained with an $SrFeCo_{0.5}O_x$ membrane tube operated at 850°C for ≈70 h in the reactor setup shown in Fig. 1. As seen in Fig. 4, methane conversion efficiency is >98% and CO selectivity is ≈90%. Measured H_2 yield is about twice that of CO, as expected.

Observations by Liu et al. [12] indicate that not only the conductivity of the membrane material, but also the catalytic activity of the surface or interfaces, has a significant effect on the rate of oxygen permeation. Conductivity (ionic and electronic) determines the mass and charge transport rates through the membrane, while catalytic activity controls the rate of interfacial electrochemical reactions. To decouple the role of the catalyst in oxygen transport across the membrane, an $SrFeCo_{0.5}O_x$ tube was tested without the reforming catalyst. The results from a run of ≈350 h are shown in Fig. 5. The feed gases are the same as earlier (80% CH_4 and 20% Ar). In the absence of a catalyst, the oxygen that was transported through the membrane reacted with CH_4 to form CO_2 and H_2O. As seen in Fig. 5, methane conversion efficiency was ≈35% and CO_2 selectivity was ≈90%.

Further confirmation of the stability and high performance of this membrane tube is shown in Fig. 6, which illustrates reactor results over a period of 1000 h. The feed during this period was a typical mixture expected in a commercial recycling feed, namely CH_4, CO, CO_2, and H_2. Throughout the run, methane conversion was high. A small decline in oxygen permeation was observed. The high oxygen flux is consistent with the high diffusion coefficient of 9 x 10^{-7} cm^2 s^{-1} that was measured by the time-relaxation method [9].

Table 1. Electronic and ionic conductivities of various mixed oxides

Sample	Electronic σ_{el} (S·cm^{-1})	Ionic σ_i (S·cm^{-1})	Method for Measuring σ_i
$SrFeCo_{0.5}O_x$	10	7	4-terminal, YSZ electron block
$SrFe_{0.8}Co_{0.2}O_x$	76	4	4-terminal, YSZ electron block
$La_{0.6}Sr_{0.4}Co_{0.2}Fe_{0.8}O_3$	300	0.01	4-terminal, YSZ electron block
$La_{0.6}Sr_{0.4}Co_{0.2}Fe_{0.8}O_3$	300	0.003	2-terminal, electron block
$La_{0.8}Sr_{0.2}Co_{0.8}Fe_{0.2}O_3$	600	15	4-terminal, YSZ electron block
$La_{0.8}Sr0_{0.2}Co_{0.8}Fe_{0.2}O_3$	250	0.10	4-terminal, YSZ electron block
$La_{0.75}Sr_{0.25}FeO_3$	50	0.03	$^{18}O/^{16}O$ exchange

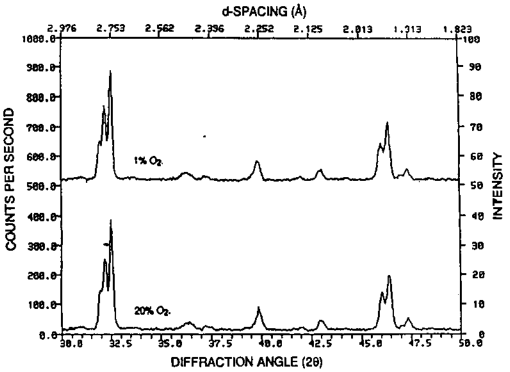

Fig. 2. XRD of $SrFeCo_{0.5}O_x$ at 850°C in 1% and 20% O_2 (balance is Ar) atmosphere.

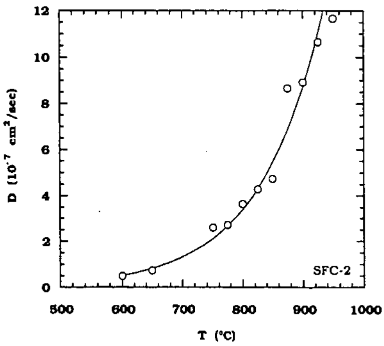

Fig. 3. Chemical diffusion coefficient in $SrFeCO_{0.5}O_x$ as a function of temperature.

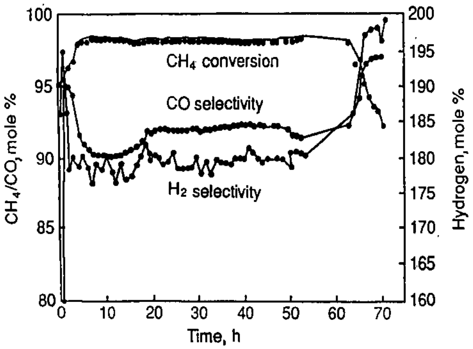

Fig. 4. Methane conversion and CO and H_2 selectivity in $SrFeCo_{0.5}O_x$ membrane reactor with reforming catalyst.

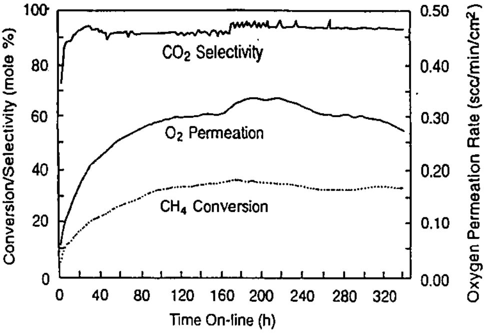

Fig. 5. Methane conversion, CO_2 selectivity, and O_2 permeation in $SrFeCo_{0.5}O_x$ membrane reactor without reforming catalyst.

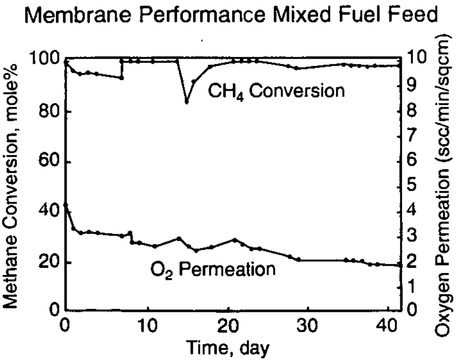

Fig. 6. Methane conversion and O_2 flux for a mixed feed in $SrFeCo_{0.5}O_x$ membrane reactor with reforming catalyst.

To use the $SrFeCo_{0.5}O_x$ membrane tube in converting methane to syngas, it appears critical to reduce the tube wall thickness. Once this is achieved, any oxygen lost from the lattice of the membrane material to the reaction stream can be replaced by the oxygen permeating from the air side at a faster rate. As a result, the material in contact with the reaction stream will not be lost by chemical decomposition. Meanwhile, the difference in oxygen content between the inside and outside surfaces of the tube becomes smaller and consequently, fracturing of the tube is less likely. Thus, a thin-wall membrane tube appears to be more promising for methane conversion in the future. A thin-wall tube will also maximize the surface-area-to-volume ratio and thereby reduce the reactor size. Several suggestions have been made for manifolded monolithic systems of the type reported by Hazbun [13]. In the area of solid-oxide fuel cells, several monolithic designs have been suggested and demonstrated [14-16]; these could be adapted for use in a monolithic reactor.

CONCLUSIONS

We have developed a mixed-conducting ceramic material of the composition $SrFeCo_{0.5}O_x$ that selectively separates oxygen from air. The separated oxygen is then utilized for partial oxidation of methane into syngas. Long tubes of $SrFeCo_{0.5}O_x$ membrane have been fabricated by plastic extrusion. Performance of the membranes has been evaluated in a methane conversion reactor, and excellent methane conversion efficiency (>98%) and good CO selectivity (≈90%) were obtained in reactors run for >1000 h at 900°C. These ceramic membranes operate without electrodes or external power supply.

ACKNOWLEDGMENT

Work at ANL is supported by the U.S. Department of Energy, Federal Energy Technology Center, under Contract W-31-109-Eng-38.

REFERENCES

1. H. D. Gesser and N. R. Hunter, Chem. Rev., 85 (1985) 235.
2. N. D. Spenser and C. J. Pereira, J. Catal., 116 (1989) 399.
3. Y. Amenomiya, V. I. Birss, M. Goledzinski, J. Galuszka, and A. R. Sanger, Catal. Rev., Sci. Eng., 32 (1990) 163.
4. Y. Teraoka, H. M. Zhang, S. Furukawa, and N. Yamozoe, Chem. Lett., 1743 (1985).
5. T. J. Mazanec, T. L. Cable, and J. G. Frye, Jr., Solid State Ionics, 111 (1992) 53.
6. A. C. Bose, G. J. Stiegel, and R. D. Srivastava, Proc. 208th American Chemical Society Meeting, Washington, DC, Aug. 20-25, 1994, Vol. 39, No. 4, p. 1006 (ed. by H. P. Stephens, D. C. Cronauer, K. S. Vorres, and J. C. Crelling, American Chemical Society).
7. U. Balachandran, J. T. Dusek, S. M. Sweeney, R. B. Poeppel, R. L. Mieville, P. S. Maiya, M. S. Kleefisch, S. Pei, T. P. Kobylinski, and A. C. Bose, Bull. Amer. Ceram. Soc. 74 (1995) 71.
8. U. Balachandran, M. S. Kleefisch, T. P. Kobylinski, S. L. Morissette, and S. Pei, U.S. Patent 5,580,497, Dec. 3, 1996.
9. B. Ma, U. Balachandran, J.-H. Park, and C. U. Segre, Solid State Ionics, 83 (1996) 65.
10. B. Ma, U. Balachandran, J.-H. Park, and C. U. Segre, J. Electrochem. Soc., 143 (1996) 1736.
11. U. Balachandran, J. T. Dusek, R. L. Mieville, R. B. Poeppel, M. S. Kleefisch, S. Pei, T. P. Kobylinski, C. A. Udovich, and A. C. Bose, Applied Catalysis A: General, 133 (1995) 19.
12. M. Liu, Y. Shen, J. Ludlow, A. Joshi, and K. Krist, Proc. Intl. Gas Research Conf. (ed. by H. A. Thompson, Government Institutes, Inc., Rockville, MD, 1992) 183.
13. E. A. Hazbun, U.S. Patent 4,791,079, Dec. 13, 1988.
14. J. P. Ackerman and J. E. Young, U.S. Patent 4,476,198, Oct. 9, 1984.
15. T. D. Claar, D. E. Busch, and J. J. Picciolo, U.S. Patent 4,883,497, Nov. 28, 1989.
16. R. B. Poeppel and J. T. Dusek, U.S. Patent 4,476,196, Oct. 9, 1984.

THE USE OF CERAMIC MEMBRANE REACTORS FOR THE PARTIAL OXIDATION OF METHANE TO SYNTHESIS GAS

M. Schwartz, J. H. White, M. G. Myers, S. Deych and A.F. Sammells
Eltron Research, Inc., 5660 Airport Blvd., Boulder, CO 80301

Keywords: Ceramic membrane reactor; partial oxidation; synthesis gas

INTRODUCTION

Materials exhibiting mixed ionic and electronic conductivity are of commercial interest due to their application in fields such as oxygen separation, membrane reactors for oxidation reactions and electrocatalysis. Much of this work has focused on metal oxides crystallizing in the perovskite structure. For example, early work[1-3] studied compounds selected from $La_{1-x}Sr_xCo_{1-y}Fe_yO_{3-\delta}$. In this work, electrical and ionic conductivities were measured on a range of compositions and it was found that oxygen ion conduction was controlled mainly through oxygen vacancies in the lattice, indicating the importance of this structural feature in achieving high oxygen permeability.

Vacancies in the perovskite lattice are formed either through doping of the lattice or through the loss of oxygen when the material is exposed to atmospheres of low oxygen partial pressures. However, both of these vacancy formation mechanisms present problems. For example, doping of cations into the lattice can cause association between the dopants and the resulting oxygen vacancies.[4] This leads to high activation energies for ionic conduction. Loss of oxygen by reaction with the atmosphere leads to increases in lattice parameters and eventual phase decomposition, limiting the usefulness of such materials in commercial applications.

To overcome such problems, Eltron has been studying ionic conductors[5] and mixed ionic and electronic conductors based on the brownmillerite structure. This structure has general composition $A_2B_2O_5$ and is attractive as an oxide ion conductor since it can support a large population of oxide ion vacancies, both ordered and disordered, as well as a variety of substituents in the A and B lattice sites. The structure consists of BO_6 octahedral layers sharing vertices with a layer of BO_4 tetrahedra (Figure 1a). This difference in coordination sphere of B metal ions lends itself to controlled substitution. Depending on the particular metal ions, some distortion may be present in the polyhedra. This structure may be compared to the perovskite structure (Figure 1b) where B metal atoms occupy only octahedral sites with no inherent oxide ion vacancies.

The rationale for selecting specific A and B lattice substituents within the $A_2B_2O_5$ brownmillerite structure has evolved in part from recent studies performed at Eltron[5-8] which have identified clear correlations between perovskite crystallographic and thermodynamic parameters relating to the activation energy for ionic transport. These parameters include: 1) the average metal-oxygen bond energy within the perovskite, 2) lattice free volumes, obtained by subtracting the ionic volumes of cations and O^{2-} in the unit cell from the overall crystallographic unit cell, 3) the parameter $r_{critical}$ (r_c) which corresponds to the radius of the opening between the two A site cations and one B site cation through which the mobile anion must pass, and 4) lattice polarizability towards ionic migration. Eltron is currently applying this rationale to the selection of new brownmillerite materials for use as mixed conducting membranes.

Of all the potential applications of mixed ionic electronic conducting materials, the partial oxidation of methane to synthesis gas (syngas) is one of the most exciting and commercially important. The partial oxidation reaction of methane and oxygen to yield syngas is:

$$CH_4 + 1/2O_2 \rightarrow CO + 2H_2 \qquad (1)$$

The syngas can then serve as a precursor for a variety of products such as methanol, higher alcohols or Fischer-Tropsch products. This process is currently performed industrially but requires oxygen on a large scale, which is expensive. By performing this reaction with a membrane reactor, the oxygen is separated directly from air. This allows air to be used as the oxidant, greatly reducing syngas production costs.

In addition to the partial oxidation reaction, Eltron has been studying the combined partial oxidation/steam reforming and partial oxidation/CO_2 reforming reactions, similar to industrial autothermal reforming. In these processes, steam or CO_2 is added to the methane feedstream. This serves two purposes. First, since the partial oxidation reaction is highly exothermic and the steam and CO_2 reforming reactions are highly endothermic, the heat generated from the partial oxidation reaction can be used to drive the reforming reactions. This will allow for better thermal control of the reactions within the membrane reactor. The second purpose for a mixed feedstream is that the composition of the syngas product can be varied. Specifically, the addition of steam in the feedstream will increase the H_2:CO ratio in the synthesis gas product stream while the addition of CO_2 will decrease the H_2:CO ratio. The specific composition desired will depend upon the eventual end use of the syngas product.

In order to promote the partial oxidation reaction utilizing a mixed conducting membrane, the ceramic membrane material needs to be formed into an appropriate reactor shape such as a thin plate, tube or monolith. In practice, one side of this reactor is exposed to air. The membrane reactor then serves to separate oxygen from the air. This oxygen is then transported as oxide ions through the membrane where it goes on to react with the methane present on the second side of the membrane yielding syngas. A schematic illustration of this process is shown in Figure 2.

In addition to Eltron, several other research groups are studying the use of mixed conducting ceramic membrane reactors for the partial oxidation of methane to syngas. One group, Mazenec et al. at BP Chemicals, have been studying materials as partial oxidation membrane reactors.[9,10] For example, they fabricated a membrane of composition $La_{0.2}Sr_{0.8}Fe_{0.8}Cr_{0.2}O_x$ into a tube and operated it for >1000hr at 1100°C as a partial oxidation reactor.[10] A second group, consisting of a team from Amoco and Argonne,[11] has been studying materials derived from intergrowths of the perovskite structure. Specifically, materials of composition $SrCo_{0.5}FeO_x$ have been fabricated into tubular membrane reactors and used to convert methane to syngas at 900°C at rates of 2-3scc/min-cm^2. High methane conversion was achieved and reactors were operated for 40 days.

As a means to develop commercially viable ceramic membrane reactors for the partial oxidation of natural gas, Eltron has prepared novel mixed conducting brownmillerite materials and successfully fabricated them into sintered disks and tubes. These disks and tubes have been incorporated into membrane reactors for the partial oxidation of methane. These materials have shown complete chemical and mechanical stability under expected operating conditions, including a long-term performance testing of >3000hr.

EXPERIMENTAL

Mixed conducting membrane materials were prepared by standard ceramic processing techniques. Metal oxides and carbonates, serving as the starting materials, were thoroughly mixed and calcined at 1200-1300°C until the desired brownmillerite phase was formed. These powders were then reduced in particle size using an attrition mill after which they were mixed with a standard binder. Membrane shapes were formed by pressing: uniaxial pressing in the case of disks and isostatic pressing in the case of open-both ends and closed-one-end tubes. After forming, the green bodies were densified by sintering in air at 1200-1400°C.

Membrane materials were characterized by X-ray diffraction (XRD) using Cuk$_\alpha$ radiation and experimental densities of sintered disks and tubes were determined using Archimedes' method. All materials studied in membrane reactors were single-phased and >90% of theoretical density.

Membrane reactors for the partial oxidation of methane to syngas were fabricated using sintered disks and open-both-end and closed-one-end tubes. Sealing of the reactors was achieved using glass seals. In all reactor experiments, air was used as the oxidant. 80% methane in helium was used primarily as the feedstock. However, experiments in which CO_2 or steam were added to the methane were also performed. CO_2 was added by mixing gases prior to entry into the reactor. Steam was added by sparging the methane:helium feedstream into a water bubbler. The concentration of the steam with respect to the methane was varied by heating the water bubbler. The humidity of the incoming and effluent streams was measured with commercial humidity sensors. Gas chromatography was used to analyze the syngas product stream as well as any leakage of air across the membrane.

RESULTS AND DISCUSSION

One of the most important properties necessary for industrial use of this technology is long-term stability of the membrane materials under actual operating conditions. An example of the long-term stability of Eltron's brownmillerite-based membrane materials is shown in Figure 3. In this experiment, a closed-one-end tube, 3.5cm long, served as the membrane reactor. The tube had an inner diameter of 8.6mm and a 1.2mm wall thickness. The outside of the tube was coated with a partial oxidation catalyst consisting of Ni supported on a perovskite-type metal oxide. The inside of the tube was coated with $La_{0.8}Sr_{0.2}CoO_3$ which served as the oxygen reduction catalyst. The experiment was performed at atmospheric pressure and 900°C.

As shown in Figure 3, the reactor has been operating for >3000hr with a syngas production rate between 10-15ml/min-cm^2 with a H_2:CO ratio that varied from 1.8 to 2, close to the expected value of 2. At ~700hr, there was a complete loss of activity because the methane tank serving the reactor ran empty. When the methane tank was replaced and the methane concentration returned to the previous value in the feed, the reactor resumed syngas production at a slightly lower, but steady rate. The reason for the lower production rate after restarting the reactor is not known but may be due to some loss of activity due to catalyst deactivation. No change in the H_2:CO ratio was observed after restarting the reactor. In addition to the syngas production, the CO_2 formed in the product was also monitored and was never more than 1-2% of the CO production rate indicating that no deep oxidation was occurring. During the course of this experiment, no evidence for mechanical or chemical instability was observed. Additionally, no leakage into the tube, as measured by the N_2 concentration in the product stream, was observed.

Further evidence of chemical stability is shown by XRD experiments performed on membrane materials operated in syngas production reactors for extended time periods. For example, a reactor fabricated from a sintered disk was operated for >1000hr at 900°C with a feed of ~80% CH_4 in helium. The oxygen partial pressure of the gas on this side of the membrane was estimated to be $<10^{-17}$atm. After the reactor was voluntarily stopped, XRD was performed on the membrane partial oxidation surface. Figure 4 shows a comparison of this membrane surface with fresh powder. The two patterns are identical which indicates that even after this extended period of syngas production, the membrane material is stable with respect to chemical decomposition under operating conditions. Additionally, the membrane disk maintained its mechanical integrity over the course of the experiment.

As discussed above, Eltron has also studied the combined partial oxidation/steam reforming reactions. In a typical example, an open-both-ends tube served as the membrane reactor. The tube had an effective length of 3.9cm, an inner diameter of 0.7cm and a wall thickness of 1.6mm. The outside of the tube was coated with a partial oxidation catalyst, specifically Ni (40wt%) supported on Al_2O_3. The inside of the tube was coated with $La_{0.8}Sr_{0.2}CoO_3$ which served as the oxygen reduction catalyst. Steam was added to the methane stream and the CH_4:H_2O ratio was varied and measured as discussed above. The experiment was performed at atmospheric pressure and 900°C.

Figure 5 summarizes the results obtained during this experiment. The amount of H_2 produced decreased initially and then increased as a function of increasing H_2O in the feedstream. Additionally, the H_2:CO ratio in the product stream increased as expected. Also important was the observation that typically greater than 90% of the H_2O in the feedstream was consumed in the combined reactions. This indicates that the premise of combining these two reactions within a ceramic membrane reactor is valid.

In a similar fashion, the combined partial oxidation/CO_2 reforming reactions have also been studied. As a typical example, a sintered disk served as the membrane reactor. The effective surface area was 0.5cm^2 and the membrane thickness was 1.4mm. One side of the disk was coated with a partial oxidation catalyst, specifically Rh (5wt%) supported on a metal oxide. The opposite side of the disk was coated with $La_{0.8}Sr_{0.2}CoO_3$ which served as the oxygen reduction catalyst. The feed gas consisted of 80% methane with CO_2 and helium making the balance. The experiment was performed at atmospheric pressure and 900°C.

Figure 6 summarizes the results of this experiment. The amount of syngas produced initially increased and then decreased with increasing CO_2 content in the feedstream. The H_2:CO ratio decreased as expected. These results validate the concept of promoting the combined CH_4 partial oxidation reaction with the CH_4/CO_2 reforming reactions within a brownmillerite-based membrane reactor.

CONCLUSION

Eltron has developed new mixed ionic and electronic conducting ceramic materials based on the brownmillerite structure. These materials have been fabricated into shapes and incorporated into membrane reactors. These membrane reactors have been used to promote the partial oxidation of methane to syngas. The long-term stability of these materials has been demonstrated by the continuous operation of a tubular partial oxidation reactor for >3000hr. Additionally, the membrane reactors have been used in an autothermal configuration using steam or CO_2 with the methane feed.

REFERENCES

1. Teraoka, Y.; Zhang, H.M.; Furukawa, S; Yamazoe, N. *Chem. Lett.* **1985**, 1743-1746.
2. Teraoka, Y.; Zhang, H.M.; Okamoto, K.; Yamazoe, N. *Mat. Res. Bull.* **1988**, *23*, 51-58.
3. Teraoka, Y.; Nobunaga, T.; Yamazoe, N. *Chem. Lett.* **1988**, 503-506.
4. Kilner, J.A.; Brook, R.J. *Solid State Ionics* **1982**, *6*, 237-252.
5. Schwartz, M; Link, B.F.; Sammells, A.F. *J. Electrochem. Soc.* **1993**, *140*, L62-63.
6. Sammells, A.F.; Cook, R.L.; White, J.H.; Osborne, J.J.; MacDuff, R.C. *Solid State Ionics* **1992**, *52*, 111-123.
7. Sammells, A.F.; Cook, R.L. *Solid State Ionics* **1991**, *45*, 311-321.
8. Cook, R.L.; MacDuff, R.C.; Sammells, A.F. *J. Electrochem. Soc.* **1990**, *137*, 3309-3310.
9. Mazenec, T.J.; Cable, T.L.; Frye, Jr., J.G.; Kliewer, W.R. U.S. Patent 5 306 411, 1994.
10. Mazenec, T.J Presented at the 188th Electrochemical Society Meeting, Chicago, IL, October 1995.
11. Balachandran, U.;, Dusek, J.T.; Mieville, R.L.; Poeppel, R.B.; Kleefisch, M.S.; Pei, S.; Kobylinski, T.P.; Udovich, C.A.; Bose, A.C. *Appl. Cat. A: Gen.* **1995**, *133*, 19-29.

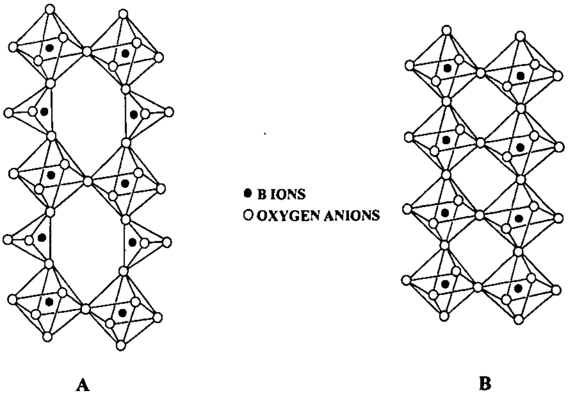
● B IONS
○ OXYGEN ANIONS
A
B

Figure 1. Comparison of brownmillerite (A) and perovskite (B) structures. A cations are omitted for clarity.

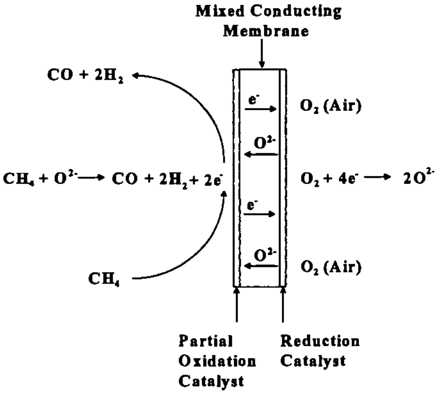
Mixed Conducting Membrane
$CO + 2H_2$
$CH_4 + O^{2-} \longrightarrow CO + 2H_2 + 2e^-$
CH_4
e^-
O^{2-}
e^-
O^{2-}
O_2 (Air)
$O_2 + 4e^- \longrightarrow 2O^{2-}$
O_2 (Air)
Partial Oxidation Catalyst
Reduction Catalyst

Figure 2. Schematic illustration of processes occurring during the partial oxidation of methane using a ceramic membrane reactor.

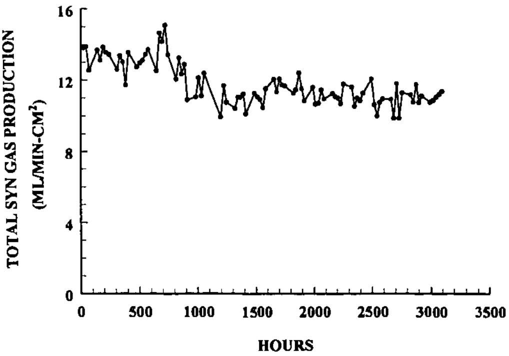

Figure 3. Plot of total synthesis gas production from the partial oxidation of methane using a tubular ceramic membrane reactor showing long-term stability.

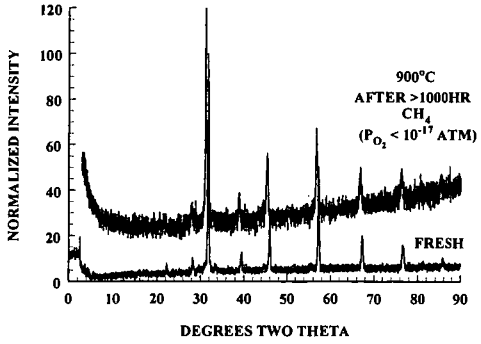

Figure 4. Comparison of XRD patterns for as-prepared membrane material and of the surface of the membrane exposed to methane during the partial oxidation reaction for >1000 hours at 900°C.

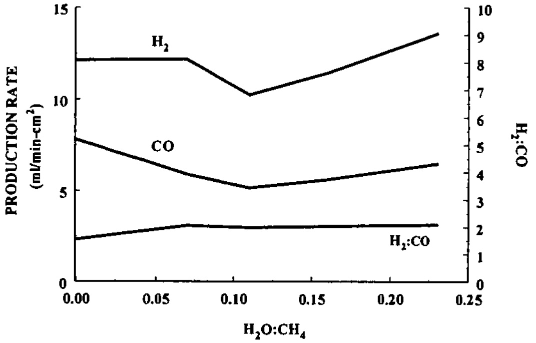

Figure 5. Plots of H_2 and CO production rates and H_2:CO ratio as a function of the H_2O:CH_4 ratio in the feedstream for the combined partial oxidation/steam reforming reactions mediated by a ceramic membrane reactor at 900°C.

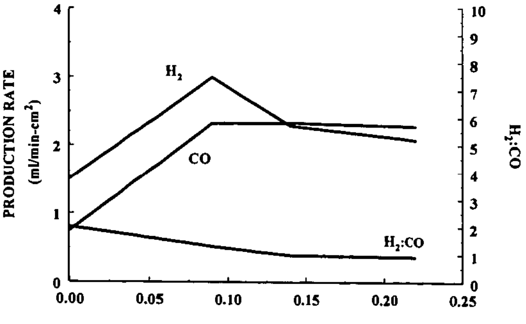

Figure 6. Plot of H_2 and CO production rates and H_2:CO ratio as a function of the CO_2:CH_4 ratio in the feedstream for the combined partial oxidation/CO_2 reforming reactions mediated by a ceramic membrane reactor at 900°C.

PARTIAL OXIDATION OF METHANE TO SYNGAS USING FAST FLOW MEMBRANE REACTORS

Michael W. Alibrando and Eduardo E. Wolf
Department of Chemical Engineering
University of Notre Dame
Notre Dame, IN 46637

Keywords: Methane, Syngas, Membranes

Previous studies have shown that high methane conversions and selectivities to syngas can be achieved while operating at very high space velocities and relatively low methane/oxygen feed ratios. This has been accomplished at relatively high temperatures (~1000°C) in a monolith reactor. (1, 2) The monolith reactor is characterized by an open pore structure which permits very fast gas flows and results not only in high syngas yields, but autothermal operation as well.

Achieving autothermal behavior is significant because a reactor which operates autothermally requires heat only during ignition. In the case of Schmidt and coworkers (1, 2), ignition occurs by passing an ammonia/air mixture over the monolith at around 300°C. Once ignited, the temperature increases rapidly to the steady state temperature, and the ammonia/air mixture is replaced by the methane/oxygen mixture. If industrial scale reactors could be operated autothermally, a significant amount of capital can be saved due to the fact that the reactor must be heated only during startup.

Although these results are very promising, this reactor configuration presents several problems. It requires operating at relatively high temperatures and the use of a different gas mixture during startup. In addition, at these high temperatures and low methane/oxygen feed ratios the potential for an explosion exists due to the possibility of flame flashback. As a result, this reactor configuration could never be implemented industrially due to safety concerns.

Therefore, we attempted to achieve high syngas yields and autothermal behavior while operating in a safer, industrially favorable environment. The intention was to operate at high space velocities, but at significantly lower temperatures. This was accomplished with the use of a highly active 3% Rh supported on TiO_2 catalyst. This catalyst was used in previous studies on the methane partial oxidation reaction in which the reactor was operated at lower space velocities and diluted gas feeds. (3)

In this case, a small amount of the 3% Rh catalyst (only 30 mg) was used in a fixed bed reactor which was operated at millisecond residence times and a methane/oxygen feed ratio of 2/1. The results are shown in Table 1. Despite the fact that the total feed rate was varied between 235 and 1500 cc/min there was very little change in conversion and selectivity. Methane conversion remained between 55 and 70% and CO selectivity remained around 90%. In addition, oxygen conversion was 100% in all cases.

However, under these conditions, relatively high conversions and selectivities were achieved at steady state temperatures in the range of 500-600°C. Although the yields are lower than Schmidt and coworkers, the reaction temperatures were significantly lower. In addition, the system was ignited under methane/oxygen mixtures at 320°C which is several hundred degrees lower than the ignition temperatures using the monolith, thus eliminating the need for the ammonia/air mixture. Another benefit of the Rh catalyst was that it was stable and did not deactivate for several days.

Despite the fact that the use of the 3% Rh catalyst in the fixed bed reactor allowed for safer operation than the monolith reactor, a difficulty still exists. Although the temperatures with the fixed bed were drastically lower than with the monolith and the possibility of explosion has been lowered, the potential for an explosive mixture still exists. An oxygen rich mixture still contacts a high temperature surface, and if the high flow reactor system is to be implemented in industry, the potential for explosion must be eliminated.

Therefore, a reactor scheme was conceived which would allow for high space velocities and overall low methane/oxygen feed ratios while separating the gas reactants until reaching the catalyst surface. The idea of using a separate oxygen feed for methane oxidation was based on previous work in our group on the distribution of oxygen during the methane oxidative coupling reaction. (4) The implementation of the new reactor scheme opens up the possibility of practical applications for the partial oxidation of methane to syngas and also the oxidative dehydrogenation of alkanes.

The membrane reactor consists of a highly porous membrane tube, with one end sealed, which is placed concentrically inside a quartz tube. The upper portion of the membrane tube is made impermeable using a ceramic glaze, leaving only a small length at the lower portion of the tube permeable. The catalyst is placed around the permeable portion of the membrane tube forming a ring in between the membrane tube and the outer quartz wall. Oxygen is fed to the membrane tube and flows exclusively inside the membrane tube until reaching the permeable portion at the bottom of the tube where it permeates to the shell side and immediately contacts the catalyst surface. Methane is fed to the shell side and flows in the annular space between the membrane wall and the quartz wall. In this scheme, the reactants mix only in the region where the catalyst is located, and because 100% oxygen conversion was achieved in every previous experiment, the possibility of oxygen rich mixtures developing is negligible. The membrane wall itself is highly permeable allowing for the use of fast flowrates in the range of millisecond residence times. Thus, the overall methane/oxygen feed ratio can remain low while operating at high space velocities in a reactor configuration which is both safe and economical.

The membrane reactor successfully achieved its goal of obtaining high conversions and selectivities while providing a safe operating environment. Table 2 shows the effect of feed rate on conversion and selectivity using 60 mg of catalyst and a methane/oxygen feed ratio of 2/1. The minimal amount of catalyst that can be used is 60 mg as this is the amount required to completely surround the permeable portion of the membrane tube.

The results are similar to those in the case of the fixed bed reactor in that for a significant change in feed rate (300 cc/min to 1080 cc/min) there is only a slight change in conversion and selectivity. Methane conversion remained primarily between 65 and 75%, CO selectivity remained around 90% and hydrogen selectivity remained primarily around 70%. Once again oxygen conversion was 100% in all cases.

Although methane conversion is slightly lower in the membrane reactor than in the fixed bed reactor, the membrane reactor is the preferred reactor due to the safety factor. Complete oxygen conversion is achieved indicating that the possibility of oxygen rich mixtures, and therefore the possibility of explosion, is negligible. Most industrial reactors are operated well below optimal yields for safety reasons, and a 5% drop in conversion is acceptable if a safe operating environment is assured.

Further experiments were conducted in the membrane reactor in an attempt to increase methane conversion. As soon as a safe reactor configuration had been developed, it was desired to determine if the yields could be improved within this system. The operational variable on which syngas production was most dependent was the methane/oxygen feed ratio. Because the methane and oxygen feeds are kept separate until contacting the catalyst, the partial oxidation reaction could be studied at lower methane/oxygen feed ratios. Table 3 shows the effect of the methane/oxygen feed ratio in the membrane reactor using 60 mg of catalyst.

Methane conversion varies from as high as 64% at the lower ratios to as low as 44% at the higher ratios. Hydrogen and CO selectivities vary from 22 and 67% at low ratios to 82 and 90% respectively at high ratios. However, even at low methane/oxygen ratios, oxygen conversion remains at 100%.

The important result obtained is that both CO and hydrogen selectivities were lower at the lower feed ratios, particularly when the ratio is less than 2/1. The hydrogen selectivity falls below 25%, and the CO selectivity falls below 70%. This is an indication that the partial oxidation reaction is no longer dominant, and the complete combustion reaction begins to occur. This effect can be explained by the fact that at the lower feed ratios, more oxygen is available to form carbon dioxide and water. At higher feed ratios, the concentration of oxygen is low and hence methane reacts to form CO instead of CO_2.

The decreasing of temperature would seem to justify the above conclusion. At lower feed ratios, the temperature is significantly greater than at the higher ratios. At feed ratios less than 2/1, the steady state temperature rises above 700°C, but at ratios greater than or equal to 2/1 the temperature is in the 500°C range. The higher temperature can be accounted for by the reaction of hydrogen and oxygen to form water and the occurrence of complete combustion which has a higher heat of reaction than partial oxidation. In addition, as methane conversion decreases the heat generated decreases and the temperature decreases.

The effect feed ratio has on methane conversion is interesting. Although 100% conversion of oxygen is achieved at low feed ratios, methane conversion levels off at 64%. This is not expected because as the concentration of oxygen increases higher methane conversions would be expected due to the fact that oxygen was the limiting reagent in all experiments. Additional oxygen should result in higher conversions, but instead results in more of the reacted methane being converted to CO_2 and water. At higher feed ratios, the reactor operates as expected as the methane conversion begins to decrease.

After it had been determined that the conversion could not be significantly increased by varying the operational parameters of the membrane reactor, an attempt was made to increase conversion by allowing the unreacted methane to participate in another reaction. For this purpose a new, double bed reactor was designed to allow for a second catalyst bed and a third reactant feed downstream from the first catalyst bed.

The double bed reactor is identical to the membrane reactor in the upper portion allowing for autothermal behavior of the partial oxidation reaction. The difference is that an additional quartz tube is placed concentrically inside the quartz reactor shell downstream from the first catalyst bed. At the top of the additional tube is a quartz cross which serves the purpose of supporting a second catalyst bed. The quartz tube is open at both ends allowing for an additional reactant to be fed over the second catalyst bed and downstream from the first catalyst bed.

The reaction chosen for the second bed was the dry reforming reaction. The hypothesis was that the unreacted methane from the partial oxidation reaction would react with carbon dioxide which would be added downstream and over the second catalyst bed. The dry reforming reaction is very endothermic, but an enormous amount of heat is evolved from the reaction in the first bed and the original hypothesis was that the heat from the first bed reaction could be used to drive the reaction in the second bed.

Initial results indicated that feeding carbon dioxide downstream would increase methane conversion, but only slightly. The reason was that the first catalyst bed did not provide enough heat to sustain the very endothermic dry reforming reaction over the second catalyst bed. It was observed that the temperature of the second catalyst bed decreased upon introduction of carbon dioxide to the reactor. This indicates that the dry reforming reaction does occur, but there is not enough heat available to sustain the reaction.

It was then decided to continue to feed carbon dioxide downstream from the first bed, but to increase the temperature of the second bed to provide enough heat for the dry reforming reaction. In this experiment, 60 mg of the Rh catalyst were used in both beds and the methane, oxygen and carbon dioxide feed rates were maintained at 500, 250 and 60 cc/min respectively as the second bed temperature was increased. Table 4 shows the effect of the second bed temperature on conversion and selectivity.

The results indicate that high methane conversions can be achieved while maintaining high CO and hydrogen selectivities. At a second bed temperature of 700°C, methane conversion reached 83% with CO and hydrogen selectivities of 85 and 64% respectively. These high syngas yields have been obtained in a reaction environment which is safe and could be modified for industrial use.

In addition, further studies with the double bed reactor indicate that both catalyst beds can be operated autothermally if oxygen is used as the downstream feed instead of carbon dioxide. In this case, the second bed temperature rapidly increases upon introduction of the downstream oxygen feed. This indicates that a second ignition occurs in the reactor and that both beds operate autothermally.

The double bed reactor served the purpose of increasing conversion, but there was still no explanation for the fact the operational parameters had little effect on conversion and selectivity in the fixed bed and membrane reactors. It was not until theoretical reactor simulations were conducted that the reason became clear.

The theoretical model is similar to the elementary step model proposed by Hickman and Schmidt (5), and is used to evaluate results from the fixed bed reactor. The mechanism consists of twenty-one elementary steps which are combined with the reactor mass balances. All of the kinetic parameters used in the model are taken from previous studies. The only modification is that the activation energy for CO desorption was lowered due to the fact that the CO surface concentration was significantly higher than the other species. Lowering the activation energy can be justified by previous studies that report the activation energy will decrease at higher surface concentrations. (5, 6) At this lower value of the activation energy for CO desorption, the model results adequately matched the experimental data.

After comparing the model results to the fixed bed experiments, a parametric sensitivity study was conducted. The study indicated that an increase in methane conversion requires and increase in the rate of methane adsorption and a decrease in oxygen adsorption. The sensitivity study also indicated that CO desorption is one of the rate determining steps and that the dry and steam reforming reactions have little effect on conversion and selectivity at these conditions.

The model also predicts that most of the reaction occurs in a very narrow region near the entrance of the bed, with the rest of the bed contribution being relatively small. In addition, all of the oxygen is consumed by the midpoint of the bed. This would explain the lack of sensitivity of the fixed bed experimental results to changes in operating variables.

Although the model results are for a fixed bed reactor, certain conclusions about the membrane reactor can be drawn. A reasonable assumption is that the profiles near the membrane tube wall are similar to the entrance of the fixed bed reactor. This would indicate that all of the oxygen is consumed near the membrane wall and most of the reaction occurs in this region. This would explain why varying the operating conditions would not result in an increase in methane conversion. All of the oxygen is consumed near the membrane wall and therefore any methane that flows near the outer portion of the reactor will not be converted. To further study the profiles and performance of the membrane reactor, a two dimensional reactor model is now under development.

In summary, very promising results have been achieved in this study. High conversions and selectivities to syngas have been achieved in the membrane reactor. In addition, the reaction is carried out in safe and economical environment without the explosive problems which exist in previous reports. Future possibilities involve the study of the oxidative dehydrogenation of alkanes, which is a very important reaction at the industrial level.

REFERENCES

1. D. A. Hickman and L. D. Schmidt. *J. Catal.* **138** 267 (1992).
2. P. M. Torniainen, X. Chu and L. D. Schmidt. *J. Catal.* **146** 1 (1994).
3. T. Shiraha. M. S. Thesis. University of Notre Dame (1995).
4. J. M. Santamaría, E. E. Miro and E. E. Wolf. *Ind. Eng. Chem. Res.* **30** 1157 (1991).
5. D. A. Hickman and L. D. Schmidt. *AIChE J.* **39** 1164 (1993).
6. V. Nehasil, I. Starva and V. Matolin. *Surf. Sci.* **331-333** 105 (1995).

Table 1. Effect of Total Feed Rate.					
Total Feed Rate (cc/min)	Temperature (°C)	Methane Conversion (%)	Oxygen Conversion (%)	CO Selectivity (%)	Hydrogen Selectivity (%)
235	401	54	100	76	34
525	558	58	100	88	77
750	564	70	100	89	70
1130	629	65	100	90	64
1500	641	68	100	90	50

Table 2. Effect of Total Feed Rate Using the Membrane Reactor.					
Total Feed Rate (cc/min)	Temperature (°C)	Methane Conversion (%)	Oxygen Conversion (%)	CO Selectivity (%)	Hydrogen Selectivity (%)
300	419	64	100	75	62
450	494	75	100	88	72
600	520	64	100	86	76
750	515	64	100	90	82
900	607	52	100	86	69
1080	680	35	100	81	90

Table 3. Effect of Methane/Oxygen Feed Ratio Using the Membrane Reactor.					
Methane/ Oxygen Feed Ratio	Temperature (°C)	Methane Conversion (%)	Oxygen Conversion (%)	CO Selectivity (%)	Hydrogen Selectivity (%)
1	710	64	100	67	22
1.33	757	64	100	81	35
1.5	702	63	100	85	45
2	515	64	100	90	82
2.6	510	52	100	90	82
3.3	410	44	100	84	80

Table 4. Effect of Second Bed Temperature Using the Double Bed Reactor.					
Second Bed Temperature (°C)	First Bed Temperature (°C)	Methane Conversion (%)	Oxygen Conversion (%)	CO Selectivity (%)	Hydrogen Selectivity (%)
300	516	73	100	87	83
400	596	74	100	77	60
500	627	75	100	78	61
600	682	78	100	81	64
700	759	83	100	85	64

GROUP (V) AND (VI) TRANSITION METAL CARBIDES AS NEW CATALYSTS FOR THE REFORMING OF METHANE TO SYNTHESIS GAS

Andrew P. E. York, John B. Claridge,[†] Carlos Márquez-Alvarez,[‡] Attila J. Brungs
and Malcolm L. H. Green[*]

The Catalysis Centre, Inorganic Chemistry Laboratory, University of Oxford,
South Parks Road, Oxford, OX1 3QR, U. K.
[†] Current address: Department of Chemistry and Biochemistry, University of South
Carolina, Columbia, SC 29208, U.S.A.
[‡] On leave from: Instituto de Catálisis y Petroleoquímica, CSIC, Campus
Cantoblanco, 28049 Madrid, Spain

Keywords: early transition metal carbides; methane dry reforming; methane partial oxidation.

ABSTRACT

High surface area group V and VI transition metal carbides, synthesised by temperature programmed reduction of the metal oxides with methane/hydrogen, have been tested as catalysts for the dry reforming of methane with carbon dioxide and partial oxidation of methane with air. Mo_2C and WC were stable and highly active catalysts for these reactions at elevated pressure, while they deactivated at ambient pressure. The product distribution obtained was close to that predicted by the thermodynamic equilibrium, except that no carbon formation was observed on the catalyst surface. The carbides of niobium and tantalum deactivated, even in the dry reforming reaction at elevated pressure, due to their greater tendency towards oxidation.

INTRODUCTION

Synthesis gas (carbon monoxide and hydrogen) is an extremely important intermediate in the production of many chemicals, for example Fischer-Tropsch synthesis of hydrocarbons (e.g. in the Shell middle distillate process or at SASOL) and alcohols [1-3], ammonia synthesis (Fe catalysts) [4], methanol synthesis ($Cu/ZnO/Al_2O_3$) [5,6], and hydroformylation (homogeneous Rh catalyst) [7], and is also used in the reduction of iron ore. Of these many products, methanol, and higher alcohols, are often discussed as environmentally friendly fuel alternatives [8], while the development of hydrogen for use as an alternative fuel or in fuel cells is currently receiving much attention [9].

At present, synthesis gas is produced in great quantities from methane, mainly by the highly endothermic steam reforming process *(1)*, and to a lesser extent by endothermic dry reforming with carbon dioxide *(2)*; an alternative route is *via* the exothermic partial oxidation reaction *(3)*.

$$CH_4 + H_2O \rightarrow CO + 3\,H_2 \qquad \Delta H^\circ_{298} = +206\ \text{kJ mol}^{-1} \qquad (1)$$
$$CH_4 + CO_2 \rightarrow 2\,CO + 2\,H_2 \qquad \Delta H^\circ_{298} = +247\ \text{kJ mol}^{-1} \qquad (2)$$
$$CH_4 + \tfrac{1}{2}O_2 \rightarrow CO + 2\,H_2 \qquad \Delta H^\circ_{298} = -38\ \text{kJ mol}^{-1} \qquad (3)$$

Currently, nickel catalysts are employed industrially for both the steam reforming and dry reforming reactions [10], while partial oxidation is carried out autothermally [11]. However, since nickel also catalyses the carbon deposition reactions, methane decomposition and CO disproportionation (Boudouard reaction), an excess of oxidants is needed in order to prevent catalyst deactivation and blockages in the reactor tubes; this results in the production of synthesis gas with product ratios that are not optimal for further conversion downstream [10,12]. Alternative catalysts are the supported noble metals [13-18], or sulphur passivated nickel [19], both of which have been shown to exhibit kinetic resistance to carbon formation at or near stoichiometric reactant ratios; however, their application has been limited by the unfavourable economics and scarcity of the former, and the low activity of the latter.

In the past two decades, it has been shown that some transition metal carbides and nitrides, particularly those of group VI, possess catalytic properties similar to the noble metals [20-22]. Since the group VI transition metals are abundant and relatively cheap, it has been suggested that they can replace the scarce and expensive noble metals for a number of catalytic applications. Initial problems centred on the synthesis of high specific surface area (S_g) materials suitable for use as catalysts. However, following the publication of a number of methods for the synthesis of metal carbides/nitrides with $S_g \leq 220\ m^2\ g^{-1}$ [23-25], it was shown that these materials were active for a number of catalytic reactions, including alkane isomerization, ammonia synthesis, and Fischer-Tropsch synthesis, to name only a few [26].

In this paper we present the results of methane dry reforming and partial oxidation over the group V and VI transition metal carbides. We have found that the high surface area carbides of molybdenum and tungsten, under stoichiometric reactant feeds and elevated pressure, are stable and highly active catalysts for these reactions; no carbon formation was observed over the carbide surface during the reactions.

EXPERIMENTAL

Catalyst Synthesis and Characterisation

The high surface area metal carbide materials were prepared using the temperature programmed reduction method pioneered by Boudart and co-workers [23]: briefly the low surface area metal oxide powder was heated in flowing 20% CH_4/H_2 mixture from room temperature to 1000-1223K, depending on the oxide (discussed later), at 1 K min^{-1}. Normally the catalysts were prepared *in situ* and tested immediately. The post-synthesis high surface area carbides are readily and exothermically oxidised by air at room temperature and, therefore, passivation in flowing 1% O_2/N_2 for 10 hours at room temperature was carried out before exposure to the atmosphere and characterization. Crystalline components of the materials were identified by X-ray diffraction (XRD) using a Philips PW1710 diffractometer with Cu-Kα radiation.

Catalyst Testing

The apparatus used in this work was a modified version of the commercial Labcon microreactor described previously [27]. The reactor was built using 1/8" and 1/16" o.d. 316 stainless steel tubing and 316 stainless steel Swagelok fittings throughout. The catalyst sample was placed between two quartz wool plugs in the centre of a 4 mm i.d. silica tube and inserted into a vertical Severn Science tube furnace, heated to the required reaction temperature and controlled from a Eurotherm 905 temperature controller. For safety reasons, in experiments carried out at elevated pressures the silica tube was placed inside a steel tube. Inlet gas flow rates were controlled using Brooks 5850TR mass flow controllers, and the exit gas stream from the reactor passed through a Tescom two stage back-pressure regulator to allow elevated pressure experiments to be carried out. All the pipework was heated to prevent condensation of the products.

Product analysis was carried out using a Hewlett-Packard 5890II gas chromatograph, fitted with both a thermal conductivity detector, and a methanator/flame ionization detector. Separation of the products was achieved using a 3m Porapak Q packed column, with argon carrier gas. In all cases stoichiometric gas mixtures were used and carbon balances were better than 97%.

RESULTS AND DISCUSSION

Synthesis and Characterisation

Synthesis of the metal carbides was carried out using temperature programmed reduction with CH_4/H_2, as mentioned above, and it was noticed, by monitoring the effluent gas by real-time mass spectrometry, that the final temperature needed for complete formation of the carbide varied from 1023K for molybdenum carbide to 1223K for tantalum carbide; this is due to the relative reducibility of the oxides.

Some of the characterising data obtained for the metal oxides and metal carbides studied are presented in Table 1. The metal carbide phase formed was determined by XRD of passivated samples; the structures were identified by comparison with the literature [28]. No metal oxide could be seen in any of the diffraction patterns, showing that the passivation method only results in the oxidation of the surface of the carbide samples, while the bulk remains unaffected. N_2 BET of passivated metal carbide samples confirmed that high surface area materials had been synthesised.

Methane Dry Reforming with Carbon Dioxide

The results obtained for the dry reforming of methane with carbon dioxide over bulk NbC_x, TaC_x, β-Mo_2C and α-WC, as well as over bulk SiC, are presented in Table 2. The silicon carbide (Norton Materials UK) used here had a low surface area (≈1 m^2 g^{-1}), and had very low catalytic activity for the dry reforming reaction. Indeed, at 1223K, the methane and carbon dioxide conversions were only 13.3% and 3.4% respectively, while at 1373K the conversions were much higher, due to the important role of autothermal processes. Thus, it can be concluded that the autothermal contribution is minor at or below 1223K, i.e. in the temperature range used for the catalytic study of the carbides.

The results obtained for Mo_2C and WC, presented in Table 2, are extremely similar to those expected from thermodynamics, demonstrating that these materials are efficient catalysts for methane dry reforming; in contrast, NbC_x and TaC_x gave relatively low conversions and yields, except when the temperature was increased to 1373 K. This indicates that the carbides of niobium and tantalum are formed, but that they are only stable at very high temperatures (and probably higher pressures). Indeed, Figure 1 shows that Mo_2C is the most stable of the carbides tested, while NbC_x and TaC_x deactivated rapidly at 1223K; NbC_x was stabilised to some extent at 1373K, but the high H_2/CO ratio given in Table 2 indicated that carbon formation was occurring at this high temperature, probably *via* autothermal reactions. The stability of WC was found to be extremely similar to that of Mo_2C under the conditions employed here (not shown), with no deactivation observed for > 72 h on stream at 8 bar and 1223 K. Further, Figure 1 shows that elevated pressures are required to stabilise the catalysts. Powder XRD of post-catalytic β-Mo_2C samples demonstrated that the deactivated sample contained a large amount of MoO_2, which has only a very low activity for methane dry reforming, while the stabilised catalyst had only peaks due to the starting carbide. The reason for the deactivation of the NbC_x and TaC_x samples is that these materials are less stable than the carbides of Mo and W, as borne out by the higher temperature needed to synthesise the carbide; this means that, under the equilibrium conditions existing during the reaction, oxidation of NbC_x or TaC_x proceeds more readily than recarbidation.

Since carbon formation is a well known problem in methane dry reforming, post-catalytic samples of β-Mo_2C and α-WC were studied by high resolution electron microscopy (not shown). No carbon deposits were observed on the catalyst surface, even under our stoichiometric reactant feeds; this compares favourably with the results published previously for commercial nickel catalysts [29].

Methane Partial Oxidation with Air

Table 3 shows the results obtained for the partial oxidation of methane with air, over β-Mo_2C and α-WC. Oxygen conversion was essentially 100% for all the experiments. As before, when the oxidation reactions were carried out at ambient pressure the catalyst deactivated by forming MO_2, although the deactivation occurred much more quickly in the presence of air than was the case with carbon dioxide, meaning that an initial activity could not be obtained. However, when the partial oxidation was carried out at elevated pressure the catalyst activity was stabilised, and no deactivation was observed for the duration of the experiments (> 72 h), as shown in Figure 2 for β-Mo_2C. Post-catalytic XRD of the samples showed that no phase changes had occurred, and that no MO_2 or MO_3 had been formed during the reaction. This is particularly important in the case of molybdenum, since the formation of MoO_3 at these high temperatures would lead to loss of catalyst by vaporisation, or movement of the catalyst along the reactor tube. HRTEM of the post-catalytic samples indicated that no carbon deposition had occurred on the catalyst surface during the reaction.

The effect of temperature and pressure on the product distribution was determined using a β-Mo_2C catalyst, at temperatures between 1073 K and 1223 K and at pressures varying from 3 to 12 bar; the results obtained are presented in Figures 3a and b. As the temperature was increased or the pressure decreased, the conversion of methane and selectivity to carbon monoxide increased; these trends can be predicted from thermodynamic calculations, and demonstrates that the carbides are efficient catalysts for this reaction.

CONCLUSIONS

We have found that high surface area molybdenum and tungsten carbides are stable catalysts for the stoichiometric carbon free reforming of methane with carbon dioxide and air at elevated pressure. These materials are much cheaper than the platinum group metals, e.g. MoO_3 is 2000 times cheaper than platinum [30], so they may be useful alternatives to conventional industrial catalysts for synthesis gas production. Methane dry reforming with niobium and tantalum carbides showed that these materials are less stable, although niobium carbide was stabilised when very high temperatures were used.

REFERENCES

1. G. Henrici-Olivé and S. Olivé, *Angew. Chem. Int. Ed. Engl.*, **15**, 136 (1976).
2. M. E. Dry, *J. Organomet. Chem.*, **372**, 117 (1989).
3. J. Eilers, S. A. Posthuma and S. T. Sie, *Catal. Lett.*, 7, 253 (1990).
4. M. V. Twigg (ed.), "Catalyst Handbook" 2nd Edn., 384 (Wolfe Publishing, London, 1989).
5. J. C. Bart and R. P. A. Sneeden, *Catal. Today*, **2**, 1 (1987).
6. G. Chichen, P. J. Denny, J. R. Jennings, M. S. Spencer and K. C. Waugh, *Appl. Catal.*, **36**, 1 (1988).
7. R. L. Pruett, *J. Chem. Ed.*, **63**, 196 (1986).
8. R. Sethuraman, H. W. Parker, T. T. Maxwell and J. C. Jones, *J. Energy Res. Tech. - Trans. ASME*, **116**, 155 (1994).
9. D. Knott, *Oil and Gas Journal*, **92**, 26 (1994).
10. J. R. Rostrup-Nielsen, in "Catalysis Science and Technology" (eds. J. R. Andersen and M. Boudart), Vol. 5, p.1. (Springer, Berlin. 1984).
11. S. T. Sie, M. M. G. Senden and H. M. H. Wechem, *Catal. Today*, **8**, 371 (1991).
12. J. M. Fox III, *Catal. Rev.-Sci. Eng.*, **35**, 169 (1993).
13. J. R. Rostrup-Nielsen, *J. Catal.*, **31**, 173 (1973).
14. A. T. Ashcroft, A. K. Cheetham, J. S. Foord, M. L. H. Green, C. P. Grey, A. J. Murrell and P. D. F. Vernon, *Nature*, **344**, 319 (1990).
15. P. D. F. Vernon, M. L. H. Green, A. K. Cheetham and A. T. Ashcroft, *Catal. Lett.*, **6**, 181 (1990).

16. A. T. Ashcroft, A. K. Cheetham, M. L. H. Green and P. D. F. Vernon, *Nature*, **352**, 225 (1991).
17. J. R. Rostrup-Nielsen and J.-H. Bak Hansen, *J. Catal.*, **144**, 38 (1993).
18. J. B. Claridge, M. L. H. Green, S. C. Tsang, A. P. E. York, A. T. Ashcroft and P. D. Battle, *Catal. Lett.*, **22**, 299 (1993).
19. J. R. Rostrup-Nielsen, *J. Catal.*, **85**, 31 (1984).
20. J. M. Muller and F. G. Gault, *Bull. Soc. Chim. Fran.*, **2**, 416 (1970).
21. R. B. Levy and M. Boudart, *Science*, **181**, 547 (1973).
22. M. J. Ledoux, C. Pham-Huu, J. Guille and H. Dunlop, *J. Catal.*, **134**, 383 (1992).
23. J. S. Lee, S. T. Oyama and M. Boudart, *J. Catal.*, **106**, 125 (1987).
24. L. Leclercq, M. Provost, H. Pastor, J. Grimblot, A. M. Hardy, L. Gengembre and G. Leclercq, *J. Catal.*, **117**, 371 (1989).
25. M. J. Ledoux and C. Pham-Huu, *Catal. Today*, **15**, 263 (1992).
26. "The Chemistry of Transition Metal Carbides and Nitrides" (ed. S. T. Oyama, Blackie Academic and Professional, Glasgow, 1996).
27. J. B. Claridge, A. P. E. York, A. J. Brungs, S. C. Tsang and M. L. H. Green, *J. Catal.*, submitted.
28. E. K. Storms, "The Refractory Carbides", Vol. 2 (Academic Press: New York, 1967).
29. M. Audier, A. Oberlin, M. Oberlin, M. Coulon and L. Bonnetain, *Carbon*, **19**, 217 (1981).
30. London Metal Exchange, 19 Sept., 1996.

TABLES

Table 1. Some characteristics of the metal carbides synthesised by CH_4 TPR.

			CH_4 TPR synthesis	
Precursor	Carbide phase	Structure	Final T / K	S_g / $m^2\,g^{-1}$
MoO_3	β-Mo_2C	h.c.p.	1023	91
WO_3	α-WC	h.c.p.	1153	39
Nb_2O_5	NbC_x	f.c.c.	1173	62
Ta_2O_5	TaC_x	f.c.c.	1223	54

x = 0.70-0.99 [NbC_x] and [TaC_x].

Table 2. Results for the dry reforming of methane over the group V and VI transition metal carbides (GHSV = 2.87 x 10^3 h^{-1}, CH_4/CO_2 = 1).

Catalyst	T / K	P / bar	C[CH_4]/ %	C[CO_2]/ %	Y[CO]/ %	H_2/CO
SiC	1223	8.0	13.3	3.4	8.1	-
	1373	8.0	76.3	75.2	75.7	0.90
NbC_x	1223	8.0	67.6	77.3	72.4	0.82
	1373	8.0	83.7	96.3	90.0	1.33
TaC_x	1223*	8.0	54.7	61.5	58.1	0.67
β-Mo_2C	1123	1.0†	92.4	92.5	92.5	0.93
	1223	1.0†	98.8	95.9	95.9	0.92
	1123	8.3	62.5	75.9	69.5	0.78
	1223	8.3	83.3	89.5	86.5	0.88
α-WC	1123	1.0†	92.0	93.1	92.6	0.94
	1123	8.3	62.7	75.4	68.6	0.79

† catalyst deactivates; * initial result could not be obtained.

Table 3. Results for the partial oxidation of methane over molybdenum and tungsten carbide catalysts (T = 1173 K, GHSV = 5.25 x 10^3 h^{-1}, CH_4/air =2/5).

Catalyst	P / bar	C[CH_4]/ %	S[CO]/ %	S[CO_2]/ %	H_2/CO
β-Mo_2C	8.7	88	92	8	2.02
α-WC	8.7	89	90	10	2.05

FIGURES

Figure 1. Stabilities of the transition metal carbides for methane dry reforming (CH_4:CO_2 = 1:1).

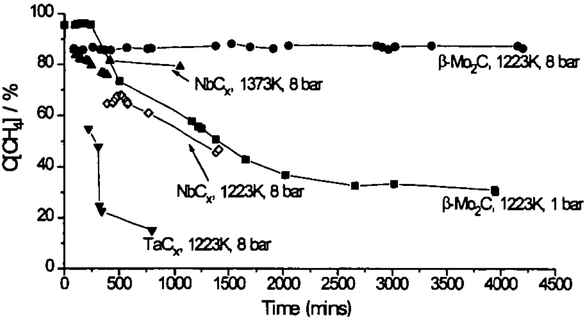

Figure 2. Lifetime study of β-Mo_2C for the methane partial oxidation reaction at 8.7 bar (T = 1173 K, GHSV = 5.25 x 10^3 h^{-1}, CH_4/air =2/5).

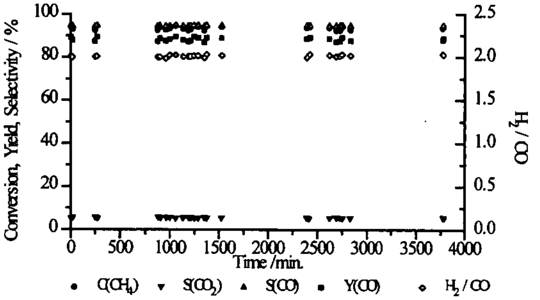

Figure 3a. Effect of temperature on the partial oxidation of methane over β-Mo_2C (8.7 bar, GHSV = 5.25 x 10^3 h^{-1}, CH_4/air =2/5).

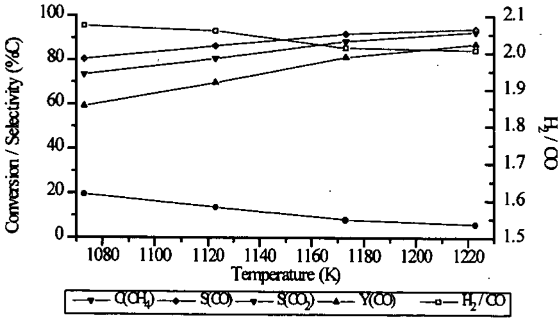

Figure 3b. Effect of pressure on the partial oxidation of methane over β-Mo_2C (1173 K, GHSV = 5.25 x 10^3 h^{-1}, CH_4/air =2/5).

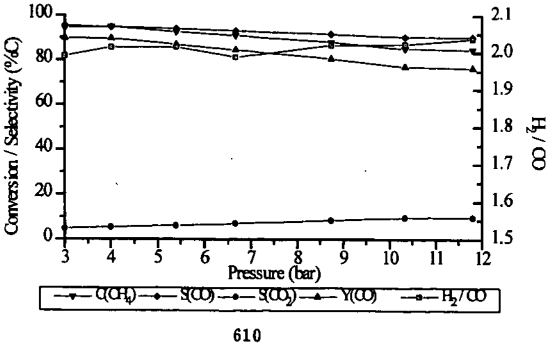

EMERGING APPLICATIONS OF HYDROGEN IN CLEAN TRANSPORTATION

Venki Raman
Air Products and Chemicals Inc.
Allentown, PA 18195

Key Words: Hydrogen, Hythane®, Hydrogen vehicles

Introduction

The present total dependence on oil supplies for our transportation systems is the major cause of air pollution in the growing urban areas of the world, and is clearly unsustainable into the future. The societal will to seek changes in this system is evidenced by the passage of stringent clean air standards that require clean alternative fuels. Emerging trends suggest that we will gradually move from this oil-dependent system to a transportation system that favors cleaner fuels such as natural gas in the near term. For the longer term, our aim will be to use pollution-free fuels derived from renewable resources. At the same time, there will also be a shift from the rather inefficient internal combustion (IC) engine that has dominated our automotive systems to highly efficient, electric motors. The combination of new fuels and new engines to use them, will ultimately produce a new transportation system built entirely on sustainable energy.

Because hydrogen can be produced cleanly from renewable energy resources, and used virtually without any pollution, it may prove to be the ideal energy carrier in the future automobile systems. A plausible strategy for the transition to hydrogen, that is widely subscribed to in the international hydrogen energy community, could involve the initial replacement of present day gasoline and diesel with natural gas, followed by the gradual introduction of hydrogen, which is similar to natural gas in the practical aspects of distribution, transfer and storage.

The key feature of past energy transitions has been the progressive move toward fuels containing less carbon and more hydrogen; witness the shift from dried wood which is mostly carbon (10% hydrogen), to coal (38% hydrogen), oil (64% hydrogen), and natural gas (80% hydrogen). The transition to hydrogen merely continues this pattern. The energy content of the fuels increases as the percentage of hydrogen increases. The shift to fuels containing less carbon has lessened air pollution over the past century (per pound burned). Particulates and carbon dioxide from oil burning are significantly lower than that from burning coal to release the same amount of energy. The shift to natural gas will cut this further and with hydrogen totally eliminated.

International Hydrogen Activities

Driven by concerns about oil dependence, and air quality, and recognizing the benefits of a hydrogen-based transportation energy system, over 30 countries worldwide, have active R&D programs underway in hydrogen energy applications. Major programs are being undertaken in Japan, the U.S. and Germany. Except for space applications which the U.S. leads, the leadership in hydrogen R&D centers in Japan and Germany. Japan has the most ambitious hydrogen energy R&D program called World Energy Network (WE-NET) which is a $2 billion effort over twenty-eight years (1993-2020). Germany has been the leader in hydrogen vehicle applications, and second to Japan in total spending on hydrogen R&D. The U.S. comes in third, followed by Canada, where the province of Quebec has undertaken a major program aimed at looking at harnessing its vast hydroelectric power resources to make liquid hydrogen for export to Europe.

In Germany, the birthplace of the automobile, Daimler-Benz and BMW have pioneered the development of hydrogen-fueled vehicles for over two decades. Daimler-Benz has developed hydrogen IC engines for cars and vans, using metal hydrides for onboard storage of hydrogen, and operated fleets of vehicles in Berlin. More recently their efforts have shifted to buses with liquid hydrogen stored onboard. Several buses are being built in conjunction with bus manufacturer MAN for operation in urban transit, and airport shuttle bus service. A joint German - Russian team including Daimler-Benz Aerospace and Tupolev are in early stages of development of a liquid hydrogen airplane called "Cryoplane". Perhaps the most exciting development at Daimler-Benz has been their unveiling in May 1996 of their second generation hydrogen fuel cell passenger minivan called "NECAR 2" with hydrogen stored onboard as compressed gas. The first prototype NECAR 1 a research vehicle had been unveiled only in 1994. This development program is clearly proceeding at an accelerated pace at Daimler-Benz. The next prototype NECAR 3 is expected to be a new small sedan.

BMW has also been active in hydrogen car developments since about 1979. The focus of BMW's efforts have been centered on liquid hydrogen from the start. BMW has developed 6 generations of cars capable of running on either gasoline or hydrogen. In conjunction with German hydrogen suppliers, they have significantly improved the insulating efficiency, and compactness of onboard liquid hydrogen storage tanks. They have also reduced fueling times from about 1 hour down to about 15 minutes. Now they are developing robotic fueling systems to fully automate the transfer of liquid hydrogen to the car. BMW also participates in a consortium that is conducting a solar-hydrogen demonstration project in Germany.

This facility is an integrated project that produces hydrogen via water electrolysis from solar generated electricity.

In Japan, active hydrogen vehicle projects are underway at Mazda, Toyota, Honda, and Musashi Institute of Technology. Mazda's work has been on hydrogen-fueled IC rotary engines using metal hydrides to store hydrogen onboard the vehicle. Toyota unveiled their first hydrogen fuel cell car in October 1996.

The U.S. Department of Energy has been researching the potential use of hydrogen as an energy carrier and fuel since the early 1970s, following the OPEC oil embargo. Originally, the driving force behind this program was the National need to develop a domestic, sustainable energy base. Basic R&D was conducted at a low level of funding ($0.5-1.0 million) throughout the 1980s. However in 1990 the U.S. Congress enacted into law the Spark Matsunaga Hydrogen Research, Development, and Demonstration Act (P.L. 101-566) which revitalized the then existing Hydrogen Program. The Energy Policy Act of 1992 (P.L.102-486) further supplemented the Matsunaga Act. These actions have resulted in a National Hydrogen R&D program under the management of the DOE which has a current budget of $15 million per year. A new Hydrogen Futures Act of 1996 (P.L. 104-271) was recently enacted authorizing expenditures of $150 million between 1997 and 2001 for hydrogen R&D and demonstration programs. In addition to the Hydrogen Program, DOE supports other hydrogen related programs including work on fuel cell technologies to the tune of $100 million per year.

In addition to the federal program, several state and regional government bodies have also initiated hydrogen vehicle programs of their own including the South Coast Air Quality Management District (SCAQMD) in Southern California, the California Air Resources Board (CARB), Cities of Palm Desert, Palm Springs, and Denver, New York State Energy Research and Development Authority (NYSERDA), Pennsylvania Energy Office (PEO), and others.

Hydrogen Transportation Demonstration Programs

In the area of hydrogen vehicles, active programs are underway in IC engines, IC engine-electric hybrids, and fuel cell engines. These programs represent a progression of increasingly more economically and technically challenging options for the transition of hydrogen into the transportation fuel marketplace.

Hythane®

From the earliest days of combustion science, experiments have established that hydrogen has a strong influence on the combustion of natural gas and other hydrocarbons. More recently, Hydrogen Components Inc., of Colorado has been actively promoting the use of dilute concentrations of hydrogen (10-20 Vol%) blended with natural gas in IC engines. They have registered the trademark Hythane®, and hold a patent on the application of Hythane in IC engines.

It has been shown in laboratory and on-the-road testing that this small level of hydrogen addition to natural gas in IC engines results in reducing levels of carbon monoxide (CO) and oxides of nitrogen (NOx) emissions from these engines an additional 50% over that achieved with "straight" natural gas. The economic rationale for such an approach involving small additions of expensive hydrogen to cheap natural gas relates to the fact that significant leverage in emissions reduction is achieved, i.e., disproportionately greater than the amount of hydrogen added. Such an approach faces a smaller economic hurdle in achieving the benefits of clean air and is more likely to be favorably received by the consumer.

The Hythane application has been developed and tested for gasoline (stoichiometric engines) and diesel type (lean burn) engines[1]. Several test and demonstration programs have been conducted in Denver, Colorado, Erie, Pennsylvania, and Montreal, Canada on small fleets of utility service vehicles and urban transit buses. In these programs optimal hydrogen additions were determined to be between 15-20 vol%. In the case of buses operating on a modified Cummins L-10 engine with natural gas, it was observed that as the hydrogen additive was increased from 0 to about 20 vol% (7% by energy content) the NOx emissions steadily decreased by about 43% due to the ability to operate the engine more fuel lean and also with less spark advance while maintaining the non-methane hydrocarbons emissions constant. Increasing hydrogen content above 20 vol% caused the NOx to increase after adjusting the engine to maintain the same hydrocarbon emissions as the baseline. A 43% NOx reduction with a 7% by energy content hydrogen addition represents a leverage factor of greater than 6. Similarly in tests with gasoline (stoichiometric) engines with three-way catalysts indicated that hydrogen addition to natural gas dramatically reduced CO but increased NOx. However by tuning the engine to operate slightly richer than the baseline operating conditions, it was seen that some of this CO advantage could be sacrificed for significantly lower NOx emissions. Thus tests done in Denver demonstrated that it is possible to operate with Hythane containing 15 vol% hydrogen (5% by energy content) and reduce both CO and NOx to about 50% of the baseline values.

A cost analysis for a 500 vehicle fleet operating on Hythane (5% hydrogen by energy content) based on current liquid hydrogen pricing indicated that Hythane price would be quite competitive with regular unleaded gasoline at about $1.13 per gallon gasoline equivalent[2].

Hydrogen IC Engines

A further enhancement of emissions reduction can be obtained by burning pure hydrogen in IC engines. As stated previously, this has been the subject of detailed investigation by Mercedes-Benz and BMW for quite some time. The approach is to use hydrogen in lean burn engines. Since the lean burn limit of air breathing hydrogen engines is so much greater than hydrocarbon fuels, it is possible to operate at very lean conditions and reduce NOx emissions to extremely low values. This is often accompanied by very low levels of CO emissions emanating from the combustion of traces of lubricating oils used in the engines. In the U.S. a demonstration program lead by Clean Air Now and Xerox Corporation operates a fleet of four service vehicles on hydrogen generated from solar energy at a fuel station in Los Angeles. A similar effort is underway in University of California's Riverside campus.

An improvement on this concept is the hydrogen hybrid electric vehicle which takes advantage of high efficiency electric drive trains and the low emissions of hydrogen IC engines. The concept involves the use of relatively small IC engines operating on hydrogen to power electric generators that charge batteries. The IC engine is sized to match the average power requirement of the vehicle and hence operates continuously at or near its optimum efficiency. The battery is sized to accommodate the peak power surge requirements. This reduces the weight of batteries needed for a given range and gives the vehicle rapid fueling capability. The hybrid electric vehicle is being actively developed for both hydrocarbon fuels and hydrogen. A hydrogen hybrid electric bus is currently undergoing testing in Atlanta by the Westinghouse Savannah River Company. This bus is slated to be put in transit service in Augusta, Georgia following this test program.

Hydrogen Fuel Cell Vehicles

Perhaps the most attractive energy conversion technology that uses hydrogen in a zero-emission vehicle is the fuel cell. Although fuel cells were first invented some 150 years ago, only recently has their pace of development accelerated dramatically. Major automobile manufacturers in the U.S., Europe and Japan all have major development programs underway in an attempt to bring this technology to the market early in the next century. In the U.S. the joint program between the federal government and the "big three" auto manufacturers is actively developing fuel cell cars under the Partnership for a New Generation of Vehicles (PNGV) program.

While fuel cell cars are still under development, hydrogen fuel cell buses are becoming a reality and small fleets (3-4 buses at each location) will begin operation in Chicago, and Vancouver, British Columbia in 1997. The Canadian company Ballard Power Systems has developed the propulsion systems for these buses using their Proton Exchange Membrane (PEM) fuel cell technology. Hydrogen refueling stations at the bus depots are being built to deliver and store hydrogen onboard the buses at 3,600 psi. The hydrogen will be delivered to these sites as liquid and pumped to high pressures using cryogenic liquid pumps. The stations are being designed for fueling a bus in about 15 minutes.

Hydrogen Fuel Supply

In the future, a truly zero emission transportation system could be based on hydrogen produced from renewable energy resources such as solar, wind, geothermal or biomass. However, renewable hydrogen production processes are still in the early stages of development and can not compete with current hydrogen production technologies. As the various hydrogen vehicle technologies rapidly progress towards commercialization, the ready availability of competitively priced hydrogen will be critical to their near term success. The perceived lack of a hydrogen fuel supply infrastructure could be the major barrier to the use of hydrogen in the transportation sector. Some major automobile companies such as Chrysler, Daimler-Benz, General Motors, and Toyota have decided to develop onboard fuel processors to generate the hydrogen required for their fuel cell vehicles from methanol or gasoline. However, it is entirely feasible to ensure an adequate hydrogen fuel supply system, at all stages of the evolution of hydrogen utilization technology, by adapting current industrial hydrogen production and distribution technologies.

About 40 million tons of hydrogen are commercially produced and consumed per year around the world. The energy content of this hydrogen is about 5 quadrillion British Thermal Units (BTU) or slightly more than 1 percent of the world's energy demand. About 95% of the 10 million tons per year of hydrogen produced in the U.S. is consumed "captively" within the producing facility to refine oil, or to produce ammonia and methanol. The rest is produced by a few industrial gas companies, and supplied to customers as a gas in high pressure cylinders and via pipelines, or as a liquid via over-the-road cryogenic tankers. This so called "merchant" hydrogen is used to manufacture specialty chemicals; to hydrogenate fats and oils; for reducing atmospheres in the manufacture of metals, glass and semiconductors; and as a coolant for large electric power generators. The only significant transportation fuel application of hydrogen - about 0.1% of the production - is as a rocket fuel, e.g., to launch NASA's Space Shuttle.

Practically all hydrogen is manufactured today, directly or indirectly, from fossil fuels. The most common commercially practiced technologies include: steam reforming of light hydrocarbons, partial oxidation of heavy oil, recovery from off-gases from the chlor-alkali industry, and refining and petrochemical processes, electrolysis of water, and methanol reformation.

The merchant hydrogen business in the U.S. is supported by well developed transportation and storage systems. Hydrogen is transported and stored as a gas, or liquid depending upon the distance from the user's location to the production plant, and usage rates and patterns, i.e., whether continuous or intermittent. Practically all commercial applications require the hydrogen in gaseous form, thus even when hydrogen is delivered and stored as liquid, it is vaporized at the customer's site prior to use. "Bulk" gaseous hydrogen is usually more expensive to store and ship than an equivalent amount of liquid hydrogen, particularly for distances greater than about 100 miles from the hydrogen production plant.

Among the various options being considered for storing hydrogen on-board the vehicle, perhaps the most challenging, from a fueling system design viewpoint, is high pressure gas at about 3,600 - 5,000 psi. The desired refueling times of about 10-15 minutes can be readily achieved with modifications to current commercial high pressure liquid hydrogen pumping systems. Fleets of up to 100 transit buses or 4,500 personal automobiles can be readily supported with liquid hydrogen deliveries and transferred at high pressure to the on-board tanks using special liquid hydrogen pumps followed by vaporization. Several high pressure hydrogen fueling systems for experimental fleets are currently being developed based on the significant experience gained in the design and operation of compressed natural gas fueling systems. The National Hydrogen Association is leading an effort to develop industry codes and standards for high pressure hydrogen fueling stations and onboard storage systems.

Hydrogen Infrastructure Options To Support Fuel Cell Vehicles

A recently completed study[3], examined how current commercial hydrogen production and supply technologies could be adapted to supply fleets of fuel cell cars at individual fueling stations and the economics of these options. Each car required 12 lbs. hydrogen stored onboard the vehicle as a gas at 5,000 psi. A typical fuel station was designed to dispense 3 tons per day (TPD) of hydrogen, sufficient to refuel 500 cars per day.

The following commercial options for hydrogen supply to the station were considered:

- Hydrogen produced from natural gas in large scale remote steam reformer plants (30-300 TPD), is delivered as liquid up to a distance of 500 miles from the plant.
- Hydrogen produced from natural gas in large regional steam reformer plants (30-300 TPD) is delivered via gas pipelines within a radius of 30 miles of the plant. Fueling stations are spaced 3 miles apart on the pipeline.
- Hydrogen is produced at the fuel station with a dedicated on-site plant (3 TPD) using natural gas steam reformer, heavy oil partial oxidation, or a methanol reformer.

Table 1 summarizes the results of this study and shows the capital investment, and hydrogen price at the pump (without taxes) for these options. Hydrogen fuel can be supplied to the vehicle using current technologies at a cost ranging from $1-2 per lb. depending on the scale of production. Taking into account the projection of a 2 to 3 times superior fuel economy of a fuel cell car over a gasoline car, the last column of Table 1 shows the maximum allowable gasoline price (without taxes) to provide the same cost per mile in an IC engine car as the fuel cell car. To compare this to a typical pump price for gasoline in the U.S., about 40¢ per gal should be added to these prices. With current regular unleaded grade gasoline prices at the pump in the U.S. at around $1.20 per gallon, this analysis indicates that several near term hydrogen production and distribution options are close to being competitive with gasoline on a cost per mile basis.

Development of a hydrogen fuel infrastructure similar to the familiar gasoline supply network, with fuel stations every few miles, in population centers across the U.S. is certainly many years into the future. Large investment in the production and distribution infrastructure are necessary to achieve the lower prices for hydrogen. This certainly dictates that such facilities will not be built until sufficient demand for hydrogen develops as hydrogen-fueled vehicle technology becomes well established and accepted by the public. Thus, the infrastructure to supply fuel cell vehicles with hydrogen will evolve with the start up and growth of this market in several stages:

In regions where merchant hydrogen infrastructure exists, when a local market starts up with a small fleet of fuel cell cars, it would first be supplied by the current commercial distribution system via hauled-in high pressure gaseous hydrogen in tube trailers (to fuel about 20 cars per day) or liquid hydrogen (to fuel 20 - 500 cars per day). As the fleet grows large enough to support the continuous operation of a small reformer, one would be built and liquid hydrogen from a large central plant used as a backup source, and to meet peak demands. As the market grows even larger it could be supplied by a large regional reformer via pipeline, with the excess capacity being liquefied for distribution to areas remote from pipelines.

In areas where merchant hydrogen is not readily available small on-site hydrogen plants would be built to support the fuel station. Recent activity in the area of small reformers for hydrogen production may result in the economic size of on-site plants being reduced from currently accepted sizes. In this connection, methanol reformers appear to offer significant advantage due to their relative simplicity and wide availability of methanol.

Natural gas supplies would probably be sufficient to supply feedstock for hydrogen production for up to several million fuel cell cars, for several decades[4]. In the longer term, other renewable hydrogen production methods such as biomass gasification, or solar energy could be phased in.

References

1. Raman V., Hansel J., Fulton J., Lynch F. and Bruderly D., "Hythane - An Ultraclean Transportation Fuel", Hydrogen Energy Progress X, Proceedings of the 10th World Hydrogen Energy Conference, Cocoa Beach, Florida, Vol. 3, p. 1797 (1994)

2. Hansel J., Kielian D., Lynch F., Ragazzi R., Raman V., and Willson B, "Hythane - A Status Report", 26th International Symposium on Automotive Technology and Automation, Aachen, Germany September 1993.

3. Moore, R. B. and V. Raman "Hydrogen Infrastructure for Fuel Cell Transportation", presented at the 7th Annual U.S. Hydrogen Meeting, National Hydrogen Association, Alexandria, VA, April 1996.

4. Ogden, J.M. et.al. "Hydrogen System Studies", presented at the U.S. DOE Hydrogen Program Review Meeting, April 29 - May 3, 1996.

Table 1. Cost Analysis for Hydrogen Infrastructure to Supply Fuel Cell Automobiles

Hydrogen Production/Delivery Method	Size, TPD	Investment $ Million	Hydrogen Price $/lb	Untaxed Gasoline Equiv. Cost $/gallon[1]
Remote Natural Gas Steam Reformer w/ Liquefier	30	63	1.52	1.12 - 1.61
	300	259	1.07	0.79 - 1.14
Regional Natural Gas Steam Reformer w/30 mile Gas Pipeline	30	82	1.32	0.97 - 1.39
	300	667	1.12	0.83 - 1.19
On-site Natural Gas Steam Reformer	3	9.6	1.62	1.19 - 1.71
On-site Partial Oxidation of Oil	3	12.5	1.80	1.33 - 1.91
On-site Methanol Reformation	3	6.8	1.70	1.25 - 1.80

---

[1] Untaxed gasoline price to produce same cost per mile in IC engine vehicle as hydrogen in a fuel cell vehicle. The price range indicates different values for fuel economy based on two variants of the Federal Urban Driving cycle.

SLURRY FISCHER - TROPSCH SYNTHESIS IN CHINA

Yu - Long Zhao Liang Bai Bi - Jiang Zhang
Institute of Coal Chemistry State Key Laboratory of Coal Conversion
P. O. Box 165, Taiyuan, Shanxi, 030001, P. R. China

Keywords: Fischer - Tropsch sythesis bubble column slurry reactor(BCSR)
Fe - Cu - K catalyst kinetic parameter solubility

INTRODUCTION

Cina is one of a few countries where coal is used as major energy source. Research and development of clean coal technology is especially important for China to solve the problems of environmental pollution and to increase supply of liquid fuel espceially the unleaded high quality gasoline. It is well known that slurry Fischer - Tropsch synthesis technology (SFTST), which has the advantages on both technology and economics over traditional fixed process as demonstrated by Sasol's Slurry Phase Distillate Process, is an advanced technology of indirect liquefaction of coal. Institute of coal chemistry has developed SFTST on both catalysts and a micro—pilot unit (MPU) as well as chemical engineering since 1986. The present paper will summarized the status and progress in R & D of SFTST.

1 CATALYST

One of the key problems in the development of SFTST is to provide a catalyst with high activity, good selectivity and long catalyst life. Iron catalysts, which are not only hydrogenation catalysts, but also active water gas shift catalysts, are indeed the most promising one as commercial catalyst for SFTST.

The catalysts used in our laboratory were prepared in a continuous multistage stirred precipitation reactor similar to those described by Kölbel[1]. Preparation conditions of catalyst including precipitation temperature, pH value and promoters were examined. Typical catalyst composition was 99. 5 Fe: 0. 5 Cu: 0. 29 K_2O by weight. The pretreatment condition and synthesis results were shown in table 1. From both hydrocarbon yield and time on stream in table 1, it is evident that the synthesis results based on temperature - programmed method are better than those based on non - programmed method. P2 pretreatment was preferred in the lone life test by considering the same ratio of H_2/CO in both pretreatment and synthesis. In order to understand the phase change during catalyst pretreatment, XRD analyses of fresh catalyst and catalyst partially induced at the initial stage and the later stage of pretreatment were compared and shown in Fig. 1. Crystal phase of a fresh catalyst is totally hematite ($\alpha - Fe_2O_3$) as shown in Fig. 1 A, XRD of the catalyst partially induced at the initial stage of pretreatment as shown in Fig. 1 B indicated that magnetic iron oxide and Hägg carbide began to appear, but Hematite still existed. Fig. 1 C is XRD spectrum of the catalyst induced at the later stage of pretreatment. Hematite disappeared totally and magnetic iron oxide and Hägg carbide were the dominant crystal phase. Above results are significant to judge the extent of pretreatment of catalysts. Three long life tests were conducted in a magnetically stirred 1L autoclave. The results are given in table 2. It is found that iron catlaysts prepared had longer life time and thus they were applied in MPU for SFTST.

2 MICRO - PILOT UNIT

Schematic of MPU is shown in Fig. 2. After being purified and preheated to a given temperature, syngas with relatively low H_2/CO ratio (0. 5 - 1. 5) was bubbled through a slurry of unsupported precipitated iron catalysts suspended in wax medium in BCSR. The gas distributor was a porous sintered metal plate. The catalyst used was the unsupported precipitated iron catalyst promoted by copper and potassium with a particle size less than 44μm. Suspended catalyst was separated from reactor - wax by sedimentation in the settling vessel. The catalyst was recirculated between the enlarged upper section and the bottom of the BCSR through a settling vessel and an 2L autoclave in sequence. Catalyst settling tests on the MPU demonstrated that catalyst concentrations were 0. 92wt% at 130℃ and 0. 66wt% 200℃ in the wax withdrawn from the section of the settling vessel for the same settling time. It is clear that increasing settling temperature makes it easier to separate catalyst from the reactor - wax. On the other hand, catalyst concentration in the reactor - wax approaches a constant value as settling time is extended. Therefore, a reasonable settling time can be set up to raise the efficiency of the settling vessel. Operation of separation was conducted every twelve hours. The reactor - wax, in which catalyst concentration was maintained at 0.5 - 0.8wt%, was regularly withdrawn through an overflow outlet. The enlargement of BCSR plays reducing the concentration of catalyst in the slurry entering the settling vessel, and the autoclave is used for the addition and activation of make - up catalyst. Fig. 3 shows variation of catalyst concentration in the reactor - wax with time on stream during the duration test lasted for over 1000h. The ranges of process variables were as follows: 260 - 280℃ (1st - stage)/320 - 340℃ (2nd - stage), 1.4 - 2.4MPa, 2.0NL/gFe · h(1st - stage)/500 - 1000h^{-1}(2nd - stage) and ratio of H_2/CO 0.5 - 1.5. Mean results of the test were as follows: syngas conversion (once - through) 65.1%, yield of C_5^+ 100g/nm^3($CO+H_2$), total hydrocarbon production >350g/gFe. When CO - rich syngas was used, the yield of C_5^+ was 110g/nm^3($CO+H_2$). Examples of matertal balances on a 12 hrs basis are given in table 3. Heat of reaction for FT syhthesis from heat balance at 280℃ for 1st - stage BCSR is 2938.5kJ/m^3($CO+H_2$), which is fairly consistent with 2829.6kJ/m^3($CO+H_2$) reported by farley[2] and 3038.9kJ/m^3($CO+H_2$) calculated by stoichemistry equation. During the duration test, catalyst samples were taken from 1st - stage BCSR at various time on stream for Mossbauer spectroscopic study of iron catalyst and the phase present in the samples were unchanged due to isolation of the sample surrounded with the reactor - wax from ambient. Fig. 5 shows the corresponding phase composition of iron catalyst in BCSR run as a function of time. It is found that the fresh catalyst was 64% of $\alpha-Fe_2O_3$ and 36% of $SP+Fe^{3+}$. The trend with time in the bulk phase composition of catalyst shows that while the extent of reduction and carburization extent of iron catalysts increased with extending time on stream and approached to the steady state with reducing fraction of magnetite. This is in accordance with the results reported by Satterfield et. al. [3] for fused magnetite catlaysts. It is therefore considered that slurry phase operation is favorable of reduction and carburization of iron catalyst to keep catalyst activity and stability constant.

The duration test demonstrated that the performance of operation in the MPU was satisfactory. Its temperature control, flow system and other equipment were reliable. Viscosity of slurry was basically constant throughout the test. The design of the slurry recirculation loop was reasonable with less loss of catalyst and stable operation.

3 Support studies

3.1 Solubilities and Mass transfer coefficients

Equilibrium gas solubilities (C_{eq}) and volumetric liquid - side mass transfer coefficients (k_La) were measured for hydrogen and monoxide in n - paraffin, n - octacosane and FT300 wax at various pressure (1.0 - 4.0MPa) temperatures (100 - 300℃), and a rotate speed of 800rpm in a 1L agitated autoclave. In the range of operating conditions investigated the relationships of gas equilibrium solubilities with temperature and heats of solution were obtained as shown in table 4. The k_La values for hydrogen and carbon monoxide in all liquid used increased with temperature and pressure, but decrease with increasing liquid molecular weight as shown in Fig. 5.

3.2 Kinetic parameter and mathematic simulation

Based on the data obtained from BCSR in MPU, the kinetic parameters of the Fischer - Tropsch synthesis (FTS) on unsupported precipitated Fe - Cu - K catalysts were estimated with a multi - component BCSR model. The main assumptions of the BCSR model under steady state conditions are as follows: 1. Plug flow gas phase and unmixed slurry phase; 2. the main mass transfer resistance to diffusion being at the liquid side of the gas - liquid interface; 3. uniform catalyst concentration throughout the BCSR; 4. FTS reaction rate expression being.

$$-R_{H_2+CO}=kC_{H_2}/(1+KC_{CO_2}/C_{CO})\ (H_2/CO\leqslant 0.8)\ \text{where } k=k_0\exp(-E_a/RT-\beta t)$$

The parameter values estimated were $k_0=1.36\times10^9 cm^3/gcat.s$, $E_a=100.0$kJ/mol, $K=0.204$. Table 5 gives comparison of kinetic parameters obtained with those reported by Kuo[4] and Sanders[5]. It is seen from table 5 that kinetic parameters estimated are very close to values reported. The results predicted from FTS rate expression indicated that activity of catalyst used will deactivated by 1% after 35 h on stream, 26% after 1000h and 50% after 2300 h. It is obvious that the stability of the catalyst used should be improved. Also, axial concentration profiles of H_2, CO, CO_2 in both gas phase and liquid phase and the effect of bubble size on syngas conversion were computed by the BCSR model and the kinetic parameters estimated. Axial concentration profiles of each component in both gas and liquid phases are depicted in Fig. 6.

3. 3 Hydrodynamics

It is known that the FT reaction is a volume reducting reaction. The volume flow rate of gas phase is gradually diminished with increasing conversion. Therefore, phase holdup and axial solids concentration were investigated in a tapered bubble column (0. 1m and 0. 2m id on the top and bottom, respectively, 3m height) with slurry circulation in a system composed of air, water and quartz sand. The axial distribution of solid concentration was measured by the synchronously sampling method and gas holdup by pressure drop method. The effect of solid particle size (142. 5μm, 180μm), solid concentration (0 - 100kg solid/m^3 slurry), slurry velocity (0 - 0. 0157m/s) and gas velocity (0 - 0. 125m/s) on gas holdup and solid axial concentration distribution were determined.

Experimental results were well agreement with the prediction made on the basis of the one dimensional sedimentation - dispersion model. The correlations of particle Peclet Number and gas holdup were obtained as follows:

$$Pe_p = 5.06(Fr_g^6/Re_g)^{0.130}(1+0.019Re_p)$$

where $0.03 \leqslant Pe_p \leqslant 0.4$; $1166 \leqslant Re_g \leqslant 18843$; $5.25 \leqslant Re_p \leqslant 10.45$; $0.0064 \leqslant Fr_g \leqslant 0.104$

$$\frac{\varepsilon_g}{(1-\varepsilon_g)^4} = 0.302(gD^2\rho_L/\sigma_L)^{0.125}\left(\frac{gD^3\rho_L^2}{\mu_L^2}\right)^{0.083}(Fr_g)^{0.958}$$

CONCLUSIONS

Unsupported precipitated Fe - Cu - K catalyst, which was prepared in a continuous precipitator, was applied in MPU. Catalyst activation proceeded well with syngas by the temperature - programmed method. THe 1000h run demonstrated the SFTST at a micro - pilot scale. Operation and performance of the MPU were good. A preliminary measure of separation of catalysts from reactor - wax was realized by a slurry recirculation loop. Under conditions of 260 - 280℃ (1st - stage)/320℃(2nd - stage), 1. 5 - 2. 5MPa, 2. 0NL/gFe · h(1st - stage), 500 - 1000h^{-1}(2nd - stage), and H_2/CO ratio 0. 6 - 0. 7, a yield of C_5^+ over 100g/nm^3($CO+H_2$) can be achieved. Engineering data and information including kinetic knowleage and solubilities are useful for further development of the process and scale - up and design of the BCSR.

REFERENCES

[1] H. Kölbel. and M. Ralek, Catal. Rev. Sci. Eng., 1980; 21,225

[2] R. Farley and D. J. Ray, The Institute of Petroleum, 1964; 50(482);27

[3] C. M. Satterfield et. al., Ind. Eng. Chem. Prod. Res. Dev., 1986; 25(3);401

[4] J. C. W. Kuo et. al., 1983; "Slurry Fischer - Tropsch/Mobil Two - Stage Process Synthesis to High Octane Gasoline" DOE Report Contract NO. DE - AC22 - 80 PC 30022

[5] E. Sanders and W. D. Deckwer, Can. J. Chem. Eng., 1987; 65(1);119

Table 1 Pretreatment conditions and results of synthesis reaction

Pretreatment						Synthesis reaction						
No.	H_2/CO	T /°C	P	HT/SV	Note	T /°C	P	HT/SV	H_2/CO	C_1^+	C_5^+	$R.T$
1	1:0	260	1.5	2	B	260~280	1.5	2.0	2.4	a little liquid		–
2	A	280	0.3	2	C	260~280	1.5	2.0	2.0	92.9	45.9	432
3	2:1	280	1.6	2	C	280	1.5	2.0	2.0	66.7	22.0	126
4	2:1		0.4/0.9	2	P1	260~280	1.5	2.7	2.0	99.5	59.0	640
5	1.5:1		0.3/1.0	2	P1	260~280	1.5/2.5	1.8/3.4	0.85	157.3	105	280
6	1:1		0.3/1.0	2	P2	260~280	1.5/2.5	2.0	1.0	113.1	77.0	1112

Note: *R.T.*–running time, h; A—$N_2/CO=9$; B—isothermal 12 h; C—isothermal 24 h; PI—increasing and decreasing temperature at isorate, then pressuring again, total time 35 h; P2—temperature programmed pretreatment

Table 2 Results of the long life test

Run No.	A-26	A-30	B-6
Temperature / °C	250~280	250~280	260~280
Pressure / MPa	1.5~3.0	1.5~2.5	1.5~2.5
WHSV / $L\cdot g(Fe)^{-1}\cdot h^{-1}$	2.96	2.88	2.96
H_2/CO in feed	1	1	1
Hours on stream / h	1112	1128	1008
X_{CO}	69.5	82.9	78.6
X_{H_2}	40.4	52.7	36.3
X_{H_2+CO}	54.5	67.4	64.4
Hydrocarbon composition /%			
CH_4	6.0	8.1	9.6
C_2H_4	4.8	5.0	4.1
C_2H_6	3.7	2.7	6.2
C_3H_6	7.3	6.2	4.7
C_3H_8	1.9	1.2	3.2
C_4H_8	6.8	4.5	7.4
C_4H_{10}	1.7	1.4	3.9
C_5^+ minus wax trap	45.0	53.5	41.1
wax trap	18.6	14.4	13.1
Hydrocarbons yield			
C_1^+ g/m^3 $(CO+H_2)$	113.8	116.9	145.1
C_5^+ g/m^3 $(CO+H_2)$	77.0	83.5	91.2

Table 3 Material balance

Temperature/℃	265	265	265	270	275	280
Pressure/MPa	2.0	2.5	2.5	2.0	2.0	2.0
WHSV NL/gFe · h	2.15	2.24	2.26	2.23	2.28	2.31
H_2/CO	0.61	0.62	1.32	0.60	0.60	0.66
X_{H_2+CO} %	69.2	70.4	58.0	75.8	77.7	81.4
Inlet feed syngas NL · h^{-1}	644	671	678	669	684	693
Outlet tail gas NL · h^{-1}	377	385	416	354	355	336
Oil/g · h^{-1}	16.5	17.3	22.8	23.1	23.8	24.8
Wax/g · h^{-1}	50	49.7	30.6	50.2	53.1	54.8
Aqueous/g · h^{-1}	10.4	12.0	26.4	11.3	12.4	16.0
Material recovery %	99.7	98.9	98.5	96.7	94.7	95.1
C_1^+/g$[Nm^3(CO+H_2)]^{-1}$	133.6	143.2	132.2	149.2	154.4	163.0
C_5^+/g$[Nm^3(CO+H_2)]^{-1}$	113.1	115.2	90.0	123.7	127.1	129.9

Table 4 The correlations of gas equilibrium solubilities with temperature and Heats of solution

medium	H_2		CO	
	Correlation	**Heats of solution**	**Correlation**	**Heats of solution**
paraffin	0.9892exp(−4697.9/T)	4697.9	0.9889exp(−2135.9/T)	2135.9
n-$C_{28}H_{58}$	0.9892exp(−5129.4/T)	5129.4	0.9889exp(−2609.9/T)	2609.9
FT300wax	0.9897exp(−8142.3/T)	8142.3	1.0108exp(−5276.6/T)	5276.6

Solubility ,kmol/kg/atm, Heat of solution ,J/mol

Table 5 Comparison of kinetic parameters

Investigator	catalyst	k_0, cm^3/gcat. s	E_A. kJ/mol	K
Kuo (1983)	Fe−Cu−K	6.7×10^9	105.0	0.089
Sanders (1987)	Fe−K	1.42×10^8	88.2	0.316
Authors	Fe−Cu−K	1.36×10^9	100.0	0.204

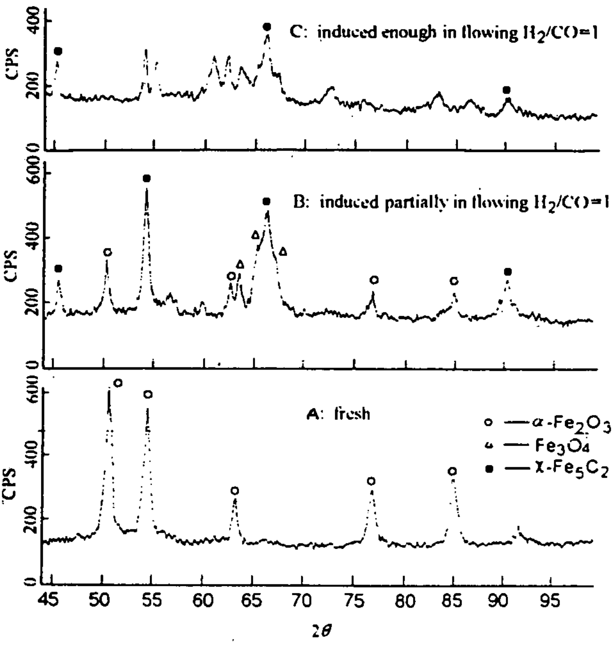

Fig. 1 XRD of the precipitated Fe - Cu - K catalyst

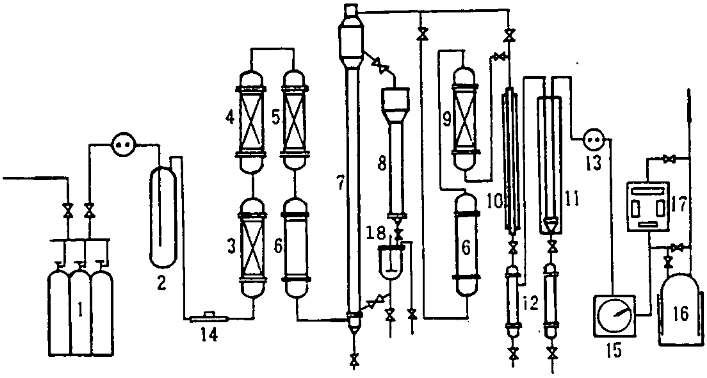

Fig. 2 A simplified flow diagram of the two - stage MPU for the synthsis of hydrocarbons

1. Syngas cylinder 2. Pressure buffer tank 3. Water trap 4. Iron carbonyl removal 5. Sulfide removal 6. preheater 7. 1st - stage BCSR 8. Settling vessel 9. 2nd - stage fixed - bed ZSM - 5 reactor 10. Air condenser 11. Chilled condenser 12. Liquid products receiver 13. Pressure let down valve 14. Mass flow meter 15. Wet - test meter 16. gas holder 16. IR gas analyzer 18. autoclave

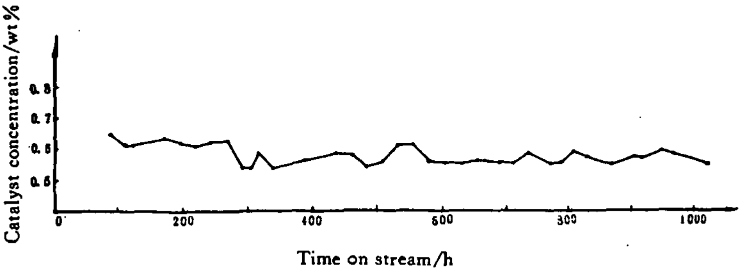

Fig. 3 Variation of catalyst concentration in the reactor - wax with time on stream

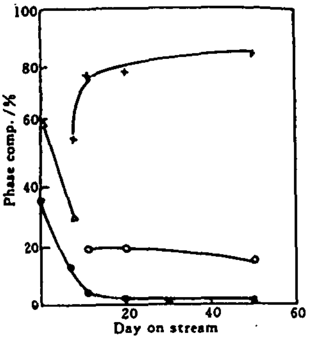

Fig. 4 Variation of bulk catalyst phase composition with time on stream

●—Fe^{3+}; Δ—α-Fe_2O_3;
○—Fe_3O_4; ×—χ-Fe_5C_2

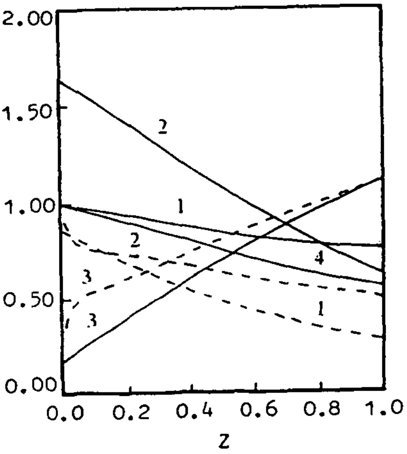

liquid ---- gas —— ; 1. H_2, 2. CO, 3. CO_2, 4. U_g

Fig.6 Dimensionless concentration profiles for each component and gas velocity profile

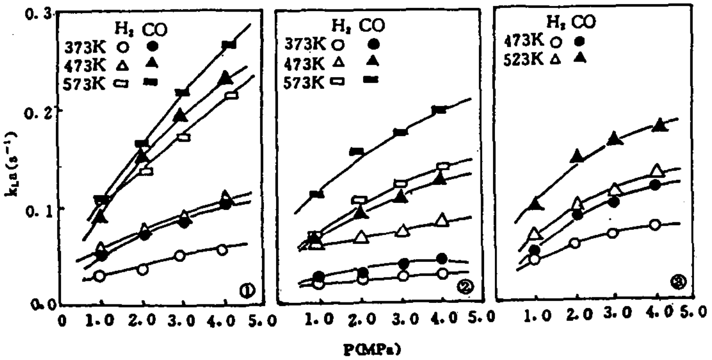

Fig. 5 Volumetric mass transfer coefficient k_La of H_2、CO in various liquids

(① n - paraffin; ② n - octacosane; ③ FT300 wax)

EFFECT OF PRETREATMENT ON CATALYST ACTIVITY AND SELECTIVITY DURING FISCHER-TROPSCH SYNTHESIS IN A SLURRY REACTOR

Dragomir B. Bukur, Xiaosu Lang and Yunjie Ding
Department of Chemical Engineering
Texas A&M University, College Station, Texas 77843

Keywords: Fischer-Tropsch synthesis, iron oxides and carbides.

INTRODUCTION

Promoted iron catalysts, reduced with hydrogen, have been used in commercial fixed bed and entrained fluid bed reactors for synthesis gas conversion to transportation fuels via Fischer-Tropsch synthesis (FTS) at SASOL in South Africa[1]. However, the purpose of pretreatment for iron FT catalysts is not clearly understood. Reduction in H_2 may lead to a zero-valent state, but upon exposure to a synthesis gas the metallic iron is rapidly converted to a carbide phase or a mixture of iron carbides[2,3]. At high syngas conversions, a reaction mixture becomes more oxidizing and magnetite is also formed[1,4,5]. During FTS, the bulk iron may be distributed among several phases: e.g. carbides, oxides and metallic iron, which often results in a lack of correlation between the catalyst bulk composition and its activity and/or selectivity[1,5]. Other pretreatments have been also employed, such as CO activation, synthesis gas pretreatment or induction, and/or H_2 reduction followed by CO treatment or vice versa[4,6].

Also, there has been a large number of related studies on model iron catalysts dealing with an issue of the role of iron phases in FTS. However, this issue still remains to be a controversial one. Briefly, some workers consider the surface carbides, with an underlying iron carbide bulk structure, to be the active phase[2,7]. In the so-called competition model of Niemantsverdriet and van der Kraan[8] iron atoms at the surface are considered as the active sites. In the latter model both bulk carbidation and FTS (hydrocarbon formation) have a common surface carbidic precursor. In addition to these two postulates concerning the nature of the active phase, Teichner and co-workers proposed that Fe_3O_4 (magnetite) is the active phase in FTS[9,10]. Validity of the latter proposal was questioned[11], but some evidence in its support was also presented[12,13].

In this paper we describe new results from our on-going studies[14-17] on the effect of pretreatment procedures on activity and selectivity of precipitated iron catalysts. Results illustrating both the initial and steady state behavior of a catalyst with nominal composition 100 Fe/3 Cu/6 K/16 SiO_2 (on mass basis) during FTS are presented, and activity/selectivity data are correlated with iron phases in the working catalyst under conditions representative of industrial practice.

EXPERIMENTAL

The reactor used in this study was a 1 dm^3 stirred tank reactor (Autoclave Engineers). Detailed description of the reactor system and operating procedures was provided elsewhere[17,18]. The feed gases (H_2>99.5% purity, and CO>99.3% purity) or a premixed gas passed through a series of traps to remove impurities. The feed gas flow rate was controlled using calibrated mass flow controllers, and the feed was introduced into the reactor below a flat blade impeller, used to agitate the slurry. After leaving the reactor, the exit gas passed through a series of product collection traps. All products collected in the steady state traps were analyzed by gas chromatography after physical separation into an aqueous and organic phase. The reactants and noncondensible products leaving ice traps were analyzed on an on-line gas chromatograph (Carle AGC 400). Powder X-ray diffraction (XRD) patterns of the catalyst samples withdrawn from the reactor were obtained on a Scintag XDS2000 system using Cu-Kα radiation (λ= 1.54 Å).

Catalyst preparation involved three steps: preparation of the iron-copper precursor, incorporation of binder/support (silicon oxide), and finally potassium impregnation. The preparation procedure was described in detail previously[19]. In brief, the catalyst precursor was continuously precipitated from a flowing aqueous solution containing iron and copper nitrates at the desired Fe/Cu ratio, using aqueous ammonia. Impregnation with SiO_2 binder/support was accomplished by addition of the appropriate amount of dilute K_2SiO_3 solution to undried, reslurried Fe/Cu co-precipitate. After a vacuum drying step, the potassium promoter was added as aqueous $KHCO_3$ solution via an incipient wetness pore filling technique. Dried catalyst was calcined in air at 300°C for 5 h, and then crushed and sieved to a diameter less than 270 mesh (53 μm). Durasyn - 164 oil (a hydrogenated 1 - decene homopolymer, ~C_{30} obtained from Albemarle Co.) was used as the initial slurry liquid medium.

All pretreatments were conducted in situ at 0.8 MPa. In runs designated SA-0946 and SA-1626 the catalyst was pretreated at 280°C, 750 cm^3/min for 8 h in CO and syngas (H_2/CO = 0.67), respectively. In run SB-2145 the catalyst was reduced with hydrogen at 240°C, 7500 cm^3/min for 2 h, whereas in run SB-2486 the catalyst was exposed to reaction conditions, without any pretreatment (unreduced catalyst). After the pretreatment, the catalyst was tested initially (baseline conditions) at 260°C, 1.48 MPa, 2.3 Nl/g-cat/h (1.4 Nl/g-cat/h in run SB-2145 only) and syngas feed with $H_2/CO = 0.67$ (molar feed ratio). In addition to baseline conditions, the catalyst was tested at different gas space velocities and reaction pressure, but these results are not reported here.

RESULTS AND DISCUSSION

Catalyst activity

Hydrogen reduced catalyst reached its steady state activity within 4 h from exposure to synthesis gas, and then its activity decreased slowly during the first 150 h of testing (Fig. 1). In the other three tests the time needed to reach a steady state activity was longer, about 20 h for the syngas pretreated and unreduced catalyst, and 80 h for the CO pretreated catalyst. Since the process conditions, including the gas space velocity, were the same in runs SB-2486, SA-1626 and SA-0946, the values of syngas conversion can be used as a measure of relative catalyst FTS activity. Initial activity of the unreduced catalyst (SB-2486) was the lowest, but at approximately 20 h on stream it was the same as that of the CO pretreated catalyst (SA-0946). After 20 h on stream the conversion (activity) of unreduced catalyst started to decline, whereas that of the CO pretreated catalyst continued to increase up to 80 h, and then became stable at about 76%. Initially, the conversion of the syngas pretreated catalyst was higher than that of the unreduced and the CO pretreated catalyst, and it reached its steady state value of ~70% at about 20 h. The steady state activity of the syngas pretreated catalyst was lower than that of the CO pretreated catalyst. Although, the conversion of the hydrogen reduced catalyst (SB-2145) up to 80 h on stream was higher than those obtained in the other three tests, this does not imply the highest catalyst activity, since the gas space velocity in run SB-2145 (1.4 Nl/g-cat/h) was significantly lower than in the other three tests (2.3 Nl/g-cat/h). In order to compare the activity of catalysts in tests under different process conditions, a simple model was used to estimate values of apparent rate constant[20]. The apparent rate constant was calculated assuming that the reaction rate has a first-order dependence on hydrogen pressure, and that the reactor can be modeled as a perfectly mixed flow reactor. At 100 h on stream the estimated values of the apparent rate constant were, in the order of increasing activity, 230 (runs SB-2145 and SB-2486), 330 (SA-1626), and 360 mmol/g-Fe/h/MPa (run SA-0946).

Crystalline phases found in samples withdrawn after the pretreatment (Fig. 4) were as follows: magnetite (hydrogen reduced catalyst); χ–carbide and possibly small amount of magnetite (CO pretreated catalyst); iron carbides (χ-carbide and/or ε'-carbide) and magnetite (syngas pretreatment). Unreduced catalyst had an amorphous structure (iron oxide/oxyhydroxide). Dominant phase in the syngas activated catalyst (SA-1626) after 137 h on stream was ε'-carbide, whereas both ε'-carbide and magnetite were found in the hydrogen reduced catalyst and the unreduced catalyst at 145 h and 147 h on stream, respectively (Fig. 5). Crystalline phases in the CO pretreated catalyst after 113 h on stream were χ-carbide and possibly magnetite.

The FTS on iron catalysts is accompanied by a reversible water-gas-shift (WGS) reaction. Values of carbon dioxide selectivity (% of CO converted to CO_2) provide indication of the WGS catalyst activity. Carbon dioxide selectivity of 50% corresponds to complete conversion of water formed by FTS to carbon dioxide. After 20 h on stream, carbon dioxide selectivities in all four tests were about 48% (Fig. 2). Hydrogen and syngas reduced catalysts reached this value after about 5 h only, the unreduced catalyst at ~8 h, whereas the CO pretreated catalyst achieved its steady state carbon dioxide selectivity at ~20 h on stream. Carbon dioxide selectivity in all tests was never greater than 50%, which would indicate that carbon dioxide is also produced via the reaction between CO and iron oxides in the catalyst.

A very rapid achievement of steady state activity of the hydrogen reduced catalyst (SB-2145) indicates either that magnetite is active for FTS or that is rapidly converted to an active carbide phase. However, the conversion of magnetite to zero-valent iron is a slow step in reduction of iron oxide, and it is unlikely that it can occur to an appreciable extent after 2 h of exposure to syngas at 260°C. For example, the unreduced iron requires about 20 h of exposure to reach its steady state activity (SB-2486). Also, as carburization of iron oxide increases with time, the catalyst activity does not increase with time, but actually decreases slowly. Activity of the unreduced catalyst (largely Fe^{3+} iron) is low initially, and it increases during the first 25 h of synthesis, due to formation of magnetite and/or ε'-carbide, indicating that one or both of these phases are active for FTS. Activity of the CO reduced catalyst is rather low initially (χ-carbide), and increases gradually with time. This behavior is not entirely consistent with hypothesis that iron carbide is the active phase for the FTS. If the latter hypothesis was correct, one would expect the initial activity of the partially carbided catalyst to be markedly greater than that of the catalyst in the form of magnetite. Also, the catalyst in test SA-0946 had a long induction period, and its activity at ~20 h on stream was similar to that of the unreduced catalyst. Initial activity of the syngas activated catalyst (mixture of iron carbide and magnetite) was the highest, but it also went through an induction period lasting approximately 25 h. Steady state activities, between 113 and 147 h on stream, of catalysts pretreated by CO and syngas were higher than those of the hydrogen and unreduced catalysts. Magnetite was virtually absent in the CO and syngas pretreated catalysts, whereas both hydrogen and unreduced catalyst contained both magnetite and ε'-carbide. All these observations are consistent with hypothesis that both magnetite and iron carbides are active for FTS, and that iron carbides have higher FTS activity than magnetite.

Methane Selectivity
During the first 20 h on stream, methane selectivities (%CO converted to CH_4/%CO converted to products other than CO_2) of the syngas and CO activated catalysts were significantly higher (3.5 - 6%) than those obtained on the hydrogen reduced catalyst and unreduced catalysts (1.5 - 2%). Methane selectivities of the CO and syngas pretreated catalysts decreased with time, whereas those of the hydrogen reduced and unreduced catalysts increased with time (Fig. 3). These data suggest that methane selectivity is low on iron oxides, and is higher on carbided catalysts. A possible reason for markedly higher methane selectivity on carbided catalysts during early periods of synthesis, is that part of methane is produced by reaction between hydrogen and surface carbon formed during the pretreatment.

SUMMARY

After pretreatments in hydrogen, carbon monoxide, syngas ($H_2/CO = 0.67$), and without pretreatment the precipitated iron catalyst was tested in a stirred tank slurry reactor at 260°C, 1.48 MPa, 1.4 or 2.3 Nl/g-cat/h and $H_2/CO = 0.67$. Hydrogen reduced catalyst quickly reached steady state activity (within 4 h), whereas the syngas, the CO activated and unreduced catalyst required longer time (up to 100 h for the CO pretreated catalyst). Initially, the CO and syngas activated catalysts, were slightly more active than the hydrogen reduced and unreduced catalyst. Methane selectivities of hydrogen reduced and the unreduced catalyst were initially significantly lower than those on the CO and syngas activated catalyst.

From these results and catalyst characterization by XRD it was concluded that both magnetite and iron carbides are active for FTS, however the activity is higher on partially carbided catalysts. Methane selectivity is lower on the catalyst which contains significant amounts of bulk iron oxides, than on partially carbided catalyst.

ACKNOWLEDGMENT

This work was supported by the U. S. Department of Energy under contract DE-AC22-94PC93069 and Texas Engineering Experiment Station.

REFERENCES

1. Dry, M. E. In *Catalysis - Science and Technology*; Anderson, J. R., Boudart, M. Eds.; Springer - Verlag: New York, 1981; Vol. 1, p. 160.
2. Amelse, J. A.; Butt, J. B.; Schwartz, L. J. *J. Phys. Chem.* 82, 558 (1978).
3. Raupp, G. B.; Delgass, W. N. *J. Catal.* 58, 348 (1979).
4. Anderson, R. B. In *Catalysis* Emmett, P. H. Ed.; Van Nostrand-Reinhold: New York, 1956; Vol. 4, p. 29.
5. Anderson, R. B. *The Fischer-Tropsch Synthesis* Academic Press: Orlando, FL, 1984.
6. Kölbel, H.; Ralek, M. *Catal. Rev - Sci. Eng.* 21, 225 (1980).
7. Raupp, G. B.; Delgass, W. N. *J. Catal.* 58, 361 (1979).
8. Niemantsverdriet, J. W.; van der Kraan, A. M. *J. Catal.* 72, 385 (1981).
9. Blanchard, F.; Reymond, J. P.; Pommier, B.; Teichner, S. J. *J. Mol. Catal.* 17, 171(1982).
10. Reymond, J. P.; Meriadeau, P.; Teichner, S. J. *J. Catal.* 75, 39 (1982).
11. Dictor, R.; Bell, A. T. *J. Catal.* 97, 121 (1986).
12. Soled, S.; Iglesia, E.; Fiato, R. A. *Catal. Letters* 7, 271 (1990).
13. Kuivila, C. S.; Stair, P. C.; Butt, J. B. *J. Catal.* 118, 299 (1989).
14. Bukur, D. B.; Lang, X.; Rossin, J. A.; Zimmerman, W. H.; Rosynek, M. P.; Yeh, E. B.; Li, C, *Ind. Eng. Chem. Res.* 28, 1130 (1989).
15. Bukur, D.B., Koranne, M., Lang, X., Rao, K. R. P. M. and Huffman, G. P., *Appl. Cat.*, 126, 85 (1995).
16. Bukur, D. B., Nowicki, L., Manne, R. K., and Lang, X., *J. Catal.*, 155, 366 (1995).
17. Bukur, D. B., Nowicki, L., and Lang X., *Energy & Fuels*, 9, 620 (1995).
18. Bukur, D. B., Nowicki, L. and Lang, X., Chem. Eng. Sci., 49, 4615 (1994).
19. Bukur, D. B.; Lang, X.; Mukesh, D.; Zimmerman, W. H.; Rosynek, M. P.; Li., C. *Ind. Eng. Chem. Res.* 29, 1588 (1990).
20. Zimmerman, W. H. and Bukur, D. B., *Can. J. Chem. Eng.*, 68, 292 (1990).

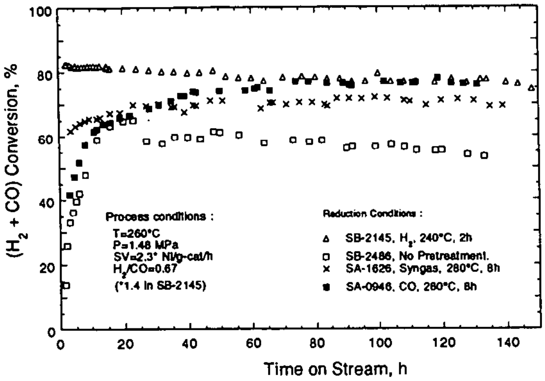

Figure 1. Effect of pretreatment conditions on synthesis gas conversion.

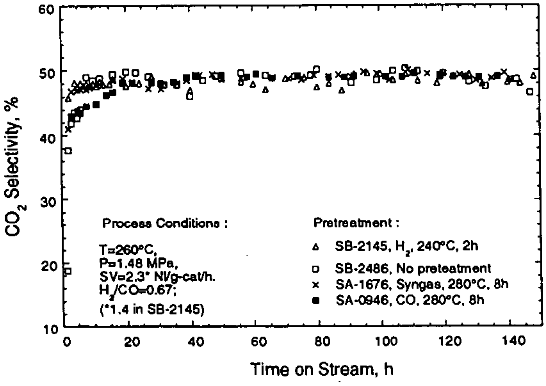

Figure 2. Effect of pretreatment conditions on carbon dioxide selectivity.

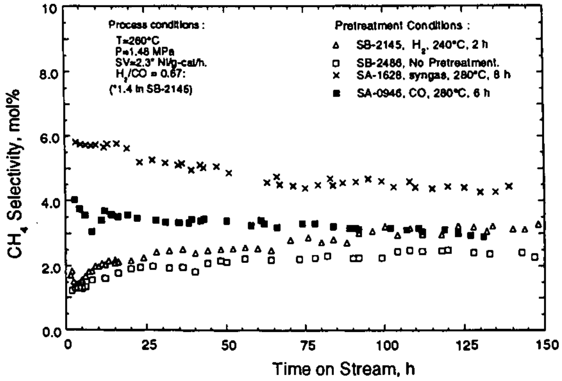

Figure 3. Effect of pretreatment conditions on methane selectivity.

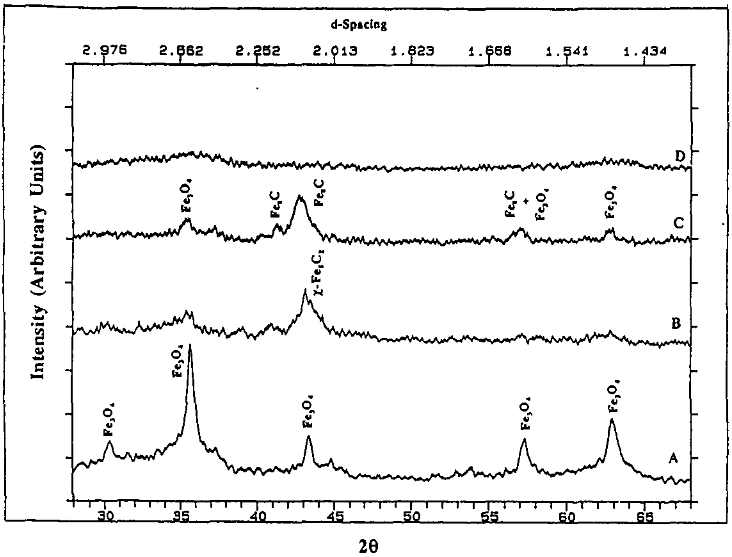

Figure 4. XRD patterns of reduced catalysts (TOS = 0 h) from slurry reactor tests:(A) SB-2145, H_2, 240°C, 2h, (B) SA-0946, CO, 280°C, 8h, (C) SA-1626, syngas, 280°C, 8h, and (D) SB-2486, No reduction.

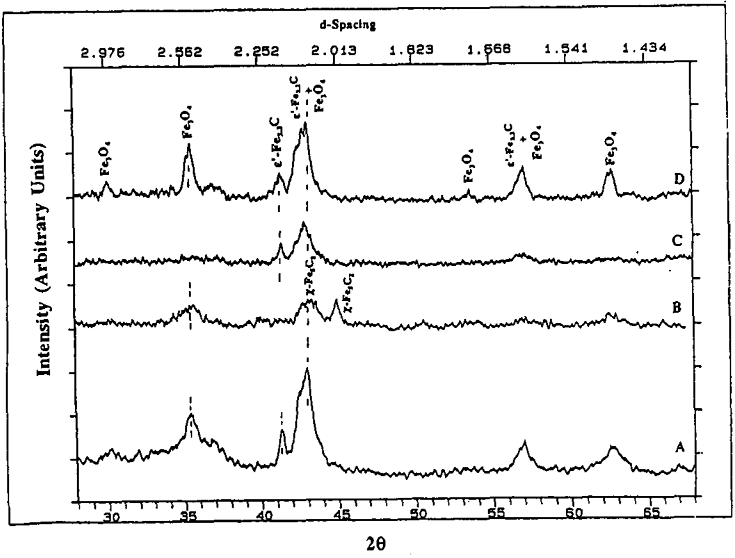

Figure 5. XRD patterns of used catalysts from slurry reactor tests:(A) SB-2145, TOS = 145 h, (B) SA-0946, TOS = 113 h, (C) SA-1626, TOS = 137 h, and (D) SB-2486, TOS = 147 h.

FISCHER-TROPSCH SYNTHESIS FOR CLEAN TRANSPORTATION FUELS

S. Bao, L. Xu, R. O'Brien, A. Raje, D. J. Houpt and B. H. Davis
Center for Applied Energy Research, University of Kentucky
3572 Iron Works Pike, Lexington, KY 40511

Keywords: Fischer-Tropsch Synthesis, Iron Catalyst, Synfuels

INTRODUCTION

The Fischer-Tropsch Synthesis (FTS) is a well established process for the production of synfuels (e.g., 1,2). Today, the process is practiced commercially in South Africa by Sasol and Mossgas and in Malaysia by Shell and partners (3). While FTS was initially envisioned as a means of producing transportation fuels, operators, such as Sasol, have recognized that the recovery of chemicals and/or chemicals feedstock provides a means of improving the profits derived from the commercial operations (e.g., 4). However, while chemicals production may be a very profitable business option for the initial FTS plant operators, as more plants are brought on-stream this will become less profitable as surpluses will drive down the prices of chemical feedstocks. Thus, the ultimate basis for FTS must be the production of transportation fuels.

The FTS process has a decided disadvantage in that the product distribution follows a normal polymerization distribution for a C_1 monomer. Thus, the plot of the log of the moles of each carbon number product versus the carbon number produces a straight line which is defined by alpha, which depends upon the rate of the propagation and termination steps. Furthermore, the value of alpha uniquely determines the product distribution such that illustrated in figure 1 (3). Today, most view the commercialization of FTS as requiring one of two options: (1) the production of heavy wax products which are subsequently hydrocracked to produce transportation fuel range products (e.g., the Shell middle distillate process (SDS); (5) and (2) the conversion of heavy products using a ZSM-5 type of catalyst (e.g., 6).

Because of the highly exothermic nature of the FTS, the ability to utilize a slurry reactor is very desirable (7). However, this operation requires the separation of the catalyst/wax slurry. When operating in a high wax mode in the temperature range of 230°C, more than half of the product must be processed to effect catalyst separation. Iron catalysts are attractive because of the highly olefinic nature of the products and because of the activity for the water-gas-shift (WGS) reaction that permits use of low H_2/CO ratios obtained by gasification of coal. However, unsupported iron catalysts have poor attrition resistance and supported catalysts have not been developed that have sufficient activity for commercial operation. Thus, one of the major operational problems associated with the use of an iron catalyst for FTS in a slurry reactor is catalyst/wax separation.

EXPERIMENTAL

The catalyst was prepared by continuous precipitation from an aqueous solution of iron nitrate containing silica derived from the hydrolysis of tetraethyl silicate using ammonia. Potassium was added to the washed and dried catalyst to provide a composition containing (atomic ratio) 100Fe/4.4Si/1.0K (8). The catalyst was activated in a flow of CO at 270°C and 175 psig during 24 hours. Following activation, synthesis was effected using a $H_2/CO = 0.7$ feed, 270°C, 175 psig and 3.4 NL/hr.g(Fe). Products were analyzed using a Carle gas analyzer for the gaseous products and g.c. with a DB-5 column for the liquid hydrocarbon products (9).

RESULTS AND DISCUSSION

A high activity iron catalyst has been prepared by precipitation; furthermore, this catalyst has a stable activity such that the decline in CO conversion is less than 1%/week during six months of operation. This catalyst produces a "low alpha" product distribution (figure 2). While this particular run was terminated after 2,000 hours (figure 3), this catalyst has been utilized for runs lasting longer than 4,000 hours with a similar slow decline in activity. When operating in this mode with an alpha value of 0.72 and assuming ideal gas and solution behavior, essentially all of the products would exit the reactor in the vapor phase (10). Thus, while a small contribution of a two-alpha product distribution (e.g., 11) and deviation from nonideality of the gas and/or liquid products may be operable, essentially all of the products should exit the reactor in the gas phase. **Provided this does occur, catalyst-wax separation would not be required.** Even if a small fraction of the product does not exit the reactor in the vapor phase, the ability to activate the catalyst external to the slurry reactor would permit catalyst to be added to make up for the small daily loss of catalyst in any liquid phase products that must be removed from the reactor. This would permit the catalyst to be utilized in the form of 1-3 micron particle sizes that result from the precipitation and activation procedure rather than having to form the precipitated catalyst into particles in the 50-100 micron range as apparently has been practiced at Sasol (11).

The kinetics of the FTS is such that the productivity of hydrocarbons depends dramatically upon the conversion of CO (12). Thus, at low CO conversion the rate of production of hydrocarbons is much higher than it is at higher CO conversion levels. At the same time, the rate of the WGS reaction is low at low CO conversions but increases as the conversion of CO increases so that at about 50-60% CO conversion the rates of hydrocarbon production and the WGS reaction become about equal and remain so as the CO conversion increases further. This is illustrated in figure 4 showing that the H_2/CO ratio initially decreases with increasing CO conversion, attains a minimum and then increases to the value of the feed gas (defined here as the equivalence point); at CO conversions above the equivalence point the reaction produces hydrogen as well as hydrocarbons and CO_2. In order to take advantage of the higher rate and higher selectivity for hydrocarbons, it has been proposed that the FTS reactor be operated at CO conversion levels that are at or below the equivalence point (12).

The hydrocarbon product distribution obtained at a CO conversion level above the equivalence point is show in Table 1. If the reactor is operated at the equivalence point or even lower CO conversions, the alkene concentrations will be higher than shown in Table 1. Thus, the following should be viewed as the minimum hydrocarbon productivity levels that could be obtained by incorporation of the process consideration described below. The Conversion of Olefins to Diesel and Gasoline (COD) process has been developed by CEF of South Africa and Lurgi of Germany and a proprietary catalyst for this process has been developed by Süd-Chemie and CEF (13). The catalyst has been utilized at the Mossgas plant in South Africa with a through-put of 68 tons/hour. The Mossgas facility is able to utilize a stream that contains oxygenates (1.5-20 wt.%) saturated with water. In this manner, the C_{2-4} olefins shown in table 1 could be converted to transportation fuel. Thus, the gasoline range (C_{4-10}) yield would be about 47% of the product from the low-alpha operation. In addition, the C_{11+} fraction could be hydrotreated as is done in the SDS process to produce even more gasoline as well as high quality diesel.

In summary, the above considerations would provide a means to eliminate the need to effect catalyst-wax separation that would allow catalyst to either be retained within or recycled to the reactor. Whether this proposed option would be a viable one would depend upon the economic impact of the higher amount of methane and ethane that are produced as well as the cost differential between the COD oligomerization and the hydrocracking processes. It appears that the potential advantages would merit an economic evaluation.

ACKNOWLEDGMENT

This work was supported by U.S. DOE contract number DE-AC22-94PC94055 and the Commonwealth of Kentucky.

REFERENCES

1. H. H. Storch, N. Golumbic and R. B. Anderson, "The fishcer-Tropsch and Related Synthesis," John Wiley & Sons, Inc., New YOrk, 1951.
2. R. B. Anderson, "The Fischer-Tropsch Synthesis," Academic Press Inc., New York, NY, 1984.
3. I. Wender, Fuel Proc. Technol., 48 (1996) 189.
4. M. Dry, Catal. & Catal. Proc., Proceedings, S. African Catalysis Society Meeting, October, 1993.
5. J. Eilers, S. A. Posthuma and S. T. Sie, Catal. Lettr., 7 (1990) 253.
6. J. C. W. Kuo, Two stage process for conversion of synthesis gas to high quality transportation fuels, Final Report, DOE Contract DE-AC22-83PC60019, October, 1985.
7. A. Geertsema, Proc. 10th Pitt. Coal Conf., 1993.
8. D. R. Milburn, R. J. O'Brien, K. Chary and B. H. Davis in "Characterization of Porous Solids III," (J. Rouquerol et al., Eds.), Elsevier, Amsterdam, 1994, pp. 753-761.
9. B. H. Davis, "Technology Development for Iron Fischer-Tropsch Catalysts," Final Report, DOE Contract #AC22-91PC90056.
10. A. P. Raje and B. H. Davis, Energy & Fuels, 10 (1996) 522.
11. B. Jager and R. Espinoza, Catal. Today, 23 (1995) 17.

12. A. P. Raje, J. R. Inga and B. H. Davis, Fuel, in press.
13. "The COD Process", published by the Süd-Chemie Group.

Table 1
Products from the Conversion of Syngas
Using a Low-alpha Iron Catalyst

Carbon Number	Product, wt.%	Olefin, wt.%
1	7,88	---
2	6.45	1.29
3	10.5	7.22
4	8.23	5.72
5	7.46	4.88
6	6.22	3.98
7	5.85	3.58
8	4.50	2.58
9	3.41	1.83
10	3.01	1.53
11+	36.5	---

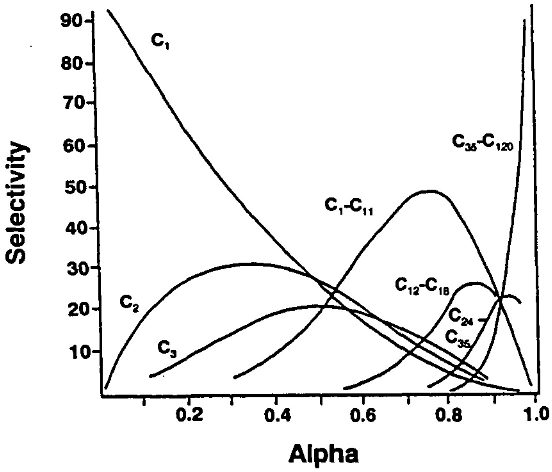

Figure 1. Product distribution dependence upon alpha.

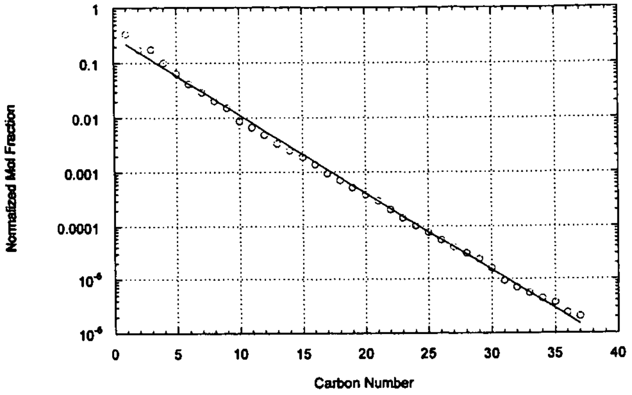

Figure 2. Anderson-Schulz-Flory plot of the products obtained from synthesis with a low-alpha (0.72) iron catalyst.

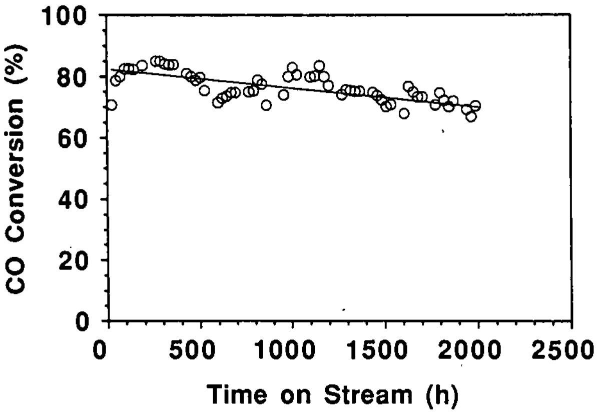

Figure 3. CO conversion with a low-alpha iron catalyst with time-on-stream.

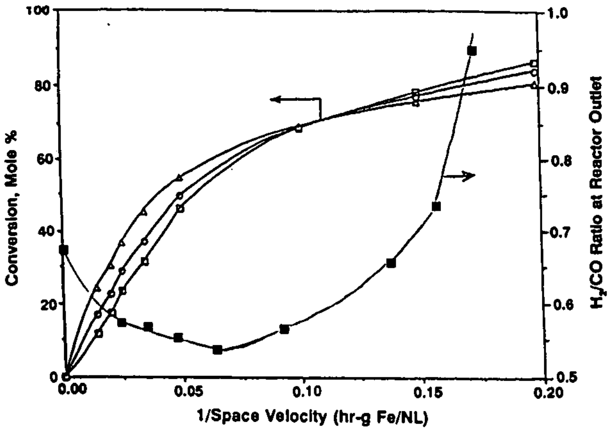

Figure 4. The conversion of CO (□), H_2 (△), (CO = H_2) (○) and the H_2/CO ratio at the reactor exit (■) for a low-alpha iron catalyst.

ALPHA-OLEFIN SELECTIVITY DURING CONVENTIONAL AND SUPERCRITICAL FISCHER-TROPSCH SYNTHESIS.

Dragomir B. Bukur, Xiaosu Lang and Zhentao Feng
Department of Chemical Engineering
Texas A&M University, College Station, Texas 77843

Keywords: Alpha-olefins, Fischer-Tropsch synthesis, supercritical fluids

ABSTRACT

Fischer-Tropsch synthesis was studied on a precipitated iron catalyst (Ruhrchemie LP 33/81) in a fixed bed reactor at several different temperatures (235°C, 250°C and 265°C) and synthesis gas feed compositions ($H_2/CO = 0.67$, 1 or 2) under both supercritical (propane as a supercritical fluid) and conventional ($P = 1.5$ MPa) operating conditions. It was found that the supercritical operation results in enhanced selectivity of α-olefins relative to conventional (normal) operation. Both total olefin content and α-olefin selectivity decreased with either increase in conversion or H_2/CO molar feed ratio, whereas olefin selectivities were essentially independent of reaction temperature.

INTRODUCTION

Alpha olefins are used as chemical intermediates for a number of important industrial and consumer products. The even-numbered carbon alpha olefins (C_4, C_6 and C_8) are used as co-monomers for ethylene and propylene polymerization, whereas the higher molecular weight olefins are used in plasticizers, household detergents and sanitizers [1]. Linear C_{10} olefins and others provide premium value synthetic lubricants. Alpha olefins are produced in significant quantities during conventional Fischer-Tropsch synthesis (FTS) in fixed bed and fluid bed reactors at Sasol in South Africa, and recently Sasol has built a large scale commercial plant for production of 1-pentene and 1-hexene utilizing raw streams from fluid bed FTS reactors [2]. The purification process employed by Sasol entails a series of distillation steps to separate desired alpha olefins from other products. Significant economic benefits can be achieved by increasing the alpha olefin content of FTS products and thus reducing the cost of product separation.

Fischer-Tropsch synthesis in supercritical fluids provides means to accomplish this objective. In recent studies of FTS, on silica supported cobalt-lanthanum and/or alumina supported ruthenium catalysts, in a supercritical n-hexane Fujimoto and co-workers [3-4] have demonstrated certain advantages of this operation, including higher olefin selectivity, relative to gas phase and liquid phase (trickle bed) operation. Lang et al. [5] studied FTS on a precipitated iron catalyst (Ruhrchemie LP 33/81), and found that supercritical operation results in enhanced selectivity of 1-olefins (α-olefins) relative to conventional FTS, but it does not have significant effect on catalyst activity and hydrocarbon product distribution.

Here, we report results from a comprehensive study study with the Ruhrchemie LP 33/81 catalyst, which was used originally in Arge fixed bed reactors at Sasol [6], over a wide range of process conditions. At a given reaction temperature and feed composition, gas space velocity was varied to achieve different levels of syngas conversion. Variations in residence time allow us to distinguish primary and secondary reaction steps that control olefin selectivity.

EXPERIMENTAL

Experimental equipment and procedures have been described previously [5]. Experiments were conducted in a conventional downflow fixed bed reactor (1.3 cm inside diameter, 40 cm^3 effective bed volume for supercritical FTS, and 1 cm inside diameter, 27 cm^3 effective bed volume for conventional FTS) embedded in an aluminum block with a two-zone heater. Carbon monoxide, hydrogen, carbon dioxide, and C_5- hydrocarbons were analyzed by on-line gas chromatography. Condensed C_5+ hydrocarbons, collected for 6-8 h after reaching steady-state at a given set of reaction condition, were analyzed using gas chromatography [5]. Premixed synthesis gas (Iweco, Inc. >99.7% purity) containing approximately 5% of argon as an internal standard, was used as the feed. Propane (Phillips 66 Co., >99% purity) was pumped from a liquid propane dip tube tank using a diaphragm metering pump (American Lewa, Inc.; Model FCMK-1). Olefin selectivities reported here are based on the analysis of gas phase (C_2-C_5 hydrocarbons) and liquid phase products (C_6-C_{15} hydrocarbons).

A precipitated iron catalyst synthesized by Ruhrchemie AG (Oberhausen - Holten, Germany) was used in this test. The nominal catalyst composition is 100 Fe/5 Cu/4.2 K/ 25 SiO_2 (on mass basis), and the preparation procedure is described elsewhere [6]. Catalyst was calcined in air at 300°C for 5 h, and then crushed and sieved to 32/60 mesh size (0.48 mm in diameter). About 3.5 g of catalyst was diluted 1:6 by volume with glass beads of same size prior to loading into the reactor. The catalyst was reduced with hydrogen at 220°C, ambient pressure and a flow rate of 5100 cm^3/min (linear superficial velocity of 150 cm/s) for 1 h.

Following reduction, the catalyst was tested initially at baseline process conditions (1.5 MPa, 250°C, 2 L (NTP)/g-cat·h, $H_2/CO = 0.67$). After 67 h of conventional FTS at the baseline conditions the total pressure was increased to 5.5 MPa using propane as a balance gas (run FA-1724), while keeping the partial pressure and the flow rate of syngas at the baseline conditions. Since the reaction pressure and temperature (5.5 MPa and 250°C, respectively) are well above the critical pressure and temperature of the propane (4.19 MPa and 96.7°C, respectively), this is referred to as supercritical FTS. Between 70 and 700 h on stream the catalyst was tested under different sets of process conditions. In another test (run FB-1644) the Ruhrchemie catalyst was evaluated under similar process conditions as those used in run FA-1724, but without supercritical propane (conventional FTS).

RESULTS AND DISCUSSION

Olefin Selectivities - Effect of gas residence time

Effects of gas residence time (i.e. gas hourly space velocity (GHSV) defined as the total volumetric (NTP) feed flow rate of synthesis gas and propane per unit bed volume, ca. 40 cm^3) and carbon number on total olefin selectivity ((1-olefin + 2-olefin)/(1-olefin + 2-olefin + n-paraffin)) and 2-olefin selectivity (2-olefin/ (1-olefin + 2-olefin)) are illustrated in Figures 1a and 1b, respectively. Data shown in Figure 1 were obtained at 250°C with $H_2/CO = 0.67$, GHSV = 330 - 1340 h^{-1} and correspond to syngas conversions of 75 to 34% (periods 2-4 in Table 1). Results obtained at gas hourly space velocities of 680 and 1340 h^{-1} were nearly identical, whereas the residence time effect was clearly observed at the gas space velocity of 330 h^{-1}. Ethylene selectivity was significantly higher at the two higher gas space velocities, whereas the increase of total olefin selectivity at higher carbon numbers was much smaller. Selectivity of 2-olefins decreased (i.e. 1-olefin selectivity increased) with increase in GHSV. The same trends were observed in experiments with different syngas feed compositions ($H_2/CO = 0.93$ and 2.03). From these observations it is concluded that 1-olefins, and to a smaller extent n-paraffins and 2-olefins, are the primary products of FTS. These conclusions are consistent with those from previous studies with iron FT catalysts [6-8]. At the present time there is no consensus whether some of n-paraffins and 2-olefins are formed by secondary hydrogenation and isomerization reactions, respectively, on sites where chain growth cannot take place, or as primary products following secondary readsorption of 1-olefins on FTS sites [9-11]. Upon readsorption, 1-olefin becomes a reaction intermediate which can either continue to grow and terminate as a longer chain 1-olefin, n-paraffin or 2-olefin, or be terminated to n-paraffin or a 2-olefin of the same carbon number.

Shapes of curves in Figure 1, reflect carbon number (molecular weight) effect on secondary reactions. Ethylene is more reactive than other low molecular weight 1-olefins, and thus its selectivity is low. Decrease in olefin content with increase in carbon number has been attributed to their greater adsorptivity [9], higher solubility in the liquid phase resulting in higher 1-olefin concentrations [8], and/or diffusion enhanced 1-olefin readsorption [10,11]. Madon et al. [10,11] proposed that larger 1-olefins spend longer times in a catalyst pore, due to their lower diffusivities, and this in turn increases probability for their readsorption on FTS active sites before exiting the pore. The increase in 2-olefin selectivity with increase in carbon number (Fig. 1b) or with increase in bed residence time (lower gas space velocity) is due to the same factors mentioned above. Longer residence time of high molecular weight 1-olefins either in the catalyst pores or in the reactor itself, increases probability for secondary 1-olefin readsorption followed by termination as 2-olefin on FTS and/or different type of sites.

Effects of gas space velocity and carbon number on olefin selectivities during conventional FTS (run FB-1644) at 1.5 MPa, 250°C, $H_2/CO = 0.67$ are shown in Figure 2. Qualitative trends are the same as those observed during SFTS (Fig. 1), i.e. the total olefin selectivity increased (Fig. 2a), whereas the 2-olefin selectivity decreased (Fig. 2b), with increase in gas space velocity (decrease in bed residence time). However, the bed residence time effect on selectivity was markedly higher during the conventional FTS, although conversions and nominal gas residence times were similar in both sets of experiments (0.9 - 4.8 min in run FB-1644 vs. 1.3 - 5.1 min in run FA-1792. Residence times were calculated from the ideal gas law, using the arithmetic average of inlet and outlet gas flow rates). Carbon number effect on total olefin and 2-olefin selectivity was also more evident in the case of conventional FTS. Changes in 1-olefin selectivity (1-olefin/(1-olefin + 2-olefin + n-paraffin)) with carbon number, for both modes of operation at syngas conversion of about 80%, are shown in Figure 3. It can be seen that selectivity of C_2 and C_7+ 1-olefins is significantly higher during supercritical FTS, and this is of potential commercial importance.

Results in Figures 1 and 2 show that gas space velocity has a marked effect on olefin selectivity during conventional FTS, and relatively small effect during SFTS. During conventional FTS the reaction mixture inside the reactor is distributed among two phases : gas and liquid. High molecular weight hydrocarbons (C_8+) are leaving the reactor preferentially in the liquid phase, the flow rate of which increases along the reactor length. In a fixed bed reactor the residence time of the liquid phase is much longer than that of the gas phase. This increases probability for readsorption of high molecular weight 1-olefins and leads to increased formation of n-paraffins and 2-olefins via secondary reactions. On the other hand during SFTS operation, there is only one phase in the reactor and the residence time of all products, regardless of their molecular weight, is the same.

Carbon number effects, can be explained in terms of diffusion enhanced 1-olefin readsorption. Larger 1-olefins spend longer time in the catalyst pores than smaller ones, due to their lower diffusivities, and this increases probability for secondary 1-olefin readsorption, double bond isomerization and hydrogenation reactions. Ethylene, which has relatively large diffusivity due to its small molecular size, is significantly more reactive than other 1-olefins [9, 10], and its selectivity is low in comparison to C_3-C_6 olefins. Ethylene selectivity during conventional FTS was smaller than during SFTS at comparable bed residence times, i.e. syngas conversions (Figures 1 and 2). However, the pore residence time of ethylene is greater during conventional FTS, because ethylene diffusivity is smaller in the liquid filled pores (conventional FTS), than in the supercritical propane. Also, at a given gas space velocity, the carbon number effect on either the total olefin or 2-olefin selectivity was much more evident during the conventional FTS. In both modes of operation diffusivity decreases with increase in carbon number (molecular weight), but since diffusivities are significantly smaller in hydrocarbon wax than in the supercritical propane, the intraparticle diffusional resistance during conventional FTS is larger and carbon number effect on olefin selectivity is stronger.

Olefin Selectivities - Effect of reaction temperature

The effect of reaction temperature on olefin selectivities during SFTS and conventional FTS (run FB-1644) at a nearly constant syngas conversion was insignificant for temperatures between 235 and 265°C. Results from previous studies with iron FT catalysts showed different types of behavior, i.e. in some cases the olefin selectivity increased with increase in temperature, but on some catalysts either no effect or the opposite trends were observed [8, 9].

Olefin Selectivities - Effect of reactant composition

Figure 4 illustrates the effect of gas feed composition on olefin selectivity during SFTS at 235°C and syngas conversion of about 30% (data from periods 6, 11 and 15 in Table 1). Total olefin selectivity was lower, and 2-olefin selectivity higher when the synthesis gas with $H_2/CO = 2.03$ was used (representative of syngas obtained from steam reforming or partial oxidation of natural gas). Olefin selectivities were similar in experiments with $H_2/CO = 0.67$ and $H_2/CO = 0.93$.

Concentration of surface hydrogen determines chain termination probabilities and olefin content, and it increases with increase in H_2/CO molar feed ratio. High surface concentrations of hydrogen favor termination reactions, and termination to paraffins rather than olefins, as well as secondary 1-olefin isomerization reactions [8, 11].

SUMMARY

Effects of reaction temperature, gas space velocity and feed composition on olefin selectivity were studied in a fixed bed reactor during conventional FTS, and FTS in supercritical propane. It was found that total olefin content decreased and 2-olefin selectivity increased with either decrease in gas space velocity or increase in H_2/CO molar feed ratio, whereas olefin selectivities were essentially independent of reaction temperature.

Results from bed residence time effect studies in both modes of operation indicate that 1-olefins are the dominant primary products of FTS. Selectivity of n-paraffins and 2-olefins increases, whereas 1-olefin selectivity decreases with increase in carbon number, due to secondary reactions of 1-olefins. At high syngas conversions (~80%), selectivities of high molecular weight 1-olefins during SFTS were significantly higher than those obtained during conventional operation. These results indicate that SFTS is a potentially attractive route for synthesis of high molecular weight alpha olefins from the synthesis gas.

ACKNOWLEDGMENT

This work was supported by the U. S. Department of Energy (University Coal Research Program) under grant DE-FG22-92PC92545 and Texas Engineering Experiment Station.

REFERENCES

1. Lappin, G. R.; Nemec, L. H.; Sauer, J. D.; Wagner, J. D. Kirk-Othmer Encyclopedia of Chemical Technology, 4 th Ed., Vol. 17, Wiley: New York, 1996; pp. 839.
2. Waddacor, M. Chemical Processing SA,. 1 (No.10), (1994).
3. Yokota, K.; Fujimoto, K. *Ind. Engng Chem. Res.* 30, 95 (1991).
4. Fan, L.; Yokota, K.; Fujimoto, K *AIChE J.* 38, 1639 (1992.
5. Lang, X.; Akgerman, A.; Bukur, D. B *Ind. Engng Chem. Res.* 34, 72 (1995).
6. Dry, M. E.*Catalysis-Science and Technology,* Vol. 1, Springer-Verlag: New York, 1981; pp. 160.
7. Schulz, H.; Gokcebay, H.*Catalysis of Organic Reactions*, Marcel Dekker: New York, 1984; pp.153.
8. Dictor, R.; Bell, A. T. *J. Catal.* , 97, 121 (1986).
9. Schulz, H.; Rosch, S.; Gokcebay, H.*Coal: Phoenix of '80s, Proc. 64th CIC. Coal Symp.* Vol. 2, Canadian Society for Chemical Engineering: Ottawa, Canada, 1982; pp. 486.
10. Madon, R. J.; Reyes, S. C.; Iglesia, E. *J. Phys. Chem.* , 95, 7795 (1991).
11. Madon, R. J.; Iglesia, E. *J. Catal.* , 139, 576 (1993).

Table 1. Process conditions and catalyst activity results in test FA-1724

Period, #	1	2	3	4	5	6	7	8	9	10	11	12	13	14	15	16	17	18
Time on stream, h	67	140	164	191	215	239	259	331	352	373	406	428	475	547	571	598	624	691
T, °C	250	250	250	250	235	235	265	265	250	250	250	235	235	250	250	235	235	250
SV, L(NTP)/g-cat·h	2.0	2.0	3.8	1.0	0.5	2.2	7.1	1.4	2.0	5.0	2.0	3.0	1.5	1.4	4.0	2.2	0.5	2.0
GHSV, h^{-1}	175	680	1340	330	288	752	2480	507	680	1750	1234	1047	529	487	1413	772	162	681
H_2/CO feed ratio	0.67	0.67	0.67	0.67	0.67	0.67	0.67	0.67	0.67	2.0	2.0	2.0	2.0	0.93	0.93	0.93	0.93	0.67
CO conv., %	48.5	48.5	32.0	74.7	62.1	26.8	29.2	77.0	43.8	34.2	92.5	48.3	77.3	70.4	26.3	26.0	75.3	33.8
H_2 + CO conv., %	43.1	50.2	34.4	75.5	65.0	29.3	32.5	76.6	46.7	22.1	60.3	30.4	51.7	64.9	27.4	27.7	69.9	35.1
H_2/CO usage ratio	0.82	0.73	0.79	0.69	0.74	0.82	0.85	0.66	0.78	0.95	0.98	0.90	1.03	0.78	1.01	1.06	0.79	0.73
H_2/CO exit ratio	0.60	0.61	0.61	0.61	0.54	0.61	0.57	0.69	0.58	2.59	15.1	3.08	5.45	1.31	0.90	0.89	1.35	0.63

Notes: Conventional FTS during period 1; SFTS during periods 2 - 18 with P_{total} = 5.5 MPa.
Syngas partial pressure P_{H_2+CO} = 0.7 MPa in periods 5 and 11, otherwise P_{H_2+CO} = 1.5 MPa.

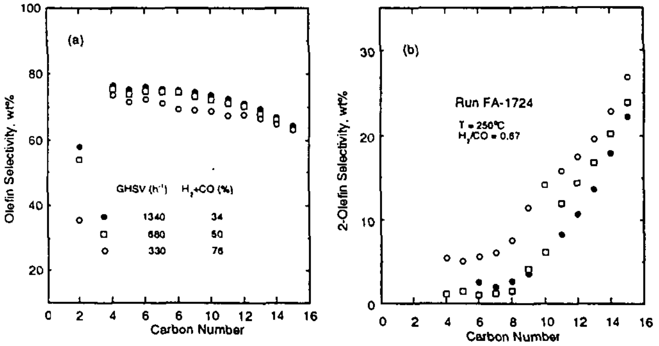

Figure 1. Effect of gas space velocity on: (a) olefin; and (b) 2-olefin selectivity during SFTS at 250°C, H_2/CO = 0.67 and 5.5 MPa (FA-1724).

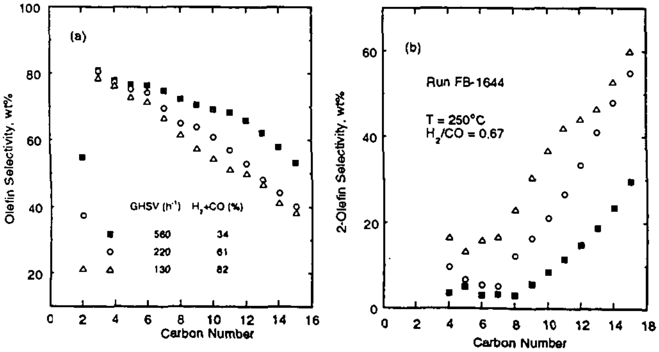

Figure 2. Effect of gas space velocity on: (a) olefin; and (b) 2-olefin selectivity during convencional FTS at 250°C, H_2/CO = 0.67 and 1.5 MPa (FB-1644).

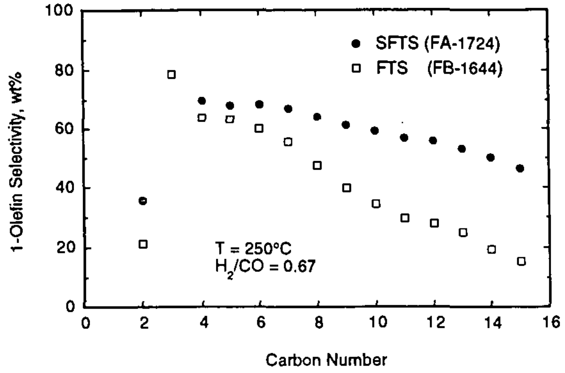

Figure 3. Comparison of α-olefin selectivities during conventional and supercritical FTS at 250°C, $H_2/CO = 0.67$ and syngas conversions of 82% (FB-1644) and 76% (FA-1724).

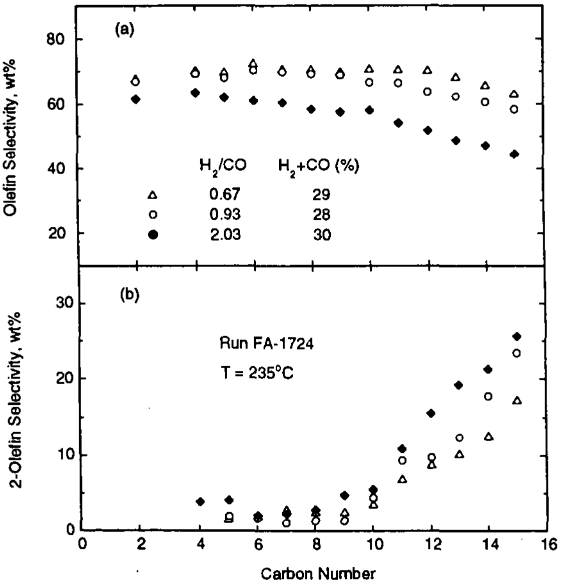

Figure 4. Effect of gas feed composition on: (a) olefin; and (b) 2-olefin selectivity during SFTS at 5.5 MPa and 235°C (FA-1724).

COMPARATIVE STUDIES OF LANTHANUM AND CERIUM AS PROMOTERS OF COBALT BASED FISCHER-TROPSCH CATALYSTS.

B. Ernst[1], A. Kiennemann[1], P. Chaumette[2]
[1]LERCSI-ECPM URA CNRS 1498
1, rue Blaise Pascal 67008 Strasbourg Cedex France
[2]Institut Français du Pétrole
1 et 4, Avenue de Bois Préau
92506 Rueil-Malmaison Cedex France

Keywords : Syngas Chemistry, Co and Co-promoted (La,Ce) catalyst reactivity

INTRODUCTION

These last years, cobalt based catalysts have been widely developed in Fischer-Tropsch synthesis, particularly for the preparation of higher molecular weight fractions (chain growth probability a > 0.9). The most studied catalysts are Co/Al_2O_3 or Co/SiO_2 undoped or doped by a second metal (Ru, Rh, Pt, Re...) and/or oxides (ZrO_2, TiO_2, rare earth oxides...) (1-5). The second metal generally favours the reduction of cobalt by hydrogen spillover phenomena or acts in regeneration of deactivated systems. The oxide operates through its interaction with the metal (TiO_2, ZrO_2), its reducibility (CeO_2), its acidic character (Al_2O_3) or the coverage of the metal particle by different processes including migration to the surface (La_2O_3). In the present work, a comparative study of Co/SiO_2 catalysts and lanthanum oxide or cerium oxide promoted Co/SiO_2 catalysts is reported. Results concerning the preparation, reduction and reactivity with syngas in a slurry type reactor are included.

EXPERIMENTALS

Preparation

A sol-gel type method has been developed (6) instead of a conventional successive impregnation technique, in order to be able to control the cobalt dispersion, even at high cobalt loadings (25 wt%). The overall scheme of preparation is as follows (Scheme 1).

Cobalt, cerium or lanthanum nitrate as well as tetraethoxysilane (TEOS) are dissolved separately in ethanol at 70°C. Once the solutions are mixed, precipitation is performed by adding an excess of oxalic acid dissolved in ethanol at 70°C. The released nitric acid makes the medium acidic, and during ethanol evaporation TEOS is slowly hydrolyzed by the water contained in the precursor salts. The evaporation is performed over a long period (6 hrs) until complete hydrolysis of TEOS. The catalysts are then dried (12 hrs, 100°C) and calcined (550°C, 4 hrs). The different catalysts prepared have the same cobalt weight content, and are described in Table 1.

Characterization Techniques

Temperature programmed reduction (TPR) :

TPR experiments were performed by passing pure hydrogen (12 $ml.min^{-1}$) over 0.2 g of calcined sample and a temperature increase rate of 1 $K.min^{-1}$ has been selected. The reduction was monitored by water formation as measured in the exit gas by a catharometer detector.

X-ray diffraction (XRD) :

The monochromatic X-ray beam was produced by a Cu anticathode (l = 1.5418 Å) in a Siemens D5000 powder diffractometer. The XRD patterns were recorder for 2 values between 10 and 90° with a 0.005° spacing. Identification of the phases were made according to the JCPDS files.

X-ray Photoelectron Spectroscopy (XPS) :

The spectrometer was a Vacuum Generator's ESCA3 fitted with a preparation and an analysis chamber (10^{-10} Torr vacuum) ($293 < T < 873$ K). The deconvolutions were made both for the $Co2p_{3/2}$ and $Co2p_{1/2}$ peaks. The binding energies were measured by taking the C_{1s} peak of contamination carbon at 284.8 eV as reference.

Transmission Electron Microscopy (TEM) :

The apparatus was a TESCON EM-002B type device (1.8Å resolution, 200kV acceleration potentiel). The analysis for chemical elements was performed by EDS with a KEVEC analyzer (selected area 14 nm). The powdered sample was suspended in ethanol and one drop of the suspension was deposited on a copper grid covered by a carbon membrane.

Reactivity test.

The catalytic tests were performed in a slurry bed reactor (7). Typical conditions were : $P = 2MPa$, $T = 493K$, $H_2/CO = 2/1$, G.S.H.V. = 2000 h^{-1}. The catalysts were reduced ex-situ at temperatures up to 513K under a flow of diluted hydrogen (5% H_2 in N_2) and then under a pure hydrogen flow with an increasing temperature up to 673K with a $1K.min^{-1}$ slope and a final step at constant temperature (400K) for 14 hrs. The syngas mixture was admitted into the reactor at room temperature. The starting time for the reaction at 493K is taken after stabilization of the catalytic system.

RESULTS AND DISCUSSION

Characterization of the catalysts

Calcined catalysts

By thermogravimetric analysis (TGA), it is shown that cobalt, mixed cobalt-cerium or cobalt-lanthanum oxalates are decomposed between 543 and 603K. At 823K, part of the lanthanum is present as an oxycarbonate. In the XRD diffractogramms and XPS spectra, cobalt is seen to be present as the Co_3O_4 spinel phase, ceria in a fluorite structure and lanthanum as a oxycarbonate but also as a $LaCoCO_3$ perovskite whose proportion increases with the amount of lanthanum added to the preparation.

The XPS analysis of the surface indicates that Co/Si ratio diminishes on the surface after calcination : 0.12 instead of the theoretical bulk 0.403 ratio for the Co/SiO_2 catalysts; 1.1 compared to 1.6 for $Co\text{-}CeO_2(A)/SiO_2$; *and* 0.3 compared to 1.5 for *Co-La(a)/SiO*$_2$).

This clearly shows that after calcination silica is segregated to the surface for the three series of catalysts. It must also be noted that cobalt *silicate* has *not been evidenced. The* NMR of silicium (MAS and CP-MAS) has shown that the initial silicagels are transformed to siloxane *groups but some isolated silanol groups are also present.*

The means size of the cerium oxide crystallites has been evaluated to be about 80-85Å even for the catalysts with the highest cerium contents which indicates a very good dispersion of the promoter. Cerium oxide is present as aggregates and at the edge of these aggregates the CeO_2 and Co_3O_4 crystallites are in close contact with each other.

The size distribution of the cobalt oxide particles has been determined by TEM. The size distribution for $Co\text{-}Ce(B)/SiO_2$ is represented on Figure 1. For Co/SiO_2 the mean size of cobalt oxide crystallites is about 300Å. It is much less (about 135Å) for $Co\text{-}Ce/SiO_2$ and for $Co\text{-}La/SiO_2$ (about 100Å). These results are in good agreement with those obtained by XRD (Figure 1).

The BET surface areas (Table 1) of the catalysts are large. They deacrease upon addition of ceria or lanthanum oxide but remain higher than 100 $m^2.g^{-1}$. It must be noted that the Co/SiO_2 catalyst is microporous and that the mesoporosity increases with the amount of rare earth oxide (porous volume for 0.22 cm^3 g^{-1} to 0.40 $cm^3.g^{-1}$).

Reduced catalysts

The reduction of all these catalytic systems has been followed by TPR and XPS. The TPR *curves up to 753K (highest reduction temperature in the reactivity studies)* for $Co\text{-}Ce/SiO_2$ and $Co\text{-}La/SiO_2$ are reported on figures 2 and 3.

The TPR curve for Co/SiO_2 shows two reduction peaks (543K, and a broad peak between 603 and 703K) (8). These two peaks are two widely separated to correspond to a two steps reduction of Co_3O_4 to Co° via CoO. It is suggested either that the reduction temperature changes is due to the change in the metal oxide particle size or that the microporosity of the **catalyst** *makes the diffusion of the water produced during the reduction difficult, thus inhibiting* the reduction process in the micropores.

For Co-Ce/SiO_2 (Figure 2) two reduction peaks are clearly present especially for the catalysts with the highest cerium contents. The first peak (483-513K) is shifted to lower temperature by increasing the cerium content. It corresponds to the reduction of Co_3O_4 to Co°. It is noteworthy that the presence of ceria lowers the reduction temperature of cobalt. The second peak corresponds to the reduction of ceria (the peak changes with the amount of CeO_2).

The Co-La/SiO_2 catalysts curves have also two maxima except for the highest loaded catalyst for which three maxima are observed (Figure 3). The three maxima are interpreted as the reduction of Co_3O_4 to Co° (~ 553K), the reduction of the perovskite structure activated by the free cobalt (~ 613K) and the decomposition of carbonate species (> 723K). The extent of reduction of all the catalysts obtained by TPR, XPS and oxygen titration are summarized on Table 2.

As can be seen on Table 2, the cerium or lanthanum promoted catalysts are less reduced than the corresponding Co/SiO_2 catalyst (except for Co-La(a)/SiO_2). This point together with the lower initial cobalt oxide particle size (Table 1) will be important in the discussion of the catalytic reactivity results.

The cobalt particle size after reduction has been measured indirectly by reoxidation to Co_3O_4 followed by XRD analysis (Table 2). Compared to the calcined catalysts (Table 1), a decrease of the cobalt oxide particle size (240Å instead of 300Å), as well as a homogeneity for that of Co-Ce/SiO_2 (170, 165, 160 and 135Å for catalysts A, B, C, D respectively) and a slight decrease for Co-La/SiO_2 (120, 105, <100, <100Å) for catalysts a,b,c,d respectively) can be noted.

Catalytic reactivity tests.

All the characterized catalyst have been tested under the conditions described in the experimental part. The results are expressed as: total conversion of CO (CO%), conversion to hydrocarbons (HC%) and CO_2 (CO_2%), and productivity in hydrocarbons (kg.kgcat^{-1}h^{-1}). The specific activity TOF^1 (mole h^{-1}) is defined as the number of CO moles transformed by gram of catalyst and unit time and TOF^2 (mole h-1) as the number of CO moles transformed by cobalt metal site and unit time. The selectivity is expressed in mass per cent on a carbon basis. Table 3 gives the reactivity results for all the catalysts.

It can be noted that the CO conversion and TOF^1 are nearly the same for all the catalysts. For the promoted catalysts, TOF^2 decreases with the promoter content. TOF^2 values are higher for ceria than for lanthana. For some catalyst samples (B and D), they are higher than for Co/SiO_2. Selectivities are reported in Table 4.

The chain growth probability α deduced from the distribution of the hydrocarbons is 0.92 for Co/SiO_2. This value decreased for catalysts doped by ceria [from 0.87 (A) to 0.82 (D,C)] or lanthana [(0.88 (b), 0.82 (a)]. It can be noted the low amounts of promoters (5wt %) are sufficient to induce this decrease. A closer examination of the selectivities obtained shows that as soon as ceria or lanthana are added (Figure 4) :

- The methane selectivity changes drastically. (The mass fraction of CH_4 is increased by a factor of 2 or 3). The formation of methane depends on the amount of ceria or lanthana added.
- The C_5+ mole % fraction decreases strongly upon addition of Ce or La (80.0% for Co/SiO_2 compared to less than 60.0% for Ce and La containing catalysts).
- The mass fraction of C_{22}+ hydrocarbons is divided by 3.
- The C_5-C_{13} fraction is favoured in the presence or cerium or lanthanum The tendency has already been reported for Co-Ce/C tested under atmospheric pressure (9).

From these results it can be seen that the cerium or lanthanum promoted catalysts have about the same activity as the unpromoted ones, however the changes in hydrocarbon distribution are more significant : lower α values, higher methane formation, increase of the C_5-C_{13} fraction and diminution of C_{22}+ yields. The change in hydrocarbon distribution can be attributed to several factors :

- The presence of smaller cobalt crystallites (240, 135-170 and 100-135Å for Co/SiO_2, Co-Ce/SiO_2 and Co-La/SiO_2) respectively.
- A higher extent of reduction for the promoted catalysts.

- The intrinsic properties of ceria or lanthana which can form hydrocarbons by themselves (10). On the catalysts containing cerium or lanthanum, hydrogen chemisorption and desorption experiments (Table 5) show clearly the influence of the promoter on hydrogen desorption. Both promoters act as hydrogen storage agents and thus probably influence the hydrocarbon selectivity of these catalysts (methane formation, decrease of chain growth).
- Modification of the nature of the cobalt site by interaction between cobalt and the rare earth, changing the CO and H_2 chemisorption properties.

CONCLUSION

The present work has evidenced the modifications of the catalytic behaviour of 25 wt%Co/SiO_2 catalysts, when they are promoted by varying amounts of ceria or lanthana. The main changes were found in the cobalt particle size, the reducibility of the metal, and the ability to desorb previously adsorbed hydrogen from the catalyst.

The changes of physical properties of the catalysts have few consequences on the catalytic activity, but strongly influence the hydrocarbons distribution. Addition of CeO_2 or La_2O_3 enhances methane formation, increases the selectivity in the C_5-C_{13} fraction and decreases the chain growth probability α.

LITERATURE CITED

(1) Iglesia, E., Adv. Catal., 39, 221 (1993).

(2) Eri, S., Goodwin, J.G., Marcelin, G., Riis, T., U.S. Patent 4,801,573 (1989).

(3) Iglesia, E., Soled, S.L., Fiato, R.A., U.S. Patent 4,794,099 (1988); 4,960,801 (1990).

(4) Gulf Reasearch Development, US Patent 4,585,798 (1986).

(5) Shell International Research, Europ. Patent 842006 (1984).

(6) Vansant, E.F., van der Voort, P., Vrancken, K.C., Stud. Surf. Sci. Catal., 96, chapter 1 and 2 (1995).

(7) Chaumette, P., Verdon, A., Kiennemann, A., Boujana, S., Am Chem. Soc. Div. Petr. chem. Prep., 37, 833 (1992).

(8) Castner, D.G., Watson, P.R., Chan, I.Y., J. Phys. Chem., 94, 819 (1990).

(9) Barsault, J., Biwole, N., Bull. Soc. Chim. Belg., 104, 149 (1995).

(10) Maruya, K., Inaba, T., Maehashi, T., Domen, K., Onishi, T., J. Chem. Soc. Chem. Comm. 487 (1985).

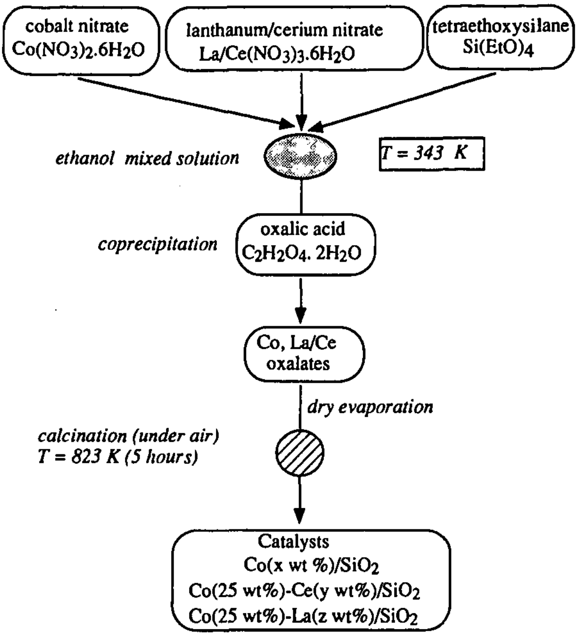
cobalt nitrate
$Co(NO_3)_2.6H_2O$
lanthanum/cerium nitrate
$La/Ce(NO_3)_3.6H_2O$
tetraethoxysilane
$Si(EtO)_4$
ethanol mixed solution
T = 343 K
coprecipitation
oxalic acid
$C_2H_2O_4.2H_2O$
Co, La/Ce oxalates
dry evaporation
calcination (under air)
T = 823 K (5 hours)
Catalysts
$Co(x\ wt\ \%)/SiO_2$
$Co(25\ wt\%)\text{-}Ce(y\ wt\%)/SiO_2$
$Co(25\ wt\%)\text{-}La(z\ wt\%)/SiO_2$

Scheme 1: Catalyst preparation procedure.

Table 1.
Characteristics of catalysts.

Catalysts	Co	Si	Ce or La	O	BET surface area ($m^2.g^{-1}$)	Particle size* cobalt oxide (Å)
Co/SiO_2	25.2	28.4	/	46.1	293	300(300)
$Co\text{-}Ce(A)/SiO_2$	25.5	7.4	38.2	26.0	137	185
$Co\text{-}Ce(B)/SiO_2$	25.5	16.9	21.5	34.6	103	170(135)
$Co\text{-}Ce(C)/SiO_2$	24.6	23.5	8.9	42.7	281	165
$Co\text{-}Ce(D)/SiO_2$	23.9	25.0	4.8	43.2	245	185
$Co\text{-}La(a)/SiO_2$	24.9	6.9	37.5	28.1	123	125(110)
$Co\text{-}La(b)/SiO_2$	24.5	16.0	21.2	34.8	131	125
$Co\text{-}La(c)/SiO_2$	24.3	20.8	9.1	43.0	340	100
$Co\text{-}La(d)/SiO_2$	24.8	26.4	4.7	43.4	384	110

* oxygen titration (TEM measurement)

Table 2.
Reducibility of catalytic systems

	Reduction extent (%)			
Catalysts	TPR	XPS	Oxygen titration	Co particle size after reoxidation (Å)
Co/SiO_2	73	82	77	240
$Co\text{-}Ce(A)/SiO_2$	66	89	89	170
$Co\text{-}Ce(B)/SiO_2$	52	-	81	165
$Co\text{-}Ce(C)/SiO_2$	51	-	77	160
$Co\text{-}Ce(D)/SiO_2$	40	-	52	135
$Co\text{-}La(a)/SiO_2$	80	84	81	120
$Co\text{-}La(b)/SiO_2$	65	-	76	105
$Co\text{-}La(c)/SiO_2$	64	-	65	<100
$Co\text{-}La(d)/SiO_2$	39	-	42	<100

Table 3.
Reactivity tests for Co/SiO$_2$, Co-Ce/SiO$_2$ and Co-La/SiO$_2$ catalysts

	Conversion			HC productivity (a)	TOF^1 (b)	TOF^2 (c)
	CO%	HC%	CO$_2$%			
Co/SiO$_2$	10.8	10.7	0.0	68.9	12.7	43.6
Co-Ce(A)/SiO$_2$	11.8	11.4	0.1	50.6	13.7	36.7
Co-Ce(B)/SiO$_2$	13.6	13.1	0.1	53.5	15.8	52.0
Co-Ce(C)/SiO$_2$	9.5	8.6	0.5	37.9	11.4	34.3
Co-Ce(D)/SiO$_2$	12.9	12.6	0.1	54.6	15.9	55.3
Co-La(a)/SiO$_2$	11.6	11.2	0.2	37.2	13.9	21.7
Co-La(b)/SiO$_2$	10.0	9.6	0.1	41.5	11.8	22.6
Co-La(c)/SiO$_2$	14.2	12.9	0.1	56.8	16.3	26.3
Co-La(d)/SiO$_2$	12.3	12.0	0.2	53.9	14.5	38.8

(a) 10^{-3} kg . kgcat^{-1}.h^{-1} (b) 10^{-3} mole h^{-1} (c) 10^{-2} mole h^{-1}

Table 4.
Selectivities obtained with Co/SiO$_2$, Co-Ce/SiO$_2$ and Co-La/SiO$_2$ catalysts.

Catalysts	Mass selectivity (%)					
	C_1	C_2-C_4	C_5-C_9	C_{10}-C_{13}	C_{14}-C_{21}	C_{22}^+
Co/SiO$_2$	15.9	2.5	3.1	11.5	24.6	42.4
Co-Ce(A)/SiO$_2$	34.0	9.2	12.3	15.4	15.9	13.2
Co-Ce(B)/SiO$_2$	30.1	9.7	16.6	16.6	15.7	11.3
Co-Ce(C)/SiO$_2$	46.6	8.3	10.0	13.9	14.8	6.4
Co-Ce(D)/SiO$_2$	49.1	5.6	5.8	10.4	17.5	11.6
Co-La(a)/SiO$_2$	48.4	6.5	7.0	16.5	14.7	6.8
Co-La(b)/SiO$_2$	47.7	7.1	3.3	8.9	12.9	20.1
Co-La(c)/SiO$_2$	38.9	5.9	15.2	15.2	14.2	10.6
Co-La(d)/SiO$_2$	43.4	6.6	6.1	14.0	16.7	13.2

Table 5.
Amount of adsorbed and temperature desorbed hydrogen
on Co/SiO$_2$, Co-Ce/SiO$_2$ and Co-La/SiO$_2$ catalysts

Catalysts	Chemisorbed H$_2$ (µmole.g cat^{-1})	Desorbed H$_2$ (µmole.g cat^{-1})
Co/SiO$_2$	11.4	4.5
Co-Ce(A)SiO$_2$	14.5	30.4
Co-La(a)SiO$_2$	14.8	28.3

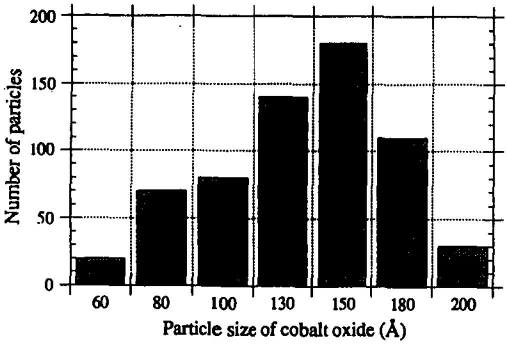

Figure 1. Cobalt oxide particle size distribution for Co-Ce(B)/SiO$_2$ catalyst.

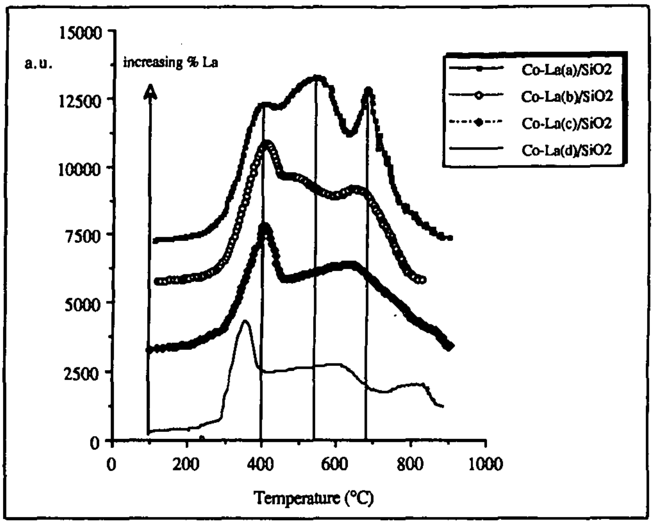

Figure 2. TPR curves for Co-La/SiO_2 catalyst.

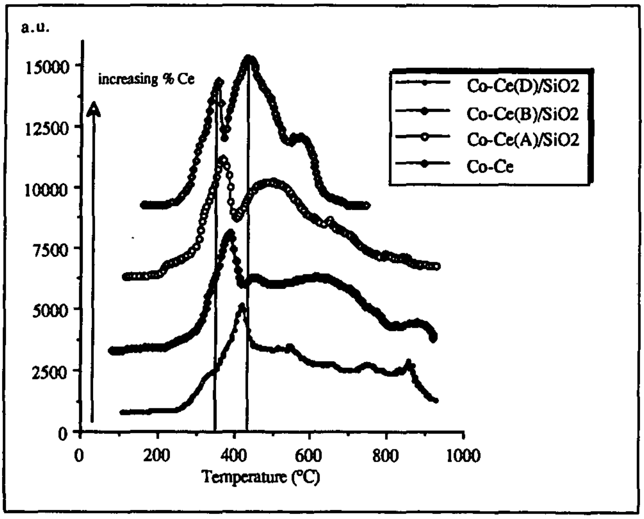

Figure 3. TPR curves for Co-Ce and Co-Ce/SiO_2 catalysts.

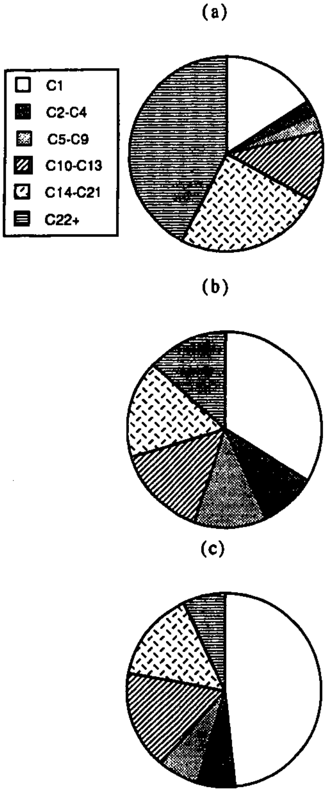

Figure 4. Weight distribution of hydrocarbons on (a) Co/SiO_2 (b) Co-Ce(A)/SiO_2 and (c) Co-La(a)SiO_2 catalysts.

MANGANESE MODIFIED NANOSCALE COBALT CATALYST TO SYNTHESIZE LONG-CHAIN HYDROCARBONS

Yongqing Zhang,Bing Zhong and Qin Wang
State Key Laboratory of Coal Conversion,Institute of Coal Chemistry,Chinese Academy of Sciences,Taiyuan,030001,PR China

ABSTRACT: Cobalt catalyst supported on ZrO_2 coated SiO_2 aerogel exhibits high FTS activity and C^{5+} selectiity at a moderate pressure in fixed bed reacter. It yields 150g liquid hydrocarbons and FT wax for every cubic meter of syngas. The effect of manganese modification on structure, texture, reduction, H_2 adsorption and FTS performance of Co/ZrO_2-SiO_2 catalyst was examined. The results show that addition of proper amount of manganese lowers the methane selectivity and raises C^{5+} selectivity ,but excessive amount of manganese added leads to opposite results. Carbon number distribution of $Co-Mn/ZrO_2-SiO_2$ no longer follows SF distribution. Distict two peaks (maximium point at C_{11} and C_{17} respectivily) are observed in the profile of carbon number distribution for $Co-Mn/ZrO_2-SiO_2$ indicating the existence of two kinds of active sites.

Keywords: Fischer-Tropsch Synthesis, Nanoscale Catalyst,Manganese Promoter

INTRODUCTION

Fischer-Tropsch synthesis is catalytic reaction of CO hydrogenation for obtaining C^{2+} hydrocarbons.Carbon number distribution of traditional FTS product obey Schulz-Flory distribution which constrains selectivity improvement of toward any product with particular carbon number.Research work of FTS has been concentrated on method and principle to control chain length distribution in last twenty years.Currently, the objective of most FTS research work is to increase the α value to as high as possible(0.95 or above) in order to synthesize long chain hydrocarbons(1).Different conclusions were drawn on the point of weather FTS reaction is structure sensitive (2-3). General result is that specific activity of FTS is affected by properties of support material and active metal crystal size of catalyst. Generally,the enlargement of active metal crystal size will increase the selectivity of long-chain hydrocarbons.It is because that in the process of FTS reaction, growing carbon chain lies on the surface of active metal crystals. So large metal crystal is required to obtain long-chain hydrocarbons. But for catalysts with some extent of metal-support interaction, such as Fe/AC(4) and Co/ZrO_2(5), opposite results were obtained. Selectivity of long-chain hydrocarbons increases with the decreasing of metal crystal size. To this kind of catalyst,minimization of particle size leads to stronger metal-support interaction.Then metal support synergism plays more important role to affect FTS activity and selectivity than metal crystal size of catalyst does. Consequently,preparation of modified ultrafine FTS catalyst with metal support interaction is a promising path to synthesis long chain hydrocarbons with high activity and selectivity.

Sol-gel method is a traditional way to produce ultrafine oxides. Previously,ultrafine SiO_2 aerogel powder was prepared by sol-gel method followed by supercritical fluid drying technique.The SiO_2 aerogel powder obtined was then coated with ZrO_2 to form ZrO_2-SiO_2 complex oxide.Cobalt catalyst supported on this complex oxide is in the category of nano material,its particle size is about 9.0nm.Under moderate pressure and in a fixed bed reactor,this catalyst was proved to be an extremely suitable catalyst for synthesis of long chain hydrocarbons,C^{5+} yield could reach 150g per cubic meter of syngas(6).

Promotion effect of manganese on iron F-T catalyst was studied extensively. The promotion effect was attributed to alkali and structure promotion. One of the characteristics of alkali promotion is to improve the selectivity of long chain hydrocarbons. Consequently, promotion effect of manganese to ultrafine Co/ZrO_2-SiO_2 catalyst on the properties of structure, texture, reduction and F-T synthesis is investgated in this paper.

EXPERIMENTAL

Catalyst preparation

Ultrafine silica aerogel was prepared by sol-gel method using TEOS as the precusor followed by supercritical fluid drying of the gels in an autoclave. The obtained monoliths were calcinated at 623K for 8hr and crushed. Zirconia coated ultrafine silica support was prepared by coating the ultrafine silica aerogel powder with solution of zirconium nitrate in a rotary evaporator. Dried sample was then calcinated at 673K in air. Preparation of cobalt catalysts was completed using incipient wetness technique with cobalt nitrate as impregnation solutions. Manganese promoted catalysts were prepared using a mixed solution of cobalt nitrate and manganese acetate as the impregnation solutions. Catalysts so obtained were then dried and calcinated before being pellesized and sieved.

Characterization

Cobalt loading of these catalysts were examined by ICP. BET surface areas and the distribution of pore volumes were measured by Micromeritics ASAP 2000 physical adsorption unit. XRD analysis were performed on a Rigaku diffractometer. X-ray photoelectron spectra were recorded with a Perkin-Elmer PHI 1600 ESCA system equiped with Al Kα X-ray excitation source and hemispherical electro analyzer. TPR tests were performed in a U-shape reaction tube with a catalyst loading of 0.2g, Ar purge temperature of 473K, temperature raising rate of 10 K/min, the carrier gas was $H_2/Ar(H_2$ 8.6V%) and the detector was TCD. TPD tests were processed after adsorption of H_2 over catalysts reduced at 673K and cooled in ambient temperature.

Reaction tests

The catalyst precursors (5g) were loaded into fixed bed laboratory reactors and reduced in situ at 673K under hydrogen. Synthesis gas (CO/H_2=1:2) was subsequently fed over the catalysts and the system was kept at steady state before mass balance data were collected. Liquid and solid condensates were collected in two seperate condensers. Product analysis for gas, liquid and solid products were all performed by GC using various columns.

RESULTS AND DISCUSSION

Texture property of Co-Mn/ZrO_2-SiO_2 catalysts

Table 1 illustrates the effect of Mn loading on texture property of Co-Mn/ZrO_2-SiO_2 catalysts. The results indicate that comparing with Co/ZrO_2-SiO_2 catalyst, the addition of manganese decreases the surface area and pore volume of Co-Mn/ZrO_2-SiO_2 catalyst and the change of average pore diameter is slight. The surface area and pore volume of three Co-Mn/ZrO_2-SiO_2 catalysts decrease with an increase of manganese loading.

Structure of Co-Mn/ZrO_2-SiO_2 catalyst

XRD spectras of Co(10.71%)-Mn(1.57%)/ZrO_2-SiO_2 catalyst before and after reaction were both recorded. We concluded that the addition of manganese increases the metal dispertion of cobalt and makes the crystal size of cobalt smaller. Furthermore, $Co_2Mn_2O_{4.5}$ spinel phase was formed after calcination of Co(10.71%)-Mn(1.57%)/ZrO_2-SiO_2 catalyst.

Surface characterization of Co-Mn/ZrO_2-SiO_2 catalysts

Surface property of Co/ZrO_2-SiO_2 and three Co-Mn/ZrO_2-SiO_2 catalysts were studied by XPS. Binding Energy and atomic ratio of the catalysts are listed in Table 2. From comparision of results of surface and bulk atomic ratio, it is evident that beneficiation of manganese at catalysts surface is significant. On the other hand, both $Co2p_{3/2}$ and $Mn2p_{3/2}$ have two BE values which verifies the formation of Co,Mn spinel phase.

TPR results of Co-Mn/ZrO_2-SiO_2 catalysts

Reduction property of Co-Mn/ZrO_2-SiO_2 catalyst was investigated by TPR. The results indicated that manganese promoter reacts with a part of CoO to form Co,Mn solid solution. Therefore the reduction of CoO is hindered and the reduction degree of catalysts in 673K decreases with the increasing manganese loading.

FTS performance of Co-Mn/ZrO_2-SiO_2 catalysts

The component of a catalyst affects the FTS performace significantly. The change of FTS performance at the same reaction temperature(493K),with the increase of manganese loading, are listed in Table 3. The following conclusions could be drawn:

1) CO conversion rate decreases.
2) Olefin to paraffin ratio increases evidently and then decreases. And olefin to paraffin ratios of all Co-Mn/ZrO_2-SiO_2 catalysts are higher than that of Co/ZrO_2-SiO_2.
3) CH_4 selectivity decreases to a minimum and then increases.
4) C^{5+} selectivity increases to maximium and then decrease.
5) Wax to oil weight ratio increases to maximium and then decreases.

The results indicate that certain amount of manganese addition could increase the selectivity of longer chain hydrocarbons,while excess amount of manganese addition leads to opposite results. FTS performance of Co-Mn/ZrO_2-SiO_2 is explained as the followings:

Decrease of CO conversion rate. (1)Addition of Mn promoter dilutes and covers the Co active sites.(2)The reduction of CoO was hindered by Mn and the degree of reduction of the catalysts at 673K decreases.

Increase of olefin to paraffin ratio. (1) Manganese as a texture promoter. Addition of Mn makes cobalt crystal size get smaller.Small crystal size makes newly produced olefines leave the surface of the catalyst quickly and increase the diffusion of olefin.Therefore, the secondary hydrogenation of olefines is restrained. (2) Group effect caused by beneficial of manganese on catalyst surface.Cobalt active sites are divided into smaller groups and this kind of surface modificaton restrains the hydrogenation of catalysts effectively.(3) Manganese as an electron promoter.Addition of Mn enhances the d-π feedback of CO to Co and therefore weakens Co-H bond.

Decrease of CH_4 selectivity and increase of C^{5+} selectivity. (1) Manganese as an alkali promoter.One of the characteristic of alkali promoter in FTS catalyst is to increase the selectivity of longer-chain hydrocarbons. (2) Group effect of manganese. The formation of methane requires a relatively large distribution of active center groups.

Fig.1 is the products carbon number distribution for Co/ZrO_2-SiO_2 and Co(10.71%)-Mn(1.57%)/ZrO_2-SiO_2 catalysts.It can be seen that carbon number distribution of Co/ZrO_2-SiO_2 catalyst follows Schulz-Flory distribution while that of Co-Mn/ZrO_2-SiO_2 catalyst deviates SF distribution and have two peaks instead.The maximium points are C_{11} and C_{17},respectively. Double-peaks distribution indicates the existence of two kinds of active centers. The author ascribes the active centers to be Co and Co,Mn spinel seperately.The assumption were verified by the results of Hongwei Xiang on Co-Mn/ZrO_2 catalyst and Yongqing Zhang on Co-Cr/ZrO_2-SiO_2 catalyst(7).

References

1.J.J.F.Scholtan,Xu Xiaoding,C.B.Von Der Decken, Intertational Journal of Energy Research,1994,18,P185-P198.
2.Liu Fu and Calvin Bartholomew,Journal of Catalysis,1985,92, P36-P387.
3.Iglesia E.,Reyes S.C.,Madon R.J.,Journal of Catalysis, 1991,129,P238.
4.Shen Jianyi,Zhang Su and Lin Liwu,Journal of Fuel Chemistry (China), 1989,17,P193
5.Xiang Hongwei,PhD Dissertation,Institute of Coal Chemistry, Chinese Academy of Sciences,1995.
6.Zhang Yongqing, Zhong Bing and Wang Qin,Proceedings of Fifth China-Japan Symposium on Coal and C1 Chemistry, Huangshan,China, 1996,P425.
7.Zhang Yongqing,Zhong Bing and Wang Qin,to be published.

Table 1 Texture property of oxidation state Co-Mn/ZrO_2-SiO_2 catalysts

Catalysts	Co/Mn	S_{BET} area	V_{PN}	r_p
	Atomic ratio	(m^2/g)	(cm^3/g)	(nm)
Co(10.73%)/ZrO_2-SiO_2		421.8	0.53	5.0
Co(10.71%)-Mn(1.57%)/ZrO_2-SiO_2	6.82	378.9	0.51	5.0
Co(11.58%)-Mn(3.28%)/ZrO_2-SiO_2	3.53	359.9	0.45	5.0
Co(11.09%)-Mn(4.36%)/ZrO_2-SiO_2	2.54	350.5	0.40	4.6

Table 2 Binding Energy and atomic ratio of Co-Mn/ZrO_2-SiO_2 catalysts

Catalysts	Binding Energy (eV)				Co/Mn atomic ratio	
	$Co2p_{3/2}$	percent	$Mn2p_{3/2}$	percent	bulk	surface
Co(10.73%)/ZrO_2-SiO_2	777.91 780.74	37.87 62.13				
Co(11.58%)-Mn(3.28%)/ZrO_2-SiO_2	777.95 780.57	41.68 58.32	641.58 645.40	81.88 18.12	3.53	2.30
Co(10.71%)-Mn(1.57%)/ZrO_2-SiO_2	779.05 781.46	72.75 27.25	641.09 644.93	86.78 13.22	6.82	4.17

Table 3. FTS performance of catalysts

Catal.No.	CO conv.	HC.distri.(wt%)		O/P^{a}ratio	Yield[g/Nm^3($CO+H_2$)]		Wax/Oil
	(%)	C_1	C^{5+}		C^{1+}	C^{5+}	(wt)
1	96.38	13.66	81.09	0.092	186.60	151.30	0.81
2	92.31	9.08	87.16	0.15	177.69	154.89	0.91
3	89.80	13.66	79.14	0.41	184.58	146.08	1.57
4	82.81	27.52	57.40	0.21	113.97	65.51	0.21

Reaction conditions: H_2/CO=2,P=2.0MPa,T=473K,GHSV=500h^{-1}

a: olefin to paraffin ratio.

No.1: Co(10.73%)/ZrO_2-SiO_2 No.2: Co(10.71%)-Mn(1.57%)/ZrO_2-SiO_2

No.3: Co(11.58%)-Mn(3.28%)/ZrO_2-SiO_2 No.4: Co(11.09%)-Mn(4.36%)/ZrO_2-SiO_2

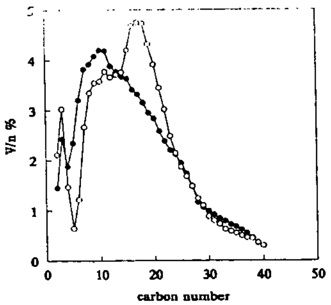

Fig 1. Carbon number distribution of products over (a): Co/ZrO_2-SiO_2 and (b): Co-Mn/ZrO_2-SiO_2

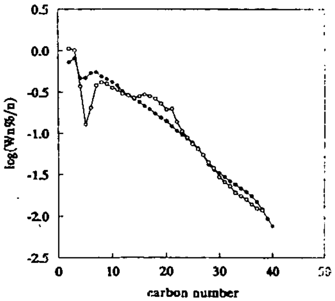

Fig 2. Schulz-Flory distribution of products over (a): Co/ZrO_2-SiO_2 and (b): Co-Mn/ZrO_2-SiO_2

FUNDAMENTALS OF CATALYSIS

M.K. Carter
Carter Technologies
P.O. Box 1852
Los Gatos, CA 95031

Keywords: theory of catalysis, transition probability, allowed catalysts

I. Background

Catalysis has been conducted for many years yet no fundamental understanding has emerged which teaches how to design a catalyst at a molecular level. Linus Pauling[1] stated, "It is thought that catalysts speed up reactions by bringing the molecules reacting together and holding them in configurations favorable to reaction." This definition offers a picture of what is to be achieved but does not suggest a mechanism of how catalysis might be accomplished. An alternative definition is proposed: *catalysis is a barrier free transformation from one electronic configuration to another*. This definition is presented as a starting point for a more formal development toward a goal of catalyst design at a molecular level. A true catalyst provides an orbital pathway for reactants to proceed to products such that the thermodynamic change in free energy for the reaction is negative. Thus, the act of catalysis will be treated as a radiationless stimulated emission - a natural transition from one electronic state to another.

II. Geometry

Consider the geometry of a set of atoms which compose a catalyst. Let r be the wave function of the reactant and let p be the wave function of the product. Catalytic conversion of a reactant to a product may be represented by a unitary transformation of r to p as $Ur = p$ so both the length of the vector and the symmetry of the wave function are preserved. This same unitary matrix transforms the wave function of the catalyst c such that $Uc = c$ since a catalyst returns to its original state following conversion of a reactant to a product. The column vectors of the unitary operator U were determined by expansion of the general form of a three by three unitary matrix to find the eigenvalues of $UU^{\dagger} = E$ so the value of the special function, c, could be calculated. The result is presented in figure 1 which shows the only geometric form allowed for a catalyst under such a unitary transformation is a one dimensional or linear geometric configuration. In this case its linear in the x-direction, but this axis is not unique. For example, catalysts represented by Y-M-Y for which M is a transition metal and Y is any appropriate electronegative atom, such as Cl-Mn-Cl or Co-Fe-Co, are described as being in linear geometric configurations. Should the molecule Y-M-Y be inherently non-linear, it may still exhibit catalytic activity during that fraction of time its bending vibration carries it through a linear configuration.

III. Symmetry Requirements

The symmetry of the reactant(s) associated with a catalyst is best described as belonging to a specific symmetry group. For example, carbon monoxide associated with a M_1-M_2-M_1 catalytic backbone, as required for Fischer-Tropsch catalytic conversion of CO/H_2 to hydrocarbons, may be represented as shown in figure 2. The two C-O molecules associated to the catalyst M_1-M_2-M_1 form a group described by the E, C_2, i, S_2', S_2'' and σ_h classes of symmetry operations. These six operations form a special D_{2S} symmetry group as shown in the character table of figure 3. During the instant of catalysis an initial chemical transformation is caused by the shifting of electrons from the catalyst, figure 2A, to form metal-carbon and metal-oxygen sigma bonds, figure 2B. These geometrical configurations represent the individual functions of the degenerate basis E1. One of the two-fold degenerate wave functions represents bonding configuration A while the other describes bonding configuration B. The transformation from one degenerate level to the other may be described as a barrier free electron shift. From the form of the mutually degenerate representations $\Gamma(E_{1A})$ and $\Gamma(E_{1B})$ different cooperative electron bonding may be inferred. Thus, $\Psi_+ = (\Psi_{E1A}+\Psi_{E1B}) = 2\varphi_1-\varphi_2-\varphi_3-2\varphi_4+\varphi_5+\varphi_6$ results from the sum and $\Psi_- = (\Psi_{E1A}-\Psi_{E1B}) = -\varphi_2+\varphi_3+\varphi_5-\varphi_6$ results from the difference of the doubly degenerate functions. The relative sign patterns are shown for both the sum and difference molecular functions in figures 2C and 2D. The sign of the wave function at carbon atoms 2 and 5 remains unchanged from Ψ_+ to Ψ_-. These atoms represent expectations of the active catalytic sites. Since no change of sign is evident, then catalysis may proceed under the barrier free condition.

The symmetry of a propene-catalyst association also belongs to the special D_{2S} symmetry group. Propene associated with the catalytic site M_2, refer to figure 4, may be represented where only one critical hydrogen atom is shown. Here the sign of the wave function on atoms 1 and 4 remains unchanged from Ψ_+ to Ψ_-. Thus, group symmetry considerations represent these two atoms as the expected catalytically activated sites. Experimental evidence shows the great majority of products formed during Ziegler-Natta catalysis do bond head-to-tail while the mechanism shows a tail-to-tail bond formation. This suggests a methylide and hydride exchange during an intermediate step to affect the apparent final head-to-tail bonded product.

IV. Transition Probability

A measure of the efficiency of catalysis may be determined by its transition probability, just as the intensity of a spectral line may be determined by its transition probability from one state to another allowed state. Such an electronic transition occurring between the product and reactant states Ψ_p and Ψ_r may be expressed by a quantum mechanical probability $|m_\mu|^2$ for which the transition moment m_μ is given by the expression

$$m_\mu = \int \Psi_p^* \mu \Psi_r d\tau$$

where μ is the amplitude of the induced electric moment. Einstein's transition probabilities[5] are seen to be wholly applicable for describing the electronic transition of molecular catalysis. Computation of the transition moment can be conducted specifically by using the set of wave functions which represent a metal-carbon monoxide complex as expressed previously, namely

$$\begin{aligned}\Phi &= \Phi_a + \Phi_b + \Phi_c + \Phi_d \\ &= (1/N_2)[1/6\varphi^{Fe}{}_{4s}+(2)^{1/2}/8\varphi^{Fe}{}_{3dxz}+(2)^{1/2}/8\varphi^{Fe}{}_{3dyz}+1/8\varphi^{Fe}{}_{3dz2}+\varphi^{O1}{}_{2py}+\varphi^{O1}{}_{2pz}]_a \\ &\quad + (1/N_2)[1/6\varphi^{Fe}{}_{4s}-(2)^{1/2}/8\varphi^{Fe}{}_{3dxz}+(2)^{1/2}/8\varphi^{Fe}{}_{3dyz}-1/8\varphi^{Fe}{}_{3dz2}+\varphi^{C1}{}_{2py}+\varphi^{C1}{}_{2pz}]_b \\ &\quad + (1/N_2)[1/6\varphi^{Fe}{}_{4s}-(2)^{1/2}/8\varphi^{Fe}{}_{3dxz}-(2)^{1/2}/8\varphi^{Fe}{}_{3dyz}+1/8\varphi^{Fe}{}_{3dz2}-\varphi^{O2}{}_{2py}+\varphi^{O2}{}_{2pz}]_c \\ &\quad + (1/N_2)[1/6\varphi^{Fe}{}_{4s}+(2)^{1/2}/8\varphi^{Fe}{}_{3dxz}-(2)^{1/2}/8\varphi^{Fe}{}_{3dyz}-1/8\varphi^{Fe}{}_{3dz2}-\varphi^{C2}{}_{2py}+\varphi^{C2}{}_{2pz}]_d\end{aligned}$$

for which the normalization constant is $N_2 = (349)^{1/2}/6$. Here all of the valance orbital functions have been given specifically and each of the four quadrants of the molecular association for the complex have been enclosed in brackets for purposes of organization. The transition moment can be computed, one quadrant at a time, replacing μ by its operator r using the system wave functions Φ as

$$\begin{aligned}m_\mu^a &= \int \Phi_a^* r \Phi_a d\tau \\ &= \int_0^\infty \int_0^\pi \int_0^{2\pi} \Phi_a^* r \Phi_a r^2 \sin\theta \, d\varphi \, d\theta \, dr\end{aligned}$$

Orthonormalized hydrogen-like one electron wave functions[2] were used and each of the four quadrant contributions to the transition moment was computed separately. The results by quadrant are

$$m_\mu = m_\mu^a + m_\mu^b + m_\mu^c + m_\mu^d = 0.2092110+0.2603221+0.2092110+0.2603221$$

$$\text{or } m_\mu = 0.9390517.$$

The value of the transition moment approaches unity supporting the requirement for a catalyst of linear geometric configuration constrained by a special D_{2S} symmetry group. Such strong transitions are not to be construed as oxidations or reductions since the time of a catalytically stimulated transition is expected to be less than the time of a molecular vibration ($< 10^{-14}$ second) following which the shifted electrons return to the original electronic configuration leaving new products in place of the reactants.

V. Catalyst Stabilization Against Permanent Oxidation

The external atoms M_1- and -M_3 in the linear catalyst cluster M_1-M_2-M_3 are present to stabilize the oxidation state of the catalytic site -M_2-. These groups possess the same or greater electronegativity[3] as -M_2- and represent the only allowed condition for catalysts. This effect is described by positioning local dipoles along the bonds pointing toward the external atoms.

A set of allowed bimetal and centrally symmetric trimetal linear catalysts formed from first row transition metal series elements is presented in figure 5. Similar sets of linear strings of symmetry allowed catalysts can be formed from the second and third row transition metal series. Noncentrally symmetric catalysts, such as Fe-Mn-Cu and interseries catalysts, are also possible provided they conform to the requirements of the theory.

Different oxidation states are required for various types of catalysis. For example, Fischer-Tropsch conversions can be accommodated by strings of zero valent metals such as Fe-Fe and Fe-Fe-Fe while Ziegler-Natta reactions seem to require higher oxidation states such as the Ti^{3+}-Ti^{3+} and Ti^{3+}-Ti^{3+}-Ti^{3+} strings.

VI. Ab Initio Computation of the Energy of a Carbon Monoxide-Catalyst Complex

Strength of the bond between the associated reactant and the active site of the catalyst was considered for the case of a carbon monoxide pi-bonded to the iron atom. A three atom model was developed in which the associated carbon monoxide was positioned symmetrically with the iron atom. Bond distances of 1.830 Angstroms for the iron to carbon and iron to oxygen bonds, and 1.210 Angstroms for the carbon to oxygen bond were assigned. Molecular bond energies were computed using the Hartree-Fock formalism for an eighteen electron spin function for a closed-shell system[4]. The symmetry determined molecular wave function is the best representation for carbon monoxide pi-bonded to the iron atom. It was derived from the same symmetry determined valence electron function employed for the transition moment computation. A single cycle bonding energy of 2.5152 eV (58 kcal/mol) was computed for the complex. The energy level was doubly degenerate as anticipated by the symmetry requirement.

VII. Recent Applications

Generation of a theoretical model based on these ideas forms the basis for identification of specific molecular catalysts for selected chemical reactions through computational methods. Several catalysts have been prepared in the laboratory, based on this work, for use in Fischer-Tropsch conversions, ambient temperature oxidation of gasoline and diesel fuel in water, and other reactions. The Fischer-Tropsch catalyst Co-Fe-Co was responsible for formation of liquid hydrocarbons directly in the C_8 to C_{22} range. GC-MS and FTIR molecular spectra show the products to be linear aliphatic hydrocarbons, refer to figures 6. Approximately half a dozen Cu-Fe and Fe-Fe based oxidation catalysts of the form $Fe(CN)_2L_3$-$FeCl_2L_3$, for L being $K_2Cu(CN)_3$ and related ligands, were prepared for destruction of 20 ppm gasoline and 100 ppm diesel fuel in water in approximately 15 minutes. Refer to figure 7.

VIII. Conclusion

Recognition of a reasonable starting point in the form of a definition of catalysis, namely that *catalysis is a barrier free transformation from one electronic configuration to another*, has became a basis from which the fundamentals of catalysis have been developed. Application of these fundamentals has produced oxidation, Fischer-Tropsch and other catalysts which generated products at good rates at room temperature without prior thermal conditioning. It is hoped that this work will add to the existing body of catalysis knowledge and give industry new opportunities for development, and expanded growth in the future.

References

1. L. Pauling, General Chemistry, W.H. Freeman & Company, San Francisco, **1959**, 2nd ed., p115.
2. L. Pauling and E.B. Wilson, Introduction to Quantum Mechanics, McGraw-Hill Book Co., New York, **1935**, p 302.
3. L. Pauling, *J.Am.Chem.Soc.* **1932**, 54, 3570.
4. W.J. Hehre, L Radom, P.v.R. Schleyer and J.A. Pople, Ab Initio Molecular Orbital Theory, pub. John Wiley & Sons, New York, **1986**, p21.

$$Uc = \begin{vmatrix} 1 & 0 & 0 \\ 0 & 1 & 0 \\ 0 & 0 & -1 \end{vmatrix} \begin{vmatrix} 1 \\ 0 \\ 0 \end{vmatrix}$$

Figure 1. Geometric Vector For A Catalyst

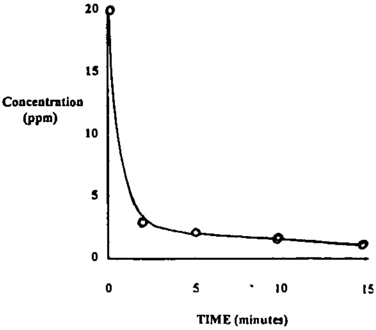

Figure 7. Oxidative Destruction Of Gasoline

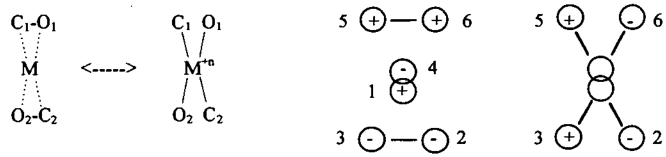

Form A Form B Form C Form D

Figure 2. Degenerate Bonding Functions And Signs For Carbon Monoxide On A Catalyst

D_{2S}	E	C_2	i	S_2'	S_2''	σ_h		
A	1	1	1	1	1	1	z, R_z	$\alpha_{x2}+\alpha_{y2}$, α_{z2}
B	1	1	1	-1	-1	-1		
E_1	2	-1	-1	-2	1	1	(x, y) (Rx,Ry)	α_{xz}, α_{yz}
E_2	2	-1	-1	2	-1	-1		$\alpha_{x2}-\alpha_{y2}$, α_{xy}
Γ(sum)	6	0	0	0	0	0		
$\Gamma(\alpha)=\Gamma(A)x\Gamma(E_1)$	2	-1	-1	-2	1	1	$=\Gamma(E_1)$	

The direct product of irreducible representations describing the polarizibility matrix, α, is $\Gamma(A) \times \Gamma(E_1) = \Gamma(E_1)$ which is also irreducible.

Figure 3. Character Table For Special D_{2S} Symmetry Group

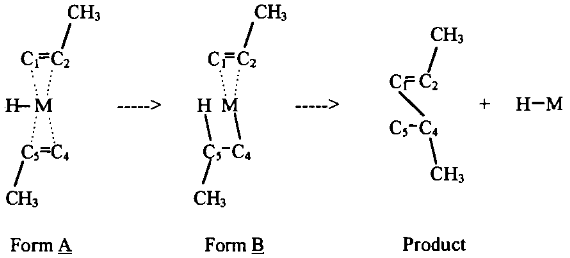

Figure 4. Barrier Free Symmetry Selected Bonding For Ethylene Dimerization

Ti-Ti
V-V
V-Ti
Cr-Cr
Cr-V
Cr-Ti
Mn-Mn
Mn-Cr
Mn-V
Mn-Ti
Fe-Fe
Fe-Mn
Fe-Cr
Fe-V
Fe-Ti
Co-Co
Co-Fe
Co-Mn
Co-Cr
Co-V
Co-Ti
Ni-Ni
Ni-Co
Ni-Fe
Ni-Mn
Ni-Cr
Ni-V
Ni-Ti
Cu-Cu
Cu-Ni
Cu-Co
Cu-Fe
Cu-Mn
Cu-Cr
Cu-V
Cu-Ti
Co-Cu-Co
Ni-Cu-Ni
Cu-Cu-Cu
Co-Ni-Co
Ni-Ni-Ni
Cu-Ni-Cu
Co-Co-Co
Ni-Co-Ni
Cu-Co-Cu
Fe-Fe-Fe
Co-Fe-Co
Ni-Fe-Ni
Cu-Fe-Cu
Ti-Mn-Ti
V-Mn-V
Cr-Mn-Cr
Mn-Mn-Mn
Fe-Mn-Fe
Co-Mn-Co
Ni-Mn-Ni
Cu-Mn-Cu
V-Cr-V
Cr-Cr-Cr
Fe-Cr-Fe
Co-Cr-Co
Ni-Cr-Ni
Cu-Cr-Cu
V-V-V
Cr-V-Cr
Fe-V-Fe
Co-V-Co
Ni-V-Ni
Cu-V-Cu
Ti-Ti-Ti
V-Ti-V
Cr-Ti-Cr
Mn-Ti-Mn
Fe-Ti-Fe
Co-Ti-Co
Ni-Ti-Ni
Cu-Ti-Cu

Figure 5. Allowed Bi and Symmetric Trimetal First Row Transition Metal Linear Catalysts

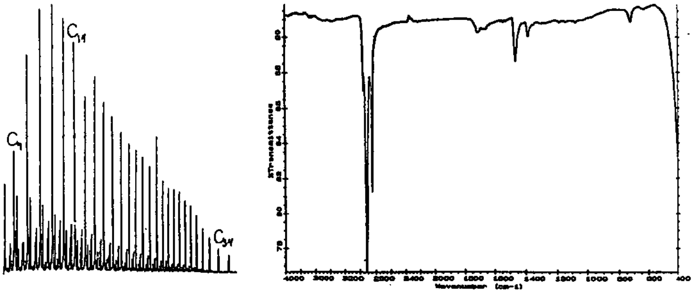

GC-MS Spectrum

FTIR Spectrum

Figure 6. GC-MS And FTIR Molecular Spectra Of Fischer-Tropsch Aliphatic Hydrocarbons

SHELL MIDDLE DISTILLATE SYNTHESIS: FISCHER-TROPSCH CATALYSIS IN NATURAL GAS CONVERSION TO HIGH QUALITY PRODUCTS

J. Ansorge
Shell International Oil Products B.V.
Badhuisweg 3
1031 CM Amsterdam

Keywords : Natural Gas Conversion, Fischer-Tropsch Synthesis, Paraffins

1. INTRODUCTION

The importance of natural gas as a source of energy has increased substantially in recent years and is expected to continue to increase. In the recent past many new gas fields were discovered around the world, leading to a large increase in the proven world gas reserves. Proven world gas reserves are now approaching those of oil and, on the basis of the current reserves situation and relative depletion rates, natural gas seems to be set to outlast oil.

The main drawback of natural gas remains its low energy density, which makes its transportation to the point of use expensive and which may even prohibit its exploration and production. Shell and others have therefore been looking at processes that chemically convert natural gas into liquid hydrocarbons. Critical for the viability of each project is the value of its products. The chemical products like ammonia, urea and methanol have shown a high price volatility in the market with a relatively low entry barrier. Production of top quality middle distillate fuels from gas is favoured by recent developments in fuel quality requirements, the ease of transport and distribution of the products, and the enormous market for the products. The middle distillates from SMDS will therefore be well positioned in the market place of quality transportation fuels.

It has been realised that there are many places in the world where gas is available, without a ready market and where, as a consequence, it would have a much lower intrinsic value compared with transportation fuels. It is this difference in value that would drive a synthetic fuel project and provide opportunities for both government and private enterprises.

The present scene in the field of oil and transportation fuels and the prospects for the near and medium term however, call for a careful and selective approach to any synfuel development. At low fuel oil prices almost no alternative energy technology can compete with existing refining. On the other hand, the crises of the early seventies and early eighties provided important lessons: emergencies come at relatively short notice, and, because of the lead times usually involved in technological development, in a crisis the answers to problems always come too late.

Next to the synthetic hydrocarbon transportation fuels, a similar role could be perceived for methanol. However, use of methanol as a transport fuel has considerable drawbacks. These include the required modifications to fuel distribution systems and to the car / engine fuel system. Synthetic hydrocarbons, on the other hand, have the advantage that they can be readily incorporated into existing fuels which can be used in today equipment. In addition, middle distillates manufactured from natural gas have very environmentally friendly properties, upon which we will elaborate in this paper. The cleanliness of natural gas is, as it were, transferred into its products. The middle distillates from SMDS will therefore be extremely well positioned in a market place with an ever increasing quality demand. Natural gas conversion has become an asset for Shell with the construction and successful operation of the first commercial natural gas to transportation fuels conversion plant , SMDS(M) Bintulu.

2. THE PROCESS

The SMDS process combines conventional and well proven technologies with advanced technology using newly developed heterogeneous catalysts.

The overall process starts with the conversion of natural gas into synthesis gas, for which there are several commercial processes available. For the production of predominantly saturated hydrocarbons, $-CH_2-$, the syngas components H_2 and CO, are consumed in a molar ratio of about 2: 1, so a production in about that ratio is desirable. This influences the choice of process, as will be explained below.

The next step of the process, the hydrocarbon synthesis, is, in fact, a modernised version of the classical Fischer-Tropsch (FT) process, with the emphasis on high yields of useful products.

The Fischer-Tropsch process developed by Shell for SMDS favours the production of long chain waxy molecules which, as such, are unsuitable for transportation fuels. The hydrocarbon synthesis step is therefore followed by a combined hydro-isomerisation and hydrocracking step to produce the desired, lighter products. By opting for the production of waxy molecules in the Fischer-Tropsch step, the amount of unwanted smaller hydrocarbons or gaseous products, produced as by-products, is substantially reduced. This means that the process, simply spoken, does not make 'gas' out of gas. Combined with the high selectivity towards middle distillates in the hydrocracking step the overall process shows a high total yield of product in the desired range.

In the final stage of the process, the products, mainly kerosene, gasoil and naphthas, are separated by distillation. By the right operating conditions in the hydrocracking step and the subsequent distillation the product slate can be shifted towards a maximum kerosene mode or towards a maximum gasoil mode depending on market circumstances.

2.1. Synthesis Gas Manufacture

For the production of synthesis gas in principle two technologies are available, viz., steam reforming and partial oxidation.

Steam Reforming (SMR)

Starting from pure methane, SMR is the most commonly used conversion process for natural gas into synthesis gas, and could theoretically produce a synthesis gas with an H2/CO ratio of about 3. This process has the advantage that it doesn't require an air separation unit for the production of pure oxygen.

For the Fischer-Tropsch process SMR turns out to be less suited since the high H2/CO ratio is a disadvantage for a reaction which is highly exothermic and obeys first order kinetics in hydrogen partial pressure. Two other disadvantages are the large size of the reformer furnace which limits the scale-up potential of this synthesis gas technology and the limitation in pressure of about 30 bar, while the Fischer-Tropsch reaction is preferably carried out at somewhat higher pressures.

On the other hand SMR technology might be favourable for small scale Fischer-Tropsch applications and for feed gases having a high content in CO_2.

Partial Oxidation

A synthesis gas with a H2/CO ratio of about 2, can theoretically be produced by partial oxidation of methane with oxygen. Without much correction such gas is suitable for the production of middle distillates. The oxygen source can be air, or pure oxygen or anything in between. The final selection depends on a number of factors and can be different from project to project. However, generally, economics favour the application of pure oxygen.

For this type of partial oxidation several processes exist amongst which Shell's own Shell Gasification Process (SGP) which has been applied for several decades for the gasification of residual oils and has been chosen for the SMDS plant in Malaysia as the most appropriate synthesis gas manufacturing process.

For the catalytic Fischer-Tropsch synthesis, the synthesis gas must be completely free of sulphur. For this requirement all sulphur components are removed upstream of the partial oxidation step. A number of well-known treating processes are available the application of which is mainly guided by the type and concentration of the sulphur components in the natural gas.

2.2. The Hydrocarbon Synthesis Step

In the Heavy Paraffin Synthesis (HPS) step, the synthesis gas is converted into long chain, heavy paraffins. The paraffinic hydrocarbons produced via the FT reaction are highly linear. The formation of the linear paraffinic molecules can be described with the Anderson Flory Schultz [AFS] distribution model. Relation between model, design, product slate, catalyst and plant operation and economics will briefly be discussed.

During the catalysed reaction of synthesis gas to the primary paraffinic product an appreciable amount of heat is released. For the classical catalyst system this requires a considerable control of the temperature in view of the following constraints:

- The temperature window of stable operation is rather small
- A high space-time yield demands a high temperature
- At only moderately higher temperature a side reaction leading to methane formation becomes more dominant, reducing selectivity and, eventually, stability.

Because of these shortcomings, Shell has developed a new and proprietary catalyst system which establishes substantial improvements in all these areas. Its robustness allows the use of a multitubular fixed bed reactor system at a temperature level where heat recovery, via production of medium pressure steam, leads to an efficient energy recovery. The catalyst self can be regenerated in situ whereby the cycle time depends on a number of factors like process conditions, changes in feedgas composition and production planning.

2.3. Heavy Paraffin Conversion (HPC)

One of the prerequisites for obtaining a high selectivity towards n-middle distillates is a sufficiently high average molecular weight of the raw product. This product, which is predominantly waxy but contains small amounts of olefins and oxygenates, has to be hydrogenated to remove the olefins and oxygenates, has to be hydrocracked into the right molecule lengths for kerosene and gasoil and has to be isomerised to improve the cold flow properties. A commercial Shell catalyst is used in a trickle-flow reactor under rather mild conditions of pressure and temperature. The HPC product is subsequently fractionated in a conventional distillation section. The product fraction which is still boiling above the gas oil range is recycled to the HPC section. By varying the process severity or the conversion per pass one can influence the selectivity towards a preferred product. Hence one may opt for a kerosene mode of operation yielding some 50% kerosene on total liquid product or for a gas oil mode of operation producing up to 60% gas oil.

The principle of combining the length-independent chain growth process (in the HPS) with a selective, chainlength dependent conversion process has been applied to selectively produce middle distillates from synthesis gas. The two stage approach creates flexibility for differentiated product slates since the primary Fischer-Tropsch liquid product can be converted into different product distributions by adjusting the cracking severity in the heavy paraffin conversion step.

For the SMDS Bintulu project, the technology was extended to include the production of specially chemicals. This addition was required to support the economy of a relatively small pioneer project. It takes advantage of the high quality of all the products respectively intermediate streams produced. Linear paraffins of varying length are isolated as solvents, detergent feed stocks and waxes. Isomerised molecules boiling below the gasoil range are worked up into lube oils. Their product properties are discussed below in some more detail. Figure 1 depicts a block diagram of the SMDS Bintulu complex.

3. THE PLANT

The first commercial SMDS plant is located in Bintulu, Malaysia. At this place, in the state of Sarawak, sufficient remote natural gas is available for conversion. About 100 MMSCFD are converted into liquid products whereas a much larger amount is liquefied in the Malaysia LNG plant. As an advanced gas conversion technology, SMDS technology is of great interest for Malaysia with its significant gas reserves. A joint venture were formed by Petronas, Sarawak State, Mitsubishi and Shell. The project was developed by Shell Internationale Petroleum Maatschappij (SIPM today SIOP), constructed by Japan Gasoline Corporation (JGC) and is operated by Shell.

A short history of construction, commissioning and start-up including some useful lessons learnt when bringing new technology into life on an industrial scale will be presented during the presentation.

Plant throughput, availability of the complex and reliability of the process units increased over the last three years. It forms a tremendous source of experience and know-how and represents a valuable basis when entering into the next generation SMDS plants.

4. THE PRODUCTS AND THEIR MARKETS

The Fischer-Tropsch synthesis for transportation fuels has the great disadvantage that first the hydrocarbonaceous feedstock has to be gasified and converted into synthesis gas before the route to the transportation fuels can be taken. On the other hand, it turns into an advantage since the target products are built from their molecular building blocks H2 and CO. As described above, after having converted olefins and oxygenates into paraffins separation into valuable products and further conversion / isomerisation into clean transportation fuels can start. Studies and experimental programmes were undertaken to identify and develop the unique SMDS products. The marketing of these products was and is a challenge, but creates simultaneously many opportunities, for example, legislation related to improvement of air quality. To be able to comply with the regulations, components of the purity provided by SMDS products are welcome and very well accepted in the market place.

In fact, SMDS products are extremely clean. They contain no sulphur, no nitrogen and aromatics at the limit of detection. The SMDS products have impurities that are several orders of magnitude lower than highly refined crude oil derived products. Hence, several normal 'oil impurities' are not detectable by the standard methods. Below some typical properties for the product groups as indicated in Figure 1 are briefly discussed.

4.1. Middle Distillates

Naphtha

The naphtha or C5-C8 fraction from SMDS is highly paraffinic. These paraffins are known to have a rather bad combustion behaviour (expressed in a low octane number), When isomerised (predominantly one methyl branch) the front end components can be used in the automotive gasoline pool whereas the heavier molecules (C7, C8) need further upgrading for the gasoline market. This will become important for future SMDS plants since applications as described below can only absorb a limited amount of these products. However, the transportation fuel market is immense, spread all over the world and expanding in some important areas. Actually, the consumption of gasoline is estimated to about 600 million metric tonnes per year and that of gasoil (diesel) to about 370 million metric tonnes per year.

Besides blending SMDS into the gasoline pool it can be used as chemical feed stock for petrochemicals. Its paraffinic nature makes it an ideal cracker feed stock for ethylene manufacture. The paraffinic nature and the purity of the SMDS naphtha results in about 10 percent higher conventional ethylene yields compared to petroleum-derived naphtha feed stock. Expectations have been met when processing SMDS naphtha on large scale in industrial steam crackers, e.g. in Singapore.

The ethylene world market presents about 70 million metric tonnes per annum and is expected to grow with a rate of about 5 % per year in the next 5 to 10 years. The market share of East Asia is estimated to represent about 15 % of the world-wide market by the year 2000. This would represent a doubling of the demand in a relatively short period of time and present opportunities for SMDS naphtha despite the fact that new capacity is planned respectively under construction.

Kerosene

Today, around 90 % of jet-fuel demand is for civil aviation and the remainder for the military sector. In 1992 the world demand for jet fuel was over 125 million tpa. North America accounted for slightly more than half of this, mainly as result of its important domestic aviation market. Outside North America and CIS, civil aviation jet fuel demand has risen between 1982 and 1992 from about 40 million tons to more than 60 million tons. Future growth is predicted at ca 4.5 % per annum. SMDS kerosene can be used to upgrade kerosene fractions having low smoke point and high aromatics, which would otherwise be unsuitable for use in jet fuel.

For the first SMDS plant in Bintulu the produced kerosene is too small to play a significant role in the regional kerosene market. However, a fraction boiling in the kerosene range can be tailored to an iso-paraffinic solvent of high purity. It has a low odour and water-clear appearance and is particularly attractive in applications as printing ink, cosmetics, dry cleaning etc. It is marketed under the tradename SMDS SARASOL 150/200 and some typical properties important for this application are summarised in table 4.

Gasoil/Diesel

Some properties indicating that the SMDS gasoil, too, is of exceptional quality are shown in table 1. Given this quality, the SMDS gasoil is an ideal blending component for upgrading of lower-quality gasoils which don't meet for example the cetane specifications. Alternatively, the SMDS gasoil could enter in a market where premium specifications are valued to meet local requirements. For example, the Californian Air Resources Board (CARB) requires commercial fuels to give lower emissions than a reference fuel, which has a minimum cetane number, low sulphur and aromatics. More details on the environmental impact of SMDS gasoil are described below.

Additionally, SMDS fuels are suitable for special applications, like. high quality lamp oils and e.g. underground truck fuel (in mining), provided that precautions are taken to mitigate the effects of low lubricity and low density. The gasoil has excellent combustion properties, as the typical product data, given in table 3 and compared with important standards, show.

Waxy Raffinate (Base Oils)

The hydrocracker (HPC) in which the linear paraffins are cracked and isomerised to prepare the right boiling range of the middle distillates operates at relatively mild severity. After having distilled the middle distillates a bottom stream remains which is recycled to the hydrocracker. This stream contains a fraction called waxy raffinate which upon solvent dewaxing leads to a stream which combines extremely high viscosity index with very low Noack volatility and forms the main part of a range of wholly synthetic top-tier lubricating oils. These base oils are fit to fulfil ever increasing quality demands like less oil consumption, ability to at higher temperatures and for longer periods, keep modern engines in a better shape.

SMDS Bintulu (Malaysia) presently supplies Shell refineries in France and Japan where SMDS waxy raffinate is processed into finished top-tier motor oils..

4.2 Products on basis of linear paraffins

In Figure 1 it is shown schematically that not all linear paraffins are converted in the HPC into middle distillates. Part of the primary Fischer-Tropsch product which contains a certain percentage of olefins and oxygenates is hydrogenated under such operating conditions that olefins and oxygenates are converted into the corresponding linear paraffins without any isomerisation. The resulting stream of pure, linear paraffins is subsequently separated by distillation to gain access to a range of special products. These products are further characterised below.

Solvents

The C5-C10 SMDS n-paraffins fall into a class of specific solvents. They are completely free of aromatics and sulphur compounds and have a low odour. These solvents fit particularly well into the current environmental requirements since the n-paraffins show the best biodegradability results. The market represents a wide variety of different solvents of which the world-wide demand in aggregate is estimated to be 100,000 tpa. Presently, solvents in this carbon range, particularly hexane and Special Boiling Point (SBP)- types are used in oil-seed extraction, polymerisation and the rubber industry. In view of their application they need to be guaranteed low in aromatics, particularly in benzene. The SMDS solvent cut (and the naphtha fraction too) are suitable for these applications.

Detergent Feedstocks

The next distillation cuts are the C10-C13 and the C14-C18 fractions which are used in further processing steps to obtain industrial detergents and flame retardant materials. The purity of the products satisfies all the performance requirements in the production of linear alkyl benzene, chlorinated paraffins and paraffin sulphonates. The C10-C13 fraction (LDF) is used most widely in laundry applications where its higher than normal C13 content gives the improved detergency. The C14-C18 fraction (HDF) is used in making chloroparaffins of exceptional quality in terms of heat stability and colour. The biodegradability, which is critical in such applications, has been demonstrated to be fully satisfactory since the limited amount of branching present is mostly biodegradable methyl groups (in the alpha position). Some typical properties of the chemicals are shown in table 4.:

Waxes

Linear paraffins above C20 belong to the world of the waxes. Four fractions are separated in Bintulu called SX30, SX50, SX70 and SX100 were SX stands for Sarawax and the figure indicates the typical congealing point of that material. Typical properties of the waxes are given in table 5. Special precautions have been taken to conserve the purity even of the heaviest wax streams. For example, Wiped Film Evaporators (WFEs) are applied to separate the heaviest wax grades. The WFEs operate at a vacuum of about a factor 500-1000 below what is conventional high vacuum technology in standard refinery processing. The low pressure allows a rather mild distillation temperature which together with a very short residence time avoids thermal degradation of the products. Possible ingress of air and formation of unwanted oxygenates can be counteracted by a subsequent final hydrofinishing step. The resulting products (especially SX70 and SX100) are applied in industry segments where extreme purity, high Sayboldt colour quality, thermal stability and specific viscosity behaviour are required. Applications are diverse and vary from candles, paper & packaging, rubber, cosmetics and medicines, electrical use to various outlets, like chewing gum.

The total world paraffin wax consumption is about 3 million tonnes per annum and has over the last 15 years displayed an average annual growth of little over 4 %. Particular growth areas are Asia and Western Europe.

Important markets for waxes are the USA, the central European countries, the Pacific Basin, Japan and Taiwan, India, Brazil and South Africa.

5. ENVIRONMENTAL ASPECTS

The use of the SMDS products as transportation fuels has minimal impact on the environment, based on the excellent product properties. In some countries, notably in the USA, legislation has been proposed, which aims at limiting particulate and sulphur dioxide emissions originating from the combustion of transportation fuels by restricting their aromatics and sulphur levels. From product properties described above it is obvious that SMDS kerosene and gasoil meet such requirements without any problem. In the following section fuel quality aspects of SMDS gasoil will be highlighted, although it should be remembered that engine design and maintenance have an equally important or even greater impact on overall emissions:

Fuel Quality Effects on Vehicle Exhaust Emissions

Extensive work in and outside Shell Laboratories has established the effect of fuel properties on vehicle exhaust emissions.

For example, fuel sulphur has a dominant effect on particulate levels The conversion of fuel sulphur to particulate sulphur is engine dependant but within a relatively narrow range of 1-2%. Thus reduction to 0.05% m from earlier levels of 0.20 %, or higher in some countries, produces a significant emission reduction but further reduction below 0.05%m has only a relatively small influence.

Fuel density has been identified as an important parameter in particulate emissions. Lower density usually gives lower emission. Changes of emission properties in the Federal Test Procedure cycle caused by density changes arise from effects introduced by transient conditions. For example, air/fuel mixture excursions are caused by turbo charger lag during periods of hard acceleration. Reduction in fuel density increases the volumetric fuel consumption at all loads, although the increase in the fuel H2 to C ratio counterbalances the effect to some extent.

Aromatics content has been examined very carefully inside and outside Shell and it has been shown that "total aromatics" have no influence on particulate emissions. In some engines the addition of polyaromatics produces small increases in particulate emissions.

Cetane number is the fuel property having the greatest influence on regulated gaseous emissions (NO., hydrocarbons, and CO) and having a large influences on the cold start performance of an engine. Higher cetane numbers give better performance. However, the benefit in regulated gaseous emissions by increasing the ignition quality through an increase in cetane is limited by the possible steps the markets would and can accept.

In California regulations are quite advanced in controlling exhaust emissions. However, compliance can be achieved in several ways. Application of SMDS gasoil can present an advantage in several of these options depending on the specific market situation and specific conditions in the refineries. Especially where cetane enhancement is required SMDS gasoil can act as cetane improver additives.

6. OUTLOOK

It is not surprising that the conversion of natural gas into middle distillates for the transportation fuel market has by the nature of the process a disadvantage compared to the manufacture of transportation fuels via crude oil distillation : part of the energy content of the feedstock is consumed for the conversion process itself. Moreover, the feedstock (natural gas) itself has alternatives to reach the market, i.e. by pipeline or by liquefaction. On the other hand, the SMDS technology can provide the bridge between vast reserves of natural gas and the large transportation fuel market. This bridge can be built already today if some specific factors come together :

- the investment has to be reasonably low
- the alternative value of the natural gas should be low
- the products fit into the longer market trends.

Above we have shown in detail that every product produced with the SMDS technology provides by the way of its manufacture from the molecular building blocks top quality and fits into increasing efforts of conserving the environment.

If a natural gas reserve cannot be exploited by pipeline or by liquefaction it can be left in the ground or used in a conversion plant. In that case a reasonable natural gas price would be about US$ O.5 per MMBTU (equivalent to a feedstock cost element in the product of about US$ 5/bbl) to make the products competitive in the transportation fuel market. The total fixed and other variable operating costs are estimated at a further US$ 5/bbl. The total required selling price for the product will depend on numerous factors, including fiscal regimes, local incentives, debt/equity ratio, type of loans and corporate return requirements. The premium that may be realised for the high quality products can be anything between 0 and 8 US$/bbl over and above the normal straight run middle distillate value depending on local circumstances.

An important factor when realising a natural gas to middle distillate conversion complex are the capital costs. These are highly dependent on location. At a location with an industrial infrastructure available specific capital cost would be around US$ 30,000 per daily barrel, whereas for a similar plant in a remote location and on a greenfield site the cost could be substantially higher.

In addition to these factors, the capacity of the plant is of great importance. Especially for remote locations, where self-sufficiency of the plant is essential, larger plants, in the 25,000 to 50,000 bbl/d range, have a much better economy of scale.

Whilst the process is ready for commercialisation, further developments are underway, directed at increasing the efficiency of the process and reducing the capital cost. An important area for these efforts is the synthesis gas manufacturing plant, which constitutes more than 50% of the total process capital cost. Other fields of interest include further catalyst improvement, the design of the synthesis reactors and general process integration within the project. Here the factor 'moving up the learning curve' is of pivotal importance: construction and several years of operation of the SMDS Bintulu complex has provided an extensive know-how which will be applied the next time. It is expected that know-how combined with further improvements for larger size plants, will bring the specific capital costs for remote areas further down.

SMDS technology has been developed to a stage where it can be considered as technically proven and, subject to local circumstances, commercially viable. Installation of SMDS plants can bring significant national benefits to countries with uncommitted gas reserves, either through export from the plant or inland use of the products, thereby reducing the need to import oil and oil products and saving on foreign exchange,

The successful application of the technology in Bintulu presents an important advance in the commercialisation of SMDS conversion technology and an asset in Shell's portfolio of technologies to make natural gas transportable. It provides exciting opportunities'in terms of marketing hydrocarbon products of a quality that fits ideally in a business environment, requiring increasingly higher performance standards.

REFERENCES

Eilers, J. Posthuma, S.A, and Sie, S.T., 'The Shell Middle Distillate Process (SMDS)', paper presented at the AICHE Spring National Meeting, Orlando, Florida, USA, March 18-20, 1990.

Post, M.F.M., Van 't Hoog , A., Minderhout, J.IC. and Sie, S.T. (1 989), 'Diffusion limitations in Fischer-Tropsch catalysts' AICHE J. 35 (7),1107-1114

Oerlemans, T.W., Van Wechem, H.M.H., and Zuideveld, P.L., 'Conversion of Natural Gas to Middle Distillates via the SMDS Process', paper presented at the 18th World Gas Conference, Berlin, FRG, July 8- I 1, 1991.

Senden, M.M.G., Sie, S.T., Post, M.F.M., and Ansorge, J. (1 99 1), 'Engineering aspects of the conversion of natural gas into middle distillates', paper presented at NATO Advances Study Institute Conference at the University of Western Ontario, Canada, September 4.

Van der Burgt, M., Van Klinken, J. and Sie, S.T. "The Shell Middle Distillate Synthesis Process", paper presented at the 5th Synfuels Worldwide Symposium, Washington D.C. USA, November 11-13,1985.

Van den Burgt, M.J., Sie, S.T., Zuideveld, P.IL and Van Wechem, H.M.H., 'The Shell Middle Distillate Process, paper presented at the Institution of Chemical Engineers Conference on Natural Gas Conversion, London, UK, January 12, 1988.

Tijm, P.J.A., Van Wechem, H.M.H., and Senden, M.M.G., 'New opportunities for marketing natural gas: The Shell Middle Distillate Synthesis Process', paper presented at the GASTECH 93, 15th International LNG/LPG Conference & Exhibition, Paris, France, February 16-19, 1993.

Booth, M, et al., 'Diesel Fuel Quality in an Environmentally Conscious World', paper presented at 1. Mech. E. International Seminar 'Fuels for Automotive and Industrial Diesel Engines', London, UK, 6-7, April 1993, London

Stradling R.J. et al. (1993) 'The Influence of Fuel Properties and Test Cycle Procedures on the Exhaust Particulate Emissions from Light-Duty Diesel Vehicles' paper presented at I. Mech. E. International Seminar 'Fuels for Automotive and Industrial Diesel Engines', London 6-7, April 1993, London

Cowley T. et al. (1993) 'The Influence of Composition and Properties of Diesel Fuel on Particulate Emissions from Heavy-Duty Engines', paper presented at Fuels and Lubricants Meeting and Exposition, Philadelphia, Pennsylvania October 18-21, 1993

Tijm, P.J.A., Marriott, J.M., Senden, M.M.G and Van Wechem, H.M.H., 'Shell Middle Distillate Synthesis: The Process, The Products, The Plant, paper presented at the Alternate Energy '94, La Quinta, Ca, USA, April 26-29, 1994.

van Herwijnen, Th., 'Shell MDS (Malaysia) Plant On Stream', paper presented at GASTECH 94, in Kuala Lumpur, Malaysia, October 23-25,1994.

Table 1 Typical properties of SMDS Middle Distillates

Property		Unit	**Naphtha**	**Kerosene**	**Gasoil**	method
Density (at 15 oC)		lkg/m3	690	740	780	ASTM D1298
Saybolt colour		-	+30	+30	n/a	ASTM D156
Distillation range	IBP	°C	40	150	200	ASTM D86
	FBP	°C	160	200	360	
Sulphur		PPM	b.d.l.	b.d.l.	b.d.l.	ASTM D1266
Cetane number		-	n/a	60	75	ASTM D976
Smoke point		mm	n/a	>> 50	n/a	ASTM D1322
Flash point		°C	n/a	40	90	ASTM D93
Aromatics		% vol	b.d.l.	b.d.l.	b.d.l.	ASTM D5186

b.d.l. = below detection limits n/a = not applicable

Table 2 Typical properties of Detergent Feedstocks from SMDS

Property	unit	LDF	HDF	Method
Saybolt colour		+30	+30	ASTM D156
Bromine index	mg Br / 100 g	5	6	ASTM D2710
Sulphur		b.d.l.	b.d.l.	ASTM D3120
Carbon distribution				by GC
C9- / C13-	% m	0	1	
C13- / C17-	% m	99.3	99	
C14+ /	% m	0.7		
..... / C18+	% m		0.2	
N-paraffins content	% m	96	95	

b.d.l. = below detection limit

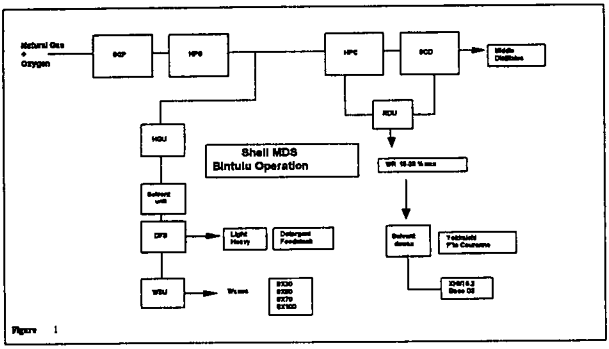
Natural Gas
+
Oxygen
SGP
HPS
HPC
SCD
Middle Distillates
RDU
HGU
Shell MDS
Bintulu Operation
Solvent unit
DFS
Light
Heavy
Detergent Feedstock
WSU
Waxes
SX30
SX50
SX70
SX100
XHVI 5.2
Base Oil

Figure 1

Table 3 **Gasoil Properties compared to CARB specifications**

Gasoil	SMDS product	Californian CARB	CEN Specs
	Commercial Spec.	Reference fuel Spec.	
Cetane number	76	48 min	49 min
Density (kg/m3)	780	N/S	820-860
Sulphur (ppmm)	n/d	500	500 (1996)
Aromatics (% m/m)	n/d	10 max.	N/S
Cloud point oC	1	-5	N/S
CFPP oC	-2	N/S	+5 to -20*
90 % recovery (oC)	340	288-338	
95 % recovery (oC)	350		370 max.

N/S = No Specification * depend on regional application

Table 4 **Typical Properties of SMDS normal paraffin products**

Property	Unit	SARAP AR 059	SARAP AR 103	SARAP AR 147	SARASOL 150/200	Method
Saybolt colour		+30	+30	+30	+30	ASTM DI56
Bromine index	mg Br/ 100g	10	5.0	5.5	20	ASTM D2710
Sulphur	PPM	zero	zero	zero	zero	ASTM 3120
Carbon distr.	% m					GC
n-C5		10				
n-C6		17				
n-C7		19			1	
n-C8		19			3	
n-C9		18			7	
n-C10		8	9		20	
n-C11			30		12	
n-C12			30		8	
n-C13			27	<1	1	
n-C14			<1	26		
n-C15				27		
n-C16				25		
n-C17				17		
n-C18				<1		
N-paraffins tot	% m	91	96	95	50	
Avg. mol. mass		122	167	213	166	
Density	kg/m3	690	750	775	735	ASTM D4052
Distillation	IBP °C	35	190	250	155	
	FBP °C	160	230	280	195	
Flash Point	°C	N/A	75	110	43	ASTM D93
Aniline Point	QC	70	83	93	82	ASTM D611
Pour Point	°C	N/A	-20	5	-35	ASTM D97
Visc. 25 OC	mm/s	0.6	1.7	3.3	1.5	ASTM D445

Table 5 **Typical Wax Properties**

Property	Unit	**SX30**	**SX50**	**SX70**	**SX100**	Method
Congealing point	oC	31	50	70	98	ASTM D938
Saybolt colour	-	+30	+30	+30	+30	ASTM D196
Odour		1.5	1.0	0.5	0.5	ASTM D1833
Oil content (-32 oC)	% m	5	2.5	0.4	0.1	ASTM D721
UV absorptivity		< 0.01	< 0.01	< 0.01	< 0.01	ASTM D2008

ENGINE EVALUATION OF FISCHER-TROPSCH DESEL FUEL, PHASE I

Thomas W. Ryan, III and Daniel A. Montalvo
Southwest Research Institute
San Antonio, Texas

INTRODUCTION

Engine manufacturers and refiners have long recognized the importance of fuel quality on diesel engine performance and emissions. The Coordinating Research Council examined this issue in some detail in a series of projects designed to quantitatively document the relationships between engine performance and emissions and fuel properties and composition[1-5]. This work was performed in what has been called a "prototype" Series 60 Detroit Diesel engine. The results of this work have indicated that cetane number and aromatic content are the primary fuel properties controlling the emissions. Additional work performed at Southwest Research Institute (SwRI) has also indicated that the types of aromatic materials are more important that simply the total mass of aromatic material in the fuel[6]. This same work demonstrated that significant emissions benefits were associated with the use of diesel fuels derived from Fischer-Tropsch processing of coal.

The test protocol used in the Prototype Series 60 testing involved the use of the Federal Heavy Duty Transient Test Procedure (FTP), as specified in the Federal Register. More recently, this same engine and the FTP have been adopted as the basis for the CARB Protocol for certifying reformulated diesel fuels in California.

OBJECTIVE

The main objective of this study was to evaluate Fischer-Tropsch (FT) diesel fuel as a low emissions diesel fuel.

EXPERIMENTAL APPROACH

The work reported in this presentation involves the comparative testing of three Fischer-Tropsch diesel fuels and two different conventional petroleum derived fuels; one representing a national average low sulfur diesel fuel, and one representing a typical low aromatic content California reformulated diesel fuel. The tests were performed in the same Series 60 engine used in the CARB Protocol, following the same basic procedures as used in the protocol.

As indicated, the group of fuels included a low-sulfur emissions 2D reference fuel, identified as Fuel 2D, three FT candidate fuels identified as Fuels B1, B1, and B3, and a "pseudo" California reference fuel, designated Fuel PCR. Transient cycle emissions of HC, CO, NO_X, total particulate (PM), sulfate, soluble organic fraction (SOF) of PM, and volatile organic fraction (VOF) of PM were obtained over repeat hot-start tests.

TEST RESULTS

Figure 1 illustrates that average hot-start transient emission levels of HC, CO, NO_X, PM, and SOF obtained with Fuels B1, B2, and B3, were all lower than those using Fuels PCR and 2D. Compared to Fuel 2D, the FT fuels showing the largest decrease in emissions were Fuel B1 for HC (46%), Fuel B2 for CO (47%), both Fuels B1 and B3 for NO_X (9%), Fuel B2 for PM (32%), and both Fuels B1 and B3 for SOF (47%).

SUMMARY

The main objective of this study was to evaluate the effects Fischer-Tropsch (FT) derived diesel fuels have on emissions from a heavy-duty truck engine. A screening test procedure was used based on transient emissions measurement procedures developed by the EPA for emissions regulatory purposes.

Average emissions of HC, CO, NO_X, PM, and SOF obtained with Fuels B1, B2, B3, and PCR were all less than with reference fuel, Fuel 2D. Furthermore, all these emissions were lower with FT fuels than on Fuel PCR. Fuel B1 had lowest HC, and Fuel B2 had lowest CO. Both Fuels B1 and B3 had low NO_X, but Fuel B2 had lowest PM.

REFERENCES

1. Terry L. Ullman, "Investigation of the Effects of Fuel Composition on Heavy-Duty Diesel Engine Emissions," SAE Paper No. 892072, SAE International Fuels and Lubricants Meeting and Exposition, Baltimore, MA, Sept. 25-28, 1989.

2. Terry L. Ullman, Robert L. Mason, and Daniel A. Montalvo, "Effects of Fuel Aromatics, Cetane Number, and Cetane Improver on Emissions from a 1991 Prototype Heavy-Duty Diesel Engine," SAE Paper No. 902171, SAE International Fuels and Lubricants Meeting and Exposition, Tulsa, OK, Oct. 22-25, 1990.

3. Terry L. Ullman, Kent B. Spreen, and Robert L. Mason, "Effects of Cetane Number, Cetane Improver, Aromatics, and Oxygenates on 1994 Heavy-Duty Diesel Engine Emissions," SAE Paper No. 941020, SAE International Congress & Exposition, Detroit, MI, Feb. 28-March 3, 1994.

4. Kent B. Spreen, Terry L. Ullman, and Robert L. Mason, "Effects of Cetane Number, Aromatics, and Oxygenates on Emissions From a 1994 Heavy-Duty Diesel Engine With Exhaust Catalyst," SAE Paper No. 950250, SAE International Congress & Exposition, Detroit, MI, February 27-March 2, 1995.

5. Terry L. Ullman, Kent B. Spreen, and Robert L. Mason, "Effects of Cetane Number on Emissions From a Prototype 1998 Heavy-Duty Diesel Engine," SAE Paper No. 950251, SAE International Congress & Exposition, Detroit, MI, February 27-March 2, 1995.

6. Thomas W. Ryan III, Jimell Erwin, Robert L. Mason, and David S. Moulton, "Relationships Between Fuel Properties and Composition and Diesel Engine Combustion Performance and Emissions," SAE Paper No. 941018, SAE International Congress & Exposition Detroit, MI, Feb. 28-March 3, 1994.

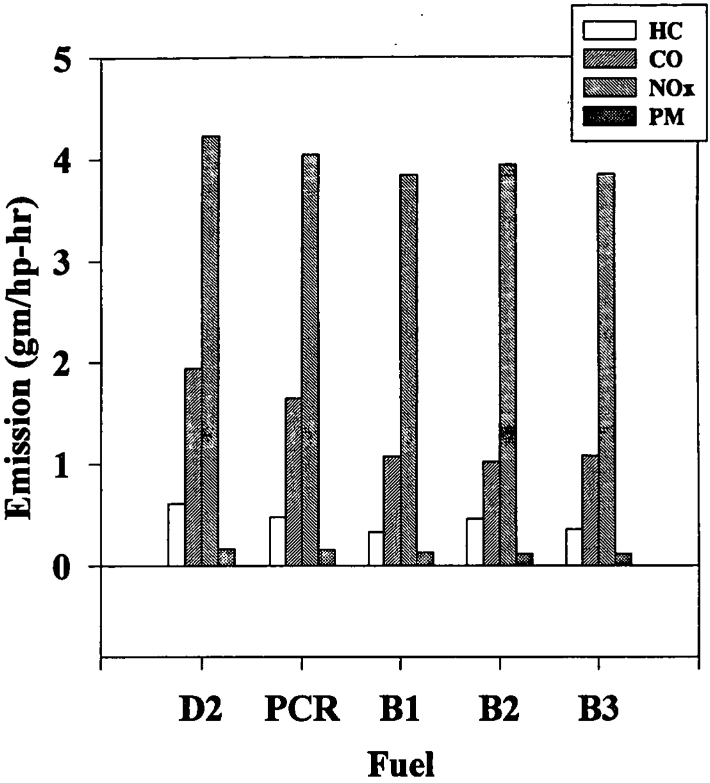

FIGURE 1. HOT-START TRANSIENT EMISSION LEVELS

DESIGN AND ECONOMICS OF A FISCHER-TROPSCH PLANT FOR CONVERTING NATURAL GAS TO LIQUID TRANSPORTATION FUELS

Gerald N. Choi, Sheldon J. Kramer and Samuel S. Tam
(Bechtel Corporation, San Francisco, CA)
Joseph M. Fox III (Consultant)

Keywords: Fischer-Tropsch, natural gas liquefaction, economics

ABSTRACT

There is considerable interest in the development of an economic process for the conversion of natural gas to liquid transportation fuels. Such a process will allow the commercialization of many remote natural gas fields which are not now viable. Under DOE sponsorship, a conceptual plant design, cost and economics were developed for a grass-roots plant using Fischer-Tropsch technology to produce about 45,000 bbls/day of liquid transportation fuels from 410 MMSCF/day of natural gas. The natural gas is converted to synthesis gas via a combination of non-catalytic partial oxidation and steam reforming. This synthesis gas is then converted to liquid hydrocarbons in a two-stage, Fischer-Tropsch slurry-bed reactor system. The Fischer-Tropsch wax and liquid hydrocarbons are upgraded to high quality naphtha and diesel blending stocks by conventional petroleum refinery processes. Economics are dependent on both plant and natural gas costs. At a location where construction costs are equivalent to the US Gulf coast and natural gas costs are low, this plant can be competitive at today's crude oil prices.

INTRODUCTION

Bechtel, along with Amoco as the main subcontractor, has developed a Baseline design (and a computer process simulation model) for indirect coal liquefaction using advanced Fischer-Tropsch (F-T) technology under DOE Contact No. DE-AC22-91PC90027. In 1995, the original study was extended to add four additional tasks; one of which was to develop a case in which natural gas, instead of coal, is used as the feedstock to produce high-quality, liquid transportation fuels. This paper describes the results of this task. It discusses the design of this plant and the economics of liquefying natural gas using F-T technology to produce liquid transportation fuels.

OVERALL PLANT CONFIGURATION

Figure 1 is a simplified block flow diagram showing the overall process configuration of the conceptual design for the natural gas-based F-T liquefaction plant. This design uses proven commercial technology for syngas generation, non-catalytic partial oxidation in combination with steam reforming. A cobalt-based catalyst in slurry-bed reactors is used for the F-T synthesis. The plant is located at a hypothetical southern Illinois mine-mouth location to be consistent with the previous coal based F-T liquefaction study. It produces about 43,200 BPD of high quality gasoline and diesel blending stocks from about 410 MMSCF/day of natural gas. In developing this natural gas case, where applicable, individual plant designs and cost estimates were prorated directly from the coal-based Baseline design.[1]

The overall natural gas-based F-T plant consists of three main processing areas; synthesis gas preparation, F-T synthesis, and product upgrading. In addition, there are eighteen ancillary offsite plants which are similar to those which were developed for the Baseline design with minor modifications as required for this natural gas case.

Synthesis Gas Preparation Area (Area 100)

This area consists of three major plants; air separation, partial oxidation, and steam reforming (sulfur is removed from the natural gas before syngas generation). Most of the syngas is generated by partial oxidation using 99.5% pure oxygen which produces a syngas with a molar H_2/CO ratio of 1.8/1. The steam reforming plant, produces a syngas with a H_2/CO ratio of 5.9/1. This is a relatively small plant. It is used only to supplement the syngas production by the partial oxidation plant by increasing the H_2/CO ratio of the total syngas going to the Fischer-Tropsch synthesis area to a H_2/CO ratio of about 1.9/1.

Fischer-Tropsch Synthesis Loop (Area 200)

This area consists of five plants; F-T synthesis, CO_2 removal, recycle gas compression and dehydration, hydrocarbon recovery, and hydrogen recovery. Hydrogen is recovered from the unconverted syngas. After satisfying the downstream hydroprocessing needs, the excess hydrogen is recycled back to the F-T reactors. The remaining unconverted syngas is used for fuel.

A cobalt-based catalyst was selected for F-T synthesis because it has negligible activity for the water-gas shift reaction compared to an iron-based catalyst, and thus, it requires a syngas with a molar H_2/CO ratio near the stoichiometric value of 2.0/1. Since methane, the principal component in natural gas, has a molar H_2/C ratio of 2.0/1, syngas produced from it has a similar H_2/CO ratio. Also, for iron-based catalyst with a high water-gas shift activity, CO_2 is the primary byproduct from the Fischer-Tropsch synthesis. With cobalt-based catalyst, water is the primary byproduct.

A total of 24 slurry-bed reactors process the syngas from Area 100. These reactors are arranged in eight trains with each train having two first-stage slurry-bed reactors feeding a single second-stage slurry-bed reactor. The unconverted syngas leaving the first-stage reactors is cooled and flashed to condense and remove liquids before being reheated and fed to the second-stage reactors. The CO conversion in each of the parallel first-stage reactors is about 56%, and in the second-stage reactors, the CO conversion is about 59%. This gives an overall CO conversion per pass of about 82%. The first-stage F-T slurry-bed reactors operate at about 428 °F and 335 psig, and the second-stage reactors operate at 428 °F and 290 psig. Excess heat is removed by the generation of 150 psig steam from tubes within the reactors.

Slurry-bed reactor sizing is based on an improved version of the kinetic reactor model which originally was developed by Viking Systems, International.[2] The primary modification to this model was the insertion of the kinetic parameters developed by Satterfield et al for cobalt-based catalyst.[3]

Product Upgrading and Refining Area (Area 300)
This area consists of eight processing plants. Fischer-Tropsch synthesis produces a wide spectrum of hydrocarbon products, similar to crude oil except that naphthenes and aromatics are absent. Upgrading is required to produce high-quality transportation fuels. For consistency with the coal-based Baseline design, Area 300 uses the same conventional petroleum processing technologies to upgrade and refine the F-T products to high quality liquid transportation fuels. This area consists of a wax hydrocracker, distillate hydrotreater, naphtha hydrotreater, catalytic reformer, C5/C6 isomerization unit, C4 isomerization unit, C3/C4/C5 alkylation unit, and a saturated gas plant. Area 300 is designed to produce maximum amounts of high-octane gasoline and high-cetane diesel blending stocks.

PLANT SUMMARY

The conceptual plant consumes about 410 MMSCF/day of natural gas and produces about 45,000 BPD of liquid products. The primary liquid products are C3 LPG, a C5-350 °F fully upgraded gasoline blending stock, and a 350-850 °F distillate. The gasoline product has a clear (R+M)/2 octane of about 88 and is basically a mixture of C3/C4/C5 alkylate, C5/C6 isomerate and catalytic reformate. The distillate product also is high quality and has a high cetane number, on the order of 70. Both products are essentially free of sulfur, nitrogen and oxygen containing compounds.

The plant uses all of the byproduct steam and fuel gas to generate electric power. In addition to supplying its entire power requirement, about 25 MW of excess electric power is sold. The only materials delivered to the plant are natural gas, raw water, catalysts, chemicals and some normal butane which is used as a feed for C4 isomerization and, subsequently, alkylation.

Following the philosophy of the previous indirect coal liquefaction study, the overall plant is designed to comply with all applicable environmental, safety and health regulations. Air cooling is maximized, wherever possible, in order to minimize cooling water requirements. A brief summary of the major feed and product streams entering and leaving this natural gas liquefaction plant is shown in Table 1.

Capital Cost Estimate
Total capital cost for this natural gas F-T plant is about 1.84 billion dollars. This is a mid-1993 cost, consistent with the coal-based F-T study. The estimated plant cost is about 40% less than that for the corresponding coal-based design. A different syngas preparation area and a smaller CO_2 removal plant account for most of the cost reduction. A brief summary of the estimated capital cost breakdown is given in Table 2.

ECONOMIC SENSITIVITY STUDIES

A discounted-cash-flow analysis on the production cost of the F-T products for a 15% internal rate of return on investment was carried out to examine the economics of the natural gas F-T design using similar financial assumptions to those employed for the coal-based F-T study.[4] Inflation projections are based on the 1996 Energy Information Administration forecast.[5] Results are expressed in terms of a crude oil equivalent price (COE) which is defined as the current hypothetical break-even crude oil price where the F-T liquefaction products are competitive with products from crude oil at a typical PADD II refinery.

The primary liquefaction products are gasoline and diesel blending stocks. Their relative values to the crude oil price were determined using a PIMS linear programming model of a typical PADD II refinery using current crude oil prices, processing costs and margins. The methodology of and results from this study are documented in a 1994 ACS paper.[6] For the Baseline coal case, the F-T gasoline blending stock had a value of 10.07 $/bbl more than crude oil, and the F-T diesel blending stock had a value that was 7.19 $/bbl more than crude oil. These same margins are used for this natural gas F-T study since the properties of these F-T gasoline and diesel blending stocks are essentially the same as those from the coal-based Baseline design.

Figure 2 shows the results of the natural gas F-T economic calculations at the southern Illinois siteas a function of the natural gas price using the economic parameters given in Table 3. With natural gas priced at 2.0 $/MMBtu, the calculated COE price is 30.7 $/bbl in current dollars. The economics are strongly dependent on the natural gas price. If natural gas is available at 0.5 \$/MMBtu, the COE drops to only 19.1 \$/bbl.

Figure 2 also shows the effects of increased capital cost (by 25 and 50%) and decreased capital cost (by 10, 25 and 50%). The former are included to show the effect of higher construction costs at remote sites. The latter are included to show the potential improvement in the economics via advanced technologies and/or location at sites where construction costs are lower. Emerging technologies for synthesis gas generation include combined autothermal reforming and ceramic membranes oxidation. These offer a potentially significant reduction in plant cost. If the syngas generation cost can be cut in half, it would correspond to a 33% decrease in total capital. As shown in Figure 2, the effect on the overall process economies would be substantial.

Figure 3 shows the portion of the calculated COE price attributable to various capital and operating cost items at the hypothetical southern Illinois site with 2.0 \$/MMBtu gas. At this gas price, the natural gas cost dominates the process economics. It contributes about 51% of the calculated COE price. Capital servicing costs account for about 34% of the COE price. Other items contribute the remaining 15% of the COE price with the operating and maintenance labor accounting for about half of this amount.

For a potential remote site where low cost natural gas is available (e.g., 0.5 \$/MMBtu), the COE distribution is very different, as shown in Figure 4. Capital servicing costs now predominate and drive the overall project economies. It constitutes about 55% of the calculated COE price. The contribution of advanced technologies to reducing the total capital cost will be greatly enhanced at a remote site.

CONCLUSIONS AND RECOMMENDATIONS

A conceptual plant design with cost estimates has been developed for a Fischer-Tropsch natural gas liquefaction plant producing 43,200 BPD of high-quality, liquid transportation fuels from about 410 MMSCF/day of natural gas. In addition, this plant produces about 1,700 BPD of liquid propane and 25 MW of surplus electric power for sale. The capital cost of this plant is estimated at about 1.84 billion mid-1993 dollars. Since US Gulf coast construction costs are somewhat lower than those in southern Illinois, the above plant at a US Gulf coast location will produce liquid transportation fuels from 2.00 \$/MMBtu gas which will be competitive with those produced from crude oil priced below 30 \$/bbl. With 0.50 \$/MMBtu natural gas, the crude oil equivalent (COE) price will drop still lower, to below 19 \$/bbl.

Thus, it is evident that attractive natural gas F-T economics currently only can be attained with low cost gas. There are numerous reserves located at remote areas and/or offshore where the gas has little value because transportation systems are not available to ship it to market. F-T synthesis offers an option to convert these resources into liquid hydrocarbons which can be easily transported to existing refineries. Under this scenario, capital servicing costs are the predominant factor driving the overall process economics. However, there are various opportunities to reduce the plant cost. Examples include:

- Simplifying the F-T design at the expense of a minor sacrifice in overall process thermal efficiency. It is also possible (and probably desirable) to eliminate and/or simplify the upgrading area to produce only a F-T syncrude which can be shipped to a conventional petroleum refinery where it would be coprocessed with crude oil.

- Integrating the F-T design with the existing infrastructure. This will be relevant, for example, for a F-T plant at the Alaskan North Slope which converts either the 'gas-cap' or 'associated' gas into a transportable syncrude. The design will utilize the considerable assets/infrastructure at the North Slope and available pipeline capacity as crude production declines to maximize cost savings.

- Investigating and incorporating more advanced processes for syngas generation such as combined autothermal reforming, fluid-bed autothermal reforming, and ceramic membranes oxidation (e.g., DOE Contract No. DE-AC22-92PC92113). Such processes have the potential to significantly reduce the plant cost and improve the economics.

- Developing a practical design for larger diameter slurry-bed reactors. The current plant design has 24 slurry-bed F-T reactors, each about 16 feet in diameter. Larger slurry-bed reactors can significantly reduce the cost of the F-T synthesis plant.

ACKNOWLEDGMENT

Bechtel, along with Amoco who was the main subcontractor for a major portion of this study, expresses our appreciation to the DOE/Pittsburgh Energy Technology Center for both technical guidance and financial funding under Contract No. DE-AC22-91PC90027.

REFERENCES:

1. Topical Report, Volume I, Process Design - Illinois No. 6 Coal Case with Conventional Refining, Baseline Design/Economics for Advanced Fischer-Tropsch Technology, Contract No. DE-AC22-91PC90027, October, 1994.
2. Final Report, Design of Slurry Reactor for Indirect Liquefaction Applications, Contract No. DE-AC22-89PC89870, December, 1991.
3. Final Report, An Innovative Catalyst System for Slurry-Phase Fischer-Tropsch Synthesis: Cobalt Plus a Water-Gas Shift Catalyst, Contract No. DE-AC22-87PC79816, July 1991.
4. Choi, G. N., Kramer, S. J., Tam, S. S. and Fox, J. M. III, "Simulation Models and Designs for Advanced Fischer-Tropsch Technology," Proceedings of the Coal Liquefaction and Gas Conversion Contractors Review Conference, Pittsburgh, PA, Aug. 29-31, 1995.
5. "Annual Energy Outlook 1996 with Projections to 2015," Energy Information Administration, Washington, DC, January 1996.
6. Marano, J. J., Rogers, R., Choi, G. N., and Kramer, S. J., "Product Valuation of Fischer-Tropsch Derived Fuels, Symposium on Alternative Routes for the Production of Fuels," ACS National Meeting, Washington, D.C., August 21-26, 1994.

Table 1

Overall Plant Major Input and Output Flows

Feed			
Natural Gas	412	MMSCF/day	(17,800 MMBtu/hr)
Raw Water Make-up	21	MMGal/day	
N-Butane	3	Mlbs/hr	(340 Bbl/day)
Primary Products			
F-T Gasoline	180	Mlbs/hr	(17,000 Bbl/day)
F-T Diesel	295	Mlbs/hr	(26,200 Bbl/day)
Propane	13	Mlbs/hr	(1,700 Bbl/day)
Electric power	592	MW-hr/day	

Table 2

Cost Breakdown of the Natural Gas Liquefaction Plant

Area	Description	Cost (MM$)	% ISBL
100	Syngas Preparation	707	66
200	F-T Synthesis	226	22
300	Upgrading & Refining	132	12
	Offsites	426	
	HO Service/Fee and Contingency	351	
	Total Cost:	1842	

The above plant costs are estimated to have an accuracy range of +/- 30%.

Table 3

Economic Parameters

N-Butane price, $/bbl	14.5
Electricity, cents/kwh	2.5
Plant life, years	25
Depreciation, years	10
Construction period, years	4
Owner's cost, % of initial capital	5
Owners initial equity, %	75
Bank interest rate, %/year	8
General inflation, %/year	3.2
Escalation above general inflation, %/year	
Natural gas	0.3
Crude oil	2.4
Electricity	-0.1
Federal income tax rate, %	34
State and local tax rates, %	0
Maintenance and insurance, % of capital	1
Labor overhead factor, % of salary	40
On-stream factor, %	90.8

Figure 1
Natural Gas Fischer-Tropsch Study
Overall Process Configuration

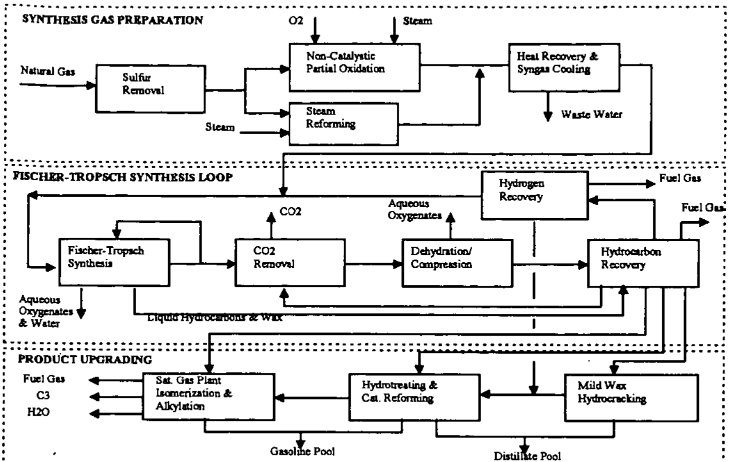
SYNTHESIS GAS PREPARATION
O2
Steam
Natural Gas
Sulfur Removal
Non-Catalytic Partial Oxidation
Heat Recovery & Syngas Cooling
Steam Reforming
Steam
Waste Water
FISCHER-TROPSCH SYNTHESIS LOOP
Hydrogen Recovery
Fuel Gas
CO2
Aqueous Oxygenates
Fuel Gas
Fischer-Tropsch Synthesis
CO2 Removal
Dehydration/ Compression
Hydrocarbon Recovery
Aqueous Oxygenates & Water
Liquid Hydrocarbons & Wax
PRODUCT UPGRADING
Fuel Gas
C3
H2O
Sat. Gas Plant Isomerization & Alkylation
Hydrotreating & Cat. Reforming
Mild Wax Hydrocracking
Gasoline Pool
Distillate Pool

Figure 2
COE Price as a Function of Natural Gas Price and Capital Cost

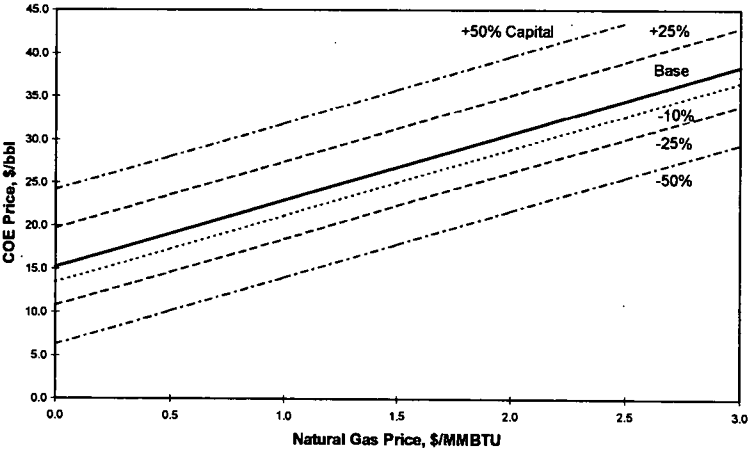

Figure 3
COE Cost Distribution @ 2.00 $/MMBTU Gas
COE = 30.7 $/bbl at Southern Illinois

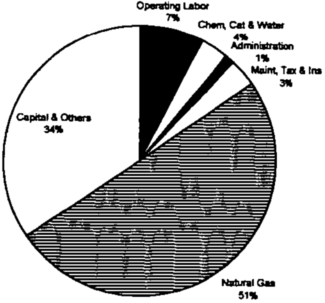

Figure 4
COE Cost Disrtibution @ 0.50 $/MMBTU Gas
COE = 19.1 $/bbl at Southern Illinois

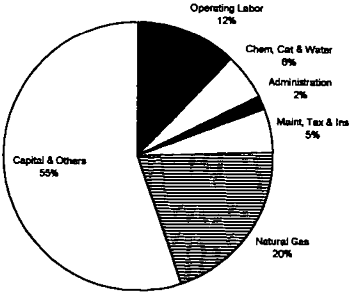

ECONOMIC CONVERSION OF NATURAL GAS TO SYNTHETIC PETROLEUM LIQUIDS

Mark A. Agee
Syntroleum Corporation
400 S. Boston, Ste. 1000
Tulsa, OK 74103

Key Words: Converting Natural Gas into Liquid Fuels Economically

Introduction. Fischer-Tropsch chemistry has been applied for more than 50 years to produce clean synthetic fuels. In recent years, the feedstock focus has shifted away from abundant, available coal to abundant but stranded natural gas. The incentive to do so is huge: Most of the world's proven and discovered, undeveloped reserves of natural gas are unmarketable in their present form. Available technology has offered few options to monetize these remote resources. If they could be economically converted into clean liquid fuels, which could then be economically transported to world commodity markets, the rewards would be enormous: Instead of being locked up, representing an expensive burden of unrecovered costs, a significant percentage of idle reserves would suddenly have the potential to be converted into booked assets of great value. At a conversion rate of 10 to 1--10 MMCF of pipeline quality gas converts to 1 barrel of synthetic product--stranded reserves are equal to several hundred billion barrels of oil.[1]

It is not surprising that a prize of that magnitude would draw a crowd. Some of the world's leading research organizations, galvanized by the prospects, have poured hundreds of millions of dollars into the search. Today, we can state with confidence, these efforts have succeeded. Fischer-Tropsch chemistry can be used in many cases to convert natural gas to synthetic liquid fuels at a cost that is competitive with conventional petroleum products at current prices. In a variety of designs developed by Syntroleum Corporation, economical conversion of gas to synthetic liquids (GTL) can be accomplished in a wide range of sites and circumstances, from small plants in remote locations, onshore and offshore, to very large "natural gas refineries."

The process is competitive at crude oil prices below $20/BBL--roughly $10/BBL less than the level previously considered to be economic for synfuels from natural gas. It has been licensed to one major international oil company for use in projects it has under consideration. Syntroleum is negotiating similar licensing arrangements with several others.

Synfuels Products and Quality. One reason for the ready marketability of synfuels is their superior quality, earning them very high marks in performance tests.[2] Synthetic fuels produced via Fischer-Tropsch chemistry are known for being among the cleanest fuels in the world. The liquid fuels produced by the new process are free of sulfur, metals, and aromatics, and are clear in appearance. They will offer industry a timely option just as refiners are seeking ways to avoid costly "have-to" compliance capital investments that are hard to justify by market conditions.

Characteristics of Syncrude. Synthetic crude made from natural gas is characteristically extremely clean. In the Syntroleum Process, the syncrude produced tends to be mostly saturated, straight chain hydrocarbons, essentially free of sulfur, aromatics and contaminants such as heavy metals commonly found in natural crude. These characteristics make syncrude a valuable blending stock for upgrading natural crude streams.

Because of its purity, high API gravity and highly paraffinic nature, syncrude can be blended with natural crude to gain significant improvements in yields and product quality in many conventional refining applications.

Synthetic Fuels. Synthetic hydrocarbon fuels are superior in many ways to products derived from conventional crude oil (Table 1). The naphtha fraction (C_5-C_8) from syncrude is highly paraffinic. The light end components are more suitable for gasoline production than the heavy end components. However, the heavy ends can be further upgraded via conventional naphtha reforming for the gasoline market.

Synthetic kerosene makes a good linear blending component for upgrading lower-quality stock (Table 1). Because of its outstanding combustion properties, synthetic kerosene can be used to upgrade petroleum kerosene products with low smoke point and high aromatics content which would otherwise be unsuitable for use as jet fuel.

Synthetic diesel, with its high cetane index and absence of sulfur and aromatics, is an ideal blending component for upgrading lower-quality stocks to meet current and future environmental specifications. Because of its superior combustion properties, synthetic diesel is an option for compliance with the most stringent current CARB and CEN standards (Table 2).

The Syntroleum Process. Alternative F-T technologies, as well as LNG, have sought to improve their economics through large plant capacities. They have focused on sizes as large as 50,000 BPD of product as a starting point, requiring 180 BCF of gas per year or approximately 5.4 TCF over a 30-year life. One recently announced proposal for a plant of that size, costing $24,000 per barrel of daily capacity, was a significant development, but limited to a small number of possible fields. Only 2% of the 4,448 identified gas fields outside the U.S. and Canada have the reserves to qualify, and some 30 of these already have significant commitments to large LNG projects.[3]

At plant capacities as small as 5,000 BPD, the Syntroleum Process offers a potential solution for almost 40% of the world's gas fields. In various combinations, the design menu can be adapted to apply to much smaller fields. The plant's relatively small footprint also lends itself to certain offshore, platform-mounted applications. Portable (barge or ship mounted) plants could allow many of the smaller offshore fields to be monetized without the need for long-term reserves.

The Syntroleum Process is a proprietary method for converting natural gas into liquid hydrocarbons (GTL). Research was aimed at developing a process that would achieve two primary objectives: (1) commercial viability with oil prices of $15 to $20/BBL, and (2) design flexibility that would permit a wide range of economic plant sizes suitable for a multitude of site conditions and a significant share of the world's remote gas fields.

The first objective was met by significantly reducing complexity and capital costs in every area of the process. This was vital because of the crucial role of capital efficiency in the economics of synfuels processes. The second was met by creating a menu of design components which, in varying combinations, can be economically applied to plant sizes ranging from as small as 2,000 BPD of liquids production--even smaller in special circumstances--to as large as 100,000 BPD.

Syntroleum uses the same two-step chemistry found in other Fischer-Tropsch processes: Natural gas is converted into synthesis gas, then the synthesis gas is reacted in a Fischer-Tropsch reactor to polymerize hydrocarbon chains of various lengths. But the Syntroleum Process is markedly different in several important ways.

Step One: Synthesis Gas Production. In typical F-T processes, more than 50% of the capital cost relates to the production of synthesis gas, usually generated from natural gas via partial oxidation with oxygen, steam reforming, or a combination of the two. These methods are relatively expensive because the production of oxygen requires an air separation plant. They also have inherent problems that must be solved in various ways to produce an acceptable ratio of hydrogen to CO in the syngas for the F-T reaction. In these approaches, nitrogen is eliminated from the syngas stream as an unwanted inert, but not in the Syntroleum Process.

The Syntroleum syngas step is based on Autothermal Reforming (ATR) with air instead of oxygen in a reactor of proprietary design. The reactor is mechanically simple, easy to start up and shut down, and relatively inexpensive to build (Figure 1). It does not require large scale to be cost effective. Its lower cost is a large contributor to the cost savings realized in the Syntroleum Process.

The ATR consists primarily of a refractory-lined carbon steel reactor vessel and a catalyst. Air and natural gas are fed in at proper ratio and pressure, producing a nitrogen-diluted synthesis gas within the desired H_2/CO ratio of approximately 2.0. The syngas ratio can be adjusted further by the introduction of a small amount of steam or CO_2 into the ATR reactor. Synthesis gas diluted with approximately 50% nitrogen raises an obvious concern that any savings from the much simpler ATR reactor would be lost due to the increased F-T reactor section needed to handle the added inert volumes. However, in the Syntroleum Process, this is not the case.

Step two: Fischer-Tropsch synthesis. Other processes have been careful to avoid the introduction of any inerts such as nitrogen. The Syntroleum Process, on the other hand, incorporates nitrogen into the process. This is possible because its F-T section has no recycle loop. The one-pass design avoids any build-up of nitrogen in the system, thus allowing the use of nitrogen-diluted syngas without impairing performance. The Syntroleum F-T reactor configuration is comparable in size but less expensive than comparable systems with recycle: The recycle compressor loop, which must handle and be rated for hydrogen service, has been eliminated (Figure 2).

Nitrogen plays a significant role in removing the large amounts of heat generated by the Fischer-Tropsch reaction. Removing the exothermic heat of reaction and controlling reactor temperatures within close tolerances is a critical element of reactor design.

Process Development, Demonstration. After 5 years' research on the process, the company obtained its first patents in 1989. This was followed by construction and operation of a 2 BPD pilot plant in 1990 and 1991. These runs were successful but confirmed the need for a proprietary catalyst system tailored to fit the unique syngas environment created by the process. Syntroleum has since developed several proprietary catalyst systems for use with different variations of the process and continues to focus a significant amount of the company's resources in this area.

The pilot plant continues to be used to evaluate process improvements, including new catalyst systems, reactor designs, and heat integration. It is also used to provide technical information necessary for scale-up and engineering of commercial plants. The company plans to maintain the pilot plant indefinitely to support future development work.

Surplus heat generated from the two reactions combined with combustion of the low-BTU tail-gas stream provides more than enough power for all plant needs. Also, there is a surplus for potential commercial sale, either as steam or electricity, if circumstances permit. The major energy consumer is compression. The energy integration is a key component of a cost effective design and the subject of several patent applications. The only other byproduct of the process is synthesized water, which can be used as boiler feed water or made potable with proper treatment.

Catalyst Technology, Downstream Processing. The process requires a special catalyst system tailored to operate in the unique syngas environment created by the ATR. Syntroleum began development of the Fischer-Tropsch catalysts optimized for such syngas in 1991. The company's high alpha catalyst system is a proprietary, highly active cobalt catalyst. It produces a waxy syncrude that is primarily uniform straight-chain hydrocarbon molecules with relatively low yields of methane (below 10%). Test runs with commercially manufactured batches have demonstrated the viability of the high alpha catalyst system at commercial scale.

Plants designed around the high alpha catalyst produce a waxy syncrude which requires hydrocracking, similar to competing processes, for the production of fuels. With conventional hydrocracking and fractionation, the syncrude can be tailored to optimize diesel yield or kerosene yield.

Work on a "chain-limiting" F-T catalyst began in 1994, with partial funding from three major oil companies. The goal was a catalyst that limits the growth of hydrocarbon chains to eliminate wax production and minimizes the production of light hydrocarbons (C_1-C_4). Recent multiple-week test runs in a fluid bed reactor yielded a product profile that indicates success.

This catalyst promises several additional efficiencies to the process configuration, including a lower operating pressure for the process, use of higher capacity fluidized-bed reactors that cannot be effectively used with the high-alpha, wax-producing catalyst, and elimination of a hydrocracking step.

Multiple Design Combinations. In keeping with initial objectives and the needs expressed by oil and gas companies, Syntroleum focused on a broad approach, one that could be adapted to a wide range of conditions and circumstances. This led to emphasis on commercialization of a menu of components:

- Two ATR (Autothermal Reforming) designs;
- Three heat integration designs which are the subject of several patent applications.
- Four Fischer-Tropsch reactor designs to allow a wide range of flexibility. For example, the "horizontal" reactor lends itself to platform, barge and ship-mounted application.
- Two F-T catalyst systems, the latest of which offers several additional cost saving changes to the process configuration.

Economics, Capital Costs. Syntroleum has collaborated with Bateman Engineering, of Denver, to develop several commercial scale design and capital cost estimates. This was done in parallel with various technical development work over the last several years. These efforts involved refining process models and evaluation of equipment designs. Considerable attention was given to alternative compression designs, reactor designs and system integration in an effort to minimize capital costs.

A 1995 study was made for a nominal 5,000 BPD first generation plant equipped to produce three fuel feedstocks (diesel/kerosene/naphtha). The estimated installed cost for the facility was $135 million. That translated to $27,000 per barrel of daily capacity, or about $3,000 below the capital cost calculated to be the break-even point for a gas-to-synfuels plant. A more recent study of a second generation design of 5,600 BPD capacity yielded a reduction to $97 million fully installed, or $17,300 per barrel of daily capacity--well within commercial range even at product prices below current levels.

Estimates encompass all process and auxiliary facilities for a complete operating plant located on the U. S. Gulf Coast, including allowance for reasonable infrastructure and utility supply to the site (i.e., gas pipeline, cooling water, rail service, etc.), capital spares, start-up expenses and the like. On-site power generation for plant loads are also included.[4]

Further cost reductions are expected from improvements in the technology which are under development. There will also be normal "learning curve" benefits from commercial experience. Significant economies of scale are achievable with the Syntroleum Process, particularly in the air compression trains. Preliminary review of a "maximum train size" configuration indicates the likelihood of constructing a 20,000 to 25,000 BPD single-train facility for $12,000 to $14,000 per barrel of daily capacity. That is the roughly the same cost as a worldscale conventional refinery--a truly revolutionary development.

Because of the limited opportunities for large plants, Syntroleum's major goal in developing this technology has been to achieve low capital costs at relatively small scales. The company is confident that, with further development, designs will be available for the majority of the world's fields. At one end of the scale is a possible 500 BPD plant for isolated areas, justified by enabling the producer not only to monetize the gas that cannot be flared, but also to produce and sell the oil shut in by the inability to dispose of the associated gas. Syntroleum currently is working with a major company to adapt a design for a 2,000 to 2,500 BPD barge-mounted plant to be installed at a very remote location; the initial estimated cost is $55 million. At the other end of the scale is the possibility of a 100,000 BPD "natural gas refinery" in an industrial area. Between these two extremes there are myriad possibilities for tapping fields now beyond the commercial reach of gas markets.

Implications. For the energy industry, the Syntroleum Process offers a new option with potential application to a wide range of situations where current technology falls short. As the new technology is applied, there will be two immediate effects: (1) supply, with a giant boost in the size and diversity of the world's oil and gas reserves, and (2) financial, as stranded reserves are converted to booked assets on the ledgers of companies and countries that own them. Refiners and power plants will have another option to satisfy their need for cleaner fuels for themselves and their customers. Meanwhile, upstream, industry will completely re-evaluate its strategy--everything from how to retarget exploration to whether to abandon LNG and heavy oil projects or pursue them in conjunction with synfuels.

These are just a few of the possibilities. Oil and gas companies, examining their own project lists and strategies, will see many others. As always happens with any new technology, the users will find applications that the developers never thought of.

REFERENCES

[1] *Oil & Gas Journal, June 19, 1995, p. 37.*

[2] Ryan, Thomas W., III, and Daniel A. Montalvo, "Emissions and Performance of Fischer-Tropsch Diesel Fuels in a Modern Heavy Duty Diesel Engine." Southwest Research Institute paper, 1996.

[3] Ivanhoe, L. F., and George G. Leckie, *Oil & Gas Journal*, Feb. 15, 1993, p. 87.

[4] Manpower requirements, labor costs estimated by Process Technical Services, Houston, specialists in start-ups and contract plant operations.

[5] Compiled from data published by Shell and Syntroleum test data.

Table 1—Typical Properties of Fuel Feedstocks from Syncrude

Property	Test Method	Unit	Naphtha[5]	Kero./JetFuel[5]	Diesel[5]
Density @ 60 °F	ASTM D1298	lb/ft^3	43.6	46.0	48.7
Distillation range	ASTM D86				
IBP		°F	109	311	394
FBP		°F	381	376	676
Sulfur	ASTM D1266	ppm	n.d.	n.d.	n.d.
Cetane number	ASTM D976	—	n/a	58	76
Smoke point	ASTM D1322	mm	n/a	>50	n/a
Flash point	ASTM D93	°F	n/a	108	190
Aromatics	ASTM D5186	%V	n.d.	n.d.	n.d.

n.d. = not detectable/below detection limits; n/a = not applicable.

Table 2—Combustion Properties of Synthetic Diesel

Property	Synthetic Diesel[5]	CARB Specs	CEN Specs
Cetane number	76	48 min.	49 min.
Density (kg/m^3)	771	n/s	820-860
Sulfur (ppm)	n.d.	500	500 (1996)
Aromatics (%m/m)	n.d.	10 max.	n/s
Cloud point (°C)	-48	-5	n/s
CFPP (°C)	-2	n/s	+5 to -20*
Distillation			
90% recovery (°C)	340	288-338	
95% recovery (°C)	350		370 max.

* Depending on climatic band chosen; n/s = no specification; n.d. = not detectable/below detection limits.

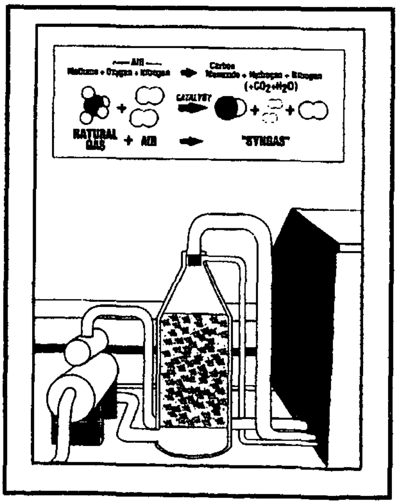
AIR
Methane + Oxygen + Nitrogen
Carbon Monoxide + Hydrogen + Nitrogen
(+CO2+H2O)
CATALYST
NATURAL GAS + AIR
"SYNGAS"

Figure 1

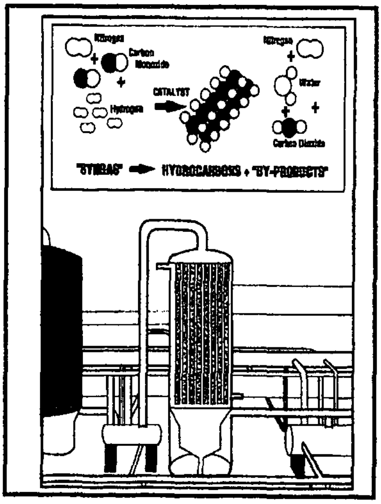
Nitrogen
Carbon Monoxide
Hydrogen
CATALYST
Nitrogen
Water
Carbon Dioxide
"SYNGAS" → HYDROCARBONS + "BY-PRODUCTS"

Figure 2

OPPORTUNITIES FOR EARLY COMMERCIAL DEPLOYMENT OF INDIRECT LIQUEFACTION

David Gray and Glen Tomlinson
MITRETEK
7525 Colshire Drive
McLean, Virginia 22102

KEYWORDS: Indirect coal liquefaction, Fischer-Tropsch Synthesis, Pioneer Plants.

Introduction:

Petroleum use worldwide is about 65 million barrels per day (MMBPD) and the Energy Information Administration (EIA) predicts that by 2015, worldwide demand will increase to between 89 and 99 MMBPD[1]. Over 55 percent of world petroleum is used in the transportation sector. Liquid hydrocarbon fuels are ideal for transportation since they are convenient, have high energy density, and a vast infrastructure for production, distribution, and end use is already in place. The estimated ultimate world resource of oil and natural gas liquids (NGL) is 2.5 trillion barrels; the sum of 1.2 trillion barrels for OPEC and 1.3 trillion barrels for non-OPEC[1]. Estimates of proven reserves of oil vary over time because more of the oil *resource* moves into the *reserve* category as a result of variations in the world oil price (WOP) and available technologies. However, the estimated ultimately recoverable world conventional oil resource (EUR) has been remarkably similar for the last 25 years. James MacKenzie of the World Resources Institute[2] cites an analysis of 40 estimates of ultimately recoverable oil, for the years 1975 to 1993, conducted by David Woodward of the Abu Dhabi Oil company. In this analysis, Woodward concluded that " there is a fair degree of consistency among the estimates with the average being 2,000 billion barrels (BBO) and 70 percent falling in the range of 2,000 to 2,400 BBO."

Mitretek has performed analyses of world oil demand and potential supply from the present until the year 2100[3]. The results of these analyses show that when the projected world oil demand is plotted on the ultimate resource curve, it becomes clear that conventional world oil production is likely to peak in a timeframe from about 2015 to 2020 and then irreversibly decline because of resource limitations.

Since oil is the primary fuel for the transportation sector, Mitretek has also examined the potential impact of the above world oil supply scenario on the U.S. transportation sector[3]. This analysis concludes that, even with a rapid penetration schedule for alternatively fueled vehicles, there is likely to be a significant shortfall in petroleum supply in the United States before 2015.

It is, therefore, essential to simultaneously pursue a number of options to mitigate the future domestic petroleum shortfall. These options are: to continue domestic exploration and production using the best technologies available, to continue to develop and deploy alternative fueled vehicles, and to continue to improve efficiencies in all sectors of transportation. Yet, even with all these efforts, this analysis indicates that the domestic demand for liquid fuels will exceed our potential sources of supply. Continuing to increase our reliance on oil imports to alleviate the shortfall is not a long term solution. Rapidly increasing oil demand worldwide will put ever increasing pressure on oil supply and the WOP will rise. The inevitable conclusion is that additional options will be necessary to insure that the U.S. will have the necessary liquid fuels supply to be able to continue its economic growth into the 21 st century. One of these additional options is to produce liquid fuels from our huge domestic coal resources.

Proposed Strategy to Deploy Indirect Coal Liquefaction:

It is estimated that continued R&D in indirect coal liquefaction can reduce the cost of coal-derived fuels from $34 per barrel to about $27 per barrel for a grass-roots stand-alone coal liquefaction facility. However, there is the opportunity to deploy indirect liquefaction plants at existing facilities, for example petroleum refineries and IGCC facilities, and greatly reduce costs. These plants integrated with existing facilities are called "entrance plants" and preliminary economic analysis has shown that they can be competitive with crude at around $19-23 per barrel. This observation that "entrance plants" have the potential to be competitive with petroleum in the short term presents an opportunity for the early commercialization of coal liquefaction. They also provide a technology bridge to the eventual deployment of stand-alone coal liquefaction facilities. However, private investors and process developers are not likely to design and construct an "entrance plant" until both technical and economic risks are acceptable. Continued bench-scale and proof-of-concept testing of indirect liquefaction technology will result in sufficient data to design and construct pioneer plants. These pioneer plants are small-scale commercial plants that will demonstrate the ability to scale the integrated technologies and thus reduce both the technical and economic risks. Once these risks have been shown to be acceptable by successful operation of pioneer plants, larger "entrance plants" would be constructed and deployed. Eventually, when the most appropriate sites for "entrance plants" have been utilized and the technologies have continued to mature and improve, stand-alone, grass-roots commercial facilities will be deployed.

Pioneer plants will be necessary to reduce technical and economic risks and allow "entrance plants," and eventually stand-alone commercial plants to be deployed. For indirect liquefaction, the pioneer plant is assumed to be located adjacent to an existing petroleum refinery and uses petroleum coke as feed to a gasification/gas cleaning plant to produce clean synthesis gas. In the simplest case, petroleum coke would probably be used as the feed but, if the plant is to be increased in size, coal can be introduced into additional gasifiers. Because the pioneer plant is located adjacent to a refinery, it is assumed that the plant will utilize some of the existing refinery facilities. In this case it is assumed that acid gas from the gas cleaning section can be processed in the existing refinery Claus unit for sulfur recovery. Also the refinery is assumed to process the waste water from the pioneer plant. The clean synthesis gas from petroleum coke gasification is passed once-through a slurry Fischer-Tropsch reactor to produce liquid fuels that are recovered in product separation, and the tail gas is sent to power generation. The pioneer plant sells electric power to the refinery and the liquid fuels are sent over the fence to the refinery for upgrading and blending. In the configuration analyzed here, 3,500 BPD of naphtha, diesel, and wax are produced together with 42 MW of power. Further additions to this pioneer plant could include pressure swing absorbers (PSA) so that hydrogen could be sold to the refinery in addition to power. The F-T unit enhances the refiner's ability and flexibility to make high value products by synthesizing high quality diesel and naphtha. The F-T diesel can be blended with FCC cycle oils to produce high cetane fuel and the naphtha can be blended in the gasoline pool or, since F-T naphtha is an excellent feed, cracked to give ethylene. The wax can be fed to a catalytic cracker to produce more high value diesel and naphtha.

Another example of a pioneer plant configuration for indirect liquefaction is one that could be located at an existing IGCC plant. The additional units required include a polishing reactor for residual sulfur removal, the F-T reactor, product recovery, and a cracker for the wax product. In this case, the IGCC plant would coproduce about 4,200 BPD of fuels in addition to 250 MW of power. Because the synthesis gas from the coal gasifier is now being fed to the F-T unit, natural gas must be imported for combustion in the gas turbines to keep the power output at 250 MW. The synthesis gas is passed once-through the F-T reactors and the tail gas, after product separation is used in the turbines. As the future cost of natural gas increases, it would be less expensive to add additional coal gasifiers and phase out use of the natural gas.

There are both technical and economic risks associated with the design, construction, and operation of the pioneer plant configurations outlined above. The desired strategy is to minimize federal government expenditures in the deployment of these technologies. For this to happen, the private sector must feel confident enough to take the initiative in deployment. If the commercial sector is to take the lead in this deployment, both types of risk must be acceptable. The objective of the pioneer plant concept is to bring the level of risk into an acceptable regime so that commercial entities will continue deployment through future "entrance" and stand-alone facilities. The government (federal or state) must encourage the private sector to finance the design, construction, and operation of the pioneer plants by providing financial incentives that will allow the products to yield an acceptable return on the investor's capital.

For the indirect pioneer plant located adjacent to the refinery a detailed economic analysis has been performed. It is shown that adequate return on investment can be obtained for these plants if it is assumed that these high quality F-T liquids can command a premium of 20 cents per gallon ($8.40 per barrel) over conventional petroleum. If the average of the nation's state fuel tax (17 cents per gallon) is exempted, effectively making the total incentive 37 cents per gallon, then the ROE rises to over 20 percent. If both state and federal fuel taxes are exempted, then a ROE of over 25 percent would be realized from this investment. Exemption of fuel taxes would appear to result in a net loss in revenue to the government. However, although this is true for the first few years of plant operation, this is generally not so if revenues over the entire 25 year life of the plant are considered. Once the pioneer plant is constructed and operating, the objectives would be for this plant to, not only confirm proof-of-concept integrated operations so that the technical risk is reduced, but also to operate for 25 years as a commercial entity so that the investors would reap the expected ROE. Even if the WOP remains at the low level of projection ($16 per barrel) for the life of the plant, taxes accruing to the government are greater than the cost of incentives to the government. The net result is that in all of these cases the government's net revenue is positive.

Conclusion:

It is concluded that domestic coal is a viable future alternative feedstock to petroleum for the production of high quality transportation fuels that are compatible with the existing liquid fuels infrastructure. These fuels are high quality distillates that in many cases are higher quality than current petroleum fuels. It is recommended that the current program of research and development be continued and extended so that sufficient performance data can be obtained for the design of "pioneer" plants. These plants would be located adjacent to existing facilities, for example, refineries or IGCC plants, and would be operated to demonstrate the integrated technical feasibility of the configurations. These plants would be constructed with private capital and, although incentives may be provided by state or the federal government, net revenues to the government, over the life of the plant, as a result of taxes on net profits would be positive. Once technical risks have been reduced as a result of "pioneer" plant operations, the continued deployment of coal liquefaction technologies would proceed with no further government involvement based on economic feasibility under market conditions.

This project is funded by the United States Department of Energy under contract number DE-AC22-95PC95054.

References:

1) Annual Energy Outlook 1996 With Projections to 2015. Energy Information Administration January 1996. DOE/EIA-0383(96).
2) MacKenzie, James J., *Oil as a Finite Resource: When is Global Production Likely to Peak?* Paper from the World Resources Institute March 1996.
3) Gray, David, and Glen Tomlinson, *Rationale and Proposed Strategy for Commercial Deployment of Coal-Derived Transportation Fuels,* Mitretek Report MP 96W0000209, June 1996.

CAN CARBON DIOXIDE BE REDUCED TO HIGH MOLECULAR WEIGHT FISCHER-TROPSCH PRODUCTS?

Imre Puskas
Research Services, 939 Brighton Drive
Wheaton, IL 60187. Tel.(630) 653-4897

Keywords: clean fuel production, carbon dioxide, Fischer-Tropsch products, methanol, remote natural gas.

INTRODUCTION.

Our interest in the title originates from our efforts to develop an economically viable clean fuel process from natural gas. Natural gas, with its high calorific value (210.8 kcal/g-mol methane) is one of the most preferred fuels from the environmental point of view because of its clean burning characteristics. However, natural gas found in remote areas, far from markets, inaccessible to pipeline transportation, cannot be readily utilized. Currently several alternatives are practiced for remote natural gas utilization (1). Natural gas can be liquified by cooling to its boiling point (-163°C) and shipped in refrigerated containers. Natural gas can also be converted to methanol or hydrocarbon liquids (syncrude) or ammonia at its source, and these products shipped to market.

Both methanol and the Fischer-Tropsch (FT) hydrocarbon liquids are "clean fuels". Their fuel uses have been evaluated (2,3). Currently they cannot compete with the less expensive crude oil-derived fuels. Methanol commands a higher price as a "chemical", but this market is relatively small (estimated 27 MM tons per annum, worldwide) compared to the huge fuel market. Increasing percentage of the methanol production originates from remote gas using giant plants (800-975 M ton/annum capacity), taking advantage of the low gas costs and the economics of large scale production. Historically, the methanol market can be characterized by periods of shortages and periods of overproduction and low capacity utilization. Recently we proposed the development of a methanol-syncrude coproduction technology (4) which could keep the methanol plants running at full capacity even in case of methanol oversupply. The co-production scheme of Figure 1 would provide both economic and technological advances. In the first step, the compressed synthesis gas would be partially converted to methanol. This reaction has equilibrium limitations. The unconverted syngas from the methanol reactor would be converted to hydrocarbons. This latter reaction has no equilibrium limitations. We are currently working on the details of a research and development plan to demonstrate the viability of a co-production technology. The key to success depends on the demonstration that the effluents of the methanol reactor (a mixture of H_2, CO and CO_2) can be efficiently converted to high molecular weight FT products. The percieved difficulty is caused by the presence of carbon dioxide, which is known to yield preferentially methane rather than high molecular weight FT products in reductions (5). This study was undertaken to provide a stimulus for the development of a methanol-syncrude coproduction technology. Reported cases of carbon dioxide reductions to reasonably high molecular weight FT products already exist. The study should be helpful to set the stage for further progress.

HISTORICAL OVERVIEW OF CARBON DIOXIDE REDUCTIONS.

The reactions, utilization and sources of carbon dioxide have recently attracted considerable interest because of the possible ecological effects arising from large scale carbon dioxide emissions into the atmosphere. An information update is provided in very recent reviews by Xiaoding and Moulijn (6) on CO_2 reactions and usage; by Krylov and Mamedov (5) on its heterogeneous catalytic reactions; by Jessop, Ikariya and Noyori (7) on its homogeneous catalytic hydrogenations; by Tanaka on its fixation catalyzed by metal complexes (8); and by Edwards on its potential sources and utilizations (9). One of the most important reactions of carbon dioxide is its reduction to methanol:

$$CO_2 + 3H_2 \xrightleftharpoons{\text{Cu-ZnO, 200-260°C, 5-10 MPa}} CH_3\text{-}OH + H_2O \qquad [E-1]$$

Although carbon dioxide has been reduced to methanol in the past in commercial operations (10,11), current methanol plants use mixtures of carbon dioxide and carbon monoxide. An alternative potential use of carbon dioxide would be its complete reduction to methane or to mixtures of Fischer-Tropsch type hydrocarbons:

$$CO_2 + 4H_2 \xrightarrow{\text{Ni (or Co, Fe, Ru), 250-400}^{\circ}\text{C}} CH_4 + 2H_2O \qquad [E-2]$$

$$nCO_2 + 3nH_2 \xrightarrow{\text{Fe or Co (Ru, Ni), 200-300}^{\circ}\text{C}} (CH_2)_n + 2nH_2O \qquad [E-3]$$

Franz Fischer and coworkers were the first to try to reduce carbon dioxide to hydrocarbon oils, after their development of hydrocarbon synthesis from carbon monoxide. They have found, that carbon dioxide gives preferentially methane, with some gaseous homologues (12). However, liquid and solid hydrocarbons were also obtained in some experiments (13). These early reports have noted, that carbon monoxide was a reaction intermediate (12) and that liquid hydrocarbons were observed in those experiments, when the catalyst was alkalized or it contained a Cu component (13).

In the last decades, many chemists and surface scientists have extensively studied the reduction of carbon dioxide to hydrocarbons and the chemisorption of carbon dioxide on catalytic surfaces. It is out of the scope of this study to review the literature. However, a restricted number of references are cited (14-35) to sample the diversity of worldwide interests. The citations exclude the literature on carbon dioxide reductions to hydrocarbons which proceed via methanol intermediate.

The cited studies unanimously agree with the early conclusions that carbon monoxide is an intermediate formed by the reverse Water Gas Shift (WGS) reaction:

$$CO_2 + H_2 \xrightleftharpoons{\text{catalyst}} CO + H_2O \qquad [E-4]$$

The reduction of carbon monoxide proceeds by the methanation reaction or FT synthesis. Falconer and Zagli have proposed (34) that the preferential formation of methane over higher hydrocarbons is caused by the high H_2:CO ratio on the catalyst surface. While the major product was methane in most of the studies, a few cases of liquid hydrocarbon formation were also reported. Table 1 compiles the best examples of higher hydrocarbon formations. In the Table, we have converted the reported hydrocarbon selectivity data to Anderson-Schulz-Flory (ASF) growth probability values (alphas) to provide a basis for easy comparison of the product molecular weight distributions. ASF alpha values in the 0.6-0.7 range have been achieved, mostly on potassium-promoted Fe catalysts. Kuester (13) has evaluated different variations of unsupported, alkalized Co and Fe catalysts. In their work, reported in 1936, the formation of solid hydrocarbons (waxes) was often observed. Unfortunately, the reported product analyses were qualitative in nature and we were unable to derive chain growth probability values for product characterization. However, the isolation of waxes suggests that the chain growth probability values must have been substantially higher than 0.70, and probably were the highest in Table 1. In the penultimate example of Table 1, the primary olefinic products were converted to aromatic hydrocarbons over the ZSM-5 component of the catalyst. The last example of Table 1 is a case of higher hydrocarbon formation over Rh/Nb_2O_3. This appears to be an interesting case, since Rh is not known for FT catalysis.

In order to understand better how CO_2 reduction can be channeled toward higher hydrocarbon formation, relevant fundamental knowledge on the WGS and FT reactions will be reviewed and discussed below.

THE REVERSE WATER GAS SHIFT REACTION STEP.

The reduction of carbon dioxide to carbon monoxide, known as the reverse WGS reaction [E-4], has been extensively studied (36-39) because of its industrial importance in synthesis gas reactions and hydrogen manufacture. The most efficient heterogeneous catalysts for the WGS reaction are the Cu-based catalysts, particularly Cu-Zn systems, the iron oxide based catalysts and the alkalized, sulfided Co-Mo catalysts (39). Other metals, oxides also have some catalytic effect, but they have received much less attention. However, alkalization was found to increase substantially the WGS activity of many substances (39). The alkalized FT catalysts have been extensively studied (13,40-43). Their WGS activity has been long known, but most of the cited studies focussed on the effect of alkali promotion on the changes in the rate and the products of the FT reaction. The alkalized FT catalysts seem to be excellent candidates for the reduction of carbon dioxide to FT hydrocarbons as the examples of Table 1 also suggest. Surface scientists have found (44-45) that alkalization of FT catalysts changes the relative chemisorptions of CO and H_2 and that alkalization activates the surfaces for CO_2 chemisorption (24,46).

Carbon dioxide hydrogenation to carbon monoxide [E-4] is a reversible reaction and leads to equilibrium. The equilibrium is independent of the pressure, but is very much influenced by the temperature. In the temperature ranges useful for the FT reaction, the equilibrium is not favorable. Figure 2 illustrates the equilibrium CO_2 conversions as a function of the temperature for 1:1, 3:1 and 4:1 H_2:CO_2 gas compositions. Higher CO_2 conversion can be obtained if the H_2 reagent is used in stoichiometric excess. The equilibrium will be also favorably shifted if the CO is removed from the system. This happens during reductions to the hydrocarbon stage.

THE FISCHER-TROPSCH REACTION STEP.

The FT reaction (E-3) has been very extensively studied because of its commercial significance and because of its scientific complexity and diversity. This brief review will be restricted to certain aspects of FT chemistry which are relevant to our objectives.

In first approximation, the products of the FT synthesis are defined by a single parameter, the chain growth probability (α or alpha) according to the ASF equation:

$$C_n = (\ln^2 \alpha) n \alpha^n \qquad \text{(E-5)}$$

where C_n is the carbon selectivity (mass fraction in the ideal case when the products are olefins) of the product with n carbon number and α is the chain growth probability. In practice, a multiplicity of α-s is produced, but an "averaged α" still reasonably defines the products unless the range of the α-s is very broad (47). Deviations from the AFS distribution have been widely reported. Some of the deviations are predictable and well defined (48); others, notably the C1 selectivities, are not well defined.

For the purpose of this treatment, it is proposed, that methanation (E-2) is an extreme case of the FT reaction (E-3) when the chain growth probability value is zero or very low. This understanding seems to be supported by the numerous reports that small amounts of ethane and propane are usually also observed during methanation. The methanation catalysts are very active hydrogenation catalysts, and they hydrogenolize the metal-C1 intermediates on the catalyst surface before they could grow. Furthermore, the methanation catalysts can also hydrogenolize the higher hydrocarbons already formed, which reactions also produce methane. Because of these reactions, the ASF equations may increasingly fail to define the product distributions as the chain growth probability value decreases.

Recently we have proposed for Co/SiO_2 catalysts (47), that the chain growth probability is a function of the catalyst, of the reagent and inert concentrations and of the temperature of the catalyst surface:

$$\alpha = f(C, S_1, \ldots, S_i, T) \qquad \text{(E-6)}$$

Even though the function f cannot be defined, it may be beneficial to review our qualitative knowledge about the factors which together should define α. In E-6, C is the catalyst factor which is composed of numerous elements. The catalytic metal is important. Co, Fe and Ru are known to be able to produce very high α values. There are reports in the literature (49-51) suggesting that the dispersion of the metal can influence chain growth. Promoters incorporated into the catalysts can also influence chain growth. Alkali metal salts, particularly K salts, were found to greatly increase chain growth (13,40-43). In addition, alkalization had a tremendous influence on the reaction characteristics by changing the relative strengths of H_2, CO and CO_2 chemisorptions. The hydrogenating character of the catalyst was reduced by alkalization, resulting in high olefin yields.

In E-6, $S_A,...S_Z$ represent the concentrations of the reagents and inerts (including products). The question is how to define these concentrations in light of the knowledge, that in most FT reactions diffusion controls the rates (47). Due to complex diffusion effects, the concentrations of the components in the immediate vicinity of the catalyst surface might be quite different, than their concentrations in the bulk gas phase. To eliminate the need for considering diffusion effects, $S_A,...S_Z$ concentrations represent the concentrations of components A to Z in the immediate vicinity of the catalyst surface. The values of $S_A,...S_Z$ are related to their respective bulk gas phase concentrations and are dependent on the prevailing diffusional conditions. Of course, their values can be changed by changing the pressure of the system. Qualitative examples on the influence of component concentration, pressure, diffusion on the chain growth probability are available in the literature. Thus, increasing H_2:CO ratio was shown to give lower alpha values (47). Dilution of the feed with inert gases was also shown to result in lower chain growth probability (47). Diffusional changes were also suggested for observed changes in rate and chain growth probability (52).

The influence of the reaction temperature (T) on the value of the chain growth probability has been long known. Recently we have shown, that over Co catalysts, the alpha value sharply decreases with increasing T (47). Over alkalized Fe catalysts, as reviewed by Dry (43), the effect of T appears to be much more gradual. With these catalysts, chain growth probability of about 0.7 can be obtained even over 300°C. In Table 1, we can see an example of 0.72 chain growth probability from CO_2 reduction at 400°C over a "heavily alkalized" Fe catalyst.

CATALYST AND PROCESS DESIGN REQUIREMENTS.

From the above review it is clear, that a combination of appropriate catalyst design and process design is required for obtaining high molecular weight FT products in CO_2 reductions. The catalyst must contain a WGS component and a FT component. The WGS component must provide fast rates for CO formation and accumulation. Furthermore, the surfaces must be modified for obtaining a proper balance in the chemisorptions of CO_2, CO and H_2. Concerning the process design, the process parameters (T, P, SV, feed composition) need to be optimized for the individual catalyst to provide the most favorable H_2:CO ratios on the catalyst surface for high molecular weight FT products. Conceptually, diffusion control might also serve to regulate the H_2:CO ratio. If gas phase diffusion controls the reagent concentrations on the catalyst surface, the surface is expected to be enriched in hydrogen, because of its high diffusivity arising from its small molecular size [52]. If diffusion through liquids were to control the reagent concentrations on the catalyst surface, the excessive hydrogen concentration on the catalyst surface may be avoided, due to differences in the solubilities of the reagents in hydrocarbon liquids [53]. We are optimistic that utilization of knowledge in catalyst and process design will lead to significant increases in the ASF growth probability values during CO_2 reductions.

REFERENCES.

1 J.M. Fox, Catal.Rev.-Sci.Eng., 35 (1993) 169.
2 M.D. Jackson and C.B. Moyer in Encyclopedia of Chemical Technology, 4th Ed., Vol 1, p.826. Wiley, New York, 1991.
3 P.J.A. Tijm, ACS Fuel Division Preprints, 39 (1994) 1146.
4 I. Puskas, Chemtech, December 1965, p.43.
5 C.V. Krylov, A.Kh. Mamedov, Rus.Chem.Rev., 64 (1995) 877.

6 X. Xiaoding, J.A. Moulijn, Energy&Fuels 10 (1996) 305.
7 P.J. Jessop, T. Ikariya, R. Noyori, Chem.Rev., 95 (1995) 259.
8 K. Tanaka in Advances in Inorganic Chemistry, Ed. A.G. Skyes, Vol. 43, p. 409. Academic Press, San Diego, 1995.
9 J.H. Edwards, Catal.Today, 23, 59 (1995).
10 M.L. Kastens, J.F. Dudley, J. Troeltzsch, Ind.Eng.Chem., 40 (1948) 2230.
11 Anonymous, Chem.Eng., February 11, 1980, p. 49.
12 H. Kuester, Brennst.Chem., 17 (1936) 203.
13 H. Kuester, Brennst.Chem., 17 (1936) 221.
14 P.H. Choi, K-W. Jun, S-J Lee, M-J Choi and K-W Lee, Catal. Lett., 40 (1996) 115.
15 J.A. Fisher and A.T. Bell, J.Catal., 162, (1996) 54.
16 G. Froehlich, U. Kestel, J. Lojewska, T. Lojewski, G. Meyer, M. Voss, D. Borgmann, R. Dziembaj, G. Wedler, Appl.Catal., A134 (1996) 1.
17 S. Mori, W-C. Xu, T. Ishidzuki, N. Ogasawara, J. Imai, K. Kobayashi, Appl.Catal., A137 (1996) 255.
18 K-W Jun, S-J Lee, M-J Choi, K-W Lee, ACS Fuel Division Preprints 41 (1995) 1411.
19 Y. Huang, X. Meng, Z. Dang, S. Weng and C. Zhang, J.Chem.Soc. Chem.Commun., 1995, p. 1025.
20 Y. Kou, Z-h. Suo, J-z. Niu, W-z. Zhang, H-l. Wang, Catal.Lett., 35 (1995) 271.
21 U. Kestel, G. Froehlich, D. Bergmann, G. Wedler, Chem.Eng. Techn. 17 (1994) 390.
22 J-F. Lee, F-S. Chern, M-D. Lee and T-Y Dong, Can.J.Chem.Eng., 70 (1992) 511.
23 T. Kai, T. Matsumura, T. Takahashi, Catal.Lett., 16 (1992) 129.
24 F. Solymosi, J.Mol.Catal., 65 (1991) 337.
25 T. Inui, T. Takeguchi, Catal.Today, 10 (1991) 95.
26 T. Suzuki, K. Saeki, Y. Mayama, T. Hirai, S. Hayashi, React. Kinet.Catal.Lett., 44 (1991) 489.
27 C-K. Kuei, M-D. Lee, Can.J. Chem. Eng., 69 (1991) 347.
28 M-D Lee, J-F Lee, C-S. Chang, Bull.Chem.Soc.Jpn., 62 (1989) 2756.
29 F. Nozaki, T. Sodesawa, S. Satoh, K. Kimura, J.Catal., 104 (1987) 339.
30 K.R. Thampi, J. Kiwi, M. Graetzel, Nature, 327 (1987) 506.
31 A.D. Thomsett, T. Hagiwara, A. Miyamoto, T.Inui, Appl. Catal., 26 (1986) 391.
32 G.D. Weatherbee, C.H. Bartholomew, J.Catal., 87, (1984) 352.
33 J. Barrault, C. Forquy, J.C. Menezo, R. Maurel, React.Kinet. Catal. Lett., 17 (1981) 373.
34 J.L. Falconer, E. Zagli, J.Catal., 62 (1980) 280.
35 D.J. Dwyer, G.A. Somorjai, J.Catal., 7 (1978) 291.
36 C.V. Ovesen, B.S. Clausen, B.S. Hammershoi, G. Steffensen, T. Askgaard, I. Chorkendorff, J.K. Norskov, P.B. Rasmussen, P. Stoltze, P. Taylor, J.Catal., 158 (1996) 170.
37 C. Rhodes, G.J. Hutchings, A.M. Ward, Catal.Today, 23 (1995) 43.
38 S-I. Fujita, M. Usui, N. Takezawa, J.Catal., 134 (1995) 220.
39 D.S. Newsome, Catal.Rev.-Sci.Eng., 21 (1989) 275.
40 D.B. Bukur, D. Mukesh, S.A. Patel, Ind.Eng.Chem.Res., 29 (1990) 194.
41 L. Koenig, J. Gaube, W. Meisel, P. Guetlich, W. Gerhard, C. Plog, Ber.Bunsenges.Phys.Chem., 91 (1987) 116.
42 G. Henrici-Olive, S. Olive, J.Mol.Catal., 16 (1982) 116.
43 M.E. Dry in Catalysis Science and Technology, J.R. Anderson and M. Boudart, Eds., Springer Verlag, Berlin, 1981, Vol 1, p.159.
44 M.E. Dry, T. Shingles, L. Boshoff, G.J. Oosthuizen, J.Catal., 15 (1969) 190.
45 J. Benzinger, R. Madix, Surf.Sci. 94 (1980) 119.
46 G. Meyer, D. Borgmann, G. Wedler, Surf.Sci., 320 (1994) 123.
47 R.S. Hurlbut, I. Puskas, D.J. Schumacher, Energy&Fuels, 10 (1996) 537.
48 I. Puskas, R.S. Hurlbut, R.E. Pauls, J.Catal., 139 (1993) 591
49 A.S. Lisitsyn, A.V. Golovin. V.L. Kuznetsov, Yu.I. Yermakov, Cl Mol.Chem., 1 (1984) 115.
50 K. Fujimoto, T. Nobusawa, T. Fukushima, H. Tominaga, Bull. Chem.Soc.Jpn., 58 (1985) 3164.
51 C.S. Kellner, A.T. Bell, J.Catal., 75 (1982) 251.
52 I. Puskas, B.L. Meyers, J.B. Hall, Catal.Today, 21 (1994) 243
53 J.S. Chou and K-C. Chao, Ind.Eng.Chem. Res., 31 (1992) 621.

Table 1. Reported Examples of Carbon Dioxide Reductions to Higher FT Hydrocarbons.[a]

Catalyst	T (°C)	P (kPa)	% CO_2 conversion[b]	α value[c]	Reference
Fe-K/Al_2O_3	400	2026	69.6; 66.9	0.72	14
Fe-K/Al_2O_3	300	1013	57.7; 50.4	0.66	18
Fe-Mn-K	320	1013	33.8; 29.0	0.56	22
Fe-K	320	1013	34.7; 28.4	0.65	28
Fe-Cu-KCl/ TiO_2-Al_2O_3	270	1520	10.0; 5.3	0.68	33
Co,Fe-Cu,K	150-250	101	?	see text	13
Fused Fe-ZSM-5	350	2100	38.1; 32.6	see text	27
Rh/Nb_2O_5	350	101	11; 10	0.21	29

[a] The H_2/CO_2 feed ratios varied between 4:1 and 1:1.

[b] The first number gives the total conversion (CO + hydrocarbons); the second number the conversion to hydrocarbons.

[c] Our best estimates of the chain growth probabilities from the reported data, unless provided in the publication.

Figure 1. Conceptual Methanol-Syncrude Coproduction Scheme.

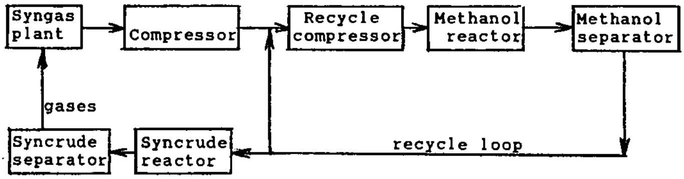
Syngas plant
Compressor
Recycle compressor
Methanol reactor
Methanol separator
gases
recycle loop
Syncrude separator
Syncrude reactor

Figure 2. CARBON DIOXIDE CONVERSIONS IN REVERSE WGS EQUILIBRIA

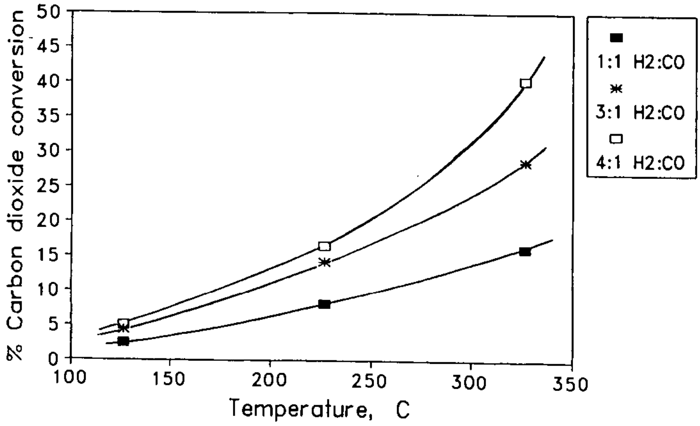

Table 1. Reported Examples of Carbon Dioxide Reductions to Higher FT Hydrocarbons.[a]

Catalyst	T (°C)	P (kPa)	% CO_2 conversion[b]	α value[c]	Reference
Fe-K/Al_2O_3	400	2026	69.6; 66.9	0.72	14
Fe-K/Al_2O_3	300	1013	57.7; 50.4	0.66	18
Fe-Mn-K	320	1013	33.8; 29.0	0.56	22
Fe-K	320	1013	34.7; 28.4	0.65	28
Fe-Cu-KCl/ TiO_2-Al_2O_3	270	1520	10.0; 5.3	0.68	33
Co,Fe-Cu,K	150-250	101	?	see text	13
Fused Fe-ZSM-5	350	2100	38.1; 32.6	see text	27
Rh/Nb_2O_5	350	101	11; 10	0.21	29

[a] The H_2/CO_2 feed ratios varied between 4:1 and 1:1.

[b] The first number gives the total conversion (CO + hydrocarbons); the second number the conversion to hydrocarbons.

[c] Our best estimates of the chain growth probabilities from the reported data, unless provided in the publication.

Figure 1. Conceptual Methanol-Syncrude Coproduction Scheme.

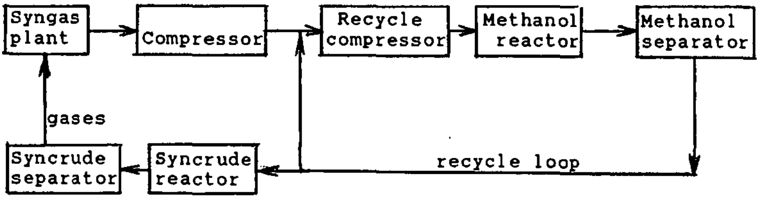
Syngas plant
Compressor
Recycle compressor
Methanol reactor
Methanol separator
gases
recycle loop
Syncrude separator
Syncrude reactor

Figure 2. CARBON DIOXIDE CONVERSIONS IN REVERSE WGS EQUILIBRIA

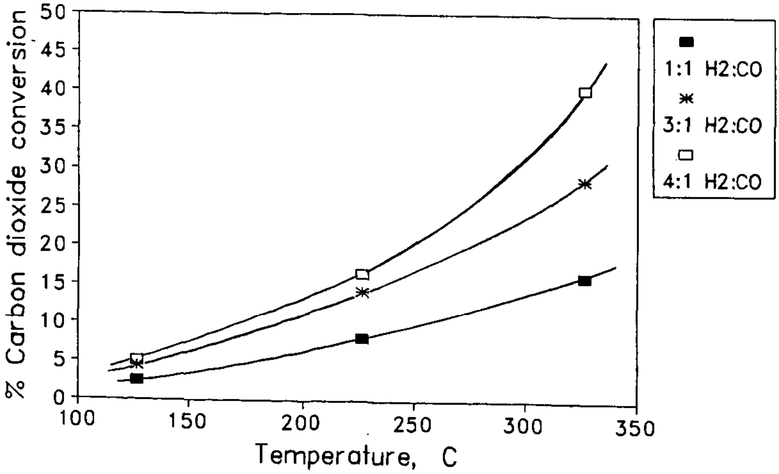

IMPROVED DIMETHYL CARBONATE SYNTHESIS AND PROCESS DESIGN VIA OXIDATIVE CARBONYLATION OF DIMETHYL ETHER METHANOL MIXTURES.

Gary P. Hagen, Arun Basu, Michael J. Spangler, and Michael A. Pacheco
Amoco Corporation
Amoco Research Center
Naperville, Illinois

Keywords: dimethyl carbonate synthesis, dimethyl ether, process design

INTRODUCTION

Enichem has commercialized a continuous solution/slurry-phase process for preparation of dimethyl carbonate (DMC) via the copper (II)-catalyzed oxidative carbonylation of methanol.(1) As of 1993 the capacity of this plant is 22 million pounds/year with worldwide demand approximately half of this amount. Recently in Japan Ube industries has completed construction of a semicommercial plant with a capacity of 11-22 million pounds per year.

DMC has strong growth potential as a phosgene replacement in some applications and as a high-oxygen high-octane fuel additive . As a phosgene replacement, there is a strong environmental incentive to use DMC since it would replace a very toxic compound with a relatively nontoxic one and eliminate environmental concerns resulting from hydrogen chloride production and recycle.

DMC also has strong potential to replace part of the growing worldwide MTBE market, which is expected to reach 66 billion pounds/year by the end of the century. As a gasoline blending agent, DMC has an oxygen content of 53% and a blending octane value of 105 (R+M/2), and these high values dictate a somewhat higher overall value for DMC in comparison to MTBE.

The key to entering this market and the phosgene replacement market lies in the development of an efficient low-cost DMC process based on inexpensive starting materials. Its current cost of $1.40/lb (non-contract) is prohibitively expensive. There are inherent problems in the Enichem process which limit per-pass methanol conversion to about 20% as the result of coproduction of water. This coproduction also results in catalyst degradation/deactivation and hardware corrosion. Production rates of 0.1 LHSV are reported for this system. Similar problems also exist in gas-phase processes such as that developed by Dow Chemical which utilize a copper (II) catalyst supported on carbon. Catalyst modifications have reportedly solved some the deactivation problems but methanol conversion is still limited to about 25%.

BACKGROUND AND OBJECTIVES

Liquid and gas-phase processes for synthesis of DMC via Cu(II)-catalyzed oxidative carbonylation of methanol (MeOH) offer limited reactor performance as the result of the effects of water formed as a coproduct.(2) Reactor water inhibits the catalytic reaction and limits reactant conversion to 30-40%. In halide-containing fixed bed catalyst systems water leaches halide away from the catalyst resulting in long-term deactivation and excessive corrosion of metallic reactor and downstream hardware components. A major goal of this project is to limit water formation and improve gas-phase reactor performance by incorporation of dimethyl ether (DME) as a dehydrated methanol equivalent into the reactor feedstream. DME is less expensive to produce than MeOH on a methanol-equivalent basis and its oxidative carbonylation to DMC would not produce water as a coproduct.

RESULTS AND DISCUSSION

A catalyst consisting of $CuCl_2$/C (Darco-active carbon), known to be active for the oxidative carbonylation of methanol/CO to DMC was found to be inactive for oxidative carbonylation of DME. At all conditions tested, low levels of CO_2 was the only product detected. A catalyst consisting of $CuCl_2$/AMSAC (an acidic molecular sieve) was also inactive and produced significantly more CO_2, suggesting that the sieve-supported Cu(II) species was more of a deep oxidation catalyst than the C-supported material. In the presence of a small amount of water added to promote initial hydrolysis of DME to methanol, the sieve-based catalyst generated a significant amount of MeOH in addition to the CO_2 but no DMC product. A third catalyst, consisting of an admixture of $CuCl_2/C$ and AMSAC was tested with DME/water feed. In this case methanol was formed but with no DMC production. Very little CO_2 was formed with this catalyst so returning the Cu(II) to the carbon support eliminated the deep oxidation activity.

Productive results were obtained with the admixture catalyst and with a DME/MeOH cofeed consisting of DME/MeOH/CO/O_2 (1/1.1/7.2/1.2 mole ratio). Throughout a 1100-minute test, carried out at 126°C, conversion of DME was steady at 30-33%. Methanol conversion was **negative**, at -20% to -30%, thus indicating net production of methanol via hydrolysis of DME. Two principle products, DMC and dimethoxymethane (DMM), were formed, each in about 50% selectivity, and methyl formate and methyl chloride were observed in trace quantities. The net conversion of the total methoxy functionality (CH_3O) in the feed to take into account the negative conversion (or production) of methanol has been calculated. This value ranged from 10-16% over the course of the study. To our knowledge this finding represents the first known net conversion of DME to DMC in an oxidative carbonylation reaction.

The high production of DMM in this study was not anticipated. . The formation of this compound, the dimethyl acetal of formaldehyde, suggests that some of the methanol has undergone conversion to formaldehyde and subsequently reacted with methanol to form the acetal. Acidic molecular sieves are well known catalysts for acetal formation, and this reaction would be heavily favored in a low-water reaction environment.

At a more optimum level of $CuCl_2$ (7.6% Cu) and with a new bimodal carbon support, a developmental material obtained from the Mega Carbon Company, significantly higher conversions were obtained with higher selectivities to the desired DMC product. Results are shown in Figure 1. Throughout the course of a 900-minute study, net conversion of CH_3O was maintained at 42-53%. At a typical sample point methanol conversion was 39% and DME conversion was 48%. Selectivity to DMC was 73-81% and selectivity to DMM was 17-25%. These results suggest significantly higher yields than those reported for the commercial liquid-phase process or those obtained in gas-phase studies which utilize only methanol as the oxidative carbonylation substrate.

CONCLUSIONS ON CATALYSIS STUDIES

A traditional catalyst for the oxidative carbonylation of methanol and CO to DMC admixtured with a mildly acidic molecular sieve catalyst allows for the oxidative carbonylation of DME/methanol mixtures to DMC. The results of this study clearly indicate the potential for obtaining high net methoxy conversions via the application of in situ dehydration with DME.

CONCEPTUAL DMC PROCESS TAILORED FOR GASOLINE BLENDING

Based on the initial laboratory data obtained under this DOE-sponsored research and previous Amoco-sponsored work on DMC recovery from a product mixture containing methanol plus water, we have initiated an economic evaluation for the production of DMC as a gasoline oxygenate. In this paper we have briefly summarized some of our initial work on the process integration of syngas production (from natural gas) and DMC synthesis steps, including cost savings ideas on DMC recovery and blending as a gasoline oxygenate. While the initial cost studies will be based on using natural gas as the feedstock, the data can be revised in future to include syngas generation via coal and biomass gasification.

Background on DMC Separation

Separation is a critical aspect of DMC production and is one of the more expensive steps. In a conventional DMC synthesis process via oxidative carbonylation of methanol (e.g., ENIChem technology), DMC is produced at low concentrations (20-40%) and it's recovery involves a separation of the ternary system of methanol/DMC and water. This system comprises at least two binary azeotropes which makes the DMC recovery quite challenging:

Component	Normal Boiling Temperature, (°C)
Methanol	65
DMC	90
Water	100
70% Methanol + 30% DMC	62.7
89% DMC + 11% Water	7.5

Based on the patent literature, there are numerous claims on various separation techniques, including extractive distillation, liquid-liquid extraction, evaporation and selective absorption.(1)

In the past, Amoco had evaluated various engineering options for recovering DMC from a mixture of methanol/DMC and water. In related R&D work, Amoco had obtained three patents on novel liquid/liquid extraction methods using various hydrocarbon solvents.(3-5) In one of these methods, specifically tailored for the use of DMC as a gasoline additive, specific gasoline blendstocks are used to extract DMC from the ternary mixture of DMC, methanol and water. Additional water is used to prevent co-extraction of methanol. In this scheme, distillation of a DMC azeotrope is completely avoided, and a gasoline blendstock with reasonably high oxygen concentration can be produced. The use of gasoline blending components as the extraction solvent eliminates any need for separation and recovery of the extraction solvent. A conceptual flowscheme of the proposed idea is shown in Figure 2.

Various laboratory studies have indicated that with suitable gasoline-range blendstocks, the DMC recovery can approach 90-95% level with (a) very low levels of water (<0.01 wt%) and methanol (<0.5 wt%) in the DMC-rich extract and (b) low levels of DMC (<0.4%) and the extraction solvent (<0.1 wt%).

Conceptual Process Flowscheme

As shown in Figure 2, the key process steps in the production of DMC based on the use of a methanol/DME mixture are: syngas generation from natural gas and oxygen (from air liquefaction), methanol plus DME synthesis from syngas, DMC synthesis from methanol, DME, carbon monoxide and oxygen, carbon dioxide and hydrogen recovery from unreacted gases in the methanol/DME synthesis step and DMC extraction from methanol/DMC/water mixture. For this specific study, DMC is extracted with a refinery hydrocarbon stream (e.g., a reformate stream) that can blended directly with gasoline.

One key consideration for the overall process scheme is that if the hydrogen from the syngas production step is to be used as fuel only, we need to select a suitable syngas generation process that will minimize hydrogen/carbon monoxide ratio (e.g., a partial oxidation process rather than a steam reformer). Regarding methanol/DME synthesis, various publications from Haldor Topsoe and Air Products have indicated that suitable catalysts can be developed to tailor to specific methanol/DME product ratio. In general, the co-production of DME and methanol is favored (namely, needs lower reactor severity) over the production of methanol alone. We are currently evaluating various options for the recovery of unconverted DME, carbon dioxide and hydrogen, and integration of various processing steps to minimize overall capital and operating costs.

References:

1. PERP Report, Chem Systems, Inc., 90S7, "DMC Via Ethylene Carbonate", Dec. 1991

2. Romano, Ugo, et al, "Synthesis of DMC from Methanol, CO, and O_2 Catalyzed by Copper Compounds", IEC Prod. Res. Dev., V-19, 396-403 (1980)

3. US Patent: 5,328,615, July 12, 1994, Amoco Corp., Inventors: M. A. Pacheco and F. D. Darrington

4. US Patent 5,338,878, Aug. 16, 1994, Amoco Corp., Inventors: M. A. Pacheco, F. D. Darrington and A. L. Hensley

5. US Patent 5,489,703, Feb. 6, 1996, Amoco Corp., Inventors: M. A. Pacheco, F. D. Darrington, J. C. Reier, and B.D. Alexander

Figure 1

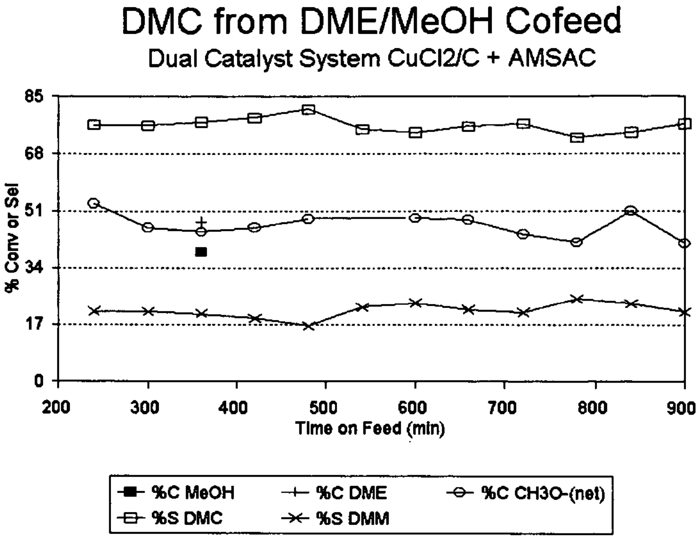

Figure 2

Conceptual Amoco DMC Synthesis Process

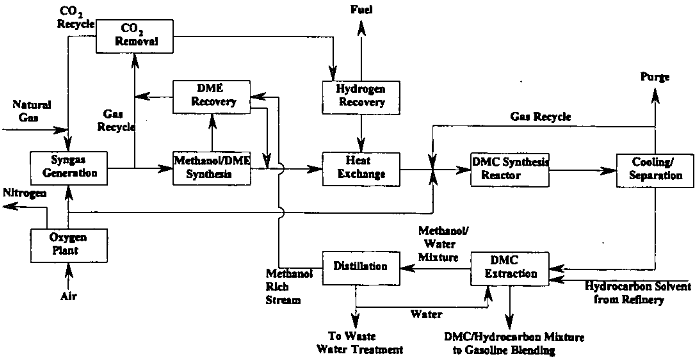
CO2 Recycle
CO2 Removal
Fuel
Natural Gas
Gas Recycle
DME Recovery
Hydrogen Recovery
Purge
Gas Recycle
Syngas Generation
Methanol/DME Synthesis
Heat Exchange
DMC Synthesis Reactor
Cooling/ Separation
Nitrogen
Oxygen Plant
Air
Methanol/ Water Mixture
Distillation
DMC Extraction
Methanol Rich Stream
Hydrocarbon Solvent from Refinery
Water
To Waste Water Treatment
DMC/Hydrocarbon Mixture to Gasoline Blending

ADVANCES IN LIQUID PHASE TECHNOLOGY

Peter J.A. Tijm*, William R. Brown, Edward C. Heydorn, and Robert B. Moore
Air Products and Chemicals Inc., Allentown, PA

ABSTRACT

The liquid phase methanol (LPMEOH™) process uses a slurry reactor to convert synthesis gas (primarily a mixture of hydrogen and carbon monoxide) to methanol. Through its superior heat management, the process is ultimately suitable to handle synthesis gas generated through gasification of coal, petroleum coke, natural gas, residual oil, wastes, and other environmentally disadvantaged hydrocarbon feedstocks. Apart from production of chemical grade methanol, the process provides economic advantages in the Integrated Gasification Combined Cycle (IGCC) power generation application. Co-production of power and methanol via the IGCC and the LPMEOH™ process provides opportunities for energy storage for peakshaving of electrical demand and/or clean fuel for export. The LPMEOH™ technology has been developed by Air Products and Chemicals, Inc. since the 1980's, extensively proven in a Department of Energy (DOE) - owned process development unit in LaPorte, Texas and selected for demonstration under the DOE Clean Coal Technology Program. The slurry reactor being demonstrated is also suitable for other exothermic synthesis gas conversion reactions, like synthesis of dimethyl ether and other alcohols/oxygenates. This paper presents an overview of LPMEOH™ and other liquid phase technology aspects and highlights the demonstration project at Eastman Chemical Company's coal gasification facility in Kingsport, TN. Commercial aspects of the LPMEOH™ process are also discussed.

INTRODUCTION

With increasing methanol market demand, it was realized by various companies that a breakthrough in technology was required to provide methanol to the market place in a cost competitive way. In the early 1960's an important technology improvement was achieved by Imperial Chemical Industries Ltd. (ICI). They introduced low pressure technology, which was made possible through the development of higher activity catalysts. Since that time, low pressure gas phase methanol process technology has dominated the market. Only in the early 1980's was the potential of liquid phase technology realized by Chem Systems and Air Products and Chemicals, Inc. As result of technology consolidation between both these companies the LPMEOH™ technology was developed, with the financial support of the U. S. Department of Energy (DOE). The concept was proven in over 7,400 hours of test operation in a DOE-owned, 3,200 gallons (U.S.) of methanol per day process development unit located at LaPorte, Texas. (Ref. a). The commercial-scale demonstration plant for the technology has been constructed and is now being commissioned at Eastman Chemical Company's coal gasification facility in Kingsport, Tennessee under the DOE's Clean Coal Technology Program. The LPMEOH™ plant will demonstrate the production of at least 80,000 gallons of methanol per day, and will simulate operation for the IGCC co-production of power and methanol. Construction began in October of 1995 and was, in a record period of 15 months, completed in December of 1996. Commissioning was completed and startup initiated in January of 1997, and will be followed by four years of operation to demonstrate the commercial advantages of the technology.

Air Products and Eastman formed the "Air Products Liquid Phase Conversion Co., L.P." limited partnership to execute the demonstration project. The partnership owns the LPMEOH™ demonstration plant. Air Products manages the demonstration project and provides technology analysis and direction for the demonstration. Air Products also provided the design, procurement, and construction of the LPMEOH™ demonstration plant (i.e., a turnkey plant). Eastman provides the host site, performs the permitting and operation of the LPMEOH™ unit, and supplies the supporting auxiliaries, the synthesis gas, and takes the product methanol.

Most of the product methanol will be refined to chemical-grade quality (99.85 wt % purity via distillation) and used by Eastman as chemical feedstock in their commercial facility. A portion of the product methanol will be withdrawn prior to purification (about 98 wt % purity) and used in the off-site product-use tests.

I. COMMERCIAL APPLICATION

Technology Description

The heart of the liquid phase technology, in this case the LPMEOH™ process, is the slurry bubble column reactor (Figure 1). The liquid medium is the feature that differentiates the LPMEOH™ process from conventional technology. Conventional methanol reactors use fixed beds of catalyst pellets and operate in the gas phase. The LPMEOH™ reactor uses catalyst in powder form, slurried in an inert mineral oil. The mineral oil acts as a temperature moderator and a heat removal medium, transferring the heat of reaction from the catalyst surface via the liquid slurry to boiling water in an internal tubular heat exchanger. Since the heat transfer coefficient on the slurry side of the heat exchanger is relatively large, the heat exchanger occupies only a small fraction of the cross-sectional area of the reactor. The slurry reactor can thus achieve high syngas conversion per pass, due to its capability to remove heat and maintain a constant, highly uniform temperature through the entire length of the reactor. Thus an essentially exothermic process has been converted to an isothermal process.

Because of the LPMEOH™ reactor's unique temperature control capabilities, it is able to directly process syngas which is rich in carbon oxides (carbon monoxide and carbon dioxide). Gas phase methanol technology would require such a feedstock to undergo stoichiometry adjustment by the water gas shift reaction (to increase the hydrogen content) and carbon dioxide (CO_2) removal (to reduce the excess carbon oxides). In a gas phase reactor, temperature moderation is only achieved by recycling large amounts of hydrogen (H_2)-rich gas, utilizing the higher heat capacity of H_2 gas as compared to carbon monoxide (CO) gas. Typically a gas phase reactor is limited to about 16% CO gas in the inlet to the reactor, in order to limit the conversion per pass to avoid excess heating. Hence recycle ratios of 6 - 10 are typically applied. In contrast, with the LPMEOH™ reactor, CO gas concentrations in excess of 50% have been routinely tested without any adverse effect on the catalyst activity.

A second differentiating feature of the LPMEOH™ reactor is its robust character. The slurry reactor is suitable for rapid ramping, idling, and even extreme stop/start actions. The thermal moderation provided by the liquid inventory in the reactor acts to buffer sharp transient operations that would not normally be tolerable in a gas phase methanol synthesis reactor.

A third differentiating feature of the LPMEOH™ process is that a high quality methanol product is produced directly from syngas which is rich in carbon oxides. Gas phase methanol synthesis, which relies on hydrogen-rich syngas, results in a crude methanol product with up to 20% water by weight. The product from the LPMEOH™ process typically contaitns only 1% water by weight. This methanol product, coproduced with IGCC, is therefore suitable for many applications, and at a substantial savings in purification costs. The steam produced in the LPMEOH™ reactor is suitable for purification of the methanol product (for upgrading to a higher quality) or for use in the IGCC power generation cycle.

Another unique feature of the LPMEOH™ process is the ability to add fresh catalyst online. Methanol catalysts deactivate at a slow rate. With the LPMEOH™ reactor, spent catalyst slurry may be withdrawn and fresh catalyst slurry added on a periodic batch basis. This allows continuous, uninterrupted operation, i.e maximum number of streamdays per year, and also the maintenance of a high productivity level in the reactor. Furthermore, choice of replacement rate permits optimization of productivity versus catalyst replacement cost.

Finally the simplicity of reactor construction is an advantage to the LPMEOH™ process.

Other Liquid Phase Reactions

The technology and process characteristics/advantages as described for the LPMEOH™ process above are also applicable to a variety of other exothermic syngas reactions. In essence it is the combination of technology elements such as the following:

- exothermicity of the chemical reaction of syngas to product
- successful reactor engineering and scale up
- selectivity towards desired reaction products and
- maintenance of catalyst(s) activity

which will determine the competitiveness of the liquid phase technology.

Following the successful development of the LPMEOH™ technology, which hereinafter will be used as an example, Air Products, sponsored by DOE, broadened the scope of its liquid phase technology interest. Air Products, together with various subcontractors, further developed and/or improved the liquid phase technology for the following chemical processes:

- 1. New C_1 - chemistry to Methyl Tertiary Butyl Ether (MTBE)
- 1. a. Liquid Phase Isobutanol/Methanol
- 1.b. Liquid Phase Isobutylene (LPIBE)
- 2. Liquid Phase Di-Methyl Ether (LPDME)
- 3. Liquid Phase Water Gas Shift
- 4. Liquid Phase Fischer-Tropsch

The new C_1-chemistry to MTBE depends on two critical steps. The first is the efficient production of both methanol and isobutanol direct from syngas, and the second is dehydration of isobutanol to isobutylene. Following laboratory autoclave pioneering and suitable catalyst system(s) determination, the LPIBE technology was proven in the LaPorte Alternative Fuels Development Unit (AFDU). Isobutanol conversion as high as 98% with an isobutylene selectivity of 92% was achieved. High conversion/selectivity is necessary in this, as in many, processes as the product separation of reaction products is difficult and expensive. The Liquid Phase Isobutanol/Methanol production from synthesis gas is presently under further research/demonstration, as previous successful demonstrations are deemed to operate at too high pressures and/or temperatures.

LPDME has been recognized as a possible spring-board molecule for synthesis of fuels and chemicals. Laboratory tests on a dual catalyst system (to perform both methanol synthesis and dehydration in the same reactor vessel) were successful on a laboratory stirred tank reactor scale. Preliminary economics led to high interest in this liquid phase technology and demonstration in the AFDU in LaPorte. LPDME technology is expected to be Air Products' next step in the commercialization of liquid phase technology. Development/cost improvement activities are on-going.

IGCC Coproduction Options

The LPMEOH™ process is a very effective technology for converting a portion of the H_2 and CO in an IGCC electric power plant's coal-derived syngas to methanol. The process is very flexible in being able to process many variations in syngas composition. The LPMEOH™ process can be used with an IGCC electric power plant (Ref. b), to provide the once-through methanol production as depicted in Figure 2. The process can be designed to operate in a continuous, baseload manner, converting syngas from oversized gasifiers or from a spare gasifier. The process can also be designed to operate only during periods of off-peak electric power demand to consume a portion of the excess syngas and allow the electricity output from the combined-cycle power unit to be turned down. In this latter circumstance, the gasification unit continues to operate at full baseload capacity, so the IGCC facility's major capital asset is fully utilized.

In either baseload or cycling operation, partial conversion of between 20% and 33% of the IGCC plant's syngas is optimal, and conversion of up to 50% is feasible. The degree of conversion of syngas (or the quantity of methanol relative to the power plant size) determines the design configuration for the LPMEOH™ process. In its simplest configuration, syngas (feed gas) at its maximum available pressure from the IGCC electric power plant is passed once, without recycle through the LPMEOH™ plant (Figure 3), and partially converted to methanol. The unreacted feed gas is returned to the IGCC power plant's combustion turbines.

If greater amounts of syngas conversion are required, different once-through plant design options (Figure 3) are available. The feed gas pressure to the reactor is a prime determinant of the degree of syngas conversion, as shown in Figure 4. Reaction pressure for methanol synthesis design is usually 750 psia or higher. The higher the pressure at which the syngas is available, the greater is the degree of conversion and the lower the conversion cost. The LPMEOH™ process design options for greater syngas conversion are:

- Once-Through, with Feed Gas Compression:

When the feed gas pressure from the IGCC electric power plant is low (e.g. below 750 psia), feed gas compression may be added to the LPMEOH™ process design, to increase reactor productivity and the overall conversion of syngas to methanol.

- Limited Gas Recycle:

One design technique to increase the degree of syngas conversion is to condense out methanol from the reactor effluent and to recycle part of the unreacted feed gas back to the reactor inlet. With the LPMEOH™ process, this simple recycle refers to recycle of CO-rich gas. The recycle ratio required for the LPMEOH™ is moderate, for example, one part unreacted syngas to one part fresh feed gas. This 1 to 1 recycle ratio is usually quite effective in optimizing the methanol production. At higher recycle ratios, little is gained since most of the available H_2 has already been converted to methanol.

- Once-Through with Water Addition:

Of course, the richer the once-through syngas is in CO, the more the production is limited by the availability of H_2. If additional conversion is desired, the LPMEOH™ process design can be altered to generate additional H_2. The inherent shift activity of the methanol catalyst can be utilized to accommodate a modest amount of shift activity within the reactor. This is done by the addition of water, as steam, to the syngas before it passes through the liquid phase methanol reactor. Within the reactor, the additional steam is converted to H_2 which is, in turn, converted to methanol. In the water addition case, the increase in conversion is accompanied with a modest increase of water in the crude methanol product and of CO_2 in the reactor effluent gas.

Any combination of these LPMEOH™ process design options may be used to achieve the desired degree of syngas conversion. There is still no need for upstream stoichiometric adjustment of the feed gas by the water-gas shift reaction and CO_2 removal; so the simplicity of once-through CO-rich gas processing is retained.

Baseload Coproduction of Methanol and Power

Process design study work for the LPMEOH™ process has been directed towards converting a portion of coal-derived syngas produced in an IGCC electric power plant to methanol. A feed gas containing 35% H_2, 51% CO, 13% CO_2 and 1% inerts (nitrogen) was used for preparing the baseload methanol coproduction economics.

With a given gasification plant size, the IGCC coproduction plant can be designed to accommodate a range of methanol to power output ratios. For example (Ref. c, d), a gasification plant, with two gasifiers of 1735 million Btu (HHV) per hour output each (equivalent to some 2200 tonnes per day of coal input), could be sized for baseload power output of 426 megawatts of electricity (MWe) and for baseload methanol coproduction of 152,000 US gallons per day (G/D). Other methanol and power plant size options for this gasification plant size are shown in Table 1.

Table 1. Methanol Plant to Power Plant Size Ratio

% of Syngas Converted to Methanol (%)	Baseload Power Plant Size (MWe)	Baseload Methanol Plant Size (G/D)	Methanol Plant to Power Plant Size Ratio (G/D per MWe)
0	500	0	0
13.8	**426**	**152,000**	**357**
20.0	394	210,000	533
30.0	342	330,000	965

The IGCC coproduction plant with 426 MWe of power and 152,000 G/D of methanol is used for the baseload production cost estimate for coproduced methanol, shown in Table 2. If the baseload fuel gas value is $4.00 per million Btu, then 152,000 G/D of methanol can be coproduced from coal for under 50 cents per gallon.

As expected, the methanol production cost is lower at larger methanol plant sizes. Figure 5 shows the effect of plant size for once-through methanol coproduction. Methanol production costs for two of the LPMEOH™ plant design options for higher syngas conversion: 1 to 1 gas recycle, and 1 to 1 gas recycle with water addition, are also shown.

Today, new methanol plants are being built where natural gas is inexpensive (Chile, Saudi Arabia). These new world scale plants range in size from 700,000 to 900,000 G/D (2000 to 2700 metric tons per day) in size. The economy of scale savings; in natural gas gathering, syngas production, and in methanol storage and ocean transport facilities; drive these plants to a large size. Estimates (Ref. e, f) show that an 836,000 G/D remotely located methanol plant (with the same 20% per year capital charge as in Figure 5), with natural gas at $0.50 to $1.00 per million Btu, has a total ex-plant methanol production cost of 46 to 50 cents per gallon. Adding ocean freight, duty and receiving terminal storage typically adds 8 to 10 cents per gallon; giving a total delivered U.S. Gulf Coast methanol cost (Chemical Grade) of 55 to 60 cents per gallon.

Figure 5 is interesting because it provides an unexpected result. Methanol coproduction with IGCC and the once-through LPMEOH™ process does not need large methanol plant sizes to achieve good economics. The gasification plant is already at a large economical scale for power generation; so the syngas production economics are already achieved. Methanol storage and transport economics are also achieved by serving local markets, and achieving freight savings over the competing methanol, which is usually shipped via the U. S. Gulf coast from areas with inexpensive feed gas (like natural gas or associated gas).

The 50 cents per gallon coproduction cost for a 152,000 G/D once-through LPMEOH™ plant size is in local markets competitive with new world scale natural gas based methanol plants. Figure 5 shows an additional 3 to 4 cent per gallon saving for a 365,000 G/D LPMEOH™ plant size. These additional savings might be used to off-set higher freight costs to more distant local customers; while still maintaining a freight and cost advantage over the imported methanol from the Gulf Coast.

The 50 cents per gallon coproduction cost for a 152,000 G/D once-through LPMEOH™ plant size in local markets is competetive with new world scale natural gas-gased methanol plants. Figure 5 shows an additional 3 to 4 cent per gallon savings for a 365,000 G/D LPMEOH™ plant size. These additional savings might be used to offset higher freight costs to more distant local

customers, while still maintaining a freight and cost advantage over the imported methanol from the Gulf Coast.

TABLE 2. Production Cost Estimate for Coproduced Methanol
LPMEOH Plant Capacity: 152,000 gallons per day (500 sT/D)
Capital Investment: $29 million

	Baseload
Methanol Plant Operation:	7884 hr/yr
Methanol Production (million gall./year):	49.9
Methanol Production Cost	**cents/gallon**
Syngas cost:	
Feed Gas @ fuel value ($4.00/mmBtu)	98.7
Unreacted (CO-rich) gas @ fuel value ($4.00/mmBtu)	(68.4)
Sub-total; net cost of syngas converted:	**30.3**
Operating cost:	
Catalyst and chemicals	2.6
Export steam	(2.9)
Utilities	0.9
Other (fixed) costs	4.0
Sub-Total; Operating Costs:	**4.6**
Capital charge @ 20% of investment per year	**11.6**
Total Methanol Production Cost:	**46.5**

Basis:
U. S. Gulf Coast Construction, 4thQ 1996 $
Includes owner costs and 30 days of Product Storage
CO-rich feed gas from IGCC electric power plant at 1000 psia, with 5ppm (max.) sulfur. Once-through LPMEOH process design with 1562 mmBtu/hr in, 1082 mmBtu out tHHV). Excludes License and Royalty fee. Air Products is the LPMEOH process technology licensor. Product methanol with 1 wt % water; Chem. Grade would add 4 to 5 cents per gallon.

II. DEMONSTRATION PLANT - STATUS

Development of the LPMEOH™ technology came to further fruition through cooperation between Air Products, DOE and Eastman Chemical Company under the DOE Clean Coal Technology Program (Ref. g).

Kingsport Site

Eastman has an extensive chemical complex at the Kingsport site, where originally methanol was produced by distillation of wood and later changed to conversion of coal-derived syngas. Coal gasification operations at Kingsport began in 1983. Figure 6 shows an aerial view of Eastman's Kingsport gasification facility. Texaco gasification is used to convert about 1,000 tons-per-day of high-sulfur, Eastern bituminous coal to synthesis gas for the manufacture of methanol, acetic anhydride, and associated products. Air Products provides the oxygen for gasification by a pipeline from an over-the-fence air separation unit. The crude synthesis gas is quenched, partially shifted, treated for acid gas removal (hydrogen sulfide and carbonyl sulfide, and CO_2, via Rectisol), and partially processed in a cryogenic separation unit to produce separate H_2 and CO streams. The H_2 stream is combined with clean synthesis gas to produce stoichiometrically balanced feed to a conventional gas phase methanol synthesis unit. Methanol from this unit is reacted with recovered acetic acid to produce methyl acetate. Finally, the methyl acetate is reacted with the CO stream to produce the prime product, acetic anhydride (and acetic acid for recycle). Figure 7 shows the process block flow diagram for the Kingsport gasification facility including the LPMEOH™ demonstration plant.

LPMEOH™ Demonstration Plant Design

The site available at Kingsport provides a 270 ft. by 180 ft. plot for the demonstration plant and tank truck loading areas. An area next to the site was made available for establishing the construction trailer, fabrication, and laydown areas. Figure 8 is an aerial view of the site prior to the start of construction. Air Products was responsible for the engineering design and construction of the project. Eastman was responsible for the outside battery limits design and construction, the permitting, and for providing the digital control programming. Eastman reviewed the detailed design of the demonstration plant.

Because the gasification facility produces individual streams of clean synthesis gas, CO, and H_2-rich gas, there is the capability to blend gases and mimic the gas compositions of a range of gasifiers. Hence, the broad applicability of the LPMEOH™ technology could be proven and formed part of an elaborate test program, to be discussed later. Those test objectives also provided a design challenge for the Air Products/Eastman design team. Of primary importance was the integration of the LPMEOH™ demonstration plant within the Kingsport gasification complex. Since the feed composition to the reactor was to be varied from H_2-lean to H_2-rich (25% to 70+%H_2) and the flow to the reactor by at least a factor of two, all of the product and byproduct streams within and outside the battery limits were affected. Control valves and instrumentation for the demonstration plant were required to have functionality over and beyond those for a normal commercial facility. Extreme cases of about twenty different heat and material balances were considered for specification of each piece of equipment, flow measurement device, control valve, and safety relief device.

The DOE approved Eastman's Kingsport, TN facility as the site of the LPMEOH™ Demonstration Plants in October of 1993. Air Products and Eastman worked with the DOE to define the size of the plant and develop a Statement of Work for the LPMEOH™ Demonstration at Kingsport. This Project Definition phase including a cost estimate was completed in October of 1994. Preliminary detailed design work on equipment layouts and development of P&ID's began shortly after this. Full authorization from the DOE for Design and Construction was effective February 1, 1995. The reactor was the first piece of equipment to be placed on order in November of 1994. Equipment deliveries began in November of 1995. The State air permit was received in March of 1996. The DOE completed its National Environmental Policy Act (NEPA) review and issued a Finding of No Significant Impact (FONSI) in June of 1995. Construction at the site began in October of 1995. Construction was essentially completed in December of 1996.

Instrument Loop Checking began in October 1996. Commissioning began in December of 1996, followed by startup in late January of 1997. Thereafter a four-year methanol test operation was started in February of 1997. The operating test program will end in the year 2001. The off-site fuel use tests will be performed over an 18 to 30 month period, beginning in May of 1998.

III. DEMONSTRATION PLANT - TEST PLANS

Methanol Operations - Demonstration Test Plan

Three key results will be used to judge the success of the LPMEOH™ process demonstration during the four years of operational testing:

- Resolution of technical issues involved with scaleup and first time demonstration for various commercial-scale operations
- Acquisition of sufficient engineering data for commercial designs
- Industry acceptance

The demonstration test plan has been established to provide flexibility in order to meet these success criteria. Annual operating plans, with specific targeted test runs, will be prepared and revised as necessary. These plans will be tailored to reflect past performance as well as commercial needs. User involvement will be sought.

The LPMEOH™ operating test plan outline, by year, is summarized in Table 3. The demonstration test plan encompasses the range of conditions and operating circumstances anticipated for methanol coproduction with electric power in an IGCC power plant. Since Kingsport does not have a combined-cycle power generation unit, the tests will simulate the IGCC application. Test duration will be emphasized in the test program. The minimum period for a test condition, short of the rapid ramping tests, is 2 weeks. Numerous tests will have 3-6 week run periods, some 8-12 weeks, and a few key basic tests of 20 to 30 weeks.

Table 3. **LPMEOH™ Demonstration Test Plan Outline**

Year 1
- Catalyst Aging
  - Catalyst Life Versus LaPorte process development unit and Lab Autoclaves
- Process Optimization / Maximum Reactor Productivity
  - Catalyst Slurry Concentration
  - Reactor Slurry Level
  - Catalyst Slurry Addition Frequency Test
- Establishment of Baseline Condition

Years 2 & 3
- Catalyst Slurry Addition and Withdrawal at Baseline Condition
- Catalyst Attrition/Poisons/Activity/Aging Tests
- Simulation of IGCC Coproduction for:
  1. Synthesis Gas Composition Studies for Commercial Gasifiers
     - Texaco, Shell, Destec, British Gas/Lurgi, Other Gasifiers
  2. IGCC Electrical Demand Load Following:
     - Rapid Ramping, Stop/Start (Hot and Cold Standby)
  3. Additional Industry User Tests
- Maximum Catalyst Slurry Concentration
- Maximum Throughput/Production Rate

Year 4
- Stable, extended Operation at Optimum Conditions
- 99% Availability
- Potential Alternative Catalyst Test
- Additional Industry User Tests

Applications for the Coproduced Methanol Product

The methanol coproduction process studies show that the LPMEOH™ process can produce a clean high quality methanol product at less than 50 cents per gallon from an abundant, non-inflationary local fuel source (coal). As previously indicated the quality of the methanol produced approaches closely that of chemical grade methanol. This allows in certain applications for limited distilling of the product and, hence, another advantage for the LPMEOH™ process. Serving local markets, the methanol coproduced at central IGCC electric power plants, can be a valuable premium fuel or fuel feedstock for many applications, such as:

1. An economical hydrogen source for small fuel cells being developed for transportation applications. Methanol is a storable, and transportable, liquid fuel which can be reformed under mild conditions to provide an economical source of hydrogen for fuel cells.
2. Reformed under mild conditions, liquid phase methanol may be an economical hydrogen or carbon monoxide source for industrial applications.
3. A substitute for chemical grade methanol being used for MTBE manufacture.
4. An environmentally advantaged fuel for dispersed electric power stations. Small packaged power plants (combustion turbine, internal combustion engine, or fuel cell) provide power and heat locally, at the use point; without any competition like natural gas pipelines and high voltage power lines. Since methanol is an ultra-clean (zero sulfur) fuel which burns with very low (better than natural gas) emissions of nitrogen oxides, the incremental power is very clean.
5. Finally, the coproduced methanol may be used by the utility owning the IGCC facility (see Figure 2). Potential uses are: a) as a backup fuel for the IGCC plant's main gas turbines; b) as a fuel for a separate, dedicated cycling combined-cycle unit at the same site; c) as the fuel exported to the utility's distributed power generation system(s); or d) as the transportation fuel for the utility's bus or van pool. Since the methanol is derived from the coal pile, the IGCC facility can be truly independent and self-sufficient for fuel needs. In addition, should the external prices for methanol command higher value to the IGCC plant's owner, the methanol can be exported for additional revenues.

Many of the applications listed above are embryo developments. Their ultimate market size potential for transportation applications, for industrial applications and for distributed power generation could become large. The methanol product specification for the applications is not adequately known. Therefore, part of the LPMEOH™ demonstration project's program is to confirm the suitability of the methanol product for these (and other) uses. Product-use tests will allow development of final methanol product specifications. During the demonstration, in the 1998 to 2000 time-frame, about 400,000 gallons of the "as-produced from CO-rich syngas" methanol will be available for off-site product-use testing. The final off-site product-use test plan is now under development. More details will be provided to interested parties.

CONCLUSION

The LPMEOH™ process is now being demonstrated at commercial scale under the DOE Clean Coal Technology Program. The demonstration plant, located at Eastman Chemical Company's Kingsport, Tennessee coal gasification facility site, will produce at least 80,000 gallons-per-day of methanol from coal-derived synthesis gas. Startup was effected in January of 1997, followed by a four-year demonstration test period beginning in February of 1997.

Successful demonstration of the LPMEOH™ technology will add significant flexibility and dispatch benefits to IGCC electric power plants, which have traditionally been viewed as strictly a baseload power generation technology. Now, central clean coal technology processing plants, making coproducts of electricity and methanol, can meet the needs of local communities for dispersed power and transportation fuel. The LPMEOH™ process provides competitive methanol economics at small methanol plant sizes, and a freight and cost advantage in local markets vis-a-vis large remote gas methanol. Methanol coproduction studies show that methanol at less than 50 cents per gallon can be provided from an abundant, non-inflationary local fuel source (coal). The coproduced methanol may be an economical hydrogen source for small fuel cells, and an environmentally advantaged fuel for dispersed electric power.

BIBLIOGRAPHY

Ref. a. "An Update on Liquid Phase Methanol (LPMEOH™) Technology and the Kingsport Demonstration Project"; E. S. Schaub, et. al. (Air Products and Chemicals, Inc.), Fourth Annual Clean Coal Technology Conference; September 5-8, 1995.

Ref. b. "Flexible Electric Power Generation - The Integrated Gasification/Liquid Phase Methanol (LPMEOH™) Demonstration Project", W. R. Brown, et. al. (Air Products and Chemicals, Inc.), Third Annual Clean Coal Technology Conference; September 6-8, 1994.

Ref. c. "IGCC Cost Study"; D. M. Todd (GE Company), J. R. Joiner (Fluor Daniel, Inc.), EPRI Conference on Gasification Power Plants, October 19-21, 1994.

Ref. d. "Gasification Systems - Advanced turbines hold the key to economic IGCC"; Modern Power Systems, August 1995.

Ref. e. "Putting the Future of Methanol in Proper Perspective"; J. R. Crocco, (Crocco & Associates, Inc.), World Methanol Conference, December 5-7, 1989.

Ref. £ "Methanol 93-1, Process Evaluation Research Planning (PERP) Report"; Chem Systems Inc., April 1995.

Ref. g. "Fuel and Power Coproduction - The Liquid Phase Methanol (LPMEOH™) Process Demonstration at Kingsport"; D. P. Drown, et. al. (Air Products and Chemicals, Inc./Eastman Chemical Company/U.S. Department of Energy), Fifth Annual DOE Clean Coal Technology Conference; January 7-9, 1997.

DISCLAIMER/ACKNOWLEDGMENT

This report was prepared by Air Products & Chemicals, Inc., pursuant to a Cooperative Agreement partially funded by the U.S. Department of Energy, and neither Air Products & Chemicals, Inc., nor any of its aubcontractors nor the U.S. Department of Energy, nor any person acting on behalf of either:

(A) Makes any warranty or representation, express or implied, with respect to the accuracy, completeness, or usefulness of the information contained in this report, or that the use of any information, apparatus, method, or process disclosed in this report may not infringe privately-owned rights; or

(B) Assumes any liabilities with respect to the use of, or for damages resulting from the use of, any information, apparatus, method, or process disclosed in this report.

Reference herein to any specific commercial product, process, or service by trade name, trademark, manufacturer, or otherwise, does not necessarily constitute its endorsement, recommendation, or favoring by the U.S. Department of Energy. The views and opinions of authors expressed herein does not necessarily state or reflect those of the U.S. Department of Energy.

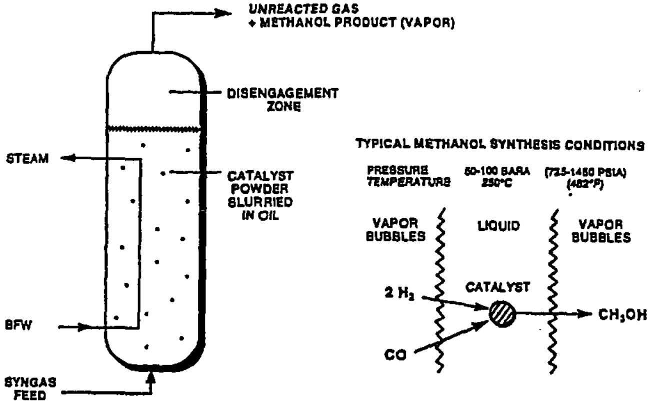
UNREACTED GAS
+ METHANOL PRODUCT (VAPOR)
DISENGAGEMENT ZONE
STEAM
CATALYST POWDER SLURRIED IN OIL
BFW
SYNGAS FEED
TYPICAL METHANOL SYNTHESIS CONDITIONS
PRESSURE 50-100 BARA (725-1450 PSIA)
TEMPERATURE 250°C (482°F)
VAPOR BUBBLES
LIQUID
VAPOR BUBBLES
CATALYST
2 H$_2$
CO
CH$_3$OH

Figure 1. LPMEOH™ Reactor and Reaction Schematics

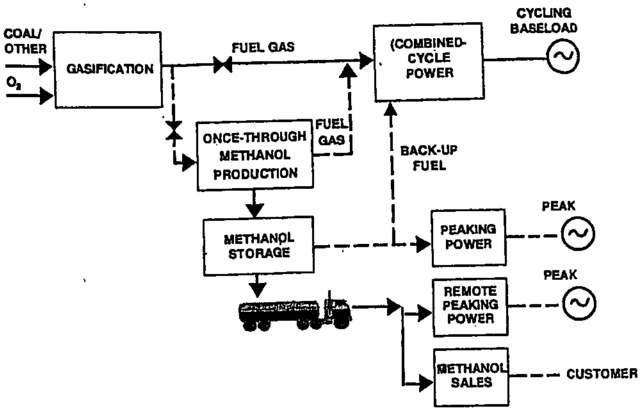
COAL/ OTHER
O_2
GASIFICATION
FUEL GAS
COMBINED-CYCLE POWER
CYCLING BASELOAD
FUEL GAS
ONCE-THROUGH METHANOL PRODUCTION
BACK-UP FUEL
METHANOL STORAGE
PEAK
PEAKING POWER
PEAK
REMOTE PEAKING POWER
METHANOL SALES
CUSTOMER

Figure 2. Once-through Methanol Coproduction with IGCC Electric Power

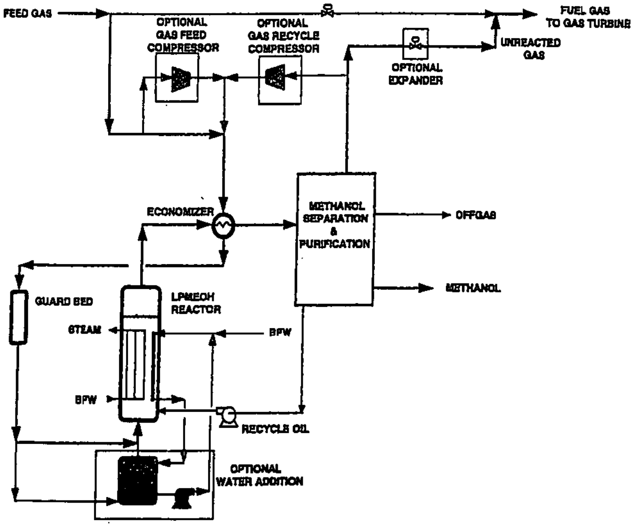
FEED GAS
OPTIONAL GAS FEED COMPRESSOR
OPTIONAL GAS RECYCLE COMPRESSOR
FUEL GAS TO GAS TURBINE
UNREACTED GAS
OPTIONAL EXPANDER
ECONOMIZER
METHANOL SEPARATION & PURIFICATION
OFFGAS
METHANOL
GUARD BED
LPMEOH REACTOR
STEAM
BFW
BFW
RECYCLE OIL
OPTIONAL WATER ADDITION

Figure 3. Once-through LPMEOH™ Process Design Options

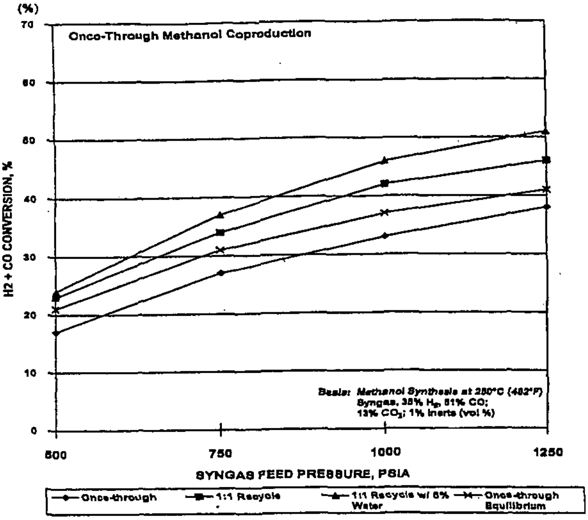

Figure 4. Synthesis Gas Conversion to Methanol

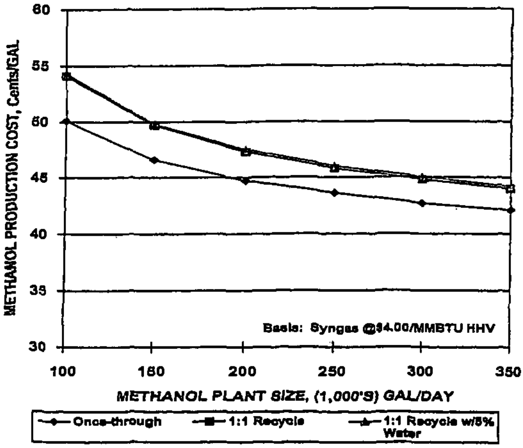

Figure 5. Coproduct Methanol Cost versus Methanol Plant Size.

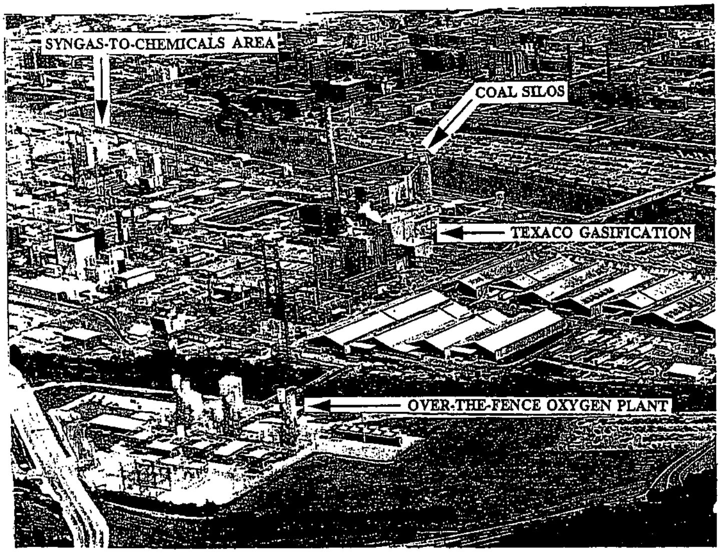
SYNGAS-TO-CHEMICALS AREA
COAL SILOS
TEXACO GASIFICATION
OVER-THE-FENCE OXYGEN PLANT

Figure 6. Aerial View of Eastman's Kingsport Complex

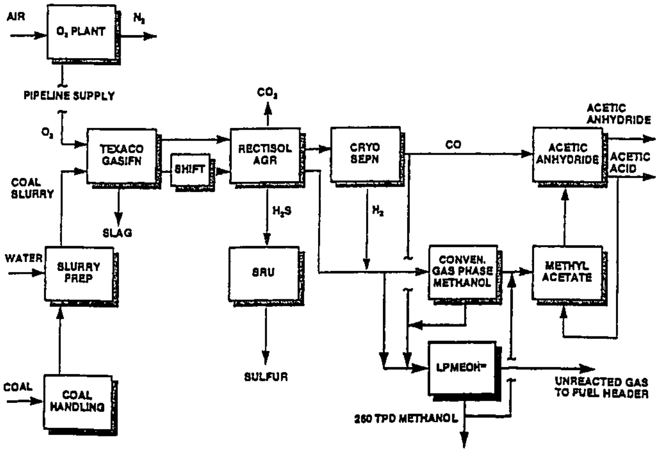
AIR
O_2 PLANT
N_2
PIPELINE SUPPLY
O_2
TEXACO GASIFN
COAL SLURRY
SLAG
WATER
SLURRY PREP
COAL
COAL HANDLING
SHIFT
CO_2
RECTISOL AGR
H_2S
SRU
SULFUR
CRYO SEPN
H_2
CO
CONVEN. GAS PHASE METHANOL
LPMEOH™
260 TPD METHANOL
UNREACTED GAS TO FUEL HEADER
METHYL ACETATE
ACETIC ANHYDRIDE
ACETIC ANHYDRIDE
ACETIC ACID

Figure 7. Process Block Flow Diagram of Kingsport Facility Including LPMEOH™ Demonstration Plant.

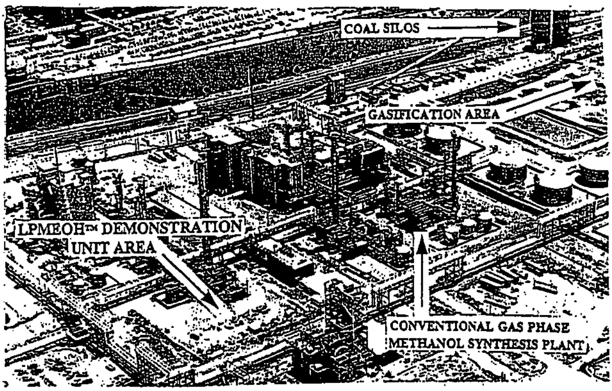
COAL SILOS
GASIFICATION AREA
LPMEOH™ DEMONSTRATION UNIT AREA
CONVENTIONAL GAS PHASE METHANOL SYNTHESIS PLANT

Figure 8. Aerial View of the Site for the LPMEOH™ Demonstration Plant

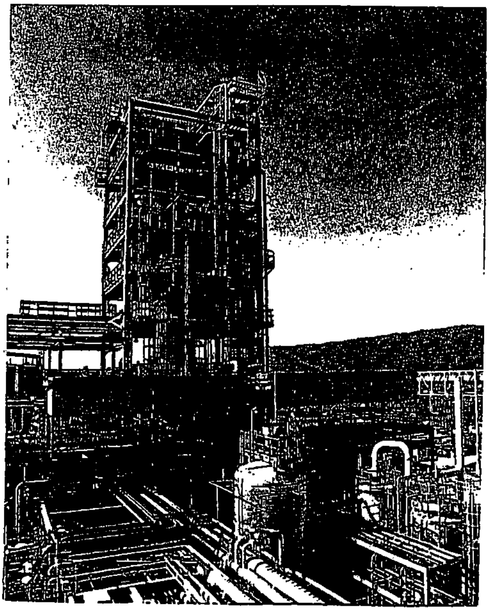

Figure 9. Photograph of the installed LPMEOH™ Demonstration Plant

NEW CLEAN FUEL FROM COAL- DIMETHYL ETHER -

Y. Ohno, T.Shikada, T.Ogawa, M.Ono and M.Mizuguchi ,NKK Corporation,Tokyo 100 and K.Fujimoto ,The University of Tokyo,Tokyo 113,Japan

Keywords: Dimethyl ether , Coal, Clean fuel

1. Introduction

In Asian countries and regions including China, ASEAN and NIES , high speed economic growth is spurring a rapid increase in energy consumption, which means that there is a high probability of this part of the world eventually facing [1] a tight energy supply and demand situation and [2] serious environmental problems (CO2,SOx, NOx, etc.).

On the energy supply side, an increase is forecast in the total volume of crude oil and oil products imported from the middle east and other production regions outside this part of Asia, but it will be necessary to also use unexploited energy resources as lignite, sub-bituminous coal, coal bed methane and unexploited small deposits of natural gas within the region.

Looking at the environmental preservation situation, to deal with existing solid pollutant sources such as relatively large electric power plants and factories ,desulfurization and denitrification plants are effective. For the consumption of fuel in residential and commercial sector and transportation sector, as the sources of pollutants are widely dispersed, measures to clean the fuel itself must be taken.

Forecasts of sharp rises in demand for the clean fuels, natural gas (LNG) and LPG, have aroused fears of a jump in the prices of these products. For this reason, the production of dimethyl ether (DME)--a clean fuel as convenient to transport as LPG--by synthesizing from gas obtained by coal gasification at coal mine for shipment to users in the surrounding countries and regions is extremely significant from the point of view of environmental preservation.

Recently, the DME synthesis from H2/CO has been studied for coproduction with methanol to increase the productivity beyond the methanol equilibrium(3,4).

NKK, which has been studying the synthesis of DME from H2/CO since 1989 (1,2) , is now conducting research on a 50kg/day bench plant.

In this report, we present an overview of the physical properties, uses and synthesis reaction of DME, and an estimation to commercial plant of DME.

2. Physical Properties and Uses of DME

2.1 Physical Properties of DME

Table 1 shows the physical properties and combustion characteristics of DME and various fuels. DME, a colorless gas with a boiling point of -25℃ , is chemically stable and easily liquefied. With properties similar to those of propane and butane, which are principal constituents of LPG, it can be handled and stored using the same technology used to handle and store LPG.

While its net calorific value of 6.903 kcal/kg is lower than that of propane, butane, and methane, it is higher than that of methanol. In gaseous state, its net calorific value is 14,200 kcal/Nm3, which is higher than that of methane. Turning to its combustion properties, its explosion limit is wider than those of propane and butane, but almost identical to that of methane and narrower than that of methanol. Its cetane number is high, ranging from 55 to 60, so that it can be used in diesel engines. Actual engine tests show that its fuel consumption rate is lower than that of diesel oil at the same NOx level and confirm that it is an extremely clean fuel, generating an extremely small quantity of soot(5). Its flame is a visible blue flame similar to that of natural gas, and it can be used just as it is in an LPG cooking stove, and it does not produce aldehyde.

A toxicity study of its use as a propellant for spray cans to replace fluorocarbons has confirmed that its toxicity is extremely low; about the same as that of LPG (6). The study has shown that the toxicity of DME is even lower than that of methanol.

Table 1 Physical Properties and combustion characteristics of DME and other fuels

Properties	DME	Propane	n-Butane	Methane	Methanol
Chemical formula	CH_3OCH_3	C_3H_8	C_4H_{10}	CH_4	CH_3OH
Boiling point (℃)	-25.1	-42.0	-0.5	-161.5	64.6
Liquid density (g/cm^3, 20℃)	0.67	0.49	0.57	–	0.79
Specific gravity (vs. air)	1.59	1.52	2.00	0.55	–
Heat of vaporization (kcal/kg)	111.7	101.8	92.1	121.9	262
Saturated vapor pressure (atm, 25℃)	6.1	9.3	2.4	246	–
Burning velocity (cm/s)	50	43	41	37	52
Ignition energy (10^{-4}J)	45	30	76	33	21
Ignition temperature (℃)	350	504	430	632	470
Explosion limit (%)	3.4~17	2.1~9.4	1.9~8.4	5~15	5.5~36
Cetane number	55~60	(5)	(10)	0	5
Net calorific value ($kcal/Nm^3$)	14,200	21,800	28,300	8,600	–
Net calorific value (kcal/kg)	6,903	11,100	10,930	12,000	5,040

( ) : estimated Value

It does not corrode metal but it does corrode rubber type sealant, so these materials must be selected carefully (6).

2.2 Uses of DME

Some is used as solvents, refrigerants, etc., but most is used as a propellant (paint, chemical fertilizers, cosmetics), with 8,000 tons/year produced in Japan and about 100,000 tons/year produced world wide. Its only use as a fuel has been as an intermediate product during the conversion to synthetic gasoline, but to take advantage of its properties similar to those of LPG, China has begun producing DME by dehydration reaction of methanol as a fuel substitute for LPG. Table 2 shows potential uses of DME as a fuel and the energy it will replace. When it is possible to produce it cheaply from coal or natural gas, it will be used widely as a clean fuel which is as convenient to transport as LPG.

Table 2 Potential use of DME as substitute fuel

Transportation	: diesel oil
Domestic use	: coal, coal briquette, fuel gas from coal, natural gas, LPG
Power generation	: coal, natural gas, heavy oil, LPG

3. Synthesis of DME

3.1 DME Synthesis Reaction

Table 3 shows the reactions concerning DME synthesis and the heat of reaction. As shown in Table 3, the DME synthesis reaction (e) from H2/CO consists of three steps: the methanol synthesis reaction (a), the dehydration reaction(b), and the shift reaction (c). Without the shift reaction, the reaction can be carried out following the formula(d) which is given by combining reactions (a) and(b). Because generally the methanol synthesis catalyst encourages the shift reaction(c), the total reaction is likely to proceed between (d) formula and (e) formula.

Because the total reaction is highly exothermic, if the excess reaction heat is not efficiently removed and the reaction temperature is not carefully controlled, there is a risk of the catalyst deactivation by the rising temperature.

Table 3 Reaction concerning DME synthesis and reaction heat

	Reaction			Reaction heat (kcal/mol-DME)
(a)	$2CO + 4H_2$	$\rightarrow$	$2CH_3OH$	+ 43.4
(b)	$2CH_3OH$	$\rightarrow$	$CH_3OCH_3 + H_2O$	+ 5.6
(c)	$CO + H_2O$	$\rightarrow$	$CO_2 + H_2$	+ 9.8
(d)	$2CO + 4H_2$	$\rightarrow$	$CH_3OCH_3 + H_2O$	+ 49.0
(e)	$3CO + 3H_2$	$\rightarrow$	$CH_3OCH_3 + CO_2$	+ 58.8

Figure 1 shows how the (H2 + CO) equilibrium conversion for these two DME synthesis reaction formulae (d) and (e) and methanol synthesis reaction(a) varies as function of the initial H2/CO ratio and reaction pressure. In each reaction, the equilibrium conversion has its peak where the H2/CO ratio of the reactant gas corresponds to the stoichiometric value, that is, H2/CO = 2 (reaction (d) and reaction(a)) and with H2/CO = 1 (reaction(e)). The equilibrium conversion of DME is higher than that of methanol. For DME synthesis, the maximum value of the equilibrium conversion is higher for the reaction formula (e). This clearly indicates the significance of the fact that the shift reaction (c) proceeds in response to reaction (a) and reaction (b).

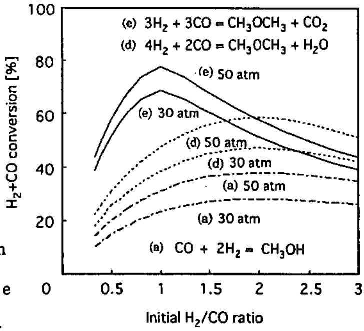

Fig.1 Equiliblium (H_2+CO) conversion to DME or methanol as function of initial H_2/CO ratio and pressure (at 280 ℃)

3.2 Slurry Bed Reactor

The reactor types for catalytic reaction are categorized in fixed bed, fluidized bed and slurry bed. Because DME synthesis reaction is highly exothermic, a fluidized bed and a slurry bed reactor are recommended. Their heat transfer characteristic is so excellent that the temperature distribution in the reactor is flat and that the structure of reactor can be simple.

A slurry bed does not restrict the shape and mechanical strength of the catalyst compared with a fluidized bed. The catalyst in the slurry bed can be easily exchanged by slurry pomp without disturbing the operation when the activity of catalyst decreases. But in the slurry bed, the solubility in the solvent of the water generated on the dehydration catalyst is low, the most of water emerges directly into the gas bubbles and there is a strong tendency for it to emerge from the reactor without reacting with the CO, and overall, the CO conversion becomes low. So adding a shift reaction function to the dehydration catalyst to convert generated water with the CO immediately to H2 and CO2 has been designed. Because H2 has high solubility and diffusion rate in the solvent, it is consumed by the methanol synthesis reaction, and overall it is possible to obtain a high CO conversion (1,2).

3.3 DME Synthesis Reaction Test

A bench scale experiment was performed based on beaker scale research (1,2). An outline of the test plant is presented in Figure 2. The reactor is a slurry bed bubble tower with an internal diameter of 90 mm and a height of 2 m. The plant capacity is of 50 kg/day of DME. Figure 3 and Figure 4 present, as examples of the results of the experiment, the CO conversion and selectivity of all constituents of the product (CO2 is excluded and the total of DME, methanol, CH4 is considered to 100%) produced in one through operation. There is no other heavy byproduct than methanol and methane.

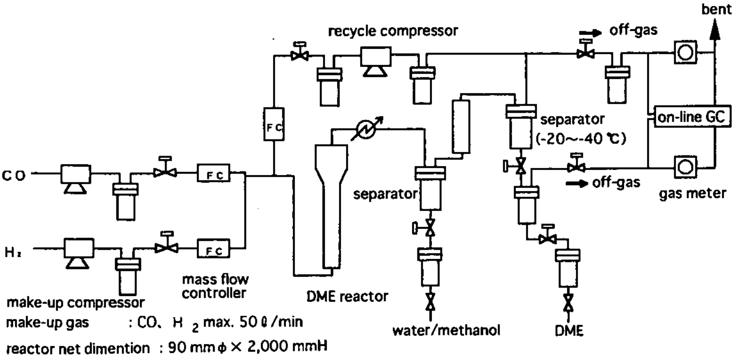
bent
recycle compressor
off-gas
on-line GC
separator
(-20~-40 ℃)
off-gas
gas meter
FC
CO
FC
separator
H₂
FC
mass flow
controller
make-up compressor
DME reactor
water/methanol
DME
make-up gas : CO, H $_2$ max. 50 ℓ/min
reactor net dimention : 90 mmϕ × 2,000 mmH

Fig.2 Flow diagram of Bench Plant

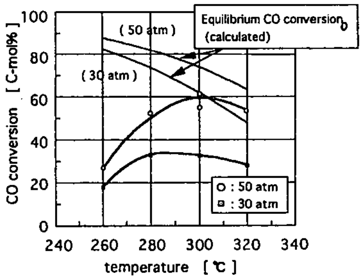

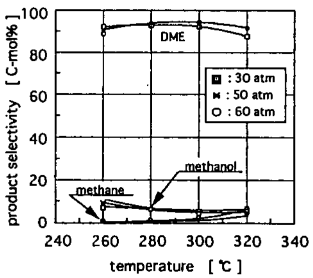

Fig. 3 CO conversion as function of temperature and pressure(one-through,make-up H2/CO=1)

Fig. 4 Product selectivity as function of temperature and pressure

The CO conversion rises as the temperature climbs, and it has the maximum value. This is considered to represent the effect of the equilibrium restrictions caused as the conversion approaches the equilibrium and of the fall in the soluhility of the reaction gas as the temperature rises. A CO conversion greater than 50% and a DME selectivity in excess of 90% were obtained at a pressure of 50 atm and a temperature of 300℃.

As for the catalyst life, as shown in Figure 5 ,during 700 hours of consecutive testing, no deactivation was observed.

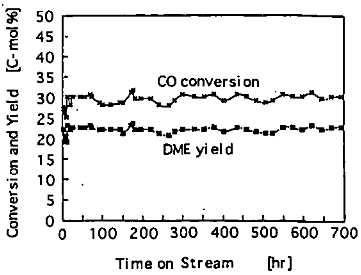

Fig. 5 Catalyst activity as function of time on stream (H2/CO=1,280g,30atm,W/F=12g-cat hr/mol)

4. Synthesis of DME from Coal and Natural Gas and its Uses

4.1 DME Synthesis Process Flow

Figure 6 shows a block diagram to produce DME from coal. Because the H2/CO ratio of synthesis gas obtained by the coal gasification ranges from 0.5 to 1.0, the gas composition is adjusted by the shift reaction so that H2/CO = 1, and it is then supplied for DME synthesis. In this synthesis step where the reaction (e) (H2/CO=1) is achieved, the difference of H2/CO ratio to be adjusted is so narrow in comparison with the reaction(d) (H2/CO=2) that the equipment size and utility consumption for the shift conversion step are smaller.

The effluent from the slurry reactor is cooled and chilled in order to separate the liquid phase (DME , CO2 and small amount of methanol and water) from the gaseous phase containing unreacted H2 and CO. Most of the separated gas is recycled to the reactor. Because the one-through reaction rate is high, the recycle ratio is sufficient at 1:1. After CO2 removal, the product DME is obtained by removing the impure water and methanol to a required level.

In case of natural gas, it can be converted to synthesis gas of H2/CO = 1 by means of CO2 reforming and used to the DME synthesis.

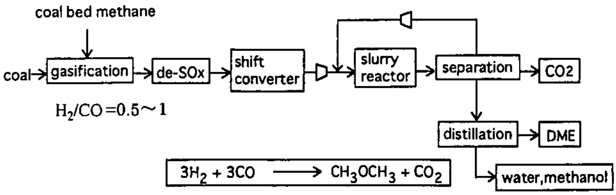

Fig. 6 DME synthesis from coal derived synthesis gas

4.2 Uses of DME

It is expected that DME will be introduced as a LPG-like home use fuel to replace coal and coal briquette and as an engine fuel to replace the light oil used in diesel engines in China, India, Indonesia, and other heavily populated countries with rich coal resources.

In Japan, 25 million tons of non-coking coal is imported to Japan to be consumed in electric power plants. It is forecasted that the future construction of more coal-burning power plants will be accompanied by an increase in the amount of coal consumed for this purpose to 57 million tons/year by 2005; three times as much as that is consumed now.

In Asian region besides Japan, the electricity demand is expected to increase at a rate of 7-8%/year and the coal consumption for power plant will be immense and the environmental pollution will be aggravated.

A concept of a system in which coal is gasified and converted to DME at coal mine, then transported to final consumption area as Japan for use in electric power production has been created as shown in Figure 7 . This system would provide the following potential benefits in comparison with the conventional coal flow.

At coal mine , [1] coal is prepared to reduce transportation costs and provide assurance of sufficient quality, but coal preparation would be unnecessary and all could be used effectively. [2] It would be possible to use low quality coal, for example, lignite coal with high moisture content or inflammable coal which is inadequate to the transportation. [3]Coal bed methane produced as a byproduct of coal mining is generally an unexploited energy resource. As it has a higher greenhouse effect than CO2, its proper treatment will be necessary. Although the coal bed methane generation varies over time, it could be used effectively by injecting it into the coal gasification reactor in which the methane is reformed to synthesis gas.

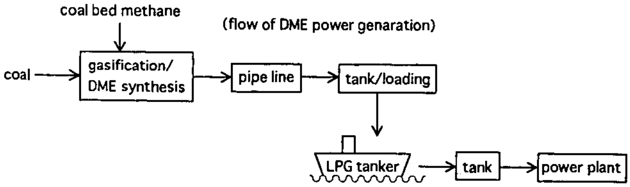

condition		· DME 2,500 t/d (over sea) · 500,000 k W power plant
DME production	plant cost	55 ~ 75 billion yen
	DME cost	2.2 ~ 2.9 yen/10^3 kcal
power genaration cost		8.2 ~ 9.4 yen/kWh

Fig. 7 Power generation through DME flow system and its cost estimation

At the transportation stage, [1] it could be handled in the same way as LPG, so the shipping and receiving base equipment could be simple, and would produce no dust.

In final consumption area , [1] the use of this ash-free clean fuel would eliminate the need for desulfurization and ash disposal treatment, [2] as a gaseous fuel, it would be sure to provide high power generation efficiency with combined cycle power generation, and the problems of providing a coal yard and dealing with ash would be resolved so it could be constructed in the suburbs of cities, thereby reducing transmission power loss.

4.3 Cost estimation of DME production and Electricity from DME burning power generation

Figure 8 shows an example of DME production cost (at coal mine and Japan CIF) in a case where equipment cost varies according to DME plant size with DME production of 910,000 tons/year as a constant condition. As the plant size increases, the cost of producing DME falls to the same level as the price of light oil and of LPG, whose cost is forecast to rise, in regions near coal mine at a production rate of 2,500 tons/day.

In this calculation, the cost of the total plant for DME production from coal is estimated to be 55 billion yen. If the plant costs climb from 55 billion to 75 billion yen, as shown in Figure 7, the DME production cost will be 2.22 yen/10 3 kcal to 2.86 yen/10 3kcal at the production site, while the electric power generation cost rises from 8.2 yen/kwh to 9.4 yen/kwh in Japan. These costs of electricity would be either equal to or lower than the cost of coal burning power generation.

4.4 Comparison of the Environmental Load of Coal burning and DME burning Power generation

The total environmental load produced between the coal production stage in coal mine over sea and the production of power and disposal of waste material in Japan has been compared. Figure 9 shows a result of this study. A switch over to DME flow system is sure to sharply cut the environmental load as follows.

[1] The volume of CO2 emissions would remain almost unchanged. When coal bed methane is emitted in the air, its effective utilization in the coal gasification reactor can cut 20% equivalent to CO2.

[2] No sulfur compounds would be discharged into the atmosphere in the DME flow system.

[3] As DME does not contain nitrogen, there would be no fuel NOx. By incorporating denitrification measures, the amount discharged into the atmosphere could be cut to approximately 1/9 of that discharged from a coal powered plant.

[4] Ash would be discharged as molten slag, it would be easier to use than fly ash, and no heavy metal elution would occur.

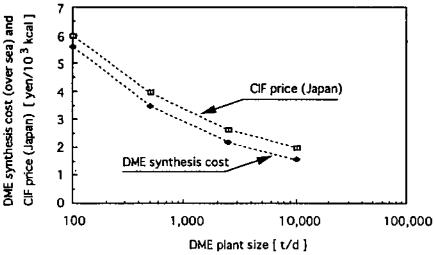

Fig. 8 Cost estimation of DME production

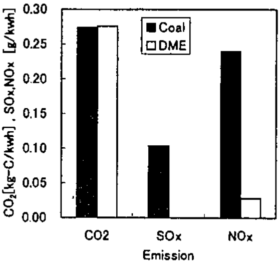

Fig.9 Environmental load of DME flow system and coal flow for power generation

5. Summary

If DME is developed to the stage where it is a practical product and is then distributed as an energy source for home use, transportation, and electric power generation, it will make a significant contribution to the resolution of energy and environmental problems, not only in the country using it for these purposes, but in other Asian countries.

Because DME is not a standard fuel which is already in use, integrated all-encompassing efforts must be made to prepare for its introduction and use from the production through the distribution stage.

References

(1) Y.Z. Han, K. Fujimoto, and T. Shikada: 4th Japan-China symposium on coal and C1 Chemistry proceedings (Osaka 1993), p. 515.
(2) Y.Z. Han, K.. Fujimoto, and T. Shikada: Ind. Eng. Chem. Res (to be published).
(3)Air Products and Chemicals: DOE/PC/90018-T7 (June, 1993).
(4) J.B. Hansen,B.Voss,F.Joensen and I.D.Sigurdardottiv.: SAE950063 (Feb. 1995).
(5)T.Fleisch,C.McCarthy,A.Basu,C.Udovich,P.Charbonneau,W.Slodowske, SE.Mikkelsen and J.McCandless.: SAE950061 (Feb. 1995).
(6) J.Daly and E.Osterman: Chemical Times &Trends,(October,1982),p.38.

LIQUID/CATALYST INTERACTIONS IN A SLURRY REACTOR FOR METHANOL SYNTHESIS USING "ZINC CHROMITE" CATALYST

George W. Roberts, Marco A. Márquez, M. Shawn McCutchen[1] and Carol A. Haney[2]
Department of Chemical Engineering, North Carolina State University, Box 7905,
Raleigh, NC 27695-7905
[1] - Current Address: E. I. Du Pont de Nemours and Company, Inc.,
Jackson Laboratory, Chambers Works, Deepwater, NJ 08023
[2] - Department of Chemistry, Box 8204

Keywords: Methanol, Slurry Liquid, Slurry Reactor, Zinc Chromite

INTRODUCTION

The synthesis of methanol and higher alcohols from mixtures of H_2 and CO (synthesis gas) is a promising approach to producing high-value fuels and chemicals from feedstocks such as natural gas, coal, coke and waste biomass. Slurry bubble column (SBC) reactors have been the focus of considerable attention for alcohol synthesis because the reactions are highly exothermic. Close temperature control is necessary to prevent excessive catalyst deactivation and to achieve high selectivity to oxygenates. The technology for producing methanol in a SBC reactor has been developed on a pilot scale, and is currently being commercialized [1,2,3]. This work has been based on Cu/ZnO, the conventional, low-pressure methanol synthesis catalyst. In addition, laboratory and pilot-plant studies have been conducted using cesium-promoted Cu/ZnO catalyst in a slurry reactor for the synthesis of higher alcohols [4,5]. Alkali-metal-promoted catalysts for higher-alcohol synthesis have evolved from the early work of Anderson and co-workers and Klier and co-workers [e.g., 6-9]. Unpromoted Cu/ZnO catalysts for methanol synthesis typically are operated at about 250°C, and the promoted Cu/ZnO catalysts for higher-alcohol synthesis have been evaluated over a temperature range of roughly 250 to 325°C.

"Zinc chromite", the high-pressure methanol synthesis catalyst, also is a promising starting point for the synthesis of higher (C_2^+) alcohols. However, this catalyst requires a much higher operating temperature, about 400°C, than Cu/ZnO. The liquids that traditionally have been used to slurry the Cu/ZnO catalyst are not thermally stable at this temperature [10-12]. In previous research, a family of liquids was identified that are sufficiently stable, thermally and chemically, to be used in a slurry reactor with the "zinc chromite" catalyst [10-13]. The objective of the present investigation was to explore the performance of an unpromoted "zinc chromite" catalyst in three of the most stable liquids, decahydronaphthalene (DHN or Decalin®, $C_{10}H_{18}$), tetrahydronaphthalene (THN or tetralin, $C_{10}H_{12}$) and tetrahydroquinoline (THQ, $C_9H_{11}N$). Unpromoted "zinc chromite" is essentially a methanol-synthesis catalyst. It is no longer competitive for methanol synthesis with the Cu/ZnO catalyst, which is more active and therefore can operate at lower pressures and temperatures. However, when promoted with alkali metals, "zinc chromite" can produce substantial yields of higher alcohols, particularly 2-methyl-1-alcohols such as isobutanol [14-17]. These alcohols might serve as alternative raw materials for the synthesis of established octane enhancers such as methyl tertiary butyl ether (MTBE). Thus, the present study of interactions between the unpromoted "zinc chromite" catalyst and the three slurry liquids was intended to provide a basis for using of one or more of these liquids as a slurry medium for an alkali-metal-promoted "zinc chromite" catalyst.

EXPERIMENTAL

The equipment used for this research has been described previously in some detail [10-13]. Basically, gases were fed from cylinders through activated carbon traps to remove impurities, including metal carbonyls, and then through mass flow controllers to measure and control the flow rates. The individual gas streams were mixed and compressed to the desired pressure. The compressed gas was passed through another activated carbon trap to remove any iron and/or nickel carbonyls that may have formed during and after compression. The gas was then fed into a 300 cm^3 stirred autoclave reactor. The reactor was charged with 20 grams of catalyst and 80 grams of the slurry liquid. The catalyst was a commercial, high-pressure methanol synthesis catalyst (Zn-0312 T1/8) from Engelhard Corporation, which was obtained in a reduced and stabilized form. The catalyst contained 60 wt% Zn and 15 wt% Cr, with the ZnO and $ZnCr_2O_4$ phases detectable by x-ray diffraction. The as-received BET surface area was 145 m^2/g. The gas leaving the reactor passed into a gas/liquid separator containing a cooling coil to control the temperature of the separator. The gas then passed through a back pressure regulator, through heated lines to prevent condensation and through a wet test meter to measure the gas flow rate. Samples of the reactor feed and effluent were periodically diverted to a dual-column gas chromatograph containing a Carboxen 1000 column followed by a thermal conductivity detector and a Poroplot Q column followed by a flame ionization detector. The former system was used to measure the fixed gases, H_2, N_2, CO, CO_2 and H_2O. The organic species were measured on the second system.

The autoclave reactor was mechanically agitated to ensure complete backmixing, and to ensure that gas/liquid mass transfer did not influence the reaction rate. Because the reactor was backmixed, the rates of formation or disappearance of the various species could be calculated directly from the inlet and outlet compositions and flow rates. The system was operated continuously for periods of one to four weeks. All data was taken at steady state conditions.

A matrix of four experiments was run in each liquid. Two experiments were at a temperature of 375°C, one with a H_2/CO ratio of 0.5 in the feed gas and the other with a feed ratio of 2. The remaining two experiments were at 325°C, at the same two H_2/CO feed ratios. For all experiments, the total pressure was 13.8 MPa and the space velocity was about 5000 sL/kg(cat)-hr.

RESULTS

Figure 1 shows the fractional conversion of carbon monoxide at each of the four operating conditions, in each of the three slurry liquids. The difference in conversion between slurry liquids was substantial. At all four operating conditions, the ratio of the highest conversion to the lowest was between about 2 and 6. The difference in apparent catalyst activity from liquid to liquid was even greater, since the actual partial pressures of CO and H_2 in the reactor were lower in the high-conversion experiments than they were in the low-conversion experiments. The CO conversion was lowest in DHN at all four conditions. At three of the four conditions, the CO conversion was highest in THN. The exception was at 325°C and a H_2/CO ratio of 0.50, where the conversion was higher in THQ than THN.

Figure 1
Effect of Slurry Liquid Composition on CO Conversion

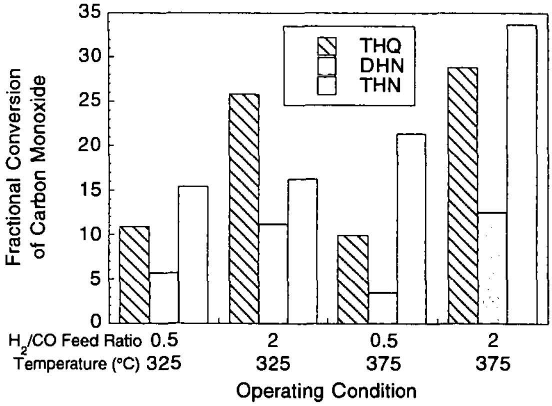

The CO conversion generally increased as the H_2/CO ratio increased from 0.5 to 2. The influence of temperature on conversion depended on the liquid employed. With THN, "normal" behavior was observed, i.e., conversion increased substantially with temperature. However, with DHN and THQ, the effect of temperature on conversion was small. The reason for this difference in behavior is discussed below, in connection with Figure 3.

Figure 2 shows the concentration of methanol in the outlet gas from the reactor at each of the four operating conditions, in each of the three slurry liquids. For comparison, the equilibrium methanol concentration at the specified reactor temperature, with the specified feed gas, also is shown.

Figure 2
Effect of Slurry Liquid Composition on Methanol Production

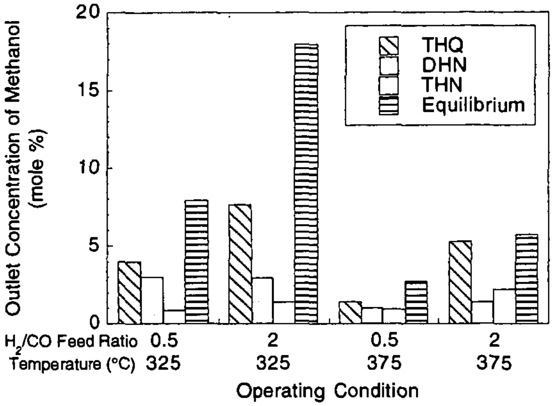

Once again, there was a substantial difference in catalyst performance from liquid to liquid. At all four conditions, the rate of methanol production was higher when THQ was used as the slurry liquid than with either THN or DHN. With the exception of the condition at 375°C and $H_2/CO = 2$, the rate of methanol synthesis was lowest in THN. At the lower temperature, where the reaction is not as close to equilibrium, the effect of liquid composition on the methanol production rate was substantial. For example, at $H_2/CO = 2$ and 325°C, this rate was about a factor of 6 higher in THQ than in THN and about a factor of 2.5 higher in THQ than in DHN.

At both temperatures, the methanol concentration generally increased as the H_2/CO ratio increased, with a given liquid. However, the effect was not as significant with DHN as with the other liquids. In fact, at 325°C with DHN, there was a slight decrease in methanol concentration as H_2/CO increased from 0.5 to 2.

The methanol production rate decreased with temperature at both H_2/CO ratios in THQ and DHN, reflecting the lower equilibrium concentration at the higher temperature. The methanol concentration increased as the temperature increased with THN, probably because the reaction was far from equilibrium in this liquid, at both temperatures.

Figure 3 shows that liquid composition also had a pronounced effect on reaction selectivity. The oxygenates were mostly methanol, plus some dimethyl ether and minor amounts of higher alcohols, primarily ethanol and isobutanol. The hydrocarbons were mostly methane, ethane and ethylene, plus lesser amounts of higher olefins.

Figure 3
Effect of Liquid Composition on Selectivity

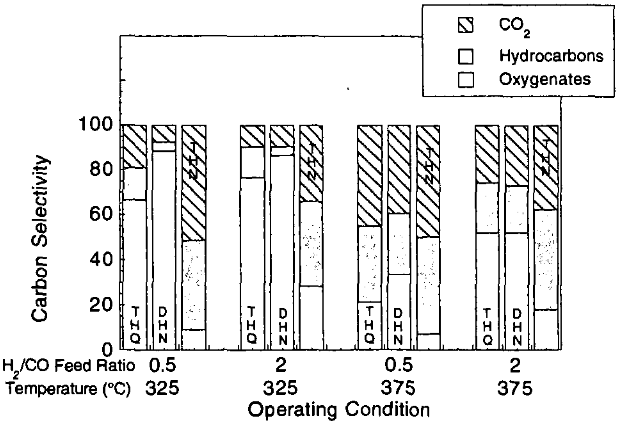

The most significant difference between liquids was the low oxygenate selectivity and high hydrocarbon selectivity in THN, relative to the other two liquids. These effects were especially pronounced at 325°C. The oxygenate selectivity, which never exceeded 30% in THN, was always a factor of about 3 to 10 higher in the other two liquids. Moreover, the high CO_2 selectivity with THN is a direct consequence of the high hydrocarbon selectivity, since "zinc chromite" is an excellent catalyst for the water-gas-shift reaction.

The selectivity to both hydrocarbons and CO_2 increased as the temperature was raised from 325 to 375°C, for all three liquids. The increase was especially pronounced for THQ and DHN since the oxygenate selectivity at 325°C was quite high for both of these liquids. In part, this reflects the fact that the methanol synthesis reaction is close to equilibrium in THQ and THN at 375°C, as shown in Figure 2. This close approach to equilibrium limited the quantity of methanol, the major component of the oxygenates, that could be produced. The oxygenate selectivity generally increased as the H_2/CO ratio was raised from 0.5 to 2 at constant temperature, for all three liquids.

The different product distributions that occur with the three liquids are consistent with the effect of temperature on CO conversion, as noted in connection with Figure 1. The primary products with THN are hydrocarbons and CO_2, and there are no significant equilibrium limitations to the formation of these products at the conditions of these experiments. Therefore, the CO conversion increases with temperature, reflecting the "normal" influence of temperature on reaction kinetics. With THQ and DHN, methanol is the primary product at 325°C. The equilibrium concentration of methanol decreases with temperature, partially offsetting the effect of temperature on reaction kinetics. As a result, the effect of temperature on CO conversion with THQ and DHN is relatively weak.

DISCUSSION

The chemical mechanism(s) that are responsible for the large differences in apparent catalyst activity and selectivity from liquid to liquid are not clear at this time. There has been very little detailed information published on the behavior of the unpromoted "zinc chromite" catalyst in the absence of a liquid, e.g., in a fixed- or fluidized-bed reactor. The problem of comparison is compounded by the fact that the present studies were carried out at a much lower total pressure than typically is used in a methanol synthesis plant employing the "zinc chromite" catalyst. This low pressure probably is characteristic of those that would be used with the promoted "zinc chromite" catalyst for higher-alcohol synthesis. However, the pressure difference makes it difficult to determine which of the liquids most closely approximates "normal" behavior. It is clear that the very low oxygenate selectivity that was observed with THN cannot be typical of conventional, vapor phase operation. The high hydrocarbon and CO_2 selectivities of this liquid, coupled with the high CO conversions, suggest some sort of liquid/catalyst interaction that inhibits methanol synthesis and dramatically increases the rate of hydrocarbon formation.

The methanol-synthesis activity of the "zinc chromite" catalyst in THQ is probably greater than the vapor-phase activity, based on the fact that the methanol synthesis reaction essentially came to equilibrium at 375°C and a H_2/CO ratio of 2 with THQ as the slurry medium. This enhanced rate of reaction may be related to the ability of secondary amines such as THQ to react with oxygenate and/or hydrocarbon fragments on the surface of the catalyst. Analyses of samples of THQ taken during and after reactor operation showed that some alkylation of THQ took place. Moreover, the alkylation of other amines has been reported to occur over various Fischer-Tropsch catalysts during vapor-phase operation, at substantially lower temperatures than those used in this research [18-22]. A mechanistic understanding of the chemistry of the interactions between THQ and the catalyst surface may lead to further improvements in rate and selectivity that can be applied to the synthesis of higher alcohols.

CONCLUSIONS

The composition of the slurry liquid had a major effect on both the apparent activity and selectivity of "zinc chromite" catalyst for the synthesis of methanol in a slurry reactor. Tetrahydronaphthalene (THN) does not appear to be a promising liquid because it causes low rates of oxygenate formation and low oxygenate selectivities. In contrast, the rate of methanol synthesis was very high in tetrahydroquinoline (THQ), and the oxygenate selectivity was good, especially considering that the rate of the methanol synthesis reaction was retarded by a close approach to equilibrium.

ACKNOWLEDGMENTS

This work was supported in part under a contract with the U. S. Department of Energy, Pittsburgh Energy Technology Center

REFERENCES

1. Studer, D. W., Brown, D. M., Henderson, J. L. and Hsiung, T. H., "Status of the Development of Methanol Synthesis by the LPMEOH* Process", paper presented at U. S. Department of Energy, Pittsburgh Energy Technology Center Indirect Liquefaction Contractor's Review Meeting, Pittsburgh, PA, November 13-15 (1989)

2. Roberts, G. W., Brown, D. M., Hsiung, T. H. and Lewnard, J. J., *Ind. Eng. Chem. Res.*, **32**, 1610 (1993)

3. "Methanol-Producing Clean Coal Technology Project Moves Into Construction In Kingsport, Tennessee", DOE News, October 16, 1995

4. Breman, B. B., Beenackers, A. A. C. M., Schuurman, H. A. and Oesterholt, E., *Catalysis Today*, **24**, 5-14 (1995)

5. Heydorn, E. C., Schaub, E. S., Stein, V. E. E., Underwood, R. P. and Waller, F. J., "Recent Progress on Syngas Conversion to Isobutanol", paper presented at U. S. Department of Energy, Pittsburgh Energy Technology Center Coal Liquefaction and Gas Conversion Contractor's Review Conference, Pittsburgh, PA, September 7-8 (1994)

6. Smith, K. J. and Anderson, R. B., *Preprints, Div. Fuel Chem., ACS*, **29** (5), 269 (1984)

7. Caverley, E. M. and Anderson, R. B., *J. Catal.*, **104**, 434-440 (1987)

8. Klier, K., Herman, R. G. and Young, C. W., *Preprints, Div. Fuel Chem., ACS*, **29** (5), 273 (1984)

9. Vedage, G. A., Himelfarb, P. B., Simmons, G. W. and Klier, K., *ACS Symp. Series*, **279**, 295-312 (1985)

10. McCutchen, M. S., "Synthesis of Alcohols from Carbon Monoxide and Hydrogen in a Slurry Reactor", Ph. D. Thesis, North Carolina State University (1996)

11. McCutchen, M. S., Márquez, M. A. and Roberts, G. W., *Chem. Engng. Sci.*, **51**, 2959 (1996)

12. Roberts, G. W., Màrquez, M. A. and McCutchen, M. S., "Alcohol Synthesis in a High-Temperature Slurry Reactor", *Catalysis Today* (in press)

13. Márquez, M. A., "The Stability of Liquids and the Effect of their Composition on the Production of Methanol in a Slurry Reactor", M. S. Thesis, North Carolina State University (1996)

14. Tronconi, E., Lietti, L., Groppi, G., Forzatti, P. and Pasquon, I., *J. Catal.*, **124**, 376-390 (1992)

15. Tronconi, E., Lietti, L., Forzatti, P. and Pasquon, I., *Applied Catalysis*, **47**, 317-333 (1989)

16. Tronconi, E., Ferlazzo, N., Forzatti, P and Pasquon, I., *Ind. Eng. Chem..Res.*, **26**, 2122-2129 (1987)

17. Tronconi, E., Christiani, C., Ferlazzo, N., Forzatti, P., Villa, P. L. and Pasquon, I., *Appl.Catal..*, **32**, 285 (1987)

18. Wang, C. J. and Ekerdt, J. G., *J. Catal.*, **80**, 172-187 (1983)

19. Wang, C. J. and Ekerdt, J. G., *J. Catal.*, **86**, 239-244 (1984)

20. Kliger, G. A., Glebov, L. S., Popova, T. P., Marchevskaya, E. V., Beryezkin, V. G. and Loktev, S. M., *J. Catal.*, **111**, 418-420 (1988)

21. Glebov, L. S., Kliger, G. A., Popova, T. P., Shiryaeva, V. E., Ryzhikov, V. P., Marchevskaya, E. V., Lesik, O. A., Loktev, S. M. and Beryezkin, V. G., *J. Mol. Catal.*, **35**, 335-348 (1986)

22. Kliger, G. A., Lesik, O. A., Mikaya, A. I., Marchevskaya, E. V., Zaikin, V. G., Glebov, L. S., and Loktev, S. M., *Izv. Akad. Nauk SSSR, Ser. Khim.*, 503 (1991)

SYNTHESIS OF FUEL ALCOHOLS AND MTBE FROM SYNGAS USING SPINEL OXIDE BASED CATALYSTS

David M. Minahan, Walter M. Hart
Technical Center, Union Carbide Corporation, P.O. Box 8361, South Charleston, WV 25303

William S. Epling and Gar B. Hoflund
Department of Chemical Engineering, University of Florida, Gainesville, FL 32611

Keywords: Higher Alcohol Synthesis, Fuel Alcohols, MTBE, Syngas

ABSTRACT

An equal mole mixture of methanol and isobutanol produced from syngas would be an ideal for the production of MTBE for use as a gasoline additive. The best present day syngas to alcohols catalysts and catalyst systems make too much methanol to be economically attractive, with typical methanol/isobutanol mole ratios of 3 or greater. We have investigated a Zn/Cr commercial methanol synthesis catalyst promoted with potassium and find that it is very selective for isobutanol when run under high temperature (> 400 C) and high pressure (>1000 psi) conditions due to both kinetic and thermodynamic considerations. Isobutanol rates >100 g/kg-hr are observed with a methanol/isobutanol mole ratio of 1.9. Surface characterization (via ISS and XPS) shows that the surface of the catalyst changes upon reduction and with use. Movement of potassium and chromium within the surface and near surface region of the catalyst is observed which can be correlated with catalytic performance

INTRODUCTION

Oxygen-containing hydrocarbon compounds can be added to gasoline to both reduce emissions and increase the octane rating of the fuel. Typical additives that have been examined are ethers such as MTBE and TAME and alcohols such as methanol. Methanol can be produced from syngas in high selectivity and can be used as an octane enhancer, but addition to gasoline can cause problems: the presence of water can cause phase separation and the Reid vapor pressure of the mixture is increased, leading to increased emissions from the gas tank. Mixtures of methanol and higher alcohols are a better alternative to methanol alone as ethanol raises the octane rating of the fuel and higher alcohols act as co-solvents, minimizing phase separation and lowering the overall vapor pressure of the additive. For long chain alcohols, branched alcohols are preferred over linear alcohols for enhancing the octane rating, whilst linear alcohols are preferred over branched alcohols for co-solvency characteristics. Ethers such as MTBE and TAME are preferred as additives due to their excellent co-solvent properties, lower volatility as compared with methanol and ethanol and their octane enhancing properties. Nonetheless, branched alcohols such as isobutanol and its higher homologs would still be of interest in their own right or as potential precursors to accepted additives such as MTBE or TAME. Alternatively, an equimolar mixture of methanol and isobutanol could be used as a direct precursor for the manufacture of MTBE.

Higher alcohol synthesis (HAS) catalysts have primarily evolved from modified methanol synthesis catalysts. The original methanol synthesis catalysts were based on a zinc/chromium spinel oxide operated around 400°C, and could tolerate some sulfur impurities in the syngas feed [1]. With the advent of effective desulfurization techniques for the syngas, a second generation methanol synthesis catalyst was developed, based on a more active copper metal based formulation which could operate at substantially lower temperatures (250-300°C) [2]. In both cases, the addition of alkali to the system resulted in the formation of higher alcohols, albeit at a substantially lower overall productivity. Other catalyst systems have been developed based on molybdenum sulfide (Dow/Union Carbide) [3], supported rhodium metal (Union Carbide) [4] and supported Cu/Co clusters (IFP) [5]. Once again, alkali is commonly added to the formulations. An interesting contrast between "modified methanol" catalysts and other systems is in the types of alcohols produced: the "modified methanol" catalysts produce mainly branched alcohols with a non Anderson-Schulz-Flory (ASF) distribution via an aldol condensation mechanism, the major products being methanol and isobutanol. The others produce linear alcohols via classical CO insertion/hydrogenation, producing the characteristic ASF distribution similar to that observed in linear condensation polymerization.

The following major reactions can take place over the catalyst or tube walls:

Alcohol Formation

$$n\,CO + 2n\,H_2 = C_nH_{2n+1}OH + (n-1)\,H_2O$$

Hydrocarbon Formation

$$nCO + (2n+1)\,H_2 = C_nH_{2n+2} + n\,H_2O$$

Water-Gas-Shift Reaction Equilibrium

$$CO + H_2O = CO_2 + H_2$$

Boudouard Reaction (CO disproportionation)

$$2CO = C + CO_2$$

Catalyst Selection and Testing Protocol

The catalysts examined here are materials consisting of a spinel oxide support (general formula AB_2O_4, where $A = M^{2+}$ and $B = M^{3+}$), promoted with potassium. The spinel itself consists of the traditional zinc/chromium oxide formulation, modified by the inclusion of excess zinc oxide and was obtained from Engelhard Corporation. The catalysts were tested first at low temperatures in stainless steel reactor tubes, then at higher temperatures (> 340 °C) in copper lined tubes to avoid the Boudouard reaction and hydrocarbon formation, known to be catalyzed by stainless steel (Fe, Ni) at these higher temperatures.

Reaction Mechanism

HAS requires at least two complimentary, yet competing reactions: carbon-carbon bond formation and hydrogenation. In the copper metal based, low temperature system, carbon-carbon bond formation is thought to occur via a classical CO insertion mechanism, followed by hydrogenation. In contrast, the high temperature catalysts utilize an aldol condensation mechanism to form the carbon-carbon bonds. The aldol reaction can proceed via acid or base catalysis.

The selection of elements other than copper as hydrogenation catalysts is a crucial feature of the high temperature formulations. Copper cannot be used as it sinters rapidly above 300°C, resulting in catastrophic loss in activity. Thus, temperature cannot be used as a lever in a copper catalyst system in order to improve alcohol activity. Nonetheless, both kinetics and thermodynamics favor HAS at higher temperatures. Methanol synthesis is at equilibrium under reaction conditions and higher alcohols are formed by consecutive reactions from methanol, thus higher temperatures will accelerate the secondary, higher alcohol forming reactions while the equilibrium of the methanol synthesis implies lower methanol concentrations. The net result is a considerable improvement in both the rate and selectivity to higher alcohols at higher temperatures at the expense of methanol. However, higher temperatures also enhance the formation of methane and higher hydrocarbons, so overall catalyst acidity must be carefully controlled. Thus alkali addition (in the form of potassium) helps by both providing basic sites for higher alcohol synthesis via the base-catalyzed aldol condensation and by neutralizing acid sites responsible for hydrocarbon formation.

The thermodynamic equilibrium for methanol formation dictates that methanol concentration grows quadratically with total pressure, while the concentration of higher alcohols exhibits a weaker dependence, resulting from kinetic considerations. Thus, pressure does increase reaction rate, but is not an effective handle for boosting HAS vs. methanol. However, hydrocarbon production is minimized at higher pressures, so total alcohol selectivity should rise.

RESULTS & DISCUSSION

Experiments were run in two different reactors. At lower temperatures (≤340°C) we used a stainless steel tubular microreactor. Low temperature runs were conducted at 12000 GHSV, $H_2/CO=1$ and 1000 psig. Most experiments were run in duplicate.

Low Temperature Operation (up to 340°C): The results are displayed in Table 1 below:

Table 1
K-impregnated Zn/CrO Catalysts - Low Temperature Operation

Temperature (°C)	260			
Potassium Loading	0% K	1% K	3% K	5% K
%CO2-free MeOH Selectivity	92	88	55	59
%CO2-free HC Selectivity	8	12	43	35
%CO2-free ROH Selectivity	92	88	57	65
%CO2-free C2+ ROH Selectivity	0	0	2	6
Isobutanol Rate (g/kg-hr)	0	0	0	0
Total Alcohol Rate (g/kg-hr)	206	104	35	20
Methanol Rate (g/kg-hr)	206	104	34	19
n-Propanol Rate (g/kg-hr)	0	0	0	0
Hydrocarbon Rate (g/kg-hr)	9	7	12	6
% CO Conversion	0.1	0.7	3.5	1.1

Temperature (°C)	300			
Potassium Loading	0% K	1% K	3% K	5% K
%CO2-free MeOH Selectivity	77	57	41	29
%CO2-free HC Selectivity	20	28	44	52
%CO2-free ROH Selectivity	80	72	56	48
%CO2-free C2+ ROH Selectivity	3	15	15	19
Isobutanol Rate (g/kg-hr)	0	0	0	0
Total Alcohol Rate (g/kg-hr)	327	197	99	73
Methanol Rate (g/kg-hr)	318	170	77	50
n-Propanol Rate (g/kg-hr)	4	14	10	9
Hydrocarbon Rate (g/kg-hr)	39	40	40	43
% CO Conversion	3.6	6.7	5.5	3.6

Temperature (°C)	340			
Potassium Loading	0% K	1% K	3% K	5% K
%CO2-free MeOH Selectivity	56	37	23	13
%CO2-free HC Selectivity	39	50	61	64
%CO2-free ROH Selectivity	61	50	39	36
%CO2-free C2+ ROH Selectivity	5	13	16	23
Isobutanol Rate (g/kg-hr)	0	0	0	3.7
Total Alcohol Rate (g/kg-hr)	428	361	197	177
Methanol Rate (g/kg-hr)	405	288	134	84
n-Propanol Rate (g/kg-hr)	7	34	31	45
Hydrocarbon Rate (g/kg-hr)	134	190	172	191
% CO Conversion	11.2	17.4	15.1	20.7

In all cases, higher alcohol production was low. Isobutanol was observed only for the case with the highest potassium loading (5%) at the highest temperature (340 °C). CO conversion increased with temperature as expected. Although higher temperatures increased methanol, total alcohol and total hydrocarbon activities, higher temperatures also promoted hydrocarbon formation at the expense of methanol synthesis. C2+ alcohol selectivity appeared to increase from 260 °C to 300 °C, but a further increase in temperature (to 340 °C) did not result in a corresponding increase in selectivity, probably due to interference from the stainless steel reactor walls. Catalysts impregnated with potassium had higher C2+ alcohol selectivity than the bare support at all three temperatures, and C2+ alcohol selectivity increased with potassium loading. However, total alcohol rates decreased as the loading of potassium on the catalyst increased due mostly to the suppression of methanol synthesis.

These results led us to believe that even higher operating temperatures would be beneficial, provided unwanted side reactions catalyzed by the stainless steel reactor walls could be eliminated. Further tests were performed in copper lined tubes. It should be noted that reaction *rates* are not dramatically increased by increased temperatures, rather the product distribution between methanol/higher alcohols and hydrocarbons is shifted; it seemed prudent, therefore, to explore the use of higher pressures as a means of boosting reaction rates, so pressures in excess of 1000 psig were also examined.

High Temperature/High Pressure Operation (400°C and above, up to 1500 psig): The results at 12000 GHSV and $H_2/CO = 1$ are displayed in Table 2 below:

Table 2
K-impregnated Zn/CrO Catalysts - High Temperature Operation

Catalyst	Unpromoted Spinel			
Temperature (°C)	400	400	440	440
Pressure (psig)	1000	1500	1500	1000
%CO2-free ROH Selectivity	65	77	43	27
Total Alcohol Rate (g/kg-hr)	111	236	133	59
Methanol Rate (g/kg-hr)	105	223	102	41
n-Propanol Rate (g/kg-hr)	0	0	18	10
Isobutanol Rate (g/kg-hr)	6	13	13	5
MeOH/I-BuOH Mole Ratio	73	68	31	36
Hydrocarbon Rate (g/kg-hr)	30	35	94	86

Catalyst	1% Potassium			
Temperature (°C)	400	400	440	440
Pressure (psig)	1000	1500	1500	1000
%CO2-free ROH Selectivity	61	75	53	53
Total Alcohol Rate (g/kg-hr)	133	251	167	129
Methanol Rate (g/kg-hr)	78	170	49	70
n-Propanol Rate (g/kg-hr)	8	0	9	6
Isobutanol Rate (g/kg-hr)	47	81	103	47
MeOH/I-BuOH Mole Ratio	6.6	8.4	1.9	6.0
Hydrocarbon Rate (g/kg-hr)	48	46	101	6

Catalyst	3% Potassium			
Temperature (°C)	400	400	440	440
Pressure (psig)	1000	1500	1500	1000
%CO2-free ROH Selectivity	80	88	70	70
Total Alcohol Rate (g/kg-hr)	75	159	99	67
Methanol Rate (g/kg-hr)	38	92	26	8
n-Propanol Rate (g/kg-hr)	4	10	0	0
Isobutanol Rate (g/kg-hr)	34	57	67	57
MeOH/I-BuOH Mole Ratio	4.5	6.4	1.5	0.54
Hydrocarbon Rate (g/kg-hr)	11	12	29	21

Catalyst	5% Potassium			
Temperature (°C)	400	400	440	440
Pressure (psig)	1000	1500	1500	1000
%CO2-free ROH Selectivity	96	97	84	83
Total Alcohol Rate (g/kg-hr)	82	159	130	70
Methanol Rate (g/kg-hr)	59	123	47	16
n-Propanol Rate (g/kg-hr)	0	0	23	10
Isobutanol Rate (g/kg-hr)	23	34	51	38
MeOH/I-BuOH Mole Ratio	10	14	3.7	1.7
Hydrocarbon Rate (g/kg-hr)	2	3	15	10

The non-promoted catalyst gives mostly methanol and a small amount of isobutanol. The total alcohol rate more than doubles when the pressure is increased from 1000 to 1500 psig, showing the beneficial effect of pressure on reaction rate. Increasing the temperature to 440°C cuts the totoal alcohol selectivity and the methanol rate in half and almost triples the hydrocarbon rate.

1% potassium promotion does not substantially affect total alcohol selectivity, but the alcohol distribution shifts dramatically in favor of isobutanol. Isobutanol rates >100 g/kg-hr are observed at the highest operating conditions of temperature and presssure (440°C and 1500 psig) with a methanol/isobutanol mole ratio of 1.9. Total alcohol selectivities are above 50%.

Increasing the level of potassium on the catalyst results in an increase in selectivities to total alcohols, but a decrease in total alcohol rate. A methanol/isobutanol mole ratio < 1 (0.54) can be obtained for the 3 wt% potassium catalyst at 440°C and 1000 psi, but the isobutanol rate is reduced to < 60 g/kg-hr. The 5 wt% material is the most selective for alcohols, but the methanol rate has increased and the isobutanol rate has decreased.

Surface Science Characterization

Surface characterization (via ISS and XPS) shows that the surface of the catalyst changes upon reduction and with use. Reduction under hydrogen (250°C for 4.5 hrs in 1 x 10-7 torr hydrogen) induces the migration of potassium to the topmost monolayer resulting in complete surface coverage as observed by ion scattering spectroscopy (ISS). X-ray photoelectron spectroscopy (XPS) data are consistent with these observations and also reveal that the near-surface region of the catalysts consist primarily of zinc oxide. Chromium is observed, and appears to be present as potassium chromate or potassium dichromate.

The used catalysts exhibit a potassium rich surface, but the near surface contains much less potassium and again consists essentially of zinc oxide. The chromium now appears to be present as chromium(III) oxide, hydroxide and some chromium metal. These results suggest that the active phase of the catalyst is potassium supported on zinc oxide, possibly promoted with chromium.

ACKNOWLEDGMENTS

The present work was sponsored by the United States Government Department of Energy (DOE) under DOE Contract No. DE-AC22-91PC90046 through the Pittsburgh Energy Technology Center. Our thanks to Engelhard Corporation for supplying the catalysts and to Paul Ruppert and Dana Jividen for catalyst testing.

REFERNCES

1. Satterfield, C. N., *Heterogeneous Catalysis in Industrial Practice*, 2nd Edition, McGraw-Hill, New York, (1991) p. 454.
2. Forzatti, P., Tronconi, E. and Pasquon, I., Catal. Rev. Sci. Eng. 33(1&2) 109-163 (1991).
3. SRI PEP Review "Dow/Union Carbide Process for Mixed Alcohols from Syngas", March (1986).
4. Bhasin, M. M. ,Bartley, W. J., Ellgen P. C. and Wilson, T. P., *J.Catal.* 54, 120 (1978).
5. Courty, P., Durand, D., Freund, E., and Sugier, A., *J. Mol. Cat.* 17, 241 (1982).

KINETICS OF HIGHER-ALCOHOL FORMATION FROM SYNTHESIS GAS USING STATISTICALLY DESIGNED EXPERIMENTS

Anil Gunturu, Jean B. Cropley, Edwin L. Kugler and Dady B. Dadyburjor
Department of Chemical Engineering, West Virginia University,
P.O. Box 6102, Morgantown WV 26506-6102

Keywords: Statistical design, Synthesis gas, Higher alcohols, Promoted molybdenum sulfide catalyst

Introduction

Alcohols containing upto five carbon atoms can be added to the gasoline pool to improve the octane number without an excessive impact on the environment. The Dow patents [1,2] describe a promoted molybdenum sulfide catalyst for the production of these alcohols from synthesis gas even in the presence of sulfur. Screening studies in our laboratory [3] have indicated that a carbon-supported, potassium-promoted cobalt-molybdenum sulfide catalyst yields exceptionally good results, in terms of the space-time yield (STY) of each higher alcohol.

For the purpose of reactor design, it is necessary to obtain a set of kinetic equations for this catalyst, to represent the formation rates of the alcohols in a range of realistic conditions for a large number of variables. However, the kinetic equations need not necessarily reflect the mechanism(s) of the reactions. The present work describes such a set of equations for methanol, ethanol, propanol and total hydrocarbons. The range of conditions used to obtain the experimental data, and in which the set of equations is valid, was based on the screening study and is characterized by: temperature, 300-350°C; total pressure, 400-1000psi; CO/H_2 ratio, 0.5-2; and methanol, 0-1.2ml/h. A fractional factorial set of experiments was designed to incorporate this large set of parameters. A Berty-type internal-recycle reactor was used, to ensure that the reaction rate corresponded to known (outlet) concentrations of reactants and products.

Experimental

The K-Co-MoS/C catalyst was prepared by incipient-wetness impregnation. The catalyst contained 18wt% Mo with a Co/Mo ratio of 0.34 and a K/Mo ratio of 1.3. The catalyst was reduced to the sulfide form inside the reactor, and thereafter purged in hydrogen. The reactor system is computer controlled and all operating conditions can be set by a PC. The system has four lines for gas feed and one line for the liquid methanol feed. The 16 factorial experiments were performed in random order, so as to make the catalyst age an independent variable as well. An additional, center-point, experiment was repeated after every four runs. Product STYs were obtained every 2h, and each experiment was conducted for at least 12h.

Results

The products were found to be linear alcohols, and follow an Anderson-Schultz-Flory distribution. A detailed examination of the experiments with methanol addition showed (1) that the higher alcohols are generated from secondary reactions involving methanol, (2) that a simple condensation reaction involving only alcohols can be ruled out, and (3) that the most likely process involves CO insertion into a lower-carbon-number alcohol to form a higher alcohol. These observations are consistent with the isotopic-labelling results of Santiesteban [4].

Based on this reaction scheme, a two-step process was used to obtain the kinetic equations. First, simple power-law representations were used to quantify the "gross" rates of formation of each of the alcohols (other than methanol) and the hydrocarbons. By the "gross" rate of formation, we refer to the total rate of formation, regardless of the fact that some of the particular species may react further. Then the rate of formation as actually measured (*i.e.*, after some of the particular species reacts further) would be the "net" rate of formation. Since we assume sequential reactions:

$$\mathrm{MeOH + CO \rightarrow EtOH,}$$

$$\mathrm{EtOH + CO \rightarrow PrOH,}$$

etc, therefore the "gross" rate of methanol formation is the sum of the "net" rates of methanol, ethanol, *etc.* formation, and so on.) For an alcohol of carbon number n, the power-law rate expression included terms for the partial pressures of CO, H_2, inert, and the alcohol of carbon number n-1, as well as terms for the catalyst age (t), the temperature (T), the pre-exponential factor (A) and the activation energy (E). The general power-law expression used can be centered around the center-point values of the parameters as:

$$r_{\mathbf{n}}^{\mathrm{gross}} = k_{\mathbf{n}}\,(P/P_{cp})_{CO}^{\mathbf{an}}\;(P/P_{cp})_{H2}^{\mathbf{bn}}\;(P/P_{cp})_{I}^{\mathbf{cn}}\,(P/P_{cp})_{\mathbf{n-1}}^{\mathbf{dn}}\,(t/t_{cp})^{-\lambda\mathbf{n}} \tag{1a}$$

where

$$k_{\mathbf{n}} = A_{\mathbf{n}}\exp[-(E_{\mathbf{n}}/R)(1/T - 1/T_{cp})] \tag{1b}$$

Here the subscripts I and cp denote inert and a center-point value respectively. Note that a power-law expression for methanol, for which $\mathbf{n}=1$, was not obtained in this first step. Because methanol is used as a reactant in many of the runs in this work, the rate of formation could be positive or negative, and a simple power-law model cannot be used for this purpose. For the other alcohols, the best fit of the power-law models yield values of $A_{\mathbf{n}}$, $E_{\mathbf{n}}$, $a_{\mathbf{n}}$-$d_{\mathbf{n}}$, and $\lambda_{\mathbf{n}}$ as shown in Table I. Further, a statistical analysis of the results indicated which parameters were statistically significant for each product.These parameters are identified in Table I.

These parameters were then used in the second step, where a Langmuir-Hinshelwood-type rate expression was used for each product, incorporating only the statistically significant parameters for each product. Now a methanol rate expression can be written, incorporating both forward- and reverse-reaction terms to allow for net rates of formation or net rates of reaction.Kinetic rate constants, equilibrium constants, and activation energy constants representing each statistically significant parameter were obtained by a non-linear best fit of the Langmuir-Hinshelwood-type rate expression. The final expressions can be written as:

$$r_{MeOH}^{\mathrm{gross}} = \frac{4.9047\exp[-(117\mathrm{x}10^{3}/R)(1/T-1/T_{cp})]\,\{\pi_{CO}\pi_{H2}^{2} - (0.3359K_{cp}/K_{eq})\,\pi_{MeOH}\}}{(1 + 0.0696\,\pi_{CO} + 0.64\,\pi_{H2}^{2} + 0.694\,\pi_{MeOH})^{2}} \tag{2}$$

$$r_{EtOH}^{\mathrm{gross}} = \frac{1.5259\exp[-(25.0\mathrm{x}10^{3}/R)(1/T-1/T_{cp})]\;\pi_{MeOH}}{1 + 0.7367\,\pi_{MeOH}} \tag{3}$$

$$r_{PrOH}^{\mathrm{gross}} = \frac{0.1159\exp[-(86.8\mathrm{x}10^{3}/R)(1/T-1/T_{cp})]\;\pi_{EtOH}}{1 + 0.640\,\pi_{EtOH}} \tag{4}$$

$$r_{HC}^{\mathrm{gross}} = \frac{4.6965\exp[-(95.3\mathrm{x}10^{3}/R)(1/T-1/T_{cp})]\;\pi_{MeOH}}{1 + 1.2479\,\pi_{MeOH}} \tag{5}$$

Conclusions

The forms of the final rate expressions obtained imply that, under the present conditions, the rate expressions refer to the intrinsic kinetics and are not strongly governed by internal pore diffusion. Further, it would appear that the chemisorption of alcohol is the rate-limiting step, and that the individual steps of hydrogen cleavage, hydrogenation, dehydration and CO insertion (in the overall CO-insertion mechanism) are not rate limiting.

Acknowledgments

This work was supported by the US Department of Energy under Contract Number DE-AC22-91PC91034.

References

1. M.M. Conway, C.B. Murchison and R.R. Stevens, *US Patent 4,675,344*, (1987).
2. R.R. Stevens, *US Patent 4,752,622* (1988).
3. Z. Liu, X. Li, M.R. Close, E.L. Kugler, J.L. Petersen and D.B. Dadyburjor, *Ind. Eng. Chem. Res.*, submitted (1996).
4. J.G. Santiesteban, Ph.D. Dissertation, Lehigh University (1989).

Table I
Results of Fit to Power-Law Model for Gross Reaction Rates

Species	A_n	E_n	a_n	b_n	c_n	d_n	λ_n
Ethanol	0.959	-38,252	0.1242	-0.3067	-0.0411	0.7307(*)	-0.1511
Propanol	0.0904	-97,852	0.0893	-0.6406	0.0216	0.5642(*)	-0.3226
Hydrocarbons	2.68	-106,478	-0.0273	-0.5212(*)	-0.0123	0.6636(*)	-0.2682(*)

(*) These parameters considered statistically significant

THE PERFORMANCE CHARACTERISTICS OF C_1-C_5 ALCOHOL - GASOLINE BLENDS WITH MATCHED OXYGEN CONTENT IN A SINGLE CYLINDER SI ENGINE

Yasser Yacoub, Reda Bata, Mridul Gautam, Daniel Martin
Department of Mechanical and Aerospace Engineering
West Virginia University
Morgantown, WV 26506

Keywords: alcohol-gasoline blend, engine knock , brake thermal efficiency

ABSTRACT

Alcohols with carbon numbers ranging from C_1 to C_5 were individually blended with unleaded test gasoline (UTG-96). All of the alcohol-gasoline blends had the same oxygen mass content. The performance characteristics of the blends were quantified using a single cylinder spark ignition engine. The knock limiting spark timing was determined by analysis of the third derivative of the measured in-cylinder pressure versus crank angle. The engine operating conditions were optimized for each (C_1-C_5) blend with two different values of matched oxygen content. Adding lower alcohols (C_1,C_2,C_3) to UTG96 improved knock resistance. Further improvement was achieved by increasing the oxygen content of the fuel blend. Blends with higher alcohols (C_4,C_5) showed degraded knock resistance when compared to neat gasoline.

INTRODUCTION

Alcohols are being used as fuel blending components to improve unleaded gasoline octane quality. Normally, methanol and ethanol are the main blending components [1][1]. Addition of small amounts of alcohols, with carbon numbers greater than one, improves fuel blend water tolerance, material compatibility, and volatility characteristics [2-7]. Increasing the alcohol content, which also increases oxygen content, up to a certain concentration (when blended with gasoline) improves the blends' knock resistance. Further increase in alcohol content does not lead to any further improvements in knock resistance [2,8,9].

The global objective of the current study is to examine individual alcohols, when blended with gasoline, with regard to engine knock. The specific objective is to determine whether the improved knock characteristics of an alcohol-gasoline blend is solely dependent on its oxygen content or if other factors are involved.

THE PHYSICAL AND CHEMICAL PROPERTIES

Selected chemical and physical properties of gasoline and alcohols are shown in table 1. When higher alcohols are blended individually with gasoline, larger amounts are needed in the blend in order to match the oxygen content of lower alcohols blends, as shown in figure 1. The changes in properties of blends with oxygen mass contents of 2.5% and 5.0%, relative to neat gasoline, are shown in figures 2 - 5. In general, as the alcohol concentration increases so does the blend's specific gravity, as shown in figure 2. Fuel blends with higher alcohols are slightly denser than those with lower alcohols for given oxygen mass contents of 2.5% and 5.0%. The energy-mass density for each blend is predicted by summing up the mass weighted heating values of the neat components[2]. The higher the oxygen content in the blend, the lower its energy mass-density value, as shown in figure 3. The decrease in the heating value is almost the same for blends with matched oxygen content. The energy-volume density for each blend is computed by multiplying its energy-mass density and its specific gravity. Blends with higher alcohols have larger energy-volume densities, when compared to those with lower alcohols for the given oxygen mass contents of 2.5% and 5.0%, as shown in figure 4. For the same operating conditions, engines burning a stoichiometric mixture need to consume more alcohol-gasoline blend than neat gasoline, as shown in figure 5. It should be noted that other important properties of gasoline-alcohol blends, such as distillation characteristics, reid vapor pressure, and water tolerance, are not discussed.

Table 1. Comparison of selected fuel properties

	Methanol	Ethanol	N-Propanol	N-Butanol	N-Pentanol	Gasoline
Formula	CH_3OH	CH_3CH_2OH	$CH_3CH_2CH_2OH$	$CH_3(CH_2)_2CH_2OH$	$CH_3(CH_2)_3CH_2OH$	—
Oxygen content (mass fraction)	0.50	0.35	0.27	0.22	0.18	0.00
Molecular weight	32.04	46.07	60.10	74.12	88.15	111.21
Specific gravity	0.79	0.79	0.80	0.81	0.81	0.74
Energy-mass density (KJ/gm)	19.93	26.75	30.94	33.22	34.84	42.91
Energy-volume density (KJ/cm^3)	15.78	21.11	24.86	26.90	28.38	31.87
Stoichiometric air/fuel ratio	6.43	8.94	10.28	11.12	11.68	14.51

---

[1] Numbers in parentheses designate references at end of paper.

EXPERIMENTAL

The engine used is a Waukesha single cylinder spark ignition cooperative fuel research engine with variable compression ratio. The engine bore and stroke are 3.25 and 4.5 in; respectively, giving a displacement of 0.612 L. A DC current General Electric dynamometer is used to motor and load the engine. Unleaded test gasoline (UTG-96) and high purity straight chain (n-) alcohols are used. Table 2 lists the engine conditions which are held constant throughout this investigation.

Table 2. Engine test conditions

Speed (rev./min.)	1000
Equivalence ratio	1.0 ± 0.02
Load	wide open throttle
Coolant temperature (°F)	209
Oil temperature (°F)	153 ± 4
Mixture temperature (°F)	110 ± 3
Air relative humidity (%)	25 ± 4

Alcohols with carbon numbers ranging from C_1 to C_5 are individually blended with unleaded test gasoline (UTG-96). The resulting alcohol-gasoline blends have oxygen mass contents of 2.5% and 5.0%. For each fuel blend, the compression ratio (CR) is changed from a value of 7, to the high knock limiting value in increments of 0.5. The spark timing (ST) is varied from a value of 30 to 5 degrees crank angle (CA) before top dead center (BTDC) in decrements of 5.

ANALYSIS PROCEDURE

For a fixed CR, a polynomial (up to fourth order) in ST is fit to brake thermal efficiency (η) values using the least squares method. The fitted polynomial is used to determine the spark timing for maximum η.

The magnitude of the third derivative of the measured in-cylinder gas pressure is used to quantify the engine knock strength [10]. A value of 50 psia/CA^3 is observed as a maximum threshold to characterize a single pressure trace that does not exhibit any knocking. Figure 6 shows that at low knocking operations, the time-averaged knock strength value is less than the threshold value, over a set of consecutively sampled in-cylinder pressure traces for different operating conditions (CR,ST). It also shows that the percentage of traces that exhibits knocking correlates linearly with the time averaged knock strength over that range. This linear relation is used to calculate values of time averaged knock strength that corresponds to a range of traces that exhibit knock.

For a fixed CR, a polynomial (up to fourth order) in ST is fit to the time-averaged knock strength values using the least squares method. The fitted polynomial is used to determine the spark timing for a range (5-20%) of traces that exhibit knock.

The intersection of the knock limiting spark timing curve ,and that of maximum η, identifies an optimum operating point (ST,CR), as shown in figure 7. The line of maximum BMEP is shown as well. Another operating point of interest is that of the maximum possible CR within the tested range. This is the point of intersection of the 5 CA BTDC spark timing line with the knock limiting spark timing curve.

RESULTS AND DISCUSSION

For the investigated CR range, all blends with 2.5% and 5.0% oxygen content have higher maximum η values as compared to neat gasoline, with the exception of ethanol-gasoline blend with a 2.5% oxygen content, as shown in figures 8 and 9. The increase in brake thermal efficiency with increased alcohol content is attributed to the faster burning rate, and higher cylinder pressure, than those of neat gasoline [2,11]. Detailed thermodynamic analysis of the power cycle is required to explain the improvement in η values for all blends and, specifically, the degradation for the ethanol-gasoline blend with 2.5% oxygen.

Figures 10 and 11 show the knock limiting spark timing at different compression ratios for 5% traces exhibit knocking. The C_1 to C_3 alcohol-gasoline blends show a wider range of operation relative to neat gasoline. On the other hand, higher alcohol (C_4,C_5)-gasoline blends show degraded knock resistance when compared with neat gasoline. These trends are common for the 2.5% and 5.0 % oxygen blends.

In order to quantify each blend's knock resistance characteristics, the areas under the curve in figures 10 and 11 are computed and compared to that of neat gasoline, as shown in figure 12. Adding lower alcohols (C_1,C_2,C_3) to gasoline has improved knock resistance. Ethanol-gasoline blends show the highest knock resistance improvement (~ 20%-35 %). On the other hand, blends with higher alcohols (C_4,C_5) show degraded knock resistance, when compared to gasoline. The pentanol-gasoline blend shows the highest knock tendency (~30%-60%). For the 5.0% oxygen blends, both the improvement and degradation trends of knock resistance are more pronounced when compared with the 2.5% oxygen blends.

For an engine operating at optimum conditions, the improvement in the values for η and CR for different blends, relative to neat gasoline, are shown in figures 13 and 14 respectively. For the 2.5% oxygen blends, the methanol-gasoline blend shows the highest improvement in η (~2%). The ethanol-gasoline blend, however, has the highest improvement (~6.0%) for η when compared with the 5.0% oxygen blends. Blends with higher alcohols (C4,C5) have degraded η values, with the exception of butanol-gasoline blend with 2.5% oxygen. For the 5.0% oxygen blends, both the improvement and the degradation trends for the η values are more pronounced, when compared with the 2.5% oxygen blends with the exception of 2.5% oxygen butanol-gasoline blend. The slight improvement in η value for the butanol-gasoline blend with 2.5% oxygen, is attributed to the blend's higher η value when compared to gasoline at the same CR value. Both 2.5% and 5.0% oxygen ethanol-gasoline blends show the highest improvement (~ 2.5% and 10.0%, respectively) in optimum CR value, when compared with matched oxygen content blends.

For an engine operating at the maximum possible CR and ST of five degrees BTDC, all blends (with the exception of pentanol-gasoline blends) show improvement for the values of η and CR relative to neat gasoline, as shown in figures 15 and 16 respectively. For the 2.5% oxygen blends, methanol-gasoline blends show the highest improvement in η (~4%). On the other hand, the propanol-gasoline blend has the highest improvement in η (~7.5%), when compared with the 5.0% oxygen blends. For the 2.5% oxygen blends, the ethanol-gasoline blend operates at the highest (~15%) CR value and the methanol-gasoline blend operates at the highest (~20%) CR value among the 5.0% oxygen blends.

CONCLUSIONS

Adding lower alcohols (C_1,C_2,C_3) to unleaded test gasoline improves its knock resistance from 8% to 20% for blends with a 2.5% oxygen mass content, when compared to neat gasoline. The knock resistance is further improved (20% - 35% compared to gasoline) by increasing the oxygen content of the blend to 5.0%. Ethanol-gasoline blends show the highest knock resistance improvement (~ 20% - 35 %) among all tested blends.

Blends with higher alcohols (C_4,C_5) show degraded knock resistance when compared to gasoline. Pentanol-gasoline blend exhibits the highest knock tendency, ~ 30% more, than gasoline for 2.5% oxygen blends. The knock tendency is further promoted (~60% more than gasoline) by increasing the oxygen mass content in the blend to 5.0%.

All tested alcohol-gasoline blends have a higher brake thermal efficiency than neat gasoline operating, when compared at the same compression ratio, with the exception of ethanol-gasoline blend with 2.5% oxygen mass content.

For an engine optimized for maximum brake thermal efficiency and knock limiting operating conditions, (C_1,C_2,C_3) alcohol-gasoline blends operate at higher efficiency (~ 2% for C_1-UTG 2.5% O_2 and ~6% C_2-UTG 5.0% O_2) when compared to neat gasoline, due to its higher optimum compression ratio. Ethanol-gasoline blends show the highest improvement in optimum compression ratio (~2.5% for 2.5% O_2 and ~10.0% for 5.0% O_2).

For an engine optimized for knock limiting operating conditions and five degress BTDC spark timing, (C_1,C_2,C_3) alcohol-gasoline blends operate at higher efficiency (~ 4% for C_1-UTG 2.5% O_2 and ~7.5% C_3-UTG 5.0% O_2), when compared to neat gasoline, due to their higher compression ratios (15-20%).

Detailed thermodynamic analysis of the power-gas exchange cycle is required to explain the improved/degraded trend of different blends.

ACKNOWLEDGMENTS

The authors wish to thank the US-DOE Pittsburgh Technology Center, especially Gary Stiegel, Project Manager, for funding this project, Contract No. DE-AC22-91PC91034. Thanks are also due to the National Research Center for Coal and Energy (NRCCE), specifically, Dr. Caulton Irwin, Project Coordinator. Thanks are also due to our project team colleges at WVU Chemical Engineering Department and Union Carbide Company, Charleston, West Virginia.

REFERENCES

1. N. E. Gallopoulos, "Alcohols for Use as Motors Fuels and Motor Fuel Components", Presented at the Coordinating European Council Second International Symposium, Wolfsburg, West Germany, 1985.
2. K. S. Patel , S. Kuma, and O.Y.Kwo, " The Performance Characteristics of Indolene-MPHA Blends in a Spark Ignition Engine", SAE 872069.
3. M. Sposini, R. Pea, et al., Proceedings of the Fifth International Alcohol Fuel Technology Symposium, Vol. II, Auckland, NZ, May 1982.
4. "Alcohols and Ethers A Technical Assessment of Their Application as Fuels and Fuel Components", API Publication 4261, Second Edition, July 1988.

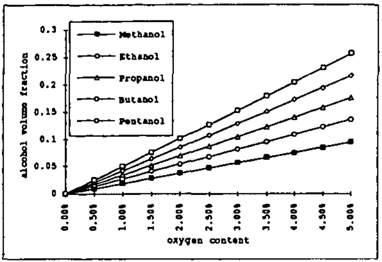

Fig.1 Alcohol volume fraction in C_1-C_5 alcohol-gasoline blends with matched oxygen content.

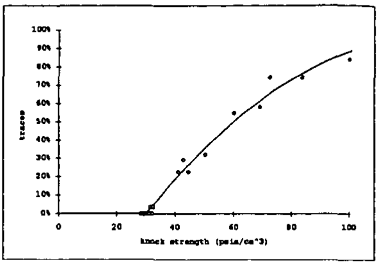

Fig.6 Percentage of knocking traces versus time averaged knock strength for different operating conditions.

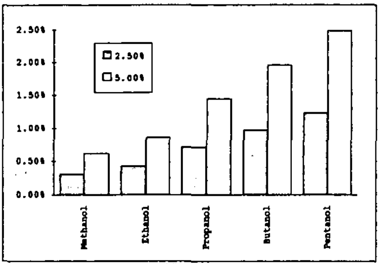

Fig.2 The change in specific gravity of C_1-C_5 alcohol-gasoline blends relative to neat gasoline.

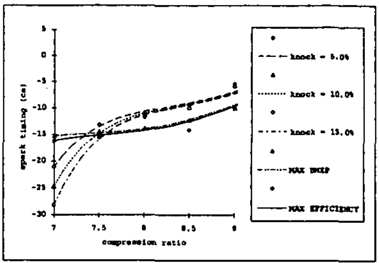

Fig.7 Determination of optimum operating compression ratio and spark timing.

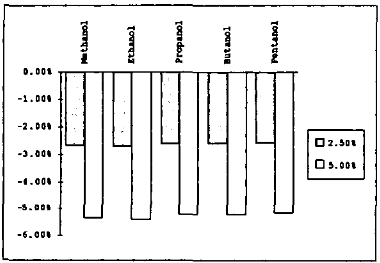

Fig.3 The change in energy-mass density of C_1-C_5 alcohol-gasoline blends relative to neat gasoline.

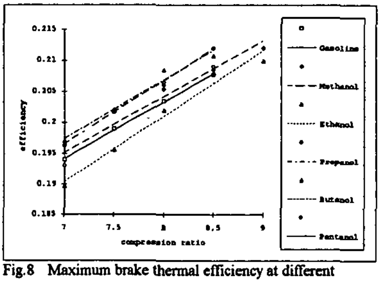

Fig.8 Maximum brake thermal efficiency at different compression ratios for blends with 2.5% oxygen.

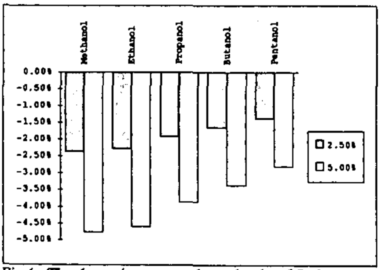

Fig.4 The change in energy-volume density of C_1-C_5 alcohol-gasoline blends relative to neat gasoline.

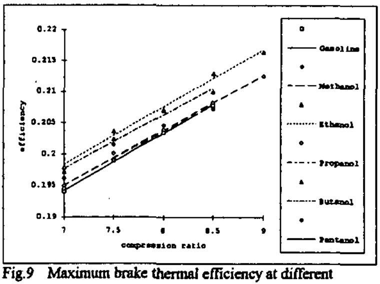

Fig.9 Maximum brake thermal efficiency at different compression ratios for blends with 5.0% oxygen.

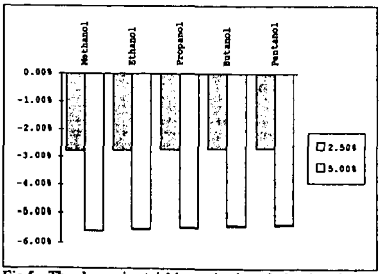

Fig.5 The change in stoichiometric air to fuel ratio of C_1-C_5 alcohol-gasoline blends relative to neat gasoline.

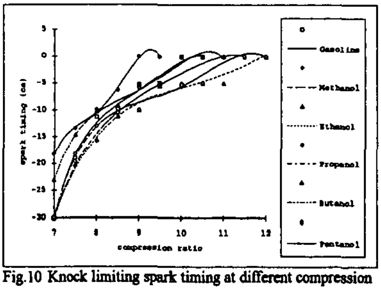

Fig.10 Knock limiting spark timing at different compression ratios for blends with 2.5% oxygen content.

5. E. I. Dupont De Nemours and Company, Inc., "Clean Air Act Waiver Application Section 211(f)", Application to the US. Environmental Protection Agency, Vol. 3, Sect. XIII, 1984.

6. R. L. Furey, "Volatility Characteristics of Gasoline-Alcohol and Gasoline-Ether Fuel Blends", SAE 852116.

7. K. Owen and T.Coley, "Automotive Fuels Reference Book", Second Edition, Society of Automotive Engineers, Inc., 1995

8. K. S. Patel and N.A.Henein, "Burning velocities in Methanol-Indolene Air Mixtures in a CFR Engine", SAE 850111.

9. A. R. Sapre, "Properties, Performance and Emissions of Medium Concentration Methanol-Gasoline Blends in a Single-Cylinder, Spark-Ignition Engine", Paper 881679, Presented at The International Fuels and Lubricants Meeting and Exposition, Portland, Oregon, Oct, 1988.

10. M. D. Checkel and J.D. Dale, "Computerized Knock Detection from Engine Pressure Record", SAE 860028

11. N. D. Brinkman, "Ethanol Fuel - A Single-Cylinder Engine Study of Efficiency and Exhaust Emissions", SAE 810345

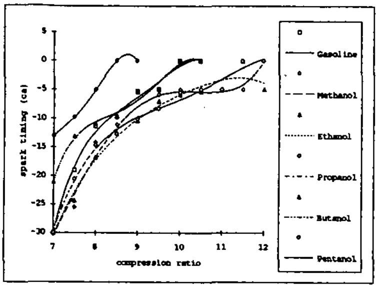

Fig.11 Knock limiting spark timing at different compression ratios for blends with 5.0% oxygen content.

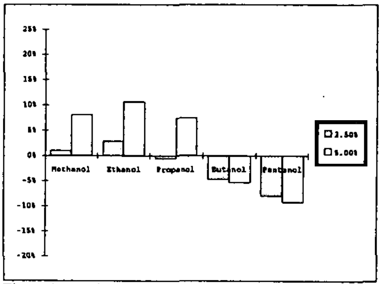

Fig.14 Comparison of alcohol-gasoline blends (2.5% and 5% oxygen mass content)compression ratio to neat gasoline at optimum operation.

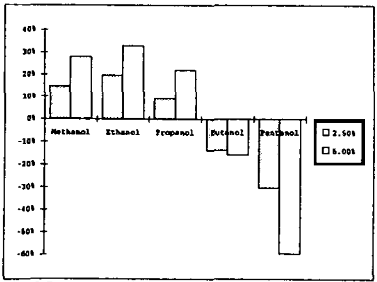

Fig.12 Improvement in knock resistance for alcohol-gasoline blends (2.5% and 5% oxygen mass content) relative to neat gasoline.

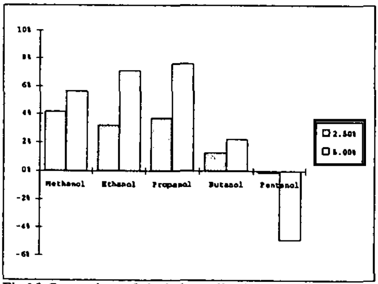

Fig.15 Comparison of alcohol-gasoline blends (2.5% and 5% oxygen mass content) brake thermal efficiency to neat gasoline at maximum compression ratio.

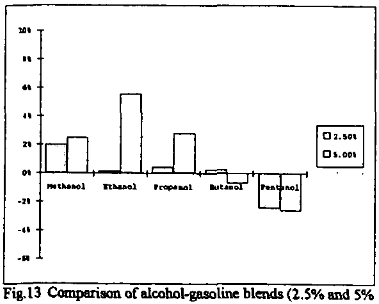

Fig.13 Comparison of alcohol-gasoline blends (2.5% and 5% oxygen mass content)brake thermal efficiency to neat gasoline at optimum operation.

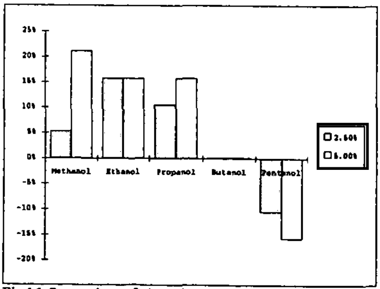

Fig.16 Comparison of alcohol-gasoline blends (2.5% and 5% oxygen mass content) maximum compression ratio to neat gasoline.

ACTIVATION OF LIGHT ALKANES IN THE PRESENCE OF Fe- AND Mn-PROMOTED SULFATED ZIRCONIA

T.-K. Cheung and B. C. Gates
Department of Chemical Engineering and Materials Science, University of California, Davis, CA 95616

ABSTRACT

A strong solid acid prepared by impregnation of sulfated zirconium hydroxide with iron nitrate and manganese nitrate was tested for conversion of *n*-butane, propane, and ethane in a packed bed flow reactor at 40-450°C. At 40°C, the predominant reaction of *n*-butane was catalytic isomerization (with disproportionation). Propane and ethane reacted at 200°C, each of these alkanes being converted predominantly into butanes. The occurrence of *n*-butane isomerization at temperatures <200°C suggests that the catalyst is strongly acidic, and the observations of butane formation from propane and from ethane are consistent with chemistry analogous to superacidic solution chemistry, but not to the exclusion of conventional strong-acid catalysis. The catalyst appears to offer good prospects for low-temperature butane conversion, although it deactivates rapidly. If acid catalysis were to be applied for propane and ethane conversion, more active catalysts would be needed.

INTRODUCTION

Environmental concerns are leading to the replacement of aromatic hydrocarbons in gasoline by branched alkanes and oxygenated compounds such as methyl *tert*-butyl ether. The ether is produced from the reaction of methanol with isobutylene, and the latter can be formed from *n*-butane by isomerization followed by dehydrogenation. Alkane isomerization reactions are catalyzed by very strong acids such as aluminum chloride supported on alumina, which has the disadvantages of being corrosive and expensive to dispose of. Thus, there is a need for improved catalysts and processes for the isomerization of *n*-butane and other straight-chain alkanes. Propane and ethane, which are present in natural gas, could also in prospect be converted by acid catalysis, giving valuable higher-molecular-weight hydrocarbons and liquid fuels (1), but practical catalysts for such conversions are lacking.

Researchers have long been searching for strong solid acids that are noncorrosive and active enough to activate light alkanes at low temperatures. A good candidate is sulfated zirconia, which catalyzes isomerization of *n*-butane at temperatures as low as 25°C (2). The addition of iron and manganese promoters increases the activity of sulfated zirconia for *n*-butane isomerization by three orders of magnitude (3). The discovery of such a highly active acidic catalyst has provided a good opportunity to explore the reactions of light alkanes at low temperatures. Our goals were to investigate the reactivities of ethane, propane, and *n*-butane with iron- and manganese-promoted sulfated zirconia (FMSZ), emphasizing low conversions to allow investigation of the reactivities of these alkanes under conditions of the simplest possible chemistry. Here we summarize new and published results for reactions of these alkanes with FMSZ and, for comparison, with zeolites.

EXPERIMENTAL

FMSZ was prepared by stepwise incipient wetness impregnation from sulfated zirconium hydroxide (Magnesium Elektron, Inc.) that was impregnated with iron and manganese nitrate solutions. The impregnated material was calcined at 650°C. The weight percentages of iron, manganese, and sulfur in the catalyst were determined to be 1, 0.5, and 1.8 %, respectively.

Before each reaction experiment, the FMSZ in flowing N_2 [30 mL(NTP)/min] was heated from 20 to 450°C at a rate of 7.1°C/min, and the temperature was then held at 450°C for 1.5 h. Reactions were carried out in a once-through plug-flow reactor at atmospheric pressure and temperatures in the range of 40-450°C. Some experiments were also conducted to characterize the reactivities of propane and of ethane in the presence of HZSM-5 and USY zeolite.

RESULTS

Conversion of n-Butane. In the presence of FMSZ, *n*-butane was converted catalytically into *i*-butane, propane, *i*-pentane, and *n*-pentane at temperatures <200°C. The selectivity for *i*-butane formation was >95% for *n*-butane conversions <10%. The overall *n*-butane conversion and the conversions of *n*-butane into products as a function of time on stream in the temperature range of 40-100°C are characterized by a break-in period followed by a period of rapid deactivation. The molar ratio of propane to pentanes approached a value of about 1 at 40°C, after about 25 h on stream. The initial (5 min time on stream) rate of *n*-butane conversion at 75°C and 0.0025 atm *n*-butane partial pressure was 4×10^{-8} mol/(s · g).

Conversion of Propane. The gas-phase products formed from propane in the temperature range of 200-300°C with FMSZ were methane, butanes, and pentanes. The conversion of propane was characterized by an initial break-in period followed by a declining period. The initially formed products were mostly methane and butanes. The selectivity to butanes increased with time on stream initially and then declined slowly, with the selectivity to pentanes increasing. The selectivity to methane simply declined with time on stream. At 250°C, the number of turnovers per sulfate group was greater than 1 after 16 days of operation. At temperatures >300°C, the only gas-phase products observed were methane, ethane, ethene, and propene. The rates of formation of methane and ethene were approximately the same at low conversions. The initial (5 min time on stream) rate of propane conversion with FMSZ at 250°C and 0.01 atm propane partial pressure was 3×10^{-10} mol/(s · g).

USY zeolite was active in converting propane into propene, methane, and ethene only at temperatures >400°C. At a propane conversion of 0.1%, the products observed were methane, ethene, and propene. Because the experiments were not run long enough, the number of turnovers (per Al site) was less than 1.

Conversion of Ethane. In the presence of FMSZ, the products observed for ethane conversion were H_2, methane, ethene, and butanes; at 200°C the products were predominantly butane and ethene. Selectivity to butanes decreased from 30% (at 0.01% conversion) at 200°C to 10% (at 0.1% conversion) at 400°C. In the temperature range of 200-350°C, the conversion to butane, ethene, and methane decreased with time on stream. At temperatures >350°C, the conversion to butanes decreased with increasing time on stream, but the conversion to ethene and to methane decreased and then increased with time on stream, followed by another declining period (Fig. 1). H_2 was observed only at temperatures >400°C; its rate of formation was characterized by an initial increase, followed by a slow decline with time on stream. Because experiments were run for only a few hours, the number of turnovers (per sulfate group) was less than 1. The initial (5 min time on stream) rate of ethane conversion in the presence of FMSZ at 450°C and 0.2 atm ethane partial pressure was 4×10^{-8} mol/(s · g).

With HZSM-5, ethane was converted into ethene in the temperature range of 300-450°C; butane and methane were also formed, but only at temperatures >400°C. In contrast, ethene and H_2 (at nearly the same rates) were formed from ethane in the presence of USY zeolite at temperatures >300°C, and traces of butane were sometimes observed at 450°C. Conversion of ethane with either of the zeolites decreased with time on stream.

The initial (5 min on stream) selectivities observed for FMSZ, HZSM-5, and USY zeolite at low ethane conversions, 450°C, and 0.2 atm ethane partial pressure are summarized in Table 1. At about 0.1% conversion, FMSZ is characterized by the lowest ethene selectivity (94%), whereas USY zeolite is characterized by the highest (99%). Butane formed with a selectivity of 4.1% with FMSZ and 1.8% with HZSM-5; it was not observed for USY zeolite, except for a trace at 0.3% conversion. At 400°C and an ethane conversion of 0.1%, the selectivity to butane with FMSZ was 10%, whereas the selectivity to butane with HZSM-5 was negligible.

DISCUSSION

Alkane Reaction Data. The data allow a rough comparison of reaction rates and product distributions for conversions of relatively unreactive alkanes in the presence of several strong solid acid catalysts, namely, FMSZ, HZSM-5, and USY zeolite. The product distributions obtained at low conversions provide some insight into the reaction mechanisms and how the reactions were initiated.

Because the rates of *n*-butane conversion with FMSZ were high, the butane conversion data demonstrate catalytic reactions. However, the rates of propane and of ethane conversion with FMSZ and with the zeolites were much lower than that of butane conversion, and catalysis was not demonstrated for these reactions.

Carbenium Ion Reactions. Classical acid catalysis of alkane conversion involves reactions of carbenium ions, $C_nH_{2n+1}^+$, which can be formed by protonation of alkenes or hydride abstraction from alkanes. In the presence of FMSZ, the low-temperature (40-100°C) *n*-butane conversion data are consistent with such chemistry, whereby $C_4H_9^+$ reacts with butene (formed by dehydrogenation of butane) to give $C_8H_{17}^+$, which rearranges and undergoes β-scission to give isobutylene, which then undergoes protonation and hydride transfer to yield *i*-butane (4-7). The observation of a nearly 1 to 1 molar ratio of propane and pentanes suggests the occurrence of stoichiometric disproportionation, involving the $C_8H_{17}^+$ intermediate. A question still remains about how the carbenium ion and the butene may be formed at low temperatures with FMSZ.

With FMSZ, the data for propane conversion in the temperature range of 200-300°C are also consistent with classical carbenium ion reactions. Propene formed by dehydrogenation of propane can react with the secondary carbenium ion $C_3H_7^+$ to form $C_6H_{13}^+$, which reacts with propene to form $C_9H_{19}^+$, which then rearranges and undergoes β-scission to give butene and $C_5H_{11}^+$. Butene would undergo protonation and then hydrogen transfer to form butane.

At temperatures >300°C, the observed formation of butane from ethane in the presence of FMSZ, HZSM-5, or USY zeolite could also be explained by carbenium ion chemistry, with butane being formed by reaction of $C_2H_5^+$ and ethene. However, the chemistry now involves a highly unstable primary carbenium ion, and one would expect the reaction to form butane from ethane to be more than the observed two or three orders of magnitude slower than that of propane.

Thus, the results raise the question of whether there is more to the chemistry than carbenium ion reactions. The suggestion of very strong acidity raises the possibility of the involvement of carbonium ions.

Carbonium Ion Reactions. The reactions involving the formation of penta-coordinated carbonium ions, $C_nH_{2n+3}^+$, which can be formed by protonation of alkanes, occur in superacidic solutions (1). This non-classical chemistry has been invoked to explain zeolite-catalyzed cracking of alkanes at low conversions (8). According to a simplified picture of the chemistry, a zeolite catalyst at a temperature of approximately 500°C protonates alkanes to give carbonium ions, which collapse to give alkanes + carbenium ions or H_2 + carbenium ions. Thus, the observations of H_2 in this work suggests the occurrence of such chemistry.

In the temperature range of 40-100°C, the *n*-butane data observed with FMSZ are consistent with carbonium ion and oligocondensation chemistry, whereby *n*-butane is protonated to form $C_4H_{11}^+$, which collapses to give H_2 and $C_4H_9^+$, which reacts (undergoes oligocondensation) with *n*-butane to form $C_8H_{19}^+$; $C_8H_{19}^+$ then rearranges and collapses to yield *i*-butane and $C_4H_9^+$.

At temperatures <300°C, the propane and ethane conversion data observed with FMSZ are also consistent with the hypothesis that oligocondensation occurs. $C_2H_5^+$, formed from protonation of propane, followed by cleavage to give methane, could react with propane to form $C_5H_{13}^+$, which would collapse to give methane and $C_4H_9^+$, which would abstract a hydride to form butane. Similarly, ethane could be protonated to form $C_2H_7^+$, which would decompose to give H_2 and $C_2H_5^+$ or methane and CH_3^+; $C_2H_5^+$ would then combine with ethane to form $C_4H_{11}^+$, which would be deprotonated to give butane.

Thus, the results mentioned in the preceding two paragraphs are consistent with both carbenium ion and carbonium ion chemistry. However, the occurrence of simple stoichiometric dehydrogenation of ethane observed with USY zeolite at low conversions is explained only by a carbonium ion mechanism. Ethane is presumably protonated to form $C_2H_7^+$, which decomposes into H_2 and $C_2H_5^+$, which is deprotonated to form ethene, giving a 1 to 1 molar ratio of H_2 to ethene.

Similarly, propane is protonated to form $C_3H_9^+$, which decomposes into H_2 and $C_3H_7^+$ or methane and $C_2H_5^+$. Propene and ethene are formed after deprotonation of $C_3H_7^+$ and $C_2H_5^+$, respectively. The nearly equal rates of formation of methane and ethene from propane in the presence of FMSZ suggest the occurrence of carbonium ion reactions rather than carbenium ion reactions at low conversions.

Similarly, with HZSM-5 (9), the *n*-butane data at about 500°C are consistent with the hypothesis that $C_4H_{11}^+$ is formed by protonation of *n*-butane. At low *n*-butane conversions, the observation of nearly equal rates of formation of H_2 and of butenes; of methane and of propene; and of ethane and of ethene with HZSM-5 provides further evidence of the occurrence of the carbonium ion mechanism.

However, we emphasize that once alkenes are formed, carbenium ion chemistry takes over because alkenes are readily protonated, and the classical carbenium ion reactions are much faster than those involving protonation of alkanes.

Chemistry of Alkane Conversions. Thus, in summary, the data for light alkane reactions in the presence of solid acids are consistent with chemistry analogous to that occurring in superacidic solutions, provided that conversions are low. As conversions increase, alkenes are increasingly formed via carbonium ion reactions, and classical carbenium ion reactions dominate. The implication is that carbonium ion chemistry appears to play a role in initiation of light alkane conversions with strong solid acids. The lower the temperature at which an alkane is to be activated, the stronger is the acid required; thus, the data suggest that FMSZ may be much more strongly acidic than the zeolites.

However, the chemistry involving FMSZ and alkane conversions is still not fully elucidated, in part because the roles of Fe and Mn are not well understood; the reactions of light alkanes at low temperatures may not be entirely acid-catalyzed. Although there is no evidence in the high-temperature product distribution data of any enhancement in dehydrogenation activity of sulfated zirconia resulting from addition of iron and manganese to sulfated zirconia, these promoters may act as catalysts (10) or redox initiators (11) to produce alkenes, which would then be protonated to form carbenium ions and kick off the conventional catalytic cycles. Alternatively, the promoters may be catalytically involved in alkane conversions as they may somehow increase the acidity of the sulfated zirconia, so that it is capable in protonating alkanes at low temperatures.

CONCLUSIONS

In the presence of FMSZ at 40°C, *n*-butane was catalytically isomerized into *i*-butane and disproportionated into propane and pentanes. Propane and ethane reacted to give butane with FMSZ at 200°C; however, the rate of ethane conversion was about 2 to 3 orders of magnitude less than that of propane conversion, which is 3 to 4 orders of magnitude less than that of *n*-butane conversion. At temperatures >300°C and in the presence of FMSZ, HZSM-5, or USY zeolite, these alkanes are inferred to be protonated to form carbonium ions, which then collapse to give smaller alkanes or H_2 and (after deprotonation) alkenes. The comparison of the product distributions for ethane and for propane conversion suggests that there is no evidence of enhancement in dehydrogenation activity of sulfated zirconia resulting from incorporating Fe and Mn. The chemistry by which these alkanes are converted in the presence of FMSZ is complicated; both classical carbenium ion and non-classical carbonium ion mechanisms seem to contribute to the products observed, and the roles of Fe and Mn promoters are not yet resolved.

ACKNOWLEDGMENTS

We thank Magnesium Elektron, Inc., for providing the sulfated zirconium hydroxide. The research was supported in part by the U.S. Department of Energy, Pittsburgh Energy Technology Center.

REFERENCES

1. Olah, G. A., Halpern, Y., Shen, J., and Mo, Y. K., J. Amer. Chem. Soc., 95, 4960 (1973).
2. Hino, M. and Arata, K., Chem. Commun., 851 (1980).
3. Hsu, C.-Y., Heimbuch, C. R., Armes, C. T., and Gates, B. C., Chem. Commun., 1645 (1992).
4. Bearez, C., Chevalier, F., and Guisnet, M., React. Kinet. Catal. Lett., 22, 405 (1983).
5. Guisnet, M., Avendano, F., Bearez, C. and Chevalier, F., Chem. Commun., 336 (1985).
6. Bearez, C., Avendano, F., Chevalier, F., and Guisnet, F., Bull. Soc. Chim. Fr., 36 (1985).
7. Adeeva, V., Lei, G. D., and Sachtler, W. M. H., Appl. Catal., 118, L11 (1994).
8. Haag, W. O. and Dessau, R. M., in "Proceedings, 8th International Congress on Catalysis, Berlin, 1984," Vol 2, p.305, Dechema, Frankfurt-am-Main, 1984.
9. Krannila, H., Haag, W. O., and Gates, B. C., J. Catal., 135, 115 (1992).
10. Wan, K. T., Khouw, C. B., and Davis M. E., J. Catal., 158, 311 (1996).
11. Lange, F. C., Cheung, T.-K., and Gates, B. C., Catal. Lett., 41, 95 (1996).

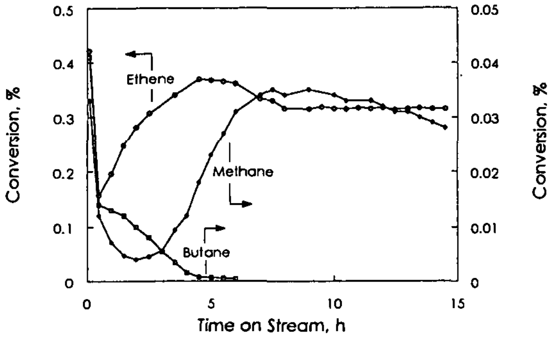

Figure 1. Conversion of ethane into ethene, butane, and methane with FMSZ at 450°C. Feed ethane partial pressure = 0.2 atm, inverse space velocity = 3.7×10^5 (s · g)/mol.

Table 1. Comparison of initial selectivity[a] for ethane conversion in the presence of FMSZ, HZSM-5, and USY zeolite at 0.2 atm ethane partial pressure and 450°C.

Solid acid	$10^{-5}\times$ Inverse space velocity, (s · g)/mol	Ethane Conversion, %	Normalized Selectivity, %		
			Methane	Ethene	Butane
FMSZ	1.83	0.38	3.4	89.7	6.9
FMSZ	1.14	0.29	2.6	91.1	6.3
FMSZ	0.46	0.13	1.7	94.2	4.1
HZSM-5	0.28	0.11	0.9	97.3	1.8
USY zeolite	7.32	0.30	1.7	96.8	1.5
USY zeolite	1.83	0.08	0.7	99.3	0

---

[a] Data taken at 5 min on stream.

HYDROGEN SPILLOVER CATALYSIS IN PACKED BED REACTORS: KINETICS OF 1-BUTENE HYDROISOMERIZATION OVER DUAL BEDS OF Pt/GRAFOIL AND FeCe/GRAFOIL

John Weigle and Jonathan Phillips*
Penn State University
Department of Chemical Engineering
133 Fenske Lab
University Park PA 16802
PWA@PSU.EDU

Keywords: catalysis, olefins, hydrogen spillover, carbon supports

INTRODUCTION

Recently a new family of very selective and active olefin double bond shift catalysts was discovered (1). These catalysts have potential value for increasing the octane of petroleum components both directly (β-position olefins generally have far higher octane value than α-olefins) and indirectly (improved input to alkylation units leads to higher octane product). This family of catalysts consists of one metal from the first row of the transition metals (typically iron or cobalt), one metal from the lanthanide series (typically cerium or praseodymium) and a relatively small amount of one noble metal (typically palladium). The multimetallic catalysts (e.g. Fe:Ce:Pd, 1:1:0.1) have some catalytic properties of each parent material. For example, FeCePd/Grafoil has selectivity (excellent) similar to FeCe/Grafoil, but high activity similar to that of Pd/Grafoil, a material with poor selectivity.

The following model was proposed to explain the unusual activity and selectivity of the multimetallic catalysts (1). First, the particle surfaces are 'compound'. They consist primarily of 'alloy' transition metal-lanthanide metal zones, but there are also postulated to be small zones of unalloyed noble metal. Second, each zone on the surface performs a different chemical function, and these functions add together to yield highly active and selective catalysts. Specifically, the alloy zone selectively isomerizes the 1-butene, and the noble metal zone provides hydrogen atoms via 'spillover' to allow this process to take place at a high level of activity. This model was shown to be consistent both with the known mechanism of bond shift and with information regarding hydrogen spillover.

Recent results support the above hypothesis. For example, it was shown that a physical mixture of the two components (e.g. FeCe/Grafoil and Pt/Grafoil) is as much as an order of magnitude more active than the sum of each component tested separately for 1-butene isomerization. The synergism also resulted in dramatically improved selectivity (2). It was also found that physical mixtures showed strong synergism for selective conversion of butadiene to butene (3).

These are not the first reports of physical mixtures demonstrating synergistic catalytic properties. Two models exist to explain synergism of physical mixtures. The classic model is the 'polyfunctional catalyst model' (4), and the second is the hydrogen spillover model (5). The earlier results strongly support the hydrogen spillover model. Indeed, it is difficult to identify an intermediate between 1-butene and 2-butene. Such an intermediate is required for the 'polyfunctional catalyst' model. Moreover, as discussed in earlier papers (2,3) the improvement in selectivity found in all cases and the 'limit' on synergism found in the hydroisomerization of butadiene are clearly consistent with the spillover hypothesis, but difficult to explain using any alternative model.

The present study was an attempt to test for spillover leading to synergism in segregated bed reactors. Specifically, the present work was designed to test the hypothesis that hydrogen spillover will lead to synergism in packed bed reactors with two stages, a graphite supported noble metal section and a graphite supported FeCe section. Synergism was found, but surprisingly the bed order was found to significantly impact the results.

EXPERIMENTAL

Catalyst Preparation. Two catalysts, FeCe/Grafoil and Pt/Grafoil, were prepared via the incipient wetness technique (1,6). GTA-grade Grafoil (Union Carbide) is a moderately high surface area (22 m^2/gm), high purity, graphitic material (7). More detail on the catalysts is available elsewhere (1-3).

Kinetics. The bond shift in 1-butene was studied using a differential Pyrex microreactor operated at 1 atmosphere pressure (8). Reaction gas was purchased from Matheson and mixed with rotameters to yield a reaction gas with 2% butene, 18% hydrogen, and helium as balance. Analyses were done using a 6840 Hewlett Packard gas chromatograph equipped with a TC detector, a packed column containing Carbopac C/ 0.19% picric acid obtained from Supelco. In all studies intended for the purpose of comparing levels of activity total conversion was kept to less than 12% in order to justify the 'differential reactor' approximation.

In order to test the impact of physical mixtures on catalytic activity and selectivity physical mixtures containing different absolute amounts and different relative amounts of each material were required. In each case a section of 2 mg of Pt/Grafoil mixed with 18 mg of unloaded Grafoil was placed in the reactor. Variable amounts (zero to seventy mg) of FeCe/Grafoil were also placed in the reactor. Caution was taken to assure that the two beds were firmly in contact, but not mixed. In this configuration the reaction mixture encountered FeCe/Gr first. Beds with the components loaded in the opposite order, so that the reaction gas encountered the Pt/Gr first, were also tested. Next, all the catalyst material was reduced in flowing hydrogen at 400 C for four hours. After cooling the reaction gas mixture was added and the system allowed to stabilize.

RESULTS/DISCUSSION

In previous work (2,3) many relevant control studies were reported, including the impact of Grafoil addition on catalytic behavior (very minor), the activity of FeCe/Grafoil in the absence of any metal (extremely low at temperatures of interest) and the initial activity of noble metal only. This last 'control' was repeated in the present case as well. That is, the activity and selectivity of a bed consisting of 18 mg of Grafoil and 2 mg of Pt/Grafoil at 373 K was determined after 15 minutes or less on stream.

The next studies were designed to determine the activity and selectivity of beds with noble metal on top (first contact with feed mix) and to contrast this with the activity/selectivity of beds in which the alloy fraction is on top and the noble is on the bottom (at reactor exit).

The behavior of systems in which the noble metal is on the bottom are easy to explain. Each addition of FeCe/Grafoil resulted in a significant increase in measured activity (Figure 1). As the FeCe/Grafoil in the absence of noble metal has barely any activity at the temperatures employed, these results indicate synergism. In all likelihood hydrogen atoms generated on the noble metal surface diffuse 'upstream' and activate FeCe in the 'upper bed'.

It should be noted that the data shown in Figure 1a (except for the Pt/Grafoil only case) was collected after the catalysts had been on stream for between two and five hours. In all instances this was found to correspond to a period in which the overall activity of the bed declined relatively little (Figure 2). In most cases the activity dropped by less than 10% during this period.

Selectivity data for the case of the platinum bed on bottom is shown in Figure 1b and it is clear that the selectivity decreases as the activity synergism increases. This is different than that observed previously for well mixed beds with the same net catalyst composition (2). In those studies selectivity was found to improve with each increment of FeCe/Grafoil. A possible explanation for the surprising impact of bed segregation is that all products must pass through a bed of noble metal prior before leaving the reactor. Platinum may be a better catalyst for converting 2-butenes than 1-butene. In contrast, in a well mixed bed much of the 2-butene formed on FeCe may not encounter platinum before leaving the reactor.

Defining synergism in beds in which the noble metal is on top is more difficult. In all cases deactivation was rapid. After one hour on stream the catalysts bed had lost more than 35% of their initial activity in most cases, after two hours activity loss approached 50% and the decline in activity continued rapidly thereafter. Thus, at present no plots of activity or synergism are available.

In sum, it is clear that the present work demonstrates that synergism is found in integral bed reactors, containing segregated beds of platinum and FeCe/Grafoil. The nature of the synergism is a function of several factors, including the relative placement of the beds. In the event that the platinum is on top the overall deactivation rate is rapid. This can be fully explained by the deactivation of platinum. Apparently platinum at the bottom of a bed of FeCe is protected from deactivation and the spillover process continues for a far longer period of time. A second finding is that the overall selectivity of segregated beds is different than that of well mixed beds of the same composition. A third finding is that there appears to be a limit to the 'reach' of spillover. That is, the degree of activity enhancement per gram of FeCe appears to gradually diminish as more FeCe is added.

REFERENCES

1. W.C. Lu, H. Chang and J. Phillips, *J. Catal.* 146, 608 (1994).
2. H. Chang and J. Phillips, *Langmuir* 12, 2756 (1996).
3. H. Chang and J. Phillips, *Langmuir*, in press.
4. P.B. Weisz, *Adv. Catal.* 13, 137 (1962).
5. W.C. Conner, Jr, G.M. Pajonk and S.J. Teichner, *Adv. Catal.* 34, 1 (1986).
6. S.C. Lin and J. Phillips, *J. Appl. Phys.* 58, 1943 (1985).
7. S. Bukshpan, T. Sonnino and J.G. Dash, *Surf. Sci.* 52, 460 (1975).
8. H. Durr and J. Phillips, *J. Catal.* 126, 619 (1990).

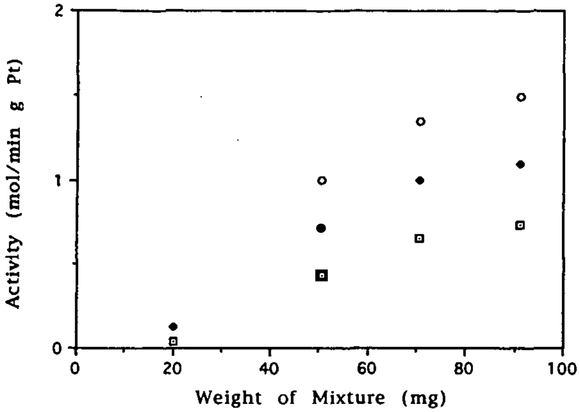

Figure 1a. Activity increase upon addition of FeCe/Grafoil
▣ 80C ● 100C ○ 120C

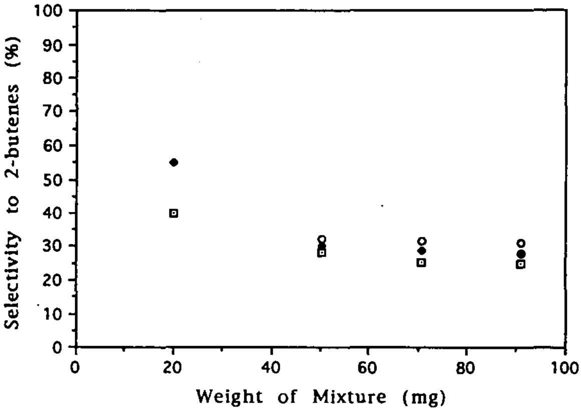

Figure 1b. Selectivity upon addition of FeCe/Grafoil
▣ 80C ● 100C ○ 120C

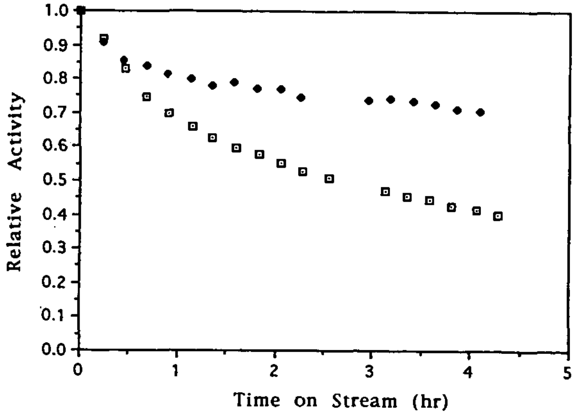

Figure 2. Impact of bed configuration on deactivation rate
▣ Pt/Grafoil on top ● Pt/Grafoil on bottom

ALTERNATE FUELS FROM THE CO-LIQUEFACTION OF COAL, OIL, AND WASTE PLASTICS

A. G. Comolli, L .K. (Theo) Lee, Vivek Pradhan
Hydrocarbon Technologies, Inc.
1501 New York Avenue
Lawrenceville, New Jersey 08648 U.S.A.

INTRODUCTION

The United States generates about 45 million tons of hydrocarbon waste, over 7 million tons of residual oil waste, and 73 million tons of waste paper per year. The approximately 25 million tons of plastic waste generated are discarded after use and end up in sanitary landfills. With existing recycle efforts, only 4% of the waste plastics are re-used. Waste plastics occupy about 21% by volume of U.S. landfills. Currently, the disposal of these wastes represents not only a significant cost ($ 3 billion/year) but also concerns such as loss of a valuable resource, a health hazard, and pollution resulting from conventional disposal methods, such as landfilling and incineration.

Through the efforts of the U.S. Department of Energy at the Pittsburgh Energy Technology Center and Hydrocarbon Technologies, Inc. (HTI), a new and promising application for direct liquefaction has been found. This application involves the combined processing of random waste plastics and waste hydrocarbons with coal and/or petroleum residuum to produce clean transportation fuels and to recover the starting chemicals used for production of new plastics. HTI' CoPro Plus™ process refers to the combined processing of coal with other hydrocarbon feedstocks. Historically this has consisted of various petroleum-derived heavy oil feedstocks; however more recent work has included waste plastics and used rubber tires. The coal feedstocks used are those typically utilized in direct coal liquefaction: bituminous, subbituminous, and lignites. Petroleum-derived oil is typically a petroleum residuum, containing at least 75 W% material boiling above 524°C. The waste plastics and tires are those collected by municipal recycling programs. The feedstocks are combined and processed simultaneously with the dual objective of liquefying the solid feed and upgrading the residuum from either the liquefied solids or petroleum oil to lower boiling (< 524°C) premium products. The new approach of the combined processing of organic wastes with coal and/or heavy petroleum resid strives to:

- Direct organic waste away from landfills.
- Produce valuable products, basic and intermediate chemicals, and fuels
- Solve existing environmental problems created by current disposal methods
- Reduce refinery waste oil pond and land fill inventories
- Enhance domestic resources
    - Supplant oil and fuel supply imports
    - Reduce energy consumption through recycling
    - Improve the trade balance
    - Create a new industry and U.S. jobs

HTI's investigation of the co-processing technology has included work performed in laboratory scale (20 cc microautoclave and a two-stage continuous stirred tank system equipped with one liter reactors), bench scale (25 kg/day throughput) and PDU scale (4 tons/day throughput) operations. In a continuous operation the waste plastics/used tires feedstock and the coal feedstock would be prepared separately and combined with the oil feedstock to form a slurry immediately prior to hydroconversion. The products are then separated downstream and the light oils are sent to an in-line hydrotreater for further upgrading. HTI's approach to coal/oil co-processing has traditionally used a two-stage reaction system with either extrudate catalyst in both reactors or more recently a combination of a dispersed and a supported catalyst in the reactor stages. Current work has been performed with dispersed catalyst in both reactors eliminating the need for handling a supported catalyst. In-line hydrotreating of the light oil products have produced a naphtha fraction with sulfur and nitrogen levels less than 10 ppm, which is below current US requirements for transportation fuels.

PROCESS DESCRIPTION

HTI CoPro Plus™ process (*Figure 1*) entails co-liquefaction of organic wastes with coal and/or oil is a liquid phase hydrogenation process that takes place at temperatures of about 425°C and pressures of 15 MPa. Under these conditions, large molecules are cracked, hydrogen is added and sulfur, nitrogen, and chlorine, etc. are easily separated and recovered after conversion to their basic hydrogenated form. Also, because the process is contained under pressure, all gases and inert components can be captured and reused if desired. Additionally such a coprocessing approach is very energy efficient, with efficiencies of greater than 80%. Co-liquefaction of random waste organic materials with coal provides for the efficient recovery and recycle of problem wastes back into the economy as premium transportation fuels and feedstocks for virgin plastics. Direct liquefaction is also applicable to the conversion and liquefaction of densified solids refuse derived fuels (RDF), formed from municipal and industrial wastes and automobile shredder residue (ASR). On a conversion to transportation fuel basis the recycle and conversion of waste plastics, waste oils, tires and organic wastes with only 50% of the waste being recovered shows that this process can supplement 10% of the United States' daily transportation fuel requirements:

Waste Type	Quantity Per Year	Oil Equivalent Million Barrels/Year
Plastics	3.5 Million Tons	200
Used Waste Oil	1.4 Billion Gallons	33
Rubber Tires	350 Million PTE*	8
Other Organic	34.4 Million Tons	212
Total		453
Total with Coal (1:1)		806
Total at 50% Waste Recovery		453+

* Passenger Tire Equivalents

+ About 10% of daily U.S. Transportation Fuel Use

A techno-economic analysis for a site specific waste/coal direct liquefaction plant at 10,000 bbls/day adjacent to and integrated with an oil refinery with random waste delivered to the plant shows an average required selling price at zero acquisition cost and at 15% ROI of about $16.00 per barrel. If tipping fees are included and if high value plastic feedstocks are recovered, the price could be less than $14/bbl and is cost effective today. This selling price will be in the competitive range by the end of this century, even with a + $20/ton acquisition cost, particularly if the environmental cost benefits of recycling are included. The current national average tipping fee is $28/ton for landfilling and $54/ton for incineration.

EXPERIMENTAL

The results from continuous bench-scale operations at HTI, conducted during 1995-96 as a part of the Proof-of-Concept Bench Option Program, which is co-sponsored by the U.S. Department of Energy, are discussed in this paper. These bench-scale operations, which were conducted at a nominal thrpoughput of about 3 lb/h and spanned over a period of 75 days, studied the coprocessing of waste plastics (from curb-side recycling in Northern NJ) with sub-bituminous coal (Wyoming Black Thunder mine) and petroleum resid (California Hondo-VTB). The bench-scale tests were carried out using HTI's proprietary iron-based dispersed slurry catalyst in hydroconversion reactors. The dispersed slurry catalyst employed was a combination of HTI's proprietary iron catalyst and Molyvan-A. Between 1000-5000 ppm of iron and 50-100 ppm of molybdenum were used for continuous co-liquefaction operations. The highlights of the reactor configuration included a two-stage hydroconversion reactor system, an interstage high pressure separator and an in-line fixed-bed hydrotreater. The overall schematic of the configuration for bench-scale testing was similar to that showed in *Figure 1* for the HTI CoPro Plus™ process.

RESULTS AND DISCUSSION

The reaction operating parameters, in terms of relative severity index for each operating condition, are presented in *Table 1*. The process performance discussed is that actually achieved at these operating conditions. The basis for the economic evaluation is defined by previous work and the assumptions described below and the process performance has been adjusted accordingly for this comparison. These conditions were carried out using a combination of dispersed slurry catalysts, based upon iron and molybdenum.

Typical feed conversions (based on the solubility of pressure filter solids in quinoline), obtained during equilibrium periods are presented in *Table 1*. As can be seen the feed conversions (W% maf feed) varies from 96.1 to 99.9 W% maf. The lowest conversion is for those conditions that contain coal as part of the feed. The conditions without coal are both over 99W% maf feed conversion. This indicates that little or no char (quinoline insoluble material) was formed in the reactors. The 524°C+ residuum conversion varies from 82.7 to 84.0 W% maf feed. Comparing the oil only condition to the oil/plastics condition shows an increase in the residuum conversion. Not surprisingly, the addition of plastic to the coal/oil condition also results in an increase in residuum conversion. The upgrading of the oil only results in a C4-524°C distillate yield of 76.0 W% maf feed. The addition of coal decreases the distillate yield by 6.3%. The addition of plastic to either of these conditions increases the distillate yield; though, more dramatically for the coal/oil condition than for the oil only condition.

Extremely significant to this comparison of process performance is the effect of plastic addition on hydrogen consumption. Not only does the addition of plastic to either oil only operation or coal/oil operation improve performance it also decreases hydrogen consumption. This is due to the plastic feed having a much higher relative concentration of hydrogen than either the coal or oil feedstock, 11.42 W% or 1.70 H/C atomic ratio for the plastic as compared to 10.13 W% or 1.45 H/C atomic ratio for the oil and 4.5 W% dry basis or 0.77 H/C atomic ratio for the coal. The light gas yield, C_1-C_3, also indicates the positive impact of adding plastics to either oil or coal/oil processing. Oil only operation results in a light gas yield of 5.0 W% MAF feed; coal/oil co-processing raises this by 2.4%. The addition of plastics to oil only operation decreases light gas yield by 0.7% and coal/oil co-processing by 2.1%. Plastics not only reduces the total hydrogen consumption but also uses it more efficiently in producing liquid and not gas products.

Figure 2 depicts the significant effect of waste plastics upon reducing the light gas-make and hydrogen consumption in heavy resid conversion or in coal/oil coprocessing. The overall quality of the light distillate products (*Table 2*) has also been excellent. The separator overhead product (SOH) coming out of the in-line hydrotreater are of premium quality with API gravities as high as 50 and H/C atomic ratios close to 2.0. The nitrogen and sulfur contents of the SOH product are very low (below 15 ppm sulfur and 1 ppm nitrogen), as shown in *Table 2*. It is also clear from *Table 2* that the addition of waste plastics either to heavy resid feed alone or to a mixture of coal and heavy petroleum resid, results in a substantial increase in the API gravities of the light distillate product; the lightest boiling naphtha (IBP-177°C) fraction also increases noticeably upon the addition of MSW plastics to the feed. The increase in the percent aromatic character of the SOH distillate during Conditions employing waste plastics in the feed can be attributed to the monomers of styrenic polymers present in the MSW plastic mixture.

The economic evaluation studies were based on construction of a fully-integrated grass-roots commercial coal/oil/plasties co-liquefaction complex to manufacture finished gasoline and diesel fuel liquid products. Byproducts from the complex include propane and butane, as well as elemental sulfur and anhydrous ammonia. The co-liquefaction plant in the complex is a multi reactor-train facility, and the total feed processing capacity has been seleeted assuming thc construction of maximum-sized heavy-walled pressure vessels to carry out the co-liquefaction reactions. Coal and waste plastics required in the co-liquefaction plant are prepared on site, and storage is provided for the oil received. Unconverted feed plus residual oil from the co-liquefaction plant are gasified to meet a part of the hydrogen requirements of the complex. Part of the fuel requirement is met by the waste process gases. Natural gas is imported to meet the remaining fuel requirements and to satisfy the remainder of the hydrogen requirements.

The costs and operating requirements of the other process facilities and the off-sites have been estimated from the Bechtel Baseline Design Study, which was developed for the Department of Energy. Total plant costs have been adjusted to a current year time frame with construction at a US Gulf Coast location. The Bechtel Baseline Design Study also provided the economic criteria and financing model used in this evaluation. A four-year construction period was assumed, followed by an operating project life of 25 years. Capital costs including working capital were depreciated over a ten-year period, using straight-line depreciation. A federal tax rate of 34 percent was assumed for the life of the project. Feed costs and product selling prices were inflated at an annual rate of 3 percent. Labor and maintenance staffing requirements and wage rates were developed based on the Baseline Design. Catalyst and chemicals costs were calculated for each plant within the complex, as factored from the Baseline Design. The results of the economic analyses are reported in *Table 3*.

The most significant criterion reported is the equivalent crude oil price. This concept was developed by Bechtel in their Baseline Design Study, and modified slightly for use in this study. From analysis of published data, a correlation was found between crude oil and product prices, depending on the specifie product and the price of the product. Relationships were developed for the ratio of the prices of crude oil to the price of the wholesale finished products (gasoline and distillate fuel oil). For a given product slate and product cost, multiplying the product cost by the ratio produces the equivalent crude oil price. This is the price that crude oil on the world market would minimally need to sell at for the proposed facility to have a 15% rate of return on the invested equity. The addition of plastic to either the coal/oil or the oil only feedstock decreases the equivalent crude oil price by 6.07 - 6.71 dollars/barrel. The oil/plastics operation in this grass-roots plant achieves an extremely low value of 20.48 dollars/barrel, putting it nearly in the range of economically commercializing.

The liquid products from these coprocessing operations were clean and good feedstocks for the refining operations, including hydrotreating, reforming, and hydrocracking. For these distillates, heteroatoms could be easily reduced, if needed; also, better FCC gasoline yields require less hydrocracking capacity for coal liquids than petroleum.These distillates made acceptable blendstock for diesel and jet fuel, due to their high cetane number (42-46) and high naphthenes (over 50 v%) content. The superior quality of distillate products from HTI's coprocessing runs (attributable to HTI's in-line hydrotreating operation) was found to fetch a three-dollar premium over the neat petroleum liquids.

CONCLUSIONS

Co-processing of waste plastics with either oil only feedstock or coal/oil feedstock results in a significant improvement in process performance. Total feed conversion is enhanced as are 524°C+ residuum conversion and C_4-524°C distillate yield. The addition of waste plastics to the feed increases hydrogen efficiency as both hydrogen consumption and C_1-C_3 light gas yield decrease. Co-processing of plastics with oil reduced the equivalent crude oil price required to have a 15% rate of return on equity to 20.48 dollars/barrel. This puts the technology in the reach of immediate commercialization with either a small increase in world crude oil prices or minor improvements in the technology to further reduce the product cost.

TABLE 1: Performance Comparison - Yields

	Oil	Coal/Oil	Coal/Oil /Plastics	Oil /Plastics
Feed Composition, W%				
Coal	0	50	33.3	0
Plastic	0	0	33.3	50
Oil	100	50	33.3	50
Relative Severity Index, STTU*				
First Stage	0.78	0.98	1.08	0.90
Second Stage	1.07	1.28	1.47	1.19
Process Performance, W% maf feed				
Feed Conversion	99.9	96.1	96.7	99.7
C_4-524°C Distillate Yield	76.0	69.7	73.9	76.2
524°C+ Conversion	83.3	82.7	83.7	84.0
Hydrogen Consumption	1.72	4.21	3.17	1.35
C_1-C_3 Gas Yield	5.00	7.37	5.31	4.31

*The relative severity index (STTU) is based upon a standard severity index of 1.0 at a space velocity of 800 kg/h/m^3 each reactor and a temperature of 440°C.

TABLE 2: Performance Comparison - Quality

	Oil	Coal/Oil	Coal/Oil /Plastics	Oil /Plastics
Feed Composition, W%				
Coal	0	50	33.3	0
Plastic	0	0	33.3	50
Oil	100	50	33.3	50
SOH Distillate, ASTM D86, W%				
IBP-177°C	39.6	42.1	52.4	53.4
177-343°C	52.1	50.9	40.7	41.7
343°C+	8.3	7.0	6.9	4.9
SOH Quality				
Gravity, °API	49.0	46.1	46.3	51.0
H/C Ratio	1.99	1.96	1.90	1.97
Nitrogen, ppm	32.2	15.5	17.9	5.4
Sulfur, ppm	96.9	52.7	46.2	17.5
%Aromaticity	7.25	17.82	23.49	14.89

TABLE 3: Economic Comparison (12,000 tons/day total feed)

	Oil	Coal/Oil	Coal/Oil /Plastics	Oil /Plastics
Feed Rate				
Coal, tons/day	0	6,000	4,000	0
Oil, barrels/day	66,730	33,365	22,243	33,365
Plastics, tons/day	0	0	4,000	6,000
Liquid Products, barrels/day				
Gasoline	15,148	14,339	15,192	15,328
Diesel Fuel	36,787	34,822	36,896	37,225
Total	51,935	49,161	52,088	52,553
Total Plant Investment, $MM	1,945	2,379	2,078	1,733
Net Operating Cost, $MM/yr	566.8	561.4	486.1	449.7
Net Product Cost, $/barrel	33.22	34.76	28.41	26.05
Equivalent Crude Oil Price,	**27.19**	**28.70**	**22.63**	**20.48**

Figure 1. Simplified Schematic of HTI's CoPro Plus™ Process

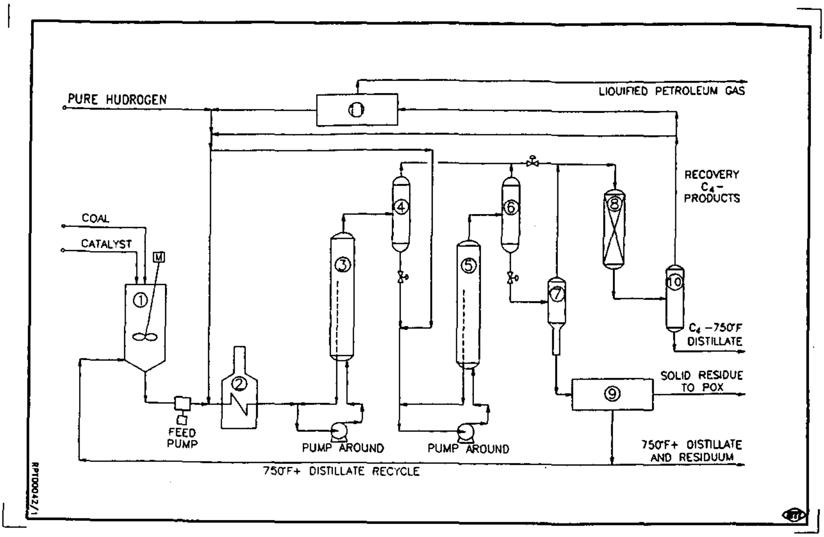
PURE HUDROGEN
LIQUIFIED PETROLEUM GAS
RECOVERY
C_4-
PRODUCTS
COAL
CATALYST
M
①
②
③
④
⑤
⑥
⑦
⑧
⑨
⑩
C_4 -750°F
DISTILLATE
SOLID RESIDUE
TO POX
FEED
PUMP
PUMP AROUND
PUMP AROUND
750°F+ DISTILLATE
AND RESIDUUM
750°F+ DISTILLATE RECYCLE
RPT00042/1

Figure 2. Effect of Waste Plastics on Liquid and Gas Yields, and H_2-Consumption

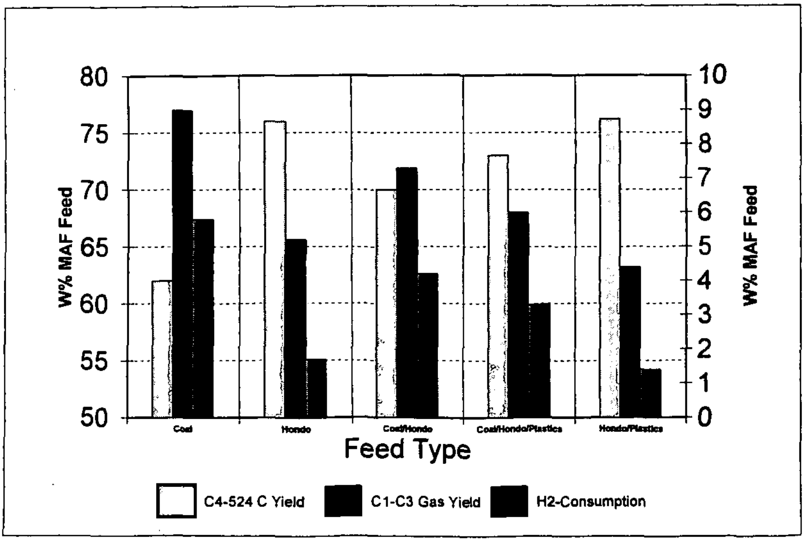

POTENTIAL USES FOR THE TIRE DERIVED PARTICLES PRODUCED BY THE WOMBAT PROCESS.*

David L. Wertz, Rachel Eschette, Ricky Cummings, Jeff Quin,
Mary Martin and Stephen DuBose
Department of Chemistry & Biochemistry
University of Southern Mississippi
Hattiesburg, MS 39406. USA.

Key Phrases: Tire-derived particles, extraction of the inorganics, blended fuels.

Approximately 275 million scrap tires are produced in the United States annually. Most of these tires are not being recycled. At best, they are an expensive nuisance. At worst, they cause significant air, water and soil pollution.

The typical modern tire is composed of a complex inert organic matrix into which several inorganic species have been impregnated to enhance the performance of the tire. Any potential uses of the scrap tires, other than simple (and expensive) reshaping of the physical appearance of the tires, must deal with these inorganic species and the C-C bonding network, both at the molecular level. The Wertz Oxidative Molecular Bombardment at Ambient Temperature (WOMBAT) process attacks the tires at this level. The final product of the WOMBAT process is referred to as tire-derived particles (TDP).

Shown in Figure 1A is the wavelength dispersive x-ray spectrum (WDXRS) of a scrap tire. The peaks in a WDXRS may be related to the presence of an element in the sample by a combination of Bragg's law and Moseley's law, i.e., $Z_J = 1 + \{n/[2 \cdot d_{mono} \cdot Q \cdot \sin\theta]\}$; where Z_J is the atomic number of element J, n is the order of the reflection, d_{mono} is the d-spacing of the crystal monochromator, and 2θ is the angle at which the peak P_J (caused by element J) appears in the x-ray spectrum of the sample. The K_β and K_α peaks for zinc (first, second, and third order reflections), the K_β and K_α peaks for calcium, and the K_α peak for sulfur are clearly discernible in the spectrum, along with the peaks from the exciting radiation -- chromium. Shown in Figure 1B is the WDXRS of TDP which has been produced by the WOMBAT solvent in the closed reactor, indicating that the zinc and sulfur originally contained in the tire have been reduced to < the lower limit of detection for each element in the TDP.

The intensities of the peaks due to different elements (eg. zinc and sulfur in this WDXRS) may not be directly compared to evaluate the relative abundances of these elements without extensive absorption-enhancement corrections being applied to the intensity of the K_α peak characteristic of each element. However, the peak intensity of the K_α and/or K_β peaks in the WDXRS of this sample and in subsequent samples may be used to estimate the change in abundance of that element in a series of samples of similar composition. These WDXRS analyses may be made at least semi-quantitative via comparison to a series of external standard curves containing the element(s) of interest dispersed into a matrix which is similar to that of the TDP. Studies to develop the appropriate absorption-enhancement corrections for zinc and sulfur in a high carbon matrix are on-going.

A two-step process for converting scrap tires to more useful material is being developed in our laboratory. This process involves the use of oxidizing solvent(s) at ambient conditions to separate the scrap tire into (a) steel belts, (b) polymeric cords, and (c) chunks of black solid which have irregular sizes and shapes. These chunks of black solid are the subject of part two of the WOMBAT process, which involves further reaction of the black solid with an oxidizing solvent. The result of process step two is a pulpy material which may be easily washed, dried, and ground into particles.

The partial compositions (measured by gas chromatography) of two samples of TDP and a sample of the rubbery part of an untreated tire are compared in Table I. This comparison shows that the WOMBAT process reduces the carbon, sulfur, and hydrogen abundances, while significantly increasing the oxygen abundance. The results also shown that the largest changes in the carbon and oxygen abundances occur when the process was carried out in an "open" container; i.e., where an infinite supply of atmospheric oxygen and of moisture were present. However, when the black chunks were subjected to the WOMBAT process in a closed system for a much shorter period of time, the resulting changes in the carbon and oxygen abundances were much reduced. Under these conditions, the resulting TDP is principally carbon (ca. 75%), but it also contains a considerable amount of oxygen (ca. 13%). Studies are currently underway to determine the effect of reaction parameters on the carbon/oxygen ratio produced in the TDP. The sulfur content of the TDP was reduced to 0.8%, while the nitrogen content was increased to 2.6%, when the chunks were reacted in the closed WOMBAT container. Studies are currently being conducted to determine the effect(s) of reaction time and other parameters on the sulfur and nitrogen abundances in the resultant TDP.

All of the results discussed below were obtained from the sample produced in the closed container (TDPA).

^{13}C NMR indicates the absence of aromatic carbons in the WOMBAT TDP.

After minimal grinding, the TDP range in diameter from 1-100 μm and have highly irregular surfaces.

The WOMBAT particles produce a high temperature ash which is 2.4% of the original weight of the TDP. The principal components of the ash are zinc, calcium, iron, and titanium, as shown in Figure 2.

The WOMBAT TDP has been evaluated as a fuel. Shown in Table II is its specific heat compared to that of other, more conventional, fuels as measured in our laboratory using conventional oxygen bomb calorimetry. Our analyses indicate that the specific heat of the WOMBAT TDP is considerably higher than that of bituminous coal. When combusted in our entrained flow thermal reactor at 850°C for an extended period, there is no measurable production of soot from the TDP.

The TDP may be mixed with materials of lesser fuel value to produce synthetic fuel blends. Shown in Figure 3 are the specific heats measured for a series of mixtures containing the TDP mixed with sawdust. The linear relationship between composition and heat content ($R^2 = 0.996$) indicates that such a mixture may be predesigned to produce a synthetic fuel blend of preselected specific heat. Combustion of such a mixture offers significantly reduced $SO_x(g)$ in the effluent gas and significantly less ash than produced by combustion of typical bituminous coals. Combustion of such a mixture also offers a useful method for utilizing, and thus not landfilling, two nuisance solid wastes -- scrap tires and sawdust.

Experiments with mixtures containing municipal garbage, wood shavings, and other low fuel content solids are on-going.

In addition, preliminary tests indicate that the TDP are capable of extracting some metal ions and some anions from water. Shown in Figure 4 is the WDXRS of a TDP which has been treated with a solution containing $CdCl_2$. New peaks indicating the presence of both Cd(II) and of Cl^- are easily discernible, indicating that the TDP has sequestered each from an aqueous solution. Experiments designed to evaluate and then exploit these capabilities of the TDP are ongoing.

Preliminary evaluation of the TDP as a component for inclusion in specialized polymeric matrices has recently been initiated.

[*] Financial support by the U.S. DOE, the Mississippi Department of Environmental Quality, and an Aubrey K. Lucas Faculty Excellence Endowment Grant from USM are gratefully acknowledged.

TABLE I. PARTIAL COMPOSITION OF THE TDP COMPARED TO THE COMPOSITION OF THE UNTREATED TIRE.

ELEMENT	SAMPLE		
	TIRE	TDPA	TDPB
C	82.4%	76.3%	48.3%
H	7.8%	2.8%	4.6%
S	2.0%	0.8%	0.4%
N	0.5%	2.6%	3.8%
O	2.4%	13.5%	33.9%

A The process was conducted in the enclosed WOMBAT reactor for 72 hours.

B The process was conducted in a flask which was exposed to atmospheric conditions for 168 hours.

TABLE II. COMPARISON OF THE SPECIFIC HEAT OF THE TDP TO THE SPECIFIC HEAT OF OTHER FUELS USING OXYGEN BOMB CALORIMETRY.

FUEL	SPECIFIC HEAT (kJ/g)	FUEL	SPECIFIC HEAT (kJ/g)
bituminous coal	23	sawdust	18
sub-bituminous coal	21	wood chips	18
lignite	19	garbage	16
WOMBAT TDP	32		

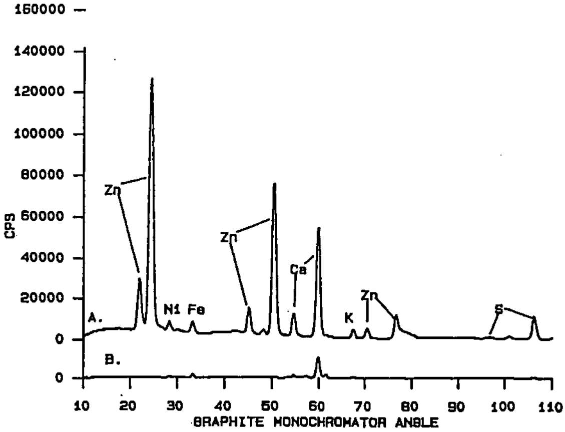

Figure 1. WDXRS of (A) a scrap tire, and (B) TDP produced from the tire.

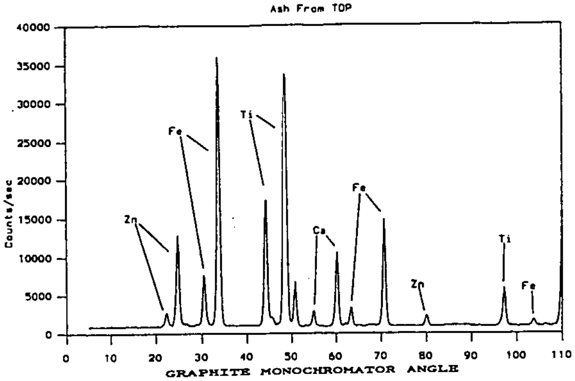

Figure 2. WDXRS of the high temperature ash produced from the TDP.

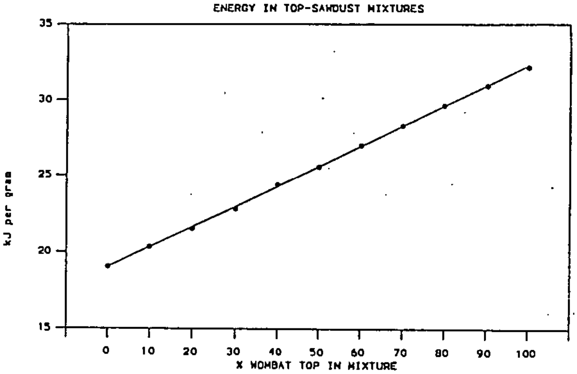

Figure 3. Specific heats of some TDP-sawdust mixtures.

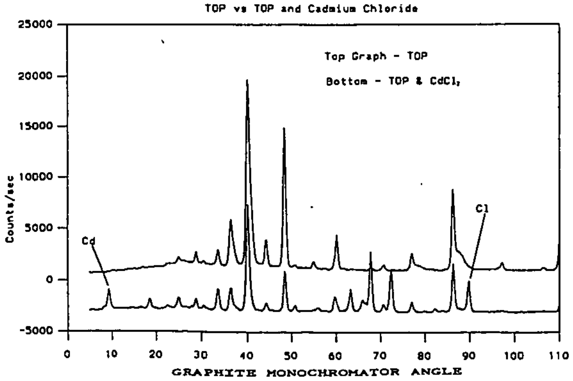

Figure 4. WDXRS of TDP treated with an aqueous solution of $CdCl_2$.

USE OF NET PRESENT VALUE ANALYSIS TO EVALUATE AND SELECT PUBLICLY FUNDED BIOMASS-TO-ETHANOL RESEARCH AND DEVELOPMENT PROGRAMS AND VALUATE EXPECTED PRIVATE SECTOR PARTICIPATION

Norman D. Hinman and Mark A. Yancey
Center for Renewable Fuels and Biotechnology
National Renewable Energy Laboratory
Golden, CO 80401-3393

INTRODUCTION

One of the main functions of government is to invest tax dollars in programs, projects, and properties that will result in greater social benefit than would have resulted from leaving those tax dollars in the private sector or using them to pay off the public debt. One traditional area for investment by government is R&D. According to Battelle, U.S. R&D expenditures reached $164.5 billion in 1994, and federal support represented $69.8 billion (42.4%) of the total (1). If invested wisely, these tax dollars can lead to greater social benefit than would be obtained by leaving them in the private sector or using the money to pay off the federal debt. However, if not invested wisely, this could result in less than optimal social benefit or, even worse, in less social benefit than could be obtained from the other two options. The purpose of this paper is to describe an approach to analyzing and selecting investment opportunities for federal money in public R&D programs and valuating expected private sector participation in the programs and to apply this approach to a specific biomass-to-ethanol R&D opportunity.

BASICS OF INVESTMENT ANALYSIS

For all investment situations there are five basic variables: (1) costs; (2) profits or benefits; (3) time; (4) the discount rate; and (5) risk. In the analysis of investment alternatives for a given situation, the alternatives under consideration may have differences with respect to costs and profits or benefits, project lives, and uncertainties. If the effects of these factors are not quantified systematically, correctly assessing which alternatives have the best potential is very difficult.

Many methods are available to decision makers to systematically evaluate investment options. These methods, described in detail in a variety of books and articles (2), include present, annual, and future value; rate of return; and break-even analysis. The application of each method depends on whether the analysis is for a single opportunity, two mutually exclusive opportunities, or several non-mutually exclusive opportunities. For the single opportunity situation, the decision maker is simply trying to decide if the single investment option meets a minimum expected financial return. For the mutually exclusive situation, the decision maker has two investment options and is trying to decide whether the options meet the minimum expected financial return, and, if both do, which is the best choice. For the non-mutually exclusive situation, the decision maker has several investment options and is trying to decide which of these meets the minimum expected financial return, and, of those that do, which combination of these will provide the maximum return on total investment dollars available.

One must be careful in applying rate of return analysis to mutually exclusive and non-mutually exclusive situations. If one simply calculates the rate of return for each alternative and then chooses the alternative or alternatives with the largest rates of return, this can, and often does, lead to the wrong choice. The correct application of rate of return analysis to either situation is known as incremental rate of return and can be very tedious and time consuming, and one must take extra steps to account for differences in project lives. Net present value (NPV) is the tool of choice for evaluating mutually exclusive or non-mutually exclusive investment options because it is much less time consuming, is straightforward, does not require additional steps or considerations for projects with different lives, allows direct comparison between projects of widely differing objectives and scopes, and allows a rational approach to valuating private sector participation in public programs.

NPV APPROACH TO NON-MUTUALLY EXCLUSIVE INVESTMENTS

A non-mutually exclusive investment situation is one where more than one investment option can be selected, depending on available capital or budget restrictions. The objective is to select those projects that maximize the cumulative profitability or benefit from the available investment dollars. To maximize the cumulative profitability or benefit, the decision maker selects the combination of projects that maximize the cumulative net present value.

To apply NPV to non-mutually exclusive alternatives, the NPV for each alternative is calculated by determining the present value of the profit/benefit stream calculated at the minimum rate of return (hurdle rate) and subtracting the present value of investment dollars and other costs, also calculated at the minimum rate of return.

$$\begin{aligned}\text{Net Present Value (NPV)} &= \text{Present Value Revenues @ } i^* \\ &\quad - \text{Present Value Costs @ } i^*\end{aligned}$$

i^* = minimum rate of return

If the project NPV is zero, there is enough revenue or benefit to cover the costs at a rate of return that is equal to the minimum rate of return required by the investor. Projects with an NPV less than zero are dropped from further consideration because their rate of return is less than the minimum required return. If the NPV is greater than zero, the NPV represents how many present value dollars will be returned to the investor above and beyond those that will be returned at the minimum rate of return. Once the NPV for each project is calculated, the decision maker looks at all possible combinations of projects to determine which combination (whose total investment does not exceed the amount of money available) has the largest cumulative NPV. This is the best possible investment portfolio. Often, selecting the best portfolio does not involve selecting projects with the largest individual project net present value and does not necessarily involve selecting projects with the highest rates of return.

If one is faced with the daunting task of selecting an investment portfolio when there are dozens of investment options, an alternate method may be used to simplify the process. Growth rate of return or ratio analysis may be used to rank non-mutually exclusive alternatives rather than cumulative NPV analysis (2). Large companies and government programs are often faced with the task of evaluating literally hundreds of potential projects. Many combinations of projects must be analyzed to determine the optimum group of projects that will maximize the cumulative NPV for a given budget. The use of growth rate of return or ratio analysis only requires the calculation of the respective values for each project and then ranking the projects in the order of decreasing values. The illustration of these concepts will not be demonstrated here, but the reader should be aware of these methods to evaluate a complex investment portfolio.

SPECIAL CONSIDERATIONS FOR NON-MUTUALLY EXCLUSIVE GOVERNMENT INVESTMENTS

Converting Intangible Benefits and Costs into Dollar Values

A basic tenant of this paper is that to make rational investments of pubic dollars one must have some approximate, quantitative idea of the value of critical costs and benefits. Moreover, as a practical matter, it is essential that the measure of value be the same for both costs and benefits so that direct comparisons between costs and benefits can be made. The most universal measure of value is the dollar. In the private sector this is the measure of cost and benefit. In the public sector, particularly with respect to R&D programs, it's the established measure of cost. However, on the benefit side, there is no established measure of value. The authors contend that the dollar should be the measure of benefit so that direct comparisons can be made with costs and so that the established and the well recognized investments analysis methodology described above can be employed in the public sector.

In many cases converting benefits and costs to dollars is fairly straightforward. For example, a key benefit that the U.S. Department of Energy (DOE) is interested in is reducing imported petroleum. The dollar value of the yearly benefit can easily be calculated from the present and projected price of petroleum (3). As another example, it is possible to estimate the net annual increase or decrease in jobs that results from introducing new technology. In addition, it is fairly straightforward to place a dollar value on these jobs (4). Other possible costs and benefits are environmental and social, which are more difficult to quantify. Nevertheless, the U.S. Environmental Protection Agency has studied these issues carefully and has given dollar estimates of health costs associated with various types and levels of pollution.

Minimal Rate of Return for Public Projects

Establishing a minimal rate of return for public projects requires some special considerations, which have been reviewed extensively by Terry Heaps (5) for Canadian public projects. He concluded that the correct social discount rate for Canada was 3-7%. In another study performed by Wilson Hill Associates (3) a discount rate of 7% was used for Projects evaluated for the Office of Transportation Programs in DOE.

SELECTING PUBLIC R&D PROGRAMS AND VALUATING EXPECTED PARTICIPATION BY THE IMPLEMENTING INDUSTRY

Commonly, a government R&D program is initiated without the private sector, but the private sector is expected to "come on board" at some point to carry the ball forward into the commercial arena. For these situations, the government and the private sector make investments in R&D and technology commercialization in order to obtain what each desires—social benefit in the case of government, and profit in the case of the private companies.

Analysis of the value of these programs demands answers to three questions: (1) What portion of the R&D cost can the private sector incur and still obtain its minimum return from implementing the technology?; (2) When this private sector cost allowance is subtracted from the total estimated cost to carry out R&D so as to obtain an estimate of the R&D cost that must be borne by government, is the estimated government R&D cost justified given the expected social benefit from implementing the technology?; and (3) If the answer to questions 2 is positive, does the program represent one of government's best opportunities for its limited investment dollars?

The NPV approach to investments provides the answer to all three questions. For example, to answer the first question one calculates the **industry NPV**. To do this, one estimates over time the capital and operating costs the industry at large will incur to implement a new technology and, using the average minimum interest rate for the industry, calculates the present value of these costs to industry at the initial time of commercialization. One also estimates over time the present value at the time of commercialization of the expected increased revenues or savings the industry should experience from implementing the technology. Subtracting the present value costs from the present value revenues gives the industry NPV at the time when commercialization is expected to begin. If the NPV is negative, the industry cannot afford to contribute to the R&D effort and cannot afford the capital and/or operating costs of commercialization. As a result, it will not "come on board" and the government should drop consideration of the program. If the industry NPV is zero, industry cannot afford to contribute to the R&D costs, but can afford the capital and operating costs to implement the technology. In this situation the government will have to incur all the R&D costs in order for industry to adopt the technology. If the industry NPV is positive, the government can expect the industry to participate in the R&D costs at a level equivalent to the NPV. This participation may be provided in the form of cost sharing or through licensing arrangements.

To answer the second question, one calculates the **government NPV**. To do this, the expected social benefits are estimated over time and dollar values are assigned. Then the present value of these benefits is calculated at the time the program was initiated using the social discount factor. Next, the entire R&D costs over time are estimated and discounted to the time the program began using the social discount factor. Next, the expected R&D contribution from industry, calculated above as industry NPV is discounted to the time of initiating the program using the industry discount factor. This industry R&D contribution, discounted to when the program began, is then subtracted from the entire R&D costs, also discounted to when the program began, to obtain the governments expected R&D costs discounted to the time the program began. These discounted government R&D costs are then subtracted from the discounted benefits to obtain the government NPV for the program at the time the program was initiated. If the government NPV is less than zero, the program should not be considered for investment of tax dollars. If the government NPV is zero or greater, it should be thrown in the pot of possible government investments.

To answer the third question, government should list all investment options with a NPV greater than zero and select that combination of projects that will maximize the **governments cumulative net present value.**

VALUATING EXPECTED PARTICIPATION BY INDIVIDUAL COMPANIES

If, from the above analysis, the industry NPV is positive, individual companies that are members of the industry can be expected to cost share in the R&D phase of a program or purchase licensing arrangements. However, the level of cost sharing or license fees will depend on each company's circumstances. The expected level of cost sharing or the licensing fee for a given company can be calculated using **company NPV** derived from projected revenues and costs a company will experience in implementing the technology in commercial use. If the company NPV is negative, the particular company cannot afford to implement the technology even if the technology is provided free. Such a company is not a viable partner to the government program. If the company NPV is zero, the company may be a partner only in the sense that it will implement the government-developed technology if it is free to the company. If the company NPV is positive, the company can afford to cost share the R&D effort or purchase a licensing arrangement at a level equal to the company NPV. Such companies are potentially the most valuable partners to the program.

APPLICATION TO BIOMASS-TO-ETHANOL R&D OPPORTUNITIES

The authors will supply a detailed example of the use of NPV analysis to a biomass-to-ethanol opportunity.

REFERENCES

1. *Manufacturing Engineering*, Vol. 112; No. 2, 1994.
2. Stermole, F.J. (1984), *Economic Evaluation and Investment Decision Methods*, Fifth Edition, Golden, CO.
3. Santone, L.C. (1981), *Methods for Evaluating and Ranking Transportation Energy Conservation Programs Final Report*, Washington, DC, April 30, 1981.
4. Tyson, K.S., Putsche, V., and Bergeron, P. (1996), *Modeling the Penetration of the Biomass-Ethanol Industry and its Future Benefits*, Golden, CO, March 15, 1996.
5. Heaps, T., and Pratt, B. (1989), FRDA Report 071, *The Social Discount Rate for Silvicultural Investments*, Victoria, B.C, March, 1989.

CLEAN GAS TURBINE FUEL FROM PETROLEUM COKE

.Satyan Katta and Gunnar B. Henningsen

The M. W. Kellogg Company
601 Jefferson Ave., Houston, Texas 77210

Keywords: Petrleum coke, partial oxidation and gasification

Introduction

Oil refiners in the United States often rely on coking to reject excess carbon from heavier crudes, resulting in an ever-increasing supply of petroleum coke. Marketing of coke as a fuel is hampered by its high sulfur and metals content which makes it unsuitable for conventional combustors. Several major IGCC projects, based on the low value refinery stocks, are currently progressing through detailed engineering, procurement and construction (1).

In a cost-shared contract with DOE/PETC, Bartlesville, The M. W. Kellogg Company has been investigating the gasification and combustion of high-carbon containing refinery by-products using a laboratory-scale fluidized bed and a sub-pilot scale transport reactor located at Kellogg's Technology Development Center where both fluid bed and transport reactors have been developed for coal gasification (2). The transport reactor process pioneered by The M. W. Kellogg Company, makes use of enriched air to partially oxidize and gasify the petroleum coke. Results of the laboratory and pilot plant program are presented in the paper along with proposed process flow diagram that incorporates some recent advances made in sulfur removal and recovery.

The objective of the study was to develop a process to convert high-carbon refinery byproducts such as petroleum coke and ROSE^{TM} (Residuum Oil Supercritical Extraction) pitch to fuel gases suitable for power generation. Experiments were conducted in the transport reactor (TRTU) to study partial oxidation, gasification and devolatilization of the coke at temperatures up to 1800°F in a continuous mode. In order to extend the data obtained in the TRTU to higher process temperatures (1850 to 2250°F), experiments were conducted in the Bench-scale Reactor Unit (BRU) to study partial oxidation and gasification in a batch mode. The BRU is capable of heating a bed of solids up to 2250°F and above with oxidant injection.

Experimental

Description of Bench-scale Reactor Unit: A simplified flow schematic of the BRU test facility is shown in Fig. 1. It consists of a 2.067-in. inside diameter (i.d.) section of 10-in. height and an expanded section of 3.068-in. i.d. of 12-in. height. It is made of Incoloy 800H alloy and consists of some ancillary equipment including a steam supply system. The reactor is surrounded by two independently-controlled electrical heaters (for top and bottom zones) and contained within a pressure vessel. Only a small pressure differential is used across the hot reactor vessel. The feed gas is electrically preheated. Product gas leaves the reactor, and is sent to a water-cooled condenser and then to a particulate filter. Water collected in the knockout drum is periodically drained from the unit. An on-line GC, that requires 12 min to complete the gas analysis, is connected to the BRU for gas analysis. It is possible to analyze the concentration of hydrocarbons and carbon oxides (CH_4, C_2H_4, C_2H_6, CO, CO_2, H_2, N_2 and the unsaturates) in the effluent gas of the BRU by using gas sample bags. The BRU facility can be operated at temperatures up to 1950°F at pressures up to 450 psig. A particulate filter, maintained at a temperature of 600 to 700°F, was used to capture the fines for analysis of vanadium and nickel which are present in the coke feed.

Petroleum coke was subjected to partial oxidation (POX) in the BRU over a peak temperature range of 1850 to 2250°F. The tests involved heating the bed to a base temperature followed by introducing the oxidant. Within a short period, the bed temperature reached a peak value and then stabilized or decreased gradually. Tests on combined POX and steam gasification and tests with steam gasification only were performed in the BRU.

Description of Transport Reactor Test Unit (TRTU)

A simplified sketch of the reactor system, shown in Fig. 2, consists of a mixing zone, a riser, a cyclone, and a standpipe. The mixing zone of the reactor, which can be operated either as a dense-phase fluid bed or as an entrained reactor, consists of a 10-foot tall section of 1.338 in. i.d. Solids from the standpipe are returned to the bottom of this zone. Fluidization gas, which can be air, O_2, steam, N_2, or any combination of these, is fed to the bottom of the mixing zone through a gas distributor. During standby periods, mixture of steam and N_2 was used. During testing, the steam flow was maintained and N_2 to the mixing zone was replaced with air.

Above the mixing zone is a 32-foot tall riser of 0.815 in. i.d. At the base of the riser is an injection nozzle that is used for feeding petroleum coke. At velocities of 15 to 30 ft/s used during partial oxidation/gasification, the gas residence time was about 1 to 2 sec in the riser. Gas and solids leaving the top of the riser flow to a high-efficiency cyclone, that separates the solids and returns them, via the standpipe, to the mixing zone. Gas leaving the top of the cyclone is cooled, measured, and sampled for analysis.

The standpipe consists of a 33-foot tall section with the same i.d. as the mixing zone. The use of a relatively small diameter standpipe requires a low solids inventory and minimal solids holdup time. Fresh solids are added for make-up, if necessary, to the top of the standpipe to compensate for attrition losses. Solid samples are withdrawn from the bottom of the standpipe. Solids are returned to the bottom of the mixing zone via a lateral leg that is aerated.

The nominal size cuts of coke used in the TRTU and the BRU were 40x140 and 40x80 mesh, respectively. The proximate analysis of the petroleum coke (wt%) was: volatile matter-9.4%, fixed carbon-89.6%, moisture-0.5% and ash-0.5%.

Results and Discussion

Testing in BRU

Tests were conducted in the BRU, in a batch mode, using a bed weight of 200 gm of Lyondell/Citgo petroleum coke with an O_2 concentration range of 15 to 30 vol% in nitrogen over an initial temperature range of 1800 to 1950°F at pressure of 100 psia. The peak bed temperature varied from 1850 to 2250°F. Results from fluidized bed testing show that a sulfur- and metals-free gas, suitable as a gas turbine fuel, can be produced from petroleum coke. The gas residence time in the BRU is about the same as in the TRTU, and hence the BRU results are applicable to the TRTU. The CO/CO_2 ratio was observed to be a function of O_2 partial pressure and temperature. At 30% O_2 concentration and 2000°F, the CO/CO_2 ratio was found to be 3.5. This was the highest ratio that was obtained over the temperature range and O_2 concentrations investigated. The steam gasification rate was determined to be 0.5 lb/lb.hr. The carbon partial oxidation reactions and the carbon gasification reaction in the presence of steam are represented by $C + O_2 \dashrightarrow CO_2$; $C + CO_2 \dashrightarrow 2CO$; and $C + H_2O \dashrightarrow CO + H_2$.

It was also determined that the carbon consumption rate by the combined partial oxidation and gasiification by steam is the sum of individual rates obtained in the two processes. The water gas shift reaction was found to be at equilibrium. The devolatilization of coke was studied in the TRTU at a lower temperature, but not in the BRU.

The bed and filter samples obtained at the end of tests were analyzed for vanadium in order to determine if it accumulates in the fines produced during testing. Runs 22 through 25 were done at lower temperatures and the results, presented in Table 1, show that the vanadium present in the feedstock does accumulate in fines. Hence, it should be possible to remove vanadium during coke processing via the fines generated. The nickel content in the bed and filter samples is not meaningful as the thermocouples used in the BRU tests had an Incoloy 800 (high nickel alloy) sheath and were corroded during the tests as a result of high temperatures. In future BRU tests, the thermocouples will be protected by ceramic tubes so that the bed and fines can be analyzed for nickel. Surface areas of fresh and bed samples of petroleum coke from BRU tests were measured by N_2 absorption (BET method). The results are given in Table 2.

The above measurements show up to a ten-fold increase in BET surface area as carbon is converted. After a significant carbon conversion is achieved, the coke partial oxidation rate increases since it becomes more reactive due to the increased surface. Thus, a transport reactor is most efficient in processing coke due to staging which utilizes all the O_2 to react with solid carbon to produce CO and CO_2 without burning volatiles. The recirculating solids have a significantly higher carbon conversion and, so, are more reactive than the fresh feed. Therefore, the coke consumption rate is higher in a transport reactor compared to a fluidized bed.

The temperatures measured in the bed and the gas composition determined using infrared analyzers in test 26 are shown in Fig. 3 and 4. The bed temperature, after reaching a peak value gradually decreased with time showing that the carbon consumption rate increased steadily. The gas composition measured using a GC is also shown in Fig. 4. Additional results, shown in Table 3, indicate that the steam gasification rate is very low as shown by the low conc. of H_2 and that the carbon consumption (cons.) rate increases by a factor of nine as the carbon in the bed is consumed.

The gas composition and temperatures measured in test 22 at a nominal bed temperature of 1900°F are shown in Fig. 5 and 6, respectively. These results show that the CO/CO_2 ratio is very low at this temperature. Results obtained at an O_2 concentration of 30% at initial bed temperature of 1950°F are shown in Table 4. Results for sample 1 correspond to O_2 conc. of 40% which was used for a short period as the peak temperature reached 2300°F.

Testing in TRTU

Petroleum coke was processed with riser and mixing zone densities of 4 and 14 lb/ft^3, respectively at a solid circulation rate of about 600 lb/hr in the TRTU in both partial oxidation and steam gasification modes at temperatures close to 1800°F. These tests confirmed that the inability of operating the TRTU at temperatures exceeding 1800°F prevented complete thermal cracking of volatiles produced, causing coke-like deposits to be formed in the reactor.

Testing in the TRTU showed that the fuel gas produced at temperatures lower than 1800°F has a CO/CO_2 ratio less than or equal to 0.5. This gas has a very low heating value and is not suitable for power generation. The partial oxidation and gasification of petroleum coke could not be studied at higher temperatures in this unit due to equipment limitations. The devolatilization of coke was also studied at temperature of 1800°F and yielded a H_2/CH_4 molar ratio of 4.0.

A product gas heating value of 124 BTU/scf was estimated for a transport gasifier with enriched air-blown (30% oxygen) mode of operation utilizing the results obtained in the BRU and the TRTU.

Flowsheet Development / Process Advantages

Based on the results obtained in the BRU and the TRTU, the process flow diagram, shown in Fig. 7, has been developed to partially oxidize/gasify petroleum coke. This flow diagram incorporates the direct sulfur recovery process, developed by Research Triangle Institute, as this process was deemed best suited for this application. It also incorporates a transport desulfurizer and a transport regenerator for sulfur removal from the product gas. These two units were developed recently by The M.W. Kellogg Co. for the Sierra Pacific project and will be demonstrated shortly. A detailed flowsheet, based on the above flow diagram to generate power from the fuel gas produced from gasification and partial oxidation was developed. Economic analysis of the proposed process is in progress.

The advantages of a transport gasifier over entrained gasifiers, which are being demonstrated to process petroleum coke and other refinery waste streams such as API wastes, acid-soluble oils from alkylation unit, and waste water treatment sludges, are the following:

- It has appreciable carbon inventory while there is none in an entrained gasifier. This factor makes the transport reactor safer and easier to operate.
- Individual refinery waste streams can be injected at different locations where as in an entrained gasifier, these have to be mixed with the main feedstock. The need

for mixing poses significant disadvantages for the latter depending upon the feedstreams.

- There is no short term need for balancing carbon, hydrogen and oxygen in the transport gasifier due to substantial carbon inventory where as it becomes essential to maintain this balance in an entrained gasifier.
- It is thermally more efficient due to a lower operating temperature with less material constraints compared to entrained gasifiers.
- The feeding of petroleum coke can be staged so that the combustion of volatile matter can be prevented in order to increase the heating value of the fuel gas produced. This is not feasible in entrained gasifiers.

Summary

At temperatures close to 2000°F, a CO/CO_2 molar ratio of 3.5 in the product gas was obtained in the BRU. This shows a great improvement in the gas composition over a value of 0.5 obtained in the TRTU at temperatures lower than 1750°F, and that a temperature of 2000°F is required to process petroleum coke to produce a fuel gas of acceptable heating value. A fuel gas heating value of 124 BTU/scf is estimated for a commercial transport gasifier based on these results. These results were used to develop a flowsheet, and a conceptual design for the transport reactor has been completed to perform economic analysis.

References

(1) D. L. Heaven, "Gasification Technologies and World Wide Refining Trends," Presented at NPRA Annual Meeting, San Antonio, March 17-19, 1996.

(2) H. Simons and W. Campbell, "Status of Kellogg's Fluid Bed and Transport Gasification processes," Presented at Institution of Chemical Engineers Conference on Gasification, London, England, November, 1995.

Abbreviations

BRU	bench-scale reactor unit
BET	Brunauer, Emmett, and Teller method based on nitrogen adsorption
DOE	Department of Energy
DSRP	direct sulfur recovery process
FCC	fluid catalytic cracker
GC	gas chromatograph
PG	Product Gas
POX	Partial oxidation
PETC	Pittsburgh Energy Technology Center
ROSE™	Residuum Oil Supercritical Extraction
TRTU	Transport Reactor Test Unit

Table 1 - Analyses of bed and filter samples from BRU tests

Run number	Sample	Vanadium, ppm
Run 26	filter	42,255
	bed	5,760
Run 25	filter	61,710
	bed	4,888
Run 24	filter	14,891
	bed	4,362
Run 23	filter	19,875
	bed	9,838
Run 22	filter	32,873
	bed	5,843
	Fresh	1,752

Table 2 - Surface Areas of Bed Samples

Sample	Surface area (m^2/gm)
24	9.7
25	5.7
26	2.6
Fresh	0.9

Table 3 - Petroleum Coke POX Studies - (Test 26)

	sam. 1	sam. 2	sam. 3	sam. 4	sam. 5
time, min	4	16	29	42	55
bed temp upper, °F	2300	2147	2101	2034	1987
H_2, vol%	0.97	0.21	0.14	0.11	0.12
CO, vol%	30.6	27.1	29.3	29.2	34.4
CO_2, vol%	5.0	13.2	12.9	11.9	9.3
CO/CO_2 ratio	6.14	2.05	2.27	2.46	3.72
C cons.,gm/min	2.18	2.71	2.93	2.80	3.11
C cons. rate, 1/min	0.01	0.02	0.03	0.04	0.09

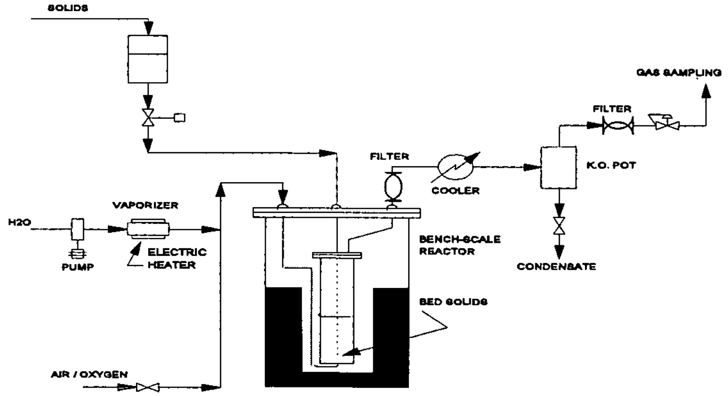
SOLIDS
GAS SAMPLING
FILTER
FILTER
COOLER
K.O. POT
H2O
VAPORIZER
PUMP
ELECTRIC HEATER
BENCH-SCALE REACTOR
CONDENSATE
BED SOLIDS
AIR / OXYGEN

Fig. 1 Bench-scale Reactor Unit for Petroleum coke Processing

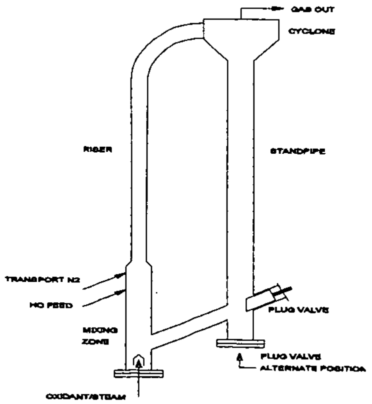
GAS OUT
CYCLONE
RISER
STANDPIPE
TRANSPORT N2
HO FEED
PLUG VALVE
MIXING ZONE
PLUG VALVE ALTERNATE POSITION
OXIDANT/STEAM

Fig. 2 Schematic of Transport Reactor

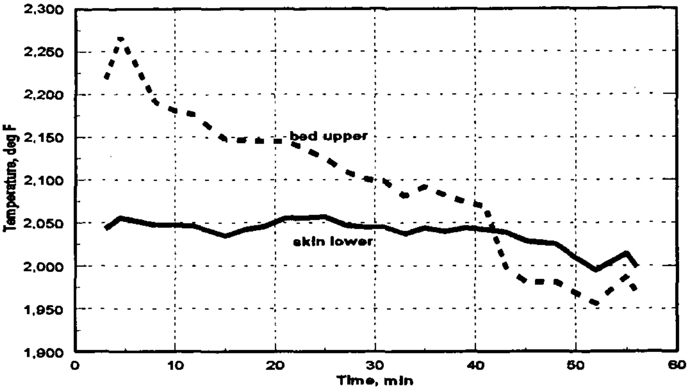

Fig. 3 Temperatures in BRU (Test 26)

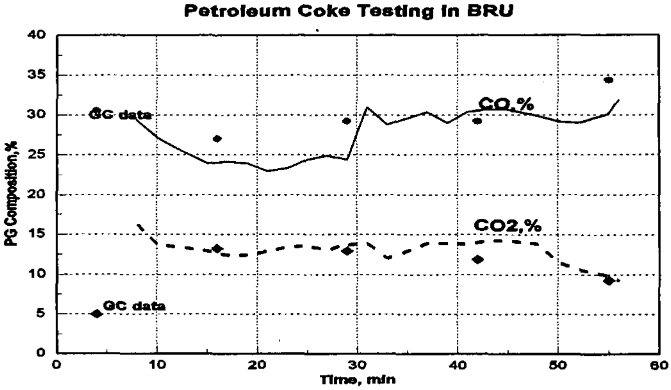

Fig. 4 PG Analysis as per IR analyzers and GC

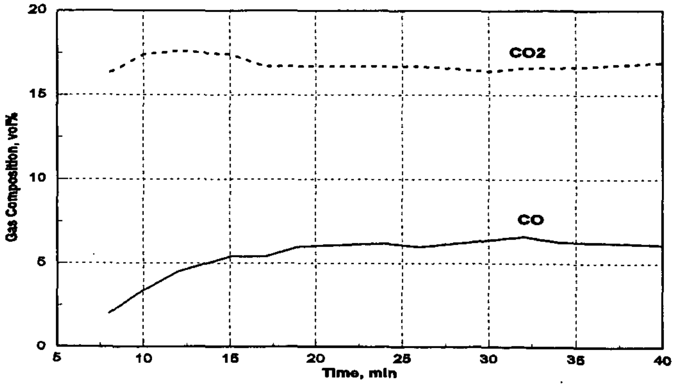

Fig. 5 Product Gas Composition - Test 22A

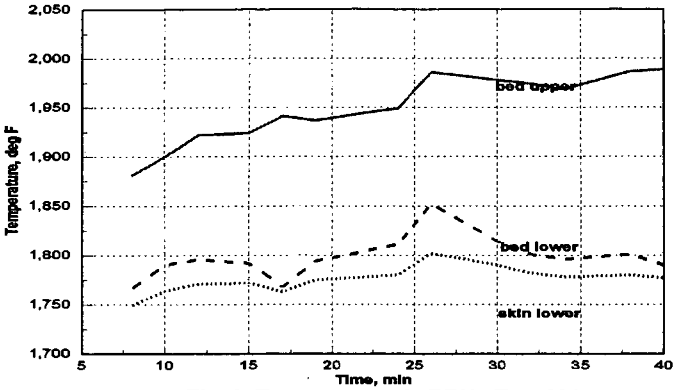

Fig. 6 Temperatures in BRU - Test 22A

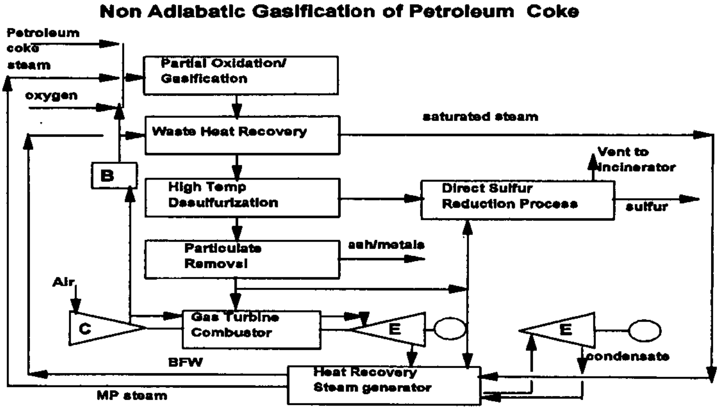
Non Adiabatic Gasification of Petroleum Coke

Petroleum coke
steam
oxygen
Partial Oxidation/ Gasification
Waste Heat Recovery
saturated steam
B
High Temp Desulfurization
Direct Sulfur Reduction Process
Vent to incinerator
sulfur
Particulate Removal
ash/metals
Air
C
Gas Turbine Combustor
E
E
condensate
BFW
Heat Recovery Steam generator
MP steam

Figure 7. Block Flow Diagram for Petroleum Coke Processing

BIODESULFURIZATION OF FLUE GASES USING SYNTHESIS GAS DELIVERED AS MICROBUBBLES

Punjai T. Selvaraj*, Marshall D. Bredwell,
Mark H. Little, and Eric N. Kaufman
Bioprocessing Research and Development Center
Oak Ridge National Laboratory
Bldg. 4505, MS 6226
Oak Ridge, Tennessee 37831-6226

Keywords: Biodesulfurization, synthesis gas, microbubbles

Introduction

Anaerobic treatment processes for biodegradation of hazardous materials have increasingly been gaining attention in environmental applications. Microbial processes utilizing sulfate reducing bacteria (SRB), in particular, have found potential applications in variety of treatment processes such as flue gas desulfurization [1,2], gypsum reclamation [3], sulfur recovery from sulfite/sulfate wastewater from pulp and paper, chemical and mining industries [4], and degrading explosive materials [5]. However, in all these applications, the source of electron donor is a major factor on the economics of the process. Previously, we have proposed a microbial process with sewage digest as an attractive low-cost feedstock for SRB cultures in the desulfurization of flue gases and sulfite/sulfate-laden industrial waste water [6]. In that process, a columnar reactor with mixed SRB cultures immobilized in BIO-SEP^{TM} polymeric porous beads with sewage digest as a carbon and energy source exhibited conversion rate of 16.5 mmol sulfite/h•L (32 kg/d•m^3) with 100% conversion to H_2S. Though municipal sewage digest is a readily available low-cost carbon source, the real cost of the medium depends on the location of the sewage treatment plant and power plant and on the transportation involved in bringing the sewage back and forth from the sewage plant. Therefore, the current research has been focused on an alternative low-cost feedstock. Various groups have demonstrated that SRB could be supported by carbon dioxide and/or carbon monoxide as the sole carbon source and hydrogen as the energy source [7-11]. Du Preez et al. [8,10] operated a sulfate-reducing reactor with a mixed SRB population to demonstrate the feasibility of using syn-gas as the feed source for SRB. Recently, van Houten et al. [9] reported the operation of a gas-lift sulfate-reducing reactor that was fed a CO-H_2 mixture (up to 20% CO) and yielded a maximum sulfate conversion rate of 30 g SO_4^{2-}/ d•L.

In our study, we have focused our research on utilizing gas mixture containing 36% H_2, 47% CO, 10% CO_2, 5% CH_4 and balance N_2 as a model coal synthesis gas as a low-cost feedstock. This composition is typical of an oxygen blown, coal fed gasifier. Coal synthesis gas will be readily available in power plants and the biological utilization of syn-gas as a carbon and energy source produces no organic end product that has to be processed prior to its disposal. Coal synthesis gas is, however, sparingly soluble in aqueous phase. Our process utilizing SRB with syn-gas feedstock may be mass transfer limited and methods to enhance the mass transport have been investigated. A CSTR with cell recycle and a trickle bed reactor with cells immobilized in BIO-SEP^{TM} polymeric beads were operated with syn-gas feedstock to obtain maximum productivity for SO_2 reduction to H_2S. The CSTR reactor was then fed with syn-gas as microbubbles in an effort to improve the mass transfer properties.

Materials and Methods

Microbial Culture and Media

Mixed SRB cultures were originally isolated from sewage solids obtained from the DAF unit of a municipal sewage treatment plant at Oak Ridge, TN. The cultures were grown in lactic acid media (LA) which consists of 3.6 g/L citric acid, 0.8 g/L $CaCl_2$, 1.0 g/L NH_4Cl, 0.5 g/L K_2HPO_4, 1.0 g/L yeast extract, 0.52 g/L $FeCl_2$, 5.8 mL/L of sodium lactate (60% syrup), 0.518 mL/L butyric acid, and 0.05 g/L cysteine HCL. A minimal salts media (MS) was also used; 1.2 g/L Na_2HPO_4, 1.8 g/L KH_2PO_4, 0.7 g/L $MgCl_2$, 0.2 g/L NH_4Cl, 0.04 g/L $FeCl_3$, 50 mL/L mineral water, 0.2 mL/L Batch vitamin solution, and 15 mL/L heavy metal solution (HMS). The Batch vitamin solution contains the following: 2.0 mg/L biotin, 2.0 mg/L folic acid, 10.0 mg/L pyridoxine hydrochloride, 5.0 mg/L thiamine hydrochloride, 5.0 mg/L riboflavin, 5.0 mg/L nicotinic acid, 5.0 mg/L DL-calcium pantothenate, 0.1 mg/L vitamin B-12, 5.0 mg/L p-amino benzoic acid, and 5.0 mg/L lipoic acid. The HMS solution contains the following: 1.5 g/L EDTA, 0.1 g/L $ZnSO_4{\bullet}7H_2O$ and 6 mL/L of a trace element solution (0.0507 g/L $AlCl_3$, 0.139 g/L KI, 0.139 g/L KBr, 0.139 g/L LiCl, 3.060 g/L H_3BO_3, 0.280 g/L $ZnCl_2$, 0.326 g/L $CuCl_2{\bullet}2H_2O$, 0.513 g/L $NiCl_2{\bullet}6H_2O$, 0.513 g/L $CoCl_2{\bullet}6H_2O$, 0.139 g/L $SnCl_2{\bullet}2H_2O$, 0.163 g/L $BaCl_2{\bullet}2H_2O$, 0.139 g/L $Na_2MoO_4{\bullet}2H_2O$, 0.139 g/L $CuSeO_4{\bullet}5H_2O$, and 0.024 g/L $NaVO_3$).

In serum bottles, the sulfate source was provided by the addition of up to 4.0 g/L of Na_2SO_4 or $MgSO_4$. In the reactors, the sulfite source was provided by a gas mixture containing 5% SO_2, 5% CO2, and balance N2. For growth on synthesis gas, a mixture of 47% CO, 36% H_2, 10% CO_2, 5% CH_4, and the balance N_2 was used. For serum bottle studies, 100 mL of MS media was put into a ~150 mL bottle and sealed with butyl rubber stopper. A nitrogen headspace was placed on top of the media and the bottles were sterilized by steam. When inoculated from an actively growing culture in a 2 L chemostat, synthesis gas was bubbled through the culture. The headspace was monitored for synthesis gas components and hydrogen sulfide and was replenished with fresh synthesis gas when needed. The bottles were usually shaken at 100 rpm at 30°C.

Syn-Gas Utilization by Mixed SRB

Utilization of syn-gas by mixed SRB culture developed from municipal sewage was investigated in a serum bottle containing minimal salt medium and SO_2 as terminal electron acceptor. The head space of the bottle was then filled with synthesis gas mixture containing 36% H_2, 47% CO, 10% CO_2, 5% CH_4, and balance N_2. The bottle was inoculated with mixed SRB culture and incubated at 30°C with shaking at 200 rpm. The syn-gas concentration was then regularly monitored using a Gas Chromatograph as described below.

Microbubble Generation and Characterization

Microbubbles are small, surfactant coated bubbles of gas that are generated by creating a gas-liquid interface in a high-shear zone. The bubbles are between 50 µm and 100 µm in diameter and the surfactant coating helps to prevent coalescence by electrostatic repulsion from the diffuse electric double layer around the bubble. In our work, the microbubble dispersions were generated using a spinning disk apparatus first described by Sebba [12]. This microbubble generator (MBG) uses a high speed motor (Talboys #37830, Cole Parmer, Chicago, IL) that spins a 4 cm disk as speeds above 4000 RPM in close proximity to baffles (within 3 mm) to generate a localized high-shear zone. The stainless steel disk and baffles are mounted in 4 L glass vessel with a ground glass lip to fit the headplate. A second headplate mounted above the first supports the motor and allows easy alignment. Stainless steel sealed bearings insure minimal wobble.

The bubble size measurements were performed on a Coulter LS 130 particle size analyzer (Coulter) using laser diffraction. The microbubble foam sample was loaded into both the constant volume module and hazardous fluids module for the instrument. The constant volume module could contain 15 mL of sample and had a magnetic stirrer in the bottom of the cell to maintain a well-mixed system. The hazardous fluids module used a recirculating pump. Dispersion was added to water in each module until 8% to 12% obscuration was obtained. Data was collected for ninety seconds in each case. Between runs the constant volume module was rinsed with double distilled water and the hazardous fluids modules had the recirculating liquid drained, refilled, and filtered.

CSTR and Trickle Bed Reactors

A 2 L Virtis Omni-culture chemostat (Virtis Co., Gardiner, NY) with temperature and agitation control was used as the primary reactor vessel. The vessel headplate was modified for acid/base additions and gas and liquid inlets and outlets. The pH was controlled at 6.8 with a Chemcadet controller with 6 *N* NaOH and 6 *N* H_3PO_4. The reactor was maintained at a temperature of 30°C and agitated at 250 rpm for all experimental runs. The reactor was operated in a continuous mode with a feed rate of fresh MS medium at 0.2 mL/min. To retain biomass in the reactor, a filtration system consisted of two Amicon Diaflo hollow fiber cartridges was attached to the reactor. All pumps used were Masterflex peristaltic. A sparge of 50 mL/min of nitrogen was added to the reactor vessel to strip off the produced H_2S from the reactor. The synthesis gas was fed directly at a rate of 10 mL/min to the reactor during the control runs through a stainless steel sparger. The flow rate of SO_2 gas fed separately into the reactor was monitored using gas flow meter. In the microbubble-fed system, the permeate from the filters was returned to the MBG. the syn-gas microbubbles were generated by bubbling syn-gas into minimal salt medium containing Tween-20 (240 mg/L) as surfactant. The microbubbles were then fed to the CSTR at a rate of 15 mL/ min. which was equivalent to 10 mL/min of synthesis gas as fed during the control run.

The trickle bed reactor consisted of fully jacketed glass column of internal dimensions 2.5 x 30 cm with a total volume of 180 mL and a working volume of 81 mL with BIO-SEP^{TM} beads. BIO-SEP^{TM} beads, encapsulated activated carbon (50-80%) in aromatic polyamide (Aramid) (20-50%) were obtained as the kind gift of Dr. Carl Camp from the DuPont Chemical Co. (Glasgow, DE). The reactor was operated at a temperature of 30°C. A 500 mL bottle with a specially made headplate was used for pH control, H_2S stripping by nitrogen, gas outlet, and ports for continuous operation. The reactor had biomass loaded on to the BIO-SEP beads by operation in a packed bed mode on lactate media. The liquid inside of the reactor was completely recycled. When switched to a synthesis gas feed, the reactor was operated in a trickle bed mode with the liquid and both gas feeds entering at the top of the reactor. Gas samples were taken from a gas disengagement bottle. The reactor was operated in a continuous mode with a fresh minimal salt medium at a feed rate of 12 mL/h. In trickle bed mode, the liquid flow rate across the bed was 600 mL/h.

In all runs the reactor was monitored for sulfite. The off-gas from the reactor was also monitored for H_2S and synthesis gas components. The off-gas flow rates were monitored with a wet test meter for two hour periods.

Analytical

The sulfite in the reactor was analyzed spectrophotometrically by the reaction of fuchsin and formaldehyde in sulfuric acid [13]. The sulfide in the reactor was precipitated using zinc acetate in a basic solution followed by resuspension and measurement using the formation of methylene blue [14].

Hydrogen sulfide in the off gas was analyzed using a gas chromatograph (Hewlett Packard HP 5890 Series II) equipped with a teflon column (30 in x 1/8 in) packed with Super Q (80/100 mesh) (Alltech, Waukeegen, WI). Temperatures of the column, injection port, and thermal conductivity detector were 70°C, 125°C, and 125°C respectively. The carrier gas was helium at 25 mL/min. The calibration was based on 1%, 5%, and 10% H_2S in nitrogen standards. Synthesis gas components were measured using a gas chromatograph (Hewlett Packard HP 5890 Series II) equipped with a HP PLOT molecular sieve 5 Å capillary column (30 m x 0.32 mm) with a 12 μm film thickness. Temperatures on the column, injection port, and thermal conductivity detector were 55°C, 100°C, and 240°C respectively. Liquid samples were filtered through a 0.22 μm syringe filter and analyzed by gas chromatography using a HP 5890 Series II with a HP WAT (crosslinked PEG) capillary column (30 m x 0.53 mm) with a 1.0 μm film thickness. The column temperature program was initially 70°C followed by ramping to 200°C at 25°C/min with a 1.2 min hold then followed by ramping to 225°C at 25°C/min with a 3.0 min hold. The injection port temperature was 245°C while the flame ionization detector was 265°C.

Results and Discussion

Syn-Gas Utilization by Mixed SRB

Initially, a decrease in CO concentration was observed with no change in H_2 concentration. However, hydrogen sulfide was detected during this time in the head space of the serum bottle. This indicates that the CO was utilized by certain type of bacteria and produced H_2 as shown in the equation below:

$$CO + H_2O \rightarrow H_2 + CO_2$$

With limited SO_2 reduction due to a possible CO inhibition at higher concentration, the H_2 concentration declined only after the CO concentration was less than about 5% in the mixture. This suggests that the mixed culture developed from sewage solids would be able to use CO as sole carbon and energy source and produce H_2. Kinetically, the CO utilization was much faster than H_2 utilization by SRB cultures.

Serum bottle experiments with mixed SRB showed that we could switch between lactate and syn-gas for carbon and energy source that would help us to start the reactor operation moe quickly.

CSTR with syn-gas feed

The CSTR in the control mode in which the syn-gas was fed directly into the reactor was able to convert 1.2 mmol SO_2/h•L with no sulfite detected in the effluent (Fig. 1). The off-gas analysis through GC showed 100% conversion of SO_2 into H_2S. With continuous N_2 purging in the liquid medium, the sulfide concentration in the aqueous phase was measured to be less than 5 mg/L. When the SO_2 feed was increased above 1.2 mmol/h•L, sulfite accumulation of greater than 25 mg/L was observed in the reactor medium. This indicated that the reactor reached the maximum productivity of 1.2 mmol SO_2/h•L under the operating conditions. The synthesis gas content in the feed and the off-gas showed the stoichiometric conversion of 1.8 mol H_2 and 2.3 mol CO per mol of SO_2. The reactor was then operated at 1.2 mmol/h•L, for 3 d and switched over to microbubble-fed system. With syn-gas fed as microbubbles, the SO_2 feed rate was increased incrementally and the maximum productivity of 2.1 mmol/h•L was obtained with 100% conversion to H_2S in 33 h. The biomass concentration in the reactor prior to the microbubble operation was 5 g/L. The increase of productivity from 1.2 to 2.1 mmol/h•L within the span of 33 h at the same biomass concentration of 5 g/L indicated that the mass transport of syn-gas was the limiting parameter in the above process.

Trickle-bed reactor with syn-gas feed

Initially, the immobilization of mixed SRB cells in BIO-SEP beads in a trickle-bed reactor was started-up with lactate medium as described earlier. This was achieved in 14 d. Following the immobilization, the reactor was fed with syn-gas at a rate of 10 mL/min as a sole carbon and energy source and 5% SO_2 at rate of 4 mL/min (2.7 mmol/h•L). The immobilized SRB cells grown on lactate medium were able to switch to syn-gas at once. The SO_2 feed rate was then increased incrementally with no sulfite detected in the effluent. As shown in Fig. 2, complete conversion of SO_2 into H_2S was achieved at a maximum SO_2 feed of 8.8 mmol/h•L with syn-gas utilization of 1.0 mol H_2 and 1.2 mol CO per mol of SO_2. This compares to previous studies which achieved 4.3 mmol SO_4^{2-}/h•L [9] and 0.5 mmol/h•L [10] with synthesis gas as feedstock.

Conclusion

The model coal synthesis gas containing 36% H_2, 47% CO, 10% CO_2, 5% CH_4, and balance N_2 has been found as a low-cost feedstock for mixed SRB in the desulfurization processes. With syn-gas fed as microbubbles, productivity in the CSTR increased from 1.2 to 2.1 mmol/h•L in 33 h. This has been observed at the same biomass concentration of 5 g/L. This shows the mass transport limitation in the above process. In the trickle bed reactor, maximum productivity of 8.8 mmol/h•L was achieved with less carbon and energy requirement (1 mol H_2 and 1.2 mol CO per mol of SO_2) indicating better surface to volume ratio with cells immobilized in the pores of polymeric beads. The mass transfer coefficients in these systems will be determined in future studies to develop better reactor configuration for biodesulfurization of flue gases and other sulfur wastes.

References

1. Selvaraj, P.T., and Sublette, K.L. (1995), Biotechnol. Prog. **11**, 153-158.1.
2. Paques B.V. and Hoogovens Technical Services (1995), Bio-technological Flue Gas Desulfurization Report.
3. Kaufman, E.N., Little, M.H., and Selvaraj, P.T. (1996), J. Chem. Technol. Biotechnol. **66,** 365-374.
4. Hammack, R.W., Edenborn, H.M., and Dvorak, D.H. (1994), Water Res. **28**, 11, 2321-2329.
5. Boopathy, R., and Manninig, J.F. (1996), American Academy of Environmental Engineers, Washington DC. pp 61-75.
6. Selvaraj, P.T., Little, M.H., and Kaufman, E.N. (1996), submitted to Bioremediation.

7. van Houten, R.T., Pol, L.W.H., and Lettinga, G. (1994), Biotechnol. Bioeng. **44**, 586-594.
8. Du Preez, L.A., Odendaal, J.P., Maree, J.P., and Posonby, M. (1992), Environ. Technol. **13**, 875-882.
9. van Houten R.T., van der Spoel, H., van Aelst, A.C., Hulshoff Pol, L.W., and Lettinga, G. (1996), Biotechnol. Bioeng. **50**, 136-144.
10. Du Preez, and Maree, J.P., (1992), Water Sci. Tech. **30**, 275-285.
11. Kaufman, E.N., Little, M.H., and Selvaraj, P.T. (1996), Appl. Biochem. Biotechnol. (in press).
12. Sebba, F. (1985), Chemistry and Industry, 91-92.
13. Steigman, A. (1950), Anal. Chem. **22**, 492-493.
14. Tanner, R. S. (1989), J. Microbiological Methods.

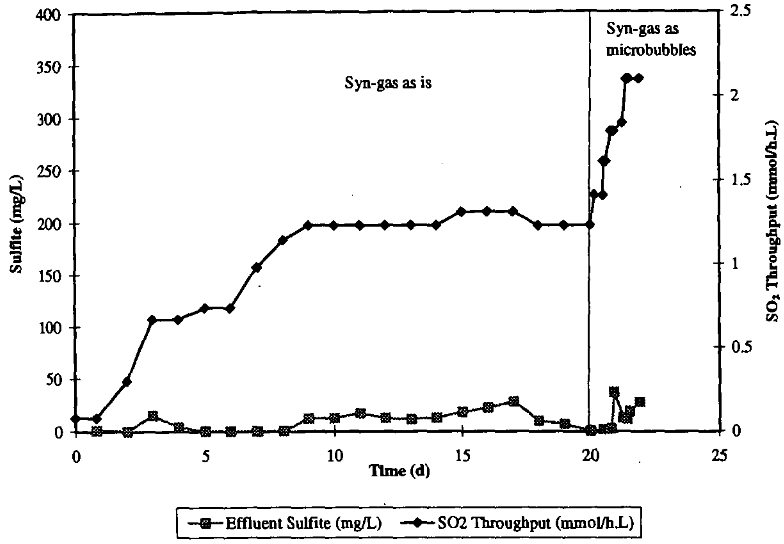

Figure 1. Sulfite conversion in a CSTR with syn-gas as feedstock. With syn-gas fed as microbubbles, the reactor productivity was increased from 1.2 to 2.1 mmol/h.L in 33 h.

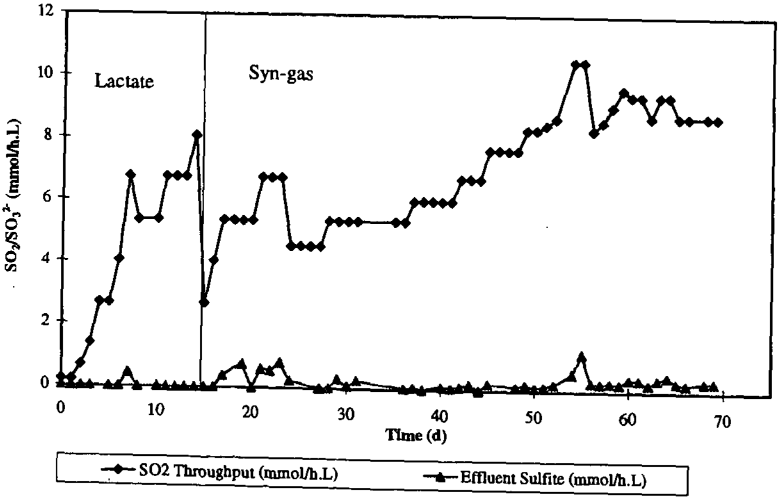

Figure 2. Sulfite conversion in a trickle-bed reactor with mixed SRB immobilized in BIO-SEP™ beads. The liquid medium and gas mixture (syn-gas and SO_2) were fed co-currently at the top of the reactor.

MICROBIAL DESULFURIZATION OF DIBENZOTHIOPHENE AND ITS DERIVATIVES

Yoshikazu Izumi and Takashi Ohshiro
Department of Biotechnology, Faculty of Engineering,
Tottori University, Tottori, 680 JAPAN

Keywords: desulfurization, dibenzothiophene, Rhodococcus

INTRODUCTION

The serious environmental problem of acid rain is at least partly caused by the combustion of sulfur compounds present in the fossil fuels, releasing sulfur dioxide into the atmosphere. Though inorganic sulfur can be reduced by physical or chemical means, none of them can be applied to removing organic sulfur from petroleum. Therefore, microbial processes that can do so have recently received much focus. Dibenzothiophene (DBT) and its derivatives have been widely used as model organic sulfur compounds in petroleum (1). Three pathways of DBT degradation have been reported. The first is the ring-destructive pathway, in which the sulfur of DBT remains (2-5), the second is the completely destructive pathway, in which DBT is mineralized to carbon dioxide, sulfite and water (6), and the third is the sulfur-specific pathway, in which only sulfur is removed from DBT (7-9) as illustrated in Fig. 1. Strains having the second or third pathways should be applied to the microbial desulfurization process. In other studies, we also isolated a DBT-degrading bacterium, Rhodococcus erythropolis D-1, which has the sulfur-specific pathway (10) and observed an enzyme system catalyzing this conversion (11). Many research groups have since studied the desulfurization of DBT by the sulfur-specific pathway (12-14) . The genes involved in DBT degradation have been identified (15-17). However, there has so far been little report on the DBT desulfurization in the presence of hydrocarbon. Since petroleum should ideally be desulfurized, we isolated a strain with the capacity to desulfurize DBT in the presence of hydrocarbon. Here we describe the desulfurization of DBT by growing whole cells of Rhodococcus erythropolis H-2 in the presence of n-tetradecane (TD) and other hydrocarbons. We also describe the desulfurization of substituted DBTs which actually exist in petroleum by R. erythropolis H-2 in the presence of TD.

MATERIALS AND METHODS

Medium A-1 was the same as medium A described elsewhere (10) except that glucose was omitted. Cells were cultivated at 30°C in test tubes containing 5 ml of medium or in 2-liter flasks containing 500 ml of medium with reciprocal shaking (300 rpm for test tubes and 100 rpm for flasks).

To isolate bacteria which could desulfurize DBT in petroleum, several soil samples from various areas in Japan were transferred to test tubes containing medium A-1 supplemented with 5.4 mM DBT as a sole source of sulfur and 0.5% TD. Single colony isolation was repeated on the same medium containing agar. Among the DBT-utilizing strains in the presence of TD, we selected strain H-2.

Strain H-2 was cultivated in medium A-1 with 0.5 % glucose and 0.27 mM DBT in 2-liter flasks for 2 days. Cells were harvested at 4°C by centrifugation at 10,000 x g for 15 min, washed once with 0.85 % NaCl and resuspended in the same solution. The suspension was lyophilized and kept at -20°C until use. The reaction mixture contained, in 1 ml, TD, DBT which was dissolved in TD, 0.1 M potassium phosphate buffer (pH 7.0) and lyophilized cells. The reaction proceeded in test tubes at 30°C with reciprocal shaking (300 rpm).

DBT and 2-HBP were determined by gas chromatography or high performance liquid chromatography as described (10). TD was measured by gas chromatography under the same conditions. When the strain was cultivated in the medium with hydrocarbon, the cells floated on the surface of the medium. Therefore, growth could not be measured turbidimetrically. We centrifuged the culture broth at 15,000 x g for 45 min and the cell pellet was resuspended in 0.85% NaCl containing 5% polyoxyethylene lauryl alcohol ether (Brij 35). Cell growth was determined by measuring the optical density of this suspension. OD660 was proven to be proportional to the number of viable cells.

RESULTS AND DISCUSSION

Characterization of a DBT-utilizing bacterium in the presence of hydrocarbon

Among the isolates, a strain designated H-2 utilized DBT most rapidly in the presence of TD. The taxonomic properties were examined at the National Collection of Industrial and Marine Bacteria Ltd. (Aberdeen, Scotland, United Kingdom). As a result, the strain was identified as Rhodococcus erythropolis. There are some differences between our previous strain D-1 (10) and the present strain H-2 grown on carbon source such maltose, L-tyrosine and D-mannose: in strain H-2, these were possibly positive. Since this strain assimilated TD as a carbon source in addition to DBT as a sulfur source, several hydrocarbons were investigated to determine whether or not they could support the growth of R. erythropolis H-2. As shown in Table 1, this strain grew on n-alkanes with carbon chains longer than C8 with and without glucose, whereas it did not grow on n-hexane, styrene, p-xylene, cyclooctane and toluene even in the presence of glucose.

Growth of R. erythropolis H-2 in the medium containing DBT and TD

The strain was cultivated in medium A-1 with TD as a sole source of carbon and DBT as a sole source of sulfur. The strain showed maximal growth (OD660=ca. 3.0) after 2 days of cultivation. DBT completely disappeared before this point. The metabolite 2-HBP was formed from DBT and it was almost equimolar to the amount of DBT degraded. The level of TD decreased slightly, and the pH decreased concomitantly with the increase of cell growth.

DBT degradation by whole cell reactions

To prepare whole cells for DBT degradation, R. erythropolis H-2 was cultivated in medium containing either 0.5% glucose or 0.5% TD as a carbon source. Cells were lyophilized after harvesting and used for each reaction by resting cells. When the whole cell reactions proceeded with 50% TD for 4 h, the DBT degradation rates by cells pregrown in glucose and TD were 60 and 33%, respectively. Therefore, the following studies of whole cells reactions were performed using cells grown in glucose. DBT degradation was investigated using various amounts of lyophilized cells. The reaction proceeded most efficiently when the cells were added to the reaction mixture at a concentration of 80 mg/ml. However, DBT degradation was suppressed in the reaction mixture at elevated concentrations of the lyophilized cells. The limitation of oxygen may lower DBT degradation as found in R. erythropolis D-1 (10). DBT degradation in reaction mixtures containing various amounts of TD or DBT were examined. The reaction proceeded more efficiently with, than without TD . Even with as much as 70% TD, the degradation was enhanced compared with the situation without TD. The optimal concentration of TD was about 40%. TD at a concentration higher than 80% suppressed the degradation. In a reaction mixture supplemented with 40% TD and 80 mg/ml of the lyophilized cells, DBT up to 3 mM was completely degraded within 4 h. Figure 2 shows the time course of DBT degradation and 2-HBP accumulation. The amount of 2-HBP formed was almost stoichiometric to that of DBT degraded. It seemed that the level of TD was slightly decreased.

Degradation of DBT and its derivatives by whole cell reactions

R. erythropolis H-2 was cultured in medium AG with DBT or its derivatives (Fig. 3) as the sole source of sulfur at 50 mg/l. The strain grew more or less on the four aromatic sulfur compounds tested: Growth (OD660) on DBT, 2,8-dimethyldibenzothiophene (2,8-dimethylDBT), 4,6-dimethyldibenzothiophene (4,6-dimethylDBT) and 3,4-benzodibenzothiophene (3,4-benzoDBT) in 4-day culture: 5.7,4.7, and 1.7, respectively. Though 3,4-benzoDBT was not a good sulfur source for this strain, the two dimethylDBTs as well as DBT also supported the growth of this strain.

The reaction using lyophilized cells cultured with DBT, proceeded with DBT derivatives at 1 mM in the presence of TD. New peaks appeared on all the elution HPLC profiles with concomitantly decreasing substrate peaks. When DBT, 3,4-benzoDBT, 2,8-dimethylDBT, and 4,6-dimethylDBT were the substrates, the retention times of the new peaks were 3.5, 5.2, 4.6, and 5.2 min, respectively. The new peak in the DBT reaction profile corresponded to 2-HBP. The products in the reaction mixture using 2,8-dimethylDBT and 4,6-dimethylDBT as substrates were analyzed by gas chromatograph-mass spectrometry. Mass ions at m/z 198 corresponding to the molecular mass of monohydroxy dimethylbiphenyls were detected. With 3,4-benzoDBT, the mass ion of the product at m/z 220 was also obtained. These results indicated that the microbial desulfurization of these DBT derivatives and of DBT proceeded in a similar manner and gave the corresponding hydroxylated biphenyls as products. And it was interesting to know whether the hydroxy group of the 3,4-benzoDBT product was attached to the benzene, or the naphthalene ring. To identify their exact structures, the products from 3,4-benzoDBT, 2,8-dimethyl DBT and 4,6-dimethylDBT were purified from the reaction mixtures and analyzed by NMR.

In the case of 3,4-benzoDBT, signals were observed at d 5.54 (s, 1 H), 7.04-7.09 (m, 1 H), 7.13 (d, 2 H, J=7.5), 7.24-7.25 (m, 1 H), 7.26-7.27 (m, 2 H), 7.29-7.30 (m, 1 H), 7.33 (d, 1 H, J=8.2), 7.35-7.36 (m, 1 H), 7.65 (d, 1 H, J=8.0), and 8.51 (d, 1 H, J=8.2). Since the signals at 7.07, 7.13 and 7.26 ppm were specific for one substituted benzene and those at 7.24 and 7.33 ppm were specific for 1,2,3,4-substituted benzene, this spectrum suggested that the hydroxy group is attached to the naphthalene ring. Therefore, we proposed that the structure of the product from 3,4-benzoDBT is a-hydroxy-b-phenylnaphthalene (Fig. 4).

The NMR signals in the case of 2,8-dimethylDBTand 4,6-dimethylDBT were assigned to 2-hydroxy-5,5'-dimethylbiphenyl and 2-hydroxy-3,3'-dimethylbiphenyl, respectively.

The amounts of products formed by whole cells were tentatively calculated assuming that the peak areas per mole of each product on the HPLC were the same as that of 2-HBP. Each substrate was thus converted to the corresponding product. The initial rates of degradation and desulfurization of 2,8-dimethylDBT, 4,6-dimethylDBT and 3,4-benzoDBT were about 120, 60, 20% that of DBT. The 2,8- and 4,6-dimethylDBTs were completely degraded within 6 h. Arthrobacter sp. readily attacked the sterically hindered 4,6-diethylDBT (18). Generally, there seems to be no steric hindrance of such alkyl groups against these enzyme systems. The chemical desulfurization rate for alkyl-substituted DBTs is much slower than that for DBT and it has been thought that the desulfurization of alkyl-substituted DBTs would also be less easy than that of DBT. Thus, these results indicate the feasibility of the practical microbial desulfurization of petroleum.

Although 3,4-benzoDBT was degraded slowly, the amount of the substrate was reduced to 0.1 mM after 12 h (Fig. 5). As described above, NMR analysis indicated that the hydroxy group of the identified product was attached to the naphthalene ring. These results suggest that the enzyme system involved in the microbial DBT desulfurization could distinguish between two carbon-sulfur bonds of 3,4-benzoDBT. The steric hindrance caused by the naphthalene ring might lead to this specificity.

Thus, the present work demonstrated that a new strain, identified as R. erythropolis H-2, utilized DBT as a sole source of sulfur and converted it to 2-HBP stoichiometrically even in the presence of hydrocarbon. This strain grew well in n-alkanes with relatively long carbon chains but not in hydrocarbons with higher toxicity to the organism such as toluene. The limiting log P value for the growth of our isolated strain was about 4.9 (log P value of n-octanol). From other experimental data (19), R. erythropolis H-2 revealed high tolerance against solvents compared with other Gram-positive bacteria, but it had less tolerance than Gram-negative bacteria such as Pseudomonas strains. Also in the whole cell reactions, DBT degradation proceeded in the presence of hydrocarbon and was enhanced by adding TD. TD may facilitate contact between DBT and cells since DBT is water immiscible.

The present strain was also found to have an ability to efficiently function in the presence of hydrocarbon and desulfurize DBT and DBT derivatives to form 2-HBP and the corresponding hydroxylated biphenyls, respectively. Therefore, the strain should be useful for the practical microbial desulfurization of petroleum.

ACKNOWLEDGMENTS. A part of this work has been conducted by the support of the Petroleum Energy Center (PEC) subsidized from Ministry of International Trade and Industry, Japan.

REFERENCES

(1) Klibane II , J.J. and Bielaga, B.A., Toward sulfur-free fuels. *CHEMTECH*, **20**:747-751 (1990).

(2) Kodama, K., Nakatani , S., Umehara, K., Shimizu, K., Minoda, Y., Yamada, K., Identification of products from dibenzothiophene. *Agric. Biol. Chem.*, **34**:1320-1324 (1970) .

(3) Laborde, A.L. and Gibson, D.T., Metabolism of dibenzothiophene by a Beijerinckia species. *Appl. Environ. Microbiol.*, **34**:783-790 (1977).

(4) Monticello, D.J., Bakker, D., and Finnerty, W.R., Plasmid-mediated degradation of dibenzothiophene by Pseudomonas species. *Appl. Environ. Microbiol.*, **49**:756-760 (1985) .

(5) Crawford, D.L. and Gupta, R.K., Oxidation of dibenzothiophene by Cunninghamella elegans. *Curr. Microbiol.*, **21**:229-231 (1990).

(6) Afferden, M. van, Schacht , S., Klein, J., and Truper, H.G., Degradation of dibenzothiophene by Brevibacterium sp. DO. *Arch. Microbiol.*, **153**:324-328 (1990).

(7) Kilbane II, J.J. and Jackowski, K., Biodesulfurization of water-soluble coal-derived material by Rhodococcus rhodochrous IGTS8. *Biotechnol. Bioeng.*, **40**:1107-1114 (1992).

(8) Omori, T., Monna, L., Saiki, Y.., and Kodama, T. Desulfurization of dibenzothiophene by Corynebacterium sp. strain SY1. *Appl. Environ. Microbiol.*, **58**:911-915 (1992).

(9) Olson, E.S., Stanley, D.C., and Gallagher, J.R., Characterization of intermediates in the microbial desulfurization of dibenzothiophene. *Energy & Fuels*, **7**:159-164 (1993).

(10) Izumi, Y., Ohshiro, T., Ogino H, Hine, Y., and Shimao, M., Selective desulfurization of dibenzothiohene by Rhodococcus erythropolis D-1. *Appl. Environ. Microbiol.*, **60**:223-226 (1994) .

(11) Ohshiro, T., Hine, Y., and Izumi, Y., Enzymatic desulfurization of dibenzothiophene by a cell-free system of Rhodococcus erythropolis D-1. *FEMS Microbiol. Lett.*, **118**:341-344 (1994).

(12) Gallagher, J.R., Olson, E.S., and Stanley, D.C., Microbial desulfurization of dibenzothiophene: A sulfur-specific pathway. *FEMS Microbiol. Lett.*, **107**:31-36 (1993).

(13) Kayser ,K.J., Bielaga-Jones, B.A., Jackowski, K., Odusan, O., and Klibane II, J.J., Utilization of organosulfur compounds by axenic and mixed cultures of Rhodococcus rhodochrous IGTS8. *J. Gen. Microbiol.*, **139:**3123-3129 (1993) .

(14) Wang, P. and Krawiec, S., Desulfurization of dibenzothiophene to 2-hydroxybiphenyl by some newly isolated bacterial strains. *Arch. Microbiol.*, **161**:266-271(1994).

(15) Denome, S.A., Olson, E.S., and Young, K.D., Identification and cloning of genes involved in specific desulfurization of dibenzothiophene by Rhodococcus sp. strain IGTS8. *Appl. Environ. Microbiol.*, **59**:2837-2843 (1993).

(16) Denome, S. A., Oldfield, C., Nash, L. J., and Young, K. D., Characterization of desulfurization genes from Rhodococcus sp. strain IGTS8. *J. Bacteriol.*, **176**:6707-6716 (1994).

(17) Piddington, C. S., Kovacevich, B. R., and Rambosek, J., Sequence and molecular characterization of a DNA region encoding the dibenzothiophene desulfurization operon of Rhodococcus sp. strain IGTS8. *Appl. Environ. Microbiol.*, **61**:468-475 (1995) .

(18) Lee, M. K., Senius, J. D., and Grossman, M. J. Sulfur-specific microbial desulfurization of sterically hindered analogs of dibenzothiophene. *Appl. Environ. Microbiol.*, **61**:4362-4366 (1995).

(19) Inoue A, Horikoshi K, Estimation of solvent-tolerance of bacteria by the solvent parameter Log P. *J. Ferment. Bioeng.*, **71**:194-196 (1991).

TABLE 1. Growth in the presence of hydrocarbons. The strain was cultivated in medium A-1 with 0.5% hydrocarbons with or without 0.5% glucose in test tubes for 4 days.

Hydrocarbon	(log *P* value)	+Glucose		–Glucose	
		Growth (OD660)	pH	Growth (OD660)	pH
None		4.8	4.6	n.t[a]	n.t[a]
n-Hexadecane	(7.0<)	4.9	4.2	5.2	5.1
n-Tetradecane	(7.0<)	5.6	3.8	4.9	3.8
n-Dodecane	(7.0)	2.9	4.2	3.0	4.8
n-Decane	(6.0)	1.7	5.7	2.5	6.4
n-Nonane	(5.5)	0.8	5.7	0.8	5.8
n-Octane	(4.9)	0.3	6.5	0.3	6.6
Cyclooctane	(4.5)	0	6.9	0	6.9
n-Hexane	(3.9)	0	7.0	0	6.9
p-Xylene	(3.1)	0	7.0	0	7.0
Styrene	(2.9)	0	6.9	0	6.9
Toluene	(2.8)	0	6.9	0	7.0

[a] not tested

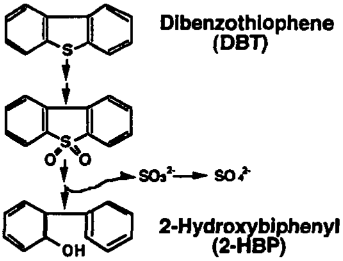

FIGURE 1. Proposed sulfur-specific pathway of dibenzothiophene (DBT)

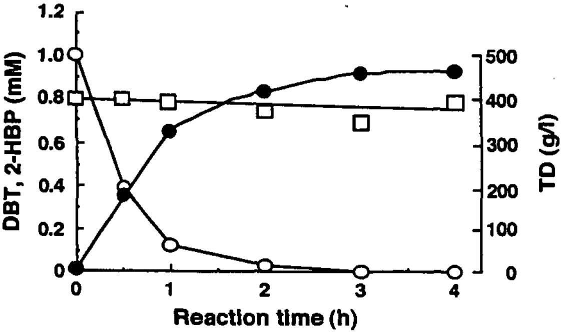

Figure 2. Time course of DBT degradation and 2-hydroxybiphenyl (2-HBP) accumulation in the whole cell reaction. ○ DBT, ● 2-HBP, □ TD

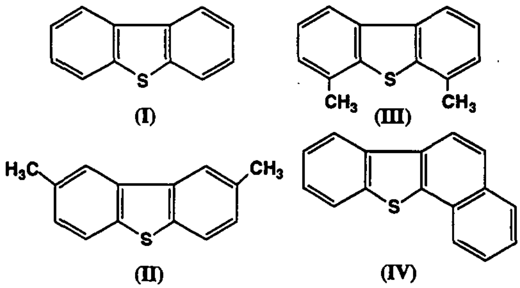

FIGURE 3. Structure of DBT and its derivatives. (I) DBT; (II) 2,8-dimethylDBT; (III) 4,6-dimethylDBT; (IV) 3,4-benzoDBT.

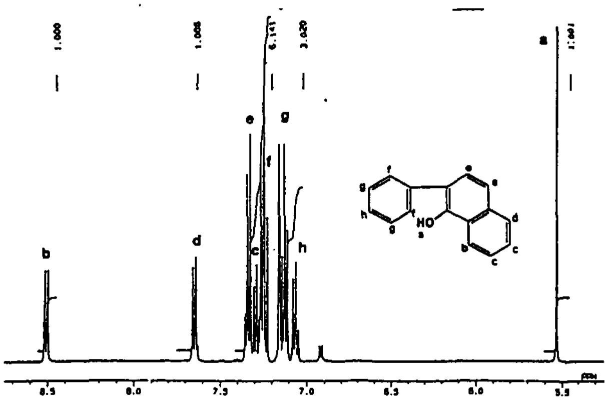

FIGURE 4. ¹H-NMR spectrum of the product from 3,4-benzoDBT.

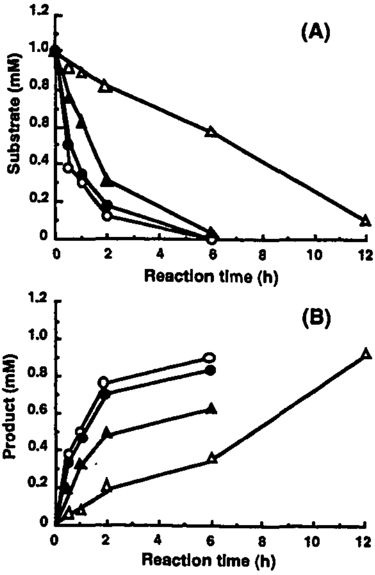

FIGURE 5. Degradation of DBT derivatives in the presence of hydrocarbon by whole cell reactions. The reaction mixture contained 100 mmol potassium phosphate buffer (pH 7.0), 40 mg lyophilized cells of the strain H-2, 400 µl TD and 1 µmol DBT (●), 2,8-dimethylDBT (○), 4,6-dimethylDBT (▲), and 3,4-benzoDBT (△) in a total volume of 1 ml. The amounts of product formed were determined by comparing the peak areas with those of standard 2-HBP. The amounts of remaining substrates and products formed are shown in (A) and (B), respectively.

ANALYSIS OF THE EXTENT OF SULFUR REMOVAL AND THE EFFECT ON REMAINING SULFUR

M. K. Lee, R. C. Prince, J. D. Senius, M. J. Grossman
Exxon Research and Engineering Co., Annandale, NJ 08801

I. J. Pickering, G. N. George
SSRL, Stanford, CA 94309

Keywords: Biodesulfurization, middle distillate, vacuum gas oil

INTRODUCTION

Hydrodesulfurization (HDS) is used to remove organic sulfur from petroleum oils in the refining process. DBTs bearing alkyl substitutions adjacent to the sulfur atom (referred to as sterically hindered compounds), are the most resistant to HDS, and represent a significant barrier to reaching very low sulfur levels in fuels[1]. Bacteria have been isolated which utilize an oxidative pathway to selectively desulfurize a variety of organic sulfur compounds found in petroleum oils[2]. The molecular mechanisms of dibenzothiophene (DBT) desulfurization by this pathway have recently been described[3]. Previous experiments with *Rhodococcus* sp. ECRD-1 (ATCC 55309) using DBT have shown that it is converted to the hydroxylated sulfur-free end product 2-phenylphenol via an analogous pathway[4]. Corresponding conversions of the sterically hindered compounds 4,6-diethyl DBT, 4,6-dimethyl DBT and 4-ethyl DBT were also demonstrated.

This study evaluates the ability of ECRD-1 to desulfurize feeds encountered in refineries and examines the fate of sulfur remaining in the oil. A middle distillate oil (232 - 343°C) and a vacuum gas oil (VGO) (343 - 496°C), representing a diesel range oil and a heavy gas oil, were tested as sole sulfur sources in batch cultures. Sulfur removal was quantified using the ratio of Flame Ionization (FID) and Sulfur Chemiluminesce (SCD) detector response factors in Gas Chromatography analysis. Results demonstrated that up to 40% of sulfur in the middle distillate cut could be removed in two week batch cultures. Compounds across the entire boiling range of the oil were affected by the treatment. Less than half that removal is evident in the heavier VGO, suggesting limitations on the range of compounds susceptible to desulfurization by this system. Analysis of the chemical state of the sulfur remaining in the treated oils by sulfur K-edge X-ray absorption spectroscopy showed that in the case of the middle distillate oil over 50% of the remaining sulfur was in an oxidized form. A lesser amount of the remaining sulfur in the treated VGO was in an oxidized state, consistent with the degree of desulfurization. The presence of partially oxidized sulfur compounds in the treated oils indicates that these compounds were en route toward desulfurization. Overall, in the case of the middle distillate oil, more than two-thirds of the initial sulfur had been affected by the microbial treatment.

EXPERIMENTAL

Bacterial Strain. *Rhodococcus* sp. ECRD-1 (ATCC 55309), previously designated Arthrobacter sp. D-1 (ATCC 55309), was isolated by enrichment culture from marine sediments based on its ability to selectively remove sulfur from the sterically hindered organic sulfur compound 4,6-DEDBT[1] using the organic sulfur compound as a sole sulfur source.

Media. Mineral Salts Sulfur-Free Medium (MSSF) containing 1% sodium acetate was prepared as previously described[1] and used for oil desulfurization experiments. Tungsten was added as 50 ug/ml $Na_2WO_4 \cdot 2H_2O$ in VGO cultures. Sulfate control media contained 0.2 g $MgSO_4 \cdot 7H_2O$ per liter.

Luria broth (LB) was used to grow cultures for use as and contained per liter: 10 g Difco tryptone, 5 g Difco yeast extract, 5 g NaCl, adjusted to pH 7.0 with 1.0 ml 1 M NaOH and autoclaved at 121°C, 15 psi.

Oils. Oregon Basin (OB) crude oil, a 450 - 650°F (232 - 343°C) middle distillate cut, represents a diesel range oil fraction. The OB oil used for experiments was artificially weathered under a stream of nitrogen to a constant weight to eliminate inconsistencies caused by evaporative loss of oil during culturing or extraction. Weathering resulted in a weight loss of less than 10% and no change in ppm sulfur content. Vacuum gas oil (VGO), a 650 - 950°F (343 - 496°C) distillate cut, represents a heavy oil fraction. The oil used was also artificially weathered under a stream of nitrogen to a constant weight to eliminate inconsistencies caused by untreated oils was determined by X-ray fluorescence sulfur analysis (XRF) and GC/FID/SCD. The percent sulfur for the Oregon Basin cut sterile control was 2.07% determined by XRF and 1.96 % by GC/FID/SCD. The percent sulfur for the VGO cut sterile control was 2.93% determined by XRF and 2.26% by GC/FID/SCD.

Biodesulfurization Assays. Biodesulfurization were performed as growing cell assays. One ml, approximately 0.84 g, of artificially weathered and heat sterilized oil was treated in one liter of culture. Inocula were prepared from overnight cultures grown from single bacterial colonies in LB at room temperature (23°C) on a VWR Orbital shaker at 200 rpm. Cells were then pelleted in a Sorval centrifuge at 3000 x g in SS34 rotor at 4°C. The pellet was washed three times with one volume of 12 mM phosphate buffer (pH 7.0) previously chilled on ice for 30 min. Cell pellets were resuspended in 1/10 the original culture volume of chilled phosphate buffer and used immediately for inoculation. Flasks were inoculated with 2 ml of the cell suspension per L medium.

Duplicate cultures were incubated with shaking at 200 rpm for 4 days for OB oils. The experiment also included a uninoculated negative control. VGO oils were incubated with shaking at 200 rpm for 5 and 7 days. The five day experiment included a positive control culture, inoculated and containing sulfate. The seven day experiment included a uninoculated negative control. Flasks were pH monitored at one to two day intervals and adjusted to pH 7.0 with 1M phosphoric acid when the pH deviated by more than 1.0 pH unit. All assays were performed in duplicate.

Before extraction, cultures were brought to a pH of 1.0 with 1N HCl. A 0.5 ml aliquot of 1% v/v dodecane in methylene chloride solution was added as an extraction standard. Each flask was then extracted 3X with 100 ml methylene chloride . The methylene chloride extracts were filtered through anhydrous sodium sulfate or calcium sulfate if water was apparent (i.e., a turbid solution was observed). The samples were then reduced to approximately 5 ml volumes under nitrogen. Samples were subsequently filtered through a 0.22 μm hydrophobic filter to remove turbidity (attributed to water condensate) appearing after volume reduction. For every liter of culture extracted, a 0.5 ml aliquot of decane/methylene chloride (0.742 g/100 ml) was added to the filtered extracts as an injection volume standard. The solutions were then concentrated to approximately 1.0 ml.

GC/FID/SCD Analysis. Gas Chromatography was performed on a Perkin-Elmer GC Autosystem (split/splitless injector). Oregon Basin oil was chromatographed on a Supelco SPB-1 column (30m x 0.32mm, 0.25um film thickness). The temperature zones for the GC were as follows: injector and detector temperature 300°C, initial oven temperature 40°C for 1 minute, followed by a 4°C /minute temperature ramp to 300°C for a final 10 minute hold. VGO was chromatographed on a Supelco SPB-1 column (15 m x 0.32mm, 4um film thickness). The temperature zones for the GC were as follows: injector temperature 275°C, detector temperature 325°C, initial oven temperature 50°C for 1 minute, followed by a 5°C /minute temperature ramp to 300°C for a final 20 minute hold. Tandem Perkin-Elmer FID (flame ionization detection) and Sievers Instruments, model 355 SCD (sulfur chemiluminescence detection) detectors were used to determine sulfur concentrations in oil samples based on response factors of model compounds. For oils and standard mixtures, 1 μl of sample was injected in duplicate and results averaged.

Response factors for OB oil and VGO were estimated based on the averaged FID and SCD response factors for a number of model compounds. These compounds were chosen to represent some of the compounds found in the oils. The standards used for calibration of the FID detector were hexane, heptane, decane, dodecane, tetradecane, fluorene, carbazole, DBT sulfone, and 4,6 DEDBT. The sulfur compounds contained in this mixture were used to calibrate the SCD. Averaged response factors for sulfur (ng/area) and for carbon (mg/area) were calculated for the standard mixtures and the sulfur/carbon ratio calculated. This ratio was multiplied by the sulfur/carbon area of the oils to give ppm S. A common baseline was drawn by the computer encompassing all area associated with the oil so that unresolved area characterized by a hump in the baseline was included in subsequent calculations.

The percent carbon loss for treated oils was determined as the difference between the GC/FID area ratio of total carbon (minus standards) to dodecane extraction standard of control and treated samples.

Sulfur K-edge X-ray absorption-edge spectroscopy. Sulfur K-edge X-ray absorption-edge spectroscopy was used to determine the effect of biodesulfurization on the remaining sulfur content of treated oils. This technique allows for the evaluation of the chemical state of sulfur

Stanford Synchrotron Radiation Laboratory. Reference compounds were run as powder films using electron yield detection, while oil samples were run as liquids using fluorescence detection[2]. Spectra of the oils were fitted to linear combinations of the spectra of reference compounds using least-squares non-linear optimization[5]. In general there is a trend toward higher absorbance energies in the order sulfidic, thiophenic, oxidized species (Fig. 1).

The procedure employed to fit the oil spectra employed a fairly broad range of model organic sulfur compounds as reference compounds to represent the majority of sulfur types expected in treated and untreated oils. Fig. 1 shows the sulfur K-edge X-ray absorption spectra of these compounds. Although the individual spectra are quite distinct, different fit results were obtained with good fits using different constraints on the fit calculations. Consequently, the fits obtained using this method are used as indicators of the likely distribution of S compounds and are not considered highly accurate for specific species.

RESULTS AND DISCUSSION

Oregon Basin Oil. The desulfurization of OB oil ECRD-1 cultures grown for four days resulted in a large reduction in sulfur containing compounds. The GC/SCD chromatograms for a sterile control and ECRD-1 desulfurized oil show that sulfur components across the entire boiling range of the oil were effected (Fig. 2). The total sulfur removed was 35 (± 30% RSD). Examination of the GC/FID profile (Fig. 3) revealed a reduction in the resolved peaks (n-alkanes) in the treated cultures. Loss of the straight chain hydrocarbons is attributed to degradation by ECRD-1 which is know to degrade these compounds. The loss of carbon in these samples was averaged 26% (± 7% RSD). Taking into account the consumption of carbon, the reduction of sulfur the maximum sulfur removed is calculated to be 58%.

Analysis of the oils by sulfur K-edge X-ray absorption-edge spectroscopy was performed to determine the effect of treatment on the remaining sulfur in the oil. The sulfur spectra of the treated, sterile control and original oils are shown in Fig. 4. The spectra of the weathered OB oil and the sterile control are virtually identical indicating no abiological effects occurred due to the culture conditions used. In contrast, the spectrum of the treated oil is markedly different, showing an increase in absorbance at approximately 2473 and 2477 eV. A shift in absorbance toward higher energies (eV) is characteristic of more oxidized sulfur species, (see Fig. 1), indicating that a significant proportion of the sulfur compounds remaining in the oil contain sulfur in an oxidized form.

Table 1 shows the best fit composition of sulfur forms in the sterile and treated oil. A small feature near 2480 eV was observed for both samples and is attributed to sulfate contaminating the graphite used for sample preparation.

Vacuum Gas Oil. Cultures of ECRD-1 grown on VGO as the sole sulfur source for five and seven days showed growth and sulfur reduction. The inoculated positive control containing sulfate also showed growth but no sulfur removal. The negative controls showed no growth. After incubation the concentration of sulfur in the VGO in the positive control and the sterile control cultures were equivalent, both approximately 2.3%. The lack of desulfurization in the presence of sulfate is consistent with previous observations that sulfate represses the expression of desulfurization activity in ECRD-1 (Table 2). The 7 day ECRD-1 cultures showed a 16% sulfur reduction as compared to only 7% for the five day cultures. The difference in desulfurization levels demonstrates that additional desulfurization of VGO is achieved with extended incubation periods. However, in comparison to OB oil, VGO appears relatively more resistant to desulfurization by ECRD-1.

Analysis of the treated VGO samples by X-ray spectroscopy showed an increase in absorbance at approximately 2477 eV in all treated samples (Fig. 5). This increase in absorbance is consistent with the production of oxidized sulfur compounds, albeit considerably less than that observed with the OB oil. No changes in the spectrum were observed for the culture amended with sulfate (data not shown) corroborating the GC results and demonstrating that no detectable desulfurization activity occurred. Due to the relatively small change in the spectrum for the treated VGO the changes in oxidized species could not be meaningfully fit with model compounds.

CONCLUSIONS

This study has shown that ECRD-1 can desulfurize complex sulfur found in a middle distillate cut and a vacuum gas oil. Consumption of hydrocarbons could impact negatively on process economics. However, there is no indication that hydrocarbon degradation is tied to desulfurization. Hydrocarbon degradation activity could be eliminated through genetic microbial treatment, complete desulfurization was not achieved. However, a significant percentage of the remaining sulfur is oxidized by the treatment indicating the potential for further desulfurization. Additionally, the ability to remove sterically hindered compounds not affected by HDS could prove valuable.

[1] Kabe, T., Ishihara, A. and Tajima, H. 1992. Ind. Eng. Chem. Res. 31:1577-1580.

[2] Grossman, M.J., in "Hydrotreating technology for pollution control: Catalysts, Catalysis, and Processes" (M. L. Occelli and R. Chianelli, eds.) Marcel Dekker, New York, pp. 345-359, 1996.

[3] Gray, K.A., Pogrebinsky, O.S., Mrachko, G.T., Xi, Lei, Monticello, D.J., and Squires, C.H. 1996. Nature Biotechnology 14:17051709.

[4] Lee, M.K., Senius, J.D., and Grossman, M.J. Appl. Environ. Microbiol. 61:4362-4366 (1995).

[5] George, G.N., Gorbaty, M.L., Kelemen, S.R., and Sansone, M. Energy & Fuels. 5: 93-97 (1991).

TABLE 1

Composition Of Sulfur Species In Treated Oregon Basin Crude Oil

Analysis by Sulfur K-edge X-ray Absorption-edge Spectroscopy

Model compound	**Relative % total S as this species**	
	Sterile control (2.0% S)	**ECRD-1 treated (1.1% S)**
2,5 Dimethylthiophene	51	24
Benzyl sulfide	47	18
Dimethylsulfoxide	-	32
Dibenzothiophene sulfone	-	24
Sulfate	2	2

TABLE 2

Sulfur Concentration in VGO Cultures

Analysis by GC/FID/SCD

Sample	**% Sulfur(±%RSD)**	**% S Removed**
5 day culture Positive Control	2.27±4%	-
5 day culture ECRD-1 Treated	2.11±0.1%	7.0
7 day culture Negative Control	2.25±1%	-
7 day culture ECRD-1 Treated	1.91±3%	15.5

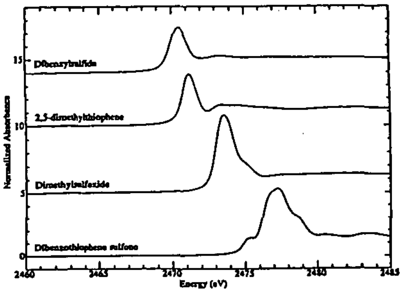

Figure 1. Sulfur K-edge X-ray Absorption Spectra of reference compounds.

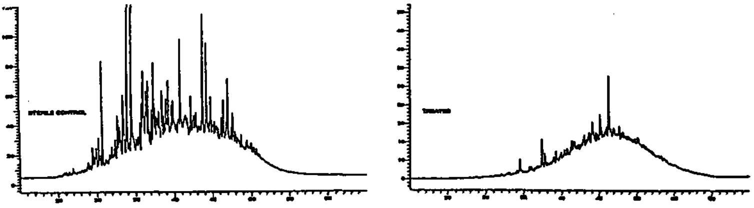

Figure 2. GC/SCD of sterile control and treated Oregon Basin oil.

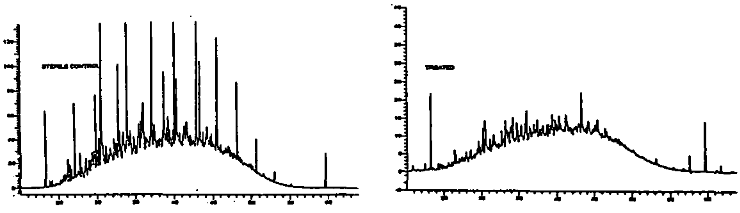

Figure 3. GC/FID of sterile control and treated Oregon Basin oil.

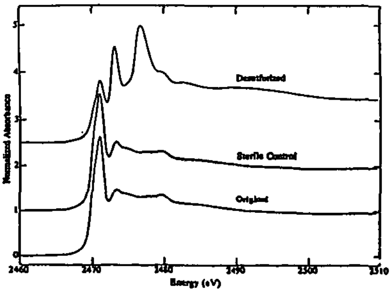

Figure 4. Sulfur K-edge X-ray absorption-edge spectra of original, sterile control and treated Oregon Basin Oil.

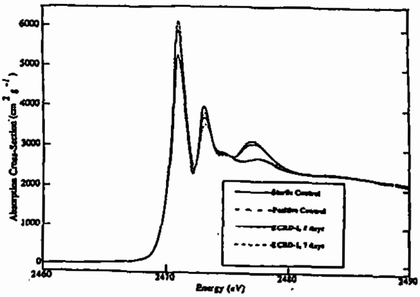

Figure 5. Sulfur K-edge X-ray Absorption spectra of Vacuum Gas Oil sterile control, positive control, and five and seven day ECRD-1 treatment

AQUATHERMOLYSIS OF ORGANIC COMPOUNDS IN THE PRESENCE OF HYDROGEN SULFIDE AND SULFATE

Gerhard G. Hoffmann and Thorsten David
German Petroleum Institute,
Walther-Nernst-Str. 7
Clausthal-Zellerfeld, G-38678
Germany

Keywords: Thermochemical reduction of sulfate, formation and decomposition of organic sulfur compounds caused by aquathermolysis, hydrogen sulfide

ABSTRACT

Thermal recovery processes are well established enhanced oil recovery techniques. At thermal recovery temperatures in the reservoir can reach 320°C. Under these specific conditions chemical reactions of the reservoir sulfate and hydrogen sulfide easily occur. The conditions at thermal recovery processes allow the thermochemical reduction of sulfate with hydrogen sulfide. In the presence of organic compounds these redox reactions lead to the formation of a variety of inorganic, as well as organic compounds in different oxidation states, including elemental sulfur.

Object of these investigations was to study the thermal induced reactions of organic compounds in the presence of hydrogen sulfide and aqueous solutions of alkali metal- as well as alkaline-earth metal sulfates. *n*-Octane, *n*-hexadecane, and 2-octanone selected as representative organic compounds were allowed to react with the inorganic components in autoclaves at temperatures up to 320°C under variation of the reaction time from 6 hrs. to 500 hrs. The amount of reduced sulfate was estimated by quantitative determination of the residual sulfate in the aqueous layer after each reaction. The organic reaction products were identified by gas chromatography and GC/MS.

INTRODUCTION

Thermal recovery processes are well established enhanced oil recovery techniques and widely applied for recovering heavy oil, heavy oil sands, and shale oil. At thermal recovery temperatures in the reservoirs can reach 320°C. Under these specific conditions decomposition reactions of organic sulfur compounds, which are already present in the crude oil, easily proceed. In addition, reactions of the reservoir sulfate and hydrogen sulfide (H_2S) take place.[1] The conditions, occurring at thermal recovery processes allow the thermochemical reduction of sulfate with H_2S. In the presence of organic compounds these redox reactions lead to the formation of a variety of inorganic and organic sulfur compounds in different oxidation states, including elemental sulfur (or its different radicals). The reduction is autocatalytic with respect to H_2S. Increasing concentrations of elemental sulfur promptly cause its reaction with organic compounds of the crude oil, which consequently leads to the formation of organic sulfur compounds and H_2S.[2-4] Thus, it is obvious that both, consumption and formation of H_2S compete with each other. The net reaction can be given with eq.1:

$$3\,SO_4^{2-} + 4\,RCH_3 \xrightarrow[p,T]{H_2S\ \text{(low conc.)}} 3\,S^{2-} + 4\,CO_2 + 4\,RH + 4\,H_2O \qquad (1)$$

From eq.1 it becomes evident that only a catalytic amount of H_2S is necessary to initiate the thermochemical reduction of sulfate. It is known that H_2S is very often present in the reservoir. It can be formed under fairly mild conditions by microbial reduction of sulfate.[5] Furthermore, H_2S can be generated by the hydrolysis of inorganic compounds like pyrite, pyrotite, and elemental sulfur.

The pH-value plays an important part in the thermal reduction, since it has a significant influence on both, the formation and the reactivity of the inorganic sulfur compounds.[6] The pH-value is strongly controlled by the metal cation of the used sulfate solutions.

The net reaction (eq.1) reveals that sour gas (CO_2 + H_2S) is formed. These compounds lead to severe problems at the recovery of crude oil, as well as at its manufacturing. Furthermore, the quality of the crude oil will be affected.[7] The changes in the composition of the hydrocarbons and heterocompounds due to aquathermolysis in the absence of sulfate and H_2S are well described in literature.[8] However, only few details concerning the very complex thermochemical reduction of sulfate in the presence of H_2S and hydrocarbons are available.[1,4,9] On the other hand, sulfate as an oxidizing agent for the synthesis of aromatic carboxylic acids, such as phthalic acids, has been earlier investigated.[10] Moreover, formation of H_2S from the reduction of gypsum has been subject of investigations.[11]

Scope of our research is to better understand the above mentioned reactions and their influences on each other with respect to the different reaction products, which are formed, depending on the reaction time, the reaction temperature, and the employed educts. The reactions were carried out in the presence of aqueous solutions of metal sulfates; moreover, in every reaction only one defined aliphatic hydrocarbon was used serving as a model compound; this was necessary to understand the complex reactions taking place.

EXPERIMENTAL

The experiments were conducted using glass cylinders, which were installed in stainless steel autoclaves. In the case of the reactions with model compounds an aqueous solution of 20 mmol of the corresponding sulfate was used, whereas in the case of crude oil a solution containing 60 mmol of sulfate was employed. Autoclaves of 90 ml and 190 ml content, respectively, were used. Reactions with $CaSO_4$ were carried out in the presence of NaH_2PO_4 (employed in the same molar ratio as $CaSO_4$). The starting pressure at ambient temperature was the steel cylinder pressure of H_2S. The reactions were performed at temperatures between 200°C and 320°C, respectively (Tab.1). After given time intervals the autoclave was cooled to room temperature (RT). The organic layer was separated from the aqueous layer. The decrease of sulfate was determined by quantitative titration, according to the method of SCHÖNINGER.[12] The pH-value of the aqueous phase was determined after the reaction at RT with a pH-meter equipped with a glass electrode. The organic layer was investigated by gas chromatography (GC) and the coupling of gas chromatography with mass spectrometry (GC/MS). GC was performed using a Hewlett Packard Model 5890 Series II instrument, equipped with a Hewlett Packard Flame Ionization Detector (FID) and a Hewlett Packard Flame Photometric Detector (FPD). The organic layer was analyzed by GC/MS using a Hewlett Packard 5890 A Series II GC coupled with a Hewlett Packard 5970 B Series MS Detector, using the same GC program as for the separation. Mass spectra were obtained by electron ionization at 70 eV. The injector system of the GC/MS was a temperature programmable Injector System from Gerstel. The analytical conditions are given in Tab.2. Reactions in the presence of crude oil were worked up in the same manner. However, the recovered crude oil was extracted by liquid sulfur dioxide in order to enrich organic sulfur compounds.[13] The enriched crude oil fractions were investigated by GC (FID, FPD).

RESULTS AND DISCUSSION

In Tab.1 the parameters of the performed reactions are summarized. To rule out artifacts and to make sure that sulfate does not react with the autoclave material, aqueous solutions of the investigated compounds were treated at elevated temperatures under helium or nitrogen pressure in stainless steel autoclaves without H_2S (Tab.1: 1-3). It could be proved that neither reduction of sulfate nor reaction of the organic compound takes place. Sulfate was recovered quantitatively, the organic compound unchanged.

In Fig.1 the amount of reduced sulfate of the reaction of different metal sulfates in the presence of *n*-octane (Fig.1; according to Tab.1: 4, 6-9, 13-17, and 23, 24) is plotted *vs.* the temperature. In these experiments the reaction time was 72 hrs. It easily can be seen that the reduction rate is strongly controlled by both, reaction temperature and metal cation of the employed sulfate. To attain the same rate of reduction reactions of $MgSO_4$ require higher temperatures than those of $CaSO_4/NaH_2PO_4$. Generally, it can be seen from Fig.1 that the rate of reduction strongly increases at temperatures higher than 250°C. The strong influence of the employed cation becomes evident by comparing the reactions of Na_2SO_4 to those of $Al_2(SO_4)_3$. In the case of sodium sulfate reduction is not as pronounced; after a reaction time of 500 hrs. only about 10% of Na_2SO_4 are reduced at 320°C (Tab.1: 4, 5). In contrast, the reduction in the presence of aluminum ions already starts at 100°C and is almost quantitative at 200°C (Tab.1: 22-24).

In Fig.2 the amount of reduced sulfate of the reactions in the presence of *n*-octane is plotted *vs.* the reaction time (Fig.2; according to Tab.1: 4, 9-12, 17-21, 24, 25). In this case, the reaction temperature was 320°C. It can be seen from the plots of $MgSO_4$ and $CaSO_4/NaH_2PO_4$ that the rate of reduction increases with increasing reaction time. It is reaching 97% within 144 hrs. for $MgSO_4$; whereas for $CaSO_4/NaH_2PO_4$ only 88% of the sulfate is reduced within the same reaction time. This indicates that the reaction is controlled by the cation, too; this feature becomes very evident for the reactions of $Al_2(SO_4)_3$ and Na_2SO_4. In the presence of aluminum cations the reduction of sulfate proceeds very fast (see for example Tab.1: 25), whereas the reactivity is very low in the presence of sodium cations (Tab.1: 4, 5). An explanation can be given with the pH-value.

By comparison of the experiments 9, 26, and 27 (Tab.1) it becomes evident that the rate of reduction of sulfate does not only depend on the reaction time and the reaction temperature; it is also influenced by the organic compound which is involved in the reaction. In the presence of *n*-octane 66% of the employed $MgSO_4$ is reduced; whereas in the presence of *n*-hexadecane or 2-octanone the rate of reduction increases significantly to approximately 80%.

Experiments 28 to 30 (Tab.1) confirm that in the presence of crude oil the rate of reduction of sulfate lies in a similar order of magnitude.

Investigations of the organic layer reveal that preferably organic sulfur compounds are formed. A strong influence of the employed metal salt on the distribution of the different newly formed organic compounds could be shown. Moreover, the reaction conditions, e.g. reaction temperature, as well as time are of main importance.

In Figures 3 to 6 an example of the identification steps of the organic compounds is given. Fig.3 shows the FID chromatogram of the organic layer of reaction 9 (Tab.1); in Fig.4 the corresponding FPD chromatogram is shown. The two chromatograms reveal that a lot of organic compounds are newly formed. In addition, the FPD chromatogram indicates that many organic sulfur compounds are generated. Most of these compounds can be assigned to mono-, as well as dialkylated thiophenes by GC/MS. Moreover, a compound containing two sulfur atoms is observed; 2,2′-bithiophene could be made plausible. The ion chromatogram of the ion mass 111 is shown in Fig.5. It can be seen that a great number of different compounds is formed, the fragmentation of which leads to ion mass 111. Mass 111 is e.g. specific for dialkylated thiophenes containing at least one methylgroup as ring substituent. By comparing the single mass spectra of the total ion current to literature data a specification of 2,5- and 2-alkylsubstituted thiophenes becomes possible. Fig.6 shows one specific example for a typical mass spectrum; it could be shown that 2-ethyl-5-methylthiophene corresponds to this particular spectrum.

The tentative overall reaction is shown in Scheme 1. It can be assumed that at the reduction of sulfate sulfur radicals are generated; these radicals subsequently react with *n*-alkanes as shown in Scheme 1a and 1b, respectively:

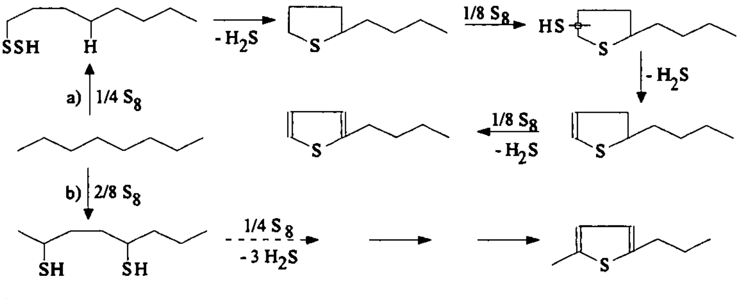

Scheme 1.

A series of insertion reactions of sulfur into carbon hydrogen bonds of the alkane, followed by a condensation reaction in the 2,5-position, as well as in the 1,4-position of the alkane lead to ring closure. Thus, 2,5-substituted and 2-substituted tetrahydrothiophene derivatives are formed. Under elimination of H_2S cyclisation may proceed as shown in Scheme 1a or 1b. The thus formed tetrahydrothiophene derivatives react in a cascade of sulfur insertion, as well as H_2S elimination steps to form the corresponding thiophenes.

In addition, other than sulfur containing compounds are formed, too. Some of these could be identified by GC/MS as ketones, e.g. 2-, 3-, and 4-octanone and aromatic compounds, like benzene and ethylbenzene.

Some of the reaction products of experiments 9, 26, and 27 (Tab.1) are identified following published sources [14] and are summarized in Tab.3. The formation of typical classes of organic compounds, such as substituted thiophenes, ketones and aromatic compounds is clearly indicated.

Furthermore, the GC- and GC/MS-spectra reveal a successive degradation of the alkyl substituents with increasing reaction time and increasing reaction temperature; a tentative overall reaction is already given elsewhere.[4]

CONCLUSIONS

In autoclave experiments the thermal reduction of sulfate in the presence of small amounts of H_2S and aliphatic organic compounds leads to the formation of a great number of organic compounds; many of these contain sulfur as a heteroatom. Alkyl substituted thiophenes are formed in substantial amounts. Evidence is given that the degradation of the alkyl substituents proceeds to form carbon dioxide.

The results of these investigations demonstrate that the conditions at thermal recovery of crude oil are responsible for thermochemical reduction of sulfate. This reaction is catalyzed by H_2S. Inorganic sulfur compounds in different oxidation states, such as elemental sulfur are formed and react with hydrocarbons of the reservoir. These reactions lead to the formation of typical types of organic compounds, such as alkyl substituted thiophenes, ketones, and aromatic compounds, respectively. Thus, at thermal recovery a rapid alteration of crude oil becomes possible and subsequently has a main impact on the quality of the recovered crude oil, as well as the quality of the reservoir.

ACKNOWLEDGMENTS

We thank the Fond der Chemischen Industrie for financial support. T.D. thanks the German Petroleum Institute for a scholarship within the BMBF program of HSP II.

REFERENCES

[1] a) Orr, W.L., Am. Ass. Pet. Geol. Bull. **58** (1974) 2295; b) Orr, W.L., Adv. Org. Geochem. **1977**, 571; c) Anisimov, L.A., Geochem. Internat., **15** (1978) 63; d) Aizenshtat, Z., 205th ACS National Meeting, Book of Abstracts, Div. Geochem. p. 76, Denver, 1993; e) Goldstein, T.P., and Aizenshtat, Z., J. Therm. Anal. **42** (1994) 241.

[2] Pryor, W.A., Ed. "Mechanisms of Sulfur Reactions", McGraw-Hill, New York, (1962).

[3] E.g.: Fromm, E., and Acker, O., Ber. Dtsch. Chem. Ges. **36** (1903) 538.

[4] Steinfatt, I., and Hoffmann, G.G., Phosphorus, Sulfur, and Silicon, **74** (1993) 431.

[5] Fedorak, P.M., in "Geochemistry of Sulfur in Fossil Fuels", Orr, W.L., and White, C.M., Eds., ACS Symposium Series 429, Washington, DC, p. 93 (1990).

[6] Hoffmann, G.G., Steinfatt, I., David, T., and Strohschein, A., DGMK Tagungsbericht 9501, Hamburg 1995, p 281.

[7] Orr, W.L., and Sinninghe Damsté, J.S., in "Geochemistry of Sulfur in Fossil Fuels", Orr, W.L., and White, C.M., Eds., ACS Symposium Series 429, Washington, DC, p. 2 (1990).

[8] E.g.: a) Siskin, M., Brons, G., Katritzky, A.R., and Balasubramanian, M., Energy & Fuels **4** (1990) 475; b) Siskin, M., Brons, G., Katritzky, A.R., and Murugan, R., Energy & Fuels **4** (1990) 482; c) Siskin, M., Glen, B., and Vaughn, S.N., Energy & Fuels **4** (1990) 488; d) Katritzky, A.R., Lapucha, A.R., Murugan, R., and Luxem, F.J., Energy & Fuels **4** (1990) 493; e) Katritzky, A.R., Balasubramanian, M., and Siskin, M., Energy & Fuels **4** (1990) 499; f) Katritzky, A.R., Lapucha, A.R., and Siskin, M., Energy & Fuels **4** (1990) 506; g) Katritzky, A.R., Lapucha, A.R., and Siskin, M., Energy & Fuels **4** (1990) 510; h) Katritzky, A.R., Luxem, F.J., and Siskin, M., Energy & Fuels **4** (1990) 514; i) Katritzky, A.R., Luxem, F.J., and Siskin, M., Energy & Fuels **4** (1990) 518; j) Katritzky, A.R., Luxem, F.J., and Siskin, M., Energy & Fuels **4** (1990) 525; k) Katritzky, A.R., Murugan, R., and Siskin, M., Energy & Fuels **4** (1990) 531; l) Katritzky, A.R., Murugan, R., and Siskin, M., Energy & Fuels **4** (1990) 538; m) Katritzky, A.R., Balasubramanian, M., and Siskin, M., Energy & Fuels **4** (1990) 543; n) Katritzky, A.R., Murugan, R., Balasubramanian, M., and Siskin, M., Energy & Fuels **4** (1990) 547; o) Katritzky, A.R., Lapucha, A.R., and Siskin, M., Energy & Fuels **4** (1990) 555; p) Katritzky, A.R., Lapucha, A.R., Greenhill, J.V., and Siskin, M., Energy & Fuels **4** (1990) 562; q) Katritzky, A.R., Lapucha, A.R., Luxem, F.J., Greenhill, J.V., and Siskin, M., Energy & Fuels **4** (1990) 572; r) Katritzky, A.R., Murugan, R., and Siskin, M., Energy & Fuels **4** (1990) 577; s) Katritzky, A.R., Allin, S.M., and Siskin, M., Acc. Chem. Res. **29** (1996) 399.

[9] a) Oae, S., Ed. "Organic Chemistry of Sulfur", Plenum Press, New York, (1977) p. 360; b) Oae, S., and Togo, H., Tetrahedron Lett., **23** (1982) 4701; c) Oae, S., and Togo, H., Kagaku (Chemistry) **38** (1983) 506; d) Oae, S., in "Review of Heteroatom Chemistry", Vol. 1, Oae. S., Ed., NYU, Tokyo, 1987, p.14; e) Hoffmann, G.G. and Steinfatt, I., Preprints, Div. of Petrol. Chem., ACS, **38**,1 (1993) 181; f) Hoffmann, G.G., Steinfatt, I., and Strohschein, A., in "Recent Advances in Oilfield Chemistry", Ogden, P.H., Ed., Special

Publication No. 159, Royal Society of Chemistry, Cambridge 1994, p. 189; g) Hoffmann, G.G., Steinfatt, I., and Strohschein, A., Proceedings SPE 29016, SPE International Symposium on Oilfield Chemistry, San Antonio, USA, Februar 1995, 745; h) Hoffmann, G.G., Steinfatt, I., and Strohschein, A., Proceedings, Vol. 1, 6th UNITAR International Conference on Heavy Crude and Tar Sands, Houston, USA, Februar 1995, p.317.

[10] a) Toland, W.G., US-Pat. 2722546, (Nov. 1, 1955) [Chem. Abstr. **57**, 11111i (1955)]; b) Toland, W.G., J. Am. Chem. Soc., **82** (1960) 1911.

[11] Biswas, S.C., Sabhurwal, V.P., and Dutta, B.K., Fert. Tech. **13** (1976) 255; loc.cit.

[12] Schöninger, W., Mikrochim. Acta, **1956**, 869.

[13] Hoffmann, G.G., Steinfatt, I., and Bode, K., Erdöl, Erdgas Kohle, **2** (1996) 70.

[14] Wiley Database, HP 59943B; a merged Wiley/NBS database.

Table 1. Parameters of the Reactions

No.	sulfate [20 mmol]	organic compounds [5 ml]	pressure [bar]	temperature [°C]	time [h]	reduction [%]	pH-value (after the reaction)
1	$(NH_4)_2SO_4$	--	162	350	46	none	7.0
2	$MgSO_4$	octane	--	320	72	none	7.0
3	$CaSO_4$	toluol	--	290	288	none	5.0
4	Na_2SO_4	octane	126	320	72	3	7.5
5	Na_2SO_4	octane	145	320	500	11	7.5
6	$MgSO_4$	octane	74	250	72	4	6.3
7	$MgSO_4$	octane	90	270	72	6	6.1
8	$MgSO_4$	octane	124	300	72	41	6.7
9	$MgSO_4$	octane	156	320	72	66	6.8
10	$MgSO_4$	octane	--	320	24	27	6.8
11	$MgSO_4$	octane	--	320	48	37	6.8
12	$MgSO_4$	octane	--	320	144	97	6.5
13	$CaSO_4$	octane	39	200	72	none	2.9
14	$CaSO_4$	octane	--	250	72	22	3.8
15	$CaSO_4$	octane	--	270	72	46	3.6
16	$CaSO_4$	octane	--	290	72	76	5.5
17	$CaSO_4$	octane	178	320	72	83	6.2
18	$CaSO_4$	octane	159	320	9	54	4.6
19	$CaSO_4$	octane	--	320	36	77	6.1
20	$CaSO_4$	octane	188	320	144	88	6.6
21	$CaSO_4$	octane	174	320	288	89	7.3
22	$Al_2(SO_4)_3$	octane	23	100	72	10	3.4
23	$Al_2(SO_4)_3$	octane	44	200	72	96	3.5
24	$Al_2(SO_4)_3$	octane	160	320	72	99	4.1
25	$Al_2(SO_4)_3$	octane	--	320	6	98	3.6
26	$MgSO_4$	hexadecane	--	320	72	83	6.4
27	$MgSO_4$	2-octanone	--	320	72	79	6.6
28	$MgSO_4$	crude oil*	101	290	72	34	7.1
29	$CaSO_4$	crude oil*	--	270	72	31	--
30	$CaSO_4$	crude oil*	--	320	72	83	6.0

*: 30 g crude oil; 60 mmol of the corresponding sulfate

Table 2a. Analytical Data of GC

Injector temperature	(°C)	280
FID temperature	(°C)	330
FPD temperature	(°C)	250
GC column	DB 5, 30 m x 0.25 mm, film thickness 0.25 µm	
Carrier gas	Helium	
Carrier gas flow	(ml/min.)	1
Sample size	(µl)	1
Split		1:35
Initial oven temp.	(°C)	35
Initial hold	(min.)	5
Program rate	(°C/min.)	5
Final oven temp.	(°C)	310
Final hold	(min.)	10

Table 2b. Analytical Data of GC/MS

Initial Injector temp.	(°C)	40
Program rate	(°C/s)	12
Final Injector temp.	(°C)	300
Final hold	(min.)	10
Purge time	(min.)	5
GC/MS column	DB 1, 30 m x 0.25 mm, film thickness 0.25 µm	
Carrier gas	Helium	
Carrier gas flow	(ml/min.)	1
Sample size	(µl)	0.15
Initial oven temp.	(°C)	35
Initial hold	(min.)	5
Program rate	(°C/min.)	5
Final oven temp.	(°C)	310
Final hold	(min.)	10

Table 3. Products of Reactions at 320°C for 72 hrs. (Tab.1: 9, 26, 27)

Products from *n*-octane	Products from *n*-hexadecane	Products from 2-octanone
1. 2-Methyltetrahydro-t.	1. 2-Methylthiophene	1. Heptane
2. Ethylbenzene	2. 2-Methyltetrahydro-t.	2. 2-Methylthiophene
3. 2-Ethylthiophene	3. 2-Ethylthiophene	3. 1-Ethyl-2-methyl-cyclopentane
4. 2,5-Dimethylthiophene	4. 2,5-Dimethylthiophene	4. Octene
5. o-Xylene	5. 2-Propylthiophene	5. Ethylbenzene
6. 2-Propylthiophene	6. 2-Ethyl-5-methyl-t.	6. 2-Ethylthiophene
7. 2-Ethyl-5-methyl-t.	7. 2-Methyl-propyl-t.	7. 2,5-Dimethylthiophene
8. 4-Octanone	8. Benzo[b]thiophene	8. o-Xylene
9. 3-Octanone	9. 3-Hexadecanone	9. 1-Ethyl-5-Methyl-t.
10. 2-Octanone	10. 2-Heptyl-5-pentyl-t.	10. 2,5-Diethylthiophene
11. 2-Methyl-5-propyl-t.	11. 2-Butyl-5-octyl-t.	11. 2-Methyl-5-propyl-t.
12. 2-Butylthiophene	12. 2-Nonyl-5-propyl-t.	12. 2-Butyltetrahydro-t.
13. 2,2-Bithiophene	13. 2-Decyl-5-ethyl-t.	13. Benzo[b]thiophen
	14. 2-Methyl-5-undecyl-t.	
	15. 2-Dodecylthiophene	

t.: abbreviation for thiophene

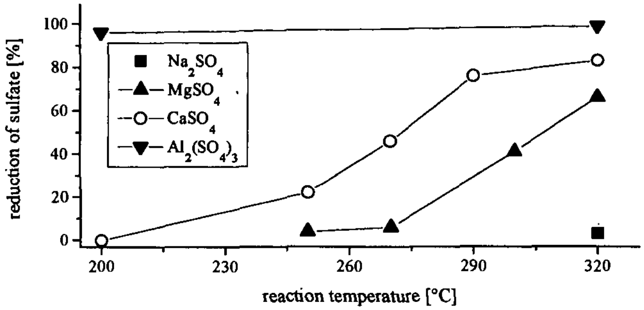

Figure 1. Influence of Temperature and Cation on the Reduction of Sulfate (t = 72 hrs.)

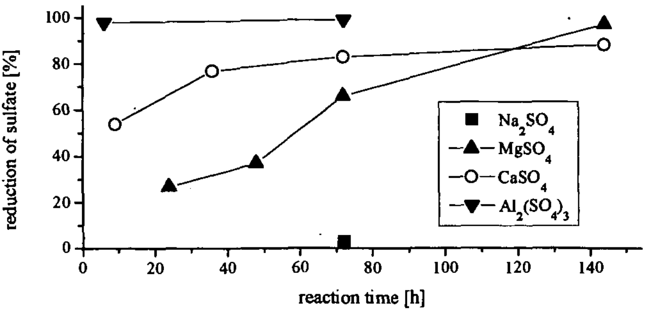

Figure 2. Influence of Reaction Time and Cation on the Reduction of Sulfate (T = 320°C)

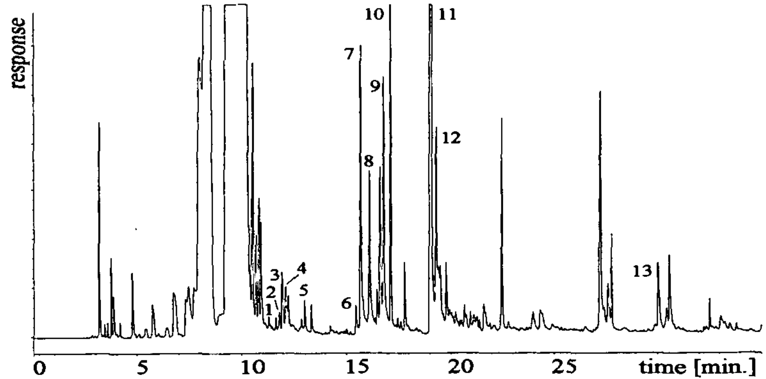

Figure 3. FID Chromatogram of the Reaction of $MgSO_4/H_2S$/Octane at 320°C (Tab.1: 9)

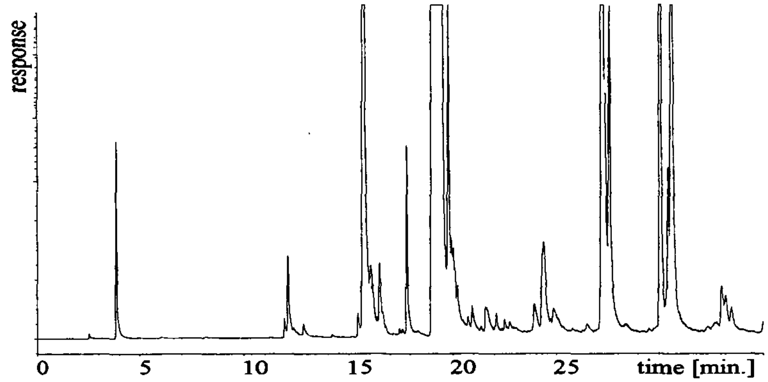

Figure 4. FPD Chromatogram of the Reaction of $MgSO_4/H_2S$/Octane at 320°C (Tab.1: 9)

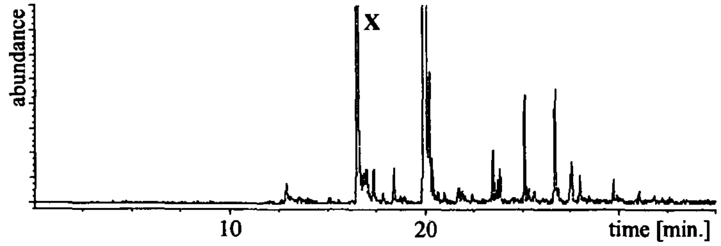

Figure 5. Ion Chromatogram of Ion 111.00 amu.

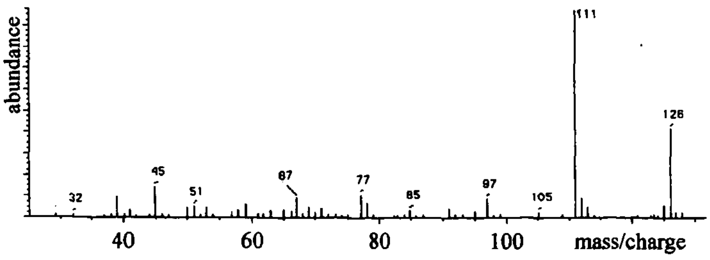

Figure 6. One (Peak Maximum) Scan of Compound **X** in Fig. 5

HYDROGEN FROM BIOMASS VIA FAST PYROLYSIS AND CATALYTIC STEAM REFORMING

D. Wang, S. Czernik, D. Montané[†], M. Mann, and E. Chornet[‡]
National Renewable Energy Laboratory (NREL)
Golden, CO 80401-3303

Keywords: Hydrogen production, biomass, catalytic steam reforming

ABSTRACT

Fast pyrolysis transforms biomass into "bio-oil", with yields as high as 75-80 wt.% of the anhydrous biomass. This bio-oil is a mixture of aldehydes, alcohols, acids, oligomers from the constitutive carbohydrates and lignin, and some water from the dehydration reactions. Tests performed using a microreactor interfaced with a molecular beam mass spectrometer and a bench-scale, fixed bed reactor have demonstrated near stoichiometric hydrogen yields from steam reforming of the bio-oil aqueous fraction obtained after precipitation and separation of the lignin-derived oxyaromatics. Reforming of the aqueous fraction required proper dispersion of the liquid to avoid vapor-phase carbonization of the feed in the inlet to the reactor. A spraying nozzle injector has been designed and successfully tested. We will present and discuss the process developed for the pyrolysis and reforming operations and some preliminary product cost estimates. The economics of the process is favored when the separated lignin-derived oxyaromatics are converted to valuable co-products and the aqueous fraction of the bio-oil is used for hydrogen production.

INTRODUCTION

Although renewable lignocellulosic biomass has been considered as a potential feedstock for gasification to produce syngas, the economics of current processes favor the use of hydrocarbons (natural gas, C_2-C_5, and naphtha) and inexpensive coal. An alternative approach to the production of H_2 from biomass is fast pyrolysis of biomass to generate a liquid product (also known as bio-oil) and catalytic steam reforming of the oil or its fractions. This latter approach has the potential to be cost competitive with the current commercial processes for hydrogen production. The yield of bio-oil can be as high as 75-80 wt.% of the anhydrous biomass.

Bio-oil is a mixture of aldehydes, alcohols, acids, oligomers from the constitutive carbohydrates and lignin, and some water from the dehydration reactions. The overall steam reforming reaction of bio-oil (or any oxygenate with a chemical formula of $C_nH_mO_k$), is given by:

$$C_n H_m O_k + (2n-k) H_2O = n CO_2 + (2n + m/2-k) H_2 \qquad (1)$$

The stoichiometric yield of hydrogen is 2+m/2n-k/n moles per mole of carbon in the feed, and k/n is usually in the fractions for the aromatic phenolics from lignin, while k/n is close to 1 for most carbohydrate-derived products such as sugars. In contrast to producer gas, *bio-oil* is easily transportable. Thus, the two key process steps, pyrolysis and reforming, can be carried out independently at different locations. This allows to minimize the costs of feedstock, transportation, and product (H_2) distribution. In this paper, we describe results on catalytic steam reforming of oxygenates. Tests performed using a microreactor interfaced with a molecular beam mass spectrometer and a bench-scale, fixed bed reactor have demonstrated near stoichiometric hydrogen yields from the bio-oil aqueous fraction obtained after precipitation and separation of the lignin-derived oxyaromatics. We will also present results of preliminary economic analysis on this process, which also produces a valuable co-product (lignin-derived oxyaromatics).

EXPERIMENTAL

Tests were carried out in two systems: a microreactor coupled to a molecular-beam mass spectrometer (MBMS) and a bench-scale fixed bed unit. Both systems have been described in detail in our previous work.[1,2] The microreactor was housed in a tubular furnace with four independently controlled temperature zones. The dual bed configuration of this reactor enabled us to study either the differences between thermolysis and catalysis or to compare the performances of two catalysts under the same temperature conditions. Gaseous products at the exit of the microreactor are sampled in real-time through a supersonic, free-jet expansion nozzle.

[†] On leave from Universitat Rovira i Virgili. Departament d'Enginyeria Química, Autovia de Salou S/N. Tarragona, 43006 Spain.

[‡] Also affiliated with Université de Sherbrooke, Sherbrooke, Quebec, Canada, J1K-2R1

This expansion cools the reaction products and forms a molecular beam that is ionized and analyzed by a quadrupole mass spectrometer.

The bench-scale reactor is a stainless steel tube (1.65 cm id x 42.6 cm length) housed in a tubular furnace equipped with three independently controlled heating zones. The reactor was packed with about 100 g of a commercial, nickel-based catalyst (particle size: 2.4-4.0 mm). Most studies were carried out using the UCI G-90C catalyst and a dual-catalyst bed of 46-1 and 46-4 from ICI Katalco. Steam was generated in a boiler and superheated. The organic feed from a diaphragm metering pump was sprayed using N_2 and mixed with superheated steam in a triple nozzle injector. Products exiting the reactor were passed through a condenser. The condensate (just water in most cases) weight, volume and compositions of the permanent gas output were recorded periodically. An on-line IR gas analyzer was used to monitor CO/CO_2 concentrations and a MTI-QUAD GC was used to measure concentrations of H_2, N_2, O_2, CO, CO_2, CH_4, and other light hydrocarbons. The reformer system was interfaced with a computer to monitor temperatures and other important parameters. All materials used were obtained from commercial suppliers, except the bio-oil and its aqueous fraction that were prepared at NREL.

RESULTS AND DISCUSSION

Rapid Screening Studies. The goal of these experiments was to demonstrate the high efficiency of catalytic steam reforming as a method for conversion of bio-oil to hydrogen, with specific objectives to evaluate and select best catalysts and operating conditions, and to gain mechanistic insight into the chemistry involved in the steam reforming reactions of oxygenates. A series of model oxygen-containing compounds, biomass and its main components (cellulose, xylan, and lignin), and *bio-oil* and its various fractions were screened under identical conditions using a commercial catalyst, G-90C, from United Catalyst Inc. (UCI). We also tested a number of research and commercial steam reforming catalysts and a WGS catalyst and determined H_2 yields using four model compounds (methanol, acetic acid, an aqueous solution of hydroxyacetaldehyde, and a methanol solution of 4-allyl-2,6-dimethoxyphenol) under the same operating conditions. All of the catalysts tested were capable of reforming the model compounds and high conversions (>99%) were observed. The H_2 yields for all catalysts and model compounds were high, averaging 90% (±5%) of the stoichiometric. Within our experimental error limit, there is no clear indication of one catalyst being better than the others. Among the most important parameters for steam reforming are catalyst bed temperature(T), molar steam-to-carbon ratio (S/C), gas hourly space velocity ($G_{C_1}HSV$), and residence time (t, calculated from the void volume of the catalyst bed divided by the total flow rate of gases at the inlet of the reactor; void fraction = 0.4). Temperature was found to have the most profound effect on steam reforming reactions. Within experimental error limits, varying residence time from 0.04 to 0.15 s and increasing S/C from 4.5 to 7.5 showed no significant effects on the yield of hydrogen under the conditions of 600°C and GHSV (gas hourly space velocity, on C_1 basis) = 1680 h^{-1}; however, this affected the yield of CH_4.

From these rapid screening studies of various classes of model oxygenate compounds, we found that steam reforming of oxygenates generally involves a significant competition from the decomposition owing to thermally-induced cracking prior to entering the catalyst bed and the acid-catalyzed reactions at the acidic sites of the catalyst support. These competing thermal decomposition reactions may result in the formation of carbonaceous materials (coke), blocking the reactor and even deactivating the catalyst. This calls for special emphasis on how to feed bio-oil or its fractions into the reactor. However, a complete conversion of both the oxygenate feed and its decomposition products to hydrogen can be achieved with commercial Ni-based catalysts under reasonable operating conditions, if char formation prior to reaching the catalyst bed and coking on the catalyst can be eliminated, or at least controlled.

Bench-Scale Tests. Tests at the bench-scale level were conducted to obtain the global and elemental mass balances and the carbon-to-gas conversion, to quantify the distribution of gas products under conditions of complete conversion of the pyrolysis oil feedstock, and to study catalyst lifetime and regeneration. We used both model compounds (methanol, acetic acid, syringol and *m*-cresol, both separately and in mixtures) and real bio-oil (its aqueous fraction), and representative results are listed in Table 1. Profiles of the output gas composition are shown for the 3-component mixture in Figure 1 and for the poplar oil aqueous fraction in Figure 2. The following discussions are focused on the reforming of a 3-component mixture and a bio-oil aqueous fraction.

The three-component mixture contained 67% acetic acid, 16% *m*-cresol, and 16% syringol. Its composition was close to the proportions of the carbohydrate fraction and the lignin fraction in bio-oil. We observed *some coke deposits* on the top portion of the UCI G-90C catalyst bed. The overall mass balance (carbon, hydrogen, and oxygen) was 99% and the carbon conversion to gas was 96% (Table 1). The other catalyst tested for steam reforming of the 3-component mixture was the 46-series from ICI Katalco (46-1/46-4). This dual catalyst bed is used in commercial naphtha reforming plants to reduce coke formation and extend catalyst lifetime. It showed an excellent and steady performance *without any coke deposition* on the catalyst. The gas composition (Figure 1) remained constant throughout the whole run. The overall mass balance (including carbon, hydrogen, and oxygen) was 104%, and for carbon 105%, indicating that there may be a systematic error in our measurement. An excellent hydrogen yield of 86% was obtained, and the total hydrogen potential may be as high as 98% with a second water-gas shift reactor. These results confirm that both the UCI G-90C and especially the ICI 46-series catalysts can efficiently convert oxygenates to hydrogen.

Steam reforming of bio-oil or its fractions was found to be more difficult than that of model compounds. The main problem that needed to be solved was feeding the oil to the reactor. Bio-oil cannot be totally vaporized; significant amounts of residual solids are often formed that block the feeding line and the reactor. Thus, the simple injection system used for model compounds had to be modified to allow spraying bio-oil and its fractions in to the catalytic reactor without prior char formation.

A poplar oil generated in the NREL vortex reactor system was extracted using ethyl acetate (EA) and water (weight ratios of 1:1:1 for oil:EA:water). The resulting aqueous fraction (55% of the whole oil) contained 25% organics and 75% water. It was successfully fed to the reactor using a triple-nozzle spraying system with minimal accumulation of char in the reactor inlet. A large excess of steam (S/C = 20-30) was used, together with a high flow rate of nitrogen, to allow for proper oil dispersion and heat transfer required to maintain a sufficiently high temperature (>500°C) at the reactor entrance. A portion of water and other volatiles in the sprayed droplets evaporate during mixing with the superheated steam and the remaining will contact the catalyst surface directly. The ICI 46-series catalysts performed satisfactorily with no coke formation. We observed a stable gas production rate and composition throughout the whole 4-hour-long experiment (Figure 2).

The carbon conversion of the aqueous fraction to gas products was almost quantitative in both runs that used the same catalyst bed (Table 1). We observed similar levels of mass balances as in the experiments using model compounds: global 99%, carbon 105%, and hydrogen 97%. The methane concentration (with N_2 excluded) increased from 0.56% in the first run (2 h, t=0.03 s) to 2.2% in the second run (4 h, t=0.02 s), and both values were much higher than that (0.01%) obtained from the 3-component model compound mixture (17 h, t=0.09 s). This was likely caused by the shorter residence time forced by the large flow rate of steam and nitrogen used in the experiment.

Process Design and Preliminary Economics. In the process being evaluated, bio-oil generated from fluid bed pyrolysis of biomass will be refined through a separation step (using water and ethyl acetate) to recover an oxyaromatic coproduct which will be used as a phenolic substitute in resin formulations. The remaining aqueous fraction will be catalytically steam reformed to produce hydrogen, using a process based on that used for natural gas reforming. Because of the low sulfur content of biomass and bio-oil, a sulfur removal system is not likely to be required. Also, according to thermodynamic simulations and the screening results, a temperature reformer ramping up to 700°-750°C (which is lower than 825°-900°C required for reforming natural gas) will be needed. The ratio of steam to oil will be determined by experimental results and economic optimization; it will be in the 5 to 7 range, based on the literature and experimental data already obtained. Laboratory experiments will provide the basis for the choice of the most suitable catalyst and reactor configuration; the base case will use a fixed-bed catalytic reactor. A pressure swing adsorption unit will be used to purify the H_2 produced.

A feasibility analysis was performed on this process to determine if the process could have economic viability and specify areas where research will help to lower the production cost.[3] Both laboratory data and standard process data, where applicable, were used. Although this analysis is not of design quality, it does provide useful information on this research project before scale-up and commercialization. The capital investment of the pyrolysis plant was taken from Beckman and Graham.[4] Biomass was considered available at a cost of $25/dry tonne. A

15% internal rate of return was assumed for both the pyrolysis and reforming facilities. The phenolics substitute coproduct was assumed to be sold for $0.44/kg, a fraction of the selling price of phenol. Steam is produced through heat integration and is be sold as a by-product.

For our conceptual process, the cost of hydrogen has been estimated to be $7.70/GJ for the base case (production capacity: 35.5 tonne of hydrogen per day), falling within the range of the current selling price of H_2 in industry ($5-14/GJ). Several parameters (for instance, a lower cost for biomass) can lower this price to $3-5/GJ.[3] The process can also sustain large changes in coproduct selling price, capital cost, and hydrogen production capacity before the hydrogen becomes more expensive than current markets will allow.

CONCLUSIONS

Reforming biomass-derived oxygenates appears to be possible using available Ni-based catalysts. It involves both thermal decomposition of the labile oxygenates and the catalytic steam reforming of the starting material and its decomposition products. At least 80% of the theoretical maximum hydrogen yield has already been obtained. The excess steam can be reduced to achieve S/C on the order of 5-10, as in cases of natural gas and naphtha reforming, by modification of reactor design. Fast pyrolysis followed by reforming represents a credible alternative to gasification with the following advantages: no oxygen is needed; a co-product strategy is possible; a regionalized system of production units coupled to a central reformer offers greater flexibility. Low biomass costs are required to produce hydrogen economically since feedstock cost is a significant component of the production cost. Co-products from the pyrolysis oil favor the economics.

REFERENCES

1. Wang, D.; Montané, D.; Chornet, E. *Applied Catalysis A: General* **1996**, *143*, 245-270.
2. Chornet, E.; Wang, D.; Czernik, S.; Montané, D.; Mann, M. In *Proceedings of the 1996 U.S. DOE Hydrogen Program Review*. NREL/CP-430-21968, May 1-2, **1996**, Miami, Florida. pp 457-480.
3. Mann, M.; Spath, P.; Kadam, K. In *Proceedings of the 1996 U.S. DOE Hydrogen Program Review*. NREL/CP-430-21968, May 1-2, **1996**, Miami, Florida. pp 249-272.
4. Beckman, D. and Graham, R. In *Advances in Thermochemical Biomass Conversion*, (ed. A.V. Bridgwater) Blackie Academic & Professional, London, **1993**. pp. 1314-24.

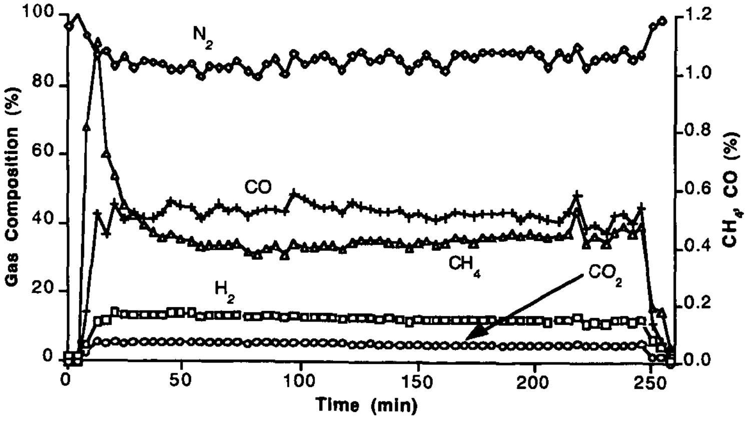

Figure 2. Composition of gaseous products during the steam reforming of a bio-oil aqueous fraction using the ICI 46-series catalyst.

Table 1. Summary of results for catalytic steam reforming experiments on the bench-scale reformer

Feed	Catalyst	S/C[a]	$G_{C_1}HSV$[b]	Temperatures (°C)			Yield (mol/100 mol of carbon fed)				% Carbon-gas conversion	% st. yield of H_2 (+WGS)[c]	Time on stream (h)
				Top	Middle	Bottom	H_2	CO_2	CO	CH_4			
acetic acid	UCI G-90C	4.7	1973	685	716	833	145.8	50.3	49.7	0.055	101	73 (98)	6
acetic acid	UCI G-90C	12.8	777	710	789	830	171.8	74.9	29.0	0.005	104	86 (100)	8
syringol (in MeOH)	UCI G-90C	6.3	2454	702	745	830	195.0	45.4	53.9	0.2	100	75 (96)	4
syringol (in MeOH)	UCI G-90C	7.4	1985	750	803	863	197.3	46.0	54.9	0.1	101	76 (97)	4
3-component mixture	UCI G-90C	6.5	1053	738	NA	833	167.6	67.4	28.6	0.00	96	78 (91)	11
3-component mixture	ICI 46-1/46-4	4.9	1053	782	753	834	187.8	79.8	27.4	0.03	105	86 (98)	17
poplar oil aq. fraction	ICI 46-1/46-4	19.3	1110	480	730	818	206.7	85.2	9.6	1.7	97	103 (108)	2
poplar oil aq. fraction	ICI 46-1/46-4	30.0	1000	530	744	821	205.8	86.6	8.4	6.9	102	103 (107)	4

[a] Molar ratio of steam to carbon. [b] Gas hourly space velocity on C_1 basis (h^{-1}). [c] Assuming all CO being converted to H_2 in a down stream WGS unit. NA = not available.

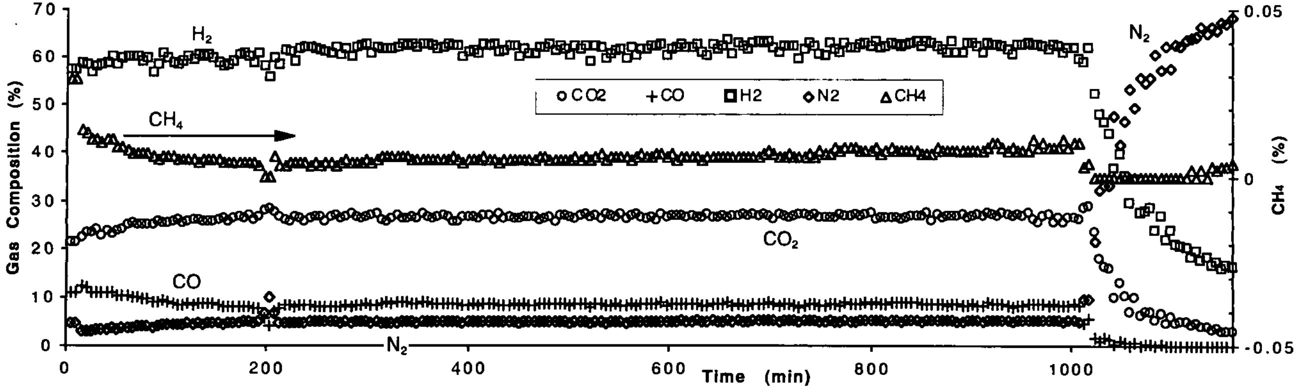

Figure 1. Composition of gaseous products during steam reforming of a 3-component mixture using the ICI 46-series catalyst.